

**UNIVERSITÄT
BAYREUTH**

Dissertation

Von der Universität Bayreuth
zur Erlangung des Grades eines
Doktors der Naturwissenschaften (Dr. rer. nat.)
genehmigte Abhandlung

**Enabling Tailored Nanostructure
Control in Organic Semiconductors
With Accelerated Nanostructural
Analysis**

von

Fabian Martin Eller
aus Ulm, Deutschland

1. Gutachter: Prof. Dr. Eva M. Herzig
2. Gutachter: Prof. Dr. Markus Lippitz
3. Gutachter: Prof. Dr. Carsten Deibel

Tag der Einreichung: 28.02.2025

Tag des Kolloquiums: 24.06.2025

English Abstract

Organic semiconductors are a continuously evolving class of semiconducting materials present in everyday life. The most common usage is in OLEDs (organic light-emitting diodes) as light emitters. Currently, they are state-of-the-art in display applications (smartphones, televisions, ...) as they enable the highest contrasts. While OLEDs are already available on the consumer mass market, other applications, e.g., OPV (organic photovoltaics) and OFETs (organic field-effect transistors), are in an earlier stage of their development. Several companies are already producing flexible and lightweight thin-film OPV devices for niche markets. Although OPV is still behind silicon solar cells in terms of power conversion efficiency (PCE) and technical maturity, it is also a much younger technology sector with a strong material development process that is still ongoing. In recent years, NFAs (non-fullerene acceptors) have led to rapid progress in the field, where laboratory records exceed 20 %, large-scale devices achieve 14.5 %, and new records are achieved yearly. Recent efforts are, therefore, targeting stability during processing and increasing the lifetime of the involved materials.

A key step in achieving record performances is controlling the nanostructure of the active layer, where the light is absorbed, exciton dissociation must take place, and charge must be transported to the electrodes. The active layer consists of blends of at least one electron acceptor and one electron donor material. The OPV performance critically depends on nanostructural parameters like phase separation, phase purity, molecular orientation, and the ordering of all components. Hence, it is important to understand the connections between nanostructure and performance.

To form a connection between the OPV performance and nanostructure, I contributed to joint projects with GIWAXS (grazing incidence wide-angle X-ray scattering) measurements and analysis (Chapters 11 and 13). GIWAXS is a valuable nanostructure characterization method that resolves the orientation, ordering, and packing distance of molecular stacking. I also identified the nanostructural reasons limiting solar cell performance in an industry collaboration with ASCA, the world market leader for organic photovoltaics with a production capacity of more than one million square meters per year. In a second step, I confirmed nanostructural improvements with GIWAXS when this problem was resolved (results from ASCA collaboration not included in this thesis due to confidentiality).

When thin films are characterized with further additional methods to GIWAXS and solar cell performance, the obtained picture of the nanostructure and structure-property relationships can be even more conclusive. Therefore, we characterized the impact of the chemical structure of the NFA, thermal annealing, solvent additives, different solvents, and molecular weight on the nanostructure, energetics, optical transitions, and thermal conductivity (Chapters 11–14). The chemical structure of the NFAs (Chapters 11 and 12) strongly impacts the nanostructure and performance of solar cells, underlining the importance of the material choice. Also, the addition of high boiling point solvents signif-

icantly affects the nanostructure and solar cell performance (Chapters 12 and 13). Some other parameters, such as the molecular weights of P3HT and the solvents in Chapter 14, hardly impact the nanostructure.

The work on influencing the nanostructure by parameter variations is highly valuable, but the achievable nanostructure changes are often limited and difficult to predict. Changes to the chemical structure often lead to strong nanostructural changes. However, no incremental nanostructural changes are possible as only discrete molecular structures exist, e.g., the sidechain length is not a continuously tunable variable. Hence, a method for tailored nanostructure control without material changes and achieving strong nanostructural changes is highly relevant.

Therefore, as the core part of my thesis, I developed a method for the pre-aggregation of P3HT solutions, namely current-induced doping (CID, Chapter 9). A strong electrical current through the solution induces this highly tunable solution aggregation. I demonstrated the range of tunability of the aggregate fraction and aggregate quality by a study of more than 600 different solutions treated with the CID treatment. Systematically screening an ample parameter space also enabled a deeper understanding of the underlying mechanisms.

The solution aggregation control directly transfers to thin film aggregation control (Chapter 10). To enable a high thin film aggregate quality, I chose the conditions of the CID treatment to yield exceptionally high backbone ordering of the pre-aggregates. The aggregate fraction of the solution then controls the thin film aggregate quality. This nanostructure control also directly leads to performance control for OFET devices. I achieved a 25-fold increase in OFET mobility in neat P3HT films (freely controllable by the solution aggregate fraction).

Blend thin films of P3HT with NFAs for OPV applications pose special nanostructural challenges. Due to the high miscibility between P3HT and most state-of-the-art Y-series NFAs, the phase separation is insufficient, leading to small, intermixed domains and poor molecular ordering. When the structure formation driven by phase separation is insufficient, the desired phase separation can sometimes also be achieved by aggregation. I followed this strategy by employing the CID treatment of P3HT for blends with the highly miscible NFA Y12 (Chapter 10). The CID treatment enables controlling the blend nanostructure from an intermixed disordered structure to a nanostructure with strong P3HT ordering. Additionally, Y12 nanostructure control can be achieved via solvent vapor annealing (SVA) post-treatment. Hence, combining the CID treatment and SVA enables a P3HT:Y12 nanostructure control between the boundaries of an intermixed disordered nanostructure and a highly ordered phase-separated nanostructure. This may be a key to overcoming the performance problems of P3HT:Y-series solar cells.

Extensive nanostructural characterization is the core of every part of this thesis described so far. However, this process is usually labor-intensive, slowing down scientific progress. For nanostructure optimizations, even several iterations are typically necessary. Hence, new hardware and software solutions are needed to accelerate nanostructural characterization and, thus, scientific progress. Therefore, I identified in the scope of the work on my thesis the bottlenecks in all involved workflows and optimized them (Chapter 3). In most cases, I could resolve the bottlenecks by automating the data acquisition and analysis process and minor modifications in the measurement procedures. In the example of

in-situ UV-Vis absorption spectroscopy during blade coating (Section 3.2), I adjusted the measurement procedure to capture dark and reference measurements along the drying automatically. A fully automated extraction of relevant spectra for the drying process and a complete data analysis give feedback on the coated film within seconds. This enables a direct feedback loop for the following processed sample, speeding up scientific progress. For GIWAXS measurements and analysis, I chose a similar approach (Section 3.3).

However, efficient UV-Vis absorption spectroscopy of strongly absorbing solutions, necessary for the ample parameter studies on the CID treatment in solution (Chapter 9), required a completely new measurement concept. Hence, I developed the Thinning Fluid Film Spectroscopy (TFFS) method, verified its validity and investigated its advantages and limitations (Chapter 8 and Section 3.1). In the TFFS method, the absorption spectra of strongly absorbing solutions can be measured through thin fluid films flowing down the measurement container walls. No dilution of the solutions is necessary, and a fully automated measurement and data analysis procedure is possible. I applied the TFFS method in my research not only to organic semiconductors but also to perovskite precursor solutions (Chapter 15). In this case, the concentration of the solutions changes their absorption spectra significantly. Hence, dilution is no option, and the previously inaccessible experimental possibilities that TFFS now enables are required.

Deutsche Zusammenfassung

Organische Halbleiter sind eine sich ständig weiterentwickelnde Klasse von Halbleitermaterialien, die auch rege Verwendung in unserem täglichen Leben findet. Am häufigsten werden sie in OLEDs (organische Leuchtdioden) als Lichtemitter verwendet. Zurzeit sind sie bei Bildschirmen (Smartphones, Fernsehgeräte, ...) der Stand der Technik, da sie die höchsten Kontraste ermöglichen. Während OLEDs bereits auf dem Massenmarkt für Endverbraucher erhältlich sind, befinden sich andere Anwendungen, z.B. OPV (organische Photovoltaik) und OFETs (organische Feldeffekttransistoren), in einem früheren Entwicklungsstadium. Mehrere Unternehmen stellen bereits flexible und leichte organische Solarzellen für Nischenmärkte her. Auch wenn OPV in Bezug auf den Wirkungsgrad und die technische Reife noch hinter Silizium-Solarzellen zurückliegt, muss berücksichtigt werden, dass es sich um einen sehr viel jüngeren Technologiesektor mit einem starken Materialentwicklungsprozess handelt, der noch nicht abgeschlossen ist. In den letzten Jahren haben in diesem Feld NFAs (Nicht-Fulleren-Akzeptoren) zu einem rasanten Fortschritt geführt. Laborrekorde übertreffen bereits 20 % Wirkungsgrad, großflächige Module erreichen bereits 14,5 % und jedes Jahr werden neue Rekorde aufgestellt. Die jüngsten Bemühungen zielen daher auf die Stabilität während der Verarbeitung und die Verlängerung der Lebensdauer der betreffenden Materialien ab.

Ein entscheidender Schritt zur Erzielung von Rekordleistungen ist die Kontrolle der Nanostruktur der aktiven Schicht, in der das Licht absorbiert wird, die Dissoziation von Exzitonen stattfinden muss und die Ladungen zu den Elektroden transportiert werden müssen. Die aktive Schicht besteht aus Mischungen von mindestens einem Elektronenakzeptor- und einem Elektronendonatormaterial. Die OPV-Leistung hängt entscheidend von nanostrukturellen Parametern wie Phasenseparation, Phasenreinheit, molekularer Orientierung und der Ordnung aller Komponenten ab. Daher ist es bedeutend, die Zusammenhänge zwischen Nanostruktur und Leistung zu verstehen.

Um eine Verbindung zwischen der OPV-Leistung und der Nanostruktur herzustellen, habe ich zu Kollaborationsprojekten mit GIWAXS (grazing incidence wide-angle X-ray scattering) Messungen beigetragen (Kapitel 11 und 13). GIWAXS ist eine wertvolle Methode zur Charakterisierung von Nanostrukturen, mit der die Orientierung, die Ordnung und der Abstand von molekularen Anordnungen bestimmt werden können. In einer Industriekooperation mit ASCA, dem Weltmarktführer für organische Photovoltaik mit einer Produktionskapazität von mehr als einer Million Quadratmetern pro Jahr, konnte ich auch die nanostrukturellen Gründe identifizieren, die die Leistung von Solarzellen einschränken. Als dieses Problem gelöst war, bestätigte ich mit GIWAXS in einem zweiten Schritt die nanostrukturellen Verbesserungen (die Ergebnisse aus der Zusammenarbeit mit ASCA sind aus Gründen der Vertraulichkeit nicht in dieser Arbeit enthalten). Wenn Dünnschichten mit weiteren zusätzlichen Methoden zu GIWAXS und Solarzellenleistung charakterisiert werden, kann das erhaltene Bild der Nanostruktur und der Beziehungen zwischen Nanostruktur und Funktionalität noch aussagekräftiger werden. Daher

haben wir die Auswirkungen der chemischen Struktur der NFAs, des thermischen Temperns, der Lösungsmittelzusätze, verschiedener Lösungsmittel und des Molekulargewichts auf die Nanostruktur, die Energetik, die optischen Übergänge und die Wärmeleitfähigkeit untersucht (Kapitel 11–14). Die chemische Struktur der NFAs (Kapitel 11 und 12) wirkt sich stark auf die Nanostruktur und die Leistung von Solarzellen aus, was die Bedeutung der Materialauswahl unterstreicht. Auch die Zugabe von Lösungsmitteln mit hohem Siedepunkt beeinflusst die Nanostruktur und die Leistung der Solarzellen erheblich (Kapitel 12 und 13). Einige andere Parameter, wie die Molekulargewichte von P3HT und die Lösungsmittel in Kapitel 14, haben hingegen kaum Auswirkungen auf die Nanostruktur.

Die Arbeit zur Beeinflussung der Nanostruktur durch Parametervariationen ist sehr wertvoll, aber die erreichbaren Nanostrukturänderungen sind oft begrenzt und schwer vorherzusagen. Änderungen der chemischen Struktur führen oft zu starken nanostrukturellen Veränderungen. Jedoch sind keine inkrementellen Nanostruktur Änderungen möglich, da nur diskrete molekulare Strukturen möglich sind, z.B. ist die Seitenkettenlänge nicht kontinuierlich veränderlich. Daher ist eine Methode zur zielgerichteten Kontrolle von Nanostrukturen, die keine Materialveränderungen benötigt und starke nanostrukturelle Veränderungen erzielt, von großer Bedeutung.

Als Kernstück meiner Dissertation habe ich daher eine Methode für die Voraggregation von P3HT-Lösungen entwickelt, nämlich current-induced doping (CID, Kapitel 9). Ein starker elektrischer Strom durch die Lösung induziert diese hochgradig kontrollierbare Lösungsaggregation. Ich habe die Reichweite der Kontrolle des Aggregatanteils und der Aggregatqualität anhand einer Studie von mehr als 600 verschiedenen Lösungen, die mit der CID-Behandlung behandelt wurden, demonstriert. Das systematische Screening eines großen Parameterraums ermöglichte auch ein tieferes Verständnis der zugrunde liegenden Mechanismen.

Die Kontrolle der Lösungsaggregation lässt sich direkt auf die Kontrolle der Aggregation einer aus diesen Lösungen hergestellten Dünnschicht übertragen (Kapitel 10). Um eine hohe Qualität der Dünnschichtaggregate zu erreichen, habe ich die Bedingungen der CID-Behandlung so gewählt, dass eine außergewöhnlich hohe Rückgratordnung der Voraggregate erreicht wird. Der Aggregatanteil der Lösung bestimmt dann die Qualität der Dünnschichtaggregate. Diese Kontrolle der Nanostruktur führt auch direkt zur Kontrolle der Leistung von OFET-Bauelementen. So konnte ich eine 25-fache Steigerung der OFET-Mobilität in reinen P3HT-Filmen erreichen (frei kontrollierbar durch den Aggregatanteil der Lösung).

Dünnschichten aus Mischungen von P3HT mit NFAs für OPV-Anwendungen stellen besondere nanostrukturelle Herausforderungen dar. Aufgrund der hohen Mischbarkeit zwischen P3HT und den meisten modernen NFAs der Y-Reihe ist die Phasenseparation unzureichend, was zu kleinen, gemischten Domänen und schlechter molekularer Ordnung führt. Wenn die Strukturbildung durch Phasenseparation unzureichend ist, kann die Phasenseparation teils auch durch Aggregation erreicht werden. Ich habe diese Strategie verfolgt, indem ich die CID-Behandlung von P3HT für Mischungen mit dem gut mischbaren NFA Y12 (Kapitel 10) eingesetzt habe. Die CID-Behandlung ermöglicht es, die Nanostruktur von einer durchmischten ungeordneten Struktur bis hin zu einer Nanostruktur mit starker P3HT-Ordnung zu kontrollieren. Darüber hinaus kann die Y12-Nanostruktur durch eine Nachbehandlung mit Lösungsmitteldampf (SVA) kontrol-

liert werden. Die Kombination von CID-Behandlung und SVA ermöglicht also eine Kontrolle der P3HT:Y12-Nanostruktur zwischen den Grenzen einer gemischten ungeordneten Nanostruktur und einer hochgradig geordneten, phasenetrennten Nanostruktur. Dies könnte ein Schlüssel zur Überwindung der Leistungsprobleme von Solarzellen aus P3HT und NFAs der Y-Serie sein.

Eine umfassende Charakterisierung von Nanostrukturen ist der Kern jedes bisher beschriebenen Teils dieser Dissertation. Jedoch ist dieser Prozess in der Regel sehr arbeitsintensiv und verlangsamt den wissenschaftlichen Fortschritt. Für die Optimierung von Nanostrukturen sind in der Regel sogar mehrere Iterationen erforderlich. Daher werden neuartige Hardware- und Softwarelösungen benötigt, um die Charakterisierung von Nanostrukturen und damit den wissenschaftlichen Fortschritt zu beschleunigen. Daher habe ich im Rahmen der Arbeit an meiner Dissertation die Engstellen in allen beteiligten Arbeitsabläufen identifiziert und optimiert (Kapitel 3). In den meisten Fällen konnte ich die Engstellen durch die Automatisierung der Datenerfassung und -auswertung sowie durch geringfügige Modifikationen der Messverfahren beheben. Im Beispiel der In-situ UV-Vis-Absorptionsspektroskopie während des blade coatings (Abschnitt 3.2) habe ich das Messverfahren so angepasst, dass Dunkel- und Referenzmessungen während der Trocknung automatisch erfasst werden. Eine vollautomatische Extraktion der für den Trocknungsprozess relevanten Spektren und eine vollständige Datenanalyse geben innerhalb von Sekunden Rückmeldung über den entstandenen Dünnsfilm. Dies ermöglicht eine direkte Rückkopplungsschleife für die nachfolgend prozessierte Probe und beschleunigt den wissenschaftlichen Fortschritt. Für die GIWAXS-Messungen und -Auswertung habe ich einen ähnlichen Ansatz gewählt (Abschnitt 3.3).

Effiziente UV-Vis-Absorptionsspektroskopie von stark absorbierenden Lösungen, die für die umfangreichen Parameterstudien zur CID-Behandlung in Lösung (Kapitel 9) notwendig ist, erforderte jedoch ein völlig neues Messkonzept. Daher habe ich die Methode der Thinning Fluid Film Spectroscopy (TFFS) entwickelt, ihre Gültigkeit überprüft und ihre Vorteile sowie Grenzen untersucht (Kapitel 8 und Abschnitt 3.1). Bei der TFFS-Methode können die Absorptionsspektren stark absorbierender Lösungen durch dünne Flüssigkeitsfilme gemessen werden, die an den Wänden des Messbehälters herunterfließen. Es ist keine Verdünnung der Lösungen erforderlich, und ein vollautomatisches Mess- und Datenanalyseverfahren ist möglich. Ich habe die TFFS-Methode in meiner Forschung nicht nur auf organische Halbleiter, sondern auch auf Perowskit-Precursor Lösungen angewendet (Kapitel 15). In diesem Fall verändert die Konzentration der Lösungen deren Absorptionsspektren erheblich. Daher ist eine Verdünnung keine Option, und die bisher unzugänglichen experimentellen Möglichkeiten, die TFFS nun bietet, sind erforderlich.

Contents

English Abstract	i
Deutsche Zusammenfassung	v
1 Introduction	1
2 Background	5
2.1 Factors Influencing Nanostructure in Solution-Processed Organic Semiconductors	5
2.1.1 Molecular Design	5
2.1.2 Solution Pre-aggregation	8
2.1.3 Processing Solvent & Additives	8
2.1.4 Coating Method	10
2.1.5 Post-deposition Treatments	11
2.2 GIWAXS of Organic Semiconductors	12
2.2.1 GIWAXS Scattering Principle	12
2.2.2 GIWAXS Applied to Organic Semiconductors	15
2.2.3 Modeling of GIWAXS Cake Cuts	17
2.3 UV-Vis Absorption Spectroscopy of Organic Semiconductors	20
2.3.1 Absorption Spectroscopy	20
2.3.2 Absorption Spectra of Organic Semiconductors	21
3 Acceleration Approach	27
3.1 Absorption Spectroscopy of Strongly Absorbing Solutions	28
3.2 In-Situ Absorption Spectroscopy	29
3.2.1 Automated In-Situ Measurements During Blade Coating	29
3.2.2 Automated Extraction of Relevant Spectra	31
3.2.3 Additional Automated Data Analysis	33
3.2.4 Automated In-Situ Characterization During Solvent Vapor Annealing	34
3.3 Accelerated GIWAXS Routine	35
3.3.1 Automated Sample Alignment Procedure	35
3.3.2 Automated Measurement Procedure	38
3.3.3 Automated Pre-analysis	40
3.3.4 Standardized Automated Material-Specific Analysis	42
4 Thesis Summary	45
4.1 Overview of Thesis Structure	45
4.2 Individual Publications	47
5 Conclusion and Outlook	51

6	Authors' Contributions	55
7	References	59
8	Facilitating Absorption Spectroscopy of Strongly Absorbing Fluids: A High-Throughput Approach	79
9	Spark Discharge Doping – Achieving Unprecedented Control over Aggregate Fraction and Backbone Ordering in Poly(3-hexylthiophene) Solutions	95
10	Tackling P3HT:Y-Series Miscibility Through Advanced Processing for Tunable Aggregation	115
11	Understanding the Role of Order in Y-Series Non-Fullerene Solar Cells to Realize High Open-Circuit Voltages	141
12	Identifying the Signatures of Intermolecular Interactions in Blends of PM6 with Y6 and N4 Using Absorption Spectroscopy	175
13	Effects of the diphenyl ether additive in halogen-free processed non-fullerene acceptor organic solar cells	207
14	Microstructural and Thermal Transport Properties of Regioregular Poly(3-hexylthiophene-2,5-diyl) Thin Films	233
15	Solvated PbI_2 Clusters preceding the Crystallization of Lead Halide Perovskites – a UV/VIS In-Situ Study	251
A.	List of Abbreviations	289
B.	Danksagung	291
C.	Eidesstattliche Versicherung	293

1 Introduction

Organic semiconductors are a versatile material class with various applications like displays, photovoltaics, and transistors. OLED (organic light-emitting diode) displays are currently state of the art in many devices, such as televisions and smartphones. OPV (organic photovoltaics) is also already commercially available, however still in niche markets. Companies like Heliatek and ASCA (formerly ARMOR) are marketing their organic solar cells mainly for facades or other architectonic solutions. As seen in Figure 1.1 (a)–(b), the possibility of fabricating solar cells in different colors, opacities, and shapes on flexible substrates enables unique energy harvesting design elements. Epishine chose another strategy and works in the niche field of indoor photovoltaics (see Figure 1.1 (c)–(d)).

While the OPV power conversion efficiency (PCE) with fullerene acceptors stagnated at about 12%, the introduction of non-fullerene acceptors (NFAs) boosted the field.^{6, 7} After continuous improvements exceeding 19%, recently, even the magic mark of 20% was surpassed by binary single-junction OPV.^{1, 8, 9} Ternary single-junction OPV surpassed 19% already in 2022 (non-certified in 2021) and recently also 20%.^{9–18} The decisive improvements leading to the record-breaking binary solar cells were mainly achieved by carefully optimizing the nanostructure.¹

In the active layer of OPV, a donor and an acceptor material are required. An exciton (bound electron-hole pair) is formed upon light absorption in the donor or the acceptor.¹⁹ For optimized light harvesting, strong absorption in a broad spectral range is necessary, which depends on the molecular structure but is also influenced by the nanostructure. That subsequently an exciton dissociation (separation of electron-hole pair) can occur, the exciton has to travel to the donor-acceptor interface. Due to a limited exciton dissociation length of about 10 nm in disordered organic semiconductors, the donor-acceptor phase separation must not be too coarse.¹⁹ After the exciton dissociation, the separated electron and hole must travel to the corresponding electrodes. Therefore, an efficient charge transport through a continuous network of the donor and acceptor phase to the corresponding electrode is required.¹⁹ Hence, absorption, exciton dissociation, and charge transport to the electrodes of an organic solar cell heavily depend on the nanostructure of the active layer, making it a decisive key factor.^{7, 20, 21}

Fulfilling the requirements in the different steps in the active layer (absorption, exciton dissociation, charge transport to the electrodes) poses a great challenge, as optimizing one requirement is prone to negatively impacting others. A strong intermixing of donor and acceptor is beneficial for the exciton separation but can be detrimental for the charge extraction as insufficient continuous percolation pathways exist.^{19, 22, 23} Such a strong intermixing occurs, e.g., when the miscibility between the acceptor and the donor is high, like in the case of P3HT blended with many Y-series NFAs.^{24–26} On the other side, large, highly ordered aggregates or crystallites can enable efficient charge transport to the electrodes, but the exciton dissociation suffers.^{19, 27, 28}



Figure 1.1: (a) Photograph of an energy-generating shade sail in the shape of the African continent made from OPV modules produced by ASCA and installed at the "Peace and Security" Building of the African Union. (b) Photograph of an artificial banana tree with 12 blue semi-transparent OPV modules as leaf imitations produced by ASCA. (c) Photograph of a remote control covered with indoor OPV produced by Epishine. (d) Advertising material of a CO₂ monitor powered by indoor OPV from Epishine. (e) Schematic sketch of a suitable OPV nanostructure. (a) Reprinted with personal permission from ASCA.² (b) Modified with personal permission from ASCA.³ (c) Modified with personal permission from Epishine.⁴ (d) Reprinted with personal permission from Epishine.⁵ (e) Reprinted from Zhu et. al.¹ Copyright 2024, with permission from Elsevier.

In the publication breaking the 20 % PCE, an approach combining controlled aggregation by using additives and a two-step layer-by-layer coating process enabled a hierarchical balanced nanostructure.¹ A sketch of the nanostructure from this publication is displayed in Figure 1.1 (e). In the finely structured mixing domain, an efficient exciton dissociation takes place. Due to the vertical phase separation and the interconnectivity between the donor and acceptor in the mixing domain with the corresponding highly ordered material in the pure fibrils, efficient charge carrier transport is also possible.¹ This work and many others impressively demonstrate the nanostructure's importance on OPV performance.

Hence, it is highly valuable to characterize the nanostructure and compare the nanostructural insights with insights from other characterization techniques to understand the structure-function relationship. Chapters 11–14 combine the expertise in our group on nanostructure characterization via GIWAXS (grazing incidence wide-angle X-ray scattering) with the expertise of other groups in complementary characterization techniques to jointly achieve this common goal. In the research conducted in this part of the thesis (Chapters 11–14), we pointed out the decisive impact of the chemical structure of the molecules in the active layer on the nanostructure, energetics, optical properties, and

performance. However, other factors, such as thermal annealing and solvent additives, also had a significant impact on these properties.^{29–32}

These insights on the influence factors on nanostructure and other relevant parameters resemble major parts of the research field on OPV. Chemical engineering (e.g., by introducing and further developing NFAs) enables major leaps in nanostructure and device performance and sets the general framework. Within this framework, changes in many processing aspects can lead to significant changes in the nanostructure and performance. Thus, the optimization of the nanostructure is usually a tedious trial-and-error process. Other applications like OFETs (organic field-effect transistors) rely to a similar extent on the nanostructure but differ in their specific requirements for an optimized nanostructure and require an independent nanostructure optimization.³³

Therefore, the ultimate goal of this thesis is to enable a tailored nanostructure control of organic semiconductors, efficiently achieving a wide variety of nanostructures. The intended nanostructure control should rely on processing alone without varying the molecular structure. The variety of nanostructures produced can be used in follow-up research, either for fundamental studies or as a starting point and tool for device optimization.

I achieved this strong nanostructure control mainly through the CID (current-induced doping) solution treatment of P3HT, which I introduce in Chapter 9.³⁴ It enables the control of the aggregate fraction and aggregate quality in solution. This study relies on the analysis of a large number of absorption spectra, which were acquired by the novel TFFS (Thinning Fluid Film Spectroscopy) method from Chapter 8.³⁵ The TFFS method allows measuring the absorption spectra of strongly absorbing solutions highly efficiently, where also full automation is realized in Chapter 8. In Chapter 15, the TFFS method is also used to measure highly concentrated perovskite precursor solutions, demonstrating its broad applicability.

Processing thin films from CID-treated solutions enables, in Chapter 10, a very tailored nanostructure control in neat P3HT films and blends with Y12.³⁶ In neat P3HT films, a 25-fold increase in OFET mobility can be achieved, while in P3HT:Y12 blends, the miscibility problem can be tackled by an approach combining the CID treatment with an SVA (solvent vapor annealing) post-treatment. Hence, the achievements of a highly tailored nanostructure control in neat and especially blend films covering a large range from highly disordered intermixed films to highly ordered films even exceed my initial goal.

The following chapter (Chapter 2) discusses the background with special relevance to this thesis. It includes an overview of factors influencing the nanostructure of organic semiconductors, as well as the two most important characterization techniques in this thesis, UV-Vis absorption spectroscopy, and GIWAXS. The acceleration approach in Chapter 3 summarizes significant advances I made during the work on my PhD thesis to accelerate nanostructure characterization. This highly increased efficiency in conducting and evaluating nanostructure measurement was crucial to exceeding my initial goals and paves the way for further highly efficient research. Chapter 4 summarizes in more detail the content of the individual publications. Finally, Chapter 5 concludes the work done in this thesis and offers an outlook for the future.

The individual contributions from all co-authors to all publications are given in Chapter 6. In Chapters 8–10, the publications of my core topics (TFFS method, solution and thin

film aggregation control via CID treatment and SVA) are reprinted, while in Chapters 11–15, the further publications of this thesis are reprinted.

2 Background

This thesis aims to obtain nanostructural control of organic semiconductors. Hence, it is highly relevant to be aware of factors in the solution-processing of organic semiconductors that are known from literature to influence the nanostructure of thin films. This knowledge on influence factors can also be used as background and framework for developing a new method to control the nanostructure actively. Therefore, in the first part of this Chapter (Section 2.1), the influence of the relevant factors on the nanostructure in solution-processed organic semiconductors is summarized.

The two further sections in this Chapter explain the fundamentals of the two most important nanostructure characterization techniques used in this thesis, GIWAXS (Section 2.2) and UV-Vis absorption spectroscopy (Section 2.3). Both sections start with the theory behind the techniques and continue with explicit information on applying these techniques to the material systems used in this thesis. Hence, this is the basis for all interpretations of the GIWAXS and UV-Vis absorption spectroscopy data in this thesis.

2.1 Factors Influencing Nanostructure in Solution-Processed Organic Semiconductors

Solution-processing organic semiconductors offers several possibilities to influence the nanostructures of the produced thin films. Due to the importance of the nanostructure for devices, much work has been done on the impact of various aspects of the processing on the nanostructure of the final films. This section leads through the relevant points of solution-processing and summarizes the effect each aspect has on the nanostructure. The section starts with selecting the molecules used in the active layer (2.1.1). Thin films are produced from solutions of these molecules. Therefore, the next relevant aspects discussed are the impact of possible pre-aggregation of the molecules in the solution (2.1.2) and the selection of the solvent and solvent additives (2.1.3). The coating method is briefly thematized (2.1.4) before finally turning to post-deposition treatments (2.1.5). This section focuses on aspects with special relevance to this thesis, while others are kept short or are just mentioned.

2.1.1 Molecular Design

The molecular design of the organic semiconductors has a decisive impact on their nanostructure. The first paragraph discusses the influence of the molecular structure of NFAs on their nanostructure. In the following paragraphs, also polymers and blends between two materials are discussed.

Even slightly different alkyl sidechains without any changes to functional groups of the NFAs can lead to substantial changes in the molecular stacking behavior (see also Chapters 11 and 12).^{28–30, 37, 38} One example is DTY6, where the only difference to Y6 is the elongated alkyl chains adding a significant steric hindrance and improving the solubility, two important points reducing the aggregation.²⁸ Changing functional groups, e.g., by changing the fluorination of Y6 to chlorination in Y7, can also substantially impact the nanostructure. However, other aspects, such as energy levels, also change significantly.³⁹ Since we only want to cover nanostructural aspects, these changes in the functional groups are beyond the scope of this work and, therefore, not discussed here.

In the case of polymers, in addition to the molecular design of the monomers, molecular weight is also a decisive aspect, especially for aggregation. With increasing molecular weight, aggregation is enhanced.^{40–42} In some cases, regioregularity is a decisive aspect for aggregation. This is prominently the case for P3HT, which is also used in this thesis. Regioregularity characterizes the percentage of monomers with a head-to-tail attachment of the sidechains at the thiophene unit rather than head-to-head. In a perfectly regioregular polymer, all sidechains adopt the head-to-tail configuration, while the configurations of the sidechains are random in a regiorandom polymer.^{33, 43–45} Regioregular polymers can usually aggregate very well, but their regiorandom counterparts possess a significantly reduced aggregation behavior.^{33, 43, 46–49} Similarly to NFAs, the sidechain and backbone design lead to nanostructural changes, while the backbone design also decisively controls the electronic properties.^{43, 50–52}

Since one of the main applications of organic semiconductors is OPV, the nanostructure in blends of electron donors and acceptors is also highly relevant. The relationship between the chemical structure of NFAs and polymers and their nanostructure discussed so far also remains important in blends. However, also the miscibility between the different materials in the blend must be considered. Therefore, one of the most decisive parameters for nanostructure formation is the Flory-Huggins interaction parameter χ_{12} between the components, which determines their miscibility. χ_{12} is decisive for the Gibbs free energy change ΔG_{mix} upon mixing materials 1 and 2.^{55, 56}

$$\Delta G_{mix} = RTn_{tot} \left[\frac{\Phi_1}{N_1} \ln \Phi_1 + \frac{\Phi_2}{N_2} \ln \Phi_2 + \Phi_1 \Phi_2 \chi_{12} \right] \quad (2.1)$$

R is the gas constant, T the absolute temperature, and Φ_1 and Φ_2 are the volume fractions of materials 1 and 2. N_1 and N_2 are the effective molecular sizes of the materials in reference units and n_{tot} is the total molar number of reference units. χ_{12} between two materials can be tuned by molecular engineering. An example of several NFAs blended with the polythiophene PDCBT-Cl is displayed in Figure 2.1 (a). The curves in Figure 2.1 (b) are the binodals which vary slightly with the molecular weight of the acceptor. The binodal is determined by the local minima of ΔG_{mix} in equation 2.1.⁵⁵ Below the binodal, a completely intermixed single phase is stable. Above the binodal, the intermixed phase is metastable or unstable. Whether the intermixed phase is metastable or unstable depends if it is below or above the spinodal (not sketched in Figure 2.1 (b)).⁵⁵ In the unstable case above the spinodal, spinodal decomposition leads to liquid-liquid demixing, as sketched in the upper branch of Figure 2.1 (c).⁵⁴ Here, a phase separation of the solubilized molecules toward the binodal occurs (indicated by arrows in Figure 2.1 (b)). In the thermodynamic equilibrium, the mixing ratios are determined by the binodal,

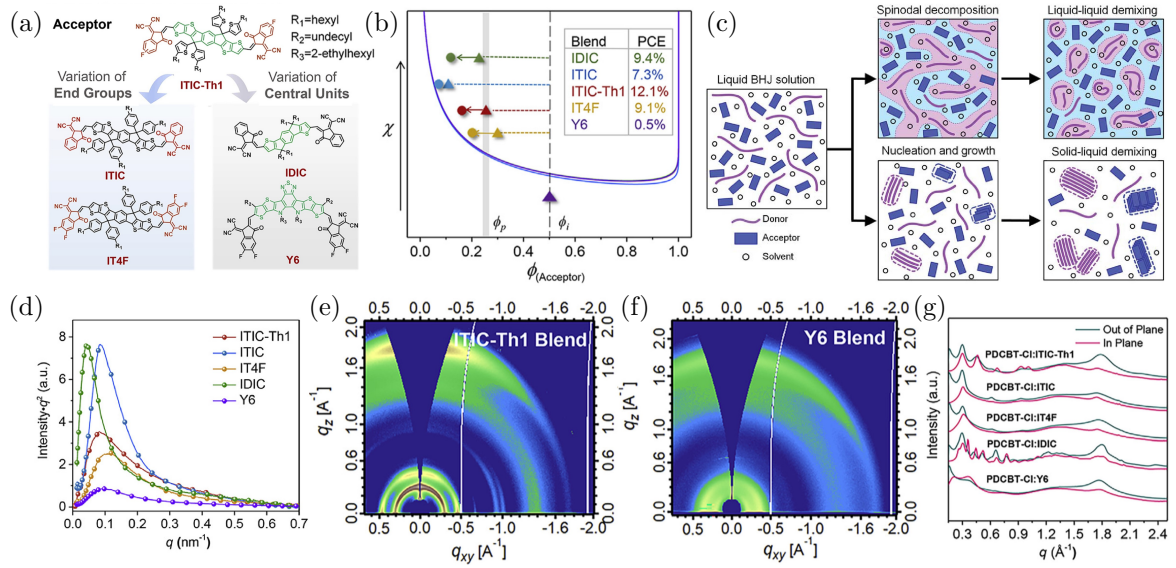


Figure 2.1: (a) Chemical structures of the five representative NFAs with a variation of end groups (ITIC, ITIC-Th1, and IT4F) and of the central units (ITIC-Th1, IDIC, and Y6) blended with the polythiophene derivative PDCBT-Cl. (b) Schematic illustration of the amorphous phase diagram based on PDCBT-Cl:NFA blends in relation to the electron transport percolation threshold (gray shadowed area). Triangles and dots represent the states in optimized devices and long-time annealed devices, respectively. The solid lines are binodals for different NFA molecular weights. (c) Scheme describing the possible paths of phase separation evolution from liquid blend solutions. (d) 1D thickness and absorption normalized RSoXS profiles of the blends processed with optimized annealing time acquired at 283.2 eV. (e) 2D GIWAXS measurement of PDCBT-Cl:ITIC-Th1 blend, and (f) of PDCBT-Cl:Y6 blend. (g) Comparison of 1D out-of-plane and in-plane profiles extracted from the 2D GIWAXS measurements of all tested blends. (a)–(b) and (d)–(g) adapted from Liang et. al.⁵³ Copyright 2020, with permission from Elsevier. (c) Adapted with permission from Yoon et. al.⁵⁴ Copyright 2022 The Royal Society of Chemistry.

leading to an almost pure NFA domain and a less pure polymer domain.⁵³ Hence, when χ is high, a strong phase separation of the components into relatively pure domains occurs, like for PDCBT-Cl with IDIC or ITIC in Figure 2.1 (b).^{53, 57} If χ is below the binodal, like for PDCBT-Cl blended with Y6, the blend is stable, remains intermixed, and no phase separation occurs. This can also be seen from the RSoXS (resonant soft X-ray scattering) measurements in Figure 2.1 (d).^{53, 57} In the intermixed phase aggregation is also suppressed, as seen by the reduced nanostructure in the GIWAXS measurements of the Y6-blend in comparison to the other blends in Figure 2.1 (e)–(g).^{53, 57} This is also the case with blends of P3HT and several Y-series NFAs.^{24–26} Chemical modifications to one of the components in the blend can increase the Flory-Huggins interaction parameter χ and thus decrease the miscibility, which already has been done on the polythiophene side as well as on the Y-series side.^{24–26, 57–61} Thus, the degree of phase separation can be effectively influenced by the interaction between the components, but only in discrete steps due to different chemical structures.

Apart from liquid-liquid demixing by spinodal decomposition, phase separation can also occur via solidification that induces solid-liquid demixing (lower branch in Figure 2.1 (c)).^{54–56, 62} When one of the components reaches its solubility limit, it aggregates. Nucleation and crystal growth lead to extended relatively pure solid domains of the aggregating component, phase separated from the remaining liquid solution.⁵⁴ Hence, an insufficient spinodal decomposition can be compensated by enhancing aggregation (see Chapter 10). Depending on the miscibility of the materials and the conditions triggering aggregation, either one of the two mechanisms dominates, or both demixing mechanisms occur simultaneously.^{54–56, 62}

2.1.2 Solution Pre-aggregation

Apart from the solutes' molecular structure, the aggregation state in solution also plays a decisive role in the final thin film morphology after coating. Instead of a fully dissolved state, polymers and small molecule acceptors can already form aggregates or clusters of several molecules in the solution. When thin films are coated from these pre-aggregated solutions, there is already some degree of phase separation of ordered molecules before the drying process starts. Thus, pre-aggregates can serve as valuable nuclei to achieve further aggregation and phase separation during the drying process.^{7, 57, 63, 64} Some polymers can even form nanowires under certain conditions in solution, a special form of pre-aggregation. These nanowires often have a diameter of just a few nanometers but a length in the micrometer range.^{20, 65, 66} Coating films from these highly conductive nanowires can yield interpenetrating networks, enabling efficient hole transport without excessive phase separation.^{20, 65–67}

There are several approaches to pre-aggregate solutions. The most common approach is aging initially fully dissolved but metastable solutions. A slow nucleation and growth mechanism leads to pre-aggregation. On the one hand, the pre-aggregation can be tuned by controlling the solubility. Changing the solvent composition and temperature are suitable methods to tune the solubility.^{7, 57, 63, 68–70} On the other hand, the aging time is a further parameter influencing the pre-aggregation. The pre-aggregation usually slowly increases with time, as in the example of P3HT:TrBTIC in Figure 2.2.^{64, 70}

An additional possibility to induce pre-aggregation in solution is to add dopants.^{71–75} The solubility of the doped polymers is reduced in the unpolar solvents being used, which can lead to aggregation.^{72, 73, 75} This controlled way of achieving highly ordered aggregates also has the downside that the dopant remains in the thin film after drying. As an alternative to doping-induced aggregation involving the addition of dopants, I developed the current-induced doping (CID) treatment, where the doping is achieved by a strong electrical current through the solution without the usage of any additives. This is the core of this thesis and is presented in detail in Chapters 9 and 10.

2.1.3 Processing Solvent & Additives

The processing solvent impacts the nanostructure formation on multiple levels during the thin film drying. The evaporation rate, which is determined by the vapor pressure of the solvent at the processing temperature, determines the drying time and, hence, the time available for phase separation and aggregation. Therefore, processing from higher boiling point solvents can lead to larger aggregates and surface roughness than

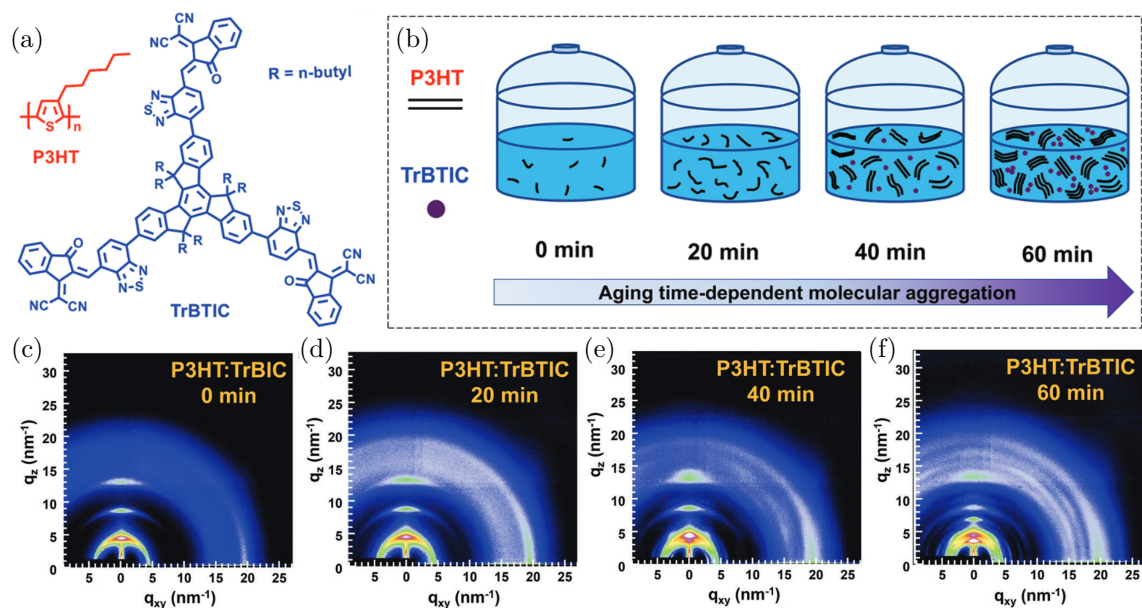


Figure 2.2: (a) Chemical structures of P3HT and TrBTIC (b) Schematic illustration of the P3HT:TrBTIC aggregation stage in TMB in dependency of the aging time. (c) 2D GIWAXS measurements of P3HT:TrBTIC without solution aging, (d) with solution aging for 20 min, (e) 40 min, and (f) 60 min. Adapted with permission from Xu et al.⁶⁴ Copyright 2019 WILEY-VCH Verlag GmbH & Co. KGaA, Weinheim.

in films cast from fast-drying lower boiling point solvents.^{28, 54, 76, 77} Apart from varying the boiling point of the primary solvent, solvent additives with a high boiling point, such as, e.g., chloronaphthalene (CN) and diiodooctane (DIO), can be added to increase the drying and thus structure formation time, as it is also done in Chapter 13 with the high boiling point green solvent diphenyl ether (DPE).^{7, 31, 78–80}

A further essential aspect of the solvent beyond the drying time is the interaction with the solute, which determines its solubility. When the concentration increases above a critical concentration determined by the solubility, aggregation of the solute can start.^{54, 81} When blends of two or more solutes are used, the critical concentrations for the different solutes are also different, impacting the nanostructure formation depending on the selective interaction of the solvent with each of the solutes.^{82–85} In the context of solubility, especially for blends, fine tunability is possible by exploiting the access to an ample parameter space in the three-dimensional Hansen solubility space by adjusting the mixing ratios of solvent mixtures.^{82, 86}

The impact of solvent additives also goes beyond the simple effect of changing the drying time. Solvent additives also change the Hansen solubility parameters of the solvent and the interactions with the solute, especially at the end of the drying process. The commonly used solvent additive CN has a much stronger affinity to backbones and other conjugated structures than to alkane sidechains, while DIO can enhance, e.g., fullerene solubility.^{7, 87}

Apart from solvent additives, solid additives have recently been gaining more attention. Solid additives can be grouped into volatile and non-volatile solid additives. Volatile solid additives, like SA1, have functionality comparable to some high boiling point sol-

vent additives. They increase the nanostructure formation during drying due to their $\pi - \pi$ interactions with the NFA molecules and volatilize during an additional thermal annealing step.^{21, 54, 88–93} Furthermore, the vacancies left by the volatilizing solid additive during thermal annealing open room for further nanostructure formation.⁸⁹ In contrast to solvent additives, they avoid the deteriorating effect of photooxidation of residual solvent additives in the active layer.^{88, 89}

A broad range of materials with different mechanisms influencing the nanostructure exist in the field of non-volatile solid additives. Ternary materials in solar cells can also be regarded as non-volatile solid additives. But as they also have several other functions beyond morphology tuning (e.g., broadening the absorption range, changing energetics), they are not discussed here.^{21, 94–96} Nucleation-inducing agents forming supramolecular structures with an epitaxial match and donor-acceptor interaction with the intended semiconducting molecule can also be grouped into non-volatile solid additives.^{97–100} Moreover, several other non-volatile solid additives shape the nanostructure formation similar to volatile solid additives.^{54, 88, 101, 102} As they remain in the film, some can also stabilize the nanostructure in the long term.⁸⁸

2.1.4 Coating Method

The drying behavior of organic semiconductor thin films is not only critically affected by the solvent and possible additives but also by the coating method. Hence, the coating method is also a relevant aspect of shaping the nanostructure. Spin coating, blade coating, and slot-die coating are the most common thin film coating methods. While blade coating and slot-die coating differ mainly from a technical point of view, spin coating leads to an entirely different drying behavior with a different structure formation, which is linked to a shorter drying time.^{54, 103–105} A further relevant difference between the coating techniques is their upscalability. Spin coating is a simple and highly suitable method for reliably producing thin films on small substrates. Hence, it is a coating method preferred in many laboratories. However, spin coating wastes much of the valuable solution since it is spun off. Furthermore, the maximum substrate size is limited. Thus, it is not suitable for industrial processing. Slot-die coating is an industrial process also used in the commercial roll-to-roll processing of large-area solar cells, e.g., by ASCA. Since knowledge transfer from lab to fab is desirable, insights from comparable coating methods, like blade coating, are highly valuable.¹⁰³ Therefore, blade coating is used in this thesis due to its comparability to the industry-relevant slot-die coating and experimental simplicity comparable to spin coating. The industry relevance outweighs the possibility of influencing the nanostructure by varying the coating method. Hence, the exact impact of the coating method on the nanostructure is not discussed here.

Even when the coating method is fixed, several options exist to process multi-component solutions. The most commonly used option is to coat blended solutions in one step. Layer-by-layer coating is a further option, where neat solutions are coated in two steps on top of each other to form a pseudo-bilayer configuration. Depending on the solubility of the material of the bottom layer in the solvent used for the top layer, the bottom layer is partially dissolved, leading to a mixed phase between relatively pure top and bottom layers.^{106–110} This principle was also used to produce the first binary single-junction OPV cells surpassing 20% power conversion efficiency.¹

2.1.5 Post-deposition Treatments

While all previously mentioned factors influencing the nanostructure exert their influence before or during the thin film formation, post-deposition treatments can also significantly impact the nanostructure. Since solvent evaporation is usually a rapid process, the resulting thin films are often in a kinetically trapped state. Thus, there is still room for further phase separation and the formation of more ordered molecular packing.^{54, 111–113} The two most common approaches are solvent vapor annealing and thermal annealing, a standard treatment in many recipes for organic solar cells.^{7, 20, 21, 43, 54, 88} A sufficient heating temperature (usually above the glass transition temperature) or sufficient swelling of the thin film exposed to solvent vapor (lowering the glass transition temperature) add mobility to one or more species of molecules in the film, allowing for a reassembly of the molecules. Both approaches often enhance phase separation and aggregation.^{7, 43, 111, 114–122}

The thermal annealing conditions are usually empirically chosen, but there are also several approaches to identify thermal transitions from temperature scans. Differential scanning calorimetry (DSC) is a powerful method to track how the dependency of the material's heat capacity changes with temperature. Thus, it enables spotting the glass transition, melting, and crystallization temperatures.^{123–125} Methods like UV-Vis absorption spectroscopy and GIWAXS also allow tracking temperature-dependent structure formation to spot structural transition temperatures.^{126–128} In Figure 2.3 (a)–(b), an example is shown, where the transition temperature of the NFA N3 was extracted from the change in absorption spectra.¹²⁶ This knowledge was then used to develop a double annealing strategy with a first annealing step slightly below the transition temperature to induce small-scale nucleation, followed by a second annealing step above the transition temperature to enhance large-scale aggregation. This can be seen by the additional small-scale structures in the RSoXS measurements in Figure 2.3 (d) compared to the large-scale structures of a single annealed film in Figure 2.3 (c).¹²⁶

While the control parameters for thermal annealing are mainly the temperature and duration, the number of relevant parameters is larger for solvent vapor annealing. The selection of the solvent for solvent vapor annealing is decisive. It depends mainly on the solubility of the materials in the solvent, but also on the ability of the solvent to permeate the layer and several other aspects.^{20, 21, 43, 118, 119, 129–131} Moreover, the saturation of the atmosphere with solvent plays an important role. The saturation depends on the vapor pressure of the solvent, on the temperature and also strongly on the experimental setup.^{43, 119, 132–136} Also, the SVA time is a decisive parameter.^{7, 132, 137}

The most common approach is placing the sample with a small amount of solvent in a closed petri dish.^{21, 88, 111} In this case, a saturated solvent atmosphere slowly builds up. Work has been done to realize controllable solvent saturation.^{132–135, 138, 139} However, there are often difficulties transferring these insights to other setups as, e.g., different sample chamber volumes may need adjustments to parameters of the SVA, e.g., different SVA times.^{7, 21, 140}

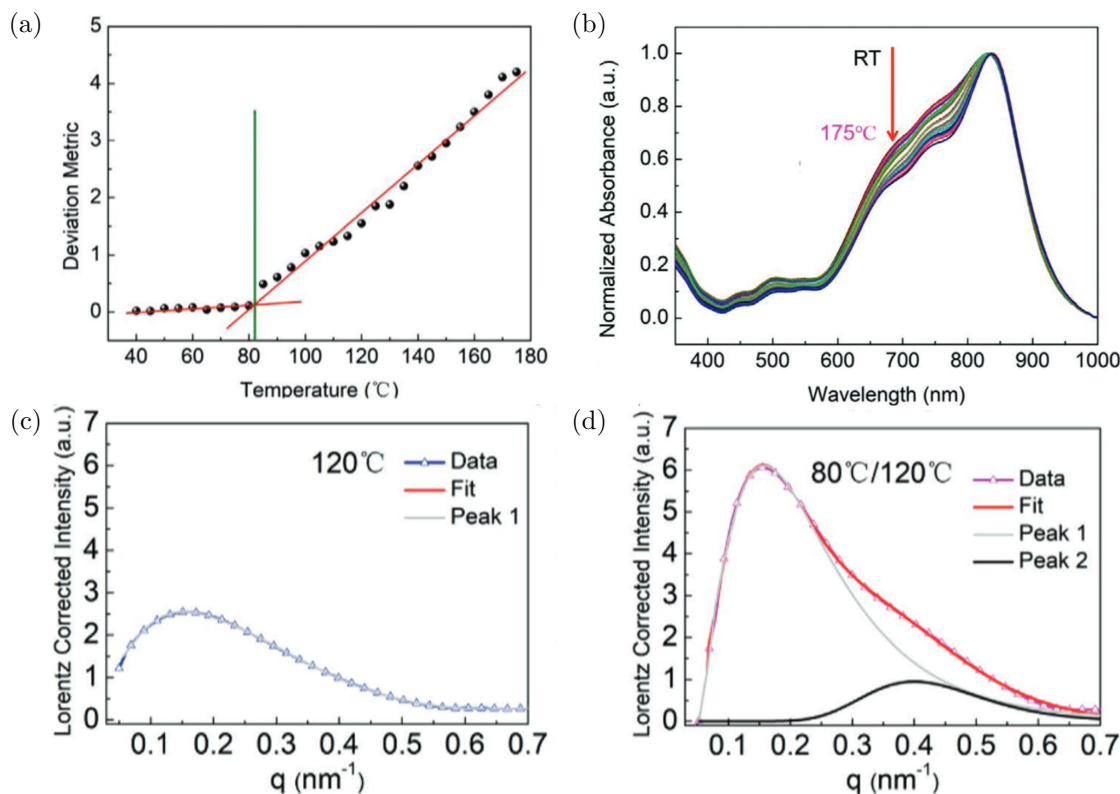


Figure 2.3: (a) N3 deviation metric extracted from the normalized UV-vis absorption spectra in (b) measured at temperatures between 40°C and 175°C. The vertical green line in (a) shows the transition temperature of N3 at $(82 \pm 1)^\circ\text{C}$. (c) Peak fit of one log-normal component to the circularly averaged RSoXS profile of a single-annealed PM6:N3:PC₇₁BM film. (d) Peak fit of two log-normal components to the circularly averaged RSoXS profile of a double-annealed PM6:N3:PC₇₁BM film. Adapted with permission from Qin et. al.¹²⁶ Copyright 2020 Wiley-VCH GmbH.

2.2 GIWAXS of Organic Semiconductors

After the most relevant possibilities of influencing the nanostructure of organic semiconductor thin films known from literature are summarized and discussed, this section turns to characterizing the nanostructure. In this thesis and the whole community, GIWAXS is the most frequently used technique to characterize the thin film nanostructure. The 2D-GIWAXS images contain important information on the abundance, orientation, and quality of ordering of different types of molecular stacking. Thus, GIWAXS is an inevitable tool when an in-depth nanostructure analysis and control is intended. In this section, at first, the general background of X-ray scattering leading to GIWAXS measurements is explained (2.2.1). This is followed by two further parts, elaborating on interpreting (2.2.2) and modeling (2.2.3) scattering features typically occurring for organic semiconductors.

2.2.1 GIWAXS Scattering Principle

The physical origin of GIWAXS is X-ray scattering, where the incident electromagnetic wave interacts with the sample's electrons. X-ray scattering can occur, when the electron

density exhibits modulations, e.g., due to electron-rich and electron-deficient parts of a molecule or due to different electron densities in different materials. The scattering strength depends on the contrast, which is based on the difference in refractive index Δn between the two materials 1 and 2, and the wavelength λ of the X-ray radiation:^{141–144}

$$\frac{|\Delta n|^2}{\lambda^4} = \frac{\Delta\delta^2 + \Delta\beta^2}{\lambda^4} = \frac{(\delta_1 - \delta_2)^2 + (\beta_1 - \beta_2)^2}{\lambda^4} \quad (2.2)$$

Where the dispersion δ and the absorption β are the real part and imaginary part of the refractive index:

$$n(\vec{r}) = 1 - \delta(\vec{r}) + i\beta(\vec{r}) \quad (2.3)$$

In a homogeneous medium far away from absorption edges the complex refractive index n can be expressed by:¹⁴⁵

$$n(\vec{r}) = 1 - \frac{\lambda^2}{2\pi} r_e \varrho(\vec{r}) + i \frac{\lambda}{4\pi} \mu(\vec{r}) \quad (2.4)$$

Hence, the complex refractive index n depends on the wavelength λ , the scattering length density $r_e \varrho(\vec{r})$ (r_e electron radius, $\varrho(\vec{r})$ electron density), and the linear absorption $\mu(\vec{r})$. Thus, changes in μ can also lead to a scattering contrast. However, GIWAXS measurements are usually conducted with hard X-rays on the order of 10 keV with photon energies away from material-specific absorption edges.¹⁴⁶ Thus, β is usually about two orders of magnitude smaller than δ , leading to a negligible impact of the absorption on the contrast.^{145, 147} In resonant scattering techniques, modulations of the contrast can be achieved with energy changes close to an absorption edge.^{141–144}

Since the refractive index is smaller than 1, total external reflection occurs at the sample surface when the incident angle is below the material-specific critical angle α_c .^{146, 148, 149}

$$\alpha_c = \sqrt{2\delta} \quad (2.5)$$

This property can be exploited in GIWAXS measurements, where very shallow incident angles below 1° are used. The shallow incident angle leads to large footprints on the sample and big probed sample volumes.^{149, 150} Often, the incident angle is chosen to lie above α_c of the thin film but below α_c of the substrate. Thus, the X-ray beam penetrates the whole thickness of the film and is then reflected off the surface of the substrate and passes the film again. Such a measurement probes the bulk of the film and reduces the contribution of substrate scattering. GIWAXS measurements can also be performed very close to or below α_c . In this case, an evanescent wave can only penetrate the top of the film, leading to surface-sensitive measurements.^{148–150}

Even in completely disordered materials, like liquids or glasses, there is a contrast in electron density, leading to diffuse X-ray scattering. When the scattering centers (e.g., atoms or molecules) are assembled periodically, constructive interference can amplify the scattering signal, leading to clear scattering peaks. The Bragg and Laue conditions are equivalent methods to evaluate the scattering angle or the scattering vector of a lattice plane. Here, only the Laue condition is discussed. It states that constructive interference occurs when the difference between the scattered wave vector \vec{k}_f and the incoming wave vector \vec{k}_i is a reciprocal lattice vector: $\vec{q} = \vec{k}_f - \vec{k}_i = \vec{G}_{hkl}$.¹⁵¹ In the case of elastic scattering ($|\vec{k}_f| = |\vec{k}_i|$), the Ewald sphere is a particularly useful visualization to determine

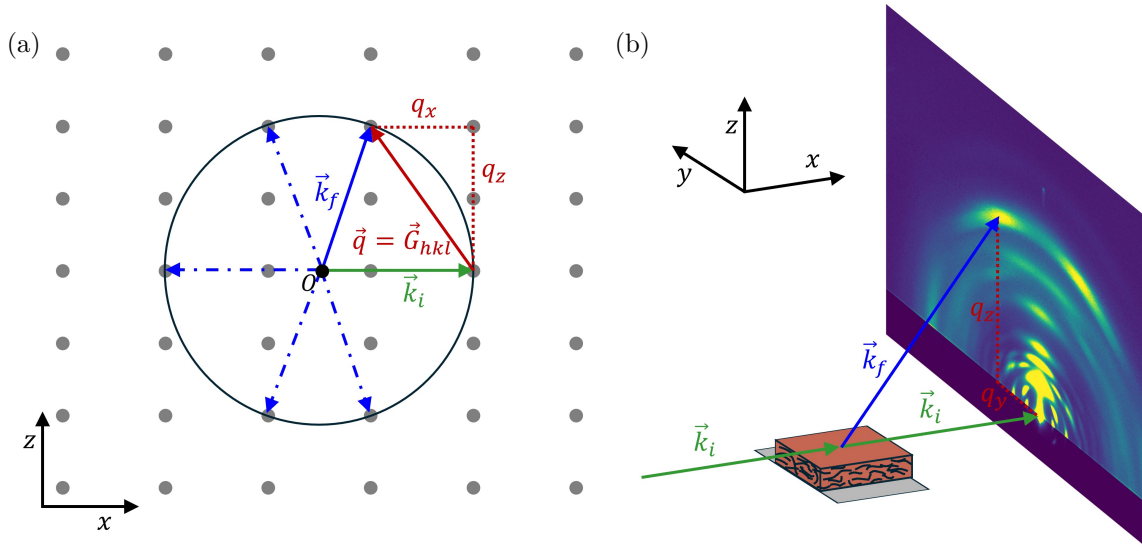


Figure 2.4: (a) Ewald sphere construction: The Ewald sphere with radius $|\vec{k}_i|$ is centered around the starting point O of \vec{k}_i . The tip of \vec{k}_i lies on an arbitrary reciprocal lattice point. Every reciprocal lattice point on the Ewald sphere leads to a scattering reflex (all blue arrows). This is a consequence of the Laue condition since the scattering vector \vec{q} is equivalent to a reciprocal lattice vector \vec{G}_{hkl} . The decomposition of \vec{q} tells, that there cannot be a vertical component q_z without a horizontal component q_x . (b) The scattered X-ray reflex travels to the 2D detector and a scattering peak is measured at a pixel attributed to q_y and q_z

scattering vectors fulfilling the Laue condition. Figure 2.4 (a) shows a 2D sketch of the Ewald sphere. The Ewald sphere with radius $|\vec{k}_i|$ is centered around the starting point O of \vec{k}_i . The tip of \vec{k}_i lies on an arbitrary reciprocal lattice point. Every reciprocal lattice point on the Ewald sphere leads to a scattering reflex.^{151, 152} Going beyond the simple picture described here, the Ewald sphere visualization can also be adapted to account for polychromatic X-ray radiation and polycrystalline materials.

The scattering reflex propagates from the sample to the detector, as sketched in Figure 2.4 (b). In GIWAXS, 2D detectors are usually placed at a sample-to-detector distance (SDD) of a few centimeters to about 50 cm (depending on the photon energy used and the q -range of interest).^{146, 149} Larger SDDs to measure smaller scattering angles and thus larger structure sizes are also commonly used, but then the method is called GISAXS (grazing incidence small-angle X-ray scattering). GISAXS is not used in this thesis and is, therefore, not discussed here. Every pixel on the detector can be attributed to a \vec{q} -vector depending on the incident angle and the scattering angle from the sample to the respective pixel.^{146, 149}

$$\vec{q} = \begin{pmatrix} q_x \\ q_y \\ q_z \end{pmatrix} = \begin{pmatrix} \cos(\psi_f) \cos(\alpha_f) - \cos(\alpha_i) \\ \sin(\psi_f) \cos(\alpha_f) \\ \sin(\alpha_i) + \sin(\alpha_f) \end{pmatrix} \quad (2.6)$$

The xy -plane lies on the sample surface and z normal to it with the origin at the point of diffraction. x is almost parallel to the beam and y perpendicular to it (see coordinate system in Figure 2.4 (b)). α is the angle in the plane spanned by the incident beam

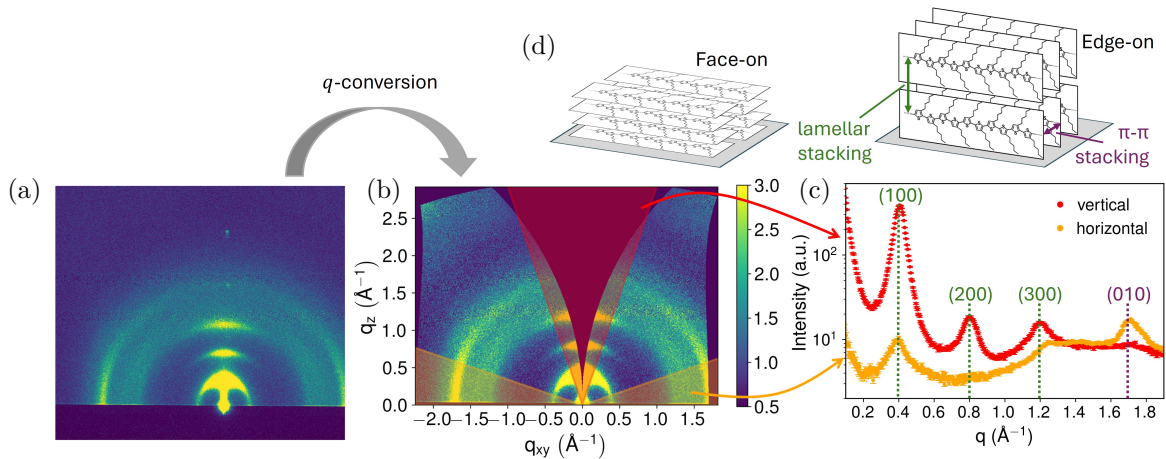


Figure 2.5: (a) GIWAXS raw data of a P3HT thin film. (b) q -converted GIWAXS data with the missing wedge. The area for the cake cuts in the vertical and horizontal direction is shaded in red and orange, respectively. (c) Cake cuts extracted from the measurement in (b). The scattering peaks are indexed. The (100), (200), and (300) peaks are three peak orders from the lamellar stacking, and the (010) belongs to the $\pi - \pi$ stacking sketched in (d). The orientation is primarily edge-on. (d) Sketches of molecular stacking of P3HT in face-on and edge-on orientation. Own unpublished data.

and the specularly reflected beam. ψ is the angle out of the plane, while the index i represents the incident beam and f the scattered beam.

Usually an in-plane isotropy in the xy -plane can be assumed so that q_x and q_y can be combined to $q_{xy} = \sqrt{q_x^2 + q_y^2}$.¹⁴⁹ Therefore, in the scope of the q -conversion, the complete 2D image can be reshaped to a new 2D-image with q_{xy} - and q_z -axis, which can be seen in Figure 2.5 (a)–(b). The most noticeable change is that there is a missing wedge around $q_{xy} = 0$.¹⁴⁹ This can be explained by the Ewald sphere construction. Therefore, we consider the case $q_y = 0$. At every $|q_z| > 0$, also $|q_x| > 0$ due to the curvature of the Ewald sphere, as also sketched in Figure 2.4 (a). At increasing $|q_z|$, the value of $|q_x|$ is strongly increasing leading to the broadening wedge in Figure 2.5 (b). The same effect also leads to the curved edges at the top and the sides.

2.2.2 GIWAXS Applied to Organic Semiconductors

GIWAXS scattering features of organic semiconductors are often arcs with varying intensity in the azimuthal direction and a certain width in the radial direction. This is also the case in the GIWAXS measurement of the exemplary organic semiconductor P3HT in Figure 2.5 (b). The highest intensity along these arcs frequently lies in the horizontal or vertical direction. Thus, it is usually beneficial for the data analysis to extract cake cuts in the horizontal and vertical direction, as sketched in Figure 2.5 (b)–(c). From the q -position of the scattering peaks, the corresponding lattice plane spacing d_{hkl} can be calculated:¹⁴⁹

$$q = \frac{2\pi}{d_{hkl}} \longrightarrow d_{hkl} = \frac{2\pi}{q} \quad (2.7)$$

The lattice plane spacing can then be attributed to typical spacings in the molecular assembly of the organic semiconductor. $\pi - \pi$ stacking ((010); see sketch in Figure 2.5

(d)) is usually at $d_{010} \approx 0.37$ nm ($q \approx 1.7 \text{ \AA}^{-1}$). At significantly smaller q (larger d), lamellar stacking is observed ((100) along sidechains; see sketch in Figure 2.5 (d)). In the case of the example P3HT, lamellar stacking is at $d_{100} \approx 1.6$ nm ($q \approx 0.39 \text{ \AA}^{-1}$). The material-specific variations in lamellar stacking distances are much larger than of $\pi - \pi$ stacking distances. This is because the sidechains and other aspects of the molecular design govern the lamellar stacking distance.¹²³ The GIWAXS measurements of some polymers also exhibit a (001) scattering peak in the third crystallographic direction, the backbone direction. This is mainly the case for donor-acceptor copolymers (e.g., PM6 or N2200), where the alternating electron-rich and electron-deficient parts in the backbone lead to a contrast in electron density. In semiconducting homopolymers like P3HT, this contrast is usually too weak.¹²³ Apart from the first-order scattering peaks (100), (010), and (001) in the three crystallographic directions, also higher order peaks (e.g., (200) and (300) of lamellar stacking in Figure 2.5 (c)) or mixed index peaks involving components in at least two crystallographic directions are often observed.

A strength of GIWAXS is that it can also resolve the orientation of the lattice planes. Since the scattering vector \vec{q} points into the direction of the reciprocal lattice vector \vec{G}_{hkl} , it is perpendicular to the corresponding lattice plane. Thus, a scattering peak in the vertical stems from horizontal planes stacking vertically. Vice versa, a scattering peak appearing in the horizontal stems from vertical planes stacking horizontally. Hence, the P3HT stacking in the measurement in Figure 2.5 (c) is primarily edge-on as the lamellar stacking is mainly in the vertical direction, and the $\pi - \pi$ stacking is primarily in the horizontal direction.^{153, 154} However, the (100) peak in the horizontal with lower intensity indicates a smaller fraction with face-on orientation. Moreover, the azimuthal extent of the scattering peaks shows that also the edge-on population exhibits a significant orientational disorder. The extreme case of orientational disorder is an isotropic orientation, which yields a ring with constant intensity in the 2D GIWAXS measurement.^{153, 154}

The description in this section was mainly focused on semiconducting polymers so far. NFAs are also an important class of organic semiconductors, where most of the concepts introduced above are equally applicable. The main differences are that due to the absence of a polymer backbone, there cannot be a backbone ordering and the nature of the lamellar stacking also changes. Usually, the nanostructure is formed by a $\pi - \pi$ stacked overlap of the end groups and central cores of the conjugated structure of the NFA molecules in several configurations (see examples in Figure 2.6 (c)). The nanostructure can range from dimers to extended, three-dimensional crystalline networks.^{155–159} Examples from the Y-series NFA 1OBO-2 (molecular structure in Figure 2.6 (a)) are displayed in Figure 2.6 (b)–(c).

Even in less ordered NFA nanostructures, at least two characteristic sizes similar to typical polymer lamellar stacking distances are usually observed in GIWAXS measurements. As neighboring molecules are usually shifted horizontally as well as vertically to each other (see Figure 2.6 (c)), some GIWAXS peaks also often appear at an inclination and not in the horizontal or vertical direction. This is especially the case in highly ordered structures, as shown in the example from Chapter 10 in Figure 2.6 (d). Here, many mixed index peaks appear. In highly ordered structures like this, with many scattering peaks off the horizontal and vertical, indexing the peaks and modeling the unit cell is often a better strategy than extracting cake cuts.

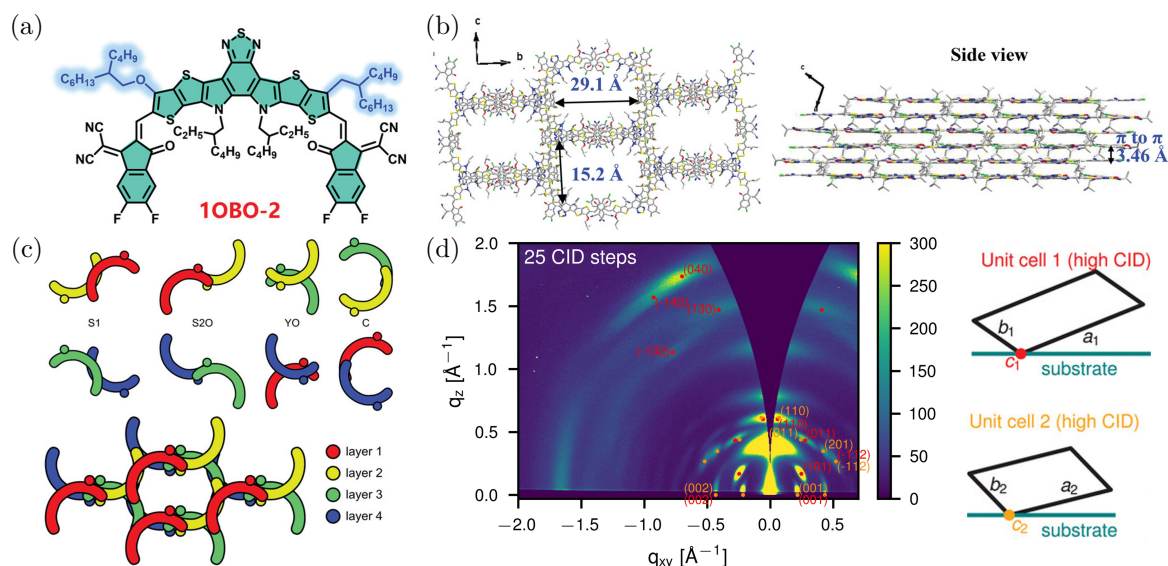


Figure 2.6: (a) Chemical structure of 1OBO-2, a Y-series NFA. (b) Crystal structure of 1OBO-2 (c) Schematical drawings of various 1OBO-2 dimers with varying overlap between the end-units and partially central cores (top) and of the crystal structure in several layers in different colors (bottom). The small circle stands for the alkoxy side chain. (d) GIWAXS measurement of a P3HT:Y12 blend thin film from Chapter 10. The dominant Y12 scattering peaks belonging to two different unit cells displayed on the right are indexed. (a)–(c) Adapted with permission from Chen et. al.¹⁵⁵ Copyright 2023 Wiley-VCH GmbH. (d) Adapted with permission according to the CC BY 4.0 license from Eller et. al.³⁶ (Chapter 10) Copyright 2024 The Authors. Advanced Energy Materials published by Wiley-VCH GmbH.

2.2.3 Modeling of GIWAXS Cake Cuts

Qualitatively comparing cake cuts in the horizontal and vertical direction extracted from 2D GIWAXS measurements can be valuable in GIWAXS data analysis. However, completely modeling the cuts can yield a magnitude of new insights that cannot be obtained from a qualitative analysis.

A closer line-shape analysis can offer information on the disorder and finite crystallite size. The most straightforward and most commonly used approach is to approximate the crystallite grain size from the width of the diffraction peaks using the Scherrer equation:^{123, 160–162}

$$L_c = \frac{2\pi K}{\Delta_q} \quad (2.8)$$

It relates the coherence length L_c with the full width at half maximum Δ_q of the peak in the q -space, further relying on the shape factor K (typically 0.8–1¹⁶⁰, often assumed as approx. 0.9¹²³). Since the coherence length can be easily evaluated with the Scherrer equation, it is widely used but frequently misused. The Scherrer equation assumes that the crystallite size dominates the peak broadening and ignores lattice disorder. However, in organic semiconductors, often strong disorder is the primary source of peak broadening, making the usage of the Scherrer equation invalid.^{123, 160} Even though, when only processing conditions are experimentally varied, the Scherrer equation can still give descriptive evidence for relative changes.¹⁶⁰

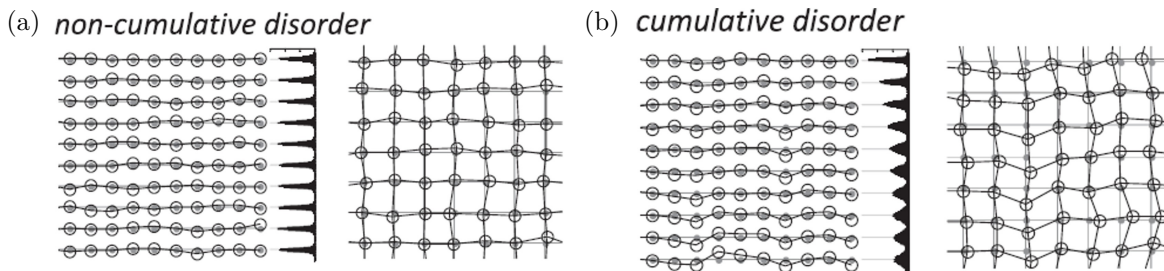


Figure 2.7: (a) Sketch of an example of non-cumulative disorder, where there are random statistical fluctuations about the ideal lattice position. (b) Sketch of an example of cumulative disorder. The correlation between lattice points decreases continuously with distance. Adapted with permission from Rivnay et. al.¹⁶⁰ Copyright 2011 by the American Physical Society.

There are two forms of lattice disorder: noncumulative and cumulative. Noncumulative disorder (see Figure 2.7 (a)) is present when random statistical fluctuations about the ideal lattice position occur. It lowers the peak intensity but does not affect the peak shape.¹⁶¹ Thus, in the case of pure noncumulative disorder, the peak width is only controlled by the crystallite size, keeping the Scherrer equation still valid. Cumulative disorder (see Figure 2.7 (b)), mainly due to paracrystalline disorder, is characterized by long-range distortions of the lattice, leading to a loss of correlation between lattice points with increasing distance.¹⁶⁰ Possible reasons include dislocations, impurities, chain backbone twists of polymers, or nonideal packing in small molecules.¹⁶⁰ In contrast to noncumulative disorder, cumulative disorder does change the peak shape, which also depends on the peak order.^{123, 160} Cumulative and noncumulative disorder often coexist, e.g., when thermal fluctuations around a paracrystalline lattice exist.¹⁶⁰

An accurate method to decouple the impact of finite crystallite size from cumulative disorder is a Fourier-transform method introduced by Warren and Averbach.^{163, 164} This is possible as in the Warren-Averbach (WA) analysis the Fourier coefficients of the peaks are products of the peak-order independent contribution from finite crystal size and peak-order dependent contribution from cumulative disorder.^{165, 166} Even though the WA-approach has been successfully applied to polymers,^{160, 165-168} it is a challenging and time-consuming approach requiring several peak-orders, which are often unavailable.¹²³

A good compromise between the oversimplification of the Scherrer-equation and the demanding WA-approach is peak fitting with a suitable function. The peak shape is best described by a Voigt profile, which is a convolution of a Gaussian and Lorentzian distribution and, therefore, challenging to use.¹⁶⁰ However, the pseudo-Voigt distribution closely resembles the Voigt distribution and is less challenging to fit than the pseudo-Voigt distribution and, thus, most suitable for modeling.^{166, 169} Hence, in this thesis, always pseudo-Voigt distributions of the following form are used for peak fitting:^{123, 160}

$$f(q) = A \cdot [\eta \cdot L(q) + (1 - \eta) \cdot G(q)] \quad \text{with } 0 \leq \eta \leq 1$$

$$G(q) = \exp \left[-\ln(2) \cdot \left(\frac{q-c}{b} \right)^2 \right], \quad L(q) = \frac{1}{1 + \left(\frac{q-c}{b} \right)^2} \quad (2.9)$$

Where A is the peak amplitude, c is the peak position, $2b$ is the full width at half maximum (FWHM) of the pseudo-Voigt peak, and η is the pseudo-Voigt mixing param-

eter. The pseudo-Voigt mixing parameter η supplies information on the type of disorder. When η is close to 1 (pure Lorentzian), cumulative disorder dominates. In the case of dominantly noncumulative disorder, η is close to 0 (pure Gaussian).^{123, 160} In the range of intermediate η , both types of disorder contribute significantly.¹⁶⁰

In the case of a pure Gaussian peak shape, i.e., noncumulative disorder, the Scherrer equation with $\Delta_q = 2b$ can be used to calculate the coherence length. In the other extreme case of a pure Lorentzian peak shape, the paracrystallinity parameter $g \approx \frac{1}{2\pi} \sqrt{\Delta_q d_{hkl}}$ can be calculated from the FWHM $\Delta_q = 2b$ and the spacing between the lattice planes of the diffraction peak of interest d_{hkl} .¹²³ The paracrystallinity parameter g is a measure of the statistical fluctuation of the individual lattice spacings reported in percent of the mean lattice spacing.¹⁶⁰ Thus, the higher the FWHM, the higher g , and the shorter the distance on which the spatial correlation is lost. In cases of intermediate η , neither a meaningful coherence length can be calculated with the Scherrer equation nor a meaningful paracrystallinity parameter. However, it can still be assumed that the order is conserved over a more extended range when the FWHM is smaller.¹⁶⁰

Thus, modeling all scattering peaks in the cuts with pseudo-Voigt distributions yields, on the one hand, information on the disorder based on the peak width and the pseudo-Voigt mixing parameter. On the other hand, the peak positions and amplitudes of the scattering peaks are also valuable information. As mentioned earlier, the peak position tells the lattice spacing. Since the lattice spacing has no constant value for a specific type of stacking but can be tighter or looser, it can characterize the packing density and quality.

The interpretation of the peak amplitude is more complicated. It is affected by several aspects, like the structure factor, the aggregate size, the quality of order, the film thickness, the aggregate fraction, and the aggregate orientation.^{123, 149, 153, 160, 170, 171} In the context of the analysis of crystalline materials, the peak amplitudes are necessary information for quantitative, in-depth structure elucidation. For more disordered organic semiconductors, peak amplitudes often rather yield qualitative information, which is especially meaningful when relative changes between different samples are analyzed. Then, the amplitude can be a measure for an increasing or decreasing quantity and/or quality of the corresponding type of stacking, as it is done for the $\pi - \pi$ stacking of P3HT and Y12 in Chapter 10. Ratios between peak amplitudes attributed to ordered and disordered material fractions, as done in Chapter 11, can also be a valuable tool for qualitatively characterizing the degree of crystallinity or ordering.¹²³ Moreover, amplitude ratios between different orientations of the same stacking feature can help quantify the molecular orientation, which is also used in Chapter 10. At this point, it must be noted that due to trigonometric reasons of the Ewald sphere, vertical scattering peaks are enhanced relative to horizontal ones. Thus, when oriented material fractions are calculated, a correction is necessary.^{153, 170}

2.3 UV-Vis Absorption Spectroscopy of Organic Semiconductors

The preceding section demonstrated the power of GIWAXS in the nanostructure characterization of organic semiconductor thin films. However, GIWAXS also has significant disadvantages. In the context of this thesis, one disadvantage is the limited high-throughput capability. Current laboratory GIWAXS machines usually require integration times in the hour timescale to achieve good data quality. At synchrotrons with high X-ray flux, high-quality measurements with short integration times below 1 s are possible. However, available beamtimes at synchrotrons are limited and require long-term planning. Hence, this thesis requires a method yielding valuable nanostructural information on short timescales.

UV-Vis absorption spectroscopy is a highly suitable technique for fulfilling these requirements. Integration times in the millisecond timescale are possible, and the absorption spectra yield valuable information on the interaction between the chromophores of the organic semiconductors. The rich information on the electronic interactions between the chromophores can be used to obtain insights into the aggregation of the polymers and other organic macromolecules and, thus, into the nanostructure. Even measurements of highly disordered samples without aggregation include valuable information on their nanostructure. These gained insights are on short-range ordering compared to long-range ordering probed with GIWAXS. Hence, the information from absorption spectra is complementary to the information from GIWAXS, making UV-Vis absorption spectroscopy and GIWAXS a powerful combination of characterization techniques. Probing short-range ordering is also needed when solutions are characterized. Thus, absorption spectroscopy is particularly useful for studying pre-aggregation in solution (Chapter 9).

The following section describes the basic principle of absorption spectroscopy measurements (2.3.1), followed by a section on the theoretical background of the nanostructural interpretation of absorption spectra of organic semiconductors (2.3.2).

2.3.1 Absorption Spectroscopy

Light passing a medium of absorbing chemical species is attenuated as a function of the photon energy E . This is described by the Beer-Lambert law:^{19, 172, 173}

$$I(E) = I_0(E) \cdot 10^{-A(E)} = I_0(E) \cdot 10^{-\mu(E)d} = I_0(E) \cdot 10^{-\varepsilon(E)cd} \quad (2.10)$$

Where $A(E)$ is the optical density (OD) or absorbance, $\mu(E)$ the attenuation coefficient, d the optical path length, $\varepsilon(E)$ is the molar decadic extinction coefficient of the attenuating species, and c the concentration of the attenuating species. The Beer-Lambert law is the most important law in optical spectroscopy and is often exploited when measuring highly diluted solutions. However, the linear relationship between the attenuation coefficient μ and the concentration c is no universal law but also has limitations. In the context of this thesis, especially the case of very high concentrations is decisive. When the concentration is as high that molecules of the analyte possess electronic interactions, the relationship between μ and c usually becomes highly nonlinear, leading to deviations from the Beer-Lambert law.^{172–177} Since electronic interactions often change the nature of specific optical transitions, the nonlinearity usually depends on the photon energy.

This does not only lead to a decreased or increased absorption but also to changes in the shape of the absorption spectrum.^{178–181} Therefore, dilution can change the shape of absorption spectra. However, measuring strongly absorbing solutions is challenging as the optical path length must be reduced to ensure that sufficient transmitted photons can be detected. To overcome this challenge, in Chapter 8 an approach is introduced that allows the measurement of absorption spectra of concentrated highly absorbing solutions, significantly broadening the measurement range compared to standard cuvettes. The path length is dynamically varied, regimes of suitable path lengths are identified, and the method’s limitations are investigated. Further circumstances that can lead to deviations from the Beer-Lambert law are, e.g., light scattering, inhomogeneous solutions, and high light intensities leading to nonlinear optical effects.^{172, 174, 175, 182}

For the acquisition of absorption spectra, a reference spectrum $I_0(E)$, a dark (background) spectrum $I_{dark}(E)$ and the measurement itself $I_{meas}(E)$ are required:¹⁷³

$$A(E) = -\log \left(\frac{I_{meas} - I_{dark}}{I_{ref} - I_{dark}} \right) \quad (2.11)$$

The dark (background) measurement accounts for counts on the spectrometer independent from the illumination and is recorded before the measurements start. The reference measurement can also be recorded before the measurements start or, in the case of a dual beam spectrometer, continuously parallel to the measurement of the sample.¹⁷³ This accounts for fluctuations of the illumination intensity but is only common for spectrometers, where a turning monochromator tunes the energy of the light impinging on the sample.¹⁷³ However, a turning monochromator has the disadvantage of low time resolution.¹⁷³ In contrast, compact spectrometers with a CCD or CMOS detector capable of acquiring a complete spectrum at once without moving parts provide a much higher time resolution, crucial for the time-resolved spectroscopy in this thesis. This applies to the spectroscopy of thinning fluid films in the TFFS method introduced in Chapter 8 (also used in Chapters 9, 10 and 15) and to the in-situ spectroscopy during solvent vapor annealing and blade coating in Chapter 10. The latter requires a time resolution on the millisecond timescale.

2.3.2 Absorption Spectra of Organic Semiconductors

After the acquisition of absorption spectra is discussed, this section deals with the origin of the absorption spectra of organic semiconductors and the way they can be interpreted. The optical transitions leading to the absorption spectra are closely related to the optical transition leading to photoluminescence (emission). Therefore, at most points in this description, photoluminescence is also described, but the focus is on absorption.

The Franck-Condon-Principle

The most crucial aspect of understanding the absorption spectra of organic semiconductors is the Franck-Condon-Principle. It exploits that only the electrons can move in resonance with the incident electromagnetic wave, while the nuclei are too heavy to respond on this time scale.¹⁹ Therefore, the configuration coordinate Q stays constant during the transition, leading to vertical transitions in the energy diagram (see Figure 2.8). The nuclei then react in the excited state on a slower time scale, leading to a shift

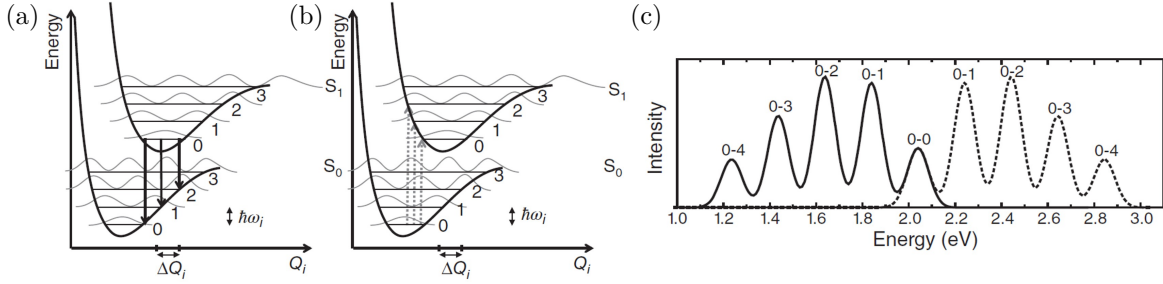


Figure 2.8: Illustration of the Franck-Condon principle, where the arrows display transitions leading to (a) emission and (b) absorption. On the schematic potential energy curves, vibrational wave functions are sketched on the vibrational levels separated by $\hbar\omega_i$. The wave function overlap determines the shape of the absorption (dotted line) and emission spectra (solid line) in (c). Adapted with permission from Köhler et. al.¹⁹ Copyright 2015 Wiley-VCH Verlag GmbH & Co. KGaA.

of the Q -position of the excited state's potential energy curve relative to the ground state's potential energy curve.¹⁹ In Figure 2.8, the vibrational modes separated by the vibrational energy $\hbar\omega_i$ are also displayed. The vibrational energies $\hbar\omega_i$ of the vibrational modes can be determined by Raman spectroscopy.

For absorption, an electron is lifted from the lowest vibrational level of the ground state S_0 to an arbitrary vibrational level of the first excited state S_1 . In the excited state, the electrons relax to the lowest vibrational level. This is the starting point for photoluminescence to an arbitrary vibrational level of the ground state. The relative intensities of the transitions are given by the wave function overlaps between the wave functions of the involved vibrational levels (also sketched in Figure 2.8).^{19, 183} Therefore, the displacement ΔQ between the configuration coordinates of S_1 and S_0 is decisive. It determines the Huang-Rhys parameter, which is a measure of the strength of the electron-phonon coupling:¹⁸⁴

$$S = \frac{M\omega}{2\hbar}(\Delta Q)^2 \quad (2.12)$$

M is the reduced mass and ω the vibrational frequency introduced above. Assuming harmonic oscillators and $\hbar\omega_i \gg kT$, the probability for a transition between the lowest vibrational level of S_0 (or S_1) and the m th vibrational level of S_1 (or S_0) is given by a Poisson distribution:¹⁹

$$I_{0-m} = \frac{S^m}{m!} e^{-S} \quad (2.13)$$

To model the absorption and emission spectra, the photon density of states of the surrounding medium must also be considered. Using the Einstein relation, the term $n(\hbar\omega) \cdot \hbar\omega$ can be introduced, resulting in the following absorption and photoluminescence spectra:¹⁹

$$I_{Abs}(\hbar\omega) = n(\hbar\omega) \cdot \hbar\omega \cdot \sum_m \frac{S^m}{m!} e^{-S} \cdot \Gamma \cdot \delta(\hbar\omega - (\hbar\omega_0 + m\hbar\omega_i)) \quad (2.14)$$

$$I_{PL}(\hbar\omega) = [n(\hbar\omega) \cdot \hbar\omega]^3 \cdot \sum_m \frac{S^m}{m!} e^{-S} \cdot \Gamma \cdot \delta(\hbar\omega - (\hbar\omega_0 - m\hbar\omega_i)) \quad (2.15)$$

Where $n(\hbar\omega)$ is the refractive index of the investigated material system at the photon energy $\hbar\omega$, $\hbar\omega_0$ is the energy of the 0-0 transition, and δ is the Delta-function determining

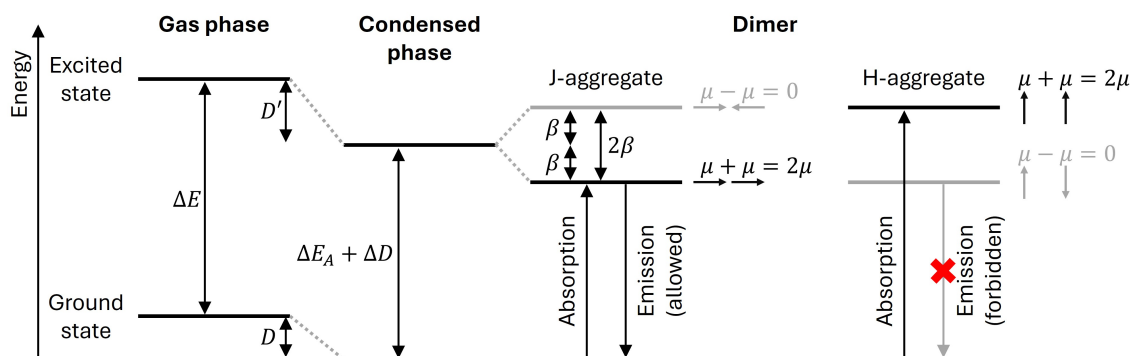


Figure 2.9: Illustration of the energetic shifts, energy level splittings, and possible optical transitions upon the dimer formation of two idealized point-dipoles. The relative orientations between the transition dipole moments in both excited state branches of each of the two aggregate types are indicated by small arrows. The resulting total transition dipole moment is listed next to the arrows.

the peak position. Γ is the line shape function describing the broadening of the peaks. Depending on the type of broadening, it can be a Gaussian or Lorentzian distribution (or a combination of both).¹⁹ Most commonly, Gaussian peaks are used for the line shape. Equations 2.14 and 2.15 assume a single vibrational mode $\hbar\omega_i$ and must be adapted when several vibrational modes are relevant.

Optical Signatures of Aggregates

The Franck-Condon-Analysis, as introduced above, describes single non-interacting chromophores. When electronic coupling with other chromophores in aggregates becomes relevant, the optical signatures change significantly, which is discussed in this section.

In the simplest form of the aggregate, the dimer, already a substantial impact of aggregation on the optical transitions can be seen. Kasha laid important fundamentals in this context, considering the interaction of two point-dipoles.^{185, 186} In the ground state, the energy is reduced by the negative van der Waals interaction between the dipoles D : $E_{GS} = E_A + E_B + D$ with E_A and E_B being the corresponding ground state energies of the isolated chromophores. In the excited state, there is an analogous van der Waals shift D' and an additional splitting by the resonance interaction energy β into two excited state energy levels: $E_{ES\pm} = E_{A^*} + E_B + D' \pm \beta$. Here, E_{A^*} is the energy of the excited molecule A , and E_B is the energy of the ground state of molecule B . These shifts are displayed in Figure 2.9. The transition energy between the shifted ground state and the shifted and split excited state is then $\Delta E_{total} = \Delta E_A + \Delta D \pm \beta$ with $\Delta E_A = E_{A^*} - E_A$ and $\Delta D = D' - D$.

The relative orientation between the two transition dipole moments is decisive for the possible optical transitions between the ground state and the two split excited state energy levels. In the following, the two extreme cases sketched in Figure 2.9 are quickly discussed:

When the transition dipole moments align straight after each other (Figure 2.9 – J-aggregate), the transition dipole moments of the energetically higher level (head-to-head)

cancel themselves out to 0. In comparison, they are doubled in the lower energy level (head-to-tail). Thus, optical transitions are only possible between the ground state and the lower energetic level. Since for absorption and emission the same energy levels are involved, the Stokes shift is small. In relation to the transitions of the isolated chromophores, the negative ΔD , as well as the downshift by $-\beta$, lead to redshifted transitions. This configuration of dipole moments is called J-aggregate or Scheibe-aggregate (after Jelley and Scheibe, who described this aggregate almost simultaneously).^{187–189}

In contrast to the J-aggregate, in the H-aggregate, the transition dipole moments stack coplanar (Figure 2.9 – H-aggregate). Thus, the transition dipole moments cancel themselves out to 0 in the lower excited state energy level (antiparallel) and sum up to the doubled value in the higher level (parallel). Consequently, the absorption then also takes place to the higher energy level. Before emission from the higher energy level to the ground state could occur, a nonradiative decay to the lower excited state occurs. Since a radiative transition from this state to the ground state is forbidden, a nonradiative decay to the ground state must occur. However, a weak emission is still possible under real conditions with non-perfect planarity and finite temperature. Absorption and emission involve different excited state energy levels, so a Stokes shift exists between the 0-0 transitions in emission and absorption.

Spano and co-workers conducted important work based on Kasha’s achievements by including static and dynamic disorder and the vibronic structure in larger systems going beyond the two point-dipoles considered so far.^{190–193} Since a detailed description of Spano’s work goes too far, only some key findings with special relevance to my work in this thesis are summarized in this paragraph. The insights on the optical transitions in aggregates gained by Kasha mainly transfer to the 0-0 transitions, while the transitions from or to higher vibronic levels are less affected. Therefore, the peak ratio between the 0-0 and 0-1 peaks bears essential information on the aggregate type (H or J) and the coupling strength between neighboring chromophores. While the 0-0/0-1 peak ratio increases with increasing coupling strength for J-aggregates, the opposite trend is seen for H-aggregates. In polymeric systems, J-aggregates stem from intra-chain coupling between adjacent monomers in the backbone, while H-aggregates stem from inter-chain coupling via $\pi - \pi$ -stacking. Thus, a higher peak ratio results from smaller inter-chain electronic couplings compared to strong intra-chain couplings. Hence, it is a sign that planar backbones with significant conjugation lengths dominate over $\pi - \pi$ -stacking.^{190, 194–196} For more information, the interested reader is referred to the thorough review from Hestand and Spano.¹⁹¹

In addition to the peak ratio, the 0-0 peak position of semiconducting polymers also includes relevant structural information about the aggregate. A redshifted peak position indicates an increased coherence length along the backbone.^{19, 194, 197} The conjugation length is the effective number of monomers over which an excitation can delocalize coherently. Thus, it behaves spectroscopically similar to an oligomer of the same length.¹⁹ The redshift in linear oligomers with increasing monomer length can be made plausible by exploiting a simple particle-in-a-box model, where the oligomer size determines the size of the one-dimensional well.¹⁹

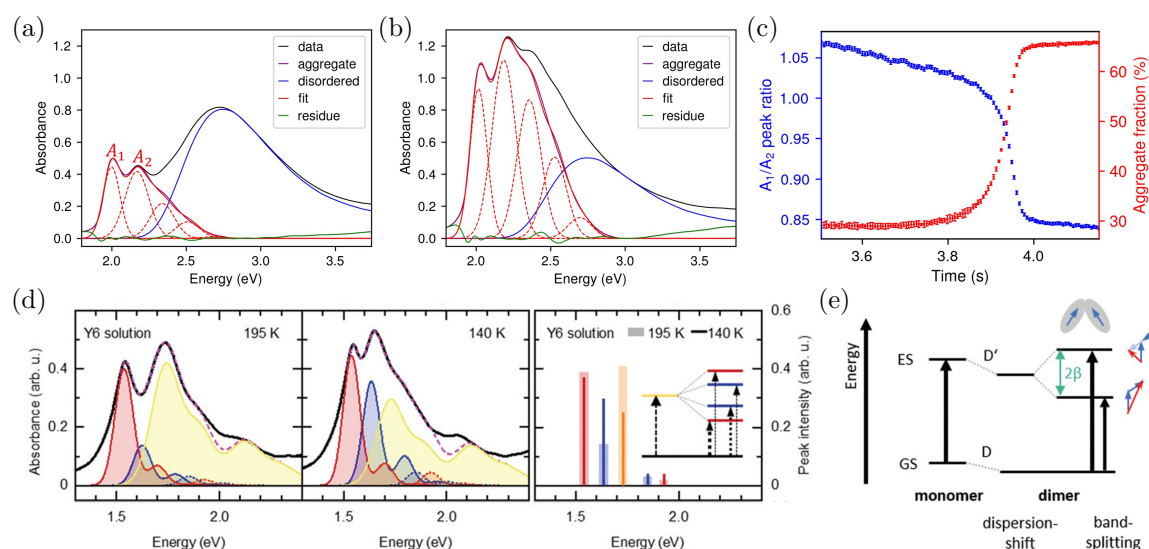


Figure 2.10: (a) Absorption spectrum of a pre-aggregated P3HT solution at the start of a blade coating process. The spectrum is decomposed into a disordered fraction and an aggregated fraction by scaling a disordered reference spectrum to the high-energy shoulder of the spectrum. The aggregate fraction can be calculated from the ratio of the areas below the disordered and aggregated contributions, considering the different molar extinction coefficients.¹⁹⁸ The aggregate absorption is modeled by five Gaussian peaks separated by the vibronic energy of 0.17 eV. The A_2 – A_5 peaks are modeled with a peak width larger by a factor of 1.45 compared to the A_1 width to account for the superposition of several vibronic modes. (b) Absorption spectrum of the dried thin film after the wet thin film from (a) is dried (with identical data analysis as in (a)). (c) Evolution of the aggregate fraction and the ratio between the A_1/A_2 peak amplitudes during the drying process of blade coating. (d) Spectral decomposition of the absorption spectra of Y6 in MeTHF at 195 K and 140 K via a Franck-Condon-Fit from Chapter 12. The disordered phase (yellow) and two aggregate species (red and blue) are considered. (e) Since the transition dipoles are not parallel to each other, transitions to the lower and higher excited states are possible (resembled by a high energy and low energy vibronic progression for each aggregate in (d)). (a)–(c) Own unpublished data. (d)–(e) adapted with permission according to the CC BY 4.0 license from Kroh et. al.²⁹ (Chapter 12) Copyright 2022 The Authors. Advanced Functional Materials published by Wiley-VCH GmbH.

As a final remark, it must be noted that absorption spectra usually consist of a superposition of several contributions, making the analysis more complicated. The spectrum can often be divided into a disordered and an aggregated part, as displayed in the examples of a P3HT solution and thin film in Figure 2.10 (a) and (b). This also allows estimating the aggregate fraction as done in Chapters 9, 10 and 14.¹⁹⁸ Higher optical transitions of the aggregate can also overlap with the spectrum of the disordered phase, leading to deviations of the spectral shape and intensity in the spectral range attributed to the disordered fraction. Hence, the disordered fraction may be overestimated. Figure 2.10 (c) displays an example of the evolution of the aggregate fraction during blade coating of a pre-aggregated P3HT solution.

In other cases, e.g., in Y-series NFAs, there can be vibronic progressions of more than one aggregate species, overlapping with each other and a disordered phase. A tedious

analysis, like that conducted by Daniel Kroh in Chapter 12, is necessary to disentangle the different contributions.²⁹ Examples of Y6 solutions at two different temperatures are displayed in Figure 2.10 (d). Since the transition dipoles are not parallel (see Figure 2.10 (e)), absorption is possible to both excited state levels in this case. In examples like this, it is important not to misinterpret the superposition of vibronic progressions as one single vibronic progression.

Moreover, even in clear vibronic progressions, as the aggregate absorption of P3HT in Figure 2.10 (a)–(b), a superposition of different vibronic modes of the same aggregate may be present. While the A_1 peak position is identical for all modes, the distance between the peaks $\hbar\omega_i$ varies, leading to a broadening and smearing out of the higher-order peaks. To account for this effect, the higher vibronic peaks can be modeled with an increased peak width.¹⁹⁹

The fitting in Figure 2.10 (a)–(b) is not a full Franck-Condon analysis but a simplified model that is also used in other parts of this thesis (Chapters 9 and 10). The peak amplitudes are fitted without restrictions, but the distances between the peaks are fixed by the vibronic energy. This still allows determining the peak position of the first peak A_1 and the A_1/A_2 peak amplitude ratio between the first two peaks. Hence, the peak position and the amplitude ratio can be interpreted in the scope of Spano's theory, as described above. The A_3 – A_5 peaks are not used for interpretations.

3 Acceleration Approach

After the theoretical background of GIWAXS and UV-Vis absorption spectroscopy of organic semiconductors was discussed in the two previous sections, this Chapter deals with the method development I did in my thesis to accelerate GIWAXS and UV-Vis absorption spectroscopy measurements.

In all parts of this thesis, nanostructural characterization plays an important role. In Chapters 8–10, UV-Vis absorption spectroscopy is an essential tool in various varieties (strongly absorbing solutions, in-situ during blade coating and solvent vapor annealing). It serves as a fast method for the determination of the aggregation state. GIWAXS is a further decisive tool for the work on thin films in Chapters 10–14.

Measuring and analyzing large amounts of data is necessary to establish nanostructure control and investigate the underlying processes. In typical screening experiments, a small subset of the complete data set often represents the relevant changes. Large fractions of data sets often contain only minor changes or lie in irrelevant regimes. It is a standard procedure to measure the whole dataset, analyze it semi-manually, identify the relevant parts of the parameter space, and repeat measurements with increased point density in these parts at a later point.

However, directly reducing obsolete measurements speeds up the parameter space exploration. Progress can be boosted if each measurement point is directly analyzed, and the result is used to decide upon the next measurement point. An optimized workflow, including such a feedback loop due to automated analysis, especially enhances the research efficiency of characterization techniques with short measurement times, such as UV-Vis absorption spectroscopy.

Therefore, I focused on enabling fast measurement procedures with direct feedback loops for different varieties of UV-Vis absorption spectroscopy. One decisive step is introducing the TFFS (Thinning Fluid Film Spectroscopy, European and US patent pending) method, which enables highly efficient automated UV-Vis absorption measurements of strongly absorbing solutions. As Chapter 8 deals with the TFFS method in detail, there is only a short description of the TFFS method below (Section 3.1). The automated measurement and analysis of in-situ absorption spectroscopy measurements during blade coating and solvent vapor annealing are discussed in the second section (Section 3.2). GIWAXS measurements at a laboratory system require very long integration times (at our current setup hour timescale) compared to UV-Vis absorption measurements (millisecond timescale). Thus, integrating the data analysis into the measurement routines is less critical. Therefore, the focus of the GIWAXS acceleration approach in the last section (Section 3.3) is the reduction of the required manual workforce by automation, enabling a more efficient usage of this routine method. When an X-ray source with higher flux is used, the necessary integration time is reduced, and the increased efficiency directly translates to a higher sample throughput.

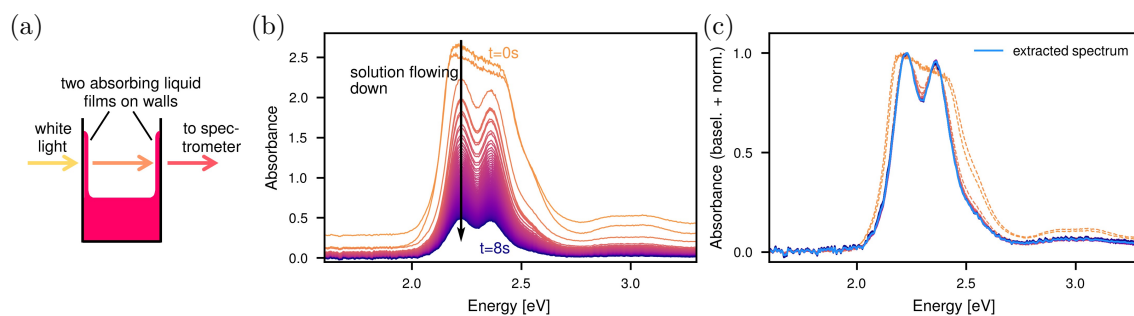


Figure 3.1: (a) Sketch of the measurement principle of TFFS. (b) Time-resolved example measurements of a solution flowing down the measurement container walls. (c) The identical absorption spectra with a baseline correction and normalization to the peak absorbance. Spectra plotted in dashed lines are disregarded as they are beyond the detection limit of the setup. The remaining spectra are averaged to the final extracted spectrum (blue). Adapted with permission from Eller et. al.³⁵ (Chapter 8) Copyright 2024 American Chemical Society.

3.1 Absorption Spectroscopy of Strongly Absorbing Solutions

To measure the absorption spectra of strongly absorbing solutions, either a strong dilution or a drastic reduction of the optical path length is necessary. Dilution can change the absorption spectra due to changed intermolecular interactions. A reduction of optical path length is possible with demountable cuvettes with low path lengths down to 10 μm . However, evaporation can be a big problem with the minute solution volumes in demountable cuvettes. Moreover, diluting solutions as well as filling the solutions into demountable cuvettes are time-consuming processes. Filling solutions into demountable cuvettes is also challenging to automate. Therefore, for efficient workflows enabling high-throughput measurements, neither the dilution nor the usage of demountable cuvettes is suitable.

To characterize the material behavior in dependency of the CID treatment strength in various solvent systems, hundreds of absorption spectra of strongly absorbing solutions were needed in Chapter 9. Therefore, a high-throughput measurement approach and fast data analysis were essential. Thus, I developed the TFFS method, which exploits the low optical path length of a thin fluid film flowing down the wall of a measurement container (see Figure 3.1 (a)). The change of optical path length over time allows the selection of the most suitable optical path lengths for the measured solution, enabling measurements in a large dynamic range of concentrations or absorptivities.

The basics of the TFFS method and its advantages, limits, and automation are extensively presented and discussed in Chapter 8. Hence, a detailed description of the TFFS method is omitted in this chapter, and the focus is on the optimizations done for Chapter 9. The first step of the TFFS procedure is to form a thin fluid film at the container walls, as displayed in Figure 3.1 (a). In Chapter 9, a special form of fluid film formation is used, which differs from the shaking and pipetting method introduced in Chapter 8. The spark discharge used for the CID treatment leads to local solvent evaporation in

the volume of the conducting channel. This rapid gas formation splashes solution to the glass walls, directly leading to the required liquid film formation. Therefore, the nature of the CID treatment can be exploited instead of taking an extra step (e.g., shaking). The remaining procedure is identical to the processes described in detail in Chapter 8. During the thinning of the fluid film, a time series of absorption spectra is measured through the vial's walls. Figure 3.1 (b) shows a time-resolved example measurement series. Measurements absorbing too strongly are omitted (dashed lines in Figure 3.1), while a weighted average of the remaining spectra yields the single extracted spectrum in Figure 3.1 (c). As weight for the average, the peak absorbance is used to reduce the impact of increased noise in weakly absorbing thin fluid films.

3.2 In-Situ Absorption Spectroscopy

Since absorption spectra of organic semiconductors contain valuable information on the interactions between chromophores and, thus, on the short-range nanostructure, time-resolved in-situ absorption spectroscopy is a powerful tool to understand structure formation processes. In this thesis, I use in-situ absorption spectroscopy during the drying of blade-coated films and during solvent vapor annealing (SVA). In these two processes, important structure formation processes take place, which strongly depend on the initial aggregation state of the solution or the thin film, respectively. Understanding these structure formation processes is crucial to understanding the reasons for nanostructure changes in this thesis.

I established in-situ absorption spectroscopy as a fully automated tool integrated into the regular blade coating procedure. Since the complete data analysis is also included in the measurement procedure, it enables in-situ measurements during the coating of every thin film, requiring no additional effort. Hence, during the work on every project, a large database of in-situ absorption spectra is generated. Therefore, even projects where the whole structure formation process is not of interest contribute to this valuable knowledge database. This can also be accessed in other projects or to correlate the absorption spectra at the same spot before and after the structure formation process.

The first section deals with the automated blade coating and acquisition process, which also captures dark and reference spectra (3.2.1). The following section discusses the automated extraction of spectra representative of the structure formation process (3.2.2). This is followed by the last step of the in-situ absorption spectroscopy procedure during blade coating, the additional automated data analysis (3.2.3). The last section explains the modifications for similar in-situ absorption measurements during SVA (3.2.4).

3.2.1 Automated In-Situ Measurements During Blade Coating

This section describes the fully automated blade coating and spectra acquisition protocol. The spectrometer continuously measures the spectrally resolved intensity. A dark spectrum and a reference spectrum of the white light passing through the bare glass substrate are required to evaluate the absorption spectra from the spectrometer signal. The coating process is designed to directly include the dark and reference spectra in the acquired time series, making additional dark and reference measurements obsolete. This

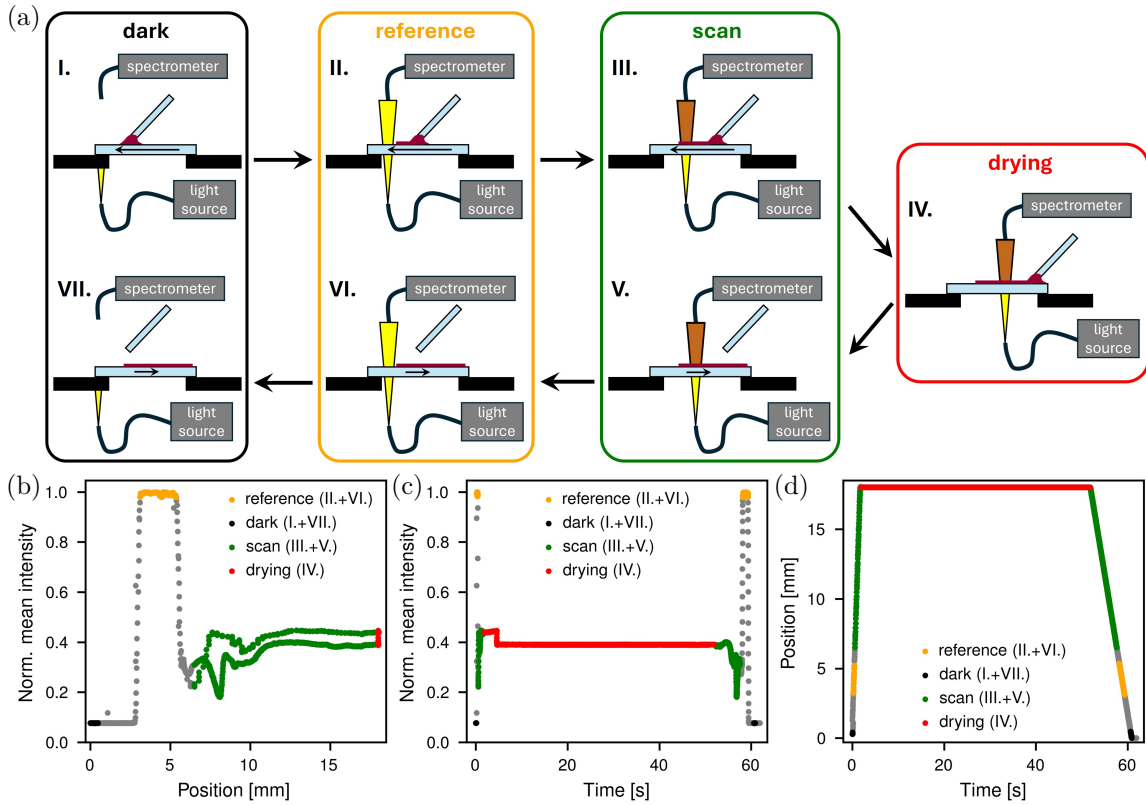


Figure 3.2: (a) Sketches of the seven different stages of in-situ measurements during the blade coating process grouped into dark measurements (I.+VII.), reference measurements (II.+VI.), scans over the sample (III.+V.), and the time-resolved drying at a fixed position (VI.). An arrow indicates the horizontal motion of the sample with the sample holder. (b)–(c) Normalized transmitted mean intensity in a selected spectral range of interest of an example measurement in dependence of (b) the position of the sample holder and (c) the elapsed time since starting the coating process. (d) Position of sample holder as a function of time. The different stages (box-colors in (a)) of the in-situ measurement are colored respectively in the data in (b)–(d). Own unpublished data.

has the additional benefit of a very short time difference between the reference measurement and measurements of the sample, minimizing the impact of possible light source instabilities.

In our blade coating process (see Figure 3.2 (a)), the substrate is moved while the blade and the measurement spot remain stationary. Thus, the measurement spot effectively moves on the sample during the horizontal motion. When the measurement spot moves over positions with the bare substrate (Figure 3.2 (a) II. and VI.), the reference measurement can be automatically extracted. The dark measurement can be extracted at positions where the sample holder blocks the beam path (Figure 3.2 (a) I. and VII.).

When the substrate moves, the blade spreads a thin fluid film on the substrate (I.–III.). When the blade reaches the end of the substrate, the substrate rests until the film is dry (IV.). Then, the blade is elevated, and the substrate is moved back to the start position (V.–VII.). The in-situ spectra during drying are measured at the end position

of the coating process (IV.). This is the most desired part of the complete time series, but also the parts of the coating process, where the measurement point moves of the sample contain valuable information. In these scans over the liquid thin film (III.) and over the dry thin film (V.), absorption spectra of the solution and thin film are measured at numerous different positions. Therefore, the whole measurement sequence can be divided into several valuable stages, also outlined in Figure 3.2 (a)):

- I. Dark measurement blocked by the sample holder
- II. Reference through the bare substrate
- III. Scan over the liquid thin film
- IV. Drying process at one position
- V. Scan over the dry thin film
- VI. Reference through the bare substrate
- VII. Dark measurement blocked by the sample holder

An accurate mapping of the spectrometer timestamps to the motor positions is necessary to distinguish between the stages. This is accomplished by precisely synchronizing the motor control and the spectrometer acquisition from the same Python script. Results of the mapping between spectrometer timestamps and the motor positions are displayed in Figure 3.2 (d). For better visualization of the coating process and the associated recorded spectra, the normalized transmitted mean intensity in a selected spectral region of interest of an example measurement is displayed in Figure 3.2 (b) and (c), depending on the position and time. The dark stages (I. and VII.) and the drying process (IV.) are uniquely linked to the positions of the sample holder and the motion's end position, respectively. The reference position can change for different samples depending on solution backflow. Thus, the analysis software dynamically adjusts the reference range.

3.2.2 Automated Extraction of Relevant Spectra

Only a small subset of the acquired data is relevant for further data analysis and plotting. In typical thin films coated from the fast-drying solvent chloroform, the relevant changes usually occur in less than 1 s. This means that out of the approximately 50 s measured in the drying stage IV. (see Figure 3.2 (c)–(d)), only less than 2 % of the spectra must be considered for further analysis as they show relevant changes. Therefore, an automated extraction of the relevant spectra is needed, which is discussed in this section.

I use two different methods to extract the data. Both involve evaluating a spectral change metric (SCM) to automatically detect the degree of spectral change over the whole spectrum between two time steps separated by Δt . To calculate the SCM, at first, a spectrum with a time shift Δt (e.g., $\Delta t = 25$ ms) before the current spectrum is subtracted from the current spectrum. The SCM is then given by the mean (averaged over the photon energy E) of the absolute value of this difference spectrum:

$$SCM(t) = \frac{1}{N} \sum_{i=0}^N |A(t, E_i) - A(t - \Delta t, E_i)| \quad (3.1)$$

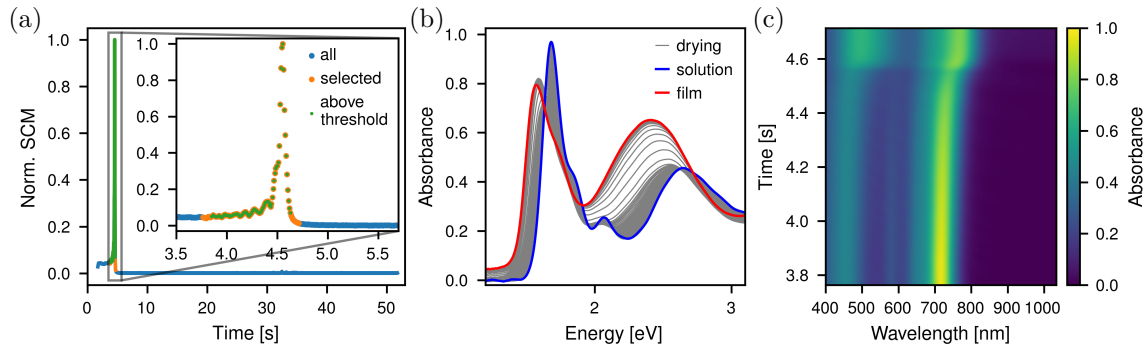


Figure 3.3: (a) Example of the normalized spectral change metric (SCM) for the whole drying phase with an inset of the more relevant range around the film formation process. The SCM is calculated by the mean of the absolute value of the difference to the spectrum 25 ms before the acquired spectrum (more details in main text). All spectra above the threshold (here 0.05) and an additional 10 spectra before and after this range are selected for further data processing. (b)–(c) All selected absorption spectra of this P3HT:Y12 sample plotted (b) as 1D profiles, and (c) in 2D in dependence on the time with color coded absorbance. Own unpublished data.

Here, A is the absorption spectrum, which depends on the acquisition time t and the photon energy E . N is the number of averaged spectrometer pixels in the relevant spectral range, and the index i enumerates the pixels with the corresponding photon energy E_i . Finally, the SCM can be normalized to obtain values of the normalized SCM between 0 and 1. An example of this normalized SCM during the whole drying stage is displayed in Figure 3.3 (a) with an inset of the more relevant range around the film formation process.

The first method of extracting relevant data is defining a threshold value for the spectral change metric, above which the drying dynamics are considered significant. In this way, the start and end points of the plotted time interval can be defined as the first and last points above the threshold. This is done in Figure 3.3 (a), where an additional 10 data points before and after the threshold were also added to soften the cutoff. With this approach, a fully automated extraction of spectra in equidistant timesteps during strong drying dynamics is possible, as shown in Figure 3.3 (b)–(c). The only disadvantage is that slow spectral changes occurring early in the solution stage or while the film is almost dry are not displayed. Alternatively, many spectra must be plotted and analyzed.

This problematic aspect is tackled in the second method of automated extraction of relevant spectra during drying. Instead of using equidistant time steps, it uses equidistant spectral change steps. This means that the density of extracted spectra is high where the SCM is high and low where the SCM is low. Therefore, the extracted spectra are scattered across the whole measured time range but still resolve the relevant spectral changes well.

To achieve this, a normalized cumulative sum over the SCM from Figure 3.3 (a) is evaluated (displayed in Figure 3.4 (a)). The cumulative sum over the SCM possesses contributions due to the drying dynamics but also due to the random noise of the spectra. Random noise results in a linearly increasing cumulative sum. Therefore, the linear increase in the dry stage at the end of Figure 3.4 (a) can mainly be attributed to random noise. A partial noise correction can be done to avoid an overrepresentation of almost

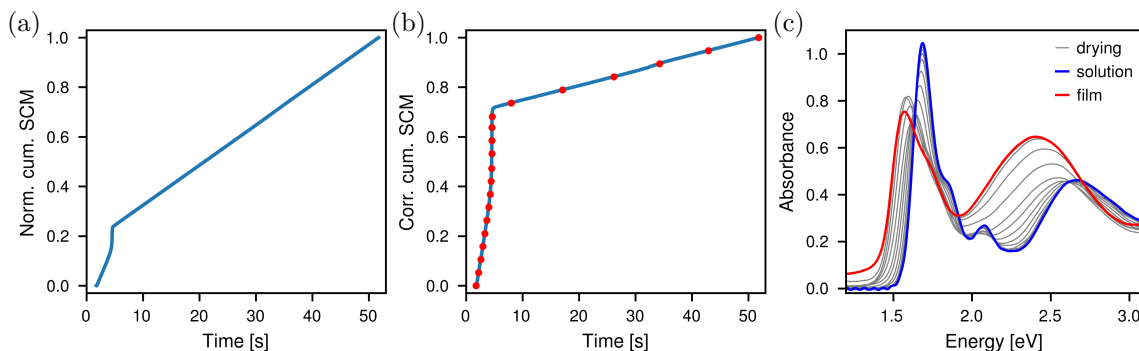


Figure 3.4: (a) Normalized cumulative sum over the SCM from Figure 3.3 (a). (b) Cumulative SCM from (a) corrected by 90% of the slope at the end of the measurement and normalized afterward. 25 spectra with equidistant corrected cumulative SCM (red points) are extracted and plotted in (c). Own unpublished data.

identical dry spectra. Therefore, a line through the origin with 90% of the slope at the end in the dry stage can be subtracted from the cumulative sum, resulting in the corrected cumulative SCM in Figure 3.4 (b).

Then, an arbitrarily defined number of spectra (here 25) is extracted from equidistant points on the corrected cumulative spectral change scale (see red points in Figure 3.4 (b)). The resulting spectra are displayed in Figure 3.4 (c). As intended, spectra from the complete measurement range are shown with a strong focus on the same strong drying stage as in the first approach with equidistant time steps. But now they also cover possible further structure formation dynamics disregarded by the first method.

Whether equidistant time steps during the strong drying phase or equidistant spectral change steps during the whole measurement are more valuable depends on the purpose of analysis. Since both methods require negligible computing time, evaluating the in-situ absorption spectra during the drying process with both methods is, therefore, the best option. This allows for the choice of a method based on direct comparison.

3.2.3 Additional Automated Data Analysis

To add further scientific value, data analysis of the extracted spectra can directly be included in the same Python script. In Figure 3.5 (a), a simple example is displayed, where the peak positions of two peaks in the absorption spectra of P3HT:Y12 blends are tracked. Beyond that, complete curve fits of the absorption spectra or other more complex analysis procedures are also possible in the same way. Figure 3.5 (b) shows an example of the time dependence of fit parameters from a drying P3HT film (the solution was pre-aggregated by the CID treatment presented in Chapter 9). The included data analysis offers the possibility for direct quantitative feedback on the processed film within a few seconds after processing. Thus, it can give direct guidance for processing the next film, making the interpretation of the experiments immediately accessible.

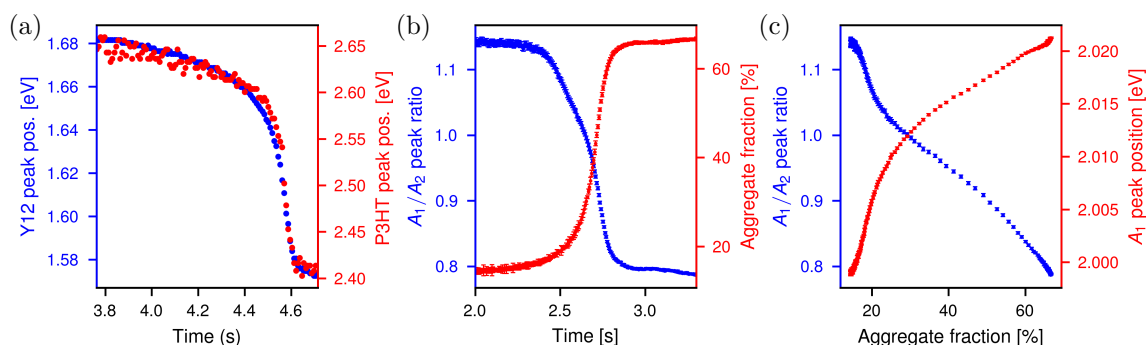


Figure 3.5: (a) Peak positions of peaks mainly attributed to Y12 and P3HT respectively tracked from the in-situ absorption spectra of the P3HT:Y12 blend in Figure 3.3 (b). (b) Aggregate fraction and peak ratio between the first two vibronic peaks extracted from fits of the in-situ absorption spectra from a drying P3HT film processed from a pre-aggregated solution treated with the CID treatment from Chapter 9. (c) Peak ratio between the first two vibronic peaks and position of the first vibronic peak from the same measurement as (b) plotted over the aggregate fraction. Own unpublished data.

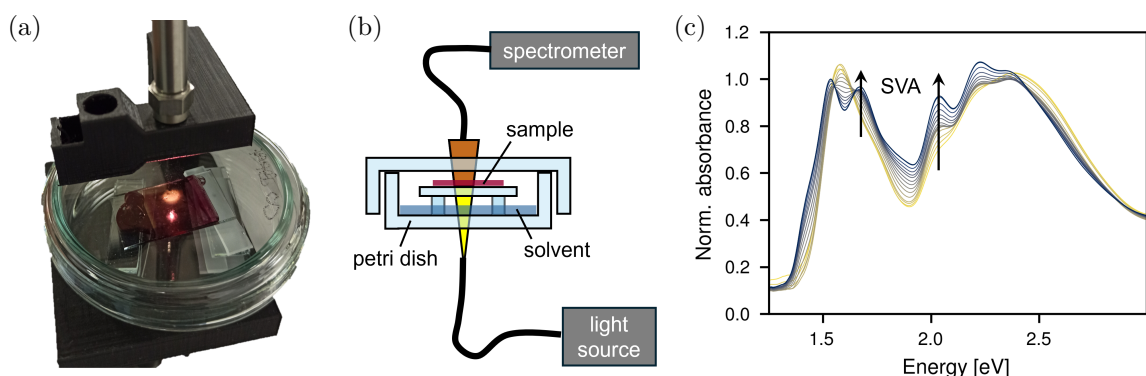


Figure 3.6: (a) Photograph and (b) sketch of the solvent vapor annealing (SVA) setup. (c) Extracted spectra with equidistant spectral change steps from SVA of a P3HT:Y12 film with Toluene from Chapter 10 (yellow before SVA, black after SVA; spectral evolution during SVA indicated by arrows). (c) Adapted with permission according to the CC BY 4.0 license from Eller et. al.³⁶ (Chapter 10) Copyright 2024 The Authors. Advanced Energy Materials published by Wiley-VCH GmbH.

3.2.4 Automated In-Situ Characterization During Solvent Vapor Annealing

The in-situ solvent vapor annealing (SVA) measurements and the corresponding analysis are similar to the in-situ measurements during blade coating but simpler. The setup for the in-situ SVA measurements is displayed in Figure 3.6 (a) and sketched in (b). The bottom of a petri dish is completely covered with solvent, the sample is placed above the fluid level, and the petri dish is closed with a lid. The white light is passed through the petri dish, the solvent, and the sample. Since no moving sample stage is involved, the reference measurement cannot be extracted from the measurement itself. Therefore, a separate reference measurement is done manually, where a blank glass substrate replaces the sample. Along with the reference measurement, a dark measurement is also

automatically done by electronically closing the shutter of the light source.

The extraction of selected relevant spectra from the complete time series of absorption spectra during SVA is identical to the spectra selection for blade coating. For SVA, the extraction method with equidistant spectral change steps over the complete time range is especially valuable as there is often more than one typical timescale involved during SVA. An example of extracted spectra during SVA with equidistant spectral change steps is displayed in Figure 3.6 (c).

3.3 Accelerated GIWAXS Routine

Since the data analysis is now completely automated and included in the in-situ UV-Vis absorption spectroscopy during blade-coating and SVA, the theoretical background from Section 2.3 allows drawing conclusions on the nanostructure in real-time. However, when an in-depth understanding of the nanostructure is desired, the vast amount of nanostructural information accessible with GIWAXS measurements (see Section 2.2) is indispensable. Therefore, the strategy in this thesis is usually fast screening using in-situ UV-Vis absorption spectroscopy followed by slower GIWAXS measurements of promising samples. Even though GIWAXS integration times are much longer, efficient workflows and quick feedback on the nanostructure are also highly beneficial here, which is the aim of this section.

An Xeuss 3.0 X-ray scattering machine in our laboratory makes almost continuous measurements possible around the year. In contrast to measurements at synchrotrons, the photon flux is much lower. Still, the extensively available measurement time allows for a huge sample throughput at any time of the year with a flexible machine booking. Thus, research does not rely on a few beamtimes a year across the world at fixed dates with a few days at each beamtime for measurements shared between several group members. A further significant advantage is that the instrumentation is always identical, so identical measurement and analysis routines are possible, and all peculiarities specific to the setup are well-known. This opens the possibility for automation routines to streamline the research. Experienced researchers benefit from a more time-efficient workflow like novices, who can use established protocols directly. I analyzed the whole workflow from the alignment of the samples (3.3.1), over the measurement of the samples (3.3.2), the standardized pre-analysis and screening of the results (3.3.3) to the material-specific peak fitting (3.3.4), identified the bottlenecks and developed automated solutions to these bottlenecks.

3.3.1 Automated Sample Alignment Procedure

The measurements can be easily automated via measurement macros with minimal human interaction. However, the measurements require a precise alignment of the samples. The semi-manual standard sample alignment procedure (see Figure 3.7) is challenging to automate and consumes a considerable workforce. Thus, it is the bottleneck in the GIWAXS measurement process, limiting its efficiency. I developed and established a very reliable, fully automated GIWAXS alignment process (see Figure 3.8), strongly enhancing the efficiency of GIWAXS measurements. Only about 10 min of working time is required to change samples and specify the measurement positions and settings. This

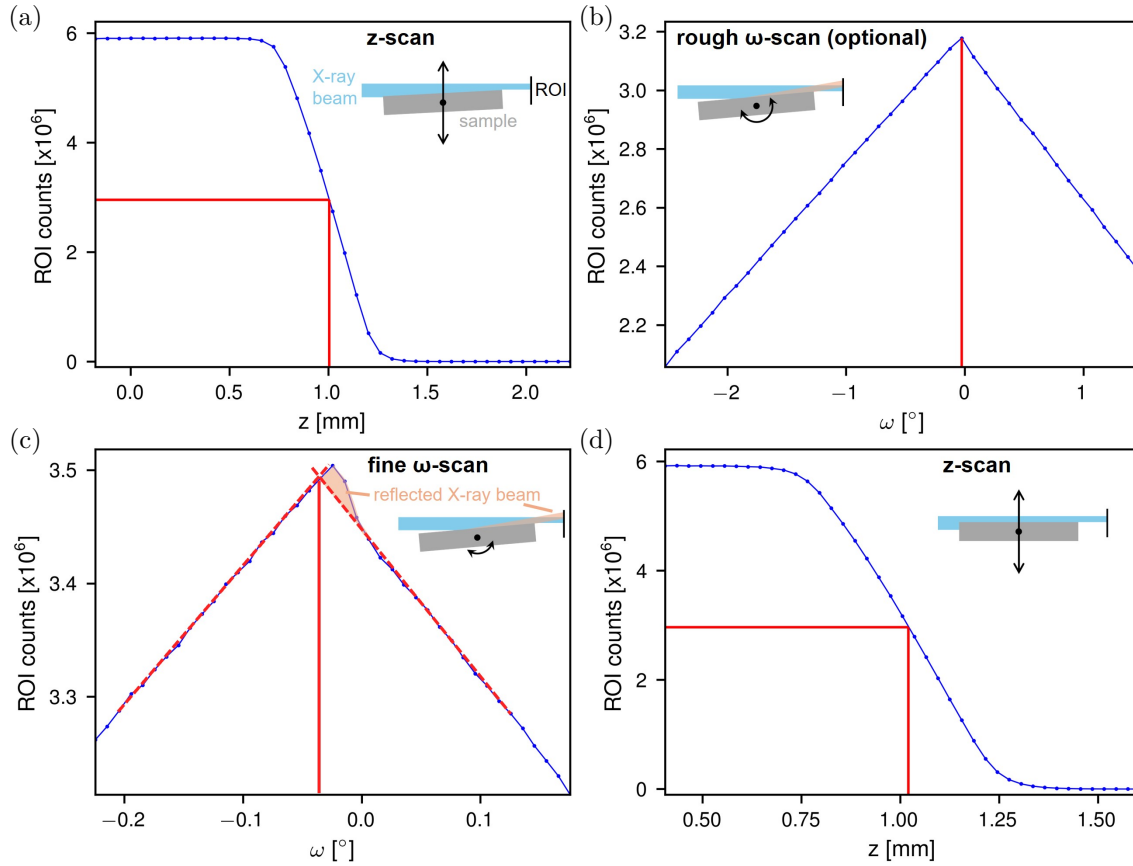


Figure 3.7: Standard semi-manual alignment procedure. The steps of the alignment procedure are (a) a z -scan for a first height calibration (go to z at half maximum), (b) optionally a rough ω -scan over a broad angular range to ensure an alignment in the right angular range (go to maximum), (c) a finer ω -scan (extrapolate the right flank, then go to intersection with left flank), (d) a further z -scan with the now flat substrate (go to z at half maximum). Own unpublished data.

section explains the automated alignment procedure in detail and compares it with the conventional semi-manual alignment procedure.

Since in GIWAXS usually very shallow angles of incidence (α_i) are used (typical values for organic semiconductors with Cu K_α X-ray source $\alpha_i \approx 0.16^\circ$), a very precise alignment of the ω -angle (tilt angle toward beam) and the z -position (height) of the sample is required. With a laboratory X-ray source, monitoring the direct beam in a suitable, freely chosen region of interest (ROI) on the detector is possible for alignment. This is usually not possible at synchrotrons, where a photodiode usually monitors the direct beam intensity to avoid beam damage on the detector.

For the vertical alignment, a scan in z -direction (vertical) is done, where the intensity in an ROI around the direct beam is tracked (see Figure 3.7 (a)). The desired position is at half of the maximum intensity, with the beam center at the sample's surface. The z -alignment is also suitable for automation in this standard procedure and does not require changes (Figure 3.8 (a)).

The standard ω -alignment (possibly split into a rough and a finer scan) is similar to the z -alignment. The intensity of the same ROI around the direct beam is tracked during an

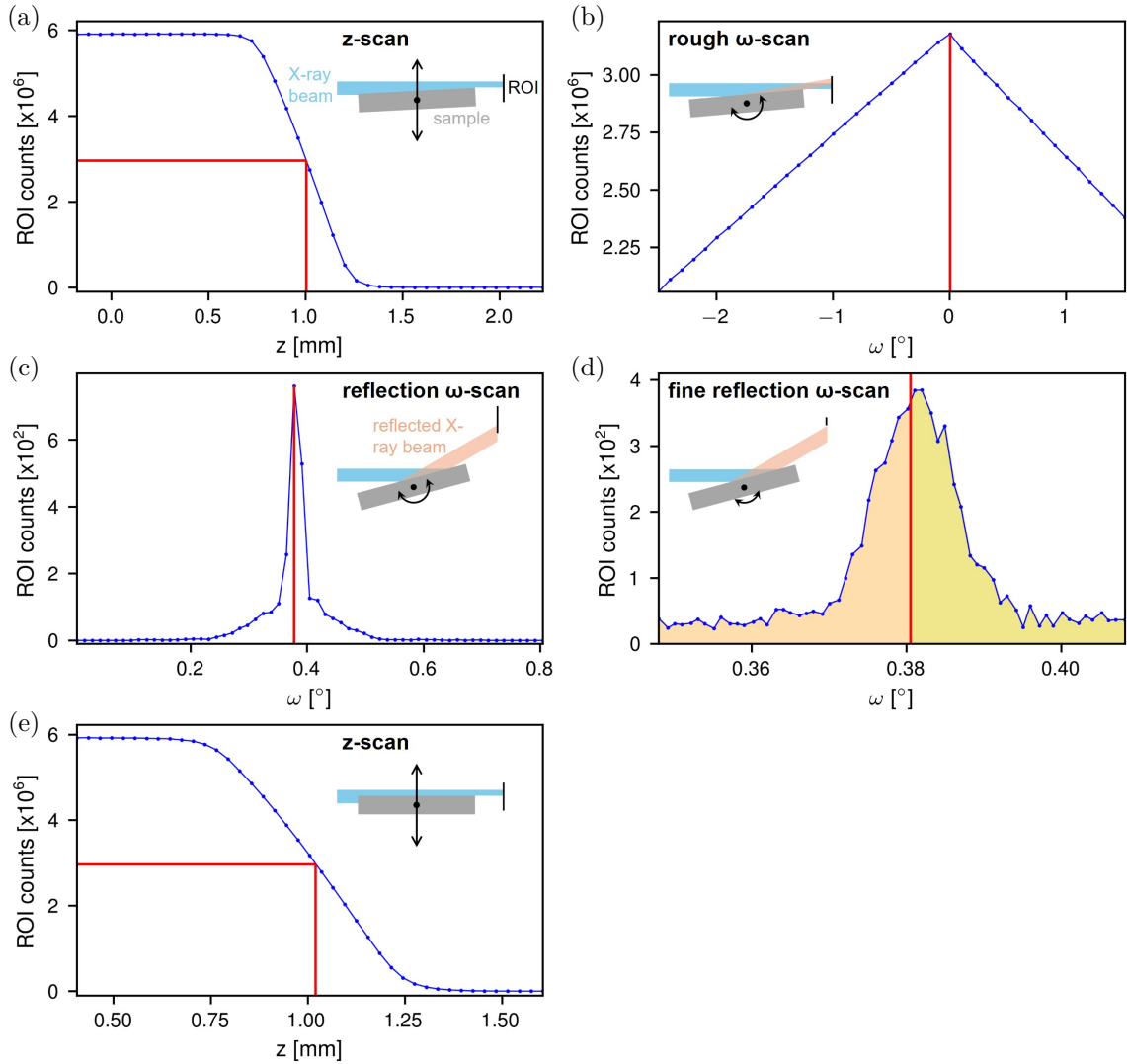


Figure 3.8: New fully automated alignment procedure exploiting the position of the reflected beam on the detector. The steps of the alignment procedure are (a) a z -scan for a first height calibration (go to z at half maximum), (b) a rough ω -scan over a broad angular range to ensure an alignment in the right angular range (go to maximum), (c) a first ω -scan around an ω -rotation of about 0.4° (go to maximum), (d) a finer ω -scan with smaller ROI (go to center of mass), (e) a further z -scan with the now flat substrate (go to z at half maximum). Own unpublished data.

ω -scan (see Figure 3.7 (b)–(c)). A larger fraction of the beam is blocked when the sample is tilted to the beam or the detector. Thus, at the ω -position of the peak intensity, the sample surface should be parallel to the beam. However, this view only considers the direct beam but not the reflected beam. The reflected beam adds intensity to the ROI at ω -values slightly above $\alpha_i = 0$, shifting the peak position to higher ω -values (see sketch in Figure 3.7 (c)). Therefore, $\alpha_i = 0$ cannot be found by searching for the peak position but at the intersection of the extrapolated slopes, where no reflection signal is in the ROI (see Figure 3.7 (c)). This selection is usually done manually using two triangle rulers on the screen. Automation of this process would be possible by fitting the slopes and calculating the intersection. However, this process possesses significant uncertainty, is prone to errors, and cannot even be used in measurement macros written

in the proprietary programming language.

Since most sample surfaces are very flat, there is a well-defined reflected beam signature on the detector. The law of reflection determines its position. In turn, the position of the reflected beam can be used to extract the α_i and, therefore, to conduct the ω -alignment. This is done by setting the ROI to an elevated position on the detector and conducting an ω -scan around the ω -value, where the reflected beam is expected to reach the ROI. When it passes the ROI, there is a sharp peak in the ω -scan (see Figure 3.8 (c)). In a second refined scan with decreased height of the ROI and finer ω step size, a very precise and reliable ω -alignment is possible (see Figure 3.8 (d)). Here, the center of mass of the measured peak is used to extract the angle of incidence α_i very precisely. The only problem with reliability, which can occur with this procedure for sufficiently smooth surfaces, is when the sample is significantly tilted compared to the previous sample and, therefore, to the starting point of the ω -alignment. Then, the range of the first reflection ω -scan (Figure 3.8 (c)) is too small to capture the reflected beam in the ROI. Instead of increasing the scan range drastically, the peak position of a standard ω -scan with the ROI on the direct beam and low resolution is used as the starting point for the ω -scan in reflection geometry (Figure 3.8 (b)).

At the first z -alignment, a possibly tilted substrate can lead to a shift in the z -alignment position. Therefore, in the standard alignment as well as in the fully automated alignment, a further z -scan with a smaller range and higher resolution finishes the alignment procedure (Figure 3.7 (d), Figure 3.8 (e)).

This fully automated alignment procedure (Figure 3.8) did not fail for a single organic semiconductor sample on glass or silicon so far after several hundred aligned samples. Compared to the standard alignment procedure (Figure 3.7), its accuracy and reliability are higher, requiring neither human interaction nor human supervision. Thus, it significantly improves precision and efficiency by removing the bottleneck in the measurement process. This impact is even more critical when X-ray sources with higher flux are used. The higher flux enables a higher sample throughput, which is only possible with an efficient, fully automated alignment procedure.

Since the alignment procedure is no longer the limiting factor, the measurements of single samples can also be split into different independently aligned positions on the sample. I usually measure three different positions on the sample to obtain a better representation of the average nanostructure and the spread of the results depending on the position. Moreover, it helps to identify artifacts or scattering features that only occur at single positions and are not characteristic of the complete sample.

3.3.2 Automated Measurement Procedure

Since the alignment procedure is now fully automated, the whole measurement procedure can be conducted in one fully automated procedure. This section elaborates on the structure of this fully automated procedure. A special focus lies here on closing the gap between the two parts of the detector to prevent the loss of important scattering information lying in the gap. Keeping the fully automated pre-analysis following the measurement procedure in mind, the gap can be easily closed without increasing the complexity of the measurement or analysis routine.

The measurement procedure consists of a large series of commands saved in a measurement macro. To minimize the required work and the risk of mistakes, just variables at the start of the measurement macro are changed between different measurement series, while the macro itself is unchanged. The variables are, e.g., the positions of the samples, the sample-to-detector distances (SDDs), and angles of incidences (α_i), which should be measured, as well as the exposure times. The macro is designed in a way that allows different numbers of samples and various numbers of measurements with different settings to maximize its versatility.

One point to consider is that the 2D detector is split into two detector parts with a horizontal gap between the detector parts. Scattering features in this detector gap are not recorded, and cake cuts including parts of the gap can have artifacts close to the gap. The manufacturer offers a measurement mode called *multidetector*, which conducts measurements at different detector positions, closing the gap and significantly broadening the measurement range. However, this comes at the cost of a reduced signal-to-noise ratio (SNR). In the *multidetector* mode, the SNR in the whole image is determined by the minimum SNR present. In the case of a *multidetector* acquisition with two measurements to close the detector gap, the measurement time is doubled at an unchanged SNR. When only the detector gap should be closed, but the measurement range is sufficient, a slight vertical detector shift is also enough. Then, most parts of the images lie in the overlap of the two detector positions, and in these parts, a better SNR is present when both measurements are considered. An automated pre-analysis (described in detail in the next section) will follow the measurements in any case. In this pre-analysis, an automated merging of the measurements at shifted detector positions can be included. Thus, the complexity of the whole workflow is not increased. In this way, the detector gap is closed while maintaining all gained data and, therefore, also SNR. The SNR is solely lower in some parts of the resulting merged images, which were part of only one detector position (see Figure 3.9 (a)).

Since the automated pre-analysis in the following section allows for fast visualization of the measurements, this tool can also be used to get an overview of the current state of the measurements while the measurements are still running. With this functionality of the pre-analysis in mind, it makes sense to divide the measurements into several loops over all samples, where the single acquisition times are relatively short (usually 30 min per detector position). This is a valuable tool as suitable acquisition times may vary between samples, e.g., due to sample thickness, amount of ordered material, and electron density contrast. Thus, there is no risk that the SNR is too low due to insufficient acquisition time. Also, strongly scattering samples do not occupy the X-ray scattering machine longer than required.

Additionally, an AgBeh calibrant and an empty beam (acquisition of direct beam without any sample) are measured in every cycle. These are especially safety features to track down possible changes in detector positioning, beam flux, or beam shape in case there are changes in measurements during the routine.

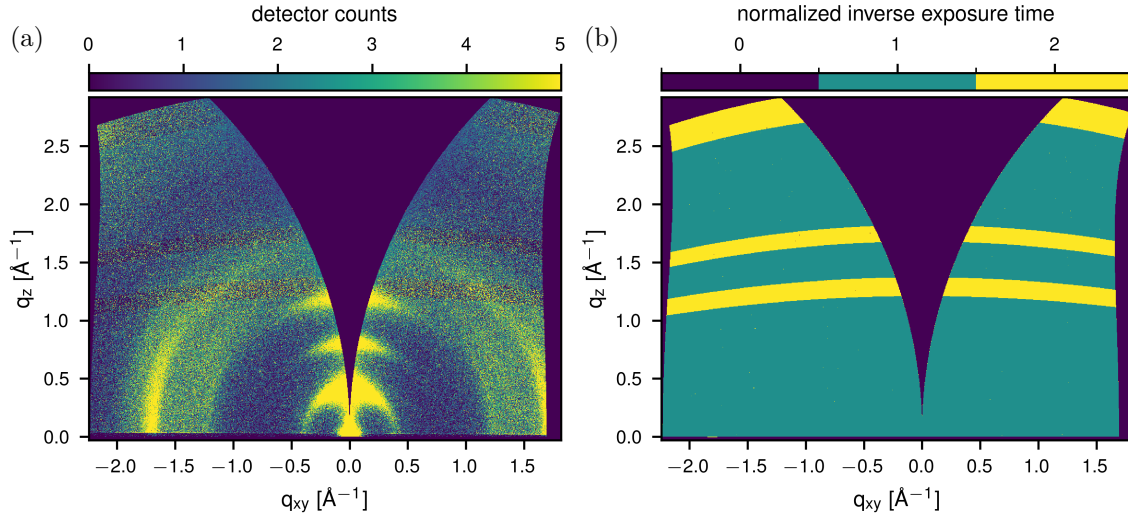


Figure 3.9: (a) Example of merged data with low counts and no interpolation between pixels, where the reduced signal-to-noise ratio (SNR) in the detector gaps is still visible (examples, where this is not the case anymore in Figure 3.10 further down and in Chapters 10, 12, 13, and 14). For comparison, (b) shows a 2D map, which was used for scaling the counts to the same virtual integration time. Own unpublished data.

3.3.3 Automated Pre-analysis

The data analysis is divided into two parts. The pre-analysis is a standardized analysis applicable to all measurements, regardless of the material system. Its role is to convert the raw data into suitable formats to start the second part of the analysis, a more detailed and material-specific analysis, like peak fitting cake cuts. The automated pre-analysis assigns the raw data to samples and measurement settings, merges measurements with identical measurement settings, and saves them with meaningful file names and meta-information. After the q -conversion of the merged data, cake cuts in the vertical and horizontal directions are extracted. Moreover, by plotting the data, the automated pre-analysis directly gives an overview of the data. In this section, I explain the different steps of the automated pre-analysis that I developed.

All measurement files contain necessary meta-information, such as motor positions and acquisition time, in their header. The x -position (horizontal shift perpendicular to beam) is used to identify the sample. The ω -position determines the angle of incidence (α_i) by the difference to the 0-position from the alignment of the sample. Therefore, an assignment of samples to positions and the alignment result of ω is first required. These positions are automatically read from dummy files saved at the end of the alignment of every sample and need a manual assignment of the sample names only once.

With this information, all measurements of the same sample with identical α_i and SDD can be identified for merging. The shift of the detector position and the acquisition times are also read from the header. This enables an automated merging of an arbitrary number of measurements at an arbitrary number of different detector positions with arbitrary acquisition times. Due to the detector gaps, dead pixels, and possibly different numbers of measurements or different acquisition times at various detector positions, the effective total acquisition time per pixel varies across the image. Therefore, the intensity

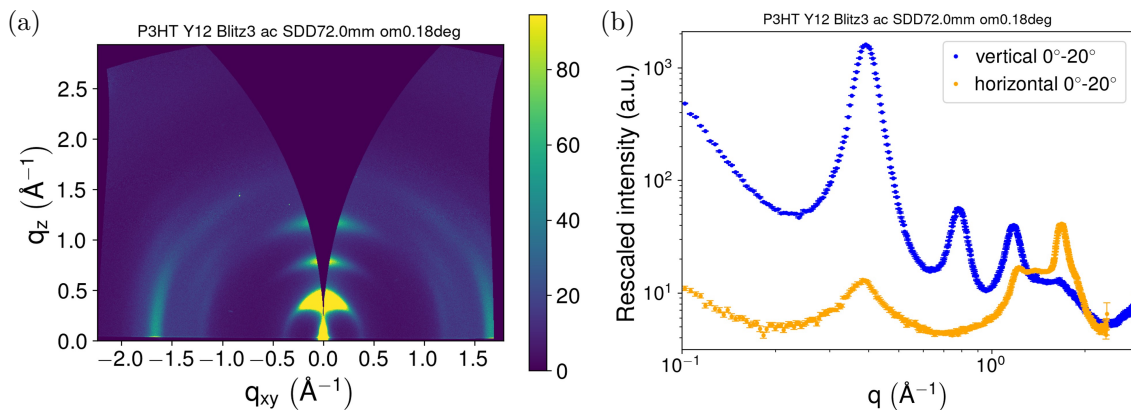


Figure 3.10: Exemplary output from the automated pre-analysis with (a) a 2D map and (b) extracted cake cuts in the horizontal and vertical direction. Apart from the plots displayed here, the data for further analysis is also saved. Own unpublished data.

of every pixel is scaled with its effective total acquisition time to a virtual acquisition time specified in the analysis routine (example of a normalized inverse acquisition time map used for rescaling in Figure 3.9 (b)). This also makes the scattering intensities of samples measured with different acquisition times easily comparable.

The merged data of every sample with every combination of α_i and SDD is saved with file names containing this information. The meta-information in the header of the files contains the meta-information describing the merged sample, making it fully compatible with any analysis applied to non-merged raw data. In the merged file headers, the correct α_i is included instead of the uncorrected ω -position from the initial measurements, allowing to read the α_i directly from the header (valuable for later batch processing).

The merged data is still raw data, where the detector gap is closed but is still not converted to reciprocal space (q -space). The conversion to q -space is essential for the data interpretation, as it is outlined in detail in Section 2.2.1. The q -conversion of the 2D data, which also introduces the missing wedge in the vertical, is done with the proprietary software XSACT via batch-processing of all files. Thus, it is the only step of the automated pre-analysis, which is outsourced to other already existing software.

In the last step, the q -converted 2D data are plotted, and cake cuts in the horizontal and vertical directions are extracted, saved, and plotted (example in Figure 3.10). The 2D and cake cut plots offer the possibility for a quick first control of the measurements and are already a valuable resource for a detailed qualitative interpretation of the data. For quantitative analysis, the cake cuts are usually fitted, which is now possible with the saved data and will be explained in detail in the next section.

The automated pre-analysis is a highly automated standard approach identical for all GIWAXS measurements, saving plenty of working time that can be spent on other tasks instead of routine work. It is only necessary to provide sample names once at the measured positions. The automation also allows dividing the measurements into shorter measurements without any extra work to get faster feedback, which would not be practical for manual data analysis. The automated pre-analysis is already widely used in

the complete working group and is valued as an important tool in every GIWAXS data analysis.

The software is designed to allow an easy implementation of further modules in the future. The different parts of the pre-analysis are performed after each other and repeated in a non-stop loop. The necessary meta-information of measurements already considered for the analysis is stored in a .json file. When further measurement files are added to the folder, the corresponding new data are directly merged with the previous data known from the .json file. Also, for plotting, only new q -converted data is considered. This fast reaction to newly added data opens the door to a continuous real-time pre-analysis on the measurement PC (or any other PC with cloud access) upon every new measured file. Therefore, only the implementation of a q -conversion module is still necessary. Then, it is possible to directly access and view the merged and plotted data at any time instead of the raw data, completely removing the standard pre-analysis task for every user.

3.3.4 Standardized Automated Material-Specific Analysis

In contrast to the universal pre-analysis, the detailed analysis of the extracted cake cuts is material-system specific. However, it is also possible to establish general routines, especially for related material systems – here, disordered organic semiconductors. This section outlines the standardized material-specific analysis of GIWAXS cake cuts of organic semiconductors. Sections 2.2.2 and 2.2.3 provide the theoretical background for interpreting the cake cuts. Hence, this section only deals with the implementation.

As introduced in Section 2.2.3, scattering peaks can be modeled by pseudo-Voigt peaks. Thus, the whole cake cuts in vertical and horizontal direction can be modeled by a superposition of a certain number of pseudo-Voigt peaks and a background consisting of a decay at small q -values (GISAXS range) and a constant contribution. Therefore, the general fitting model is the same for all samples. Still, the number of peaks, necessary constraints, and suitable starting values for different fitting parameters usually vary.

Since the fitting model is complex and involves many fitting parameters, performing the fits in a multistage process is sometimes also necessary. Therefore, only single parts of the cuts are fitted initially, while other contributions are fixed. In the end, a global optimization of all fit parameters is performed.

The multistep fitting process already ensures that all peaks are fitted reliably, but these complex fits have two main challenges. On the one hand, sometimes, even when the fitting curve fits very well, confidence intervals of single components of the fits can get very large. This often indicates that the fitting model is too unspecific and requires more constraints, e.g., to fix a peak position. Another reason can be that the model is generally unsuitable to describe the fitted cut (e.g., an essential contribution is missing, or unsuitable constraints are chosen). To identify the problem of too large confidence intervals, it is very valuable to evaluate the confidence intervals of the whole fit and every component and display them directly with the fit result. An example is depicted in Figure 3.11. Further examples are in Figure 1 (g)–(j) of Chapter 10. The example in Figure 3.11 clearly shows that most peaks are fitted with exceptional confidence but also raises awareness that, e.g., the broad peak in the q_z direction possesses significant uncertainty.

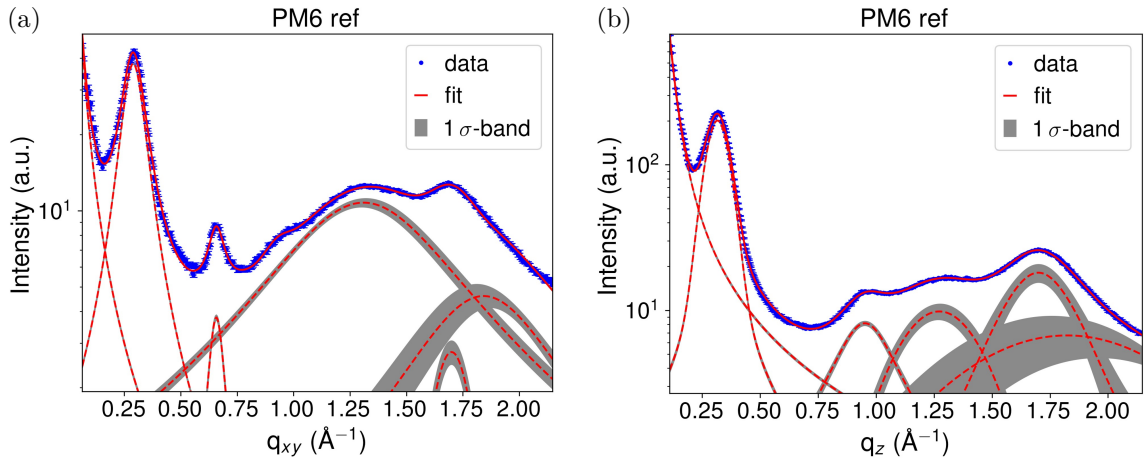


Figure 3.11: Exemplary fits of cake cuts extracted from a GIWAXS measurement of PM6 (a) in the horizontal direction and (b) in the vertical direction. The data is displayed in blue, the total fit curves are in solid red lines, and the single components of the fit are in dashed red lines. The 1σ -intervals of the uncertainty of the whole fit function and the single components are displayed as grey bands. Own unpublished data.

On the other hand, there may also be fit parameters that do not contribute sufficiently to the scattering profile to be evaluated. Critical parameters are especially pseudo-Voigt mixing parameters of minor peaks, where it is impossible to differentiate between a Gaussian and a Lorentzian peak shape. These unspecified parameters cause problems when evaluating the uncertainties of other fit parameters and the confidence intervals. To overcome this problem, I developed a fitting routine that identifies the parameters that are not significantly influencing the outcome. Subsequently, it sets them to a constant value in the next fitting cycle. This loop is repeated until all insignificant parameters are omitted, and a meaningful fit result with all uncertainties and confidence intervals can be evaluated.

Even though the explicit modeling of all scattering features is specific to the material system, the key aspects described in this section enable a reliable automated analysis for all samples of the same material system. Other material systems only require some changes to the existing routine.

4 Thesis Summary

This thesis aims to achieve tailored nanostructure control in organic semiconductors. Accelerated nanostructure analysis helps to achieve this goal. The thesis addresses its issue in eight chapters and is grouped into three blocks. These three thematic blocks and the corresponding articles are also shown in Figure 4.1. Section 4.1 gives a short overview of the structure of the thesis while Section 4.2 elaborates in more detail on the individual publications with a focus on my contribution to them.

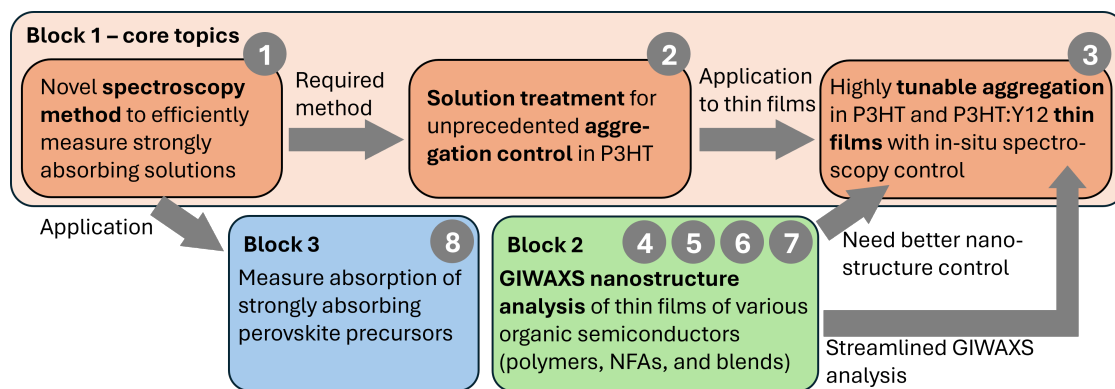
4.1 Overview of Thesis Structure

The largest block contains my personal core topics (publications 1, 2, and 3), which feature the whole process from the introduction of a new spectroscopy method to accelerate the nanostructure analysis (publication 1, Chapter 8) over the introduction of the novel CID solution treatment to control P3HT aggregation in solution (publication 2, Chapter 9), and finally nanostructure control in neat and blend thin films (publication 3, Chapter 10). Each publication requires the previous publication as the necessary starting point.

Publication 1 (Chapter 8) introduces the spectroscopy method TFFS (Thinning Fluid Film Spectroscopy, European and US patent pending), verifies its validity, and investigates its advantages and limitations. TFFS enables automated absorption spectroscopy measurements of strongly absorbing solutions within seconds. In contrast to conventional approaches involving dilution of the solutions, TFFS prevents possible artifacts from diluting solutions due to concentration-dependent interactions.

The TFFS method enabled in publication 2 (Chapter 9) a comprehensive study of more than 600 solutions treated with the current-induced doping (CID) treatment introduced in this publication. Thus, a deeper understanding of the treatment can be achieved by screening an ample parameter space influencing the solution aggregation.

With this knowledge of how the aggregate fraction and the ordering of the aggregates can be tuned via the CID treatment, in publication 3 (Chapter 10), I transfer the aggregation control in solutions from publication 2 to nanostructure control in thin films cast from CID-treated solutions. In neat P3HT films, the highly ordered aggregates from solution lead to a strongly increased molecular ordering (nanostructure control) and an up to 25-fold increase in OFET mobility (device performance control). In blends with the highly miscible NFA Y12, a strong P3HT nanostructure control is also possible via the CID treatment. Moreover, I demonstrate that Y12 nanostructure control can be achieved via solvent vapor annealing (SVA).



- 1 *Facilitating Absorption Spectroscopy of Strongly Absorbing Fluids: A High-Throughput Approach*
- 2 *Spark Discharge Doping—Achieving Unprecedented Control over Aggregate Fraction and Backbone Ordering in Poly(3-hexylthiophene) Solutions*
- 3 *Tackling P3HT:Y-Series Miscibility Through Advanced Processing for Tunable Aggregation*
- 4 *Understanding the Role of Order in Y-Series Non-Fullerene Solar Cells to Realize High Open-Circuit Voltages*
- 5 *Identifying the Signatures of Intermolecular Interactions in Blends of PM6 with Y6 and N4 Using Absorption Spectroscopy*
- 6 *Effects of the diphenyl ether additive in halogen-free processed non-fullerene acceptor organic solar cells*
- 7 *Microstructural and Thermal Transport Properties of Regioregular Poly(3-hexylthiophene-2,5-diyl) Thin Films*
- 8 *Solvated PbI_2 Clusters preceding the Crystallization of Lead Halide Perovskites – a UV/VIS In-Situ Study*

Figure 4.1: Flow chart showing the overview of the research blocks and the corresponding research articles. The numbers in the grey circles are the publication numbers attributed to the blocks.

The second block (publications 4, 5, 6, 7, Chapters 11, 12, 13, 14) consists of different publications, where I conducted the nanostructural analysis of thin films closely related to the samples in publication 3 (NFAs, blends with NFAs, and P3HT) via GIWAXS measurements in collaboration with other researchers. In these joint projects, I characterized the impact of the chemical structure of the NFA, thermal annealing, solvent additives, different solvents, and molecular weight on the nanostructure and correlated this, together with my co-workers, with device performance and results from other complementary measurement techniques to obtain conclusive pictures of the nanostructure and the structure-property relationships.

The third block (publication 8, Chapter 15) applies the TFFS method introduced in publication 1 (Chapter 8). Here, I measured the absorption spectra of perovskite precursor solutions of various concentrations and in different solvents, supplementing spectra from in-situ spin coating. The absorption spectra of the material system investigated here strongly depend on the concentration. My TFFS method enabled individual measurements of these strongly absorbing solutions with a known, constant concentration. This example nicely corroborates the need for the new, previously inaccessible, experimental possibilities that TFFS now enables for a broad range of research communities.

4.2 Individual Publications

The previous section already outlined the structure of this thesis. In this section, I want to give a more detailed summary of each article with a focus on my contributions to these articles.

In publication 1 (Chapter 8, *Facilitating Absorption Spectroscopy of Strongly Absorbing Fluids: A High-Throughput Approach*), I introduced Thinning Fluid Film Spectroscopy (TFFS), a simple and highly automatable method enabling reliable absorption spectroscopy measurements of concentrated solutions. This measurement method was necessary to allow the large parameter study of concentrated P3HT solutions with different CID treatments in publication 2 (Chapter 9) but also possesses broad application potential in many other fields. Therefore, publication 1 (Chapter 8) is more general with applications to different material systems. Beyond the basic measurement and analysis principle, I developed three exemplary measurement modes of TFFS suitable for many applications and validated the TFFS measurements with control data obtained in specialized low optical path length cuvettes. I conducted the validation over a broad concentration range to analyze the suitability of the measurement modes in dependence on the concentration.

To demonstrate the automation possibilities, I developed a spectroscopy robot covering two measurement modes that are most suitable for highly efficient and high-throughput lab work. The robot was also used for the measurements for validation and comparison of the measurement modes and for an automated temperature-dependent spectroscopy study on highly concentrated PM6 suitable for coating organic solar cells. Beyond the spectroscopy robot, I also developed an in-line setup, which can be incorporated into various pipe systems. I applied it to conduct a repeatability study and to monitor chemical reactions.

Therefore, publication 1 (Chapter 8) is the basis to enable my main research strand, with publications 2 and 3 addressing the systematic control of pre-aggregation in solution (publication 2, Chapter 9) and subsequently in dried films (publication 3, Chapter 10).

The properties of semiconducting polymers are strongly influenced by their aggregation behavior, that is, mainly their aggregate fraction and backbone planarity. However, tuning these properties, particularly the backbone planarity, is challenging. To overcome this challenge, I developed in publication 2 (Chapter 9, *Spark Discharge Doping—Achieving Unprecedented Control over Aggregate Fraction and Backbone Ordering in Poly(3-hexylthiophene) Solutions*) a solution treatment to precisely control the aggregation of semiconducting polymers, namely current-induced doping (CID). It utilizes spark discharges between two electrodes immersed in a polymer solution to create strong electrical currents resulting in temporary doping of the polymer. I designed and built a setup for reproducible CID treatments and also implemented TFFS in this setup. Therefore, I can quickly measure absorption spectra after every CID treatment step without diluting the solution. This enabled me to conduct a broad parameter study of the CID treatment of P3HT in dependency of solvent, temperature, concentration, and CID treatment strength, always as a function of the number of CID treatment steps.

Rapid doping-induced aggregation occurs upon every treatment step for the semiconducting model-polymer P3HT. Therefore, the aggregate fraction in solution can be precisely tuned up to a maximum value determined by the solubility of the doped state. I developed a qualitative model to explain the dependences of the maximum aggregate fraction, which also serves as a tool for the rational selection of suitable parameters. Besides controlling the aggregate fraction, CID also allows for strong control of the aggregate order. Remarkably, the CID treatment can yield an extraordinarily high quality of backbone order and planarization, expressed in UV-Vis absorption spectroscopy and differential scanning calorimetry (DSC) measurements. Depending on the selected parameters, an arbitrarily lower backbone order can be chosen using the CID treatment, allowing maximum aggregation control. This method may become an elegant pathway to finely tune aggregation and solid-state morphology for thin films of semiconducting polymers, which is demonstrated in publication 3 (Chapter 10).

At first, I addressed in publication 3 (Chapter 10, *Tackling P3HT:Y-Series Miscibility Through Advanced Processing for Tunable Aggregation*) neat thin films processed by blade coating the CID-treated P3HT solutions with the strongest ordering. This results in a substantial increase in aggregate ordering in the thin films, seen by UV-Vis spectroscopy and GIWAXS. Moreover, the achieved nanostructural control leads to a 25-fold increase in OFET hole mobility. The first CID treatment step is already sufficient to achieve a tenfold increase, demonstrating the great importance of the highly ordered aggregates produced by the CID treatment as nuclei for further aggregation. I could confirm this also by in-situ UV-Vis spectroscopy during drying of the thin films, where I could observe that the P3HT aggregation behavior already sets in at an earlier time with the CID treatment compared to untreated P3HT.

In addition to the study of neat P3HT thin films, the P3HT nanostructure control offers especially the potential to improve the morphology in blends with an acceptor used in organic solar cells. The high miscibility in blends of P3HT and state-of-the-art Y-series NFAs suppresses phase separation and aggregation, challenging successful charge transport to the electrodes. My approach was to use the CID treatment of P3HT solutions to enable aggregation and phase separation induced by the aggregation in blends of P3HT with Y12. This results in a broad tunability of the P3HT aggregation in the presence of Y12. At the same time, the Y12 long-range ordering is heavily suppressed by increasing P3HT aggregation.

However, I could identify solvent vapor annealing (SVA) as a post-treatment procedure leading to an extraordinarily high Y12 ordering and a further improvement of P3HT aggregation. The Y12 crystallite orientation after SVA depends on the strength of the CID treatment. I also tracked the SVA in-situ with UV-Vis absorption spectroscopy, giving immediate feedback on these nanostructure changes. The in-house GIWAXS measurements complemented the nanostructure results quickly after processing. A broad range of different degrees of aggregation of both materials can, therefore, be obtained in the final thin films solely by changing processing parameters without changing the composition of the material system.

I highly value the exchange with fellow researchers and particularly enjoyed contributing to collaborative research efforts with the common goal of understanding structure-function relationships with my expertise in nanostructural characterization using GIWAXS in publications 4–7 (Chapters 11–14).

Publications 4 and 5 (Chapters 11 and 12) are from one big joint project with a different focus on the same material systems, the polymer PM6 blended with the NFA Y6 compared to blends with the NFA N4. Blends with Y6 have better solar cell performance due to a higher V_{OC} , as also shown in publication 4 (Chapter 11). My task in this project (and the further projects in this block) was to characterize the nanostructure in thin films of the neat materials and blends via GIWAXS and contribute the nanostructural insights to the overall research question.

In publication 4 (Chapter 11, *Understanding the Role of Order in Y-Series Non-Fullerene Solar Cells to Realize High Open-Circuit Voltages*), the focus was on the different energetic disorder in the blends due to the different DOS (density of states) as a reason for the different V_{OC} . I could demonstrate with GIWAXS, that the blends with Y6 and N4 possess different packing structures and that the PM6:N4 blend exhibits a higher structural disorder than the PM6:Y6 blend. This fits the insights from the other methods used in this publication, demonstrating a higher energetic disorder in PM6:N4.

In publication 5 (Chapter 12, *Identifying the Signatures of Intermolecular Interactions in Blends of PM6 with Y6 and N4 Using Absorption Spectroscopy*), the aim was to understand the nanostructure and local interactions leading to changes in performance due to the different chemical structures of the NFAs N4 and Y6 and also due to the post-treatment of thermal annealing. With spectroscopy and GIWAXS, we could independently identify different aggregates in N4 and Y6. They also change in N4 with thermal annealing, while in Y6 hardly any changes to the nanostructure occur with thermal annealing. The detailed analysis of the N4 and Y6 UV-Vis absorption spectra in this work also laid important fundamentals for interpreting the Y12 (structurally very similar molecule) contributions to the absorption spectra in publication 3 (Chapter 10).

In publications 4 and 5 (Chapters 11 and 12), we could see the great importance of even slight changes to the chemical structure of the molecules used (only small changes in the alkyl chains) on the nanostructure and many other dependent parameters. Thus, the choice of “suitable” materials is important but does not offer a knob for an easily tunable nanostructure, as it is the case in publication 3 (Chapter 10).

Publication 6 (Chapter 13, *Effects of the diphenyl ether additive in halogen-free processed non-fullerene acceptor organic solar cells*) was a further study on the dependence of the performance of organic solar cells on the nanostructure. In this case, we used the solvent additive DPE in green-solvent processed blends of a further polymer:NFA blend (TPD-3F:IT-4F) to enhance the nanostructure formation for better solar cell performance. Therefore, I analyzed the nanostructure in the different blends via GIWAXS and could identify the desired substantial enhancement of the nanostructure of the donor polymer due to the usage of the additive DPE. This improved morphology did not only lead to an enhanced power conversion efficiency due to an increased short-circuit current and fill factor but also to a higher stability under illumination.

While the first part of block 2 with publications 4–6 (Chapters 11–13) dealt with thin films for NFA-based organic solar cells, publication 7 (Chapter 14, *Microstructural and Thermal Transport Properties of Regioregular Poly(3-hexylthiophene-2,5-diyl) Thin*

Films) is based on P3HT thin films for thermal transport. Thus, all publications in block 2 are closely related to the work on P3HT and P3HT:Y12 thin films in publication 3 (Chapter 10) in block 1. In publication 7 (Chapter 14), we used different P3HT batches with different molecular weights and solvents with varying boiling points to process the thin films. In my GIWAXS measurements of the nanostructure, the parameter variation had hardly any impact. With these little changes to the aggregates' properties, the effect on the absorption spectra and thermal transport was also minor. This again underlines the significance of the strong P3HT nanostructure control offered by the CID treatment introduced in publication 2 (Chapter 9) and applied to thin films in publication 3 (Chapter 10).

In block 3 (publication 8, Chapter 15, *Solvated PbI₂ Clusters preceding the Crystallization of Lead Halide Perovskites – a UV/VIS In-Situ Study*), I applied the TFFS method from publication 1 (Chapter 8) to highly concentrated perovskite precursor solutions in different solvents from collaborators. Publication 8 (Chapter 15) deals with modeling the early stage of the perovskite film formation during spin coating monitored by UV in-situ absorption spectroscopy. The absorption spectra change drastically with concentration, which increases during spin coating by evaporation. Hence, an independent measurement of the absorption spectra at a fixed concentration was necessary. This is possible by my newly introduced TFFS method.

The measurements were a challenging application as the absorption of the perovskite precursor solutions lies in the UV range, where light source intensities are low, and transmission through glass is reduced. However, I could adapt the standard setup to accomplish the measurements with the TFFS method in shaking mode with quartz tubes, a strong UV-light source, and increased spectrometer integration times. This demonstrates the broad applicability of the TFFS method developed in publication 1 (Chapter 8) to many applications, also demanding ones.

I am particularly proud that my efforts to enable absorption spectroscopy on highly absorbing fluid thin films have already proven useful for our research community. Hence, my work contributes to understanding structural control also beyond organic semiconductors.

5 Conclusion and Outlook

The work presented in this thesis is a close interconnection of accelerated nanostructural analysis and nanostructure control of organic semiconductors. The highly efficient research on the nanostructure control of organic semiconductors in this thesis was only possible to this extent as I developed the TFFS (Thinning Fluid Film Spectroscopy) method and strongly accelerated the work with GIWAXS and in-situ UV-Vis absorption spectroscopy.

The work on the nanostructure of organic semiconductors is split into the work on the CID treatment as a direct handle on the aggregation control and several projects involving different influence factors on the nanostructure in Chapters 11–14. The chemical structure of the NFAs in Chapters 11 and 12 has proven to have a substantial impact on the nanostructure. This underlines the high importance of the chemical design of the molecules involved. Therefore, the engineering of molecular structures will continue to play an essential role in the field of nanostructure control. Unfortunately, chemical structure changes are always discrete without the possibility of gradual changes.

In contrast, arbitrary gradual changes are enabled with the external processing parameters involved in the CID treatment. I demonstrated that the aggregate fraction and quality in P3HT solutions can be systematically controlled with the CID treatment utilizing the number of treatment steps, the treatment strength, temperature, concentration, and solvent composition. The deep understanding of the underlying working mechanism, in combination with a broad parameter study, enables a highly tailored control of the solution aggregation state over wide ranges.

The highly efficient parameter study was enabled by the TFFS method introduced in Chapter 8. Therefore, I implemented the TFFS method directly into the CID setup so that only seconds are required to measure each spectrum. This rapid automated characterization of the aggregation state in solution directly upon the CID treatment offers the possibility of precisely setting a desired aggregate fraction. The TFFS measurement coupled with an automated data analysis can immediately determine the aggregate fraction and, hence, offers a control parameter. Consequently, the CID treatment can be conducted until the desired aggregate fraction is achieved.

The unprecedented aggregation control from Chapter 9 is also the basis of Chapter 10, where thin films were processed by blade coating from CID-treated solutions. Since a high quality of the backbone ordering was desired in this study, the parameters of the CID treatment were chosen accordingly. The exceptional aggregate ordering was also transferred to the thin films when neat films were processed from the CID-treated solutions. This nanostructure control toward films with high backbone planarity and enhanced edge-on orientation led to a 25-fold increase in OFET mobility.

The possibilities of nanostructure control, which the CID treatment offers, become even more apparent in highly miscible P3HT:Y12 blends. An increasing CID treatment al-

lows to control the thin film nanostructure from a thoroughly intermixed blend to a high P3HT ordering. This high P3HT ordering suppresses at the same time the Y12 ordering. An additional SVA post-treatment also enabled a high Y12 ordering. Thus, in total, combining the CID treatment with SVA, a nanostructure control between highly disordered intermixed films, and high P3HT and Y12 ordering is possible, exceeding the initial expectations.

Chapter 10 mainly sets the boundaries of nanostructure control enabled by the CID treatment and SVA and gives guidelines on achieving different nanostructures. This nanostructure control framework offers plenty of space for optimizations of the nanostructure for various applications, e.g., organic solar cells. A controlled SVA process can also lead to intermediate Y12 ordering in this context, which is an ongoing project. Moreover, the broad range of possible nanostructures is highly valuable for fundamental research on the impact of the nanostructure in various fields. It should also be noted that Chapter 10 only utilized highly ordered pre-aggregates, but the CID treatment can also produce more disordered aggregates under different conditions. This demonstrates that the CID treatment introduced in the scope of this thesis offers a magnitude of possibilities for nanostructure control going far beyond the achievements presented here.

In this thesis, the CID treatment was only applied to P3HT. I tested to transfer the CID treatment to several state-of-the-art donor-acceptor-copolymers used for OPV but could not achieve an aggregation control like for P3HT. Hence, the working mechanism of the CID-induced aggregation is highly dependent on the molecular structure. P3HT fulfills the requirements that the backbone is planarized upon doping, and permanent $\pi - \pi$ stacking is induced. In contrast, examples like PM6 are designed to possess a planar backbone even without doping and do not favor $\pi - \pi$ stacking. Hence, aggregation control via CID treatment is unsuitable for them. There may be other semiconducting polymers where CID can also lead to aggregation control, but at least in the field of OPV donor polymers, the current trend is toward stiff donor-acceptor-copolymers like PM6.

P3HT is probably the most studied semiconducting polymer but has gained less attention in recent years due to the increasing OPV performances of other material systems. However, recently stable P3HT solar cells with PCEs exceeding 10% have been reported.^{25, 26, 59-61} Combined with the low cost of P3HT, its easy synthesis, and high stability, P3HT solar cells can increase their industry relevance again.⁶¹ Aggregation control via the CID treatment may help with incremental nanostructure tuning to optimize the nanostructure.

Moreover, applications of P3HT are not limited to OPV. P3HT can also be used for organic and hybrid field effect transistors (see also results in Chapter 10),²⁰⁰⁻²⁰³ OECTs (organic electrochemical transistors),²⁰⁴⁻²⁰⁹ transport layer for perovskite solar cells,²¹⁰⁻²¹⁷ in photocatalysis,²¹⁸⁻²²⁴ and several other applications. P3HT has even been used to give blind rats sight again.²²⁵⁻²²⁷ Therefore, the application potential of the CID treatment also lies in other fields than the prominent field of OPV.

Turning toward the automated nanostructure characterization, the achievements accelerating the research in this thesis can directly be transferred to any other research project utilizing the same methods. Thus, the increased research efficiency has a long-term effect translating to the whole group and research community. In this context, the novel

TFFS method is especially noteworthy. Through publication 1 in Chapter 8, we made all details of the TFFS method public to the whole research community, closing the gap existing so far for efficient absorption spectroscopy measurements of strongly absorbing solutions. Chapter 15 also demonstrates the necessity and value of the TFFS method in other research areas.

With the high level of automation, where the complete data analysis is included in the measurement process, the possibilities for further acceleration of this workflow are limited. The limiting factor is now often the duration of the experimental processes, e.g., processing thin films. Entire robotic systems, as also developed in this thesis for the TFFS method, can be a further improvement. Even though they cannot reduce the processing time, the required human working time is reduced. When the robotic system is coupled to a system for AI-based autonomous discovery, the efficiency of parameter space mapping can be further increased. During the work on my thesis, I also initiated an ongoing project of AI-based parameter space mapping using the robot I developed for the TFFS method. This process is still very similar to the research in this thesis. The automated analysis gives direct feedback, which is then used to determine the parameters of the subsequent measurement. In both cases, the aim is to obtain a maximized scientific output by a minimum number of necessary measurements. The only difference is that the human or the AI determines the measurement settings of the next point. Hence, this is a continuous further development and optimization of the strategy used in this thesis.

6 Authors' Contributions

In this section, the contributions of all co-authors to all included publications are summarized. My own contributions to the publications are highlighted in bold text.

Facilitating Absorption Spectroscopy of Strongly Absorbing Fluids: A High-Throughput Approach

Fabian Eller, and Eva M. Herzig

The Journal of Physical Chemistry A **2024**, 128(44), 9682-9687
(DOI: 10.1021/acs.jpca.4c04902)

FE developed the Thinning Fluid Film Spectroscopy (TFFS) method, conceptualized the project, and planned the experiments. **FE** developed and built the measurement robot for automated measurements and the in-line setup. **FE** conducted all measurements and analyzed them. **FE** wrote the manuscript, and **EMH** and **FE** edited it. **EMH** supervised the project.

Spark Discharge Doping – Achieving Unprecedented Control over Aggregate Fraction and Backbone Ordering in Poly(3-hexylthiophene) Solutions

Fabian Eller, Felix A. Wenzel, Richard Hildner, Remco W. A. Havenith, and Eva M. Herzig

Small **2023**, 19 (21), 2207537 (DOI: 10.1002/sml.202207537)

FE developed the current-induced doping (CID) method and initiated the project. **FE**, with the support of **EMH**, planned the experiments. **FE** developed a setup for reproducible CID treatment. **FE** conducted all CID treatments, measured all UV-Vis absorption spectra, and analyzed them. **FAW** conducted the DSC measurements, and **FE** analyzed the DSC data. **FE**, under the supervision of **RWAH**, conducted the DFTB3 simulations and the DFT simulations. **FE**, together with **EMH**, outlined and wrote the manuscript. All authors critically read the manuscript and commented on the manuscript. **EMH** supervised the project.

Tackling P3HT:Y-Series Miscibility Through Advanced Processing for Tunable Aggregation

Fabian Eller, Christopher R. McNeill, and Eva M. Herzig
FM, EG, and PMK in acknowledgements

Advanced Energy Materials **2024**, 14 (29), 2304455 (DOI: 10.1002/aenm.202304455)

FE initiated the project. **FE**, with the support of **EMH**, planned the experiments. **FE** conducted all CID treatments and solvent vapor annealing (SVA) treatments and prepared all samples by blade coating (for UV-Vis absorption spectroscopy, OFET devices, GIWAXS, and RSoXS measurements). **FE** conducted and analyzed all UV-Vis absorption spectroscopy measurements (static, in-situ during blade coating, and in-situ during SVA). **FE** prepared the OFET devices, measured them, and analyzed the data after introduction by **FM**. **FE** conducted all GIWAXS measurements and analyzed them. **EG** and **PMK** conducted the RSoXS measurements according to instructions of **CRM**, and **CRM** analyzed them. **FE**, together with **EMH**, outlined and wrote the manuscript. All authors critically read the manuscript and commented on the manuscript. **EMH** supervised the project.

Understanding the Role of Order in Y-Series Non-Fullerene Solar Cells to Realize High Open-Circuit Voltages

Lorena Perdigón-Toro, Le Quang Phuong, Fabian Eller, Guillaume Freychet, Elifnaz Saglamkaya, Jafar I. Khan, Qingya Wei, Stefan Zeiske, Daniel Kroh, Stefan Wedler, Anna Köhler, Ardalan Armin, Frédéric Laquai, Eva M. Herzig, Yingping Zou, Safa Shoaee, and Dieter Neher

Advanced Energy Materials **2022**, 12 (12), 2103422 (DOI: 10.1002/aenm.202103422)

LPT planned the project together with **DN**. **LPT** fabricated all samples and solar cells under investigation. **LPT** performed optoelectronic measurements and analysis, including T-dependent BACE, and J-V, and TDCF. **LQP** conducted T-dependent PIA spectroscopy studies and the corresponding data analysis. **GF** measured GIWAXS according to instructions by **FE** and **EMH**. **FE** performed the GIWAXS data analysis under the supervision of **EMH**. **FE**, guided by **EMH**, provided a draft for the GIWAXS-section of the manuscript. **ES** helped with the preparation of only-devices, performed all SCLC measurements, and contributed to the data analysis. **JIK** contributed with TRPL measurements and analyzed data under the supervision of **FL**. **QW** synthesized the N4 molecule under the supervision of **YZ**. **SZ** performed sensitive EQEPV measurements under the supervision of **AA**. **DK**, **SW**, **AK**, **FE**, and **EMH** provided important conceptual ideas regarding the interpretation of the optical and morphology data. **SS** and **DN** supervised the project. **LPT** carried out the analysis and calculations necessary for the reproduction of the OC vs. T data with help from **DN**. **LPT** wrote the manuscript and reviewer's response (GIWAXS section by **FE**). All co-authors contributed to data interpretation and proof-reading of the manuscript.

Identifying the Signatures of Intermolecular Interactions in Blends of PM6 with Y6 and N4 Using Absorption Spectroscopy

Daniel Kroh, **Fabian Eller**, Konstantin Schötz, Stefan Wedler, Lorena Perdigón-Toro, Guillaume Freychet, Qingya Wei, Maximilian Dörr, David Jones, Yingping Zou, Eva M. Herzig, Dieter Neher, and Anna Köhler

Advanced Functional Materials **2022**, 32, 2205711 (DOI: 10.1002/adfm.202205711)

AK and DN initiated the project. DK planned the experiments. DK prepared all samples (only blend samples for GIWAXS by LPT), conducted all temperature-dependent Steady-State absorption and photoluminescence experiments, and analyzed the data with support of SW and KS. SW and MD had carried out preliminary studies. QW synthesized the N4 molecule under the supervision of YZ. **GF measured GIWAXS of the blend samples according to instructions by FE and EMH, and FE measured GIWAXS of the neat samples. FE performed the data analysis of all GIWAXS measurements under the supervision of EMH. FE, guided by EMH, provided a draft for the GIWAXS-section of the manuscript. DJ, LPT, DN, FE, and EMH provided conceptual ideas regarding the interpretation of the film morphology. DK outlined and wrote the manuscript. AK edited the manuscript. All authors critically read the manuscript and commented on the manuscript. AK supervised the project.**

Effects of the diphenyl ether additive in halogen-free processed non-fullerene acceptor organic solar cells

Lorenzo Di Mario, David Garcia Romero, Meike J. Pieters, **Fabian Eller**, Chenhui Zhu, Giovanni Bongiovanni, Eva M. Herzig, Andrea Mura and Maria A. Loi

Journal of Materials Chemistry A **2023**, 11 (5), 2419-2430 (DOI: 10.1039/D2TA08603D)

LDM and MAL conceptualized the project. LDM planned the experiments. LDM, DGR, and MJP fabricated organic films and solar cells. LDM, DGR, and MJP performed device characterization on the organic solar cells, and LDM analyzed the data. LDM conducted UV-Vis, EQE, and photoluminescence (steady-state and time-resolved) spectroscopy measurements and analyzed the data. DGR measured impedance spectroscopy and analyzed the data. GB and AM conducted transient absorption spectroscopy measurements according to instructions by LDM and MAL, and LDM performed the data analysis. **CZ measured GIWAXS according to instructions by FE and EMH, and FE performed the data analysis under the supervision of EMH. LDM drafted the manuscript, and FE drafted the GIWAXS section of the manuscript. All authors critically read the manuscript and commented on the manuscript. MAL supervised the project.**

Microstructural and Thermal Transport Properties of Regioregular Poly(3-hexylthiophene-2,5-diyl) Thin Films

Kai Herrmann, Simon Freund, **Fabian Eller**, Tamino Rößler, Georg Papastavrou, Eva M. Herzig and Markus Retsch

Materials **2022**, 15 (21), 7700 (DOI: 10.3390/ma15217700)

Conceptualization, K.H.; methodology, K.H.; data analysis and validation, K.H., S.F.; investigation, K.H., S.F.; **GIWAXS measurements, F.E.; data analysis GIWAXS, F.E.**; AFM measurement, T.R.; writing—original draft preparation, K.H.; **writing—original draft preparation scattering, F.E.**; writing—review and editing, E.M.H., G.P. and M.R.; visualization, K.H.; supervision, M.R., E.M.H., G.P.; project administration, K.H.; funding acquisition, E.M.H., G.P. and M.R.

Solvated PbI₂ Clusters preceding the Crystallization of Lead Halide Perovskites – a UV/VIS In-Situ Study

Maximilian Spies, Simon Biberger, **Fabian Eller**, Eva M. Herzig, Anna Köhler

Submitted in *Advanced Electronic Materials*

PRELIMINARY AUTHOR CONTRIBUTION STATEMENT, since paper is not yet accepted.

MS and SB planned the experiments. MS modified the in-situ setup and conducted all in-situ measurements and their analysis. **FE, under the supervision of EMH, conducted the as-prepared UV-VIS absorption spectroscopy measurements with the Thinning Fluid Film Spectroscopy (TFFS) method.** MS developed the precursor states fitting, the model for the film thickness and concentration evolution, and modeled all absorption spectra. MS, SB, and AK discussed the results and outlined the manuscript. MS, with help from SB, wrote the first version of the manuscript. AK edited the manuscript. **All authors critically read the manuscript and commented on the manuscript.** AK supervised the project.

These contribution statements for each publication were approved by each co-author.

7 References

- [1] L. Zhu, M. Zhang, G. Zhou, Z. Wang, W. Zhong, J. Zhuang, Z. Zhou, X. Gao, L. Kan, B. Hao, F. Han, R. Zeng, X. Xue, S. Xu, H. Jing, B. Xiao, H. Zhu, Y. Zhang, and F. Liu (2024). Achieving 20.8% organic solar cells via additive-assisted layer-by-layer fabrication with bulk *p-i-n* structure and improved optical management. *Joule* **8** (11), 3153–3168. DOI: [10.1016/j.joule.2024.08.001](https://doi.org/10.1016/j.joule.2024.08.001).
- [2] ASCA. *OPV SAIL in shape of African continent*. URL: <https://www.asca.com/applications/projects/opv-sail/> (visited on 02/25/2025).
- [3] ASCA. *OPV SOLARTREE An energy self-sufficient installation*. URL: <https://www.asca.com/applications/projects/opv-solartree/> (visited on 02/25/2025).
- [4] Epishine. *Epishine indoor solar cells - Product Catalogue - Added Value Operation*. URL: <https://4883108.fs1.hubspotusercontent-na1.net/hubfs/4883108/Epishine%20Product%20Catalogue-2.pdf> (visited on 02/06/2025).
- [5] Epishine (2024). *Introducing AIR-sense-IQ: a CO2 Monitor Powered by Epishine's Organic Indoor Solar Cells*. URL: <https://www.epishine.com/news/introducing-air-sense-iq-a-co2-monitor-powered-by-epishines-organic-indoor-solar-cells> (visited on 02/06/2025).
- [6] P. Meredith, W. Li, and A. Armin (2020). Nonfullerene Acceptors: A Renaissance in Organic Photovoltaics? *Advanced Energy Materials* **10** (33), 2001788. DOI: [10.1002/aenm.202001788](https://doi.org/10.1002/aenm.202001788).
- [7] R. S. Gurney, D. G. Lidzey, and T. Wang (2019). A review of non-fullerene polymer solar cells: from device physics to morphology control. *Reports on Progress in Physics* **82** (3), 036601. DOI: [10.1088/1361-6633/ab0530](https://doi.org/10.1088/1361-6633/ab0530).
- [8] L. Zhu, M. Zhang, Z. Zhou, W. Zhong, T. Hao, S. Xu, R. Zeng, J. Zhuang, X. Xue, H. Jing, Y. Zhang, and F. Liu (2024). Progress of organic photovoltaics towards 20% efficiency. *Nature Reviews Electrical Engineering* **1** (9), 581–596. DOI: [10.1038/s44287-024-00080-3](https://doi.org/10.1038/s44287-024-00080-3).
- [9] K. Liu, Y. Jiang, G. Ran, F. Liu, W. Zhang, and X. Zhu (2024). 19.7% efficiency binary organic solar cells achieved by selective core fluorination of nonfullerene electron acceptors. *Joule* **8** (3), 835–851. DOI: [10.1016/j.joule.2024.01.005](https://doi.org/10.1016/j.joule.2024.01.005).
- [10] S. Guan, Y. Li, C. Xu, N. Yin, C. Xu, C. Wang, M. Wang, Y. Xu, Q. Chen, D. Wang, L. Zuo, and H. Chen (2024). Self-Assembled Interlayer Enables High-Performance Organic Photovoltaics with Power Conversion Efficiency Exceeding 20%. *Advanced Materials* **36** (25), 2400342. DOI: [10.1002/adma.202400342](https://doi.org/10.1002/adma.202400342).

-
- [11] H. Chen, Y. Huang, R. Zhang, H. Mou, J. Ding, J. Zhou, Z. Wang, H. Li, W. Chen, J. Zhu, Q. Cheng, H. Gu, X. Wu, T. Zhang, Y. Wang, H. Zhu, Z. Xie, F. Gao, Y. Li, and Y. Li (2025). Organic solar cells with 20.82% efficiency and high tolerance of active layer thickness through crystallization sequence manipulation. *Nature Materials*. DOI: [10.1038/s41563-024-02062-0](https://doi.org/10.1038/s41563-024-02062-0).
- [12] L. Zhu, M. Zhang, J. Xu, C. Li, J. Yan, G. Zhou, W. Zhong, T. Hao, J. Song, X. Xue, Z. Zhou, R. Zeng, H. Zhu, C.-C. Chen, R. C. I. MacKenzie, Y. Zou, J. Nelson, Y. Zhang, Y. Sun, and F. Liu (2022). Single-junction organic solar cells with over 19% efficiency enabled by a refined double-fibril network morphology. *Nature Materials* **21** (6), 656–663. DOI: [10.1038/s41563-022-01244-y](https://doi.org/10.1038/s41563-022-01244-y).
- [13] L. Zhan, S. Yin, Y. Li, S. Li, T. Chen, R. Sun, J. Min, G. Zhou, H. Zhu, Y. Chen, J. Fang, C.-Q. Ma, X. Xia, X. Lu, H. Qiu, W. Fu, and H. Chen (2022). Multiphase Morphology with Enhanced Carrier Lifetime via Quaternary Strategy Enables High-Efficiency, Thick-Film, and Large-Area Organic Photovoltaics. *Advanced Materials* **34** (45), 2206269. DOI: [10.1002/adma.202206269](https://doi.org/10.1002/adma.202206269).
- [14] W. Shen, Y. Zhao, and F. Liu (2023). Highlights of mainstream solar cell efficiencies in 2022. *Frontiers in Energy* **17** (1), 9–15. DOI: [10.1007/s11708-023-0871-y](https://doi.org/10.1007/s11708-023-0871-y).
- [15] L. Zhan, S. Li, Y. Li, R. Sun, J. Min, Y. Chen, J. Fang, C.-Q. Ma, G. Zhou, H. Zhu, L. Zuo, H. Qiu, S. Yin, and H. Chen (2022). Manipulating Charge Transfer and Transport via Intermediary Electron Acceptor Channels Enables 19.3% Efficiency Organic Photovoltaics. *Advanced Energy Materials* **12** (39), 2201076. DOI: [10.1002/aem.202201076](https://doi.org/10.1002/aem.202201076).
- [16] T. Chen, S. Li, Y. Li, Z. Chen, H. Wu, Y. Lin, Y. Gao, M. Wang, G. Ding, J. Min, Z. Ma, H. Zhu, L. Zuo, and H. Chen (2023). Compromising Charge Generation and Recombination of Organic Photovoltaics with Mixed Diluent Strategy for Certified 19.4% Efficiency. *Advanced Materials* **35** (21), 2300400. DOI: [10.1002/adma.202300400](https://doi.org/10.1002/adma.202300400).
- [17] W. Shen, Y. Zhao, and F. Liu (2024). Highlights of mainstream solar cell efficiencies in 2023. *Frontiers in Energy* **18** (1), 8–15. DOI: [10.1007/s11708-024-0937-5](https://doi.org/10.1007/s11708-024-0937-5).
- [18] Y. Cui, Y. Xu, H. Yao, P. Bi, L. Hong, J. Zhang, Y. Zu, T. Zhang, J. Qin, J. Ren, Z. Chen, C. He, X. Hao, Z. Wei, and J. Hou (2021). Single-Junction Organic Photovoltaic Cell with 19% Efficiency. *Advanced Materials* **33** (41), 2102420. DOI: [10.1002/adma.202102420](https://doi.org/10.1002/adma.202102420).
- [19] A. Köhler and H. Bässler (2015). *Electronic Processes in Organic Semiconductors: An Introduction*. John Wiley & Sons. DOI: [10.1002/9783527685172](https://doi.org/10.1002/9783527685172).
- [20] H. Lee, C. Park, D. H. Sin, J. H. Park, and K. Cho (2018). Recent Advances in Morphology Optimization for Organic Photovoltaics. *Advanced Materials* **30** (34), 1800453. DOI: [10.1002/adma.201800453](https://doi.org/10.1002/adma.201800453).
- [21] C. Cui and Y. Li (2021). Morphology optimization of photoactive layers in organic solar cells. *Aggregate* **2** (2), e31. DOI: [10.1002/agt2.31](https://doi.org/10.1002/agt2.31).

-
- [22] B. A. Collins, Z. Li, J. R. Tumbleston, E. Gann, C. R. McNeill, and H. Ade (2013). Absolute Measurement of Domain Composition and Nanoscale Size Distribution Explains Performance in PTB7:PC71BM Solar Cells. *Advanced Energy Materials* **3** (1), 65–74. DOI: [10.1002/aenm.201200377](https://doi.org/10.1002/aenm.201200377).
- [23] S. D. Dimitrov and J. R. Durrant (2014). Materials Design Considerations for Charge Generation in Organic Solar Cells. *Chemistry of Materials* **26** (1), 616–630. DOI: [10.1021/cm402403z](https://doi.org/10.1021/cm402403z).
- [24] J. Xiao, X. Jia, C. Duan, F. Huang, H.-L. Yip, and Y. Cao (2021). Surpassing 13% Efficiency for Polythiophene Organic Solar Cells Processed from Nonhalogenated Solvent. *Advanced Materials* **33** (25), 2008158. DOI: [10.1002/adma.202008158](https://doi.org/10.1002/adma.202008158).
- [25] B. Chang, C.-H. Chen, T.-F. Hsueh, S. Tan, Y.-C. Lin, Y. Zhao, B.-S. Tsai, T.-Y. Chu, Y.-N. Chang, C.-E. Tsai, C.-S. Chen, and K.-H. Wei (2023). High-Performance Poly(3-hexyl thiophene)-Based Organic Photovoltaics with Side-Chain Engineering of Core Units of Small Molecule Acceptors. *ACS Applied Materials & Interfaces* **15** (45), 52651–52660. DOI: [10.1021/acsami.3c13007](https://doi.org/10.1021/acsami.3c13007).
- [26] M. Gao, Y. Liu, K. Xian, Z. Peng, K. Zhou, J. Liu, S. Li, F. Xie, W. Zhao, J. Zhang, X. Jiao, and L. Ye (2022). Thermally stable poly(3-hexylthiophene): Nonfullerene solar cells with efficiency breaking 10%. *Aggregate* **3** (5), e190. DOI: [10.1002/agt2.190](https://doi.org/10.1002/agt2.190).
- [27] E. Sağlamkaya, M. Saeed Shadabroo, N. Tokmoldin, T. M. Melody, B. Sun, O. Alqahtani, A. Patterson, B. A. Collins, D. Neher, and S. Shoaee (2024). Key factors behind the superior performance of polymer-based NFA blends. *Materials Horizons* **11** (21), 5304–5312. DOI: [10.1039/D4MH00747F](https://doi.org/10.1039/D4MH00747F).
- [28] S. Dong, T. Jia, K. Zhang, J. Jing, and F. Huang (2020). Single-Component Non-halogen Solvent-Processed High-Performance Organic Solar Cell Module with Efficiency over 14%. *Joule* **4** (9), 2004–2016. DOI: [10.1016/j.joule.2020.07.028](https://doi.org/10.1016/j.joule.2020.07.028).
- [29] D. Kroh, F. Eller, K. Schötz, S. Wedler, L. Perdigón-Toro, G. Freychet, Q. Wei, M. Dörr, D. Jones, Y. Zou, E. M. Herzig, D. Neher, and A. Köhler (2022). Identifying the Signatures of Intermolecular Interactions in Blends of PM6 with Y6 and N4 Using Absorption Spectroscopy. *Advanced Functional Materials* **32** (44), 2205711. DOI: [10.1002/adfm.202205711](https://doi.org/10.1002/adfm.202205711).
- [30] L. Perdigón-Toro, L. Q. Phuong, F. Eller, G. Freychet, E. Sağlamkaya, J. I. Khan, Q. Wei, S. Zeiske, D. Kroh, S. Wedler, A. Köhler, A. Armin, F. Laquai, E. M. Herzig, Y. Zou, S. Shoaee, and D. Neher (2022). Understanding the Role of Order in Y-Series Non-Fullerene Solar Cells to Realize High Open-Circuit Voltages. *Advanced Energy Materials* **12** (12), 2103422. DOI: [10.1002/aenm.202103422](https://doi.org/10.1002/aenm.202103422).
- [31] L. D. Mario, D. G. Romero, M. J. Pieters, F. Eller, C. Zhu, G. Bongiovanni, E. M. Herzig, A. Mura, and M. A. Loi (2023). Effects of the diphenyl ether additive in halogen-free processed non-fullerene acceptor organic solar cells. *Journal of Materials Chemistry A* **11** (5), 2419–2430. DOI: [10.1039/D2TA08603D](https://doi.org/10.1039/D2TA08603D).
- [32] K. Herrmann, S. Freund, F. Eller, T. Rößler, G. Papastavrou, E. M. Herzig, and M. Retsch (2022). Microstructural and Thermal Transport Properties of Regioregular Poly(3-hexylthiophene-2,5-diyl) Thin Films. *Materials* **15** (21), 7700. DOI: [10.3390/ma15217700](https://doi.org/10.3390/ma15217700).

- [33] H. Nok Tsao and K. Müllen (2010). Improving polymer transistor performance via morphology control. *Chemical Society Reviews* **39** (7), 2372–2386. DOI: [10.1039/B918151M](https://doi.org/10.1039/B918151M).
- [34] F. Eller, F. A. Wenzel, R. Hildner, R. W. A. Havenith, and E. M. Herzig (2023). Spark Discharge Doping—Achieving Unprecedented Control over Aggregate Fraction and Backbone Ordering in Poly(3-hexylthiophene) Solutions. *Small* **19** (21), 2207537. DOI: [10.1002/sml1.202207537](https://doi.org/10.1002/sml1.202207537).
- [35] F. Eller and E. M. Herzig (2024). Facilitating Absorption Spectroscopy of Strongly Absorbing Fluids: A High-Throughput Approach. *The Journal of Physical Chemistry A* **128** (44), 9682–9687. DOI: [10.1021/acs.jpca.4c04902](https://doi.org/10.1021/acs.jpca.4c04902).
- [36] F. Eller, C. R. McNeill, and E. M. Herzig (2024). Tackling P3HT:Y-Series Miscibility Through Advanced Processing for Tunable Aggregation. *Advanced Energy Materials* **14** (29), 2304455. DOI: [10.1002/aenm.202304455](https://doi.org/10.1002/aenm.202304455).
- [37] Y. Cui, H. Yao, J. Zhang, K. Xian, T. Zhang, L. Hong, Y. Wang, Y. Xu, K. Ma, C. An, C. He, Z. Wei, F. Gao, and J. Hou (2020). Single-Junction Organic Photovoltaic Cells with Approaching 18% Efficiency. *Advanced Materials* **32** (19), 1908205. DOI: [10.1002/adma.201908205](https://doi.org/10.1002/adma.201908205).
- [38] C. Li, J. Zhou, J. Song, J. Xu, H. Zhang, X. Zhang, J. Guo, L. Zhu, D. Wei, G. Han, J. Min, Y. Zhang, Z. Xie, Y. Yi, H. Yan, F. Gao, F. Liu, and Y. Sun (2021). Non-fullerene acceptors with branched side chains and improved molecular packing to exceed 18% efficiency in organic solar cells. *Nature Energy* **6** (6), 605–613. DOI: [10.1038/s41560-021-00820-x](https://doi.org/10.1038/s41560-021-00820-x).
- [39] Y. Cui, H. Yao, J. Zhang, T. Zhang, Y. Wang, L. Hong, K. Xian, B. Xu, S. Zhang, J. Peng, Z. Wei, F. Gao, and J. Hou (2019). Over 16% efficiency organic photovoltaic cells enabled by a chlorinated acceptor with increased open-circuit voltages. *Nature Communications* **10** (1), 2515. DOI: [10.1038/s41467-019-10351-5](https://doi.org/10.1038/s41467-019-10351-5).
- [40] F. Panzer, H. Bäessler, and A. Köhler (2017). Temperature Induced Order–Disorder Transition in Solutions of Conjugated Polymers Probed by Optical Spectroscopy. *The Journal of Physical Chemistry Letters* **8** (1), 114–125. DOI: [10.1021/acs.jpcllett.6b01641](https://doi.org/10.1021/acs.jpcllett.6b01641).
- [41] F. Panzer, H. Bäessler, R. Lohwasser, M. Thelakkat, and A. Köhler (2014). The Impact of Polydispersity and Molecular Weight on the Order–Disorder Transition in Poly(3-hexylthiophene). *The Journal of Physical Chemistry Letters* **5** (15), 2742–2747. DOI: [10.1021/jz5009938](https://doi.org/10.1021/jz5009938).
- [42] W. Wang, Q. Wu, R. Sun, J. Guo, Y. Wu, M. Shi, W. Yang, H. Li, and J. Min (2020). Controlling Molecular Mass of Low-Band-Gap Polymer Acceptors for High-Performance All-Polymer Solar Cells. *Joule* **4** (5), 1070–1086. DOI: [10.1016/j.joule.2020.03.019](https://doi.org/10.1016/j.joule.2020.03.019).
- [43] F. Zhao, C. Wang, and X. Zhan (2018). Morphology Control in Organic Solar Cells. *Advanced Energy Materials* **8** (28), 1703147. DOI: [10.1002/aenm.201703147](https://doi.org/10.1002/aenm.201703147).
- [44] R. D. McCullough (1998). The Chemistry of Conducting Polythiophenes. *Advanced Materials* **10** (2), 93–116. DOI: [10.1002/\(SICI\)1521-4095\(199801\)10:2<93::AID-ADMA93>3.0.CO;2-F](https://doi.org/10.1002/(SICI)1521-4095(199801)10:2<93::AID-ADMA93>3.0.CO;2-F).

-
- [45] T.-A. Chen and R. D. Rieke (1993). Polyalkylthiophenes with the smallest bandgap and the highest intrinsic conductivity. *Synthetic Metals* **60** (2), 175–177. DOI: [10.1016/0379-6779\(93\)91240-3](https://doi.org/10.1016/0379-6779(93)91240-3).
- [46] T. A. Chen and R. D. Rieke (1992). The first regioregular head-to-tail poly(3-hexylthiophene-2,5-diyl) and a regiorandom isopolymer: nickel versus palladium catalysis of 2(5)-bromo-5(2)-(bromozincio)-3-hexylthiophene polymerization. *Journal of the American Chemical Society* **114** (25), 10087–10088. DOI: [10.1021/ja00051a066](https://doi.org/10.1021/ja00051a066).
- [47] C. H. Woo, B. C. Thompson, B. J. Kim, M. F. Toney, and J. M. J. Fréchet (2008). The Influence of Poly(3-hexylthiophene) Regioregularity on Fullerene-Composite Solar Cell Performance. *Journal of the American Chemical Society* **130** (48), 16324–16329. DOI: [10.1021/ja806493n](https://doi.org/10.1021/ja806493n).
- [48] H. Zhong, L. Ye, J.-Y. Chen, S. Byeok Jo, C.-C. Chueh, J. H. Carpenter, H. Ade, and A. K.-Y. Jen (2017). A regioregular conjugated polymer for high performance thick-film organic solar cells without processing additive. *Journal of Materials Chemistry A* **5** (21), 10517–10525. DOI: [10.1039/C7TA02391J](https://doi.org/10.1039/C7TA02391J).
- [49] R. Steyrlleuthner, R. Di Pietro, B. A. Collins, F. Polzer, S. Himmelberger, M. Schubert, Z. Chen, S. Zhang, A. Salleo, H. Ade, A. Facchetti, and D. Neher (2014). The Role of Regioregularity, Crystallinity, and Chain Orientation on Electron Transport in a High-Mobility n-Type Copolymer. *Journal of the American Chemical Society* **136** (11), 4245–4256. DOI: [10.1021/ja4118736](https://doi.org/10.1021/ja4118736).
- [50] I. Osaka, M. Saito, T. Koganezawa, and K. Takimiya (2014). Thiophene–Thiazolothiazole Copolymers: Significant Impact of Side Chain Composition on Backbone Orientation and Solar Cell Performances. *Advanced Materials* **26** (2), 331–338. DOI: [10.1002/adma.201303059](https://doi.org/10.1002/adma.201303059).
- [51] W. Li, S. Albrecht, L. Yang, S. Roland, J. R. Tumbleston, T. McAfee, L. Yan, M. A. Kelly, H. Ade, D. Neher, and W. You (2014). Mobility-Controlled Performance of Thick Solar Cells Based on Fluorinated Copolymers. *Journal of the American Chemical Society* **136** (44), 15566–15576. DOI: [10.1021/ja5067724](https://doi.org/10.1021/ja5067724).
- [52] J.-L. Wang, F. Xiao, J. Yan, Z. Wu, K.-K. Liu, Z.-F. Chang, R.-B. Zhang, H. Chen, H.-B. Wu, and Y. Cao (2016). Difluorobenzothiadiazole-Based Small-Molecule Organic Solar Cells with 8.7% Efficiency by Tuning of π -Conjugated Spacers and Solvent Vapor Annealing. *Advanced Functional Materials* **26** (11), 1803–1812. DOI: [10.1002/adfm.201505020](https://doi.org/10.1002/adfm.201505020).
- [53] Z. Liang, M. Li, Q. Wang, Y. Qin, S. J. Stuard, Z. Peng, Y. Deng, H. Ade, L. Ye, and Y. Geng (2020). Optimization Requirements of Efficient Polythiophene:Nonfullerene Organic Solar Cells. *Joule* **4** (6), 1278–1295. DOI: [10.1016/j.joule.2020.04.014](https://doi.org/10.1016/j.joule.2020.04.014).
- [54] S. Yoon, E.-Y. Shin, N.-K. Cho, S. Park, H. Young Woo, and H. Jung Son (2021). Progress in morphology control from fullerene to nonfullerene acceptors for scalable high-performance organic photovoltaics. *Journal of Materials Chemistry A* **9** (44), 24729–24758. DOI: [10.1039/D1TA06861J](https://doi.org/10.1039/D1TA06861J).
- [55] (2007). Polymer Blends and Block Copolymers. In: *The Physics of Polymers: Concepts for Understanding Their Structures and Behavior*. Ed. by G. Strobl. Berlin, Heidelberg: Springer, 105–164. DOI: [10.1007/978-3-540-68411-4_4](https://doi.org/10.1007/978-3-540-68411-4_4).

- [56] M. Kim, J. Lee, S. Byeok Jo, D. Hun Sin, H. Ko, H. Lee, S. Goo Lee, and K. Cho (2016). Critical factors governing vertical phase separation in polymer-PCBM blend films for organic solar cells. *Journal of Materials Chemistry A* **4** (40), 15522–15535. DOI: [10.1039/C6TA06508B](https://doi.org/10.1039/C6TA06508B).
- [57] Q. Wang, Y. Qin, M. Li, L. Ye, and Y. Geng (2020). Molecular Engineering and Morphology Control of Polythiophene:Nonfullerene Acceptor Blends for High-Performance Solar Cells. *Advanced Energy Materials* **10** (45), 2002572. DOI: [10.1002/aenm.202002572](https://doi.org/10.1002/aenm.202002572).
- [58] X. Yuan, Y. Zhao, Y. Zhang, D. Xie, W. Deng, J. Li, H. Wu, C. Duan, F. Huang, and Y. Cao (2022). Achieving 16% Efficiency for Polythiophene Organic Solar Cells with a Cyano-Substituted Polythiophene. *Advanced Functional Materials* **32** (24), 2201142. DOI: [10.1002/adfm.202201142](https://doi.org/10.1002/adfm.202201142).
- [59] C. Yang, S. Zhang, J. Ren, M. Gao, P. Bi, L. Ye, and J. Hou (2020). Molecular design of a non-fullerene acceptor enables a P3HT-based organic solar cell with 9.46% efficiency. *Energy & Environmental Science* **13** (9), 2864–2869. DOI: [10.1039/D0EE01763A](https://doi.org/10.1039/D0EE01763A).
- [60] C. Yang, R. Yu, C. Liu, H. Li, S. Zhang, and J. Hou (2021). Achieving over 10 % Efficiency in Poly(3-hexylthiophene)-Based Organic Solar Cells via Solid Additives. *ChemSusChem* **14** (17), 3607–3613. DOI: [10.1002/cssc.202100627](https://doi.org/10.1002/cssc.202100627).
- [61] C. Yang, S. Zhang, and J. Hou (2022). Low-cost and efficient organic solar cells based on polythiophene- and poly(thiophene vinylene)-related donors. *Aggregate* **3** (3), e111. DOI: [10.1002/agt.2.111](https://doi.org/10.1002/agt.2.111).
- [62] L. J. Richter, D. M. DeLongchamp, and A. Amassian (2017). Morphology Development in Solution-Processed Functional Organic Blend Films: An In Situ Viewpoint. *Chemical Reviews* **117** (9), 6332–6366. DOI: [10.1021/acs.chemrev.6b00618](https://doi.org/10.1021/acs.chemrev.6b00618).
- [63] D. Qian, L. Ye, M. Zhang, Y. Liang, L. Li, Y. Huang, X. Guo, S. Zhang, Z. Tan, and J. Hou (2012). Design, Application, and Morphology Study of a New Photovoltaic Polymer with Strong Aggregation in Solution State. *Macromolecules* **45** (24), 9611–9617. DOI: [10.1021/ma301900h](https://doi.org/10.1021/ma301900h).
- [64] X. Xu, G. Zhang, L. Yu, R. Li, and Q. Peng (2019). P3HT-Based Polymer Solar Cells with 8.25% Efficiency Enabled by a Matched Molecular Acceptor and Smart Green-Solvent Processing Technology. *Advanced Materials* **31** (52), 1906045. DOI: [10.1002/adma.201906045](https://doi.org/10.1002/adma.201906045).
- [65] H. Xin, O. G. Reid, G. Ren, F. S. Kim, D. S. Ginger, and S. A. Jenekhe (2010). Polymer Nanowire/Fullerene Bulk Heterojunction Solar Cells: How Nanostructure Determines Photovoltaic Properties. *ACS Nano* **4** (4), 1861–1872. DOI: [10.1021/nn9014906](https://doi.org/10.1021/nn9014906).
- [66] J. S. Kim, J. H. Lee, J. H. Park, C. Shim, M. Sim, and K. Cho (2011). High-Efficiency Organic Solar Cells Based on Preformed Poly(3-hexylthiophene) Nanowires. *Advanced Functional Materials* **21** (3), 480–486. DOI: [10.1002/adfm.201000971](https://doi.org/10.1002/adfm.201000971).
- [67] M. Kim, J. H. Park, J. H. Kim, J. H. Sung, S. B. Jo, M.-H. Jo, and K. Cho (2015). Lateral Organic Solar Cells with Self-Assembled Semiconductor Nanowires. *Advanced Energy Materials* **5** (5), 1401317. DOI: [10.1002/aenm.201401317](https://doi.org/10.1002/aenm.201401317).

-
- [68] C. Yang, N. Liang, L. Ye, H. Ade, X. Yuan, and J. Hou (2019). Enhanced JSC of P3HT-based non-fullerene polymer solar cells by modulating aggregation effect of P3HT in solution state. *Organic Electronics* **68**, 15–21. DOI: [10.1016/j.orgel.2019.01.047](https://doi.org/10.1016/j.orgel.2019.01.047).
- [69] Y. Liu, J. Zhao, Z. Li, C. Mu, W. Ma, H. Hu, K. Jiang, H. Lin, H. Ade, and H. Yan (2014). Aggregation and morphology control enables multiple cases of high-efficiency polymer solar cells. *Nature Communications* **5** (1), 5293. DOI: [10.1038/ncomms6293](https://doi.org/10.1038/ncomms6293).
- [70] X. Yu, H. Yang, S. Wu, L. Wang, Y. Geng, and Y. Han (2015). Crystallization-dominated and microphase separation/crystallization-coexisted structure of all-conjugated phenylene–thiophene diblock copolymers. *Journal of Polymer Science Part B: Polymer Physics* **53** (24), 1718–1726. DOI: [10.1002/polb.23893](https://doi.org/10.1002/polb.23893).
- [71] F. M. McFarland, C. M. Ellis, and S. Guo (2017). The Aggregation of Poly(3-hexylthiophene) into Nanowires: With and without Chemical Doping. *The Journal of Physical Chemistry C* **121** (8), 4740–4746. DOI: [10.1021/acs.jpcc.7b00816](https://doi.org/10.1021/acs.jpcc.7b00816).
- [72] L. Müller, D. Nanova, T. Glaser, S. Beck, A. Pucci, A. K. Kast, R. R. Schröder, E. Mankel, P. Pingel, D. Neher, W. Kowalsky, and R. Lovrincic (2016). Charge-Transfer–Solvent Interaction Predefines Doping Efficiency in p-Doped P3HT Films. *Chemistry of Materials* **28** (12), 4432–4439. DOI: [10.1021/acs.chemmater.6b01629](https://doi.org/10.1021/acs.chemmater.6b01629).
- [73] A. E. Mansour, D. Lungwitz, T. Schultz, M. Arvind, A. M. Valencia, C. Cocchi, A. Opitz, D. Neher, and N. Koch (2020). The optical signatures of molecular-doping induced polarons in poly(3-hexylthiophene-2,5-diyl): individual polymer chains versus aggregates. *Journal of Materials Chemistry C* **8** (8), 2870–2879. DOI: [10.1039/C9TC06509A](https://doi.org/10.1039/C9TC06509A).
- [74] M. Arvind, C. E. Tait, M. Guerrini, J. Krumland, A. M. Valencia, C. Cocchi, A. E. Mansour, N. Koch, S. Barlow, S. R. Marder, J. Behrends, and D. Neher (2020). Quantitative Analysis of Doping-Induced Polarons and Charge-Transfer Complexes of Poly(3-hexylthiophene) in Solution. *The Journal of Physical Chemistry B* **124** (35), 7694–7708. DOI: [10.1021/acs.jpccb.0c03517](https://doi.org/10.1021/acs.jpccb.0c03517).
- [75] J. Gao, J. D. Roehling, Y. Li, H. Guo, A. J. Moulé, and J. K. Grey (2013). The effect of 2,3,5,6-tetrafluoro-7,7,8,8-tetracyanoquinodimethane charge transfer dopants on the conformation and aggregation of poly(3-hexylthiophene). *Journal of Materials Chemistry C* **1** (36), 5638–5646. DOI: [10.1039/C3TC31047G](https://doi.org/10.1039/C3TC31047G).
- [76] J. Wang and Z. Liang (2016). Synergetic Solvent Engineering of Film Nanomorphology to Enhance Planar Perylene Diimide-Based Organic Photovoltaics. *ACS Applied Materials & Interfaces* **8** (34), 22418–22424. DOI: [10.1021/acsami.6b08284](https://doi.org/10.1021/acsami.6b08284).
- [77] L. Zhu, M. Zhang, G. Zhou, T. Hao, J. Xu, J. Wang, C. Qiu, N. Prine, J. Ali, W. Feng, X. Gu, Z. Ma, Z. Tang, H. Zhu, L. Ying, Y. Zhang, and F. Liu (2020). Efficient Organic Solar Cell with 16.88% Efficiency Enabled by Refined Acceptor Crystallization and Morphology with Improved Charge Transfer and Transport Properties. *Advanced Energy Materials* **10** (18), 1904234. DOI: [10.1002/aenm.201904234](https://doi.org/10.1002/aenm.201904234).

- [78] L. Ye, W. Zhao, S. Li, S. Mukherjee, J. H. Carpenter, O. Awartani, X. Jiao, J. Hou, and H. Ade (2017). High-Efficiency Nonfullerene Organic Solar Cells: Critical Factors that Affect Complex Multi-Length Scale Morphology and Device Performance. *Advanced Energy Materials* **7** (7), 1602000. DOI: [10.1002/aenm.201602000](https://doi.org/10.1002/aenm.201602000).
- [79] X. Song, N. Gasparini, L. Ye, H. Yao, J. Hou, H. Ade, and D. Baran (2018). Controlling Blend Morphology for Ultrahigh Current Density in Nonfullerene Acceptor-Based Organic Solar Cells. *ACS Energy Letters* **3** (3), 669–676. DOI: [10.1021/acsenergylett.7b01266](https://doi.org/10.1021/acsenergylett.7b01266).
- [80] M. Schubert, B. A. Collins, H. Mangold, I. A. Howard, W. Schindler, K. Vandewal, S. Roland, J. Behrends, F. Kraffert, R. Steyrleuthner, Z. Chen, K. Fostiropoulos, R. Bittl, A. Salleo, A. Facchetti, F. Laquai, H. W. Ade, and D. Neher (2014). Correlated Donor/Acceptor Crystal Orientation Controls Photocurrent Generation in All-Polymer Solar Cells. *Advanced Functional Materials* **24** (26), 4068–4081. DOI: [10.1002/adfm.201304216](https://doi.org/10.1002/adfm.201304216).
- [81] S. Pröller, F. Liu, C. Zhu, C. Wang, T. P. Russell, A. Hexemer, P. Müller-Buschbaum, and E. M. Herzig (2016). Following the Morphology Formation In Situ in Printed Active Layers for Organic Solar Cells. *Advanced Energy Materials* **6** (1), 1501580. DOI: [10.1002/aenm.201501580](https://doi.org/10.1002/aenm.201501580).
- [82] D. Corzo, D. Rosas-Villalva, A. C. G. Tostado-Blázquez, E. B. Alexandre, L. H. Hernandez, J. Han, H. Xu, M. Babics, S. De Wolf, and D. Baran (2023). High-performing organic electronics using terpene green solvents from renewable feedstocks. *Nature Energy* **8** (1), 62–73. DOI: [10.1038/s41560-022-01167-7](https://doi.org/10.1038/s41560-022-01167-7).
- [83] B. R. Aich, J. Lu, S. Beaupré, M. Leclerc, and Y. Tao (2012). Control of the active layer nanomorphology by using co-additives towards high-performance bulk heterojunction solar cells. *Organic Electronics* **13** (9), 1736–1741. DOI: [10.1016/j.orgel.2012.05.001](https://doi.org/10.1016/j.orgel.2012.05.001).
- [84] J. Zhao, S. Zhao, Z. Xu, B. Qiao, D. Huang, L. Zhao, Y. Li, Y. Zhu, and P. Wang (2016). Revealing the Effect of Additives with Different Solubility on the Morphology and the Donor Crystalline Structures of Organic Solar Cells. *ACS Applied Materials & Interfaces* **8** (28), 18231–18237. DOI: [10.1021/acsami.6b02671](https://doi.org/10.1021/acsami.6b02671).
- [85] Y. J. Kim, S. Ahn, D. H. Wang, and C. E. Park (2015). A Mechanistic Understanding of a Binary Additive System to Synergistically Boost Efficiency in All-Polymer Solar Cells. *Scientific Reports* **5** (1), 18024. DOI: [10.1038/srep18024](https://doi.org/10.1038/srep18024).
- [86] C. M. Hansen (2007). *Hansen Solubility Parameters: A User's Handbook, Second Edition*. 2nd ed. Boca Raton: CRC Press. DOI: [10.1201/9781420006834](https://doi.org/10.1201/9781420006834).
- [87] Z. Xu, K. S. Park, J. J. Kwok, O. Lin, B. B. Patel, P. Kafle, D. W. Davies, Q. Chen, and Y. Diao (2022). Not All Aggregates Are Made the Same: Distinct Structures of Solution Aggregates Drastically Modulate Assembly Pathways, Morphology, and Electronic Properties of Conjugated Polymers. *Advanced Materials* **34** (32), 2203055. DOI: [10.1002/adma.202203055](https://doi.org/10.1002/adma.202203055).
- [88] T. Yu and D. Ma (2024). Highly Efficient Nonfullerene Organic Solar Cells: Morphology Control and Characterizations. *Solar RRL* **8** (2), 2300751. DOI: [10.1002/solr.202300751](https://doi.org/10.1002/solr.202300751).

-
- [89] R. Yu, H. Yao, L. Hong, Y. Qin, J. Zhu, Y. Cui, S. Li, and J. Hou (2018). Design and application of volatilizable solid additives in non-fullerene organic solar cells. *Nature Communications* **9** (1), 4645. DOI: [10.1038/s41467-018-07017-z](https://doi.org/10.1038/s41467-018-07017-z).
- [90] R. Yu, H. Yao, Z. Chen, J. Xin, L. Hong, Y. Xu, Y. Zu, W. Ma, and J. Hou (2019). Enhanced – Interactions of Nonfullerene Acceptors by Volatilizable Solid Additives in Efficient Polymer Solar Cells. *Advanced Materials* **31** (18), 1900477. DOI: [10.1002/adma.201900477](https://doi.org/10.1002/adma.201900477).
- [91] J. Cai, H. Wang, X. Zhang, W. Li, D. Li, Y. Mao, B. Du, M. Chen, Y. Zhuang, D. Liu, H.-L. Qin, Y. Zhao, J. A. Smith, R. C. Kilbride, A. J. Parnell, R. A. L. Jones, D. G. Lidzey, and T. Wang (2020). Fluorinated solid additives enable high efficiency non-fullerene organic solar cells. *Journal of Materials Chemistry A* **8** (8), 4230–4238. DOI: [10.1039/C9TA13974E](https://doi.org/10.1039/C9TA13974E).
- [92] J. Fu, S. Chen, K. Yang, S. Jung, J. Lv, L. Lan, H. Chen, D. Hu, Q. Yang, T. Duan, Z. Kan, C. Yang, K. Sun, S. Lu, Z. Xiao, and Y. Li (2020). A “-Hole”-Containing Volatile Solid Additive Enabling 16.5% Efficiency Organic Solar Cells. *iScience* **23** (3), 100965. DOI: [10.1016/j.isci.2020.100965](https://doi.org/10.1016/j.isci.2020.100965).
- [93] Z. Chen, H. Yao, J. Wang, J. Zhang, T. Zhang, Z. Li, J. Qiao, S. Xiu, X. Hao, and J. Hou (2023). Restrained energetic disorder for high-efficiency organic solar cells via a solid additive. *Energy & Environmental Science* **16** (6), 2637–2645. DOI: [10.1039/D3EE00927K](https://doi.org/10.1039/D3EE00927K).
- [94] X. Xu, Y. Li, and Q. Peng (2020). Recent advances in morphology optimizations towards highly efficient ternary organic solar cells. *Nano Select* **1** (1), 30–58. DOI: [10.1002/nano.202000012](https://doi.org/10.1002/nano.202000012).
- [95] N. Gasparini, A. Salleo, I. McCulloch, and D. Baran (2019). The role of the third component in ternary organic solar cells. *Nature Reviews Materials* **4** (4), 229–242. DOI: [10.1038/s41578-019-0093-4](https://doi.org/10.1038/s41578-019-0093-4).
- [96] Y. Dong, Y. Zou, J. Yuan, H. Yang, Y. Wu, C. Cui, and Y. Li (2019). Ternary Polymer Solar Cells Facilitating Improved Efficiency and Stability. *Advanced Materials* **31** (52), 1904601. DOI: [10.1002/adma.201904601](https://doi.org/10.1002/adma.201904601).
- [97] F. A. Wenzel, H. Welz, K. P. VAN DER Zwan, S. Stäter, K. Kreger, R. Hildner, J. Senker, and H.-W. Schmidt (2022). Highly Efficient Supramolecular Nucleating Agents for Poly(3-hexylthiophene). *Macromolecules* **55** (7), 2861–2871. DOI: [10.1021/acs.macromol.1c02283](https://doi.org/10.1021/acs.macromol.1c02283).
- [98] F. A. Wenzel, S. Stäter, P. O’Reilly, K. Kreger, J. Köhler, R. Hildner, and H.-W. Schmidt (2024). Isolated Hierarchical Superstructures with Highly Oriented P3HT Nanofibers. *Macromolecules* **57** (21), 10389–10398. DOI: [10.1021/acs.macromol.4c01618](https://doi.org/10.1021/acs.macromol.4c01618).
- [99] S. Stäter, F. A. Wenzel, H. Welz, K. Kreger, J. Köhler, H.-W. Schmidt, and R. Hildner (2023). Directed Gradients in the Excited-State Energy Landscape of Poly(3-hexylthiophene) Nanofibers. *Journal of the American Chemical Society* **145** (25), 13780–13787. DOI: [10.1021/jacs.3c02117](https://doi.org/10.1021/jacs.3c02117).
- [100] N. D. Treat, J. A. Nekuda Malik, O. Reid, L. Yu, C. G. Shuttle, G. Rumbles, C. J. Hawker, M. L. Chabinyc, P. Smith, and N. Stingelin (2013). Microstructure formation in molecular and polymer semiconductors assisted by nucleation agents. *Nature Materials* **12** (7), 628–633. DOI: [10.1038/nmat3655](https://doi.org/10.1038/nmat3655).

-
- [101] Y.-F. Ma, Y. Zhang, and H.-L. Zhang (2022). Solid additives in organic solar cells: progress and perspectives. *Journal of Materials Chemistry C* **10** (7), 2364–2374. DOI: [10.1039/D1TC04224F](https://doi.org/10.1039/D1TC04224F).
- [102] J. Oh, S. Jung, M. Jeong, B. Lee, J. Lee, Y. Cho, S. M. Lee, S. Chen, Z.-G. Zhang, Y. Li, and C. Yang (2019). Ring-perfluorinated non-volatile additives with a high dielectric constant lead to highly efficient and stable organic solar cells. *Journal of Materials Chemistry C* **7** (16), 4716–4724. DOI: [10.1039/C9TC00762H](https://doi.org/10.1039/C9TC00762H).
- [103] E. M. Herzig, F. Gao, J. Bergqvist, M. A. Loi, and S. B. Meier (2024). Harmonizing organic photovoltaics research and development among academia and industry. *Joule* **8** (8), 2171–2178. DOI: [10.1016/j.joule.2024.07.015](https://doi.org/10.1016/j.joule.2024.07.015).
- [104] X. Gu, L. Shaw, K. Gu, M. F. Toney, and Z. Bao (2018). The meniscus-guided deposition of semiconducting polymers. *Nature Communications* **9** (1), 534. DOI: [10.1038/s41467-018-02833-9](https://doi.org/10.1038/s41467-018-02833-9).
- [105] A. S. Gertsen, M. F. Castro, R. R. Søndergaard, and J. W. Andreasen (2020). Scalable fabrication of organic solar cells based on non-fullerene acceptors. *Flexible and Printed Electronics* **5** (1), 014004. DOI: [10.1088/2058-8585/ab5f57](https://doi.org/10.1088/2058-8585/ab5f57).
- [106] R. Yu, X. Wei, G. Wu, and Z. Tan (2022). Layer-by-layered organic solar cells: Morphology optimizing strategies and processing techniques. *Aggregate* **3** (3), e107. DOI: [10.1002/agt2.107](https://doi.org/10.1002/agt2.107).
- [107] M. Ren, G. Zhang, Z. Chen, J. Xiao, X. Jiao, Y. Zou, H.-L. Yip, and Y. Cao (2020). High-Performance Ternary Organic Solar Cells with Controllable Morphology via Sequential Layer-by-Layer Deposition. *ACS Applied Materials & Interfaces* **12** (11), 13077–13086. DOI: [10.1021/acsami.9b23011](https://doi.org/10.1021/acsami.9b23011).
- [108] X. Zhang, Y. Li, D. Zhang, G. Wu, H. Zhang, J. Zhou, X. Li, Saud-uz-Zafar, J. Zhang, Z. Wei, H. Zhou, and Y. Zhang (2021). Molecular dispersion enhances photovoltaic efficiency and thermal stability in quasi-bilayer organic solar cells. *Science China Chemistry* **64** (1), 116–126. DOI: [10.1007/s11426-020-9837-y](https://doi.org/10.1007/s11426-020-9837-y).
- [109] Q. Wu, W. Wang, Y. Wu, Z. Chen, J. Guo, R. Sun, J. Guo, Y. (Yang, and J. Min (2021). High-Performance All-Polymer Solar Cells with a Pseudo-Bilayer Configuration Enabled by a Stepwise Optimization Strategy. *Advanced Functional Materials* **31** (15), 2010411. DOI: [10.1002/adfm.202010411](https://doi.org/10.1002/adfm.202010411).
- [110] L. Zhan, S. Li, X. Xia, Y. Li, X. Lu, L. Zuo, M. Shi, and H. Chen (2021). Layer-by-Layer Processed Ternary Organic Photovoltaics with Efficiency over 18%. *Advanced Materials* **33** (12), 2007231. DOI: [10.1002/adma.202007231](https://doi.org/10.1002/adma.202007231).
- [111] Z. Wang, Z. Peng, Z. Xiao, D. Seyitliyev, K. Gundogdu, L. Ding, and H. Ade (2020). Thermodynamic Properties and Molecular Packing Explain Performance and Processing Procedures of Three D18:NFA Organic Solar Cells. *Advanced Materials* **32** (49), 2005386. DOI: [10.1002/adma.202005386](https://doi.org/10.1002/adma.202005386).
- [112] K. W. Chou, B. Yan, R. Li, E. Q. Li, K. Zhao, D. H. Anjum, S. Alvarez, R. Gassaway, A. Biocca, S. T. Thoroddsen, A. Hexemer, and A. Amassian (2013). Spin-Cast Bulk Heterojunction Solar Cells: A Dynamical Investigation. *Advanced Materials* **25** (13), 1923–1929. DOI: [10.1002/adma.201203440](https://doi.org/10.1002/adma.201203440).

-
- [113] W.-R. Wu, C.-J. Su, W.-T. Chuang, Y.-C. Huang, P.-W. Yang, P.-C. Lin, C.-Y. Chen, T.-Y. Yang, A.-C. Su, K.-H. Wei, C.-M. Liu, and U.-S. Jeng (2017). Surface Layering and Supersaturation for Top-Down Nanostructural Development during Spin Coating of Polymer/Fullerene Thin Films. *Advanced Energy Materials* **7** (14), 1601842. DOI: [10.1002/aenm.201601842](https://doi.org/10.1002/aenm.201601842).
- [114] X. Liu, L. Ye, W. Zhao, S. Zhang, S. Li, G. M. Su, C. Wang, H. Ade, and J. Hou (2017). Morphology control enables thickness-insensitive efficient non-fullerene polymer solar cells. *Materials Chemistry Frontiers* **1** (10), 2057–2064. DOI: [10.1039/C7QM00182G](https://doi.org/10.1039/C7QM00182G).
- [115] W. Ni, M. Li, B. Kan, F. Liu, X. Wan, Q. Zhang, H. Zhang, T. P. Russell, and Y. Chen (2015). Fullerene-free small molecule organic solar cells with a high open circuit voltage of 1.15 V. *Chemical Communications* **52** (3), 465–468. DOI: [10.1039/C5CC07973J](https://doi.org/10.1039/C5CC07973J).
- [116] M. Osaka, D. Mori, H. Benten, H. Ogawa, H. Ohkita, and S. Ito (2017). Charge Transport in Intermixed Regions of All-Polymer Solar Cells Studied by Conductive Atomic Force Microscopy. *ACS Applied Materials & Interfaces* **9** (18), 15615–15622. DOI: [10.1021/acsami.7b00979](https://doi.org/10.1021/acsami.7b00979).
- [117] O. K. Kwon, J.-H. Park, D. W. Kim, S. K. Park, and S. Y. Park (2015). An All-Small-Molecule Organic Solar Cell with High Efficiency Nonfullerene Acceptor. *Advanced Materials* **27** (11), 1951–1956. DOI: [10.1002/adma.201405429](https://doi.org/10.1002/adma.201405429).
- [118] C. Jiao, C. Pang, and Q. An (2019). Nonfullerene organic photovoltaic cells exhibiting 13.76% efficiency by employing upside-down solvent vapor annealing. *International Journal of Energy Research* **43** (14), 8716–8724. DOI: [10.1002/er.4870](https://doi.org/10.1002/er.4870).
- [119] M. Li, F. Liu, X. Wan, W. Ni, B. Kan, H. Feng, Q. Zhang, X. Yang, Y. Wang, Y. Zhang, Y. Shen, T. P. Russell, and Y. Chen (2015). Subtle Balance Between Length Scale of Phase Separation and Domain Purification in Small-Molecule Bulk-Heterojunction Blends under Solvent Vapor Treatment. *Advanced Materials* **27** (40), 6296–6302. DOI: [10.1002/adma.201502645](https://doi.org/10.1002/adma.201502645).
- [120] B. Kan, Q. Zhang, M. Li, X. Wan, W. Ni, G. Long, Y. Wang, X. Yang, H. Feng, and Y. Chen (2014). Solution-Processed Organic Solar Cells Based on Dialkylthiol-Substituted Benzodithiophene Unit with Efficiency near 10%. *Journal of the American Chemical Society* **136** (44), 15529–15532. DOI: [10.1021/ja509703k](https://doi.org/10.1021/ja509703k).
- [121] M. Zhang, F. Zhang, Q. An, Q. Sun, W. Wang, X. Ma, J. Zhang, and W. Tang (2017). Nematic liquid crystal materials as a morphology regulator for ternary small molecule solar cells with power conversion efficiency exceeding 10%. *Journal of Materials Chemistry A* **5** (7), 3589–3598. DOI: [10.1039/C7TA00211D](https://doi.org/10.1039/C7TA00211D).
- [122] J. Vogelsang, J. Brazard, T. Adachi, J. C. Bolinger, and P. F. Barbara (2011). Watching the Annealing Process One Polymer Chain at a Time. *Angewandte Chemie International Edition* **50** (10), 2257–2261. DOI: [10.1002/anie.201007084](https://doi.org/10.1002/anie.201007084).
- [123] Z. Peng, L. Ye, and H. Ade (2022). Understanding, quantifying, and controlling the molecular ordering of semiconducting polymers: from novices to experts and amorphous to perfect crystals. *Materials Horizons* **9** (2), 577–606. DOI: [10.1039/D0MH00837K](https://doi.org/10.1039/D0MH00837K).

- [124] G. W. H. Höhne, W. F. Hemminger, and H.-J. Flammersheim (2003). *Differential Scanning Calorimetry*. Berlin, Heidelberg: Springer. DOI: [10.1007/978-3-662-06710-9](https://doi.org/10.1007/978-3-662-06710-9).
- [125] C. Schick (2009). Differential scanning calorimetry (DSC) of semicrystalline polymers. *Analytical and Bioanalytical Chemistry* **395** (6), 1589–1611. DOI: [10.1007/s00216-009-3169-y](https://doi.org/10.1007/s00216-009-3169-y).
- [126] Y. Qin, Y. Xu, Z. Peng, J. Hou, and H. Ade (2020). Low Temperature Aggregation Transitions in N3 and Y6 Acceptors Enable Double-Annealing Method That Yields Hierarchical Morphology and Superior Efficiency in Nonfullerene Organic Solar Cells. *Advanced Functional Materials* **30** (46), 2005011. DOI: [10.1002/adfm.202005011](https://doi.org/10.1002/adfm.202005011).
- [127] L. Tang and C. R. McNeill (2022). Capturing the Phase Transformation and Thermal Behavior of P(NDI2OD-T2) with In Situ Grazing Incidence WAXS. *Macromolecules* **55** (16), 7273–7283. DOI: [10.1021/acs.macromol.2c01025](https://doi.org/10.1021/acs.macromol.2c01025).
- [128] X. Jiao, M. Statz, L. Lai, S. Schott, C. Jellett, I. McCulloch, H. Sirringhaus, and C. R. McNeill (2020). Resolving Different Physical Origins toward Crystallite Imperfection in Semiconducting Polymers: Crystallite Size vs Paracrystallinity. *The Journal of Physical Chemistry B* **124** (46), 10529–10538. DOI: [10.1021/acs.jpcc.0c06763](https://doi.org/10.1021/acs.jpcc.0c06763).
- [129] J. H. Park, J. S. Kim, J. H. Lee, W. H. Lee, and K. Cho (2009). Effect of Annealing Solvent Solubility on the Performance of Poly(3-hexylthiophene)/Methanofullerene Solar Cells. *The Journal of Physical Chemistry C* **113** (40), 17579–17584. DOI: [10.1021/jp9029562](https://doi.org/10.1021/jp9029562).
- [130] W. Liu, R. Liu, W. Wang, W. Li, W. Liu, K. Zheng, L. Ma, Y. Tian, Z. Bo, and Y. Huang (2009). Tailoring Nanowire Network Morphology and Charge Carrier Mobility of Poly(3-hexylthiophene)/C60 Films. *The Journal of Physical Chemistry C* **113** (26), 11385–11389. DOI: [10.1021/jp900042h](https://doi.org/10.1021/jp900042h).
- [131] H. Chen, Y.-C. Hsiao, B. Hu, and M. Dadmun (2014). Control of morphology and function of low band gap polymer–bis–fullerene mixed heterojunctions in organic photovoltaics with selective solvent vapor annealing. *Journal of Materials Chemistry A* **2** (25), 9883–9890. DOI: [10.1039/C4TA01436G](https://doi.org/10.1039/C4TA01436G).
- [132] R. Hegde, N. Henry, B. Whittle, H. Zang, B. Hu, J. Chen, K. Xiao, and M. Dadmun (2012). The impact of controlled solvent exposure on the morphology, structure and function of bulk heterojunction solar cells. *Solar Energy Materials and Solar Cells* **107**, 112–124. DOI: [10.1016/j.solmat.2012.07.014](https://doi.org/10.1016/j.solmat.2012.07.014).
- [133] R. Lundy, S. P. Flynn, C. Cummins, S. M. Kelleher, M. N. Collins, E. Dalton, S. Daniels, M. A. Morris, and R. Enright (2017). Controlled solvent vapor annealing of a high block copolymer thin film. *Physical Chemistry Chemical Physics* **19** (4), 2805–2815. DOI: [10.1039/C6CP07633E](https://doi.org/10.1039/C6CP07633E).
- [134] H. Hulkkonen, T. Salminen, and T. Niemi (2019). Automated solvent vapor annealing with nanometer scale control of film swelling for block copolymer thin films. *Soft Matter* **15** (39), 7909–7917. DOI: [10.1039/C9SM01322A](https://doi.org/10.1039/C9SM01322A).
- [135] C. Sinturel, M. Vayer, M. Morris, and M. A. Hillmyer (2013). Solvent Vapor Annealing of Block Polymer Thin Films. *Macromolecules* **46** (14), 5399–5415. DOI: [10.1021/ma400735a](https://doi.org/10.1021/ma400735a).

-
- [136] X. Cheng, A. Böker, and L. Tsarkova (2019). Temperature-Controlled Solvent Vapor Annealing of Thin Block Copolymer Films. *Polymers* **11** (8), 1312. DOI: [10.3390/polym11081312](https://doi.org/10.3390/polym11081312).
- [137] L. Yang, S. Zhang, C. He, J. Zhang, H. Yao, Y. Yang, Y. Zhang, W. Zhao, and J. Hou (2017). New Wide Band Gap Donor for Efficient Fullerene-Free All-Small-Molecule Organic Solar Cells. *Journal of the American Chemical Society* **139** (5), 1958–1966. DOI: [10.1021/jacs.6b11612](https://doi.org/10.1021/jacs.6b11612).
- [138] S. Hüttner, M. Sommer, A. Chiche, G. Krausch, U. Steiner, and M. Thelakkat (2009). Controlled solvent vapour annealing for polymer electronics. *Soft Matter* **5** (21), 4206–4211. DOI: [10.1039/B907147D](https://doi.org/10.1039/B907147D).
- [139] C. Jin, B. C. Olsen, E. J. Luber, and J. M. Buriak (2017). Nanopatterning via Solvent Vapor Annealing of Block Copolymer Thin Films. *Chemistry of Materials* **29** (1), 176–188. DOI: [10.1021/acs.chemmater.6b02967](https://doi.org/10.1021/acs.chemmater.6b02967).
- [140] B. Jung, K. Kim, Y. Eom, and W. Kim (2015). High-Pressure Solvent Vapor Annealing with a Benign Solvent To Rapidly Enhance the Performance of Organic Photovoltaics. *ACS Applied Materials & Interfaces* **7** (24), 13342–13349. DOI: [10.1021/acsami.5b01658](https://doi.org/10.1021/acsami.5b01658).
- [141] D. Ye, S. N. Kiemle, S. Rongpipi, X. Wang, C. Wang, D. J. Cosgrove, E. W. Gomez, and E. D. Gomez (2018). Resonant soft X-ray scattering reveals cellulose microfibril spacing in plant primary cell walls. *Scientific Reports* **8** (1), 12449. DOI: [10.1038/s41598-018-31024-1](https://doi.org/10.1038/s41598-018-31024-1).
- [142] B. A. Collins, J. E. Cochran, H. Yan, E. Gann, C. Hub, R. Fink, C. Wang, T. Schuettfort, C. R. McNeill, M. L. Chabiny, and H. Ade (2012). Polarized X-ray scattering reveals non-crystalline orientational ordering in organic films. *Nature Materials* **11** (6), 536–543. DOI: [10.1038/nmat3310](https://doi.org/10.1038/nmat3310).
- [143] H. Ade and A. P. Hitchcock (2008). NEXAFS microscopy and resonant scattering: Composition and orientation probed in real and reciprocal space. *Polymer* **49** (3), 643–675. DOI: [10.1016/j.polymer.2007.10.030](https://doi.org/10.1016/j.polymer.2007.10.030).
- [144] J. M. Virgili, Y. Tao, J. B. Kortright, N. P. Balsara, and R. A. Segalman (2007). Analysis of Order Formation in Block Copolymer Thin Films Using Resonant Soft X-ray Scattering. *Macromolecules* **40** (6), 2092–2099. DOI: [10.1021/ma061734k](https://doi.org/10.1021/ma061734k).
- [145] M. Tolan (1999). *X-Ray Scattering from Soft-Matter Thin Films: Materials Science and Basic Research*. Vol. 148. Springer Tracts in Modern Physics. Berlin, Heidelberg: Springer. DOI: [10.1007/BFb0112834](https://doi.org/10.1007/BFb0112834).
- [146] A. Hexemer and P. Müller-Buschbaum (2015). Advanced grazing-incidence techniques for modern soft-matter materials analysis. *IUCrJ* **2** (1), 106–125. DOI: [10.1107/S2052252514024178](https://doi.org/10.1107/S2052252514024178).
- [147] B. L. Henke, E. M. Gullikson, and J. C. Davis (1993). X-Ray Interactions: Photoabsorption, Scattering, Transmission, and Reflection at $E = 50\text{--}30,000$ eV, $Z = 1\text{--}92$. *Atomic Data and Nuclear Data Tables* **54** (2), 181–342. DOI: [10.1006/adnd.1993.1013](https://doi.org/10.1006/adnd.1993.1013).
- [148] W. H. DE Jeu (2016). Introduction and Overview. In: *Basic X-Ray Scattering for Soft Matter*. Ed. by W. H. DE Jeu. Oxford University Press, 1–17. DOI: [10.1093/acprof:oso/9780198728665.003.0001](https://doi.org/10.1093/acprof:oso/9780198728665.003.0001).

- [149] J. Steele, E. Solano, D. Hardy, D. Dayton, D. Ladd, K. White, P. Chen, J. Hou, H. Huang, R. Ali Saha, L. Wang, F. Gao, J. Hofkens, M. Roeffaers, D. Chernyshov, and M. Toney (2023). How to GIWAXS: Grazing Incidence Wide Angle X-Ray Scattering Applied to Metal Halide Perovskite Thin Films. *Advanced Energy Materials* **13**. DOI: [10.1002/aenm.202300760](https://doi.org/10.1002/aenm.202300760).
- [150] W. H. DE Jeu (2016). Soft Matter Films and Surfaces. In: *Basic X-Ray Scattering for Soft Matter*. Ed. by W. H. DE Jeu. Oxford University Press, 103–127. DOI: [10.1093/acprof:oso/9780198728665.003.0006](https://doi.org/10.1093/acprof:oso/9780198728665.003.0006).
- [151] (2009). Die Beugung an periodischen Strukturen. In: *Festkörperphysik: Einführung in die Grundlagen*. Ed. by H. Ibach and H. Lüth. Berlin, Heidelberg: Springer, 51–80. DOI: [10.1007/978-3-540-85795-2_3](https://doi.org/10.1007/978-3-540-85795-2_3).
- [152] W. H. DE Jeu (2016). Basic Scattering by Particles. In: *Basic X-Ray Scattering for Soft Matter*. Ed. by W. H. DE Jeu. Oxford University Press, 18–38. DOI: [10.1093/acprof:oso/9780198728665.003.0002](https://doi.org/10.1093/acprof:oso/9780198728665.003.0002).
- [153] D. E. Johnston, K. G. Yager, H. Hlaing, X. Lu, B. M. Ocko, and C. T. Black (2014). Nanostructured Surfaces Frustrate Polymer Semiconductor Molecular Orientation. *ACS Nano* **8** (1), 243–249. DOI: [10.1021/nm4060539](https://doi.org/10.1021/nm4060539).
- [154] J. Rivnay, S. C. B. Mannsfeld, C. E. Miller, A. Salleo, and M. F. Toney (2012). Quantitative Determination of Organic Semiconductor Microstructure from the Molecular to Device Scale. *Chemical Reviews* **112** (10), 5488–5519. DOI: [10.1021/cr3001109](https://doi.org/10.1021/cr3001109).
- [155] Y. Chen, Z. Wu, L. Ding, S. Zhang, Z. Chen, W. Li, Y. Zhao, Y. Wang, and Y. Liu (2023). Manipulating Crystal Stacking by Sidechain Engineering for High-Performance N-Type Organic Semiconductors. *Advanced Functional Materials* **33** (50), 2304316. DOI: [10.1002/adfm.202304316](https://doi.org/10.1002/adfm.202304316).
- [156] J. Xin, W. Li, Y. Zhang, Q. Liang, C. Song, Y. Zhao, Z. He, J. Liu, and W. Ma (2023). A review of nonfullerene solar cells: Insight into the correlation among molecular structure, morphology, and device performance. *Battery Energy* **2** (2), 20220040. DOI: [10.1002/bte2.20220040](https://doi.org/10.1002/bte2.20220040).
- [157] S. Shoaee, H. M. Luong, J. Song, Y. Zou, T.-Q. Nguyen, and D. Neher (2024). What We have Learnt from PM6:Y6. *Advanced Materials* **36** (20), 2302005. DOI: [10.1002/adma.202302005](https://doi.org/10.1002/adma.202302005).
- [158] G. Kupgan, X. K. Chen, and J. L. Brédas (2021). Molecular packing of non-fullerene acceptors for organic solar cells: Distinctive local morphology in Y6 vs. ITIC derivatives. *Materials Today Advances* **11**, 100154. DOI: [10.1016/j.mtadv.2021.100154](https://doi.org/10.1016/j.mtadv.2021.100154).
- [159] G. Zhang, X.-K. Chen, J. Xiao, P. C. Y. Chow, M. Ren, G. Kupgan, X. Jiao, C. C. S. Chan, X. Du, R. Xia, Z. Chen, J. Yuan, Y. Zhang, S. Zhang, Y. Liu, Y. Zou, H. Yan, K. S. Wong, V. Coropceanu, N. Li, C. J. Brabec, J.-L. Bredas, H.-L. Yip, and Y. Cao (2020). Delocalization of exciton and electron wavefunction in non-fullerene acceptor molecules enables efficient organic solar cells. *Nature Communications* **11** (1), 3943. DOI: [10.1038/s41467-020-17867-1](https://doi.org/10.1038/s41467-020-17867-1).
- [160] J. Rivnay, R. Noriega, R. J. Kline, A. Salleo, and M. F. Toney (2011). Quantitative analysis of lattice disorder and crystallite size in organic semiconductor thin films. *Physical Review B* **84** (4), 045203. DOI: [10.1103/PhysRevB.84.045203](https://doi.org/10.1103/PhysRevB.84.045203).

-
- [161] B. E. Warren (1969). *X-ray Diffraction*. Addison-Wesley Publishing Company.
- [162] D.-M. Smilgies (2009). Scherrer grain-size analysis adapted to grazing-incidence scattering with area detectors. *Journal of Applied Crystallography* **42** (6), 1030–1034. DOI: [10.1107/S0021889809040126](https://doi.org/10.1107/S0021889809040126).
- [163] B. E. Warren and B. L. Averbach (1950). The Effect of Cold-Work Distortion on X-Ray Patterns. *Journal of Applied Physics* **21**, 595–599. DOI: [10.1063/1.1699713](https://doi.org/10.1063/1.1699713).
- [164] B. E. Warren and B. L. Averbach (1952). The Separation of Cold-Work Distortion and Particle Size Broadening in X-Ray Patterns. *Journal of Applied Physics* **23**, 497–497. DOI: [10.1063/1.1702234](https://doi.org/10.1063/1.1702234).
- [165] B. Crist and J. B. Cohen (1979). Fourier analysis of polymer x-ray diffraction patterns. *Journal of Polymer Science: Polymer Physics Edition* **17** (6), 1001–1010. DOI: [10.1002/pol.1979.180170609](https://doi.org/10.1002/pol.1979.180170609).
- [166] T. J. Prosa, J. Moulton, A. J. Heeger, and M. J. Winokur (1999). Diffraction Line-Shape Analysis of Poly(3-dodecylthiophene): A Study of Layer Disorder through the Liquid Crystalline Polymer Transition. *Macromolecules* **32** (12), 4000–4009. DOI: [10.1021/ma981059h](https://doi.org/10.1021/ma981059h).
- [167] R. Somashekar and H. Somashekarappa (1997). X-ray Diffraction-Line Broadening Analysis: Paracrystalline Method. *Journal of Applied Crystallography* **30** (2), 147–152. DOI: [10.1107/S0021889896010023](https://doi.org/10.1107/S0021889896010023).
- [168] S. M. Wecker, J. B. Cohen, and T. Davidson (1974). Study of deformation in polytetrafluoroethylene by x-ray line broadening. *Journal of Applied Physics* **45** (10), 4453–4457. DOI: [10.1063/1.1663071](https://doi.org/10.1063/1.1663071).
- [169] D. Balzar (1992). Profile fitting of X-ray diffraction lines and Fourier analysis of broadening. *Journal of Applied Crystallography* **25** (5), 559–570. DOI: [10.1107/S0021889892004084](https://doi.org/10.1107/S0021889892004084).
- [170] J. L. Baker, L. H. Jimison, S. Mannsfeld, S. Volkman, S. Yin, V. Subramanian, A. Salleo, A. P. Alivisatos, and M. F. Toney (2010). Quantification of Thin Film Crystallographic Orientation Using X-ray Diffraction with an Area Detector. *Langmuir* **26** (11), 9146–9151. DOI: [10.1021/la904840q](https://doi.org/10.1021/la904840q).
- [171] W. H. DE Jeu (2016). Diffraction Physics: Scattering by Crystals. In: *Basic X-Ray Scattering for Soft Matter*. Ed. by W. H. DE Jeu. Oxford University Press, 54–76. DOI: [10.1093/acprof:oso/9780198728665.003.0004](https://doi.org/10.1093/acprof:oso/9780198728665.003.0004).
- [172] T. G. Mayerhöfer, S. Pahlow, and J. Popp (2023). Understanding the Limits of the Bouguer-Beer-Lambert Law. *Spectroscopy*, 29–30, 58. DOI: [10.56530/spectroscopy.iq2368r9](https://doi.org/10.56530/spectroscopy.iq2368r9).
- [173] D. A. Skoog, F. J. Holler, and S. R. Crouch (2007). *Principles of Instrumental Analysis*. Thomson Brooks/Cole.
- [174] I. Oshina and J. Spigulis (2021). Beer–Lambert law for optical tissue diagnostics: current state of the art and the main limitations. *Journal of Biomedical Optics* **26** (10), 100901. DOI: [10.1117/1.JBO.26.10.100901](https://doi.org/10.1117/1.JBO.26.10.100901).
- [175] M. K. Kiteto and C. A. Mecha (2024). Insight into the Bouguer-Beer-Lambert Law: A review. *Sustainable Chemical Engineering*, 567–587. DOI: [10.37256/sce.5220245325](https://doi.org/10.37256/sce.5220245325).

- [176] S. Pradhan, J. S. Bhattarai, M. Murugavel, and O. P. Sharma (2024). *Application of an Electronic Eye to Address the Limitations of Beer-Lambert Law*. DOI: [10.26434/chemrxiv-2024-dc3ml](https://doi.org/10.26434/chemrxiv-2024-dc3ml).
- [177] F. S. Rocha, A. J. Gomes, C. N. Lunardi, S. Kaliaguine, and G. S. Patience (2018). Experimental methods in chemical engineering: Ultraviolet visible spectroscopy—UV-Vis. *The Canadian Journal of Chemical Engineering* **96** (12), 2512–2517. DOI: [10.1002/cjce.23344](https://doi.org/10.1002/cjce.23344).
- [178] W. C. Holmes (1924). The Influence of Variation in Concentration on the Absorption Spectra of Dye Solutions. *Industrial & Engineering Chemistry* **16** (1), 35–40. DOI: [10.1021/ie50169a014](https://doi.org/10.1021/ie50169a014).
- [179] J. Lavorel (1957). Influence of Concentration on the Absorption Spectrum and the Action Spectrum of Fluorescence of Dye Solutions. *The Journal of Physical Chemistry* **61** (12), 1600–1605. DOI: [10.1021/j150558a006](https://doi.org/10.1021/j150558a006).
- [180] A. Penzkofer, W. Leupacher, B. Meier, B. Runde, and K. H. Drexhage (1987). Concentration-dependent absorption and emission behaviour of a pyrimidonecarbocyanine dye in hexafluoroisopropanol. *Chemical Physics* **115** (1), 143–150. DOI: [10.1016/0301-0104\(87\)80186-6](https://doi.org/10.1016/0301-0104(87)80186-6).
- [181] R. Philip, A. Penzkofer, W. Bäumlner, R. M. Szeimies, and C. Abels (1996). Absorption and fluorescence spectroscopic investigation of indocyanine green. *Journal of Photochemistry and Photobiology A: Chemistry* **96** (1), 137–148. DOI: [10.1016/1010-6030\(95\)04292-X](https://doi.org/10.1016/1010-6030(95)04292-X).
- [182] T. G. Mayerhöfer, S. Pahlow, and J. Popp (2020). The Bouguer-Beer-Lambert Law: Shining Light on the Obscure. *ChemPhysChem* **21** (18), 2029–2046. DOI: [10.1002/cphc.202000464](https://doi.org/10.1002/cphc.202000464).
- [183] N. J. Turro (1991). *Modern Molecular Photochemistry*. University Science Books.
- [184] P. K. H. Ho, J.-S. Kim, N. Tessler, and R. H. Friend (2001). Photoluminescence of poly(p-phenylenevinylene)–silica nanocomposites: Evidence for dual emission by Franck–Condon analysis. *The Journal of Chemical Physics* **115** (6), 2709–2720. DOI: [10.1063/1.1372508](https://doi.org/10.1063/1.1372508).
- [185] M. Kasha (1963). Energy Transfer Mechanisms and the Molecular Exciton Model for Molecular Aggregates. *Radiation Research* **20** (1), 55–70. DOI: [10.2307/3571331](https://doi.org/10.2307/3571331).
- [186] M. Kasha, H. R. Rawls, and M. A. El-Bayoumi (1965). The exciton model in molecular spectroscopy. *Pure and Applied Chemistry* **11** (3-4), 371–392. DOI: [10.1351/pac196511030371](https://doi.org/10.1351/pac196511030371).
- [187] E. E. Jelley (1936). Spectral Absorption and Fluorescence of Dyes in the Molecular State. *Nature* **138** (3502), 1009–1010. DOI: [10.1038/1381009a0](https://doi.org/10.1038/1381009a0).
- [188] G. Scheibe (1937). Über die Veränderlichkeit der Absorptionsspektren in Lösungen und die Nebenvalenzen als ihre Ursache. *Angewandte Chemie* **50** (11), 212–219. DOI: [10.1002/ange.19370501103](https://doi.org/10.1002/ange.19370501103).
- [189] F. Würthner, T. E. Kaiser, and C. R. Saha-Möller (2011). J-Aggregates: From Serendipitous Discovery to Supramolecular Engineering of Functional Dye Materials. *Angewandte Chemie International Edition* **50** (15), 3376–3410. DOI: [10.1002/anie.201002307](https://doi.org/10.1002/anie.201002307).

-
- [190] F. C. Spano (2005). Modeling disorder in polymer aggregates: The optical spectroscopy of regioregular poly(3-hexylthiophene) thin films. *The Journal of Chemical Physics* **122** (23), 234701. DOI: [10.1063/1.1914768](https://doi.org/10.1063/1.1914768).
- [191] N. J. Hestand and F. C. Spano (2018). Expanded Theory of H- and J-Molecular Aggregates: The Effects of Vibronic Coupling and Intermolecular Charge Transfer. *Chemical Reviews* **118** (15), 7069–7163. DOI: [10.1021/acs.chemrev.7b00581](https://doi.org/10.1021/acs.chemrev.7b00581).
- [192] H. Yamagata and F. C. Spano (2012). Interplay between intrachain and interchain interactions in semiconducting polymer assemblies: The HJ-aggregate model. *The Journal of Chemical Physics* **136** (18), 184901. DOI: [10.1063/1.4705272](https://doi.org/10.1063/1.4705272).
- [193] F. C. Spano (2010). The Spectral Signatures of Frenkel Polarons in H- and J-Aggregates. *Accounts of Chemical Research* **43** (3), 429–439. DOI: [10.1021/ar900233v](https://doi.org/10.1021/ar900233v).
- [194] J. Clark, C. Silva, R. H. Friend, and F. C. Spano (2007). Role of Intermolecular Coupling in the Photophysics of Disordered Organic Semiconductors: Aggregate Emission in Regioregular Polythiophene. *Physical Review Letters* **98** (20), 206406. DOI: [10.1103/PhysRevLett.98.206406](https://doi.org/10.1103/PhysRevLett.98.206406).
- [195] J. Gierschner, Y.-S. Huang, B. Van Averbeke, J. Cornil, R. H. Friend, and D. Beljonne (2009). Excitonic versus electronic couplings in molecular assemblies: The importance of non-nearest neighbor interactions. *The Journal of Chemical Physics* **130** (4), 044105. DOI: [10.1063/1.3065267](https://doi.org/10.1063/1.3065267).
- [196] F. C. Spano and C. Silva (2014). H- and J-Aggregate Behavior in Polymeric Semiconductors. *Annual Review of Physical Chemistry* **65**, 477–500. DOI: [10.1146/annurev-physchem-040513-103639](https://doi.org/10.1146/annurev-physchem-040513-103639).
- [197] C. A. Sandstedt, R. D. Rieke, and C. J. Eckhardt (1995). Solid-State and Solvatochromic Spectra of a Highly Regular Polythiophene. *Chemistry of Materials* **7** (6), 1057–1059. DOI: [10.1021/cm00054a005](https://doi.org/10.1021/cm00054a005).
- [198] J. Clark, J.-F. Chang, F. C. Spano, R. H. Friend, and C. Silva (2009). Determining exciton bandwidth and film microstructure in polythiophene films using linear absorption spectroscopy. *Applied Physics Letters* **94** (16), 163306. DOI: [10.1063/1.3110904](https://doi.org/10.1063/1.3110904).
- [199] F. M. Keheze, D. Raithel, T. Wu, D. Schiefer, M. Sommer, R. Hildner, and G. Reiter (2017). Signatures of Melting and Recrystallization of a Bulky Substituted Poly(thiophene) Identified by Optical Spectroscopy. *Macromolecules* **50** (17), 6829–6839. DOI: [10.1021/acs.macromol.7b01080](https://doi.org/10.1021/acs.macromol.7b01080).
- [200] S. Srivastava, A. K. Rai, M. Shrivastava, and P. C. Ramamurthy (2024). Sub-100 nm Patterning of P3HT with Enhanced OFET Device Performance by Dose Optimization of Electron Beam-Induced Cross-Linking. *ACS Applied Electronic Materials* **6** (8), 5923–5933. DOI: [10.1021/acsaelm.4c00904](https://doi.org/10.1021/acsaelm.4c00904).
- [201] S. Sharma, D. Kar, P. D. Khanikar, A. Moudgil, P. Mishra, and S. Das (2024). Hybrid MoSe₂/P3HT Transistor for Real-Time Ammonia Sensing in Biofluids. *ACS Applied Materials & Interfaces* **16** (24), 30648–30657. DOI: [10.1021/acsaami.4c02352](https://doi.org/10.1021/acsaami.4c02352).

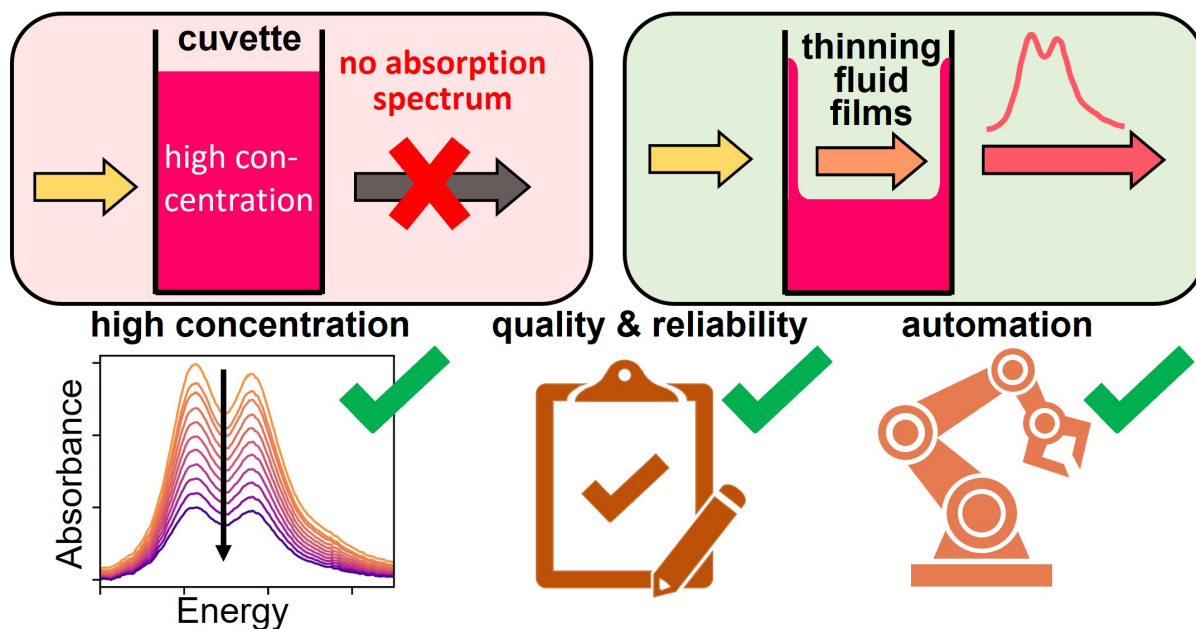
- [202] H. Runfang, Y. Yangfan, L. Leilei, J. Jianlong, Z. Qiang, D. Lifeng, S. Shengbo, and L. Qiang (2022). P3HT-based organic field effect transistor for low-cost, label-free detection of immunoglobulin G. *Journal of Biotechnology* **359**, 75–81. DOI: [10.1016/j.jbiotec.2022.09.022](https://doi.org/10.1016/j.jbiotec.2022.09.022).
- [203] P. Lin and F. Yan (2012). Organic Thin-Film Transistors for Chemical and Biological Sensing. *Advanced Materials* **24** (1), 34–51. DOI: [10.1002/adma.201103334](https://doi.org/10.1002/adma.201103334).
- [204] P. Y. Ho, O. Ditzer, A. Solgi, H. Zhang, R. Thümmel, M. Al-Hussein, H. Kleeemann, N. Sun, and F. S.-C. Lissel (2025). Boosting OECT Performance with PEGylated Gold Nanoparticles in Hydrophobic Channels. *Advanced Functional Materials* **35** (2), 2412559. DOI: [10.1002/adfm.202412559](https://doi.org/10.1002/adfm.202412559).
- [205] D.-H. Kim, J. Lee, Y. Kim, H. Yoo, and E. K. Lee (2024). Enhanced synaptic behavior of neuromorphic device based on organic electrochemical transistors by adding Aminosilane. *Organic Electronics* **131**, 107076. DOI: [10.1016/j.orgel.2024.107076](https://doi.org/10.1016/j.orgel.2024.107076).
- [206] C. Yan, L. Xiang, Y. Xiao, X. Zhang, Z. Jiang, B. Zhang, C. Li, S. Di, and F. Zhang (2024). Lateral intercalation-assisted ionic transport towards high-performance organic electrochemical transistor. *Nature Communications* **15** (1), 10118. DOI: [10.1038/s41467-024-54528-z](https://doi.org/10.1038/s41467-024-54528-z).
- [207] H. J. Kim, K. Perera, Z. Liang, B. Bowen, J. Mei, and B. W. Boudouris (2022). Radical Polymer-Based Organic Electrochemical Transistors. *ACS Macro Letters* **11** (2), 243–250. DOI: [10.1021/acsmacrolett.1c00695](https://doi.org/10.1021/acsmacrolett.1c00695).
- [208] J. Bisquert, B. Ilyassov, and N. Tessler (2024). Switching Response in Organic Electrochemical Transistors by Ionic Diffusion and Electronic Transport. *Advanced Science* **11** (36), 2404182. DOI: [10.1002/advs.202404182](https://doi.org/10.1002/advs.202404182).
- [209] C. Lee, Y. Kim, W. Kim, E. Lee, and E. Lee (2024). High-Performance Synaptic Devices Based on Cross-linked Organic Electrochemical Transistors with Dual Ion Gel. *Advanced Functional Materials*. DOI: [10.1002/adfm.202417539](https://doi.org/10.1002/adfm.202417539).
- [210] Z. Wang, G. Yang, Y. Yin, K. Li, H. Guan, X. Yu, B. Xu, S. Yin, and Y. Hao (2024). Synergistic Effect of Defects Passivation and Energy Level Alignment Realizing P3HT-Based High-Efficiency CsPbI₃ Perovskite Solar Cells. *Small* **20** (49), 2402910. DOI: [10.1002/sml1.202402910](https://doi.org/10.1002/sml1.202402910).
- [211] W. Ren, J. Ren, Y. Wu, S. Li, Q. Sun, and Y. Hao (2024). An Extraordinary Antisolvent Ethyl Cyanofornate for Achieving High Efficiency and Stability P3HT-Based CsPbI₃ Perovskite Solar Cells. *Advanced Functional Materials* **34** (8), 2311260. DOI: [10.1002/adfm.202311260](https://doi.org/10.1002/adfm.202311260).
- [212] H. Kassem, A. Salehi, and M. Kahrizi (2024). Recent Advances in Poly(3-hexylthiophene) and Its Applications in Perovskite Solar Cells. *Energy Technology* **12** (5), 2301032. DOI: [10.1002/ente.202301032](https://doi.org/10.1002/ente.202301032).
- [213] C. Seriwattanachai, S. Sahasithiwat, T. Chotchuangchutchaval, L. Srathongsian, W. Wattanathana, Z. Ning, N. Phuphathanaphong, P. Sakata, K. K. Shin Thant, T. Sukwiboon, A. Inna, T. Kanlayapattamapong, A. Kaewprajak, P. Kumnorkaew, R. Supruangnet, T. Wongpinij, H. Nakajima, D. Wongratanaphisan, P. Pakawatpanurut, P. Ruankham, and P. Kanjanaboos (2025). Ferrocene Interlayer for a Stable and Gap-Free P3HT-Based Perovskite Solar Cell as a Low-Cost Power Source for Indoor IoTs. *ACS Photonics*. DOI: [10.1021/acsp Photonics.4c01469](https://doi.org/10.1021/acsp Photonics.4c01469).

-
- [214] J. Tong, C. Dong, V. M. Arnal, M. Yao, Q. Wang, Y. Song, Y. Deng, Y. Gao, G. Yue, W. Zhang, M. I. Saidaminov, and F. Tan (2024). Synergistic potentiation between P3HT and PTAA enables blade-coated carbon-electrode perovskite solar cells with >21% outdoor and >35% indoor efficiencies. *Chemical Engineering Journal* **501**, 157577. DOI: [10.1016/j.cej.2024.157577](https://doi.org/10.1016/j.cej.2024.157577).
- [215] Y. Zhang, W. Liu, F. Tan, and Y. Gu (2015). The essential role of the poly(3-hexylthiophene) hole transport layer in perovskite solar cells. *Journal of Power Sources* **274**, 1224–1230. DOI: [10.1016/j.jpowsour.2014.10.145](https://doi.org/10.1016/j.jpowsour.2014.10.145).
- [216] S. Kundu and T. L. Kelly (2018). Improving the moisture stability of perovskite solar cells by using PMMA/P3HT based hole-transport layers. *Materials Chemistry Frontiers* **2** (1), 81–89. DOI: [10.1039/C7QM00396J](https://doi.org/10.1039/C7QM00396J).
- [217] P. Zhou, T. Bu, S. Shi, L. Li, Y. Zhang, Z. Ku, Y. Peng, J. Zhong, Y.-B. Cheng, and F. Huang (2018). Efficient and stable mixed perovskite solar cells using P3HT as a hole transporting layer. *Journal of Materials Chemistry C* **6** (21), 5733–5737. DOI: [10.1039/C8TC01345D](https://doi.org/10.1039/C8TC01345D).
- [218] Y. He, L. Han, Y. Hou, X. Qiao, and M. Zhu (2025). P3HT/*g*-C₃N₄ composite fiber membranes for high-performance photocatalytic hydrogen evolution. *Applied Surface Science* **682**, 161673. DOI: [10.1016/j.apsusc.2024.161673](https://doi.org/10.1016/j.apsusc.2024.161673).
- [219] L. Zhang, S. A. Gregory, K. L. Malinowski, A. Atassi, G. Freychet, and M. D. Losego (2024). Vapor Phase Infiltration of Titanium Oxide into P3HT to Create Organic–Inorganic Hybrid Photocatalysts. *ACS Applied Materials & Interfaces* **16** (26), 33259–33269. DOI: [10.1021/acsami.3c16469](https://doi.org/10.1021/acsami.3c16469).
- [220] K.-T. Lin, W.-H. Cheng, H.-L. Cheng, H.-H. Lin, W.-Y. Chou, B.-Y. Hsu, C.-A. Mao, Y.-C. Hou, and J. Ruan (2024). Photocatalytic Hydrogen Evolution Enabled by Oriented Phase Interactions between Monolayers of P3HT-Wrapped MoS₂ and Ferroelectric Lamellar Crystals. *Advanced Functional Materials* **34** (2), 2307262. DOI: [10.1002/adfm.202307262](https://doi.org/10.1002/adfm.202307262).
- [221] Z. Goh, A. Dolan, J. M. DE LA Perrelle, M. Jevric, X. Pan, M. R. Andersson, D. M. Huang, and T. W. Kee (2024). Preparation-Dependent Photocatalytic Hydrogen Evolution by Organic Semiconducting Nanoparticles. *ACS Applied Nano Materials* **7** (22), 25544–25555. DOI: [10.1021/acsamm.4c04625](https://doi.org/10.1021/acsamm.4c04625).
- [222] J. Bruder, K. Fischer, J. Armleder, E. Müller, N. Da Roit, S. Behrens, Y. Peng, W. Wenzel, H. Röhm, and A. Colsmann (2024). Photocatalytic Hydrogen Generation in Surfactant-Free, Aqueous Organic Nanoparticle Dispersions. *Small* **20** (47), 2406236. DOI: [10.1002/smll.202406236](https://doi.org/10.1002/smll.202406236).
- [223] D. Floresyona, F. Goubard, P.-H. Aubert, I. Lampre, J. Mathurin, A. Dazzi, S. Ghosh, P. Beaunier, F. Brisset, S. Remita, L. Ramos, and H. Remita (2017). Highly active poly(3-hexylthiophene) nanostructures for photocatalysis under solar light. *Applied Catalysis B: Environmental* **209**, 23–32. DOI: [10.1016/j.apcatb.2017.02.069](https://doi.org/10.1016/j.apcatb.2017.02.069).
- [224] B. Jana, S. Bhattacharyya, and A. Patra (2015). Conjugated polymer P3HT–Au hybrid nanostructures for enhancing photocatalytic activity. *Physical Chemistry Chemical Physics* **17** (23), 15392–15399. DOI: [10.1039/C5CP01769F](https://doi.org/10.1039/C5CP01769F).

-
- [225] D. Ghezzi, M. R. Antognazza, R. Maccarone, S. Bellani, E. Lanzarini, N. Martino, M. Mete, G. Pertile, S. Bisti, G. Lanzani, and F. Benfenati (2013). A polymer optoelectronic interface restores light sensitivity in blind rat retinas. *Nature Photonics* **7** (5), 400–406. DOI: [10.1038/nphoton.2013.34](https://doi.org/10.1038/nphoton.2013.34).
- [226] J. F. Maya-Vetencourt, G. Manfredi, M. Mete, E. Colombo, M. Bramini, S. Di Marco, D. Shmal, G. Mantero, M. Dipalo, A. Rocchi, M. L. DiFrancesco, E. D. Papaleo, A. Russo, J. Barsotti, C. Eleftheriou, F. Di Maria, V. Cossu, F. Piazza, L. Emionite, F. Ticconi, C. Marini, G. Sambuceti, G. Pertile, G. Lanzani, and F. Benfenati (2020). Subretinally injected semiconducting polymer nanoparticles rescue vision in a rat model of retinal dystrophy. *Nature Nanotechnology* **15** (8), 698–708. DOI: [10.1038/s41565-020-0696-3](https://doi.org/10.1038/s41565-020-0696-3).
- [227] S. Francia, S. Di Marco, M. L. DiFrancesco, D. V. Ferrari, D. Shmal, A. Cavalli, G. Pertile, M. Attanasio, J. F. Maya-Vetencourt, G. Manfredi, G. Lanzani, F. Benfenati, and E. Colombo (2023). P3ht-Graphene Device for the Restoration of Visual Properties in a Rat Model of Retinitis Pigmentosa. *Advanced Materials Technologies* **8** (6), 2201467. DOI: [10.1002/admt.202201467](https://doi.org/10.1002/admt.202201467).

8

Facilitating Absorption Spectroscopy of Strongly Absorbing Fluids: A High-Throughput Approach



Fabian Eller, and Eva M. Herzig

Published in
The Journal of Physical Chemistry A **2024**, 128(44), 9682-9687
(DOI: 10.1021/acs.jpca.4c04902)

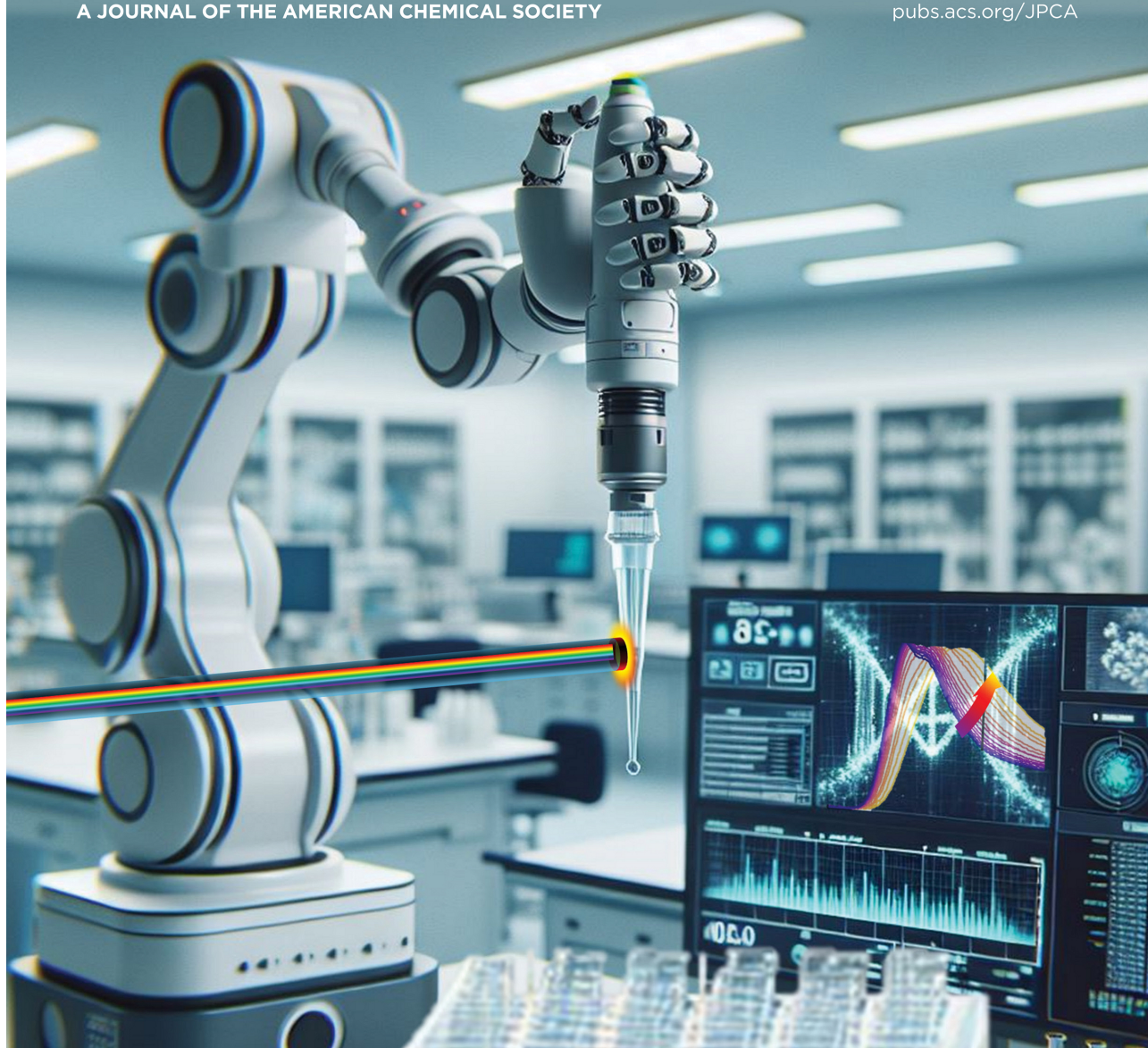
Reprinted with permission from
The Journal of Physical Chemistry A **2024**, 128(44), 9682-968
Copyright 2024 American Chemical Society

THE JOURNAL OF PHYSICAL CHEMISTRY

A

A JOURNAL OF THE AMERICAN CHEMICAL SOCIETY

November 7, 2024
Volume 128
Number 44
pubs.acs.org/JPCA



 **ACS Publications**
Most Trusted. Most Cited. Most Read.

www.acs.org

Facilitating Absorption Spectroscopy of Strongly Absorbing Fluids: A High-Throughput Approach

Published as part of *The Journal of Physical Chemistry A special issue "Spectroscopic Techniques for Renewable Energy"*.

Fabian Eller and Eva M. Herzig*



Cite This: *J. Phys. Chem. A* 2024, 128, 9682–9687



Read Online

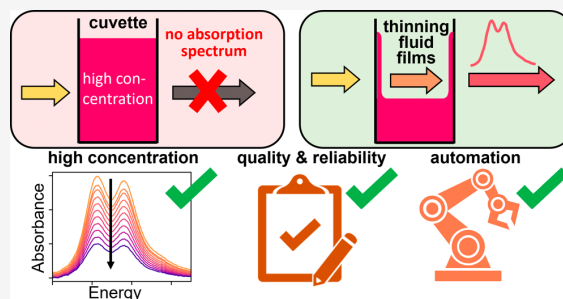
ACCESS |

Metrics & More

Article Recommendations

Supporting Information

ABSTRACT: Measuring absorption spectra of strongly absorbing solutions is usually only possible by diluting the solution. However, the absorption spectra can be heavily influenced by concentration-dependent interactions, so dilution leads to misleading results. To enable reliable absorption measurements of concentrated solutions, we introduce in this work thinning fluid film spectroscopy (TFFS), a simple and highly automatable method. We present three exemplary measurement modes of TFFS suitable for many different applications and validate the TFFS measurements with control data obtained in specialized, low optical path length cuvettes. Additionally, we compare the suitability of the different measurement modes over a broad concentration range and demonstrate the automation possibilities with a spectroscopy robot. Beyond this automated approach for highly efficient and high-throughput lab work, we also show the possibility of direct integration into production systems with an in-line setup, which can be incorporated into a variety of pipe systems. The TFFS method is not limited to samples from material science but can be transferred to a broad variety of research and industry fields, including proteins, food, and pharmaceuticals or also agriculture and forensics.



1. INTRODUCTION

UV–vis absorption measurements provide a powerful method for material investigations in solutions in many scientific communities ranging from biology, chemistry, and physics to engineering and medicine.^{1–5} Particularly when the interaction of materials is being investigated, higher solution concentrations and hence strongly absorbing solutions are of interest. However, such measurements are impossible or at least challenging in 10 and 1 mm cuvettes. Low photon counts on the detector become dominated by noise or stray light, resulting in seemingly lower absorbance and, hence, a nonlinear distortion of the overall absorbance as a function of wavelength. To compensate for this effect, the first option is to perform strong dilutions. However, the dilution of solutions can strongly change the absorption spectra of the solute as the intermolecular interactions that determine this spectrum often change with concentration or even contain the information on interest in such studies.^{6–9} Furthermore, dilution is an additional step in the measurement procedure, limiting in situ or high-throughput applications.

Second, specialized cuvettes with optical path lengths down to 0.01 mm exist to access 100-fold higher concentrations, but more strongly absorbing solutions are still inaccessible. To broaden this limited measurement range, here we introduce a

novel method, thinning fluid film spectroscopy (TFFS) where a thin fluid film is created to carry out absorption spectroscopy in transmission. After the walls of a measurement container were wetted with the desired solution, multiple absorption spectra are obtained from white light passing the thinning fluid film flowing down the walls as a function of time recorded by a spectrometer. An automated analysis procedure returns a static absorption spectrum. Due to the simplicity and flexibility of this approach, it is less costly and more reliable than working with specialized, low optical path length cuvettes and is less labor intensive, and the measurement procedure can be fully automated. Particularly, the possibility for high-throughput measurements on strongly absorbing solutions makes TFFS an attractive approach for a broad range of research and technology applications, from synthesis to processing.

Received: July 21, 2024

Revised: October 9, 2024

Accepted: October 14, 2024

Published: October 24, 2024



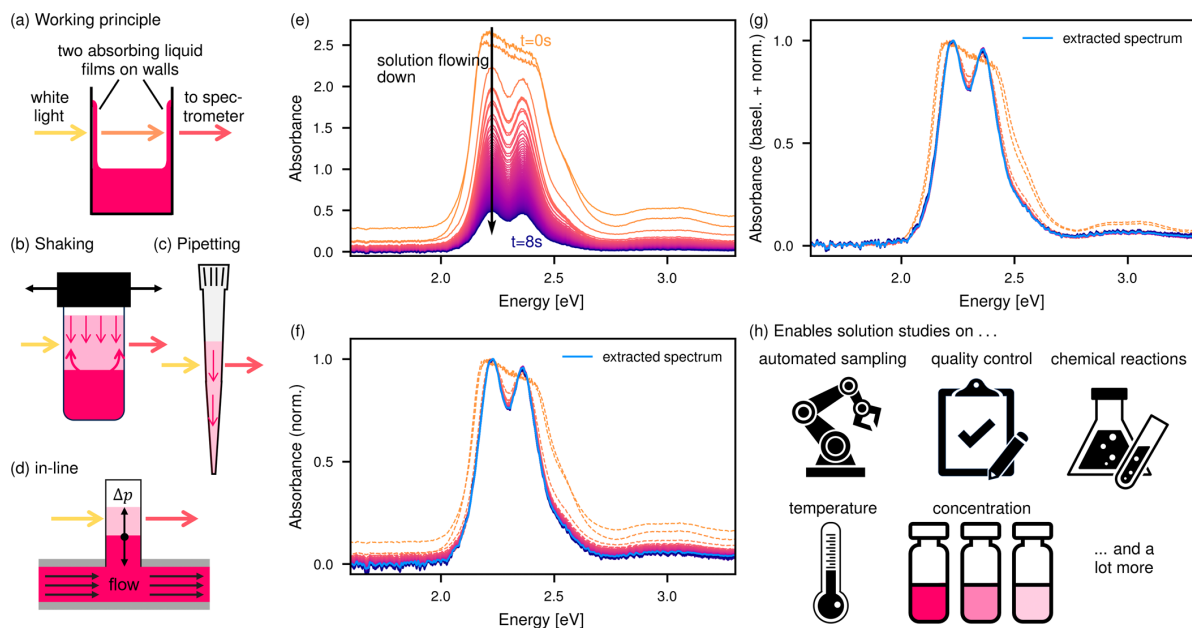


Figure 1. (a) Sketch of the measurement principle of TFFS and in (b)–(d) three exemplary measurement modes: (b) shaking, (c) pipetting, (d) in-line. All measurement modes rely on different methods to generate a thin fluid film flowing down the container walls. (e) Time-resolved absorption spectra of a 1 mg mL⁻¹ Rhodamine B in H₂O solution in the shaking mode. The same spectra (f) normalized to peak absorbance and (g) with an additional baseline correction (extracted from 1.1 eV to 1.4 eV). Dashed lines are disregarded as they are beyond the detection limit; the light blue curve is the extracted spectrum formed by the average of suitable spectra. (h) Examples of possible applications.

2. METHODS

2.1. Materials. Rhodamine B was purchased from Magnacol, PM6 ($M_n = 45$ kDa, $M_w = 93$ kDa, $PDI = 2.07$) from Brilliant Matters, o-DCB from Acros Organics, KMnO₄ from Grüssing, and NaOH from Hedinger.

2.2. Solutions. All of the solutions used were prepared by weighing the powder to be dissolved, adding the specified solvent to achieve the given concentration, and eventually heating it to dissolve all material. For the study of the chemical reaction of KMnO₄ in Figure 3c, 500 μL of a 50 mg mL⁻¹ KMnO₄ in H₂O solution was mixed with 500 μL of a 100 mg mL⁻¹ NaOH in H₂O solution (first spectrum). 20 μL aliquot of 100 mg mL⁻¹ Na₂SO₃ in H₂O solution was added for every further measured spectrum until 400 μL of total addition was reached.

2.3. Cuvettes. The used low optical path length cuvettes are Hellma Demountable Cell 106-QS with path lengths of (0.10 ± 0.005) mm and (0.01 ± 0.003) mm.

2.4. TFFS Measurements. All TFFS measurements were conducted with an AvaLight-HAL-S-Mini2 halogen white light source and an AvaSpec-ULS2048CL-EVO-RS-UA spectrometer (both from Avantes). An integration time of 1.8 ms for pipetting and shaking and 0.1 ms for in-line measurements was used throughout and averaged as described in the main text and the figure captions. The measurement times were chosen individually for every solution, depending on the time scale with which the absorbance is decreasing with. The spectrometer was controlled from the same Python scripts as the pipetting, shaking, and in-line fluid film formation enabling a measurement start still during the fluid film formation or immediately after it before the fluid film is thinned too much. In the case of the shaking mode, the measurement was started

immediately after the last shaking move is finished, while for the pipetting and in-line measurements, the measurements were started while the fluid ejection was still ongoing. In Figures 2 and S4, extracted spectra obtained from several repeated TFFS measurements were averaged to ensure a high reliability of the validation. Reference and dark measurements were used to obtain the absorbance values. In the Supporting Information, the section “Guide to conducting TFFS measurements” provides especially important guidance to find suitable measurement settings, but also other hints for successful TFFS measurements.

2.5. Automation. The home-built measurement robot includes a three-dimensional positioning system for positioning the pipet tips and glass vials as well as for shaking the glass vials (ROTH Rotilabo sample vials 4 mL, borosilicate glass, clear) and taking and dropping the pipet tips (servoprax MINIPET transparent pipet tips 200 μL), a pneumatic gripping system to pick and place vials, and a home-built syringe pump for infusing and withdrawing the solution into the pipet tips. Moreover, a temperature-controlled heating stage to heat the glass vials (including all parts of the wall) for temperature-dependent studies is included in the measurement robot. The prototypical in-line unit is realized by connecting two air pumps to a glass tube. The solution can be sucked up into the measurement tube until the desired filling level is reached, and the other pump can dispense the solution again when the hydrostatic pressure and Bernoulli’s principle are not suitable.

3. RESULTS AND DISCUSSION

In the first part of this study, we present our approach of extracting the absorption spectra from a time series of spectra acquired, as well as several exemplary measurement modes of a

fully robotic system. In the second part, the presented measurement modes are validated by measurements in specialized low optical path length cuvettes. Finally, we demonstrate the advantage of automated monitoring of spectral changes with this method.

3.1. Basic Measurement Principle and Exemplary Measurement Modes.

The first step for TFSS measurement is the generation of a thin fluid film on the walls of the measurement container. The incoming light examines simultaneously the front and back film on the container walls (Figure 1a). Here, we present three exemplary possibilities to generate such a liquid film for subsequent measurements with shaking, pipetting, and an in-line approach. These three modes are suitable for a broad range of applications. In the shaking mode, a closed vial is rapidly agitated such that the walls above the fluid level are covered by solution (see sketches in Figures 1b and S1a). In the pipetting mode, the solution is sucked up into a transparent pipet tip and ejected again. If the wetting conditions are appropriate, a thin fluid film of solution remains on the walls instead of being fully ejected (see sketches in Figures 1c and S1b). Of course, this procedure of sucking up and ejecting a solution is not only limited to pipet tips but also applies to, e.g., glass tubes. For an in-line approach, a transparent tube is mounted onto an existing pipe system through which the solution of interest flows. By applying a pressure difference, the solution is sucked up and released again by inverting the pressure difference to leave behind the desired fluid film (see sketch in Figures 1d and S2). Moreover, there are unlimited further possibilities to generate such thin fluid films, which may be more suitable for specific applications or exploit special circumstances in the application.

After the fluid film is generated, the fluid flows down the wall under gravity, thinning the film, while a time series of absorption measurements records the absorption spectra. The film thickness decreases with time, and thus, the absorbance decreases as well, as can be seen in Figure 1e. As the aim of a measurement is to obtain one single absorption spectrum of the solution, the time series of spectra requires further processing. This involves the selection of suitable spectra from the time series, an averaging procedure of these selected spectra, and optional baseline correction and normalization. When all spectra from Figure 1e are normalized to the peak absorbance in Figure 1f, it can clearly be seen that the first strongly absorbing spectra significantly deviate from later absorption spectra. As discussed before, this is due to low photon counts and stray light effects when the thickness of the film is too high. To avoid these artifacts, only spectra with sufficiently low absorbance are selected for further analysis (spectra with dashed lines in Figure 1f are omitted). The threshold for the peak absorbance can be set either manually by visual control or automatically using a deviation metric from, e.g., a median spectrum. On the other end of the time series, spectra are excluded if the films start having too weak absorption to reduce the noise in the final combined spectrum. All selected, normalized spectra are averaged to obtain one single absorption spectrum of the solution. Especially when many weakly absorbing spectra are included for averaging, the noise can be reduced by using a weighted average with a higher weight for the stronger absorbing spectra. Normalized spectra are obtained since the optical path length at each measurement is unknown. To extract the molar extinction coefficient a calibration measurement is necessary to obtain absolute spectra. To avoid misunderstandings in this regard, we

normalize the spectra to the peak absorbance or to the absorbance at other characteristic energies in this paper. While the unknown path length might seem inconvenient compared to cuvettes, it has to be noted that the uncertainty of the 0.01 mm cuvette used is 3 μm (30%), which also heavily limits the absolute precision of the results with such low path length cuvettes. Moreover, even minute evaporation can change the concentration drastically, as only a few microliters of solution are used (2.6 μL in the used cuvette). Since the complete spectrum can sometimes be slightly offset to higher or lower absorbance (most likely due to refraction effects), a baseline correction can further increase the precision of the measurement. This predominantly occurs when using relatively weakly absorbing solutions (as in Figure 1) for TFSS, where larger film thicknesses can lead to stronger refraction effects. When a spectral range without absorbance exists, this range can be used to extract the baseline subtracted from the spectrum. In other cases, baseline subtractions should be handled with care. In Figure 1g, we performed a baseline correction to all spectra (baseline extracted in the low energy range of 1.1–1.4 eV), which collapses all selected spectra to a single curve.

The minimal measurement time is determined by how quickly spectra without spectral distortions are recorded and depends on the solution, the wetting properties of the surface, the range of interest in the irradiated white light spectrum, and the spectrometer itself. The typical measurement time to obtain an averaged spectrum is dominated by the nonsuitable, initial time of thinning to an appropriate film thickness followed by further integration time for the acquisition of suitable spectra, which is in most cases below 10 s. In the Supporting Information, the section “Guide to conducting TFSS measurements” also provides guidelines to find a suitable measurement duration. As the automated analysis can be performed directly together with the measurement procedure, the duration from the start of the measurement until a single fully analyzed absorption spectrum is saved and displayed is in the same time frame. Due to this short measurement and analysis time and the simple measurement routine, TFSS is highly suitable for automation and high-throughput measurements. We developed a measurement robot, which can measure in shaking (also heated vials) as well as the pipetting measurement mode, and a prototype of an in-line system (Figure S2). Thus, this method enables a broad range of highly efficient studies on strongly absorbing solutions, e.g., automated sampling, quality control, chemical reactions, external parameter studies like temperature studies, and concentration-dependent studies, just to name a few possible examples (depicted in Figure 1h). We have applied spectroscopy to agitation-wetted walls to examine the aggregation state in semiconducting polymer solutions and used such controlled solutions to examine the resulting thin film properties.^{10,11}

3.2. Validation and Comparison of Measurement Modes.

To validate the measurements in shaking and pipetting modes, we compare them with conventional measurements in specialized low optical path length cuvettes for varying solution concentrations. Additionally, we examine the suitability of the shaking and pipetting measurement modes for different concentration regimes. In Figure 2a–c, comparisons of three exemplary concentrations of the prototypical fluorescent dye Rhodamine B in water are displayed, and comparisons of further concentrations are displayed in Figure S4. At a concentration of 8 mg mL^{-1} in Figure 2b, the spectra of both measurement modes fit perfectly

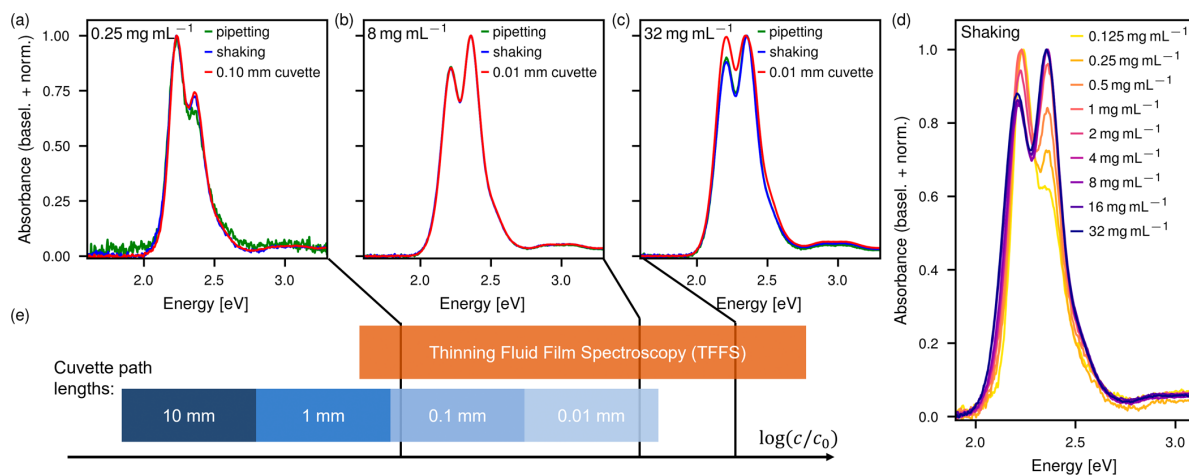


Figure 2. (a)–(c) Comparisons of the same Rhodamine B in H_2O solutions measured with the pipetting and shaking measurement mode and in a short optical path length cuvette ((a) 0.10 mm, (b) and (c) 0.01 mm) for three different concentrations: (a) 0.25 mg mL^{-1} , (b) 8 mg mL^{-1} , and (c) 32 mg mL^{-1} . (d) Concentration-dependent absorption measurements of Rhodamine B in H_2O measured in the shaking mode. (e) Schematic comparison of the dynamic concentration range of the TFFS method compared to the dynamic concentration range of different cuvette path lengths. The vertical lines schematically demonstrate the concentration of the measured solutions in (a)–(c) on the $\log(c/c_0)$ -axis, where c_0 is an arbitrary reference concentration.

to the measurement in a 0.01 mm optical path length cuvette, demonstrating the validity and high suitability of the shaking and pipetting measurements. At an even higher concentration of 32 mg mL^{-1} in Figure 2c, the shaking and pipetting measurements are also in very good agreement, but the measurement in the 0.01 mm optical path length cuvette is deviating strongly due to the detection limit of the spectrometer (as also observed in Figure 1d with too high film thicknesses). This demonstrates that we can exceed the measurement range achievable with a 0.01 mm cuvette toward higher concentrations with our method (see also Figure 2e). Mere visual control is insufficient to identify that the cuvette measurement is distorted. In the Supporting Information section “Are my static absorption spectra distorted?”, we provide guidelines to detect distorted spectra in cuvette measurements. There, we also proved in Figure S6 by tilting the cuvette (setup in Figure S5) that the 32 mg mL^{-1} cuvette measurement is distorted. At a relatively low concentration of 0.25 mg mL^{-1} , the shaking measurement is also very well in line with the measurement in a 0.1 mm cuvette (see Figure 2a), so that the shaking measurements cover a large dynamic range starting from where standard 1 mm cuvettes are not usable anymore up to very strongly absorbing solutions (see Figure 2e). The pipetting measurements show weaknesses at a concentration of 0.25 mg mL^{-1} with an increased noise level and a deviating spectrum. The reason is that the polypropylene surface of the pipet tips has different wetting properties compared to the glass vials used for shaking. Therefore, the solution flows off faster (approximately 0.1 s for complete dewetting), reducing the available measurement time drastically for water-based solutions. When a complete dewetting takes place within less than 1 s, the results should be handled with care. In the case of low concentrations, poor wetting is a disadvantage, but it turns into an advantage at high concentrations, where the waiting time until the absorbance drops to a suitable measurement level is also drastically decreased. Thus, at the lower absorbance boundary, the shaking mode (glass walls) is more suitable, while at the upper

absorbance boundary, the pipetting mode (polypropylene walls) is faster and results in thinner wetting films for water-based solutions. In the broad intermediate range, both measurement modes are highly suitable, and the selection of one measurement mode depends more on the practicability of the application. The wetting behavior heavily depends on the fluids used, and most nonwater-based solutions, e.g., solutions in organic solvents, do not feature dewetting issues, neither on polypropylene nor on glass (see more detailed note on wettability in Supporting Information).

An overview of reliable spectra obtained from different concentrations in the shaking mode is displayed in Figure 2d. The large concentration dependency of the absorption spectra of Rhodamine B clearly demonstrates that the dilution of a concentrated solution to measure its absorption spectrum can yield strongly deviating results. Therefore, a method to measure strongly absorbing solutions is inevitable for undistorted measurements and enables studies without changing molecular interactions within the investigated system.

3.3. Automated Monitoring of Spectral Changes. TFFS is highly suitable for automated characterization. Our robotic setup includes a heating station for glass vials, enabling automated temperature studies of the absorption spectrum, as shown for the semiconducting polymer PM6 in o-DCB (Figure 3a), a high-performance polymer for organic solar cells. For each temperature step, the heated glass vial is picked up by the robot and moved to the measurement position, where the shaking and measurement take place. Then it is placed back into the heating station. After reaching the new temperature and further 2 min of equilibration, the measurement is repeated. The same automated pick-and-place measurement principle can also be used for autosampling of different samples, possibly also combined with a temperature scan of a variety of samples. The resulting temperature scan in Figure 3a shows a gradual transition from an aggregated polymer phase at low temperatures to an amorphous polymer phase at high temperatures.^{12–14} Usually temperature scans like this are done on highly diluted solutions in 10 or 1 mm cuvettes, but apart

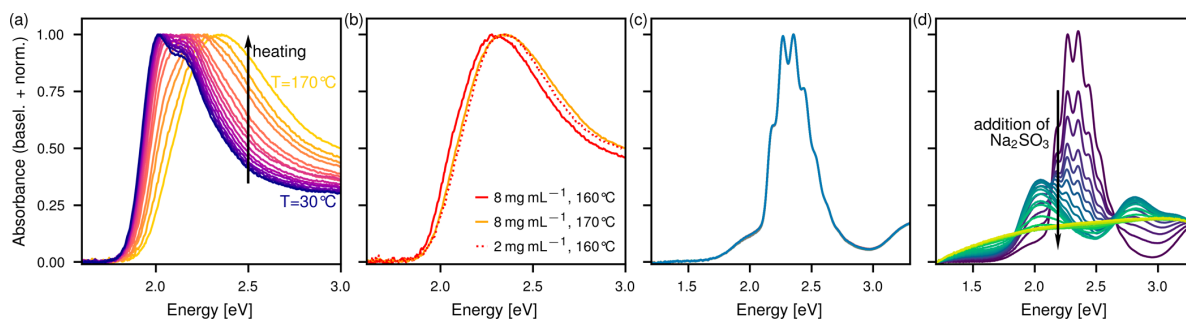


Figure 3. (a) Temperature scan of 8 mg mL⁻¹ PM6 in o-DCB solution in the shaking mode. (b) Comparison between PM6 in o-DCB solutions with 8 mg mL⁻¹ and 2 mg mL⁻¹ at 160 °C and 8 mg mL⁻¹ at 170 °C. (c) Repeatability test of an in-line measurement unit: 50 repeated spectra of an alkaline 25 mg mL⁻¹ KMnO₄ in H₂O solution. (d) Stepwise addition of a Na₂SO₃ solution to an alkaline KMnO₄ solution measured in the in-line measurement unit (baseline correction at 1.2 eV, normalization at 3.3 eV).

from changes in the absorption spectra, this can also change the transition temperatures. This can be seen in Figure 3b, where about 10 °C more is needed to achieve a similarly amorphous state in an 8 mg mL⁻¹ solution compared to a 2 mg mL⁻¹ solution due to increased polymer–polymer interactions.

Compared with the automated sampling in shaking and pipetting modes, an in-line approach offers other possibilities for automation. A liquid flowing through a pipe system can (almost) continuously be monitored, either for quality control (QC) purposes or to trigger processing actions. Especially for QC purposes, high repeatability of the measurements is important to differentiate between natural fluctuations and quality problems. Therefore, we conducted a repeatability test with our prototypical in-line measurement unit. In Figure 3c, 50 consecutively extracted static spectra of alkaline 25 mg mL⁻¹ KMnO₄ in H₂O solution using the in-line system are displayed. This clearly demonstrates a high repeatability, which is suitable for many QC applications. Additionally, in Figure 3d, we show the simple possibility of monitoring spectral changes occurring in the solution flowing through the pipe system. In a stepwise manner, we added identical volumes of a Na₂SO₃ solution to an alkaline KMnO₄ solution, monitoring the resulting absorption spectra. Due to the chemical reduction of MnO₄⁻, there is a gradual color change from pink over green (MnO₄²⁻) to brown (MnO₂).^{15–17} The color change to brown is accompanied by precipitation of the solute, leading to light scattering over the whole spectral range, which is (partially) corrected by the baseline correction.

4. CONCLUSION

We developed a novel absorption spectroscopy method, TFFS, for strongly absorbing solutions, which exploits the low optical path length through fluid films on surfaces after they are wetted with the desired solution. As the solutions gradually flow off the surface, a broad range of optical path lengths is accessible. A weighted average over normalized and background-corrected spectra extracted from path lengths suitable for the specific solution is used to extract a static absorption spectrum of the solution. Therefore, the same setup can be used to measure a large dynamic range of absorbances. We demonstrated, for an example material system (Rhodamine B in water) that the covered measurement range extends from solutions, which can still be measured in 1 mm cuvettes, to solutions with significantly higher concentrations than we can measure without distortion in 0.01 mm cuvettes. Thinning fluid films

can also be used in many other applications where longer path lengths can be an issue, like self-absorption in photoluminescence measurements of strongly absorbing solutions.¹⁸

There exists a multitude of possibilities to generate a thin liquid film, making this approach very versatile for many different applications. In this work, we introduced, validated, and compared three different exemplary measurement modes (shaking, pipetting, and in-line). There is very good agreement with measurements in specialized cuvettes, making TFFS highly suitable to obtain absorption spectra for a broad range of concentrations in an automated manner. However, it has to be noted that due to the unknown optical path length, no absolute absorbances, but only normalized absorbances, can be extracted. In cases in which an application requires absolute absorbances, possibilities may be to add marker molecules (with known absorbance and no interaction with the solute), exploit white light interference, or use separate calibration measurements.

All three introduced measurement modes are highly suitable for automated high-throughput measurements and cover a broad range of possible applications. To demonstrate the automation potential, we implemented TFFS in a spectroscopy robot combining the pipetting and shaking measurement modes, which was also used to fully automatically acquire a temperature series of polymer solution absorption spectra. Moreover, the separate in-line setup, which we used to monitor a chemical reaction, is also fully automated and can be incorporated into pipe systems, e.g., to monitor industrial processes.

■ ASSOCIATED CONTENT

Supporting Information

The Supporting Information is available free of charge at <https://pubs.acs.org/doi/10.1021/acs.jpca.4c04902>.

Sketches of experimental setups; guide to conducting TFFS measurements; comparison between shaking, pipetting, and cuvette measurements of different Rhodamine B concentrations; instructions on identifying distorted spectra; note on wettability (PDF)

CAD files for 3D-printing cuvette holder and adapter to identify distorted spectra (ZIP)

AUTHOR INFORMATION

Corresponding Author

Eva M. Herzig – Dynamics and Structure Formation – Herzig Group, University of Bayreuth, Bayreuth 95447, Germany;
 ● orcid.org/0000-0002-0151-5562; Email: eva.herzig@uni-bayreuth.de

Author

Fabian Eller – Dynamics and Structure Formation – Herzig Group, University of Bayreuth, Bayreuth 95447, Germany

Complete contact information is available at:
<https://pubs.acs.org/10.1021/acs.jpca.4c04902>

Notes

The authors declare no competing financial interest.

ACKNOWLEDGMENTS

F.E. and E.M.H. thank the Deutsche Forschungsgemeinschaft (DFG Research Unit FOR 5387 POPULAR, Project No. 461909888) for their support.

REFERENCES

- (1) Abdolkarimi-Mahabadi, M.; Bayat, A.; Mohammadi, A. Use of UV-Vis Spectrophotometry for Characterization of Carbon Nanostructures: a Review. *Theor. Exp. Chem.* **2021**, *57* (3), 191–198.
- (2) Begum, R.; Farooqi, Z. H.; Naseem, K.; Ali, F.; Batool, M.; Xiao, J.; Irfan, A. Applications of UV/Vis Spectroscopy in Characterization and Catalytic Activity of Noble Metal Nanoparticles Fabricated in Responsive Polymer Microgels: A Review. *Crit. Rev. Anal. Chem.* **2018**, *48* (6), 503–516.
- (3) Li, P.; Hur, J. Utilization of UV-Vis spectroscopy and related data analyses for dissolved organic matter (DOM) studies: A review. *Crit. Rev. Environ. Sci. Technol.* **2017**, *47* (3), 131–154.
- (4) Perkampus, H.-H. *UV-VIS Spectroscopy and Its Applications*; Springer: Berlin, Heidelberg, 1992; pp. 2680.
- (5) Rocha, F. S.; Gomes, A. J.; Lunardi, C. N.; Kaliaguine, S.; Patience, G. S. Experimental methods in chemical engineering: Ultraviolet visible spectroscopy—UV-Vis. *Can. J. Chem. Eng.* **2018**, *96* (12), 2512–2517.
- (6) Holmes, W. C. The Influence of Variation in Concentration on the Absorption Spectra of Dye Solutions. *Ind. Eng. Chem.* **1924**, *16* (1), 35–40.
- (7) Lavorel, J. Influence of Concentration on the Absorption Spectrum and the Action Spectrum of Fluorescence of Dye Solutions. *J. Phys. Chem.* **1957**, *61* (12), 1600–1605.
- (8) Penzkofer, A.; Leupacher, W.; Meier, B.; Runde, B.; Drexhage, K. H. Concentration-dependent absorption and emission behaviour of a pyrimidonecarbocyanine dye in hexafluoroisopropanol. *Chem. Phys.* **1987**, *115* (1), 143–150.
- (9) Philip, R.; Penzkofer, A.; Bäuml, W.; Szeimies, R. M.; Abels, C. Absorption and fluorescence spectroscopic investigation of indocyanine green. *J. Photochem. Photobiol., A* **1996**, *96* (1–3), 137–148.
- (10) Eller, F.; Wenzel, F. A.; Hildner, R.; Havenith, R. W. A.; Herzig, E. M. Spark Discharge Doping-Achieving Unprecedented Control over Aggregate Fraction and Backbone Ordering in Poly(3-hexylthiophene) Solutions. *Small* **2023**, *19* (21), No. e2207537.
- (11) Eller, F.; McNeill, C. R.; Herzig, E. M. Tackling P3HT: Y-Series Miscibility Through Advanced Processing for Tunable Aggregation. *Adv. Energy Mater.* **2024**, *14* (29), 2304455.
- (12) Köhler, A.; Bässler, H. *Electronic processes in organic semiconductors: An introduction*; 2022, Wiley-VCH GmbH: Weinheim, Germany, pp. 152153.
- (13) Kroh, D.; Eller, F.; Schötz, K.; Wedler, S.; Perdigón-Toro, L.; Freychet, G.; Wei, Q.; Dörr, M.; Jones, D.; Zou, Y.; et al. Identifying the Signatures of Intermolecular Interactions in Blends of PM6 with

Y6 and N4 Using Absorption Spectroscopy. *Adv. Funct. Mater.* **2022**, *32* (44), 2205711.

(14) Panzer, F.; Bässler, H.; Köhler, A. Temperature Induced Order-Disorder Transition in Solutions of Conjugated Polymers Probed by Optical Spectroscopy. *J. Phys. Chem. Lett.* **2017**, *8* (1), 114–125.

(15) Binnewies, M.; Finze, M.; Jäckel, M.; Schmidt, P.; Willner, H.; Rayner-Canham, G. *Allgemeine und Anorganische Chemie*; Springer: Berlin, Heidelberg, 2016; pp. 795796.

(16) Holleman, A. F.; Wiberg, N.; Wiberg, E. *Lehrbuch der Anorganischen Chemie*; Walter de Gruyter, 2007; pp. 16181619.

(17) Roesky, H. W.; Möckel, K. *Chemische Kabinettstücke: spektakuläre Experimente und geistreiche Zitate*; 2nd ed.; VCH: Weinheim, 2000; pp. 6566.

(18) Zhang, J.; Su, Z. C.; Cui, Y.; Hu, G.; Tang, Y. L.; Gan, Z. X.; Yang, L.; Lao, X. Z.; Bao, Y. T.; Xu, S. J. The roles of self-absorption and radiative energy transfer in photoluminescence of N-doped carbon nanodots in solution. *AIP Adv.* **2019**, *9* (3), 035135.

Supporting Information

Facilitating Absorption Spectroscopy of Strongly Absorbing Fluids: A High-Throughput Approach

Fabian Eller and Eva M. Herzig*

Fabian Eller, Eva M. Herzig

Dynamics and Structure Formation – Herzig Group, University of Bayreuth,

Universitätsstraße 30, 95447 Bayreuth, Germany

E-mail: eva.herzig@uni-bayreuth.de

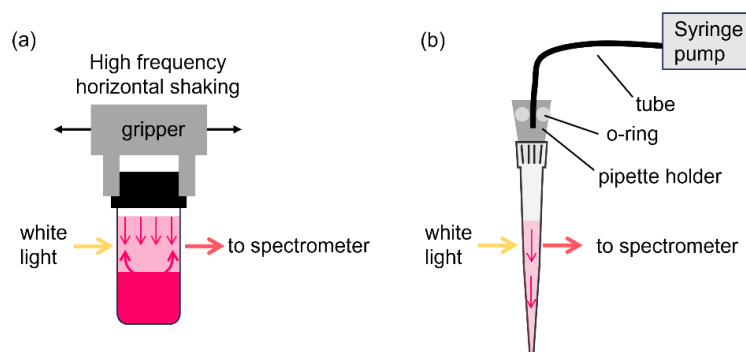


Figure S1. Sketches of the experimental realization of the (a) shaking, and (b) pipetting measurement mode used in this work: (a) A mechanical gripper places the measurement container in the white light beam and performs a horizontal shaking motion with high frequency. When the last move of the shaking motion is finished, the TFFS measurement is started immediately. (b) The pipette holder, which is mounted to the three-dimensional positioning system, takes up the pipette tip and immerses it into the desired solution. A syringe pump, which is connected via a tube and o-ring to the pipette holder, is used to suck up the solution. After positioning the pipette tip at the measurement position, the solution is ejected by the syringe pump and the measurement is started while the ejection is still ongoing.

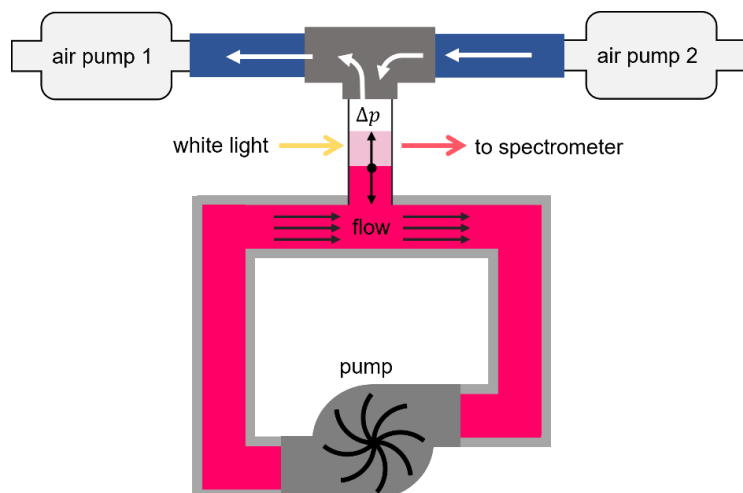


Figure S2. Sketch of prototypical in-line setup. The fluid is pumped through a pipe system, where a TFFS unit is inserted. Air pump 1 generates a negative pressure above the fluid level in the TFFS unit, which leads to a rising fluid level in the TFFS unit. The fluid level drops again when air pump 1 is switched off and air pump 2 is switched on, leading to a positive pressure above the fluid level. Absorption spectra can then be measured through the remaining liquid film on the TFFS unit.

Guide to conducting TFFS measurements

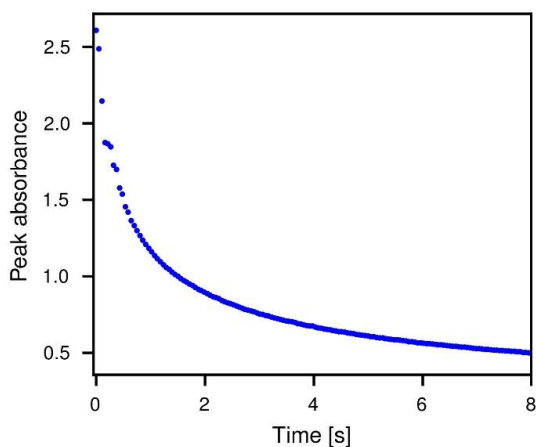


Figure S3. Decay of the peak absorbance over time extracted from the measurement displayed in Figure 1 in the main paper.

This section provides a guide to conducting TFFS measurements. It focuses on the important points for finding suitable measurement settings. To ensure that the complete relevant part of the fluid film thinning of the solution is captured, it is the safest option to start the time-resolved spectroscopy measurement directly when the fluid film thinning starts or even before. Thus,

S2

either a proper synchronization between the mechanism controlling the buildup of the fluid film and the measurement, e.g. by a trigger or control from the same software, or a sufficient time buffer before the measurement should start, is required.

Of the measurement itself the important settings are the duration of the complete measurement and the repetition rate of the time-resolved measurement. To find suitable settings an empirical approach is the best option as these settings heavily depend on the viscosity, wetting properties and absorption of the solutions. A suitable approach is to track the peak absorbance or the absorbance at another point in the absorption profile over time, as it is done in Figure S3. The timescale of the decay of the absorbance determines a suitable time resolution as well as a suitable measurement duration. The duration needs to be long enough so that the film thinning continues far enough to be in the range of undistorted measurements. A procedure to find the point, from where the spectra are undistorted is presented in Figure 1 (e)-(g) and the corresponding main part of the publication. This evaluation can be carried out once for a material to determine at which peak absorbance the detection limit roughly lies. This rough limit may also be used for other materials with similar absorption profiles but needs to be redone when the range of strong absorption lies in spectral ranges with different light source intensity, e.g. in the UV. It is important to measure sufficiently long in the undistorted regime. When the peak absorbance range for undistorted measurements is known, the measurement duration can be chosen to reach well into this regime.

When the detection limit and the suitable measurement duration are known, the repetition rate can be optimized. It is important that no averaging over strong thickness changes is taking place, hence that the peak absorbance barely changes between measurements. This is the case when the difference between the peak absorbance of two neighboring data points in the decay curve is small compared to the actual peak absorbance. If the difference is too big this may result in artifacts. In the example in Figure S3 in the early range of the measurement with peak absorbances above roughly 1.5 the changes are too big, but as this range also lies in the detection limit, this is no problem. Oversampling with a higher than required time-resolution is of course possible but increases file sizes and computing time for the analysis without improvement of the result.

When the measurement settings are chosen according to this guide, reliable measurements are conducted, which can be converted into a single absorption spectrum as described in the main part of this publication belonging to Figure 1 (e)-(g). When the used solvent is volatile in the measurement settings, e.g. due to a low boiling point or elevated temperature care has to be

taken to avoid excessive evaporation. In these cases, the shaking mode with tightly sealed containers is a particularly good choice.

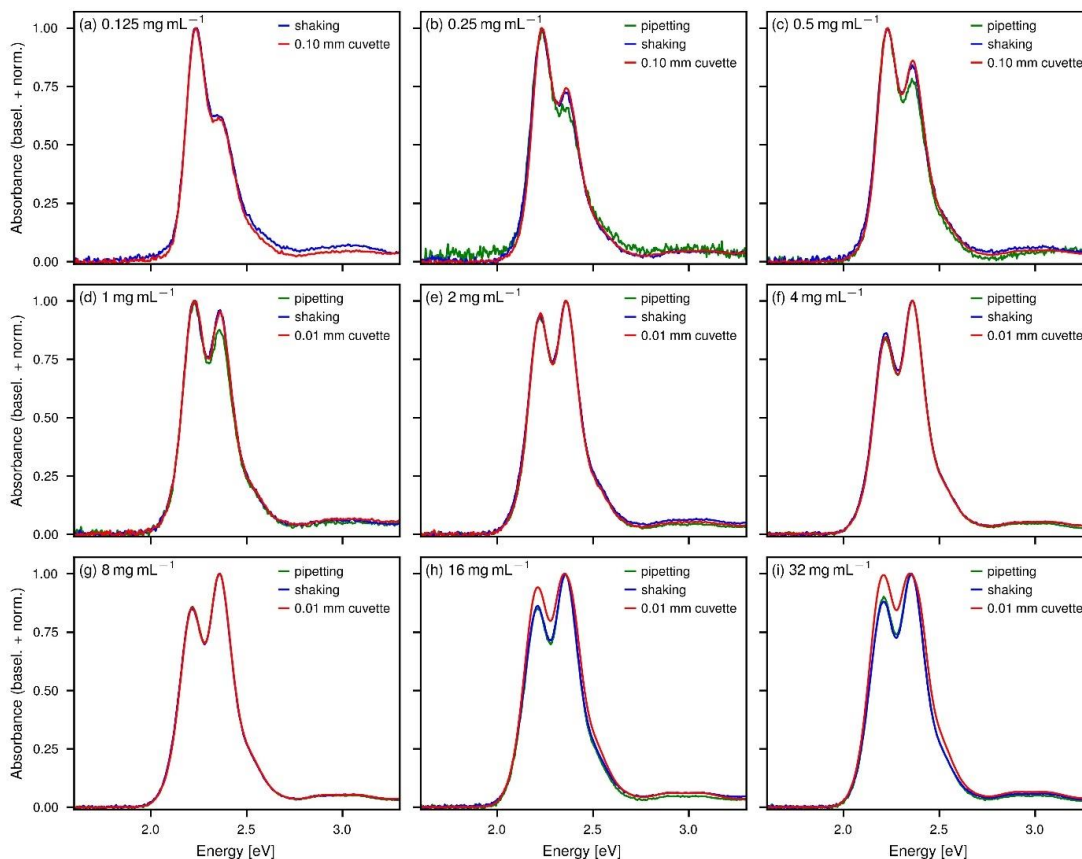


Figure S4. Comparisons of Rhodamine B in H₂O solutions with different concentrations measured with the pipetting (not for (a)) and shaking measurement mode and in short optical path length cuvettes ((a)-(c) 0.10 mm, (d)-(i) 0.01 mm): (a) 0.125 mg mL⁻¹ (concentration too low for pipetting measurement), (b) 0.25 mg mL⁻¹, (c) 0.5 mg mL⁻¹, (d) 1 mg mL⁻¹, (e) 2 mg mL⁻¹, (f) 4 mg mL⁻¹, (g) 8 mg mL⁻¹, (h) 16 mg mL⁻¹, (i) 32 mg mL⁻¹. The deviations of the pipetting measurements in (b)-(d) are due to too fast dewetting (approx. 0.1 s), while in (e)-(i), no dewetting but thinning took place, which was on the second timescale. The deviations in (h) and (i) are due to a too strong absorbance in the cuvette, resulting in low counts beyond the detection limit for the cuvette but adequate measurements for the pipetting and shaking.

Are my standard static absorption spectra distorted?

In TFFS measurements it is easy to determine when spectra are distorted due to detected light intensity below the detection limit, as it was demonstrated in Figure 1 in the main paper. This easy proof relies on changing optical path lengths, where the normalized and baseline-corrected absorption spectra must not change with path length. When the spectra deviate for higher path lengths (i.e. of the initially too thick fluid film), these spectra are not reliable as counts on the detector due to stray light contribute significantly and distort the obtained spectra.

However, varying the optical path length in standard static absorption spectra in cuvettes is less straightforward. If there is a cuvette available with lower optical path length, it can be used to check for deviations. However, when testing such limits, usually the cuvette with the lowest optical path length available is already in use. A possible method to change the optical path length without changing the cuvette is to tilt it. We designed a cuvette holder suitable for all standard cuvettes (see Figure S5), where cuvettes can be inserted perpendicular to the light path, but also tilted by 30°, increasing the path length by about 15%. The light source and spectrometer can be connected by glass fibers to the cuvette holder. The CAD-files for 3D-printing are available as further files of the supporting information and on MakerWorld (<https://makerworld.com/en/models/687708>). In Figure S6 (a)-(b) normalized and baseline corrected absorption spectra of Rhodamine B solutions with concentrations of 8 mg mL⁻¹ and 32 mg mL⁻¹ in a 0.01mm cuvette measured at 0° (perpendicular) and tilted by 30° are displayed. At 8 mg mL⁻¹ in Figure S6 (a) both spectra are almost identical, implying that the measurements are undistorted. In contrast, the analogous measurements of the 32 mg mL⁻¹ solution in Figure S6 (b) show clear deviations, which is a clear indicator, that stray light contributes significantly to the signal. Thus, a lower path length, either by a suitable cuvette (if available) or by TFFS, is required for reliable measurements. These measurements can also be done in the same cuvette holder with cuvettes with other path lengths, e.g. in Figure S6 (c)-(d) with 10 mm cuvettes, where there are also deviations visible in Figure S6 (d) in contrast to the perfect match in S6 (c).

There may also be other options to use knowledge about the solutions (e.g. peak shape analysis, use of known spectra) to identify distorted spectra due to the detection limit of the setup. However, it has to be noted that using the knowledge of the setup and solutions always includes significant uncertainty strongly depending on how good the knowledge is and may also be less sensitive than comparing measurements at different path lengths.

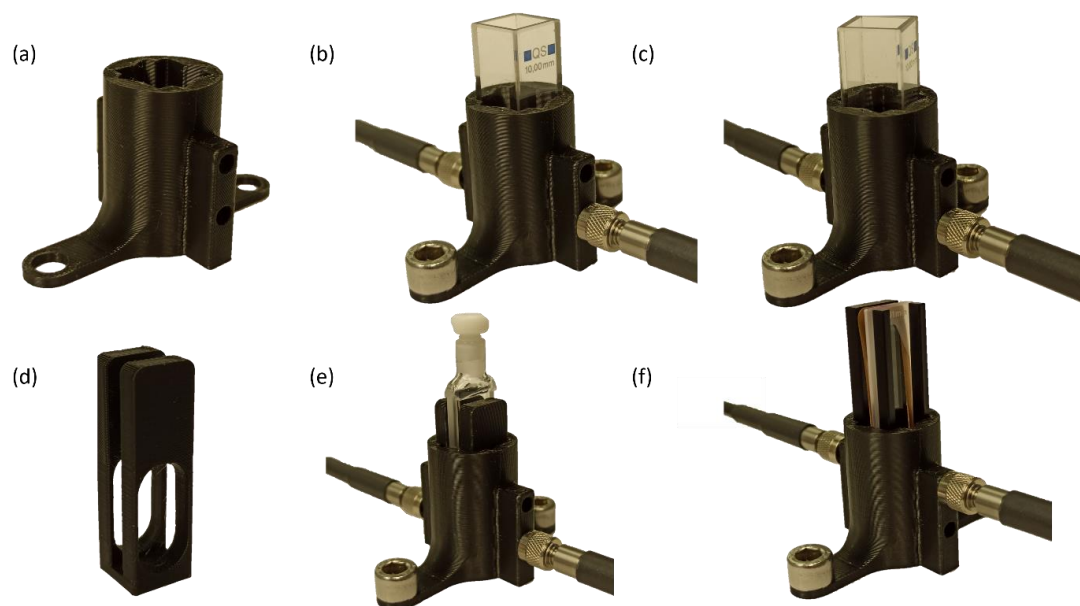


Figure S5. (a) Cuvette holder designed to measure absorption spectra through cuvettes (b) perpendicular and (c) tilted by 30° (in (b) and (c) 10 mm cuvette). (d) Adapter inset to perform same measurements on (e) 1 mm cuvettes. (f) Very thin demountable cuvettes (here 0.01 mm) can also be inserted together with the corresponding holder pressing the two parts together. The CAD files for 3D-printing the cuvette holder in (a) and the adapter inset in (d) are available as separate files in the SI and on Makerworld (<https://makerworld.com/en/models/687708>)

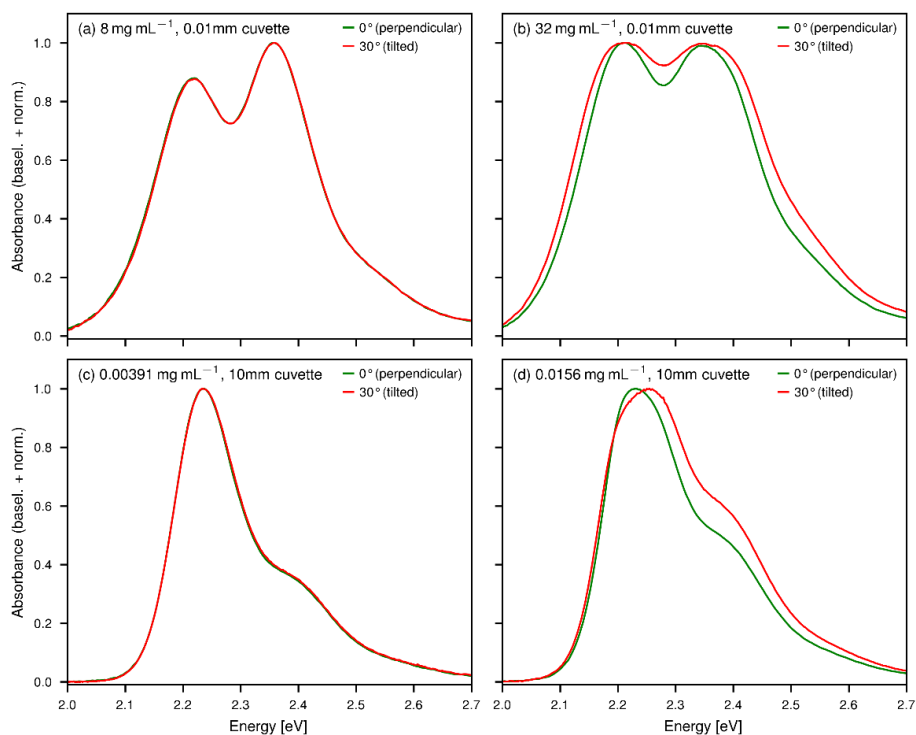


Figure S6. Measurements of Rhodamine B solutions with different concentrations in cuvettes perpendicular and tilted by 30° to the light path: (a) 8 mg mL^{-1} solution in 0.01 mm cuvette, (b) 32 mg mL^{-1} solution in 0.01 mm cuvette, (c) $0.00391 \text{ mg mL}^{-1}$ in 10 mm cuvette, (d) $0.0156 \text{ mg mL}^{-1}$ in 10 mm cuvette.

Note on wettability:

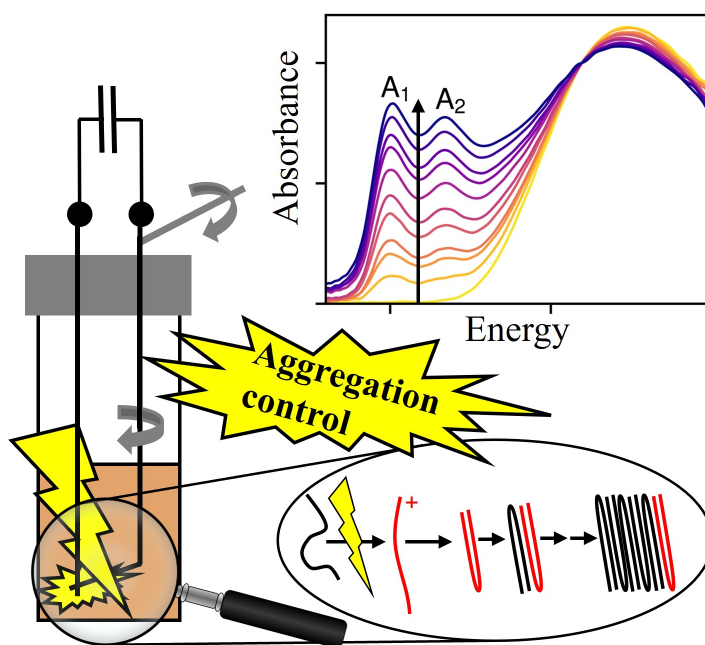
The wetting behavior heavily depends on the fluids and surfaces used as the affinity between the fluid and the surface controls its contact angle and, therefore, the wettability. The strong polarity and hydrogen bonding of water compared to the almost vanishing polarity and hydrogen bonding of polypropylene leads to dewetting issues in the extreme case of water on polypropylene, while there are no problems with water on glass due to the higher affinity and also for most other solvent-surface combinations.^[1] For example, many organic solvents possess low polarity and hydrogen bonding, leading to a high affinity to polypropylene with very low contact angles.^[1] We have successfully carried out the shaking and pipetting measurement mode with water and different organic solvents, e.g. chloroform, dichlorobenzene, and o-xylene. The wettability of arbitrary solvents can be checked via their Hansen Solubility Parameters.^[1,2] In case there are wetting issues for a certain surface-solution combination, surface treatments, e.g. plasma treatment, silanization or coatings, or alternatively surfactants in the solutions can help to increase the wettability.

References

- [1] S. Abbott, C. M. Hansen, H. Yamamoto, "Surface Energy", can be found under https://www.hansen-solubility.com/HSP-science/Surface_Energy.php.
- [2] M. Murase, D. Nakamura, *Langmuir: the ACS journal of surfaces and colloids* **2023**, *39*, 10475.

9

Spark Discharge Doping – Achieving Unprecedented Control over Aggregate Fraction and Backbone Ordering in Poly(3-hexylthiophene) Solutions



Fabian Eller, Felix A. Wenzel, Richard Hildner, Remco W. A. Havenith, and Eva M. Herzig

Published in
Small **2023**, 19 (21), 2207537
(DOI: 10.1002/smll.202207537)

Reprinted with permission according to the CC BY 4.0 license
Copyright 2023 The Authors. *Small* published by Wiley-VCH GmbH



Spark Discharge Doping—Achieving Unprecedented Control over Aggregate Fraction and Backbone Ordering in Poly(3-hexylthiophene) Solutions

Fabian Eller, Felix A. Wenzel, Richard Hildner, Remco W. A. Havenith, and Eva M. Herzig*

The properties of semiconducting polymers are strongly influenced by their aggregation behavior, that is, their aggregate fraction and backbone planarity. However, tuning these properties, particularly the backbone planarity, is challenging. This work introduces a novel solution treatment to precisely control the aggregation of semiconducting polymers, namely current-induced doping (CID). It utilizes spark discharges between two electrodes immersed in a polymer solution to create strong electrical currents resulting in temporary doping of the polymer. Rapid doping-induced aggregation occurs upon every treatment step for the semiconducting model-polymer poly(3-hexylthiophene). Therefore, the aggregate fraction in solution can be precisely tuned up to a maximum value determined by the solubility of the doped state. A qualitative model for the dependences of the achievable aggregate fraction on the CID treatment strength and various solution parameters is presented. Moreover, the CID treatment can yield an extraordinarily high quality of backbone order and planarization, expressed in UV–vis absorption spectroscopy and differential scanning calorimetry measurements. Depending on the selected parameters, an arbitrarily lower backbone order can be chosen using the CID treatment, allowing for maximum control of aggregation. This method may become an elegant pathway to finely tune aggregation and solid-state morphology for thin-films of semiconducting polymers.

particularly intensive work is done on polymer aggregation as it paves the way toward efficient charge transport.^[1–4] Moreover, the altered aggregate absorption spectrum enables harvesting a broader spectral range of light. The most common ways of influencing aggregation are thermal annealing, solvent vapor annealing, processing from a mixture of good solvents with fractions of marginal or poor solvents, and using other solvent additives.^[5–8] Some of these methods are post-treatment steps for the dried film, while others modify the aggregation behavior during the drying process. Complexity further increases moving from single materials to multi-component blends. Therefore, it is desirable to obtain a well-defined aggregation state already in solution before blending of materials and further processing.

Poor solvent additives have successfully been used to induce pre-aggregation. However, this pre-aggregation has limited control, because such additives can have further effects, like gel formation, and the

quality of backbone order is often reduced due to the lower solvent quality.^[9–12] The reason for the associated lower backbone ordering is linked to the different mechanisms responsible for the ordering in different molecular directions: backbone

1. Introduction

A major branch of organic semiconductor research deals with understanding and optimizing morphology. In this field,

F. Eller, E. M. Herzig
Dynamics and Structure Formation – Herzig Group
University of Bayreuth
Universitätsstraße 30, 95447 Bayreuth, Germany
E-mail: eva.herzig@uni-bayreuth.de

F. A. Wenzel
Macromolecular Chemistry and Bavarian Polymer Institute
University of Bayreuth
Universitätsstraße 30, 95447 Bayreuth, Germany

The ORCID identification number(s) for the author(s) of this article can be found under <https://doi.org/10.1002/smll.202207537>.

© 2023 The Authors. Small published by Wiley-VCH GmbH. This is an open access article under the terms of the Creative Commons Attribution License, which permits use, distribution and reproduction in any medium, provided the original work is properly cited.

R. Hildner
Zernike Institute for Advanced Materials
University of Groningen
Nijenborgh 4, Groningen 9747 AG, The Netherlands

R. W. A. Havenith
Stratingh Institute for Chemistry and Zernike Institute for Advanced Materials
University of Groningen
Nijenborgh 4, Groningen 9747 AG, The Netherlands

R. W. A. Havenith
Ghent Quantum Chemistry Group
Department of Chemistry
Ghent University
Krijgslaan 281 (S3), Gent B-9000, Belgium

DOI: 10.1002/smll.202207537

ordering, side-chain ordering, and π - π stacking.^[13] Depending on the driving forces of the aggregation process, different directions of molecular ordering contribute to a different extent, enabling a higher quality of order in one direction at the cost of the quality of order in one or both other directions.^[13,14] As transport properties are mostly influenced by backbone ordering, an aggregation mechanism leading to a high quality of backbone order is of interest.

Doping-induced aggregation can lead to pre-aggregation in solution with the desired high quality of backbone order. Molecular doping results in backbone planarization, which then transfers to the high quality of backbone order in the produced aggregates.^[15] Usually, doping is achieved by adding dopant molecules to the polymer solution, for example, F4TCNQ (2,3,5,6-tetrafluoro-7,7,8,8-tetracyanoquinodimethane). A charge transfer between the dopant and the polymer occurs, and the dopant counterions subsequently remain in the solution and also in produced thin films, permanently doping the system.^[15-19]

In some cases, permanent doping is desired. However, the most suitable dopant amount for aggregation control and permanent doping is not necessarily identical. Thus, decoupling doping-induced aggregation from permanent doping would be highly beneficial.

Here, we present an approach to exploit doping-induced aggregation without permanently doping the material system. Using this novel current-induced doping (CID) treatment allows us to achieve temporary doping of the polymers leading to an accompanying temporary change of solubility. We demonstrate that this electronic solution treatment works in a wide variety of solvents, including green solvents, and does not require any chemical additives. The CID treatment allows for the systematic control of the aggregate fraction as well as the quality of backbone order of the semiconducting polymer poly(3-hexylthiophene) (P3HT) in solution.

2. Temporary Doping for Aggregation Control

In general, for aggregation to occur, the backbone of a polymer needs to straighten before folding or attaching to an existing aggregate.^[20] A doping-induced aggregation pathway known from the literature occurs according to the steps shown in **Figure 1c**: The charge induced by the dopant influences the rigidity of the backbone and decreases the solubility in non-polar organic solvents compared to the neutral polymer.^[16,17,19] Hence, after planarization, the chain folds and forms a single-chain aggregate where the charge is delocalized in the conjugated system and stabilized via π - π stacking.^[16] This single-chain aggregate can act as a nucleating site for neutral chains stabilizing the charged aggregate further through additional π - π interactions.^[16]

In this paper, we actively aim to exploit this mechanism by temporarily charging some of the backbones electronically. To achieve a uniform charge distribution on the backbone in order to examine the general principle of this doping mechanism, we choose a highly investigated conjugated homopolymer, namely the model polymer P3HT. Using simulations, we demonstrate that doping this backbone results in the planarization step necessary for aggregation. Density functional theory (DFT) simulations show that dihedral rotation between two P3HT monomers is suppressed due to a strongly increased energy barrier when positive charge is added to the monomers (Figure 1a). This results in the planarization of a doped backbone section.

2.1. Proposed Process

To gain specific aggregation control, we choose a process that allows us to temporarily dope a fraction of the polymers within a solution. We achieve this with a strong current through the polymer solution. As displayed in Figure 1b,

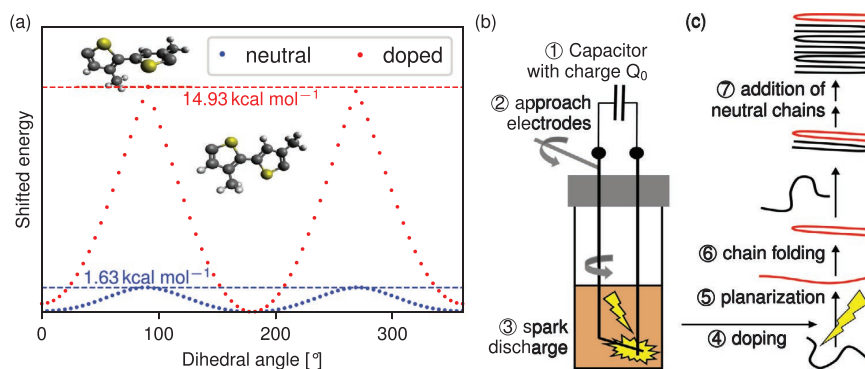


Figure 1. a) Simulation results of energetic profiles (shifted to minimum energy at 180°) upon rotating the dihedral angle between two 3-methylthiophene monomers. The energetic profiles were obtained with DFTB3 simulations and rescaled with the more precise energy barriers obtained from DFT simulations (more details in the Experimental Section and Table S1, Supporting Information). The inserted molecular structures visualize a part of the simulated molecules (consisting of four monomers) at 90° and 180°. b) Schematic diagram of the experimental setup for CID treatment consisting of two tungsten wires connected to a charged capacitor. The field strength between the wires is increased above the breakdown field strength for a spark discharge to occur. This spark results in the doping and, hence, planarization of a polymer chain. c) In doping-induced aggregation, the doped chain (red) can fold and act as a nucleating site for neutral chains (black) to form highly ordered aggregates.^[16]

we approach two tungsten wires within our polymer solution connected to a charged capacitor. When the distance between the wires in solution is decreased sufficiently that the electric field strength between the two electrodes is increased above the breakdown field strength, a conductive channel builds up, consisting of ionized solvent and polymer.^[21] The strong current flow locally induces evaporation in a small volume around the conductive channel due to Joule heating. This rapid expansion of the evaporating solvent then mixes the solution. Hence, the charged polymer and other ions and radicals generated in the conductive channel are spread across the complete solution. The ion and radical species depend on the solvent, but they are reliably produced, regardless of the solvent. The charged, that is, doped, polymer can start doping-induced aggregation in the complete volume. Moreover, certain ions and radicals can act as dopants and dope further polymer chains increasing the effect. It has to be noted that there may be more than one charge on some of the polymer chains. The doping and resulting aggregation are both demonstrated in the absorption spectra upon CID treatment of P3HT in chloroform (CF). The doped chains give rise to a polaron signature in the low energy region, and the aggregation changes the absorption in the visible region, see Figure S1a, Supporting Information. After the termination of the current and, therefore, also of the energy input, the ionization and radical generation are stopped. The remaining ions and radicals recombine again with counterions and other radicals to neutral non-reactive products. With time the excess charge dissipates in the system and, thus, the doping process and the aggregation stop.

This way, we achieve a fast, temporary, and additive-free doping-induced aggregation of the prototypical semiconducting polymer P3HT.

3. Controlled Increase of Aggregate Fraction

To demonstrate the range of control available with the proposed CID, we systematically investigate the aggregation process and the resulting aggregates as a function of experimental parameters.

Carrying out the CID treatment repeatedly, we can demonstrate a systematic increase in aggregate fraction and analyze the produced aggregates. Figure 2a shows solution spectra of 12 mg mL⁻¹ P3HT in CF solutions with an increasing number of identical CID treatment steps. Every additional treatment step leads to an increased aggregate absorption, which can be clearly identified by the A₁ and A₂ peaks in the range of 1.9–2.3 eV (related to the 0–0 and 0–1 vibronic transitions of non-aggregated P3HT). To determine the increasing aggregate fraction, we used the approach of scaling an amorphous spectrum to the high-energy shoulder of the obtained absorption spectra at ≥2.6 eV, fitting the A₁–A₅ peaks to the remaining fraction of the spectra and considering the different molar extinction coefficients of the amorphous and aggregated P3HT (details in Experimental Section).^[22,23] Figure 2b and further data in Figure 5 demonstrate that in this experiment, the aggregate fraction in solution could be tuned between 0% to at least about 57%, which is a typical value for aggregate fractions in thin films.^[24,25] Two references for P3HT without CID treatment are provided, namely, 12 mg mL⁻¹ P3HT in CF solutions were 1) left for 25 days at 20 °C (time-induced aggregation) and 2) cooled for 65 min at –18 °C (temperature-induced aggregation), see Figure 2b, blue and green dots. Both procedures yielded aggregate fractions of 2.4% and 5.1%, respectively, which meet the expectations in the good solvent CF.^[26]

The aggregate fraction is further influenced by several different parameters. We systematically studied the effect of

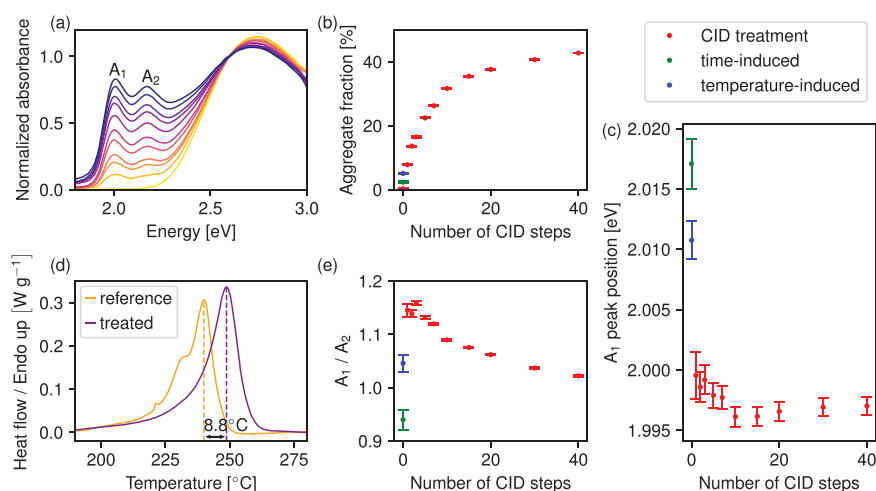


Figure 2. a) Normalized absorption spectra of 12 mg mL⁻¹ P3HT in chloroform (CF) solutions with an increasing number of spark treatment steps (from yellow (untreated) to purple (highest number of treatment steps); capacitor charged with 300 V). b, c, e) Results of fitting the vibronic structure (A₁ and A₂ first two peaks; details in Experimental Section) in spectra from (a) and reference spectra of 12 mg mL⁻¹ P3HT: 1) left for 25 days at 20 °C (time-induced aggregation) and 2) cooled for 65 min at –18 °C (temperature-induced aggregation). b) Minimum aggregate fraction, c) A₁ peak position, and e) ratio between peak amplitudes of the A₁ to A₂ peak. d) Thermogram of the first DSC heating cycle of 12 mg mL⁻¹ P3HT in CF vacuum-dried solutions with CID treatment (purple) and reference without treatment (orange).

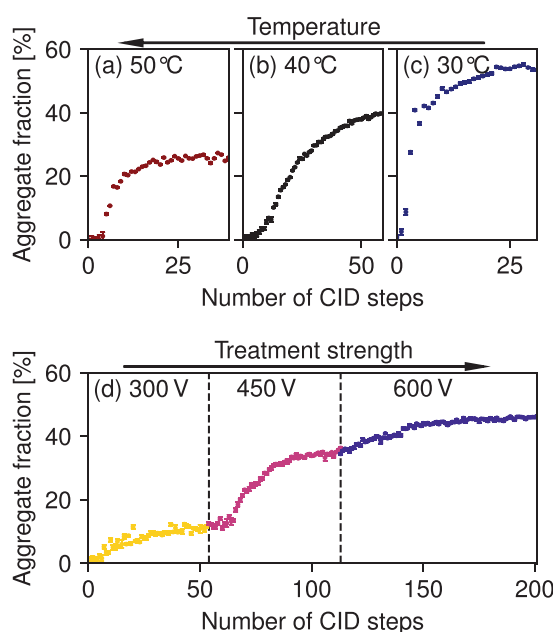


Figure 3. Fit results from associated UV-vis measurements: aggregate fraction in dependency of the number of spark treatment steps for 2 mg mL⁻¹ P3HT in tetrahydrofuran (THF) solutions; a–c) with fixed treatment strength (capacitor charged with 600 V), but different temperatures: a) 50 °C, b) 40 °C, and c) 30 °C; d) with the same temperature (40 °C) but consecutively increasing voltage for charging the capacitor from 300 (yellow) to 450 V (pink) and finally 600 V (purple).

temperature, polymer concentration, solvent, poor solvent addition, and CID treatment strength on the achievable aggregate fraction. In Figure 3a–c, the aggregate fractions upon CID treatments with 600 V discharges at three different temperatures of 2 mg mL⁻¹ P3HT in tetrahydrofuran (THF) solutions are displayed. At all three temperatures, we observe the same general trend. The first CID steps result in a rapid increase in the aggregate fraction. However, the effect due to further CID steps is getting weaker, and a constant value for the aggregate fraction is approached, which we will refer to as the maximum achievable aggregate fraction under a specific set of conditions. This maximum value increases with decreasing temperature. At 30 °C, an aggregate fraction of up to 53% can be achieved, while it is 39% at 40 °C and only 27% at 50 °C. In other words, an aggregate fraction below 27% can be achieved with all three tested temperatures by adjusting the number of treatment steps. However, a lower temperature must be chosen to reach higher aggregate fractions.

Moreover, we increase the treatment strength in a 2 mg mL⁻¹ P3HT in THF solution at 40 °C by increasing the voltage for charging the capacitor. With a higher charging voltage, more charge is stored on the capacitor for the spark discharge, and the breakdown field strength is already reached at a larger distance between the two wires. In Figure 3d, the capacitor was at first charged with a voltage of 300 V, resulting in the aggregate fraction leveling off at only 12%. Increasing the voltage to 450 V, the stronger treatment strength increases the achievable aggregate fraction up to 36%. Still on the same solution, the voltage was further increased to 600 V, yielding another increase in the achievable aggregate fraction of up to 46%. Apart from this consecutively increased treatment strength, it is also possible to use one fixed treatment strength (600 V in Figure 3b), resulting in a systematic but not identical increase in aggregate fraction.

We also tested the impact of the polymer concentration and the poor solvent content (see Figure S2, Supporting Information) on the achievable aggregate fractions. The maximum value increases with the polymer concentration and the content of the poor solvent.

4. Quality and Tunability of Backbone Order

While the aggregate fractions can be tuned over a wide range using consecutively increasing as well as a fixed treatment strength, the quality of backbone order is also of great interest in organic electronics. From the absorption spectroscopy data, we can extract information on aggregate properties. The peak positions of the A₁ absorption and the peak ratios between the A₁ and A₂ peaks of the aggregates (obtained from the corresponding fits) reveal information on the quality of backbone order. Compared to the reference samples, the peak positions of the A₁ peak (lower energy peak) show a clear redshift by ≥10 meV (Figure 2c). This shift can be attributed to a higher conjugation length and, thus, to a more planar polymer backbone within the aggregates.^[27–29]

The conclusion on the higher backbone ordering for CID aggregates is further supported by the relative changes of the peak ratios between the A₁ and A₂ peaks, where the CID aggregation leads to the highest peak ratios of up to 1.16, Figure 2e. A higher peak ratio results from smaller inter-chain electronic couplings, which result from larger conjugation lengths, and, thus, more planar backbones of the π-stacked polymer chains.^[27,30–32]

For subsequent CID steps, the peak ratios between the A₁ and A₂ peaks show a decay with increasing treatment strength. This indicates that the quality of backbone order is slightly decreasing with an increasing number of treatment steps.

The enhanced backbone planarization is further supported by the strong stability of the aggregates revealed by differential scanning calorimetry (DSC) measurements on vacuum-dried polymer solutions. The thermogram of the first heating cycle (Figure 2d) reveals the melting peak of the material with CID treatment at 248.7 °C. This melting peak is with 8.8 °C significantly higher than the melting peak of the untreated reference material at 239.9 °C, which was processed identically except for the CID steps. A peak at 248.7 °C is a surprisingly high value for P3HT. Usually, from the position of the melting peaks, it is possible to calculate ζ, the number of repeating units of the polymer along the chain axis, based on the following relationship^[33]

$$\zeta = \frac{a \cdot T_m^0}{T_m - T_m^0} \quad (1)$$

T_m⁰ is the melting temperature of a P3HT crystal of infinite size and *a* is an experimentally derived constant. Snyder et al. obtained

from their study of short P3HT chains without chain folding and oligomers $T_m^0 = (545 \pm 6)$ K (272 °C) and $a = -5.4 \pm 0.5$.^[33] Using these values and setting the results in relation to literature values of lamellar widths, we can assume an increase in lamellar width of at least 30%.^[34,35] This indicates that the planarized parts of the involved backbones need to be significantly longer for the CID-treated P3HT.

Similar results can be achieved by investigating solutions of CID-treated and reference P3HT in CF. Upon heating, the reference P3HT dissolves in CF at around 40 °C, while the P3HT with CID treatment can only be entirely dissolved in CF under sealed conditions at about 80 °C (see Supporting Information).

Re-dissolved P3HT solutions with CID treatment possess a nearly identical molecular weight distribution compared to untreated solutions (Figure S3, Supporting Information). In addition, the second heating curves of the CID-treated sample and the reference feature an almost identical melting peak (Figure S4, Supporting Information). Furthermore, the fact that the CID-treated P3HT can be completely re-dissolved demonstrates the reversibility of the CID treatment. This treatment only forms improved aggregates but does not significantly alter the chemical structure of the polymers permanently.

4.1. Role of Treatment Protocol

Evaluating the absorption spectroscopy data of the experiments with variation in treatment protocol from Figure 3 reveals further information on the formation process. The results in Figure 4a show the general tendency that after a range of relatively constant quality of backbone order, that is, constant A_1 peak position, at intermediate aggregate fractions, the quality of backbone order decreases at high aggregate fractions, reflected

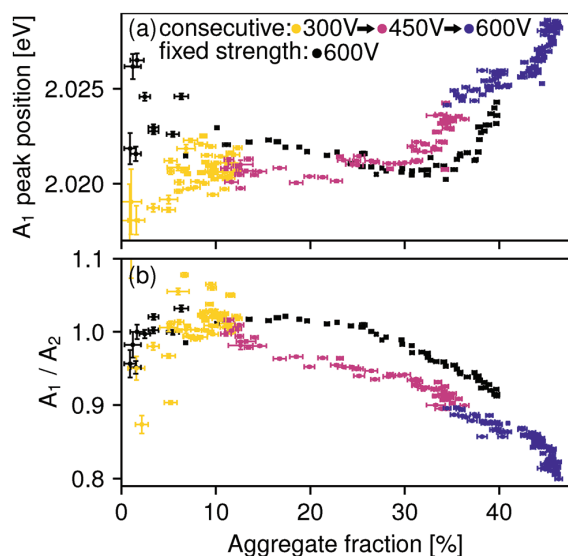


Figure 4. Fit results from associated UV-vis measurements: a) A_1 peak position and b) peak amplitude ratio between A_1 peak and A_2 peak obtained from fitting the vibronic structure from the spectra of the experiments in Figure 3b,d (same color code used).

in the blueshift of the A_1 peak. This decrease is more pronounced and sets in at lower aggregate fractions for the treatment with consecutively increasing strength. At low aggregate fractions, a higher quality of backbone order can be achieved with lower treatment strength (300 V treatment vs 600 V treatment). The values for the A_1 to A_2 peak ratio in Figure 4b, with an initial plateau and a decreasing trend for higher aggregate fractions, support the same conclusion for the impact of the consecutively increasing and fixed treatment strength on the backbone ordering.

Therefore, we can conclude that a lower treatment strength is beneficial at low aggregate fractions, however, limiting the achievable range of aggregate fractions. For high aggregate fractions, a higher fixed treatment strength yields a better aggregate quality than the consecutively increasing treatment strength.

4.2. Role of Solvent

The CID treatment allows inducing aggregation in various solvents, including green solvents. We examined the CID treatment in the following solvents: chloroform (CF), toluene (TOL), *o*-xylene (OX), tetrahydrofuran (THF), and various mixing ratios of OX and the poor solvent acetonitrile (ACN). For all tested solvents, control over the aggregate fraction can be realized. The main changes between the solvents are systematic differences in the quality of the backbone order. In Figure 5a,b, we summarize

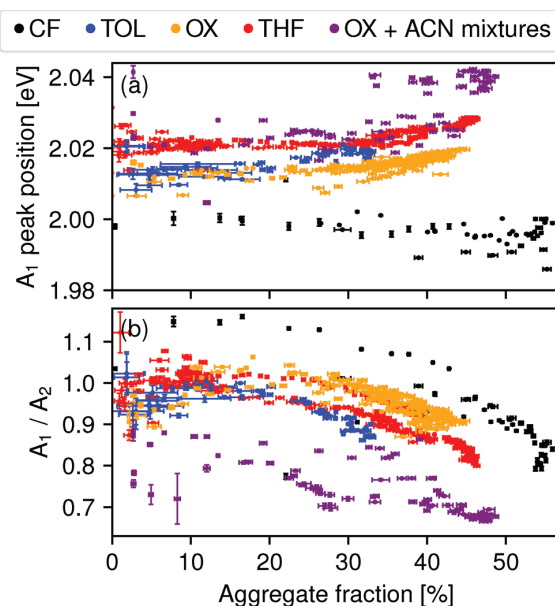


Figure 5. Fit results from associated UV-vis measurements: a) A_1 peak position and b) ratio of the peak amplitudes between the A_1 peak and the A_2 peak obtained from fitting the vibronic structure from more than 600 individual spectra obtained in more than 30 independent CID treatments series. The data are categorized by the used solvents: chloroform (CF, black), toluene (TOL, blue), *o*-xylene (OX, orange), tetrahydrofuran (THF, red), and various mixing ratios of *o*-xylene and acetonitrile (OX + ACN mixtures, purple).

the results of fitting more than 600 spectra obtained in more than 30 independent CID treatment series, mainly using various non-chlorinated solvents. All datasets from one solvent are shown in a single color. The A_1 peak position, as well as the peak ratios of the absorption spectroscopy data, shows the same systematic tendencies: The quality of the backbone order is decreasing at high aggregate fractions after relatively constant values at intermediate and low aggregate fractions. Aggregates in CF possess an exceptionally high quality of backbone order. For the other solvents, the overall quality of backbone order can be correlated with the polarity of the solvents. A high Hansen polarity parameter δ_p indicates a high solvent polarity. While *o*-xylene ($\delta_p = 1.0$ MPa) and toluene ($\delta_p = 1.4$ MPa) have the lowest polarity, they show the highest backbone ordering, THF ($\delta_p = 5.7$ MPa) shows a lower backbone ordering.^[36] The ACN ($\delta_p = 18.0$ MPa) admixture to OX further boosts the solvent polarity and results in the lowest quality of backbone order.^[36]

5. Discussion

5.1. Aggregate Formation

Examining CID in CF (see Figures 2 and 5), we showed that direct control of the aggregate fraction between 0% and at least about 57% could be achieved with the CID treatment. The extracted information on backbone ordering supports our assumed model for aggregate formation because high-quality aggregates are formed particularly for the initial CID steps, which is shown in a clear redshift of the A_1 peak, a high A_1 to A_2 peak ratio, and the strong shift to higher melting temperatures in DSC (Figure 2c–e). Combined with the apparent polaron absorption (Figure S1, Supporting Information), we conclude that the backbone's planarization occurs due to doping. Those more planar chains are then incorporated into aggregates, explaining the high planarity in the aggregates. Moreover, the increased backbone stiffness upon doping observed in the simulations in Figure 1a supports suppressed chain folding resulting in a more extended lamellar width.

In general, each CID step results in further aggregation events. Initially, mainly the long and defect-free chains aggregate.^[10,37–39] Subsequent treatment steps induce aggregates with lower quality, gradually decreasing the observed average quality of backbone order since more and more chain-ends and regio-defects must be incorporated, which causes torsional disorder along P3HT backbones within aggregates.

5.2. Tunability of Aggregate Fraction

The simplest way to control the aggregate fraction is by monitoring the aggregate fraction with UV–vis absorption spectroscopy and stopping the spark treatment when the desired aggregate fraction is achieved. In our measurements, we always observe the same characteristic dependence of the aggregate fraction on the number of treatment steps: the initial substantial increase of aggregate fraction is slowed down until it reaches a plateau at a specific constant aggregate fraction (Figures 2 and 3). Assuming that under fixed processing condi-

tions with a fixed CID treatment strength, a specific fraction of the polymer can be aggregated, this general tendency can be explained purely statistically. A certain portion of the polymer chains gets doped upon a CID treatment step. A fraction of these doped chains starts to aggregate, while another fraction does not aggregate because it cannot form aggregates under the chosen conditions (e.g., defects hampering the aggregation or tie-chains between aggregates). A third fraction of the doped chains does not aggregate because it is already aggregated. With increasing aggregate fraction, the third fraction of the already aggregated chains grows at the cost of the first fraction of chains that can be aggregated. Thus, the aggregation rate decreases with every treatment step until it is 0 because all chains that can be aggregated under the given conditions are already aggregated.

In Figure 3 as well as in Figure S2, Supporting Information, we could demonstrate that by carrying out CID for selected solution parameters (temperature, concentration, and poor solvent additive), we reach a specific achievable aggregate fraction, that is, the level of the plateau reached after sufficient treatment steps. However, the plateau does depend on the treatment strength. To explain the dependencies of the achievable aggregate fraction using CID treatment, we extend the literature models for disorder–order transitions of neutral polymers by a further dimension.

Temperature-induced disorder–order transitions in semiconducting polymers are widely studied.^[20,37,40–45] When the temperature of a polymer solution is decreased, the solvent quality decreases, and thus the polymer's solubility decreases accordingly. Upon reducing the temperature, P3HT undergoes a disorder–order transition from a random coil via a planarized coil and a disordered aggregate to a planarized aggregate and possibly a crystallized aggregate.^[20] The temperature acts as a parameter controlling the solubility, where for lower solubility, less material is in an amorphous random coil phase and increasingly more material in an aggregated phase.^[20,37] Other parameters, such as, for example, poor solvent content and polymer concentration, can have a similar effect, and also other polymers undergo similar disorder–order transitions.^[7,10–12,20,40–46] In the following, we will refer to the parameters influencing the solubility, like the polymer concentration, poor solvent concentration, and temperature as solubility parameters.

The clear polaron signature in Figure S1a, Supporting Information, suggests that the strong current flow induced by the CID treatment leads to doping (charging) of the polymer. The solubility of charged polymers is lower compared to the corresponding neutral polymers in the nonpolar organic solvents generally used for semiconducting polymers.^[16,17,19] Also, increasing the doping ratio further reduces the polymer's solubility.^[18] With a stronger CID treatment, more current is flowing, and we can expect on the one hand a higher number of doped chains and on the other hand higher doping ratios of single chains. Thus, more chains can be aggregated and there is a lower solubility. Therefore, the solubility during CID processing is a) a function of solubility parameters discussed in the previous paragraph and b) a function of the treatment strength. For simplicity, we consider only one solubility parameter in the following, but more could be considered analogously.

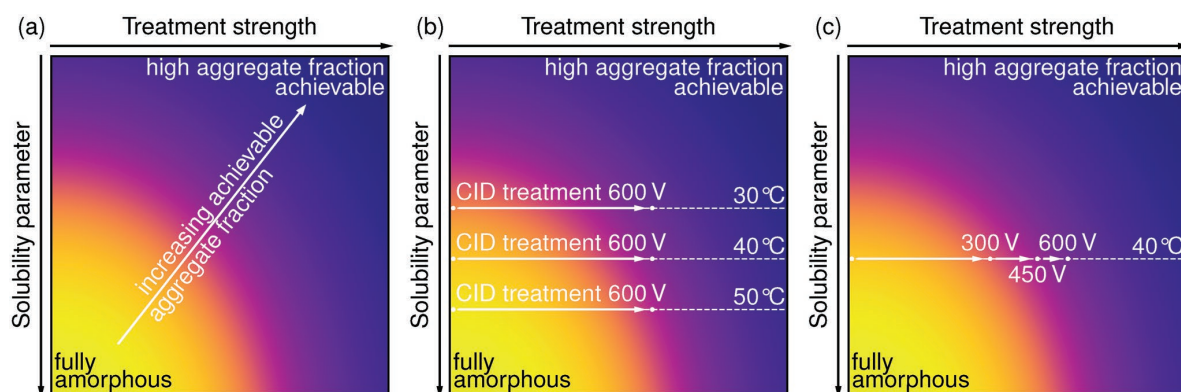


Figure 6. a) Sketch of a qualitative 2D parameter space map displaying the achievable aggregate fraction (plateau reached after sufficient treatment steps) color-coded from yellow (fully amorphous/no aggregation achievable) to purple (high aggregate fraction achievable) as a function of the treatment strength and a solubility parameter. b) Exemplary jumps for spark treatments from Figure 3a–c) with the same treatment strength (capacitor charged with 600 V) at different temperatures (30 °C, 40 °C, and 50 °C) and c) from Figure 3d) at the same temperature (40 °C), but consecutively increasing treatment strength (capacitor charged with 300 V, then increased to 450 and 600 V).

Using the solubility parameter as one dimension and the treatment strength as a further dimension, we draw a qualitative 2D parameter space map (scale of solubility and treatment strength qualitative). In this 2D parameter space, the achievable aggregate fraction (plateau reached after sufficient treatment steps) can be displayed as a measure of solubility. The lower the solubility is, the higher the achievable aggregate fraction. In Figure 6a, such a 2D map is sketched. The achievable aggregate fraction is color coded from yellow (fully amorphous/no aggregation achievable) to purple (high aggregate fraction achievable). The polymer is nearly fully amorphous with a high solubility parameter and low treatment strength.^[47] By decreasing the solubility parameter and/or increasing the treatment strength, an increasing aggregate fraction is achievable.

On this basis, the measurements in Figure 3 can be discussed. Without CID treatment, the accessible parameter space is the ordinate at 0 treatment strength. Conducting the CID treatment temporarily charging the polymer leads to a temporary, horizontal shift in the qualitative 2D map from 0 treatment strength to a specific treatment strength. These jumps in parameter space are sketched in Figure 6b for three different temperatures (= three different solubility parameters) representing the measurements in Figure 3a–c. With identical treatment strength, there is always the same horizontal jump. In the example here (Figure 6b), the starting point of the transition is vertically shifted due to carrying out the treatment at different solubility parameters (by using different temperatures). Only minimal aggregation occurs at the starting point for all three sketched temperatures (e.g., first absorption spectrum in Figure 2a). However, with the CID treatment, the now charged polymer temporarily experiences an environment with higher aggregation tendency leading to significant aggregate fractions for repeated CID treatments. The largest aggregate fractions from Figure 3a–c are achieved at 30 °C, followed by 40 °C, and the lowest at 50 °C, because the jump occurs into a region with larger (30 °C) or smaller (50 °C) aggregation tendency as seen from the 2D parameter space maps. The aggregates are still stable at the initial condition since only the formation is suppressed at that condition and not the final state.

Analogous 2D maps of the achievable aggregate fraction with the spark treatment can also be drawn in dependence on other solubility parameters as, for example, poor solvent content or polymer concentration, as shown in Figure S5, Supporting Information. It is important to note that there are also conditions where no aggregation occurs upon CID treatment (e.g., in Figure S2c, Supporting Information).

The 2D parameter space maps also explain the aggregation behavior if the solubility parameter is kept constant and the treatment strength is adjusted. Figure 6c shows the induced jumps in parameter space with different CID treatment strengths (data in Figure 3d). The jump for 300 V is still parallel to the treatment strength axis but shorter than in Figure 6b with 600 V. With the consecutive increase of voltage, the overall jump depth is increased, allowing for an increased achievable aggregate fraction.

Thus, the qualitative model presented here can explain a large variety of results of the achievable aggregate fraction and, therefore, can be used as a guide to choose experimental conditions to achieve the desired aggregate fractions for various material systems.

The different results obtained by increasing the CID treatment strength consecutively up to a specific strength compared to a treatment with the same fixed treatment strength are due to the different starting point of the 600 V treatment. From Figure 4 it is clear that the aggregate properties after the 450 V treatment are different to the aggregate properties at the same aggregate fraction with a fixed treatment strength of 600 V. This will be discussed in more detail in the following section. Depending on the properties of the already existing aggregates and the remaining amorphous chains different fractions of the involved material are accessible for aggregation.

5.3. Tunability of Aggregate Properties

Our 2D parameter space maps only allow a statement about the achievable aggregate fraction, while the aggregate properties

(e.g., quality of molecular ordering and aggregate size) must be considered separately and will highly depend on the chosen processing path. With the results from UV–vis spectroscopy, we mainly access the quality of backbone order, which is of great importance for charge transport.

Considering the basics leading to the 2D parameter space map for the achievable aggregate fraction can also explain the differences observed in the backbone ordering. A low treatment strength only achieves aggregation of long and defect-free polymer chains.^[10,37–39] Defect-free chains naturally have a higher quality of packing. Therefore, high-quality backbone ordering can be expected for the low voltage (=low treatment strength). When in contrast, a stronger treatment strength is used, it is likely that already in the first treatment steps, shorter and defective chains are among the aggregated material. Therefore, the average order is lower, supporting the results in the low aggregate fraction range in Figure 4. An increasing doping ratio due to a stronger treatment strength leads to a stronger planarization of the polymer chains prior to chain folding. This can translate to an increased backbone ordering in the aggregates, which we observe in Figure 4 at higher aggregate fractions.

Comparing the different solvents in Figure 5, the backbone ordering upon CID treatment appears to be correlated with solvent polarity (for the tested non-chlorinated solvents). Taking selective backbone and sidechain solubility into consideration, our hypothesis is that the polarity of the solvent compared to the sidechains and the charged backbone is decisive.^[48] While the hexyl sidechains are nonpolar (note, *n*-hexane, chemically similar to the sidechains, has a vanishing Hansen polarity parameter of $\delta_p = 0$ MPa), the polymer backbones charged by the CID treatment are polar.^[36] The polarity of all used solvents can be expected to lie between the polarity of the sidechain and the charged backbone. Considering a very nonpolar solvent, the aggregation would be expected to be driven by the stacking of the charged backbones leading to a strong backbone ordering. With increasing polarity of the solvent, the affinity between the sidechains is increasingly contributing to the driving forces of the aggregation. In this case, sidechain ordering and backbone ordering are both contributing, and the quality of the backbone order suffers in a more polar solvent.^[13,14]

Compared with the non-chlorinated solvents, CID treatment in CF leads to exceptionally high backbone ordering despite possessing a higher polarity ($\delta_p = 3.1$ MPa) than *o*-xylene and toluene.^[36] One reason causing an increased planarization during the CID treatment could be an exceptionally high and sufficiently long-lived doping ratio achieved in CF. For a more strongly charged backbone, the backbone aggregation dominates the side chain aggregation stronger than if less charged. If the doping is strong enough, this can then compensate for the slightly higher solvent polarity. In contrast to other solvents, we observed a characteristic polaron absorption in CF solutions upon CID treatment (Figure S1, Supporting Information), which supports the hypothesis of a high doping ratio.^[49–52] This strong doping is probably possible due to several factors. Due to the intrinsic instability of CF and its function as a Lewis acid, P3HT chains in CF are, on average, slightly positively charged even without spark treatment.^[53,54] We already demonstrated this property in a previous work by the positive electrophoretic

mobility of P3HT in CF and used it to move P3HT in a wet thin film driven by an electric field.^[55] If P3HT is further positively charged beyond this intrinsic effect, that is, further electrons are transferred from P3HT to CF, charge remains localized on the P3HT for a longer time. The reason is that the CF[−] anion is unstable, and a Cl[−] anion splits off upon charging a CF molecule negatively.^[56–58] A HCl₂C[•] radical is left behind, and the Cl[−] anion forms a quite stable and long-lived cluster anion with a neutral CF molecule stabilizing the doped P3HT.^[56,57] With this slower decay of the P3HT doping ratio, a stronger and more ordered aggregation can be achieved in CF compared to the other (non-chlorinated) solvents, explaining the exceptional role of the solvent CF we observe in Figure 5. This longer lifetime is also in line with the possibility to observe the polaron absorption in CF, but not in other solvents (Figure S1, Supporting Information).

6. Conclusion

We developed a novel solution treatment for controlled polymer aggregation. CID utilizes spark discharges between two tungsten electrodes immersed in a polymer solution. This treatment induces a fast subsequent aggregation process, which we monitor for every treatment step by absorption spectroscopy. We show that the aggregation process is a special form of doping-induced aggregation, where strong electric currents through the solution can be used to quickly switch on and off doping.

Our newly presented CID treatment aims to achieve maximum control over the polymer aggregation process in several ways. We demonstrated a stepwise control for setting the aggregate fraction in various solvents. Moreover, we introduced a qualitative model describing the achievable aggregate fraction as a function of solubility parameters (e.g., temperature, polymer concentration, or poor solvent content) and the treatment strength. The tunability of the achievable aggregate fraction proposed by our model is in good agreement with numerous experiments examining various solubility parameters (temperature, polymer concentration, and poor solvent content) and experimental settings (CID treatment strength).

Beyond the control over the aggregate fraction, we can also control the backbone ordering with the CID treatment. This is partially possible by choosing an appropriate treatment strength, but the highest control is possible by choice of solvent. Particularly the solvent polarity appears to be an essential factor where nonpolar solvents can yield the highest backbone order among the tested non-chlorinated solvents. The highest backbone order among all tested solvents could be achieved with CF. The other extreme case of the lowest backbone order could be achieved by admixtures of the highly polar solvent ACN. Therefore, a broad spectrum of backbone ordering can be achieved with the CID treatment by rationally choosing the solvent.

We demonstrated that our approach of exploiting the CID treatment can be successfully employed to control the aggregation state of P3HT in solution before further processing. Therefore, this method may become an elegant pathway to finely tune aggregation and solid-state morphology for thin-films of semiconducting polymers, especially if employed for

multi-component systems, like binary donor–acceptor mixtures. We further anticipate that this CID treatment can also be transferred to other semiconducting polymers to control their aggregation in solution. These solutions can be further processed to dried films and will be investigated next.

7. Experimental Section

Materials: P3HT with a regioregularity of 96% was purchased from Rieke Metals (size exclusion chromatography (SEC) data on molecular weight in Figure S3, Supporting Information), chloroform from Sigma-Aldrich, THF from Fisher Chemical, *o*-xylene from Alfa Aesar and toluene as well as ACN from VWR Chemicals. All materials were used as received.

CID Treatment: The untreated P3HT solutions were prepared by dissolving P3HT in the specified solvent at 50 °C for 20 min. Prior to the CID treatment, the solutions were kept for 15 min at the desired temperature to allow for proper equilibration. This temperature was also kept constant throughout the complete CID treatment. As seen in the schematic diagram of the setup for the CID treatment in Figure 1b, a capacitor (WIMA MKS 4, 3.3 μ F) was charged to the specified voltage and subsequently connected to two tungsten wires separated by several millimeters and immersed into the P3HT solution. These two tungsten wires were then approached until a spark discharge occurred below a separation of 1 mm before the wires are brought into contact. This procedure of charging the capacitor, connecting, and approaching the tungsten wires was repeated until the desired number of CID treatment steps was achieved. A photograph of the comparison between an untreated solution and a solution with CID treatment is displayed in Figure S6, Supporting Information. A safety evaluation for each solvent was carried out prior to the start of experiments.

UV–Vis Absorption Spectroscopy: For acquiring the UV–vis absorption measurements, a combined deuterium and halogen white light source from Ocean Optics and an AvaSpec-HSC1024 \times 58 TEC-EVO spectrometer from Avantes were used to measure the absorption of the solutions. Short optical path lengths in the range of 100 μ m and less were realized by time-resolved measurements of wet thin films with a time resolution of 6 ms. Spectra were evaluated before any drying dynamics occurred. Amorphous spectra measured at the same concentration and temperature in the same solvent were scaled to the high-energy shoulder of the absorption spectrum at ≥ 2.6 eV.^[22,23] This rescaled amorphous spectrum was subsequently subtracted from the absorption spectrum, which was then fitted by the sum of five equidistant (distance of 0.17 eV between peaks) gaussian peaks for the A_1 to A_5 peaks.^[22,23] While an identical peak width was fitted for the A_2 to A_5 peaks, a smaller peak width was fitted for the A_1 peak.^[59,60] The minimum aggregate fraction was calculated using the area below the fits and below the rescaled amorphous spectrum considering the different molar extinction coefficients of the amorphous and aggregated P3HT described by Clark et al.^[23] This procedure yields an estimate for the minimum aggregate fraction as higher optical transitions of the aggregate can contribute to the high energy shoulder leading to an overestimation of the amorphous absorption.

Simulations: The energy barriers upon dihedral rotation of the backbone of poly(3-methylthiophene) oligomers including four monomers without charge and with a charge of +1e were simulated using the Amsterdam Modeling Suite (AMS). In AMS, potential energy scans of the S–C–S dihedral angle were used exploiting DFTB3, an extension of the self-consistent-charge density-functional tight-binding method.^[61,62] To obtain more precise results, we also conducted DFT simulations for the syn (0°), transition state (90°), and anti (180°) conformation with AMS using B3LYP/TZ2P.^[63–67] While the minima at 0° and 180° were fully optimized, for the transition state, a constrained optimization was performed with the S–C–S dihedral angle fixed to 90° . The DFTB3 PES scans were rescaled to fit the energy difference between the transition state and the anti-conformation obtained with DFT.

Differential Scanning Calorimetry: DSC was performed using a Mettler Toledo DSC 3+. For the preparation of solid samples, differently treated solutions of P3HT were prepared, and the solvent was removed entirely under vacuum overnight. About 3–10 mg of the dried samples was weighed into DSC pans, which were then closed with a cover lid. All samples were heated from 50 to 300 °C under nitrogen. The cooling and heating rates were always 10 K min^{-1} . The reported melting temperatures refer to peak temperatures in the DSC thermograms. The DSC data were corrected by a baseline correction.

Supporting Information

Supporting Information is available from the Wiley Online Library or from the author.

Acknowledgements

F.E. and E.M.H. thank for funding from SolarEraNet (No. NFA4R2ROPV). F.E. and F.A.W. thank the Elite Study Program Macromolecular Science within the Elite Network of Bavaria (ENB) for support. The authors are grateful to Florian Meichsner (Macromolecular Chemistry, University of Bayreuth) for help with the SEC measurements. The simulation work was performed under the Project HPC-EUROPA3 (INFRAIA-2016-1-730897), with the support of the EC Research Innovation Action under the H2020 Programme; in particular, F.E. gratefully acknowledges the Stratingh Institute for Chemistry and the computer resources and technical support provided by SURF.

Open access funding enabled and organized by Projekt DEAL.

Conflict of Interest

The authors declare no conflict of interest.

Data Availability Statement

The data that support the findings of this study are available from the corresponding author upon reasonable request.

Keywords

conjugated polymers, density functional theory, green solvents, nanostructural control, organic semiconductors, solubility, solution pre-aggregation

Received: December 2, 2022

Revised: January 27, 2023

Published online: March 2, 2023

- [1] H. Sirringhaus, P. J. Brown, R. H. Friend, M. M. Nielsen, K. Bechgaard, B. M. W. Langeveld-Voss, A. J. H. Spiering, R. A. J. Janssen, E. W. Meijer, P. Herwig, D. M. De Leeuw, *Nature* **1999**, 401, 685.
- [2] H. Wang, Y. Xu, X. Yu, R. Xing, J. Liu, Y. Han, *Polymers* **2013**, 5, 1272.
- [3] R. Noriega, J. Rivnay, K. Vandewal, F. P. V. Koch, N. Stingelin, P. Smith, M. F. Toney, A. Salleo, *Nat. Mater.* **2013**, 12, 1038.
- [4] Z.-Y. Wang, L. Di Virgilio, Z.-F. Yao, Z.-D. Yu, X.-Y. Wang, Y.-Y. Zhou, Q.-Y. Li, Y. Lu, L. Zou, H. I. Wang, X.-Y. Wang, J.-Y. Wang, J. Pei, *Angew. Chem.* **2021**, 133, 20646.

- [5] S. Pröller, D. Moseguí González, C. Zhu, E. Schaible, C. Wang, P. Müller-Buschbaum, A. Hexemer, E. M. Herzig, *Rev. Sci. Instrum.* **2017**, *88*, 066101.
- [6] G. Shi, J. Yuan, X. Huang, Y. Lu, Z. Liu, J. Peng, G. Ding, S. Shi, J. Sun, K. Lu, H.-Q. Wang, W. Ma, *J. Phys. Chem. C* **2015**, *119*, 25298.
- [7] L. Li, G. Lu, X. Yang, *J. Mater. Chem.* **2008**, *18*, 1984.
- [8] G. L. Schulz, S. Ludwigs, *Adv. Funct. Mater.* **2017**, *27*, 1603083.
- [9] C. E. Johnson, M. P. Gordon, D. S. Boucher, *J. Polym. Sci., Part B: Polym. Phys.* **2015**, *53*, 841.
- [10] S. Berson, R. DeBettignies, S. Bailly, S. Guillerez, *Adv. Funct. Mater.* **2007**, *17*, 1377.
- [11] S. Ludwigs, *P3HT Revisited – From Molecular Scale to Solar Cell Devices*, Springer, Berlin **2014**.
- [12] N. Kiriya, E. Jähne, H.-J. Adler, M. Schneider, A. Kiriya, G. Gorodyska, S. Minko, D. Jehnichen, P. Simon, A. A. Fokin, M. Stamm, *Nano Lett.* **2003**, *3*, 707.
- [13] Z. Peng, L. Ye, H. Ade, *Mater. Horiz.* **2022**, *9*, 577.
- [14] J. H. Carpenter, M. Ghasemi, E. Gann, I. Angunawala, S. J. Stuard, J. J. Rech, E. Ritchie, B. T. O'Connor, J. Atkin, W. You, D. M. Delongchamp, H. Ade, *Adv. Funct. Mater.* **2019**, *29*, 1806977.
- [15] J. Gao, J. D. Roehling, Y. Li, H. Guo, A. J. Moulé, J. K. Grey, *J. Mater. Chem. C* **2013**, *1*, 5638.
- [16] F. M. McFarland, C. M. Ellis, S. Guo, *J. Phys. Chem. C* **2017**, *121*, 4740.
- [17] L. Müller, D. Nanova, T. Glaser, S. Beck, A. Pucci, A. K. Kast, R. R. Schröder, E. Mankel, P. Pingel, D. Neher, W. Kowalsky, R. Lovrincic, *Chem. Mater.* **2016**, *28*, 4432.
- [18] A. E. Mansour, D. Lungwitz, T. Schultz, M. Arvind, A. M. Valencia, C. Cocchi, A. Opitz, D. Neher, N. Koch, *J. Mater. Chem. C* **2020**, *8*, 2870.
- [19] M. Arvind, C. E. Tait, M. Guerrini, J. Krumland, A. M. Valencia, C. Cocchi, A. E. Mansour, N. Koch, S. Barlow, S. R. Marder, J. Behrends, D. Neher, *J. Phys. Chem. B* **2020**, *124*, 7694.
- [20] F. Panzer, H. Bässler, A. Köhler, *J. Phys. Chem. Lett.* **2017**, *8*, 114.
- [21] S. Ray, *An Introduction to High Voltage Engineering*, 2nd ed., PHI Learning, Delhi, **2014**.
- [22] C. Scharsich, R. H. Lohwasser, M. Sommer, U. Asawapirom, U. Scherf, M. Thelakkat, D. Neher, A. Köhler, *J. Polym. Sci., Part B: Polym. Phys.* **2012**, *50*, 442.
- [23] J. Clark, J.-F. Chang, F. C. Spano, R. H. Friend, C. Silva, *Appl. Phys. Lett.* **2009**, *94*, 163306.
- [24] M. Reichenberger, D. Kroh, G. M. M. Matrone, K. Schötz, S. Pröller, O. Filonik, M. E. Thordardottir, E. M. Herzig, H. Bässler, N. Stingelin, A. Köhler, *J. Polym. Sci., Part B: Polym. Phys.* **2018**, *56*, 532.
- [25] M. Reichenberger, S. Baderschneider, D. Kroh, S. Grauf, J. Köhler, R. Hildner, A. Köhler, *Macromolecules* **2016**, *49*, 6420.
- [26] F. Machui, S. Langner, X. Zhu, S. Abbott, C. J. Brabec, *Sol. Energy Mater. Sol. Cells* **2012**, *100*, 138.
- [27] J. Clark, C. Silva, R. H. Friend, F. C. Spano, *Phys. Rev. Lett.* **2007**, *98*, 206406.
- [28] C. A. Sandstedt, R. D. Rieke, C. J. Eckhardt, *Chem. Mater.* **1995**, *7*, 1057.
- [29] A. Köhler, H. Bässler, *Electronic Processes in Organic Semiconductors: An Introduction*, Wiley-VCH, Weinheim **2015**.
- [30] J. Gierschner, Y.-S. Huang, B. Van Averbeke, J. Cornil, R. H. Friend, D. Beljonne, *J. Chem. Phys.* **2009**, *130*, 044105.
- [31] F. C. Spano, *J. Chem. Phys.* **2005**, *122*, 234701.
- [32] F. C. Spano, C. Silva, *Annu. Rev. Phys. Chem.* **2014**, *65*, 477.
- [33] C. R. Snyder, R. C. Nieuwendaal, D. M. Delongchamp, C. K. Luscombe, P. Sista, S. D. Boyd, *Macromolecules* **2014**, *47*, 3942.
- [34] M. Brinkmann, P. Rannou, *Adv. Funct. Mater.* **2007**, *17*, 101.
- [35] R. Zhang, B. Li, M. C. Iovu, M. Jeffries-El, G. Sauv e, J. Cooper, S. Jia, S. Tristram-Nagle, D. M. Smilgies, D. N. Lambeth, R. D. McCullough, T. Kowalewski, *J. Am. Chem. Soc.* **2006**, *128*, 3480.
- [36] C. M. Hansen, *Hansen Solubility Parameters: A User's Handbook*, 2nd ed., CRC Press, Boca Raton, FL **2007**.
- [37] F. Panzer, H. Bässler, R. Lohwasser, M. Thelakkat, A. Köhler, *J. Phys. Chem. Lett.* **2014**, *5*, 2742.
- [38] P. Kohn, S. Huettner, H. Komber, V. Senkovskyy, R. Tkachov, A. Kiriya, R. H. Friend, U. Steiner, W. T. S. Huck, J.-U. Sommer, M. Sommer, *J. Am. Chem. Soc.* **2012**, *134*, 4790.
- [39] F. Paquin, H. Yamagata, N. J. Hestand, M. Sakowicz, N. Bérub e, M. C ot e, L. X. Reynolds, S. A. Haque, N. Stingelin, F. C. Spano, C. Silva, *Phys. Rev. B* **2013**, *88*, 155202.
- [40] A. Köhler, S. T. Hoffmann, H. Bässler, *J. Am. Chem. Soc.* **2012**, *134*, 11594.
- [41] L. Sun, J. Zhao, W. Huang, X. Chen, W. Zhang, Y. Ding, L. Li, *J. Polym. Sci., Part B: Polym. Phys.* **2019**, *57*, 1105.
- [42] T. Unger, F. Panzer, C. Consani, F. Koch, T. Brixner, H. Bässler, A. Köhler, *ACS Macro Lett.* **2015**, *4*, 412.
- [43] C. Scharsich, F. S. U. Fischer, K. Wilma, R. Hildner, S. Ludwigs, A. Köhler, *J. Polym. Sci., Part B: Polym. Phys.* **2015**, *53*, 1416.
- [44] M. Reichenberger, J. A. Love, A. Rudnick, S. Bagnich, F. Panzer, A. Stradomska, G. C. Bazan, T.-Q. Nguyen, A. Köhler, *J. Chem. Phys.* **2016**, *144*, 074904.
- [45] D. Kroh, F. Eller, K. Schötz, S. Wedler, L. Perdig on-Toro, G. Freychet, Q. Wei, M. D orr, D. Jones, Y. Zou, E. M. Herzig, D. Neher, A. Köhler, *Adv. Funct. Mater.* **2022**, *32*, 2205711.
- [46] J. Liu, M. Arif, J. Zou, S. I. Khondaker, L. Zhai, *Macromolecules* **2009**, *42*, 9390.
- [47] D. Raithele, S. Baderschneider, T. B. De Queiroz, R. Lohwasser, J. Köhler, M. Thelakkat, S. K ummel, R. Hildner, *Macromolecules* **2016**, *49*, 9553.
- [48] Z. Xu, K. S. Park, J. J. Kwok, O. Lin, B. B. Patel, P. Kafle, D. W. Davies, Q. Chen, Y. Diaoy, *Adv. Mater.* **2022**, *34*, 2203055.
- [49] J. Lebert, E. M. Kratzer, A. Bourdick, M. Coric, S. Gekle, E. M. Herzig, *ACS Omega* **2018**, *3*, 6388.
- [50] C. Enengl, S. Enengl, S. Pluczyk, M. Havlicek, M. Lapkowski, H. Neugebauer, E. Ehrenfreund, *ChemPhysChem* **2016**, *17*, 3836.
- [51] Y. Furukawa, *J. Phys. Chem.* **1996**, *100*, 15644.
- [52] J. Yamamoto, Y. Furukawa, *J. Phys. Chem. B* **2015**, *119*, 4788.
- [53] Sigma-Aldrich, "Solvent Stabilizer Systems", <https://www.sigmaaldrich.com/DE/de/technical-documents/technical-article/chemistry-and-synthesis/reaction-design-and-optimization/stabilizer-systems> (accessed: December 2022).
- [54] G. C. Vogel, R. S. Drago, *J. Chem. Educ.* **1996**, *73*, 701.
- [55] S. Pr oller, O. Filonik, F. Eller, S. Mansi, C. Zhu, E. Schaible, A. Hexemer, P. M uller-Buschbaum, E. M. Herzig, *ACS Appl. Mater. Interfaces* **2020**, *12*, 5219.
- [56] P. O. Staneke, G. Groothuis, S. Ingemann, N. M. M. Nibbering, *Int. J. Mass Spectrom.* **1995**, *142*, 83.
- [57] W. B. Knighton, E. P. Grimsrud, *J. Am. Chem. Soc.* **1992**, *114*, 2336.
- [58] P. O. Staneke, G. Groothuis, S. Ingemann, N. M. M. Nibbering, *J. Phys. Org. Chem.* **1996**, *9*, 471.
- [59] F. M. Keheze, D. Raithele, T. Wu, D. Schiefer, M. Sommer, R. Hildner, G. Reiter, *Macromolecules* **2017**, *50*, 6829.
- [60] F. C. Spano, *Chem. Phys.* **2006**, *325*, 22.
- [61] M. Gaus, Q. Cui, M. Elstner, *J. Chem. Theory Comput.* **2012**, *7*, 931.
- [62] E. J. Baerends, SCM, ADF2022.01, SCM, Theoretical Chemistry, Vrije Universiteit, Amsterdam, The Netherlands **2012**, <http://www.scm.com>.
- [63] G. Te Velde, F. M. Bickelhaupt, E. J. Baerends, C. Fonseca Guerra, S. J. A. Van Gisbergen, J. G. Snijders, T. Ziegler, *J. Comput. Chem.* **2001**, *22*, 931.
- [64] A. D. Becke, *J. Chem. Phys.* **1993**, *98*, 5648.
- [65] P. J. Stephens, F. J. Devlin, C. F. Chabalowski, M. J. Frisch, *J. Phys. Chem.* **1994**, *98*, 11623.
- [66] T. H. Dunning, *J. Chem. Phys.* **1971**, *55*, 716.
- [67] J. Gauss, J. F. Stanton, R. J. Bartlett, *J. Chem. Phys.* **1992**, *97*, 7825.



Supporting Information

for *Small*, DOI: 10.1002/smll.202207537

Spark Discharge Doping—Achieving Unprecedented Control over Aggregate Fraction and Backbone Ordering in Poly(3-hexylthiophene) Solutions

*Fabian Eller, Felix A. Wenzel, Richard Hildner, Remco W. A. Havenith, and Eva M. Herzig**

Supporting Information

Spark Discharge Doping – Achieving Unprecedented Control over Aggregate Fraction and Backbone Ordering in Poly(3-hexylthiophene) Solutions

*Fabian Eller, Felix A. Wenzel, Richard Hildner, Remco W. A. Havenith, Eva M. Herzig**

Fabian Eller, Eva M. Herzig

Dynamics and Structure Formation – Herzig Group, University of Bayreuth,

Universitätsstraße 30, 95447 Bayreuth, Germany

E-mail: eva.herzig@uni-bayreuth.de

Felix A. Wenzel

Macromolecular Chemistry and Bavarian Polymer Institute, University of Bayreuth,

Universitätsstraße 30, 95447 Bayreuth, Germany

Richard Hildner

Zernike Institute for Advanced Materials, University of Groningen, Nijenborgh 4, 9747 AG

Groningen, The Netherlands

Remco W. A. Havenith

Stratingh Institute for Chemistry and Zernike Institute for Advanced Materials, University of Groningen, Nijenborgh 4, 9747 AG Groningen, The Netherlands

Ghent Quantum Chemistry Group, Department of Chemistry, Ghent University, Krijgslaan 281 (S3), B-9000 Gent, Belgium

DFT results

Table S1. Energies obtained with DFT (B3LYP/TZ2P) in the different conformations between two 3-methylthiophene monomers (within an oligomer including four monomers) without charge and with a charge of +1 e. The angles refer to the S-C-C-S dihedral angle.

Charge	Energy syn (0°) [kcal mol ⁻¹]	Energy TS ^{a)} (90°) [kcal mol ⁻¹]	Energy anti (180°) [kcal mol ⁻¹]
0 e	0.13	2.63	0
+1 e	0.75	14.93	0

^{a)} Transition state

Polaron absorption signature

Upon performing an increasing number of the current-induced doping (CID) treatment steps with poly(3-hexylthiophene) (P3HT) solutions in chloroform (CF), the typical aggregate absorption increases, and also a characteristic polaron absorption in the low energy range emerges, as can be seen in Figure S1 (a).^[1–3] This polaron band is a clear sign that the CID treatment results in the doping of P3HT in the CF solution. For the tested non-chlorinated solvents, we could not observe this polaron absorption, which is exemplarily shown for a sample of P3HT in tetrahydrofuran (THF) with CID treatment in Figure S1 (b). However, it can be expected that doping also occurs in other solvents but may be short-lived, hampering the observation of these states. The reasons for the longer lifetime of polarons in CF solutions are discussed in detail in Section 5.3 of the main paper.

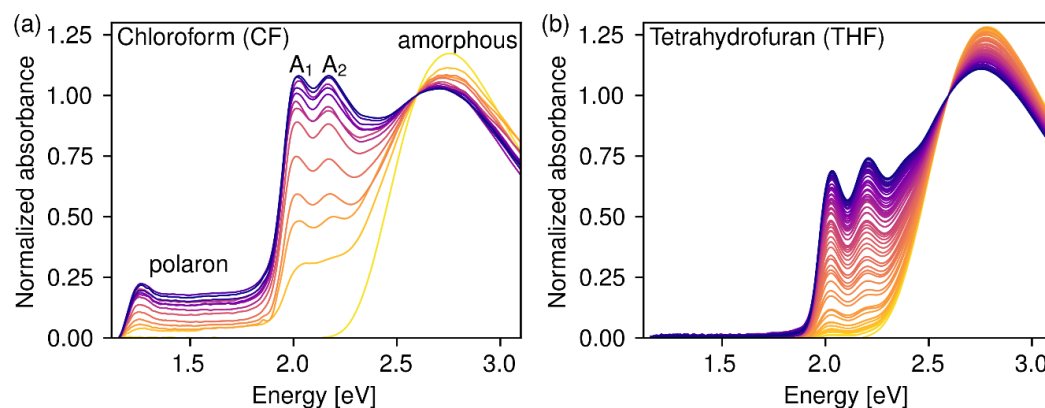


Figure S1. Normalized UV-vis absorption spectra of 2 mg ml⁻¹ P3HT in (a) chloroform (CF) and (b) tetrahydrofuran (THF) solutions with an increasing number of CID treatment steps (from yellow (first treatment step) to purple (highest number of treatment steps); 3.3 μF capacitor charged with (a) 300 V and (b) 600 V respectively). The spectra were measured about 15 ms after a CID treatment step.

Study of concentration and bad solvent additive

By decreasing the polymer concentration of P3HT in *o*-xylene (OX) from 2 mg ml⁻¹ to 0.5 mg ml⁻¹ at 20 °C, the achievable aggregate fraction decreased from 39 % to 16 %, as can be seen in Figure S2 (a)-(b). At 50 °C no aggregation could be induced by the spark treatment for a 2 mg ml⁻¹ P3HT in OX solution (Figure S2 (c)), while 30 % aggregate fraction could be achieved by adding 5% of the poor solvent acetonitrile (ACN) (Figure S2 (d)) and 44 % by adding 10 % ACN (Figure S2 (e)). The corresponding qualitative 2D parameter space maps, as introduced in section 5.2, are displayed in Figure S5 (a)-(b).

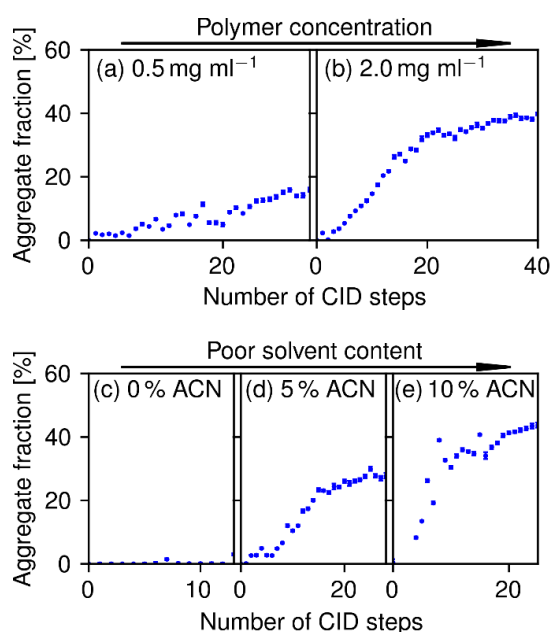


Figure S2. Aggregate fraction in dependency of the number of spark treatment steps for (a)-(b) P3HT in *o*-xylene (OX) solutions at 20 °C with the same treatment strength (3.3 μ F capacitor charged with 600 V) at different concentrations (a) 0.5 mg ml⁻¹, (b) 2.0 mg ml⁻¹. (c)-(e) P3HT in *o*-xylene:acetonitrile solutions at 50 °C with the same treatment strength (3.3 μ F capacitor charged with 600 V) with different acetonitrile (ACN) content (c) 0 % ACN, (d) 5 % ACN, (e) 10 % ACN.

Molar mass

Size exclusion chromatography (SEC) was performed using a Waters HPLC pump 515 and a Waters 2998 photodiode array detector. For the separation process, a guard column (PL, ResiPore, length: 5 cm, diameter: 0.8 cm) and two analytical columns (PL, ResiPore, length:

WILEY-VCH

30 cm, diameter: 0.8 cm) were utilized. Tetrahydrofuran (THF) was used as eluent at a flow rate of 0.5 ml min^{-1} . The molecular weight was reported with respect to narrowly distributed standards of polystyrene. Solutions of the CID treated and reference P3HT (12 mg ml^{-1}) in chloroform (CF) are dried under reduced pressure. Some of the polymer was dissolved in 2 ml of THF, and *ortho*-dichlorobenzene was added as an internal standard. Prior to the measurement, the solution was filtered using a $0.2 \text{ }\mu\text{m}$ polytetrafluoroethylene syringe filter.

Figure S3 shows the molar mass distributions obtained with SEC for the polymer with and without CID treatment. The reference sample features a number-average molar mass of 29.3 kg mol^{-1} , and the treated sample shows a slightly reduced number-average molar mass of 26.4 kg mol^{-1} . This slight shift due to the CID treatment may have multiple reasons. For example, the vacuum-dried solutions are redissolved with THF and consequently filtered, removing undissolved aggregates from the sample. As shown, aggregates produced with the CID treatment in CF are more stable than reference aggregates. Hence, more material may remain insoluble and may, therefore, be removed by the filtering step. This effect might influence the molar mass distribution as long chains are expected to be especially included in the highly stable aggregates, decreasing the overall number average molar mass of the filtered solution.^[4,5] In addition, damage to the chains by the CID treatment could also contribute to the slightly decreasing molar mass. However, it should be noted that the decrease in the number average molar mass is only slight. In other words, the effects observed by the CID treatment cannot be explained by the changes in the molar mass.

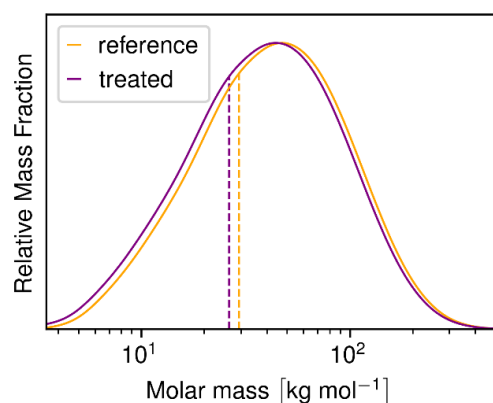


Figure S3. Relative mass fractions obtained with size exclusion chromatography of a P3HT sample with CID treatment (purple) and a reference without treatment (orange). Both curves are normalized to their area and show very similar behavior. The distribution of the treated

sample is slightly shifted to lower molar masses. The dashed lines visualize the number average molar mass M_n ($M_n = 29.3 \text{ kg mol}^{-1}$ for reference, $M_n = 26.4 \text{ kg mol}^{-1}$ for CID treatment).

Re-dissolution of aggregates

Analogously to the increased melting point of the vacuum-dried solution with spark treatment compared to the reference, we also observed an increased dissolution temperature required to dissolve the aggregates due to the CID treatment. In fact, dissolving all aggregates in chloroform (CF) at atmospheric pressure was impossible. To realize higher temperatures, despite the low boiling point of CF, we conducted DSC measurements (Mettler Toledo DSC 3+) in solution using a hermetically sealed container. To observe significant melting and recrystallization signatures of the P3HT solution (12 mg ml^{-1}) in CF with CID treatment temperatures of at least $80 \text{ }^\circ\text{C}$ were required. Comparatively, aggregates produced by cooling or drying usually dissolve in CF at around 40°C . This significant difference further emphasizes the drastically increased interactions of the aggregates due to the CID treatment.

Moreover, temperature-dependent absorption spectroscopy of P3HT in CF solutions with CID treatment diluted to the very low concentration of $25 \text{ } \mu\text{g ml}^{-1}$ in chlorobenzene (CB) and *o*-xylene (OX) showed that the last aggregates dissolved only at about $80 \text{ }^\circ\text{C}$.

Furthermore, in the classical DSC measurements of dried samples, we observe a significant melting temperature shift in the first heating cycle, as evaluated in the main text. However, starting with the second heating cycle, the melting temperatures are almost identical (Figure S4). Therefore, the CID treatment significantly changes the interaction in the aggregates, resulting in the shift at the first heating cycle. Still, it does not significantly alter the chemical structure of the polymers, as the second heating shows almost no difference.

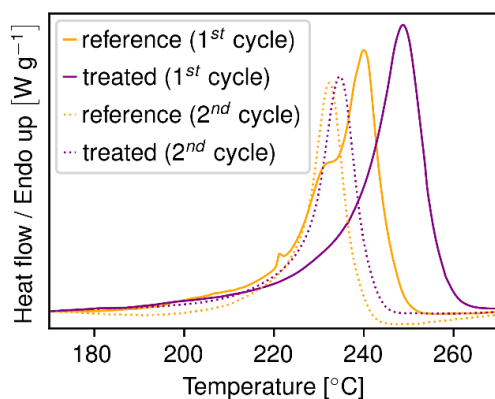


Figure S4. DSC data of the first two heating cycles of 12 mg ml^{-1} P3HT in CF vacuum-dried solutions with CID treatment (purple) and reference without treatment (orange). The solid

WILEY-VCH

lines are the data from the first heating cycle, while the dotted lines are from the second heating cycle. While the first heating cycle shows significant differences in melting behavior due to the CID treatment, the second heating cycle is almost identical for both samples.

Qualitative model

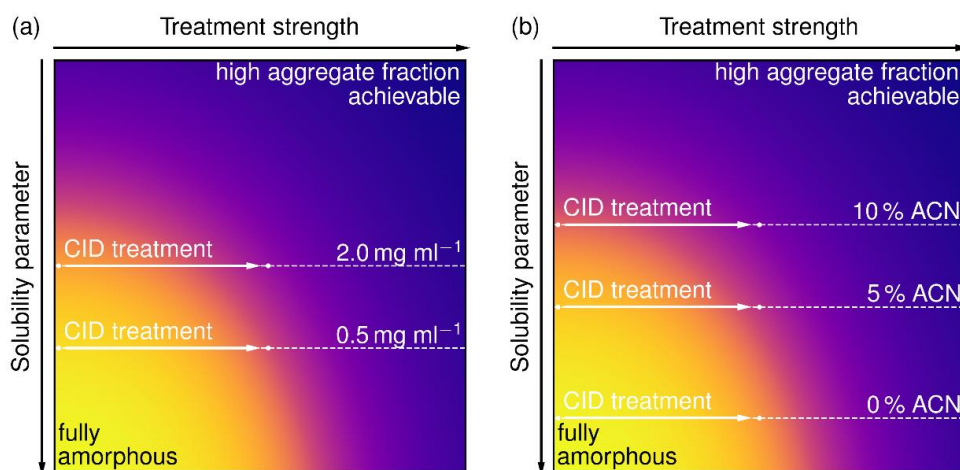


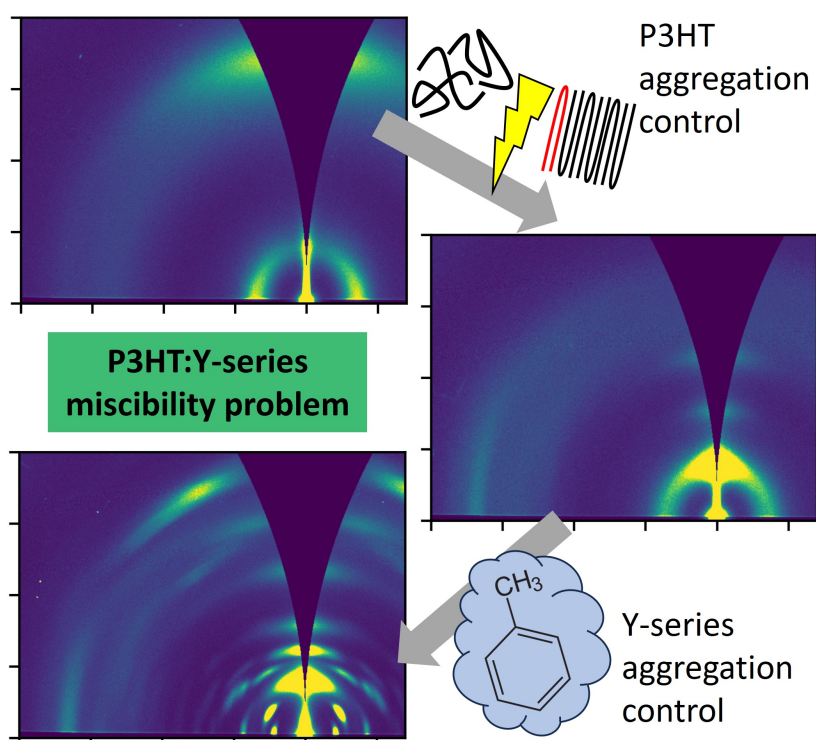
Figure S5. Sketch of a qualitative 2D parameter space map displaying the achievable aggregate fraction (plateau reached after sufficient treatment steps) color-coded from yellow (fully amorphous/no aggregation achievable) to purple (high aggregate fraction achievable) as a function of the treatment strength and a solubility parameter. Exemplary jumps for spark treatments are included: (a) P3HT in o-xylene (OX) solutions at 20 °C with the same treatment strength (3.3 μ F capacitor charged with 600 V) at different concentrations (0.5 mg ml⁻¹, 2.0 mg ml⁻¹; corresponding data in Figure S2 (a)-(b)), (b) P3HT in o-xylene:acetonitrile solutions at 50 °C with same treatment strength (3.3 μ F capacitor charged with 600 V) with different acetonitrile (ACN) content (0 %, 5 %, 10 %; corresponding data in Figure S2 (c)-(e)).

Photographs of solutions

Figure S6. Comparison of an untreated P3HT in CF solution (on the left) and a P3HT in CF solution with CID treatment (on the right).

- [1] C. Enengl, S. Enengl, S. Pluczyk, M. Havlicek, M. Lapkowski, H. Neugebauer, E. Ehrenfreund, *Chemphyschem : a European journal of chemical physics and physical chemistry* **2016**, *17*, 3836.
- [2] Y. Furukawa, *J. Phys. Chem.* **1996**, *100*, 15644.
- [3] J. Yamamoto, Y. Furukawa, *The journal of physical chemistry. B* **2015**, *119*, 4788.
- [4] F. Paquin, H. Yamagata, N. J. Hestand, M. Sakowicz, N. Bérubé, M. Côté, L. X. Reynolds, S. A. Haque, N. Stingelin, F. C. Spano et al., *Phys. Rev. B* **2013**, 88.
- [5] F. Panzer, H. Bäessler, R. Lohwasser, M. Thelakkat, A. Köhler, *The journal of physical chemistry letters* **2014**, *5*, 2742.
- [6] G. C. Vogel, R. S. Drago, *J. Chem. Educ.* **1996**, *73*, 701.

10 Tackling P3HT:Y-Series Miscibility Through Advanced Processing for Tunable Aggregation



Fabian Eller, Christopher R. McNeill, and Eva M. Herzig

Published in
Advanced Energy Materials **2024**, 14 (29), 2304455
(DOI: 10.1002/aenm.202304455)

Reprinted with permission according to the CC BY 4.0 license
Copyright 2024 The Authors. *Advanced Energy Materials* published by Wiley-VCH
GmbH



RESEARCH ARTICLE

ADVANCED
ENERGY
MATERIALS

www.advenegymat.de

Tackling P3HT:Y-Series Miscibility Through Advanced Processing for Tunable Aggregation

Fabian Eller, Christopher R. McNeill, and Eva M. Herzig*

Polymer and small molecule blend thin films are of strong interest for organic electronics and particularly organic solar cells. The high miscibility in blends of ordinary P3HT and state-of-the-art Y-series non-fullerene acceptors (NFAs) suppresses phase separation and aggregation challenging successful charge separation and transport. In a recent work, current-induced doping (CID) is introduced, a method to precisely control the aggregation of Poly(3-hexylthiophene) (P3HT) in solution. The highly ordered pre-aggregation in solution is used here to control the P3HT aggregation in neat films and blends with Y12 (BTP-4F-12). This results in a 25-fold increase in hole mobility in P3HT organic field-effect transistor (OFET) devices and tunability of the P3HT aggregate quality in the presence of Y12 over large ranges. At the same time, particularly the Y12 long-range ordering is heavily suppressed by increasing P3HT aggregation. However, solvent vapor annealing (SVA) leads to an extraordinarily high Y12 ordering, changes in the crystal orientation of Y12, and a further improvement of P3HT aggregation. A broad range of different degrees of aggregation of both materials can therefore be obtained in the final thin films solely by changing processing parameters without changing the composition of the material system.

attractive material.^[3–11] However, in recent years it received less attention due to inherently low OPV efficiencies with most Y-series NFAs.^[10,12,13] One reason is the lower open circuit voltage (V_{oc}) compared to, e.g., PM6 due to the higher HOMO of P3HT^[12,14,15] and the higher energetic disorder of the Y-series NFA in P3HT than in, e.g., PM6,^[16,17] but the detrimental problem is the high miscibility between P3HT and Y-series NFAs, which prevents the necessary phase separation for charge separation and transport.^[10,12,18] With ZY-4Cl a Y-series NFA was explicitly designed to reduce the miscibility with P3HT, enabling a PCE of $\approx 10\%$.^[11,18–20] Thus, chemical modification of NFAs is one possibility to achieve phase separation. Here we demonstrate that applying a new technique called current-induced doping (CID)^[21] to obtain high-quality P3HT aggregates in solution can improve the P3HT aggregation in dried thin films with and without a second component present and hence

causing an effective phase separation in an otherwise miscible material system.

During a CID treatment strong, electrical currents in the form of spark discharges between two tungsten electrodes immersed into the P3HT solution lead to a temporary doping of P3HT, which in turn results in aggregation. In our previous work, we demonstrated that the CID treatment allows unprecedented control over the aggregate fraction and quality of backbone ordering in solution.^[21] The number of treatment steps and the strength of the treatment are two parameters to control the aggregation in solution, which are directly related to the CID treatment. Moreover, the solvent as well as concentration, and especially the temperature during treatment play an important role.^[21]

We want to investigate the influence of the CID treatment on the film formation of neat P3HT and especially on blends with Y12, a highly miscible Y-series NFA with alkyl chains identical to ZY-4Cl. To control the aggregate fraction in the solution prior to casting the films, we varied the number of CID steps.

In the first part of this study, we examine aggregation control of neat P3HT films and the effect on organic field-effect transistor (OFET) devices. In the second part, we add untreated Y12 solution to CID-treated P3HT solution to blade-coat thin films and exploit solvent vapor annealing (SVA) to demonstrate tunable aggregation within both materials. Overall this approach only relies

1. Introduction

The introduction of Y-series non-fullerene acceptors (NFAs) like Y6, Y7, Y12, or others in the field of organic photovoltaics (OPV) led to a boost in power conversion efficiency (PCE) in combination with donor-acceptor copolymers like PM6.^[1,2] Historically P3HT played an important role in OPV research, due to its simple and cheap synthesis and its high stability, making it still an

F. Eller, E. M. Herzig
Dynamics and Structure Formation – Herzig Group
University of Bayreuth
Universitätsstraße 30, 95447 Bayreuth, Germany
E-mail: eva.herzig@uni-bayreuth.de

C. R. McNeill
Department of Materials Science and Engineering
Monash University
Wellington Road, Clayton, Victoria 3800, Australia

The ORCID identification number(s) for the author(s) of this article can be found under <https://doi.org/10.1002/aenm.202304455>

© 2024 The Authors. Advanced Energy Materials published by Wiley-VCH GmbH. This is an open access article under the terms of the [Creative Commons Attribution License](#), which permits use, distribution and reproduction in any medium, provided the original work is properly cited.

DOI: 10.1002/aenm.202304455

on processing parameters alone while conventional approaches to tune aggregation properties in thin films rely on the addition of extra components like high boiling point solvents,^[22–24] dopants,^[25–28] or changing solvents.^[29–35]

2. Results and Discussion

2.1. Increasing Backbone Planarity in neat P3HT Films using CID Treatment

Current-induced doping (CID) allows us to produce solutions with different aggregate fractions with highly ordered P3HT aggregates. Further aggregation will take place upon drying such a solution to obtain thin films.

In **Figure 1a** absorption spectra of dried neat P3HT films with an increasing number of CID treatment steps (yellow to purple) are displayed. A particularly strong spectral change can be seen between the dried P3HT film without CID treatment (yellow) and the film with 1 CID treatment step. Despite the small amount of highly ordered aggregates with 1 CID step before coating (aggregate fraction of only $\approx 8\%$ in **Figure 1c**), we observe a strongly increased A_1/A_2 ratio in the film (**Figure 1d**) accompanied by a redshift of the A_1 peak position (**Figure 1b**). These trends continue with an increasing number of CID steps finally reaching in the saturated regime an A_1/A_2 ratio of 0.85 and a peak position of 2.015 eV (redshift of 12 meV), which are both clear signs for a strong increase of backbone planarity.^[36–41]

In general, aggregation in drying thin films starts upon reaching a critical concentration.^[42] Examining the temporal evolution of the aggregate fraction for different CID treatment steps, allows us to investigate the effect of the presence of highly ordered aggregates in solution. The comparison of the slope of the temporal evolution of the aggregate fraction obtained from time-resolved in situ UV–vis spectroscopy during drying of blade coated thin films is therefore plotted without CID treatment and with 1 CID treatment step in **Figure 1e**. If no highly ordered aggregates are present (no CID treatment), the aggregation takes place within a well-defined, short time. The presence of highly ordered aggregates (with CID treatment) leads to a slow, systematic increase in aggregate fraction already in the wet film prior to the fast aggregation that occurs after reaching the critical concentration.

Combining the information from the temporal evolution with the strong increase of the backbone planarity from no solution treatment to a single CID step (**Figure 1d**) demonstrates that the aggregation process during drying is altered by the presence of the high-quality aggregates in solution, suggesting that these act as nuclei for further highly ordered aggregation.

Comparing grazing incidence wide angle X-ray scattering (GI-WAXS) cake cuts of a dry samples without CID treatment and a strong treatment of 45 CID steps in **Figure 1g–j** shows that the scattering intensity of the lamellar stacking peaks (100), (200), and (300) is strongly increased in the vertical (out of plane, OOP) direction, while the (100) peak in the horizontal (in plane, IP) direction is significantly reduced. Both aspects lead to a strongly increasing ratio between the (100) OOP to IP amplitudes from 60 to 420 (increase by a factor of 7), demonstrating an increasing edge-on character (**Figure S1**, Supporting Information). Moreover, mixed index peaks like the (11l) and (012) (peaks shown in **Figure 1h,j**) at ≈ 1.24 and 1.87 \AA^{-1} respectively) become more

prominent, which is a clear sign that aggregates are highly ordered in all three crystallographic directions.

Highly ordered aggregates with a highly planarized backbone and a strong edge-on character are ideal conditions for improving in-plane charge transport as required in OFET device geometries. Hole mobilities in the saturation regime of OFETs show this expected strong increase (**Figure 1f**, **Figure S3,S4**, Supporting Information). As in the UV–vis data, we also see here a particularly strong impact of the first CID step leading to an immediate, ten-fold increase of the mobility demonstrating the importance of the function of the highly ordered aggregates as nuclei for aggregation. Equally in accordance with the UV–vis data, a saturation in mobility sets in with a final mobility increase of a factor of 25 compared to no treatment. Applying thermal annealing does not alter the mobilities and repeated measurements after storage in the glovebox for five weeks do not show any significant changes in the mobilities (see **Figure S2**, Supporting Information).

Hence, we have demonstrated that applying CID treatment to P3HT solutions allows us to obtain highly ordered aggregates in edge-on configuration in blade-coated P3HT thin films with highly improved charge transport properties solely by changing processing conditions without changing solvents, composition, or usage of additives.

2.2. Deliberate Enhancement and Suppression of Aggregation Behavior in Blend Films

For energy materials not only neat films are of interest but also nanostructural control in blended systems. In OPV the domain sizes of the blended material and the nanostructure of the components within these domains are decisive for charge separation and transport. In the following, we show that using CID on P3HT solutions we particularly tune the aggregate properties of P3HT in the resulting blend thin film, while using solvent vapor annealing after coating we dominantly enhance the aggregation behavior of the small molecule acceptor.

2.2.1. Enhancing P3HT Aggregation in as Cast Blend Thin Films Using CID Treatment

First, we examine the highly miscible blend of P3HT and the NFA Y12. Without any CID treatment, the UV–vis spectrum of the dried thin film is dominated by a very broad absorption peak $\approx 2.4 \text{ eV}$ (red data in **Figure 2a**). In this peak, no vibronic shoulders are discernible, which is in contrast to the separated vibronic shoulders observed for neat P3HT (**Figure 1a**) or also in blends with many other acceptors (e.g., EH-IDTBR in **Figure S5**, Supporting Information). The addition of Y12 to P3HT therefore results in an increased energetic disorder, broadening the single peaks in the vibronic structure to an extent that these are no longer discernible. The behavior of the Y12 in the identical drying process in the low energy range of the in situ spectra in **Figure 2a** shows a clearly blueshifted absorption maximum in comparison to PM6:Y12 blends, and an even stronger blueshift for neat Y12 (see **Figure S6**, Supporting Information). This indicates an increased disorder not only for P3HT but also of the Y12 in the P3HT:Y12 blend, confirming the miscibility of the two materials.

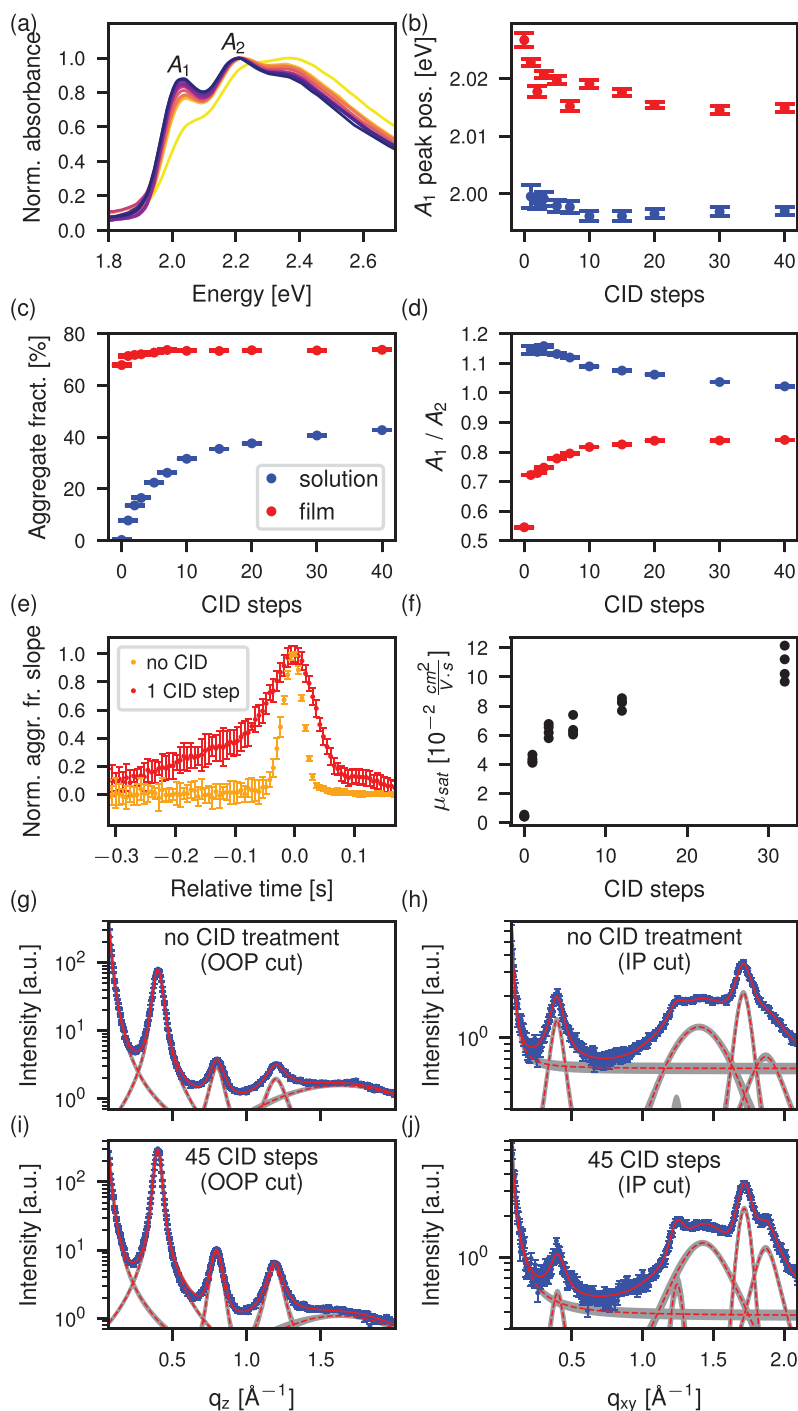


Figure 1. a) Normalized UV-vis absorption spectra of dry P3HT with an increasing number of CID steps (from yellow (untreated) to purple (45 CID steps)). b-d) Results of fitting the vibronic structure in the dry film spectra (red) from a) and the respective solution spectra (blue) before drying: b) A₁ peaks position, c) minimum aggregate fraction, and d) ratio between peak amplitudes of the A₁ to A₂ peak. e) Normalized slope of the temporal evolution of the aggregate fraction during drying without CID treatment and with 1 CID step. f) Hole mobility in the saturation regime of bottom-contact bottom-gate field effect transistors. g-j) Vertical (OOP) and horizontal (IP) cake cuts (blue) with fits (red) and 1σ confidence intervals (grey) of P3HT g), h) without CID treatment and i), j) with 45 CID steps.

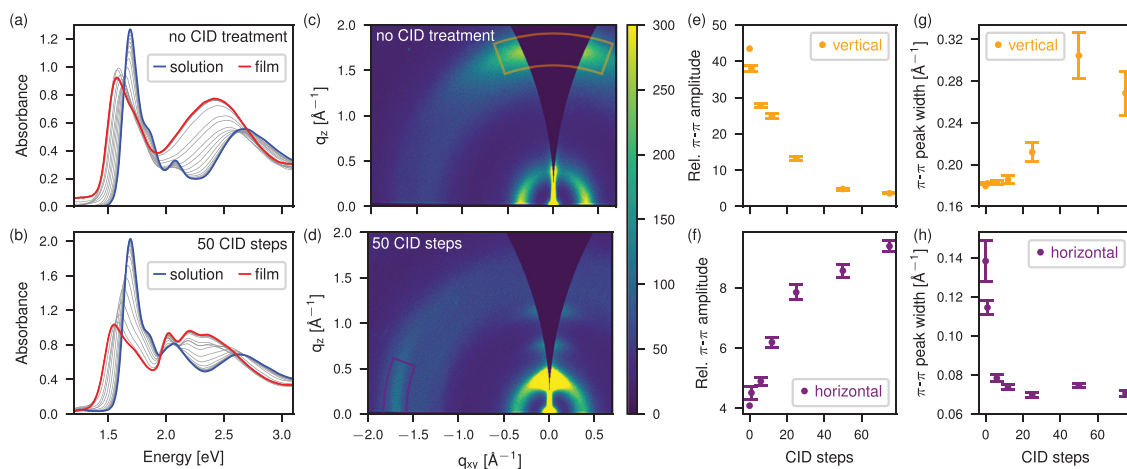


Figure 2. In situ UV-vis absorption spectra during the drying of 16.5 mg mL^{-1} P3HT:Y12 solutions: a) without CID treatment and b) with 50 CID steps. c), d) 2D GIWAXS data of P3HT:Y12 films: c) without CID treatment and d) with 50 CID steps. e–h) π - π amplitudes relative to the disordered ring at $\approx 1.4 \text{ \AA}^{-1}$ and π - π peak widths from fitting vertical and horizontal cake cuts.

For increasing numbers of CID steps **Figure 3d** shows a stronger suppression of the overall Y12 oscillator strength. This can be explained by a reduction of the in-plane orientation of the Y12 transition dipole moments since we are probing with light of normal incidence which couples to the in-plane components of the transition dipole moments. The loss of in-plane orientation

of Y12 is linked to the loss of face-on orientation as shown in GIWAXS measurements in **Figure 2c,d**, and discussed below. At the same time, the CID treatment induces a very clear P3HT vibronic structure within the final film (**Figure 2b**). The vibronic structure is already present in the solution before drying (blue curve in **Figure 2b** and Eller et. al.^[21]), but due to the superposition of a

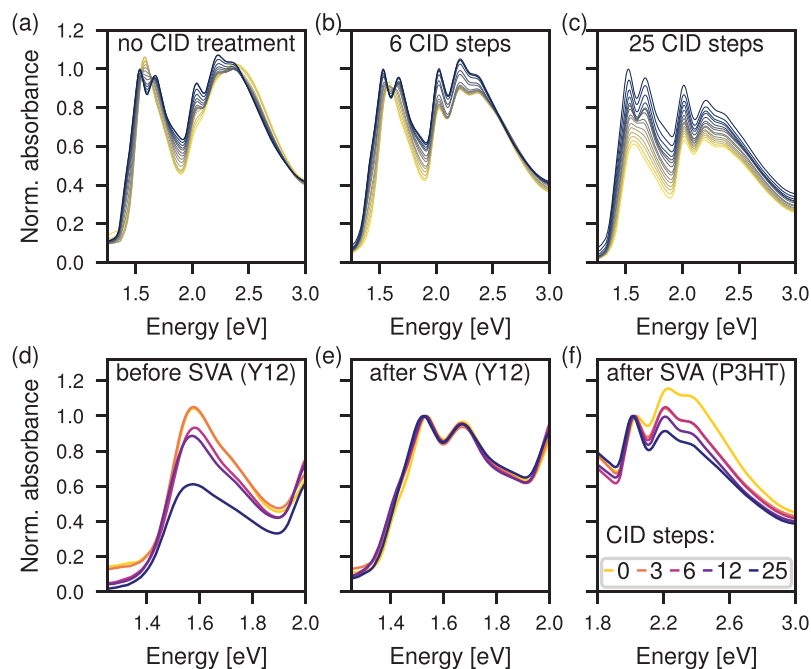


Figure 3. In situ UV-vis absorption spectra of P3HT:Y12 films: a) without CID treatment, b) with 6 CID steps, c) with 25 CID steps during SVA in a saturated toluene atmosphere (yellow before SVA, black after SVA). d–f) Comparison of absorption spectra with different numbers of CID steps: d) before SVA and e), f) after SVA. The spectra in a)–e) are normalized to the Y12 peak absorbance at the end of the SVA, while in f) the spectra are normalized to the P3HT A_1 peak after SVA.

Y12 peak at ≈ 2.1 eV, no separation of the A_1 and A_2 vibronic peak is discernible. During drying further highly ordered aggregation of P3HT occurs, probably due to nucleation at the highly ordered aggregates from the CID treatment in solution (see temporal evolution of the P3HT absorbance change in Figure S7, Supporting Information).

For the discussion of the nanostructure in the examined thin films we differentiate between short- and long-range order. With UV-vis spectroscopy we probe interactions between chromophores and therefore access information on short-range interactions. Using GIWAXS we exploit interference effects of X-rays reradiated by the electrons of the molecular units in a particular arrangement. In analogy to a diffraction grating, we obtain information on the degree of structural order beyond neighboring molecular elements, hence on the long-range ordering within the film. The weak short-range ordering of P3HT in P3HT:Y12 blends without CID treatment implies no significant long-range ordering of P3HT. This conclusion is confirmed by the GIWAXS measurement in Figure 2c, which lacks clear scattering signals of long-range ordered P3HT. The relatively strong π - π peak in the vertical (marked by orange wedge) and the scattering signal ≈ 0.35 \AA^{-1} is typical for Y12 in polymer-Y12 blends (for reference Figure S8 (Supporting Information) GIWAXS measurements of neat Y12 and PM6:Y12). However, the peak widths of both these signals are larger than in a comparable PM6:Y12 blend (see Figure S8, Supporting Information) and no onset of the nanostructure scattering of the (110) and (011) Y12 peaks (corresponding crystal structure see 2.2.2) is detected, implying that the long-range ordering of Y12 is also reduced.

A strong ordering of P3HT, however, can now be induced in the dry blend film by CID treatment. GIWAXS data of samples with strong CID treatment (Figure 2d; Figure S9, Supporting Information) show that the P3HT signal dominates the scattering pattern. The P3HT lamellar peaks (100), (200), and (300) in the vertical and the π - π stacking in the horizontal (marked by purple wedge) are observed, while no discernible scattering of the Y12 nanostructure and its π - π peak is detected anymore. It appears that the P3HT solution pre-aggregation due to the CID treatment, followed by P3HT aggregation during drying, enables P3HT long-range ordering, but hinders at the same time the formation of Y12 long-range ordering (even more than without CID treatment). To track the rise of the P3HT and the decay of the Y12 long-range ordering, the π - π peak amplitudes (relative to the disordered ring at ≈ 1.4 \AA^{-1}) and the peak widths of the π - π peaks in the vertical (OOP) and horizontal (IP) respectively are displayed in Figure 2e-h. Supported by the orientation of the neat materials, we attribute the OOP π - π peak to dominantly Y12 and the IP π - π peak to dominantly P3HT (see Figure S8, Supporting Information). The relative π - π amplitude of Y12 decays by a factor of ≈ 10 until it saturates at a low level, which may also partially stem from face-on oriented P3HT. The peak width slowly increases at low numbers of CID steps until a more drastic increase of the peak width indicates a highly disordered π - π structure of the Y12. The P3HT π - π stacking amplitude increases rapidly at low CID treatment steps and then increases more slowly, while the P3HT π - π peak width drops rapidly to a nearly constant level indicating a strongly increased long-range order of P3HT with CID treatment in the π - π stacking direction.

Furthermore, RSoXS (Resonant Soft X-ray Scattering) measurements in Figure S10 (Supporting Information) show an overall increase in scattering intensities with an increasing number of CID steps. This is consistent with an increase in domain purity. However, a more detailed interpretation is challenging since film thickness and roughness need also to be considered.

Overall, we have shown that drying CID-treated solutions allows us to systematically tune the P3HT aggregation in thin films as a function of the number of CID steps while suppressing Y12 structure formation.

2.2.2. Enhancing Small Molecule Acceptor Aggregation Using Solvent Vapor Annealing on Dry Blend Thin Films

For structural control of nanomorphology in a blended system, both components need to be accessible for tuning. We have shown that the CID treatment can control the aggregation behavior of P3HT. We therefore aim to address the small molecule acceptor using post-treatments. We tested the two most common post-processing techniques thermal annealing (TA) and solvent vapor annealing (SVA). Since the Y12 structure formation with CID treatment is heavily suppressed during drying, we need to ensure successful nucleation of Y12 in subsequent processing. Therefore, we choose a two-step TA approach, where a first short (5 min) annealing step at 90 °C (close to the transition temperature of Y12) should increase Y12 nucleation and a second longer (10 min) annealing step at 120 °C should enhance larger-scale aggregation.^[43] Even though the Y12 absorption peak is redshifted to 1.508 eV (for comparison PM6:Y12 with the same treatment 1.512 eV), GIWAXS does not reveal a significant increase in long-range ordering (see Figure S11, Supporting Information). Mainly the P3HT contributions in the GIWAXS measurement shows a longer range of ordering by significantly decreased peak widths and increased peak amplitudes after TA.

We conducted SVA in a saturated toluene environment and tracked the UV-vis absorption during the SVA in situ, as it is displayed for different numbers of CID treatment steps in Figure 3a-c. We stopped the SVA treatment after 5 min for each sample when no more changes were detectable in the UV-vis spectra. The CID treatment and SVA strongly influence the Y12 aggregation behavior.

After SVA the reduced Y12 absorption observed after drying recovers and the absorption peaks are clearly separated. We associate these two peaks with the two aggregate species (aggregate I at lower and aggregate II at higher energy) identified in similar material systems (Y6 and N4 as NFAs differing only in alkyl sidechains) by Kroh et al.^[44] We observe an increased order of Y12 after SVA obtained from the observed redshift of aggregate I and the reduction in peak width (see evolution during SVA in Figure 3a-c; values before and after SVA in Table S1, Supporting Information). Furthermore, we observe that there is no strong dependency on the number of CID treatment steps (Figure 3e, merely a slight increase of peak width in Table S1, Supporting Information), although the nanomorphology of the individual films prior to SVA is different. Thus, the Y12 absorption after SVA suggests, that Y12 strongly gains in ordering and in-plane orientation of the transition dipole moments upon SVA.

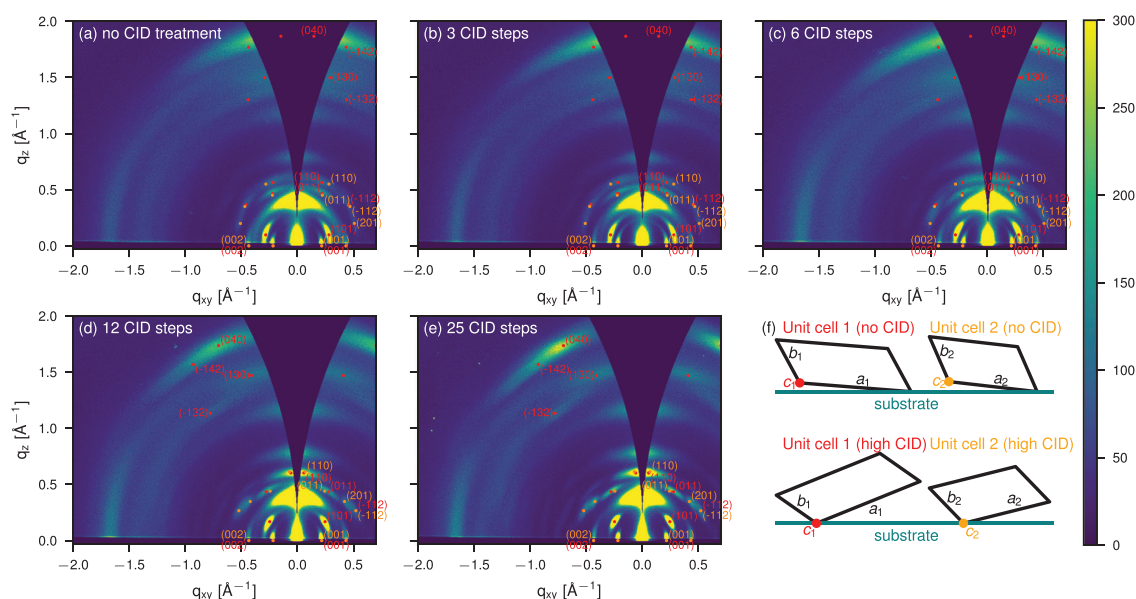


Figure 4. 2D GIWAXS data of P3HT:Y12: a) without CID treatment, b) with 3, c) 6, d) 12, and e) 25 CID steps all post-treated with SVA in a saturated toluene atmosphere. The lattice parameters of the Y12 unit cell 1 (peaks indexed in red) are $a_1 = 36.5 \text{ \AA}$, $b_1 = 16 \text{ \AA}$, $c_1 = 29 \text{ \AA}$, $\alpha_1 = 90^\circ$, $\beta_1 = 90^\circ$, $\gamma_1 = 123^\circ$, and the lattice parameters of the Y12 unit cell 2 (peaks indexed in orange) are $a_2 = 29 \text{ \AA}$, $b_2 = 16 \text{ \AA}$, $c_2 = 29 \text{ \AA}$, $\alpha_2 = 90^\circ$, $\beta_2 = 90^\circ$, $\gamma_2 = 120^\circ$. f) Sketch of side view of the two unit cells used for indexing showing the rotation around the c -axis. For up to 6 CID steps this is $\approx 4.5^\circ$ for unit cell 1 and $\approx 6.5^\circ$ for unit cell 2 (top row). From 12 CID steps onward the rotation around the c -axis is $\approx -22^\circ$ for unit cell 1 and $\approx -14^\circ$ for unit cell 2 (bottom row).

Examining the behavior of P3HT upon SVA, we see that especially without CID treatment an increase in P3HT ordering is apparent due to the increase of well-defined vibronic peaks in the UV–vis data (Figure 3a). The already well-defined vibronic structure due to the CID treatment in Figure 3b,c with 6 and 25 CID steps is further enhanced by the SVA annealing evident in the increase of the A_1/A_2 ratio. This control of P3HT backbone planarity due to the combination of CID treatment and SVA is particularly well observable when comparing the spectra after SVA normalized to the A_1 peak in Figure 3f.

Examining the long-range order of Y12 after SVA using GIWAXS (Figure 4, larger representation in Figures S12 and S13, Supporting Information) clearly demonstrates an increase for all starting conditions in line with the increase in short-range Y12 ordering as observed by UV–vis. All GIWAXS measurements show a rich Y12 nanostructure with low peak width in the radial direction (see Figure S14, Supporting Information, at a higher sample-to-detector distance with smaller footprint broadening). These observations allow the conclusion that the Y12, which was previously in a highly disordered intermixed phase, now forms domains with high purity consisting of highly ordered 3D nanostructures. While the peaks along q_{xy} without q_z -component ((001), (002), and (003)) are unchanged upon CID treatment, an increased number of CID steps leads to an azimuthal rotation of the remaining peaks without changes in the magnitude of q . To index all dominant peaks, two unit cells are required. Two unit cells also properly explain the observed (110) double peak at higher numbers of CID treatment steps (more details in Figure S15, Supporting Information). Optimizing the lattice parameters of both unit cells allows us to index all dominant Y12 peaks (Figure 4).

It is possible to model the 2D GIWAXS data with any number of CID treatment steps with the identical two unit cells (marked red and orange in Figure 4 respectively), just by varying the rotational angle of the unit cells around the horizontal c -axis (thus varying the tilt of the crystal structures with respect to the substrate). Observing an unchanged unit cell structure for all SVA-treated films implies also no changes in the intermolecular arrangements in accordance with the nearly identical spectra obtained from UV–vis spectroscopy (Figure 3e). The optimized lattice parameters are $a_1 = 36.5 \text{ \AA}$, $b_1 = 16 \text{ \AA}$, $c_1 = 29 \text{ \AA}$, $\alpha_1 = 90^\circ$, $\beta_1 = 90^\circ$, $\gamma_1 = 123^\circ$ for unit cell 1 and $a_2 = 29 \text{ \AA}$, $b_2 = 16 \text{ \AA}$, $c_2 = 29 \text{ \AA}$, $\alpha_2 = 90^\circ$, $\beta_2 = 90^\circ$, $\gamma_2 = 120^\circ$ for unit cell 2.

Since all peaks in the measurements extend over a significant azimuthal range the values of rotations extracted for the two unit cells marked with the dots in the 2D images represent the dominant orientation but occur over a broader range of unit cell rotations. Initially, for no and up to 6 CID steps, the rotation around the c -axis is $\approx 4.5^\circ$ for unit cell 1 and $\approx 6.5^\circ$ for unit cell 2. From 12 CID steps onward the rotation around the c -axis is $\approx -22^\circ$ for unit cell 1 and $\approx -14^\circ$ for unit cell 2 (shown in Figure 4f). While the sample with 6 CID steps is similar to the two data sets in Figure 4a,b, i.e., dominated by unit cells that are weakly rotated, it also contains scattering intensities of the more strongly rotated unit cells observed for the higher numbers of CID steps (Figure 4d,e). In Tables S2 and S3 (Supporting Information) the values for q_{xy} , q_z , and q of all indexed peaks are displayed.

P3HT also responds to the SVA treatment with long-range ordering probed by GIWAXS. This response is particularly strong when there is no prior CID treatment, where significant edge-on aggregates are present after SVA (Figure 4a) in comparison

to no signature of aggregation of P3HT prior to SVA (Figure 2c). For the CID treated samples, a further improvement of the pre-existing P3HT aggregation occurs during SVA (direct comparison in Figure S16, Supporting Information) but keeping the increasing strength of long-range order as a function of CID treatment steps.

Overall, the SVA treatment dominantly addresses an improved ordering of the Y12 on the nanoscale with no negative impact on P3HT aggregation. We therefore have demonstrated that independent of the pre-condition of the P3HT matrix the Y12 can be strongly aggregated resulting in high-quality aggregates by application of SVA.

3. Conclusion

We have successfully demonstrated the opportunity of CID treatments on P3HT solutions for nanostructural control in thin films. We observe that the high tunability within the solution transfers to the neat thin films of P3HT leading to a 25-fold increase in OFET hole mobility. It is especially remarkable that already the first CID treatment step is sufficient to achieve a tenfold increase demonstrating the great importance of the highly ordered aggregates produced by the CID treatment as nuclei for further aggregation.

Furthermore, we can use the CID treatment in combination with SVA to demonstrate unprecedented control over the aggregation behavior in the P3HT:Y12 blend. Using these processing approaches we can produce from the same solvent, without changing the composition or using additives, final films that are either highly disordered, show only order in the Y12 or P3HT alone, and also on the contrary highly ordered Y12 with different orientations of Y12 and different degree of order in P3HT. Moreover, our in situ UV-vis measurements during SVA suggest, that an intermediate range of Y12 ordering may be accessible by reducing the SVA time. This specific, almost separate control over the P3HT and Y12 ordering can be highly valuable for fundamental research. While transferring the mechanism of inducing aggregation via CID treatment to other polymeric materials is challenging, the choice of the NFA or additional components can be widely varied, since these materials are added after the CID treatment. Therefore, potential fundamental studies can include but are not limited to studies on charge transport, electron and hole mobility, energy levels, solar cell properties, stability, and trap densities all as a function of, e.g., the degree of aggregation or depending on crystal orientation. We are therefore convinced that CID-treated thin films will be helpful for further understanding and optimizing energy materials.

4. Experimental Section

Materials: P3HT with a regioregularity of 96% was purchased from Rieke Metals, Y12, PM6, and EH-IDTBR from Brilliant Matters, PEDOT:PSS (poly(3,4-ethylenedioxythiophene) polystyrene sulfonate) from Heraeus, chloroform from Sigma-Aldrich and toluene from VWR Chemicals. All materials were used as received.

CID Treatment: Since this work is interested to exploit highly ordered aggregates, chloroform as solvent was chosen at a temperature of 20 °C with a voltage of 300 V for charging the capacitor, which yielded the highest aggregate quality in this extensive previous study.^[21] The untreated P3HT

solutions were prepared by dissolving P3HT in chloroform at 50 °C for 20 min. Prior to the CID treatment, the solutions were kept for 15 min at 20 °C to allow for proper equilibration. This temperature was also kept constant throughout the complete CID treatment. A capacitor (WIMA MKS 4, 3.3 μF) was charged to 300 V and subsequently connected to two tungsten wires separated by several millimeters and immersed into the P3HT solution. These two tungsten wires were then approached until a spark discharge occurred below a separation of 1 mm. This procedure of charging the capacitor, connecting, and approaching the tungsten wires was repeated until the desired number of CID treatment steps was achieved.^[21]

Sample Preparation: The glass and silicon substrates were cut to the desired size and then thoroughly cleaned by sonication in Alconox, VE-water, and isopropanol for 10 min each. To ensure a comparable surface all samples were spin-coated with sonicated PEDOT:PSS at 3000 rpm. The neat P3HT samples were coated from 12 mg mL⁻¹ P3HT solutions treated with the given number of CID steps. For the P3HT:Y12 blends also 12 mg mL⁻¹ P3HT solutions treated with the given number of CID steps were used and subsequently blended with 24 mg mL⁻¹ Y12 solutions (without CID treatment) with a volume ratio of 5:3. Thus, the resulting mixing ratio of Y12 to P3HT was 1.2:1 and the concentration 16.5 mg mL⁻¹. All samples were coated with a home-built blade-coating setup at a coating speed of 10 mm s⁻¹. During every drying process on glass substrates the UV-vis absorption was tracked in situ.^[45]

UV-Vis Absorption Spectroscopy: A combined deuterium and halogen white light source from Ocean Optics and an AvaSpec-HSC1024 × 58 TEC-EVO spectrometer from Avantes were used to acquire the in situ UV-vis spectra of the neat P3HT samples during drying. For the in situ drying measurements of the blend samples and the in situ SVA measurements, an AvaLight-HAL-S-Mini2 halogen white light source and an AvaSpec-ULS2048CL-EVO-RS-UA spectrometer (both from Avantes) were used. Amorphous P3HT spectra measured at the same concentration and temperature were scaled to the high-energy shoulder of the neat P3HT absorption spectra at ≥2.6 eV.^[46,47] This rescaled amorphous spectrum was subsequently subtracted from the neat P3HT absorption spectrum, which was then fitted by the sum of five equidistant (distance of 0.17 eV between peaks) Gaussian peaks for the A₁ to A₅ peaks.^[46,47] While an identical peak width was fitted for the A₂ to A₅ peaks, a smaller peak width was fitted for the A₁ peak.^[48,49] The minimum aggregate fraction was calculated using the area below the fits and below the rescaled amorphous spectrum considering the different molar extinction coefficients of the amorphous and aggregated P3HT described by Clark et al.^[46] This procedure yields an estimate for the minimum aggregate fraction as higher optical transitions of the aggregate could contribute to the high energy shoulder leading to an overestimation of the amorphous absorption.

The in situ absorption data showing the transition from liquid to solid film or the effect of SVA was chosen to display well the occurring changes and were not necessarily equidistant in time. To determine the slope of the aggregate fraction the difference of data points 30 ms apart is considered.

GIWAXS: Grazing incidence wide-angle X-ray scattering (GIWAXS) was performed on a laboratory system at the University of Bayreuth (Xeuus 3.0, Xenocs SAS, Grenoble, France) with a Cu Kα source (λ = 1.54 Å), a Dectris EIGER 2R 1 m detector, and a sample-to-detector distance of 72 mm (and 200 mm for the measurements in Figures S14 and S15, Supporting Information) and a beam size of 500 μm. The presented 2D data were wedge-corrected scattering images with solid angle correction. Scattering experiments were carried out at room temperature under vacuum on samples on PEDOT:PSS coated silicon substrates with a length of 5 mm in beam direction. The incident angle was set to 0.18° (above the critical angle of ≈0.16°), which probes the full depth of the films. The presented q-profiles were cake cuts covering an azimuthal angle of 70°–110° for the cuts in the vertical direction and 0–20° as well as 160°–180° for the cuts in the horizontal direction.

All fits to the cuts of the GIWAXS data were Pseudo-Voigt fits, described by the following expression for a single peak:

$$f(q) = A \cdot [\eta \cdot L(q) + (1 - \eta) \cdot G(q)] \text{ with } 0 < \eta < 1 \quad (1)$$

$$G(q) = \exp\left[-\ln(2) \cdot \left(\frac{q-c}{b}\right)^2\right], L(q) = \frac{1}{1 + \left(\frac{q-c}{b}\right)^2} \quad (2)$$

where A is the peak amplitude, c is the peak position, $2b$ is the full width at half maximum (the obtained values for the peak width were the values of b) of the Pseudo-Voigt peak, and η the Pseudo-Voigt mixing parameter. To fit the superposition of various peaks, the sum of several Pseudo-Voigt peaks was fitted for both directions. Moreover, an additional background was fitted. It consists of a q^{-4} decay in the horizontal direction and a q^{-5} decay in the vertical direction with an additional q^{-2} decay and an offset in both directions.

To index the data a self-written Python program was used to calculate and superimpose the various peak positions on the original data. The program allows the rotation around individual crystal axes. In plane isotropy is assumed.

OFET-Device Fabrication and Characterization: Substrates for organic field-effect transistors with a bottom-gate bottom-contact (BGBC) geometry were purchased from Fraunhofer IPMS Dresden (OFET Gen. 4). Substrate and gate-electrode consisted of heavily n-doped silicon, while 230 nm of thermally grown silicon oxide was the gate dielectric ($C = 1.5 \times 10^{-8} \text{ F cm}^{-2}$). Interdigitated electrodes were patterned from gold (30 nm) and used as source- and drain-contacts, the used channel-widths were 20 μm . The substrates were thoroughly cleaned by sonication in isopropanol and acetone for 10 min each and the P3HT was deposited in the same way as the other films. No silanization or other surface treatment was used. Afterward, the devices were transferred into a nitrogen-filled glovebox and the transistor characteristics were measured using the Agilent Technologies B1500A Semiconductor Device Analyzer. The mobilities were extracted from the slope of the $I_D^{0.5}$ versus V_G -plots in the saturation regime, using:

$$I_D = \frac{W}{2L} \cdot \mu \cdot C \cdot (V_G - V_{Th})^2 \quad (3)$$

where I_D is the drain current, W the channel width, L the channel length, C the capacitance per unit area μ_{sat} the charge carrier mobility, V_G the gate voltage and V_{Th} the threshold voltage.^[38]

RSoXS: Resonant Soft X-ray scattering (RSoXS) measurements were collected at the Spectroscopy Soft and Tender (SST-1) beamline at the National Synchrotron Light Source II.^[50]

Measurements were carried out in vacuum with the incident beam normal to the substrate passing through the silicon nitride window prior to passing through the sample. Two-dimensional scattering patterns were recorded on a charge-coupled device (CCD) detector sensitive to soft X-rays (greateyes GmbH) at a sample-to-detector distance of 35 mm and a photon energy of 285.4 eV.

Supporting Information

Supporting Information is available from the Wiley Online Library or from the author.

Acknowledgements

F.E. and E.M.H. thank the Deutsche Forschungsgemeinschaft (DFG Research Unit FOR 5387 POPULAR, Project No. 461909888 and Project INST 91/443-1) for their support. This work was also supported by a Senior Research Fellowship (CRM) from the University of Bayreuth Centre of International Excellence "Alexander von Humboldt". The authors are grateful to Florian Meichsner (Macromolecular Chemistry, University of Bayreuth) for the introduction and support with the OFET measurements and analysis and to Eliot Gann (Brookhaven National Laboratory) and Priyanka M. Ketkar (National Institute of Standards and Technology) for help with the RSoXS measurements. This research used the Spectroscopy Soft and Tender (SST-1) beamline of the National Synchrotron Light Source II, a U.S.

Department of Energy (DOE) Office of Science User Facility operated for the DOE Office of Science by Brookhaven National Laboratory under Contract No. DE-SC0012704.

Open access funding enabled and organized by Projekt DEAL.

Conflict of Interest

The authors declare no conflict of interest.

Data Availability Statement

The data that support the findings of this study are available from the corresponding author upon reasonable request.

Keywords

current induced doping, GIWAXS, morphology, nanostructure, NFA, solvent vapor annealing, UV-vis spectroscopy

Received: December 22, 2023

Revised: March 29, 2024

Published online:

- [1] Q. He, P. Ufimkin, F. Aniés, X. Hu, P. Kafourou, M. Rimmle, C. L. Rapley, B. Ding, *SusMat* **2022**, 2, 591.
- [2] B. Lu, J. Wang, Z. Zhang, J. Wang, X. Yuan, Y. Ding, Y. Wang, Y. Yao, *Nano Select* **2021**, 2, 2029.
- [3] J. H. Bannock, S. H. Krishnadasan, A. M. Nightingale, C. P. Yau, K. Khaw, D. Burkitt, J. J. M. Halls, M. Heeney, J. C. de Mello, *Adv Funct Mater* **2013**, 23, 2123.
- [4] D. Baran, R. S. Ashraf, D. A. Hanifi, M. Abdelsamie, N. Gasparini, J. A. Röhr, S. Holliday, A. Wadsworth, S. Lockett, M. Neophytou, C. J. Emmott, J. Nelson, C. J. Brabec, A. Amassian, A. Salleo, T. Kirchartz, J. R. Durrant, I. McCulloch, *Nature Mater* **2017**, 16, 363.
- [5] N. Chander, S. Singh, S. S. K. Iyer, *Sol. Energy Mater. Sol. Cells* **2017**, 161, 407.
- [6] M. Du, Y. Xiao, Y. Geng, Y. Chen, H. Jiang, C. Dong, Q. Guo, Q. Guo, G. Li, E. Zhou, *J. Mater. Chem. C* **2022**, 10, 10114.
- [7] S. Holliday, R. S. Ashraf, A. Wadsworth, D. Baran, S. A. Yousaf, C. B. Nielsen, C.-H. Tan, S. D. Dimitrov, Z. Shang, N. Gasparini, M. Alamoudi, F. Laquai, C. J. Brabec, A. Salleo, J. R. Durrant, I. McCulloch, *Nat. Commun.* **2016**, 7, 11585.
- [8] M. Manceau, S. Chambon, A. Rivaton, J.-L. Gardette, S. Guillerez, N. Lemaître, *Sol. Energy Mater. Sol. Cells* **2010**, 94, 1572.
- [9] K. Tremel, S. Ludwigs, *P3HT Revisited – From Molecular Scale to Solar Cell Devices*, Springer, Berlin **2014**, 265, 39.
- [10] J. Xiao, X. Jia, C. Duan, F. Huang, H.-L. Yip, Y. Cao, *Adv. Mater.* **2021**, 33, 2008158.
- [11] C. Yang, S. Zhang, J. Ren, M. Gao, P. Bi, L. Ye, J. Hou, *Energy Environ. Sci.* **2020**, 13, 2864.
- [12] B. Chang, C.-H. Chen, T.-F. Hsueh, S. Tan, Y.-C. Lin, Y. Zhao, B.-S. Tsai, T.-Y. Chu, Y.-N. Chang, C.-E. Tsai, C.-S. Chen, K.-W. Wei, *ACS Appl. Mater. Interfaces* **2023**, 15, 52651.
- [13] H. Tarikhum B, F. Almyahi, B. Ali, *Karbala Int. J. Mod. Sci.* **2023**, 9.
- [14] J. Bertrandie, J. Han, C. S. P. de Castro, E. Yengel, J. Gorenflot, T. Anthopoulos, F. Laquai, A. Sharma, D. Baran, *Adv. Mater.* **2022**, 34, 2202575.
- [15] B. Yang, Y. Yuan, P. Sharma, S. Poddar, R. Korlacki, S. Ducharme, A. Gruverman, R. Saraf, J. Huang, *Adv. Mater.* **2012**, 24, 1455.

- [16] C. Wöpke, C. Göhler, M. Saladina, X. Du, L. Nian, C. Greve, C. Zhu, K. M. Yallum, Y. J. Hofstetter, D. Becker-Koch, N. Li, T. Heumüller, I. Milekhin, D. R. T. Zahn, C. J. Brabec, N. Banerji, Y. Vaynzof, E. M. Herzig, R. C. I. MacKenzie, C. Deibel, *Nat. Commun.* **2022**, *13*, 3786.
- [17] L. Perdigón-Toro, Q. Le Phuong, F. Eller, G. Freychet, E. Saglamkaya, J. I. Khan, Q. Wei, S. Zeiske, D. Kroh, S. Wedler, A. Köhler, A. Armin, F. Laquai, E. M. Herzig, Y. Zou, S. Shoaee, D. Neher, *Adv. Energy Mater.* **2022**, *12*, 2103422.
- [18] M. Gao, Y. Liu, K. Xian, Z. Peng, K. Zhou, J. Liu, S. Li, F. Xie, W. Zhao, J. Zhang, X. Jiao, Xuechen, L. Ye, *Aggregate* **2022**, *3*, e190.
- [19] C. Yang, R. Yu, C. Liu, H. Li, S. Zhang, J. Hou, *ChemSusChem* **2021**, *14*, 3607.
- [20] C. Yang, S. Zhang, J. Hou, *Aggregate* **2022**, *3*, e111.
- [21] F. Eller, F. A. Wenzel, R. Hildner, R. W. A. Havenith, E. M. Herzig, *Small* **2023**, *19*, e2207537.
- [22] L. Di Mario, D. Garcia Romero, M. J. Pieters, F. Eller, C. Zhu, G. Bongiovanni, E. M. Herzig, A. Mura, M. A. Loi, *J. Mater. Chem.* **2023**, *11*, 2419.
- [23] S. M. Hosseini, N. Tokmoldin, Y. W. Lee, Y. Zou, H. Y. Woo, D. Neher, S. Shoaee, *Sol. RRL* **2020**, *4*, 2000498.
- [24] W. Wang, L. Song, D. Magerl, D. Moseguí González, V. Körstgens, M. Philipp, J.-F. Moulin, P. Müller-Buschbaum, *Adv. Funct. Mater.* **2018**, *28*, 1800209.
- [25] J. Gao, J. D. Roehling, Y. Li, H. Guo, A. J. Moulé, J. K. Grey, *J. Mater. Chem. C* **2013**, *1*, 5638.
- [26] I. E. Jacobs, E. W. Aasen, J. L. Oliveira, T. N. Fonseca, J. D. Roehling, J. Li, G. Zhang, M. P. Augustine, M. Mascal, A. J. Moulé, *J. Mater. Chem. C* **2016**, *4*, 3454.
- [27] I. E. Jacobs, C. Cendra, T. F. Harrelson, Z. I. Bedolla Valdez, R. Faller, A. Salleo, A. J. Moulé, *Mater. Horiz.* **2018**, *5*, 655.
- [28] L. Müller, D. Nanova, T. Glaser, S. Beck, A. Pucci, A. K. Kast, R. R. Schröder, E. Mankel, P. Pingel, D. Neher, W. Kowalsky, R. Lovrincic, *Chem. Mater.* **2016**, *28*, 4432.
- [29] S. Guo, W. Wang, E. M. Herzig, A. Naumann, G. Tainter, J. Perlich, P. Müller-Buschbaum, *ACS Appl. Mater. Interfaces* **2017**, *9*, 3740.
- [30] S. Dong, T. Jia, K. Zhang, J. Jing, F. Huang, *Joule* **2020**, *4*, 2004.
- [31] X. Dong, Y. Jiang, L. Sun, F. Qin, X. Zhou, X. Lu, W. Wang, Y. Zhou, *Adv. Funct. Mater.* **2022**, *32*, 2110209.
- [32] Y. Minami, A. Hoshino, Y. Higuchi, M. Hamaguchi, Y. Kaneko, Y. Kiritani, S. Taminishi, T. Nishiji, A. Taruno, M. Fukui, Z. Arany, S. Matoba, *Nat. Commun.* **2023**, *14*, 1870.
- [33] M. A. Ruderer, S. Guo, R. Meier, H.-Y. Chiang, V. Körstgens, J. Wiedersich, J. Perlich, S. V. Roth, P. Müller-Buschbaum, *Adv. Funct. Mater.* **2011**, *21*, 3382.
- [34] K. Feng, D. Zhang, F. Liu, H. Li, J. Xu, Y. Xia, Y. Li, H. Lin, S. Wang, M. Shao, Z. Kang, J. Zhong, *Adv. Energy Mater.* **2020**, *10*, 1904234.
- [35] K. Herrmann, S. Freund, F. Eller, T. Rößler, G. Papastavrou, E. M. Herzig, M. Retsch, *Materials* **2022**, *15*, 7700.
- [36] J. Clark, C. Silva, R. H. Friend, F. C. Spano, *Phys. Rev. Lett.* **2007**, *98*, 206406.
- [37] J. Gierschner, Y.-S. Huang, B. van Averbeke, J. Cornil, R. H. Friend, D. Beljonne, *J. Chem. Phys.* **2009**, *130*, 44105.
- [38] A. Köhler, H. Bässler, *Electronic Processes in Organic Semiconductors. An Introduction*, Wiley-VCH GmbH, Weinheim, Germany, **2022**.
- [39] C. A. Sandstedt, R. D. Rieke, C. J. Eckhardt, *Chem. Mater.* **1995**, *7*, 1057.
- [40] F. C. Spano, *J. Chem. Phys.* **2005**, *122*, 234701.
- [41] F. C. Spano, C. Silva, *Annu. Rev. Phys. Chem.* **2014**, *65*, 477.
- [42] S. Pröller, F. Liu, C. Zhu, C. Wang, T. P. Russell, A. Hexemer, P. Müller-Buschbaum, E. M. Herzig, *Adv. Energy Mater.* **2016**, *6*, 066101.
- [43] Y. Qin, Y. Xu, Z. Peng, J. Hou, H. Ade, *Adv. Funct. Mater.* **2020**, *30*, 2005011.
- [44] D. Kroh, F. Eller, K. Schötz, S. Wedler, L. Perdigón-Toro, G. Freychet, Q. Wei, M. Dörr, D. Jones, Y. Zou, E. M. Herzig, D. Neher, A. Köhler, *Adv. Funct. Mater.* **2022**, *32*, 2205711.
- [45] S. Pröller, D. Moseguí González, C. Zhu, E. Schaible, C. Wang, P. Müller-Buschbaum, A. Hexemer, E. M. Herzig, *Rev. Sci. Instrum.* **2017**, *88*, 66101.
- [46] J. Clark, J.-F. Chang, F. C. Spano, R. H. Friend, C. Silva, *Appl. Phys. Lett.* **2009**, *94*, 163306.
- [47] C. Scharsich, R. H. Lohwasser, M. Sommer, U. Asawapirom, U. Scherf, M. Thelakkat, D. Neher, A. Köhler, *J. Polym. Sci. B Polym. Phys.* **2012**, *50*, 442.
- [48] F. M. Keheze, D. Raithele, T. Wu, D. Schiefer, M. Sommer, R. Hildner, G. Reiter, *Macromolecules* **2017**, *50*, 6829.
- [49] F. C. Spano, *Chem. Phys.* **2006**, *325*, 22.
- [50] E. Gann, T. Crofts, G. Holland, P. Beaucauge, T. McAfee, R. J. Kline, B. A. Collins, C. R. McNeill, D. A. Fischer, D. M. DeLongchamp, *J. Phys.: Condens. Matter* **2021**, *33*, 164001.

Supporting Information

Tackling P3HT:Y-Series Miscibility Through Advanced Processing for Tunable Aggregation

Fabian Eller¹, Christopher R. McNeill² and Eva M. Herzig^{1,*}

¹ Dynamics and Structure Formation – Herzig Group, University of Bayreuth, Universitätsstraße 30, 95447 Bayreuth, Germany
E-mail: eva.herzig@uni-bayreuth.de

² Christopher R. McNeill
Department of Materials Science and Engineering, Monash University, Wellington Road, Clayton, Victoria 3800, Australia

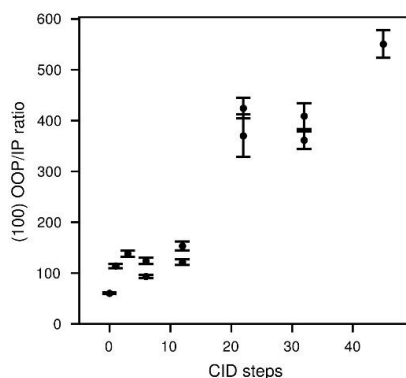


Figure S1. From GIWAXS cuts of neat P3HT film measurements: Ratio of the (100) vertical (OOP) amplitude to the (100) horizontal (IP) amplitude obtained from the fits to the GIWAXS data in Figure 1 g)-j).

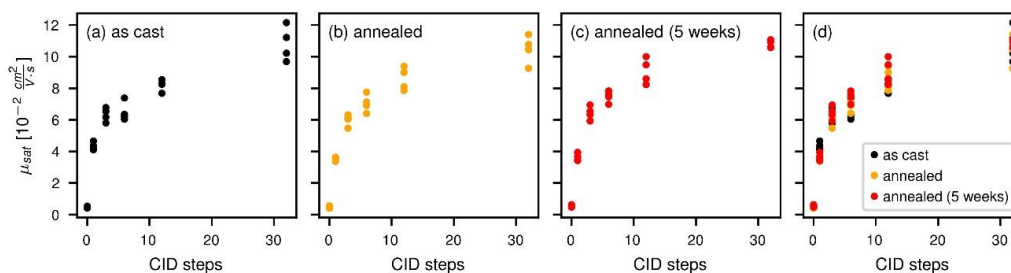


Figure S2. OFET measurements of neat P3HT: Hole mobility in the saturation regime of bottom-contact bottom-gate field effect transistors. The same devices were measured a) as cast, b) annealed at 140°C for 10 min, and c) 5 weeks after the annealing (storage in nitrogen-filled glovebox). In d) all data points from a)-c) are compared demonstrating no significant changes with annealing and storage.

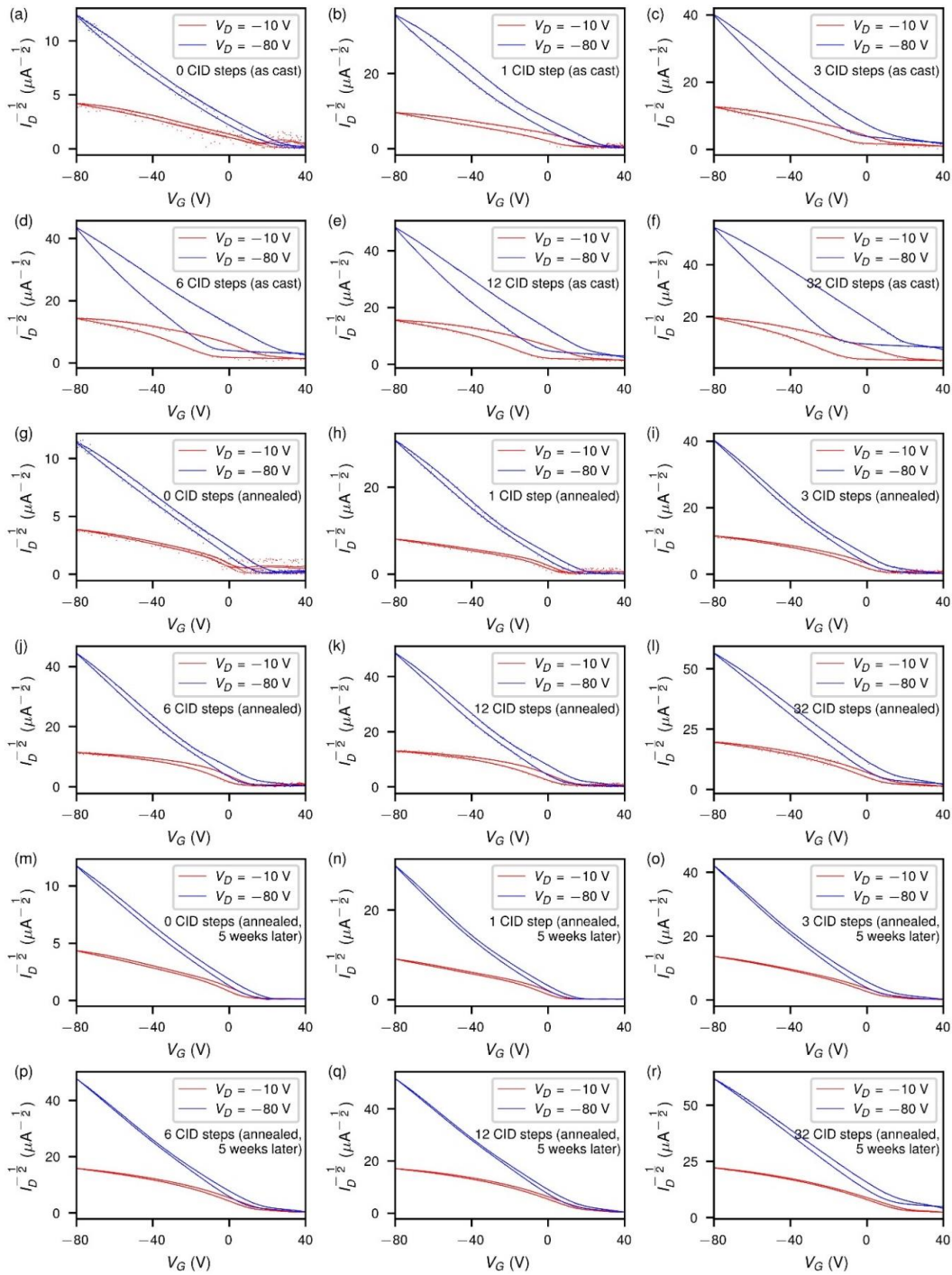


Figure S3. Exemplary OFET transfer curves used to extract the mobilities: a)-f) as cast with a) 0, b) 1, c) 3, d) 6, e) 12, and f) 32 CID steps. g)-l) same transistors measured after thermal annealing at 140°C for 10 min: g) 0, h) 1, i) 3, j) 6, k) 12, and l) 32 CID steps. m)-r) same transistors measured after thermal annealing at 140°C for 10 min and 5 weeks storage in nitrogen filled glovebox: m) 0, n) 1, o) 3, p) 6, q) 12, and r) 32 CID steps. The measurement data are plotted as points, while the solid lines serve as guide to the eye.

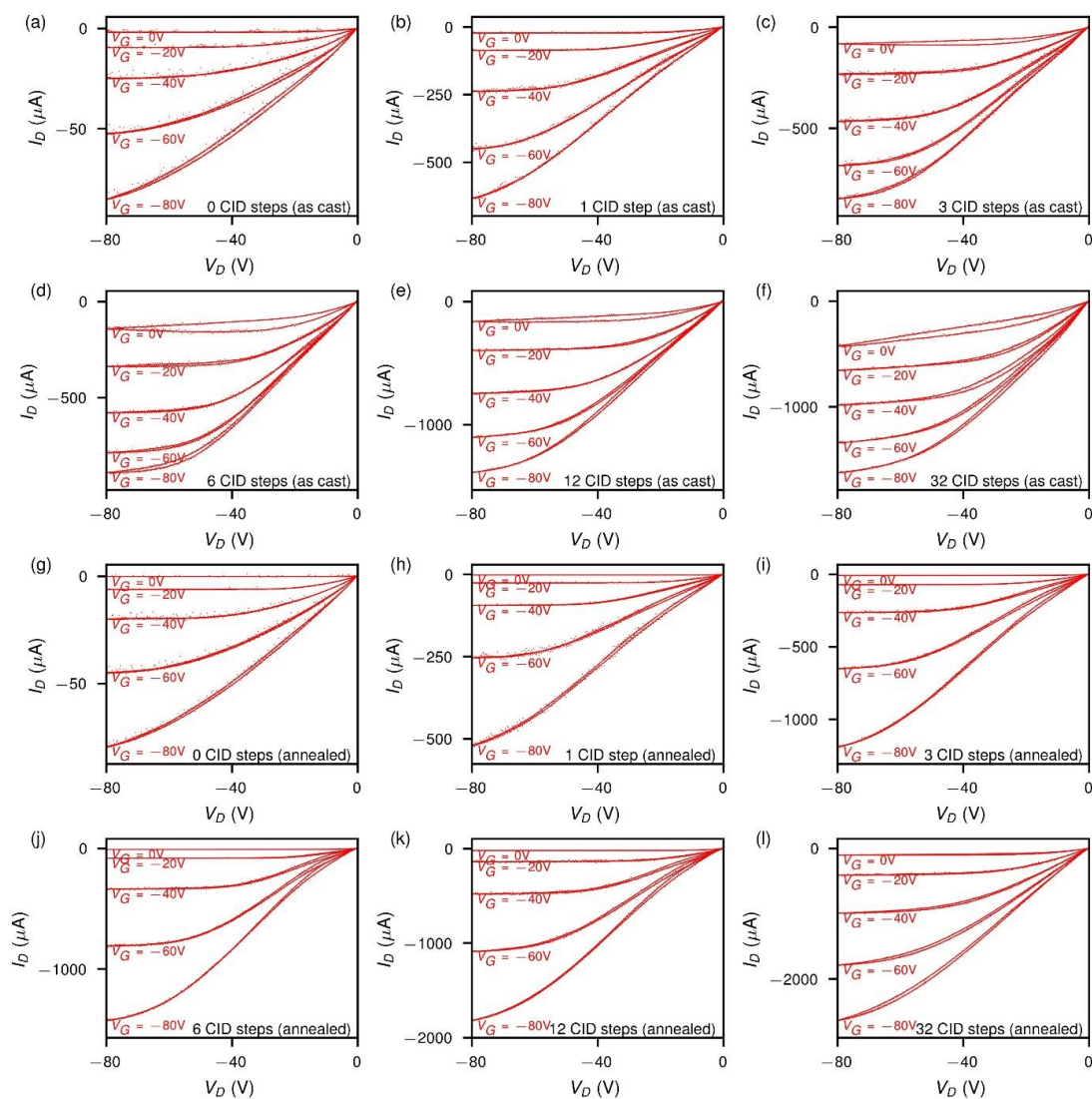


Figure S4. Exemplary OFET output curves: a)-f) as cast with a) 0, b) 1, c) 3, d) 6, e) 12, and f) 32 CID steps. g)-l) same transistors measured after thermal annealing at 140°C for 10 min: g) 0, h) 1, i) 3, j) 6, k) 12, and l) 32 CID steps. The measurement data are plotted as points, while the solid lines serve as guide to the eye.

WILEY-VCH

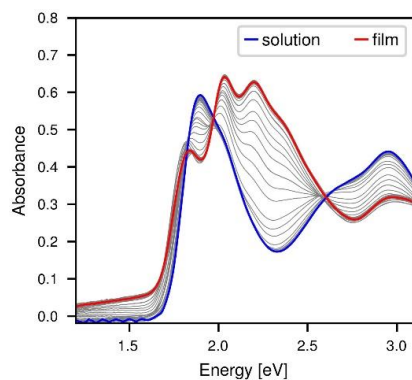


Figure S5. In-situ UV-vis absorption spectra during the drying of a 16.5 mg mL^{-1} P3HT:EH-IDTBR solution (no CID treatment).

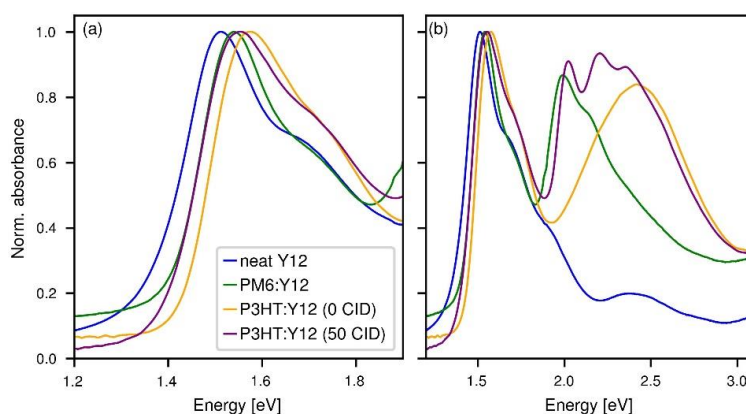


Figure S6. Film UV-vis absorption spectra: neat Y12, PM6:Y12, and P3HT:Y12 blends without CID treatment and with 50 CID steps. The full spectral range is displayed in b), while in a) a closeup on the low-energy range shows the Y12 peak shift between the films.

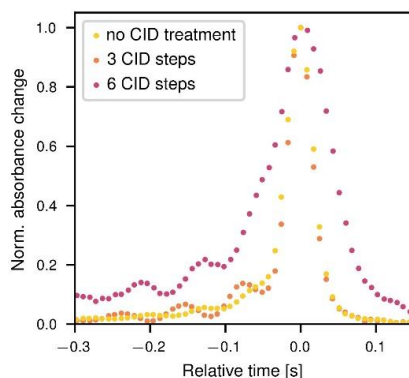


Figure S7. Normalized temporal change of the absorbance of P3HT:Y12 samples during drying averaged over the spectral range between 2.1 eV and 2.5 eV (dominant P3HT aggregate absorption). The oscillations are most likely interference effects. The results are similar to the normalized aggregate fraction slope in Figure 1 (e) with the difference, that more CID steps are necessary in the blend to achieve a significant nucleation-driven aggregation of P3HT before reaching the critical concentration.

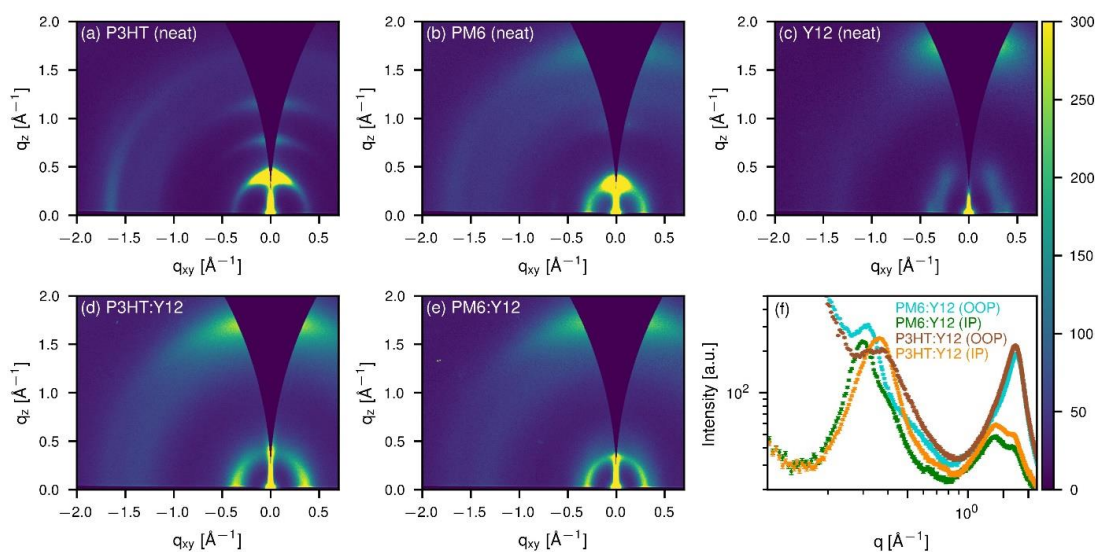


Figure S8. 2D GIWAXS data of a) neat P3HT, b) neat PM6, c) neat Y12, d) P3HT:Y12 (without CID treatment), and e) PM6:Y12 films. The intensity profiles of horizontal (IP) and vertical (OOP) cake cuts from d) and e) are compared in f).

WILEY-VCH

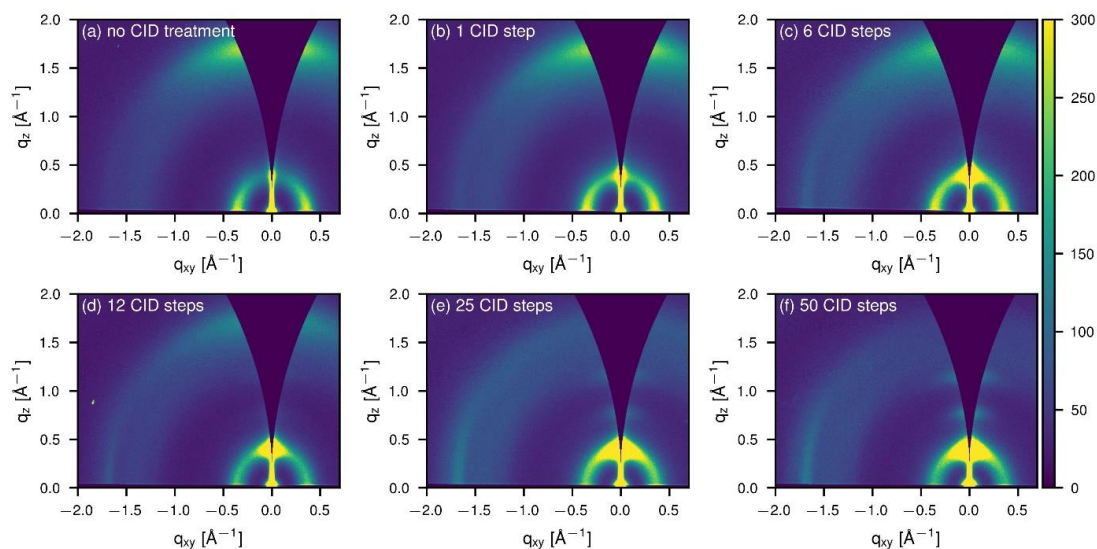


Figure S9. 2D GIWAXS data of P3HT:Y12 blends with varying number of CID steps: a) no CID treatment, b) 1 CID step, c) 6 CID steps, d) 12 CID steps, e) 25 CID steps, and f) 50 CID steps.

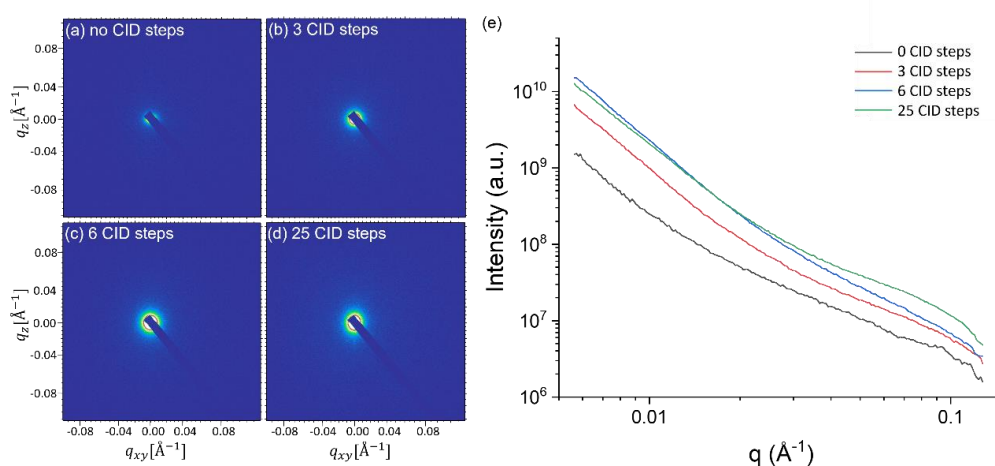


Figure S10. RSoXS (Resonant Soft X-ray Scattering) measurements of P3HT:Y12 films (as cast) with different number of CID steps. 2D-qmaps (a) without CID treatment, with (b) 3 CID steps, (c) 6 CID steps, (d) 25 CID steps. (e) Comparison of radial intensity profiles extracted from the measurements in (a)-(d).

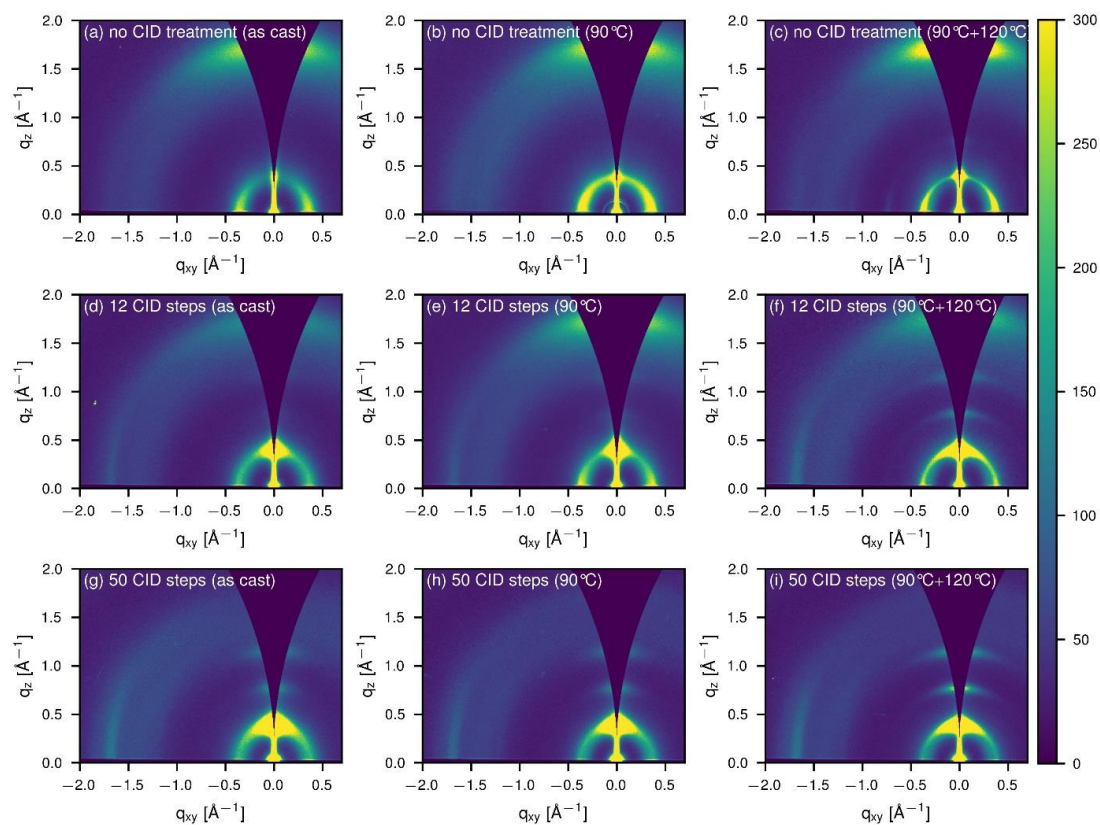


Figure S11. 2D GIWAXS data of exemplary P3HT:Y12 blends with different number of CID steps: a)-c) no CID treatment, d)-f) 12 CID steps, and g)-i) 50 CID steps and different annealing conditions: a), d), g) as cast, b), e), h) 5 min at 90°C, and c), f), i) 5 min at 90°C followed by 10 min at 120°C.

WILEY-VCH

Table S1. Peak position and peak width σ of the low-energy shoulder (main peak of aggregate I) of Y12 in dependency of the number of CID treatment steps before and after SVA in a saturated toluene atmosphere. The values were extracted by a Gaussian fit of the UV-vis absorption measurements from Figure 3 (d) and (e) within a range of 50 meV around the peak.

Number of CID steps	Treatment	Peak position [eV]	σ [meV]
0	no SVA	1.578	101
	SVA	1.537	72
3	no SVA	1.577	100
	SVA	1.528	74
6	no SVA	1.581	101
	SVA	1.532	74
12	no SVA	1.571	106
	SVA	1.531	77
25	no SVA	1.574	140
	SVA	1.524	81

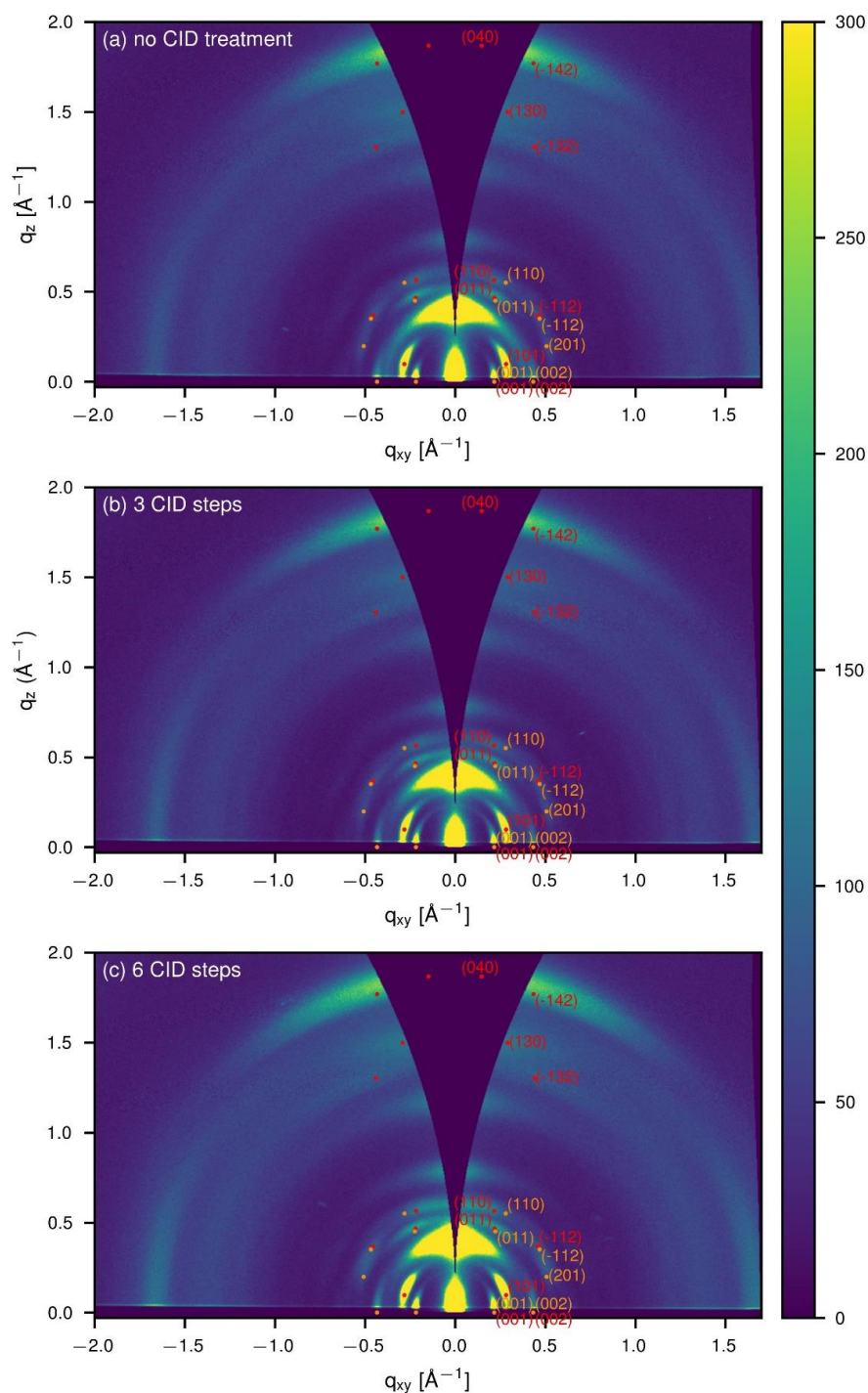


Figure S12. 2D GIWAXS data of P3HT:Y12: a) without CID treatment, b) with 3, c) 6 CID steps all post treated with SVA in a saturated toluene atmosphere. The lattice parameters of the Y12 unit cell 1 (peaks indexed in red) are $a_1=36.5$ Å, $b_1=16$ Å, $c_1=29$ Å, $\alpha_1=90^\circ$, $\beta_1=90^\circ$, $\gamma_1=123^\circ$, and the lattice parameters of the Y12 unit cell 2 (peaks indexed in orange) are $a_2=29$ Å, $b_2=16$ Å, $c_2=29$ Å, $\alpha_2=90^\circ$, $\beta_2=90^\circ$, $\gamma_2=120^\circ$. The rotation around the c -axis is about 4.5° for unit cell 1 and about 6.5° for unit cell 2.

WILEY-VCH

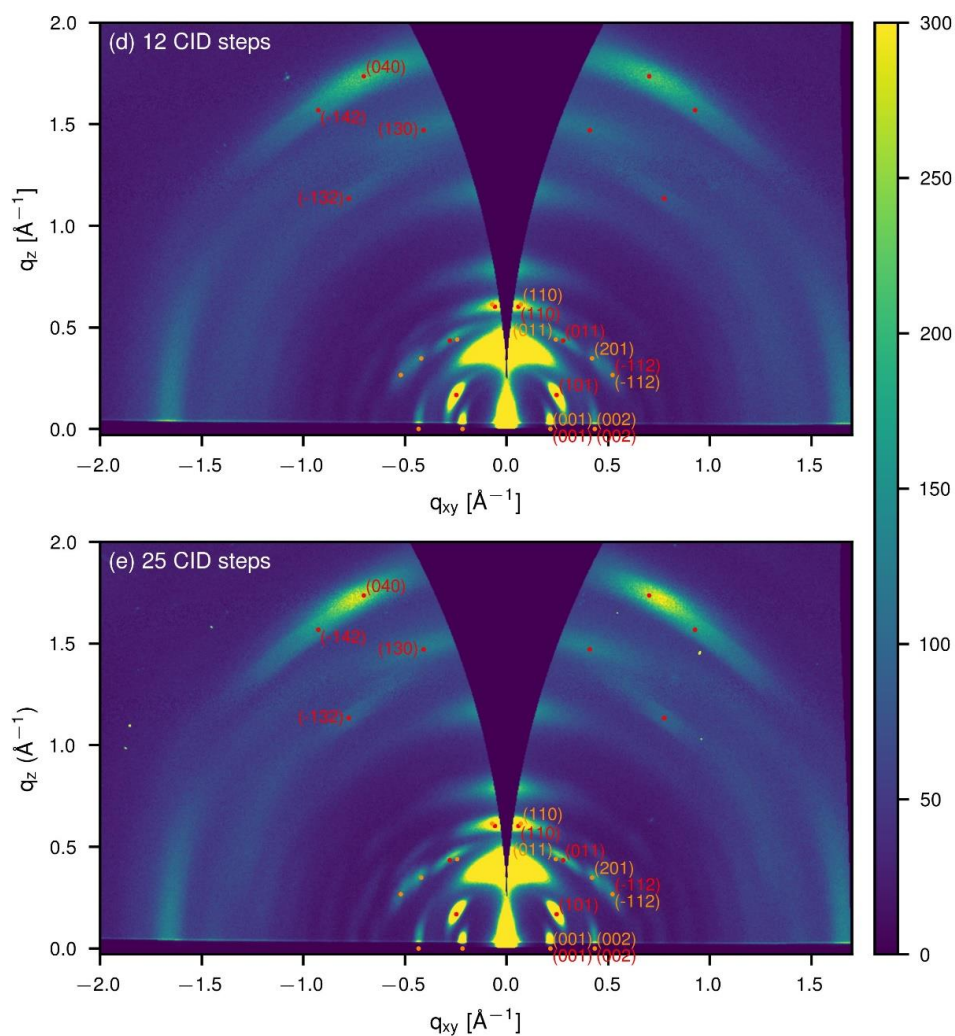


Figure S13. 2D GIWAXS data of P3HT:Y12: d) 12, and e) 25 CID steps all post treated with SVA in a saturated toluene atmosphere. The lattice parameters of the Y12 unit cell 1 (peaks indexed in red) are $a_1=36.5$ \AA , $b_1=16$ \AA , $c_1=29$ \AA , $\alpha_1=90^\circ$, $\beta_1=90^\circ$, $\gamma_1=123^\circ$, and the lattice parameters of the Y12 unit cell 2 (peaks indexed in orange) are $a_2=29$ \AA , $b_2=16$ \AA , $c_2=29$ \AA , $\alpha_2=90^\circ$, $\beta_2=90^\circ$, $\gamma_2=120^\circ$. The rotation around the c -axis is about -22° for unit cell 1 and about -14° for unit cell 2.

Table S2. Values for q_{xy} , q_z , and q of all indexed peaks of unit cell 1 (indexed in red in Figure 4, Figure S12, and Figure S13). The lattice parameters of the Y12 unit cell 1 are $a_1=36.5 \text{ \AA}$, $b_1=16 \text{ \AA}$, $c_1=29 \text{ \AA}$, $\alpha_1=90^\circ$, $\beta_1=90^\circ$, $\gamma_1=123^\circ$. Moreover, a rotation around the c -axis of 4.5° (up to 6 CID steps) and -22° (from 12 CID steps onwards) is considered.

Peak index	Rotation around c -axis [$^\circ$]	q_{xy} [\AA^{-1}]	q_z [\AA^{-1}]	q [\AA^{-1}]
(001)	4.5	0.217	0.000	0.217
	-22	0.217	0.000	
(002)	4.5	0.433	0.000	0.433
	-22	0.433	0.000	
(101)	4.5	0.282	0.098	0.298
	-22	0.246	0.168	
(011)	4.5	0.220	0.467	0.516
	-22	0.279	0.434	
(-112)	4.5	0.456	0.369	0.587
	-22	0.523	0.266	
(110)	4.5	0.217	0.565	0.605
	-22	0.058	0.602	
(-132)	4.5	0.439	1.302	1.374
	-22	0.776	1.134	
(130)	4.5	0.291	1.498	1.526
	-22	0.408	1.471	
(-142)	4.5	0.434	1.769	1.822
	-22	0.927	1.568	
(040)	4.5	0.147	1.867	1.873
	-22	0.702	1.737	

Table S3. Values for q_{xy} , q_z , and q of all indexed peaks of unit cell 2 (indexed in orange in Figure 4, Figure S12, and Figure S13). The lattice parameters of the Y12 unit cell 2 are $a_2=29$ Å, $b_2=16$ Å, $c_2=29$ Å, $\alpha_2=90^\circ$, $\beta_2=90^\circ$, $\gamma_2=120^\circ$. Moreover, a rotation around the c -axis of 6.5° (up to 6 CID steps) and -14° (from 12 CID steps onwards) is considered.

Peak index	Rotation around c -axis [°]	q_{xy} [Å ⁻¹]	q_z [Å ⁻¹]	q [Å ⁻¹]
(001)	6.5	0.217	0.000	0.217
	-14	0.217	0.000	
(002)	6.5	0.433	0.000	0.433
	-14	0.433	0.000	
(011)	6.5	0.223	0.451	0.502
	-14	0.243	0.440	
(201)	6.5	0.507	0.200	0.545
	-14	0.420	0.348	
(-112)	6.5	0.468	0.351	0.585
	-14	0.521	0.266	
(110)	6.5	0.281	0.550	0.618
	-14	0.070	0.614	

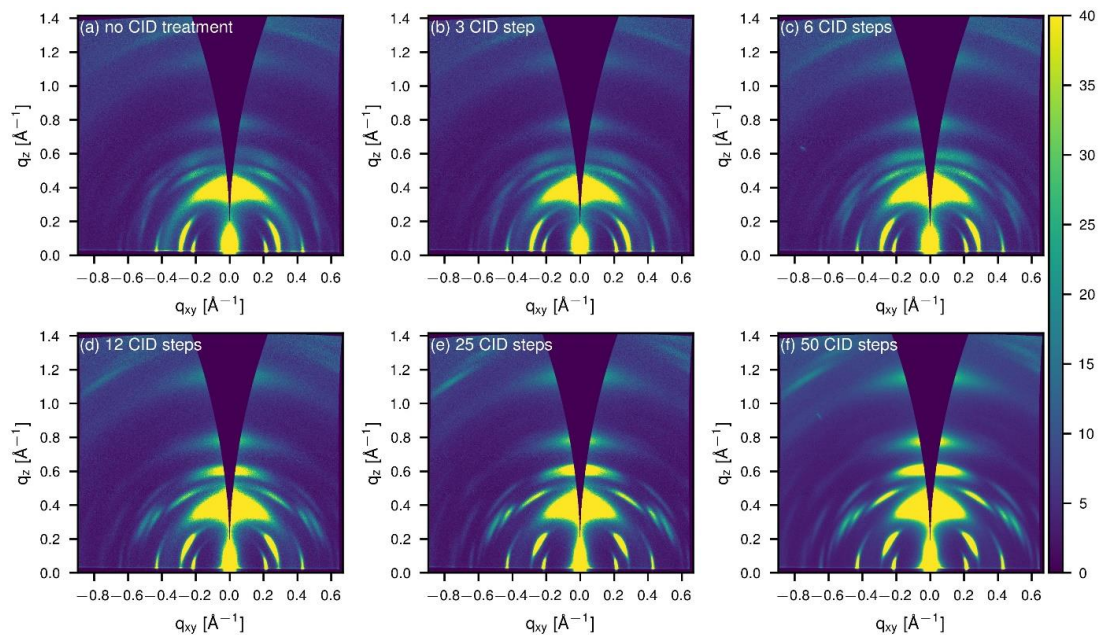


Figure S14. 2D GIWAXS data of P3HT:Y12: a) without CID treatment, b) with 3, c) 6, d) 12, e) 25, and f) 50 CID steps with additional solvent vapor annealing (SVA) in a saturated toluene atmosphere. In comparison to Figure 4 the sample-to-detector distance was increased from 72 mm to 200 mm, where a smaller q -range with a smaller impact of footprint broadening is captured.

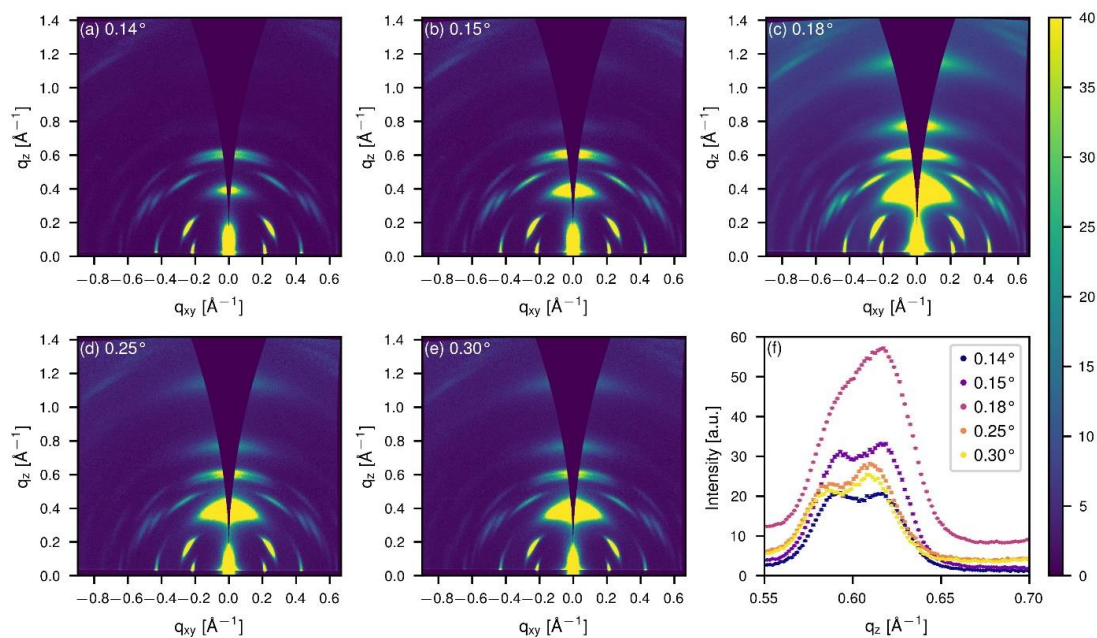


Figure S15. 2D GIWAXS data of P3HT:Y12 with 75 CID steps and additional solvent vapor annealing (SVA) in a saturated toluene atmosphere measured at different angles of incidence of the X-ray beam relative to the substrate ranging from 0.14° - 0.30° in a) to e). In f) the intensity profiles of the double peak extracted with a vertical cake cut are displayed for all different angles of incidence. As the (110) double peak is detected in the measurements at 0.14° and 0.15° below the critical angle of the film, at 0.25° and 0.30° above the critical angle of the Si substrate as well as at 0.18° between the critical angle of the film and the Si substrate and as no other clear double peaks exist, this is no artefact, but two scattering peaks of two different crystal structures.

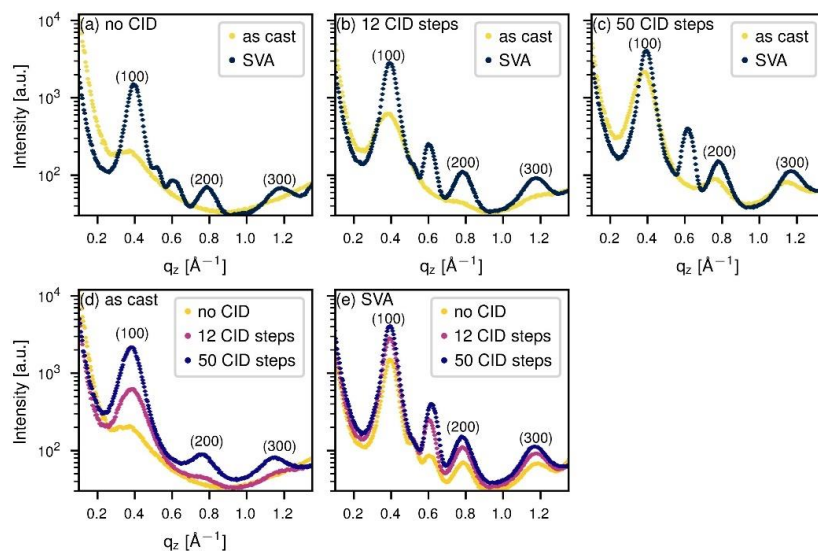
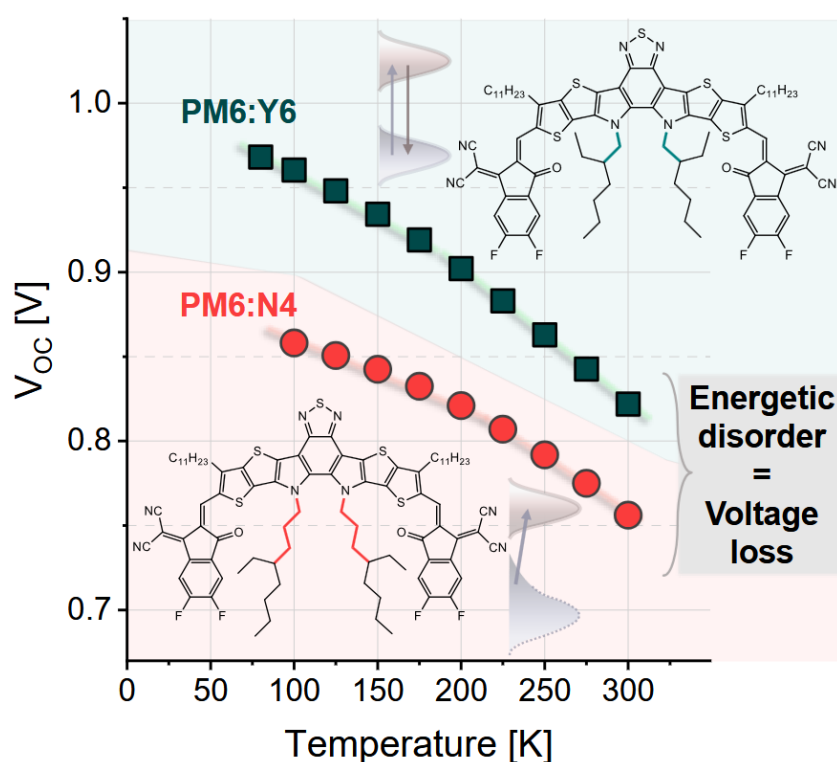


Figure S16. Comparison of GIWAXS intensity profiles extracted from vertical cake cuts of as cast films (yellow) and films with additional solvent vapor annealing (SVA) in a saturated toluene atmosphere (black): a) without CID treatment, b) with 12 CID steps, c) with 50 CID steps. The (100), (200), and (300) lamellar P3HT peaks are labelled. d) and e) comparison of samples with different numbers of CID steps (same data as in a)-c)): d) as cast, e) with SVA.

11 Understanding the Role of Order in Y-Series Non-Fullerene Solar Cells to Realize High Open-Circuit Voltages



Lorena Perdigón-Toro, Le Quang Phuong, **Fabian Eller**, Guillaume Freychet, Elifnaz Saglamkaya, Jafar I. Khan, Qingya Wei, Stefan Zeiske, Daniel Kroh, Stefan Wedler, Anna Köhler, Ardalan Armin, Frédéric Laquai, Eva M. Herzig, Yingping Zou, Safa Shoaee, and Dieter Neher

Published in
Advanced Energy Materials **2022**, 12 (12), 2103422
(DOI: 10.1002/aenm.202103422)

Reprinted with permission according to the CC BY 4.0 license
Copyright 2022 The Authors. *Advanced Energy Materials* published by Wiley-VCH GmbH

Understanding the Role of Order in Y-Series Non-Fullerene Solar Cells to Realize High Open-Circuit Voltages

Lorena Perdigón-Toro, Le Quang Phuong, Fabian Eller, Guillaume Freychet, Elifnaz Saglamkaya, Jafar I. Khan, Qingya Wei, Stefan Zeiske, Daniel Kroh, Stefan Wedler, Anna Köhler, Ardalan Armin, Frédéric Laquai, Eva M. Herzig, Yingping Zou, Safa Shoaee, and Dieter Neher*

Non-fullerene acceptors (NFAs) as used in state-of-the-art organic solar cells feature highly crystalline layers that go along with low energetic disorder. Here, the crucial role of energetic disorder in blends of the donor polymer PM6 with two Y-series NFAs, Y6, and N4 is studied. By performing temperature-dependent charge transport and recombination studies, a consistent picture of the shape of the density of state distributions for free charges in the two blends is developed, allowing an analytical description of the dependence of the open-circuit voltage V_{OC} on temperature and illumination intensity. Disorder is found to influence the value of the V_{OC} at room temperature, but also its progression with temperature. Here, the PM6:Y6 blend benefits substantially from its narrower state distributions. The analysis also shows that the energy of the equilibrated free charge population is well below the energy of the NFA singlet excitons for both blends and possibly below the energy of the populated charge transfer manifold, indicating a down-hill driving force for free charge formation. It is concluded that energetic disorder of charge-separated states has to be considered in the analysis of the photovoltaic properties, even for the more ordered PM6:Y6 blend.

1. Introduction

Organic solar cells (OSCs) stand out because of their easy processability, flexibility, light weight, and the abundance of materials that can act as electron donor (D) or acceptor (A) in the active layer of such devices. Great efforts are put into the development of even a larger library of materials, and the appearance of new non-fullerene acceptors (NFAs) has injected new life into the technology.^[1] Highest efficiencies are reported for single junction of ternary blends in which one of the components is the NFA Y6, or one of its close derivatives.^[2–6] When blended with the polymer donor PM6, PM6:Y6 devices have high and reproducible power conversion efficiencies (PCEs), thus many studies have focused on elucidating what makes this blend so special.^[7] Free charge generation was shown to be essentially

L. Perdigón-Toro, D. Neher
Soft Matter Physics and Optoelectronics
Institute of Physics and Astronomy
University of Potsdam
Karl-Liebknecht-Str. 24–25, 14476 Potsdam-Golm, Germany
E-mail: neher@uni-potsdam.de

L. Perdigón-Toro, L. Q. Phuong, E. Saglamkaya, S. Shoaee
Disordered Semiconductor Optoelectronics, Institute of Physics
and Astronomy
University of Potsdam
Karl-Liebknecht-Str. 24–25, 14476 Potsdam-Golm, Germany
F. Eller, E. M. Herzig
Physikalisches Institut
Dynamik und Strukturbildung – Herzig Group
Universität Bayreuth
Universitätsstr. 30, 95447 Bayreuth, Germany

 The ORCID identification number(s) for the author(s) of this article can be found under <https://doi.org/10.1002/aenm.202103422>.

© 2022 The Authors. Advanced Energy Materials published by Wiley-VCH GmbH. This is an open access article under the terms of the Creative Commons Attribution License, which permits use, distribution and reproduction in any medium, provided the original work is properly cited.

DOI: 10.1002/aenm.202103422

G. Freychet
NSLS-II
Brookhaven National Laboratory
Upton, NY 11973, USA

J. I. Khan, F. Laquai
KAUST Solar Center (KSC)
Physical Sciences and Engineering Division (PSE)
King Abdullah University of Science and Technology (KAUST)
Thuwal 23955-6900, Kingdom of Saudi Arabia

Q. Wei, Y. Zou
College of Chemistry and Chemical Engineering
Central South University
Changsha 410083, P. R. China

S. Zeiske, A. Armin
Sustainable Advanced Materials (S_{AM})
Department of Physics
Swansea University
Singleton Park, Swansea SA2 8PP, UK

D. Kroh, S. Wedler, A. Köhler
Soft Matter Optoelectronics
Bayreuth Institut of Macromolecular Research (BIMF)
and Bavarian Polymer Institute (BPI)
University of Bayreuth
95440 Bayreuth, Germany

barrierless which was attributed to the molecular structure of Y6 and its large quadrupole moment, which causes band bending across the heterojunction and drives charge separation.^[8] The unique molecular packing of Y6 has also been pointed out as responsible for electron delocalization at the D:A interface and consequent charge separation.^[9] In comparison to NFAs reported earlier, neat films of Y6 have more preferential face-on orientation,^[7,10,11] and clusters of Y6 are better connected, promoting faster transport of electrons, holes, and excitons.^[12] Despite a favorable morphology, the PM6:Y6 blend lags in terms of charge extraction,^[13] given its fairly high bimolecular recombination coefficient and moderate mobility.^[8,14,15] Both properties are known to be related to the energetic disorder of the charge transporting states.^[16–19] In addition, energetic disorder will reduce the open-circuit voltage (V_{OC}) because carriers accumulate in the tail of the electronic density of states (DOS).^[20–22] Therefore, detailed knowledge of the interplay between energetic disorder and the physical processes determining the photovoltaic response is needed.

Compared to inorganics, organic semiconductors have a larger positional and energetic disorder. In bulk heterojunction (BHJ) solar cells, this is primarily a result of molecular and interfacial interactions and the multiple possible morphologies upon mixing of the donor and acceptor. Research spanning over a decade attempted to link energetic disorder to the photovoltaic parameters of polymer:fullerene OSCs.^[20,22–29] Fullerene-based blends have large energetic disorder with values that can even exceed 100 meV.^[30–33] This is because of the small aggregate size of substituted fullerenes such as PCBM ([6,6]-phenyl-C₆₁-butyric acid methyl ester) but also the significant orientational and conformational disorder even within these ordered domains.^[34–36] Modern NFAs as used in state-of-the-art OSCs exhibit layers with a well-defined intermolecular nanostructure.^[10,11,37] For OSCs with Y-series acceptors, both the lowest unoccupied molecular orbital (LUMO) and the highest occupied molecular orbital (HOMO) exhibit energetic disorder values typically between 50 and 70 meV.^[14,15,38,39] Often, the effect of energetic disorder is described through a Gaussian or exponential model of the density of states and the V_{OC} can be analytically derived from the splitting of the quasi-Fermi levels in each model, while considering whether recombination occurs between free charges via bound states to the ground state, or between free charges and traps.^[20,25,40] The different mechanisms can be discerned experimentally by determining the recombination parameters from the V_{OC} dependence on carrier density (m -factor) and generation current (ideality factor, n_{id}), and the recombination current dependence on carrier density (recombination order δ), as detailed in Refs. [24,40]. So far, though, few experimental studies have tried to link energetic disorder to the V_{OC} losses, the V_{OC} dependence on temperature or the main recombination mechanism in NFA blends.^[38,41,42] An approach frequently used in literature to determine the disorder is to measure the Urbach energy from the slope of the tail of the external quantum efficiency (EQE_{pv}) spectrum.^[38,43,44] However, for a Gaussian disorder, this slope will always be equal to the thermal energy, independent of the width of the DOS, σ .^[45] Very recently, Brus et al.^[42] explained the V_{OC} as a function of temperature and light intensity for several polymer:NFA blends, using a combination of bimolecular and trap-assisted

recombination in the bulk and at the surface. To take energetic disorder into account, the recombination rates were related to a temperature-dependent mobility according to the Gaussian disorder model.^[16] This yielded values of σ between 46 and 70 meV, depending on the system. Thereby, the same disorder was assumed for the HOMO and the LUMO. As for work on the PM6:Y6 blend, information on the energetic disorder was derived from temperature-dependent space charge-limited currents (SCLC) measurements but no corresponding measurement of the V_{OC} in relation to disorder was performed.^[15] Interestingly, V_{OC} as a function of temperature data reported so far reveals a charge transfer (CT) energy, E_{CT} , of ≈ 1.1 eV when extrapolated to 0 K,^[8,46,47] which is less than 0.3 eV above qV_{OC} . This points to energetic disorder affecting the V_{OC} of PM6:Y6 solar cells, even at room temperature.

In this work, we highlight the role of energetic disorder in NFA solar cells, by comparing Y6 to a close derivative, namely, N4. Grazing-incidence wide-angle X-ray scattering (2D-GIWAXS) reveals distinct differences of the molecular orientation and order for the two acceptors blended with PM6, while temperature-dependent SCLC measurements show a significantly smaller energetic disorder in PM6:Y6. Temperature-dependent bias-assisted charge extraction (BACE) measurements reveal that the recombination mechanism is different in both blends. In PM6:Y6, recombination occurs between charges in a Gaussian HOMO DOS and a Gaussian LUMO DOS, both of narrow width, whereas the main recombination mechanism in PM6:N4 is of carriers in a broader Gaussian LUMO DOS recombining with carriers in a HOMO DOS with an exponential tail. As a consequence, the V_{OC} of PM6:N4 is considerably lower compared to PM6:Y6. The effect of disorder on the V_{OC} as a function of temperature is quantitatively described by analytical models considering the shape and disorder of the HOMO and LUMO site distributions. Because of the higher disorder, the CT emission is well discernible in electroluminescence (EL) at low temperatures in PM6:N4, which we assign to emission from lower-lying states in a broad DOS distribution, again consistent with the larger voltage loss of this blend. Finally, for a given generation rate, the free carrier density increases with decreasing temperature in both PM6:Y6 and PM6:N4. This contrasts the view that charge separation is temperature-assisted or entropy-driven. Instead, this finding supports the model that band bending in combination with energetic disorder provides a down-hill driving force for free charge formation.

2. Results

2.1. Device Characteristics

Since it is well established that PM6:Y6 has a desirable morphology and thereby low energetic disorder, we aimed at having an in-depth comparison with an alternative NFA that features a different molecular packing but has a similar molecular structure, that is, a Y-derivative. N4 is a small molecule acceptor that has an aromatic backbone identical to that of Y6 but different alkyl chains elongation, with 4th-position branching on the nitrogen atoms of the pyrrole motif of the backbone (instead of 2nd-position as in Y6, see

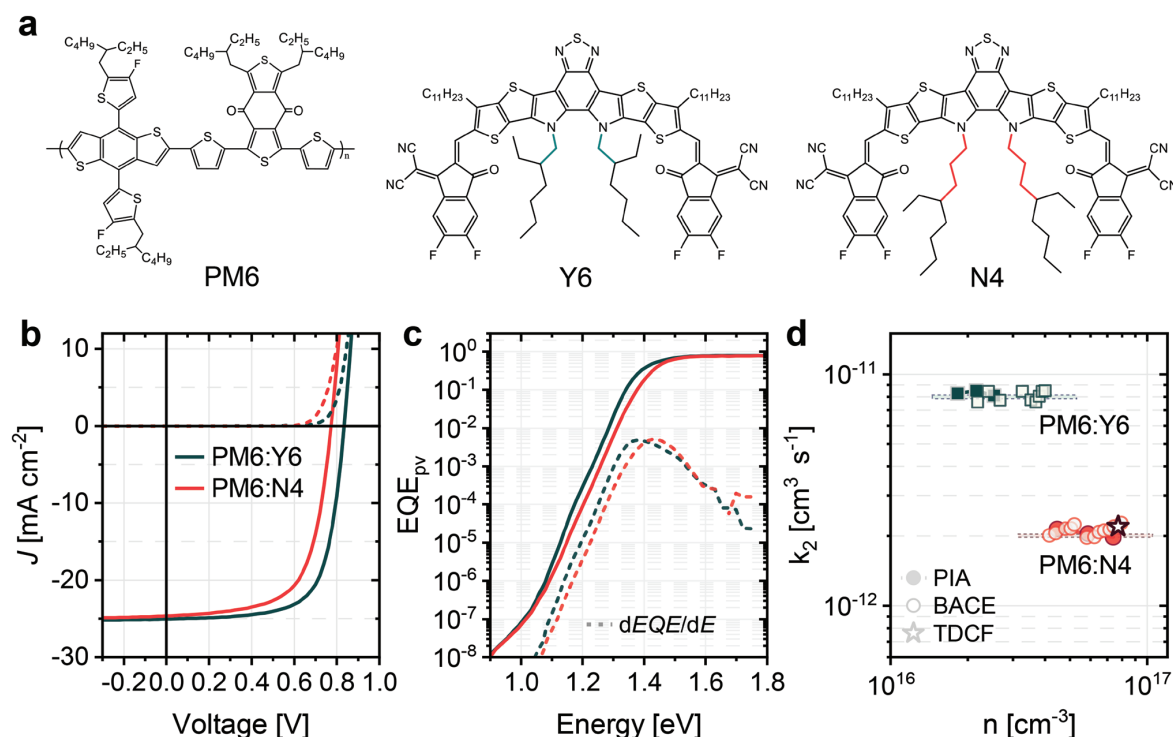


Figure 1. a) Chemical structures of PM6, Y6, and N4. b) Current density–voltage (J – V) characteristics of PM6:Y6 and PM6:N4 regular devices measured under simulated AM1.5G light (solid lines) and in the dark (dashed lines). c) Sensitive photovoltaic external quantum efficiency (s -EQE_{pv}) of PM6:Y6 and PM6:N4 devices (solid lines). The derivative $dEQE/dE$ is shown in dashed lines and the photovoltaic gap E_C is determined from its maximum. The obtained E_C is 1.38 eV for PM6:Y6 and 1.43 eV for PM6:N4. d) Bimolecular recombination coefficient k_2 as a function of charge carrier density of PM6:Y6 and PM6:N4 devices measured via PIA (full symbols) and BACE (open symbols). For PM6:N4, the value of k_2 from TDCF-delay measurements is also plotted (star symbol).

Figure 1a). This increases the solubility of the N4 molecule.^[48] Morphology studies performed by Jiang et al. showed that the PM6:N4 blend has a preferential *edge-on* orientation in contrast to the predominant *face-on* orientation of PM6:Y6. Moreover, R-SoXs experiments revealed larger but less pure domains in PM6:N4, pointing to more intermixing. As it turns out, the different molecular design and packing result in a poorer performance for the PM6:N4 devices, which have a lower V_{OC} , slightly lower fill factor (FF) but similar short-circuit current density (J_{SC}) when compared to PM6:Y6. The typical current density–voltage (J – V) characteristics of regular devices with a 100 nm layer of PM6:Y6 (1:1.2, wt%) and PM6:N4 (1:1.25, wt%) are shown in Figure 1b. Table S1 (Supporting Information) contains the averaged photovoltaic parameters of regular devices prepared in this work, while Figure S1 (Supporting Information) compares in more detail the statistics of both regular and inverted devices. Our regular PM6:Y6 devices exhibit a PCE average value of 14%, whereas the PCE of PM6:N4 is at 12%. Inspection of the photovoltaic parameters shows that the PM6:Y6 produces on average 1 mA cm⁻² more in J_{SC} than the PM6:N4 (24.9 vs 23.9 mA cm⁻²) for the same active layer thickness (Figure S2 shows the photovoltaic external quantum efficiency, EQE_{pv}, including the integrated J_{SC} for PM6:Y6 and PM6:N4, Supporting Information). In

addition, the FF is 2% higher, with an average value of 66.8%, in PM6:Y6 compared to an average of 64.7% in PM6:N4. The largest difference is in the V_{OC} , which on average is 0.84 V in PM6:Y6 and 0.77 V in PM6:N4.

The large difference in V_{OC} comes as a surprise as N4 has been reported to have a slightly deeper HOMO and higher LUMO than Y6.^[49] In accordance, the comparison in Figure 1c of the sensitive photovoltaic external quantum efficiency (s -EQE_{pv}) spectra shows that the absorption is blueshifted in PM6:N4 with respect to PM6:Y6. The same holds for the peak of the EQE derivative, which gives a photovoltaic gap of 1.38 and 1.43 eV for PM6:Y6 and PM6:N4, respectively. These results indicate that the PM6:N4 blend suffers overall from larger voltage losses. This is indeed observed in measurements of the external quantum efficiency of electroluminescence (ELQY), in Figure S3 (Supporting Information).

For a given energetics, a smaller V_{OC} would originate from faster geminate and/or nongeminate nonradiative recombination. Our previous measurements of time-delayed collection field (TDCF) on PM6:Y6 devices demonstrated that free charge generation is very efficient and independent of the electric field, pointing to small geminate losses in the blend. Similar results were obtained now for PM6:N4 (Figure S4, Supporting Information). We

investigated nongeminate recombination of regular PM6:Y6 and PM6:N4 devices with a semitransparent back electrode by means of charge extraction and optical-based spectroscopy techniques under steady-state conditions, namely bias assisted charge extraction (BACE) and quasisteady-state photoinduced absorption (PIA). In BACE, the device is held at V_{OC} under steady-state illumination and as soon as the light is turned off, a high reverse bias is applied to extract all charges.^[50,51] Provided the recombination rate, R , follows a second order dependence on charge carrier density n , k_2 is directly calculated from $R = k_2 n^2$. PIA measurements are also performed at V_{OC} , but the yield and dynamics of free carriers are recorded by measuring the differential absorption upon modulation of the intensity of the quasi steady-state illumination.^[52,53] Further experimental details on both techniques are given in the Supporting Information. The results from both methods point to second order recombination in the blends. The recombination coefficients as a function of carrier density are compared in Figure 1d, where we observe that $k_2 \approx 8 \times 10^{-12} \text{ cm}^3 \text{ s}^{-1}$ for PM6:Y6 and $k_2 \approx 2 \times 10^{-12} \text{ cm}^3 \text{ s}^{-1}$ for PM6:N4, meaning that recombination is ≈ 4 times slower in PM6:N4. This comes initially as a surprise since it is on the contrary a higher k_2 which would explain increased V_{OC} losses.^[20,22] We note that the k_2 for the PM6:Y6 regular devices in this work is lower than in our previous report, which could be related to using a newer batch of the blend materials. To confirm the conclusions about the recombination loss in PM6:N4, we additionally performed transient recombination measurements with TDCF. TDCF has been already applied to PM6:Y6 and gave excellent agreement to BACE results.^[54] The corresponding TDCF transients for PM6:N4 are shown in Figure S5 (Supporting Information). Analysis of these transients with an established model yielded the same k_2 as obtained via BACE and PIA, as marked in Figure 1d. A further source of V_{OC} losses is nonradiative recombination at the electrodes due to nonideal contacts. To rule out carrier losses due to surface recombination, we followed the same approach as for our PM6:Y6 devices,^[55] and measured PIA and electromodulation injection-induced absorption (EMIA) spectroscopy on the same PM6:N4 device with regular architecture. These two complementary techniques allow us to compare photogenerated and dark injected charges at equivalent recombination currents (Figure S6, Supporting Information). At 1 sun, the carrier concentration under dark injection is slightly lower than under photoexcitation, but this would only cause a ≈ 15 meV difference in the quasi-Fermi level splitting (QFLS). Furthermore, we compared the photogenerated carrier concentration in a full device and a PM6:N4 bare film on glass (Figure S6, Supporting Information). Here, the PM6:N4 data on device and film agree very well, as was the case for PM6:Y6,^[53] suggesting that little carriers are lost due to the incorporation of transport layers and electrodes (known as interfacial or surface recombination). Consequently, the reason for the lower V_{OC} of the PM6:N4 blend must lie in the details of the energetics and recombination mechanism in the bulk, which motivated a thorough study of the morphology and energetic disorder of the two blends and the resulting photovoltaic properties, as detailed in the following.

2.2. Morphology and Energetic Disorder

We employed grazing-incidence wide-angle X-ray scattering (2D-GIWAXS) to investigate the differences in the blend morphology of PM6:Y6 and PM6:N4 films. Figure 2a shows the 2D-GIWAXS images of PM6:Y6 and PM6:N4. In order to disentangle the contribution of the single components in the blend, we measured films of all neat materials. Figure 2b,c corresponds to the horizontal and vertical line cuts, respectively, of the neat materials PM6, Y6, and N4 (2D data can be found in Figure S7, Supporting Information), while Figure 2d,e contains the horizontal and vertical line cuts of the blends (from panel a). In Figure 2b,c, neat Y6 shows predominantly *face-on* orientation, as we observe the π - π stacking in the vertical direction while the lamellar peaks are identified in the horizontal direction, in line with previous reports.^[7,10,11] The Gaussian peak shape (coherence length of 6.4 nm) of the first lamellar peak suggests long range order within the Y6 network. On the contrary, the π - π stacking in neat N4 is in the horizontal direction, pointing to preferential edge-on orientation. In addition, the lamellar stacking of N4 shows well defined, multiple structure peaks into specified directions which are more pronounced in comparison to the N4 π - π stacking signal. Thus, the lamellar stacking seems to be the more dominant stacking mechanism for neat N4. The length of the side-chain before the branching point could be decisive in this competition, as a result of steric hindrance and/or the better solubility of N4.^[56,57] Overall, neat N4 is highly ordered but, in comparison to neat Y6, the π - π stacking is less pronounced and the width of the peak is larger due to stronger cumulative disorder in the π - π stacking of N4. For the neat PM6, there is strong lamellar stacking in the vertical direction, i.e., edge-on preferential orientation, while there is only evidence of a very weak π - π stacking (Figure S7, Supporting Information). The corresponding data for the blends are shown in Figure 2a,d,e. For PM6:Y6, we notice that the first lamellar peak at $q_{xy} = 0.29 \text{ \AA}^{-1}$ is contributed by both PM6 and Y6 (making it hard to distinguish them), but the second lamellar peak at $q_{xy} = 0.42 \text{ \AA}^{-1}$ must have a Y6 contribution, meaning there is long range order of Y6 present within the blend. We attribute the π - π stacking in the vertical direction at $q_z = 1.7 \text{ \AA}^{-1}$ almost solely to Y6 since the peak shape is nearly identical to the neat Y6 and PM6 has a weak π - π stacking. Conclusively, Y6 maintains its preferential face-on packing when blended with PM6 and spincoated from CF with 0.5% v/v CN. In PM6:N4, the N4 lamellar ordering ($q_{xy} = 0.33 \text{ \AA}^{-1}$ and $q_{xy} = 0.41 \text{ \AA}^{-1}$) appears to have completely vanished, since the observed lamellar peaks in the blend resemble those of PM6 in position and shape. The lamellar peak at $q_{xy} = 0.29 \text{ \AA}^{-1}$ of the PM6:N4 blend has a larger isotropic contribution than in the PM6:Y6 blend, i.e., PM6 is more isotropic, if blended with N4. Interestingly, the π - π stacking in the PM6:N4 blend is stronger in the vertical direction. It is unlikely that this signal is dominated by the PM6 which has a slightly preferred orientation of the lamellar stacking in the vertical. This in turn indicates that N4 is partially reoriented to face-on in our PM6:N4 blend. This contrasts with previous morphology studies,^[48] where no significant π - π stacking could be observed for PM6:N4, while the lamellar stacking appeared to be similarly dominated by PM6 and thus no information on the N4 orientation in the blend

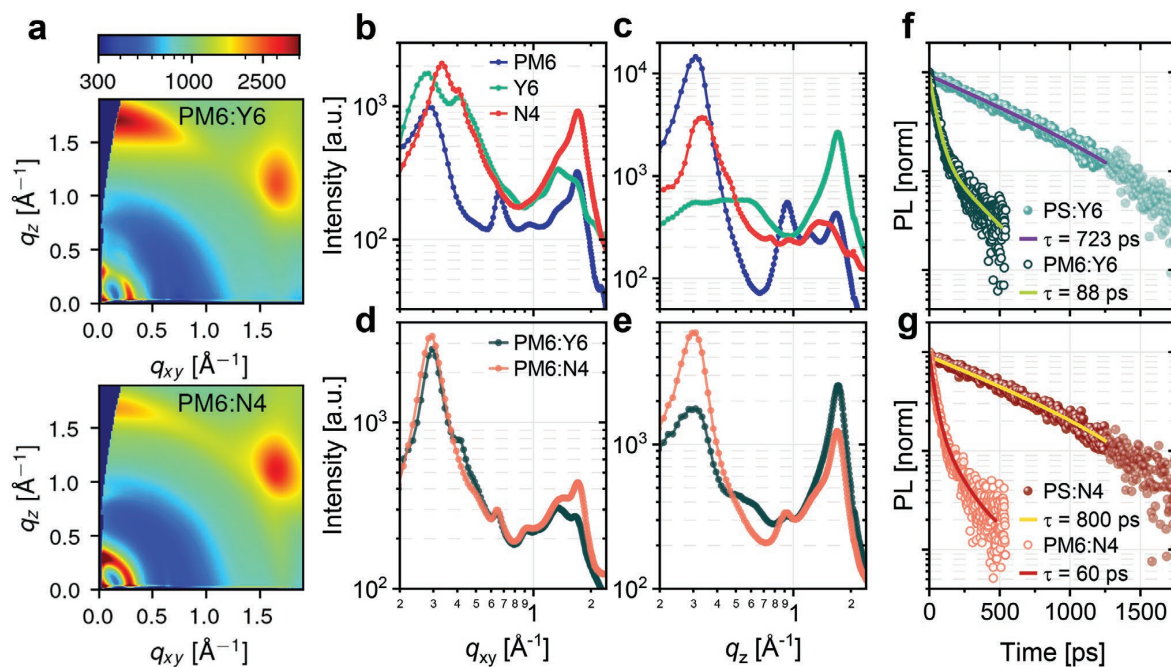


Figure 2. a) 2D-GIWAXS images of PM6:Y6 (top) and PM6:N4 (bottom) measured on Si substrates (the strong diffraction signal at about $q_{xy} = 1.7 \text{ \AA}^{-1}$, $q_z = 1.2 \text{ \AA}^{-1}$ is due to substrate scattering). b) Horizontal and c) vertical line cuts of the neat materials PM6, Y6, and N4. d) Horizontal and e) vertical line cuts of the blends PM6:Y6 and PM6:N4. Time-resolved photoluminescence measured on f) PS:Y6 and PM6:Y6 films and g) PS:N4 and PM6:N4 films, from which a quenching efficiency of 88% and 93%, respectively, were determined.

could be obtained. This difference could be a result of using a different PM6 batch, with, e.g., different molecular weight and/or polydispersity, or slightly different processing conditions. In our blends, the addition of PM6 changes the environment of the N4 leading to a clearly altered aggregation behavior of the N4 including changes in the final orientation of the π - π stacking and a loss in regular nanostructure between N4 molecules. Taking a closer look at the π - π stacking, the intensity of the peaks is larger in PM6:Y6 compared to PM6:N4, meaning quantitatively that more NFA π - π stacking in *face-on* direction is present in our Y6 blend. We finally performed Pseudo-Voigt fits to the π - π peak and the disordered contribution in the vertical direction (see Figure S8, Supporting Information). The ratio between the area of π - π peak and amorphous contribution is ≈ 2.5 for PM6:N4 and ≈ 5.4 for PM6:Y6, revealing a larger amorphous fraction in the PM6:N4 blend in comparison to the PM6:Y6 in the π - π stacking direction. Thus, all the morphological features collected here indicate a lower degree and quality of stacking of N4 in the PM6:N4 blend in comparison to the neat N4 film, as well as in comparison to the Y6 in the PM6:Y6 blend. Here, stacking refers to the lamellar as well as the π - π stacking. Particularly in the vertical direction, it becomes apparent that the PM6:N4 blend shows less order than PM6:Y6 on the short length scales that are decisive for the electronic interactions of the materials.

We noted earlier that PM6:N4 has a lower domain purity.^[48] To conveniently examine this, we measured time-resolved photoluminescence (TRPL) on films of the neat acceptors blended with the inert polymer polystyrene (PS) and on the blends with

PM6, as shown in Figure 2f,g. The PS:NFA data are fitted using a single exponential decay, while the PM6:NFA blends are fitted using two exponentials, see Note S1 and Table S2 for details (Supporting Information). As expected, the blends with PM6 exhibit shorter lifetimes due to exciton quenching. In Figure 2f, the singlet exciton lifetime obtained for PS:Y6 is 723 ps and the weighted-average lifetime of PM6:Y6 is 88 ps, which gives a quenching efficiency of 88%. For the N4 blends, PS:N4 has a lifetime of 800 ps and PM6:N4 has 60 ps, thus the quenching efficiency is higher at 93%. Stronger exciton quenching is consistent with more intermixing in PM6:N4, i.e., more interfacial area between donor and acceptor. This in turn could be a potential source for a broadening of the DOS. For example, the presence of the other molecule disrupts the intermolecular order of the majority phase, going along with a larger energetic disorder. Also, all Y-series acceptor molecules exhibit quite large electrical dipole and quadrupole moments which, when mixed at low concentrations into PM6, could increase the energetic disorder in the donor phase.^[58,59] In general, more intermixing will create larger D:A interfaces and a larger density of CT states, discerned by a broader and more significant low energy tail in EQE_{pv} measurements.^[60,61] However, as we have previously shown for PM6:Y6,^[55] the tail of the sensitive EQE_{pv} is dominated by the Y6 exciton and there is no discernible evidence for CT absorption. We concluded this by measuring the photoluminescence (PL) spectrum of the blend, which is largely dominated by emission from the Y6 singlet exciton and using the optoelectronic reciprocity by Rau^[62] to calculate the EQE_{pv} spectrum due to exciton absorption. We performed the

Table 1. Energetic disorder parameters for the LUMO ($\sigma_{L,A}$) and the HOMO ($\sigma_{H,D}$), and zero-field electron (μ_e) and hole (μ_h) mobilities in the blends PM6:Y6 and PM6:N4.

Blend	$\sigma_{L,A}$ [meV]	$\sigma_{H,D}$ [meV]	μ_e [$\times 10^{-4}$ cm ² V ⁻¹ s ⁻¹]	μ_h [$\times 10^{-4}$ cm ² V ⁻¹ s ⁻¹]
PM6:Y6	60	74	8.4	1.3
PM6:N4	66	90	1.6	0.1

same characterization for PM6:N4 in Figure S9 (Supporting Information), where we observe that emission and absorption are dominated by N4 singlets. The reciprocity of the PL perfectly reproduces the tail of the measured s-EQE_{pv} except from ≈ 1.2 eV and below, which indeed indicates additional absorption due to a low energy CT population.

To establish the effect of the different morphologies on the energetic properties, we measured space charge limited currents (SCLC) of electron-only and hole-only devices as a function of temperature (see Note S2 and Figures S10–S11, Supporting Information). This approach has been shown to be sensitive to the shape and width of the DOS. We note that in order to avoid the effect of diffusion enhanced transport,^[63] devices thicker than our typical solar cells were needed (typically larger than 150 nm). The temperature dependence of the zero-field mobility μ_0 for the PM6:Y6 and PM6:N4 blends is shown in Figure S12 (Supporting Information). Table 1 summarizes the values of μ_0 at 300 K and the energetic disorders for the HOMO, $\sigma_{H,D}$, and the LUMO, $\sigma_{L,A}$, obtained using the Gaussian disorder model (GDM), see Note S2 (Supporting Information). When it comes to the LUMO, the disorder is slightly larger in PM6:N4, at 66 meV, while it is only 60 meV in the PM6:Y6. The electron mobility is then 5 times lower in PM6:N4 compared to PM6:Y6. It is in the HOMO where striking differences in disorder values are observed. The $\sigma_{H,D}$ increases from 74 meV in PM6:Y6 to 90 meV in PM6:N4, going along with a 10 times decrease of the zero-field mobility. It seems that the lower molecular order of PM6:N4 leads to a slight increase of disorder in the LUMO, while affecting to a greater extent the width of the HOMO DOS. From the earlier TRPL results, we speculate that N4 molecules mix into PM6 domains.

In addition, it becomes meaningful to plot the logarithmic slope of the J - V curves, slope = $d(\log J)/d(\log V)$, to reveal the SCLC regime and the presence of energetic traps.^[16,64–66] This is done in Figures S10 and S11 (Supporting Information) in dependence of the applied voltage for PM6:Y6 and PM6:N4 electron- and hole-only devices. The electron-only devices of both blends follow a slope between 2 and 2.5 at higher voltages. The slight increase, especially at lower temperatures, is most likely due to a field-dependence of the mobility. The situation is the same for the PM6:Y6 hole-only data. The device that behaves differently is the hole-only PM6:N4. Here, the slope saturates at higher fields and the saturation value increases with decreasing temperature, reaching close to 4 at 223 K. This behavior is characteristic for an exponential distribution of tail states.^[67,68] For SCLCs in a pure exponential DOS, $J \propto V^{2l+1}$, with $l = T_0/T$ and T_0 being the characteristic distribution temperature of the exponential DOS (see Note S3, Supporting Information). The best fit of the PM6:N4 hole-only data is shown in Figure S13 (Supporting Information) and yields $T_0 = 585$ K. The true width

may, however, be smaller as this analysis does not consider an explicit voltage dependence of the free carrier mobility.

2.3. Nongeminate Recombination

The shape of the DOS does not only affect the free carrier transport but also its nongeminate recombination characteristics.^[21,27,69–71] In brief, the recombination rate R is defined as the decay of charge carriers n with time, $R = -\frac{dn}{dt} = \gamma n^\delta$, where δ is the recombination order and γ the recombination coefficient. As introduced earlier, bimolecular recombination gives $\delta = 2$ and the recombination coefficient is then denoted as k_2 . At V_{OC} conditions, recombination equals generation, while the generation rate G can be expressed in terms of the generation current J_G

$$J_G = qdR = qd\gamma n^\delta \quad (2a)$$

where q is the elementary charge and d is the film thickness. The steady-state recombination current is connected to the applied voltage, V , via the ideality factor, n_{id} , according to

$J_R = J_0 \exp\left(\frac{qV}{n_{id}k_B T}\right)$, with J_0 being the dark recombination current, T temperature and k_B , the Boltzmann constant. Then, at open-circuit conditions

$$J_G(V_{OC}) = J_R(V_{OC}) = J_0 \exp\left(\frac{qV_{OC}}{n_{id}k_B T}\right) \quad (2b)$$

In absence of surface recombination, the V_{OC} is equal to the quasi-Fermi level splitting in the bulk which in turn, for equilibrated electrons and holes, is a function of the electron and hole densities, n and p . For an ideal intrinsic semiconductor with sharp bands, $n = p \propto \exp\left(\frac{qV_{OC}}{2k_B T}\right)$. In general, the relation between V_{OC} and n is written as

$$n = p = N_0 \exp\left(\frac{qV_{OC}}{2mk_B T}\right) \quad (2c)$$

where the m -factor is introduced to describe the degree of disorder and N_0 is the effective density of states. In case of two Gaussians, $\delta = 2$, $m = 1$ and $n_{id} = 1$, with all parameters being independent of temperature.^[40] We already note here that for a Gaussian DOS, these considerations are only correct in the nondegenerate limit (see Note S4, Supporting Information).^[72] As we will show later, the approximation holds for $T \gtrsim 200$ K in the PM6:Y6 blend. In contrast, once an exponential DOS is involved in recombination, at least two of the above parameters depend on l , and with that on temperature,^[40] given that $l = T_0/T$ as introduced earlier. Moreover, it makes a difference whether free or trapped carriers are involved. The reason is that for an exponential DOS the free carrier density is a nonlinear function of the total carrier density according to $n \propto (n_T)^l$.

Following Equation (2a–c), we measured J - V s and $n(V_{OC})$ at different illumination intensities and as a function of

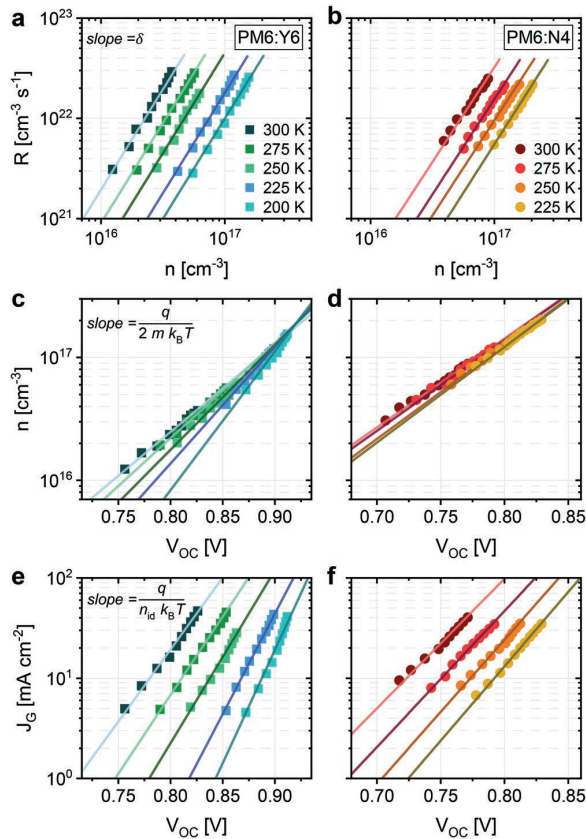


Figure 3. Recombination rate as a function of charge carrier density to determine the recombination order δ at different temperatures for a) PM6:Y6 and b) PM6:N4 devices. Charge carrier density as a function of V_{OC} to determine the m -factor at different temperatures for c) PM6:Y6 and d) PM6:N4 devices. Generation current density as a function of V_{OC} to determine the ideality factor n_{id} at different temperatures for e) PM6:Y6 and f) PM6:N4 devices. δ , the m -factor and n_{id} were extracted from the slope of the solid line fits (see equations in the left side panels).

temperature. **Figure 3a,b** shows the recombination rate R as a function of carrier density, measured using BACE, to determine δ for PM6:Y6 and PM6:N4. For both blends, we were able to fit the entire temperature range with a slope close to 2 (see the solid lines in the plots). We also notice that the recombination is slowed down at lower temperatures and the carrier density increases in both blends, which we will discuss in greater detail below. Differences between the blends appear in the charge carrier dependence on V_{OC} as shown in **Figure 3c,d**. While the slope of $\log(n)$ versus V_{OC} becomes larger with lower temperatures in the PM6:Y6 blend, it is nearly constant in PM6:N4. Remarkably, the PM6:N4 data points seem to merge onto one line, which is clearly not the case for PM6:Y6. The same effect is seen in the $\log(J_G)$ versus V_{OC} plots in **Figure 3e,f** where we observe a weak (if any) T-dependence of the slope for PM6:N4.

These findings are summarized in **Figure 4a**, where the parameters δ , m and n_{id} taken from the fits in **Figure 3** are plotted as a function of temperature. The values of the recombination order δ assemble around 2 for both blends, with no

appreciable dependence on temperature. As anticipated for the PM6:Y6 device, m and n_{id} remain constant at values of around 1.2 in the range of 300 K down to 200 K. The temperature independence and values close to 1 support the picture that the recombination of free carriers in PM6:Y6 involves mainly two Gaussians, as we reported before.^[8] This situation is sketched in **Figure 4b**. A possible cause for n_{id} being slightly above one is additional recombination through midgap traps.^[7,3] At 300 K, PM6:N4 has similar values of m and n_{id} as PM6:Y6, close to 1, but as the sample is cooled down, both parameters increase to above 1.4 at 225 K. According to Hofacker and Neher,^[40] it is only when free charges in a Gaussian recombine with trapped charges in an exponential that the recombination order is equal to 2 and independent of temperature, but m and n_{id} depend on T . For this case, $n_{id} = m = \frac{1}{2} \left(1 + \frac{T_0}{T} \right)$.

This equation gives a reasonable fit to the experimental data (dashed gray line in **Figure 4a**), yielding $T_0 = 435$ K. We will discuss the discrepancy to the value from the T-dependent SCLC measurements below. According to SCLC results of PM6:N4 we assign a purely Gaussian shape to the density of electron-transporting states, while the density of hole-transporting states is characterized by an exponential tail (see **Figure 4c** for a schematic presentation of this situation). A possible scenario is that holes become immobilized in the exponential tail of the PM6 HOMO, while electrons move more freely in the Gaussian-shaped DOS of the N4 LUMO. Recombination takes place either at the interdiffused D:A heterojunction or electrons penetrate into the PM6-rich phase via dissolved N4 molecules. As mentioned above, R-SoXS revealed a smaller domain purity in the PM6:N4 blend compared to PM6:Y6, and GIWAXS showed no significant nanostructure between different N4 molecules when blended with PM6 apart from π - π stacking.

2.4. Predicting the Open-Circuit Voltage as a Function of Temperature

The models proposed in **Figure 4b,c** suggest that the two blends will differ in their quasi-Fermi level splitting, $QFLS = E_{F,e} - E_{F,h}$, and with that in their V_{OC} and its dependence on temperature and illumination intensity. For a Gaussian-type HOMO and LUMO, $E_{F,e} = E_{L,A} - \frac{\sigma_{L,A}^2}{2k_B T} + k_B T \ln \frac{n}{N_0}$ and $E_{F,h} = E_{H,D} + \frac{\sigma_{H,D}^2}{2k_B T} - k_B T \ln \frac{p}{N_0}$, with $E_{L,A}$ and $E_{H,D}$ being the center of the respective DOSs. Under the assumption that the electron and hole densities are equal ($n = p$) under illumination at open-circuit conditions, the V_{OC} can be described analytically as

$$q V_{OC} = E_{F,e} - E_{F,h} = E_g - \frac{\sigma_{L,A}^2 + \sigma_{H,D}^2}{2k_B T} + 2k_B T \ln \frac{n}{N_0} \quad (3a)$$

where $E_g = E_{L,A} - E_{H,D}$. As discussed in the Note S4 (Supporting Information), the above expression holds in the limit of an equilibrated population at high enough temperature, where the

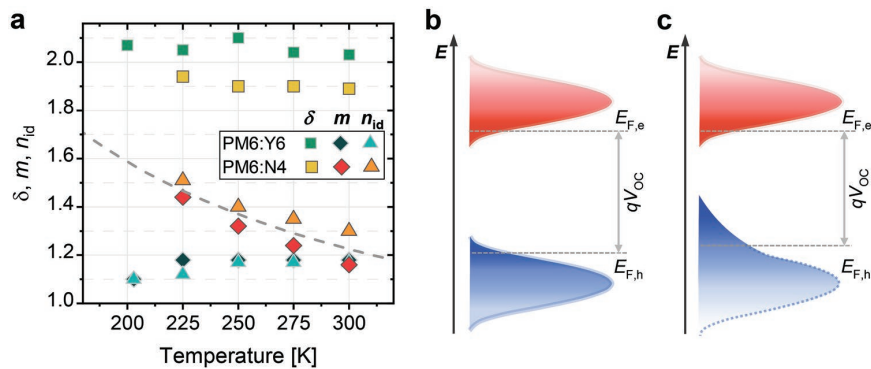


Figure 4. a) Dependencies of the parameters δ , the m -factor and n_{id} on temperature for PM6:Y6 and PM6:N4 devices. δ and the m -factor were obtained from temperature-dependent BACE and n_{id} from temperature-dependent J -Vs. The dashed line is a fit to the PM6:N4 data according to the equation $n_{id} = m = \frac{1}{2} \left(1 + \frac{T_0}{T} \right)$, as predicted for free-trapped recombination in the Gaussian-exponential model. b) Scheme of HOMO and LUMO density distributions for a Gaussian-Gaussian model. c) Model of the HOMO and LUMO for PM6:N4, where recombination is dominated by holes in an exponential tail. $E_{F,e}$ and $E_{F,h}$ are the quasi-Fermi levels for electrons and holes, respectively.

state population can be described by a Boltzmann distribution. This is the case when the quasi-Fermi levels are more than $3k_B T$ away from the so-called equilibrium energies of the Gaussian DOSs. To predict the V_{OC} at low temperatures, the degenerate case has to be considered, for which Paasch et al.^[72] provided an analytical approximation (Note S4 and Figure S14, Supporting Information).

In contrast, for holes in an exponential DOS, there is no distinction between non-degenerate and degenerate regions and $E_{F,h} \cong E_{H,D} - k_B T_0 \ln \frac{p}{N_0}$.^[74] Then, assuming again $n = p$, the V_{OC} expression for the Gaussian-exponential model in the nondegenerate limit is

$$qV_{OC} = E_{F,e} - E_{F,h} = E_g - \frac{\sigma_{L,A}^2}{2k_B T} + k_B (T + T_0) \ln \frac{n}{N_0} \quad (3b)$$

See the Note S4 (Supporting Information) for the corresponding equation in the degenerate regime.

Equation (3a) predicts that for the combination of two Gaussians, the increase of V_{OC} with decreasing temperature due to the entropic contribution becomes partially compensated by the reduction of the effective bandgap, $E_g^{eff} = E_g - \frac{\sigma_{L,A}^2 + \sigma_{H,D}^2}{2k_B T}$, especially at low temperatures. For the Gaussian-exponential case, the temperature dependence of both terms is reduced because $E_{F,h}$ does not depend explicitly on temperature.

These trends are indeed observed in the experimental $V_{OC}(T)$ data plotted in Figure 5a. Not only is the V_{OC} higher for PM6:Y6, due to smaller disorder, but it also displays a steeper slope of the $V_{OC}(T)$ dependence at higher temperatures. For low temperatures, the temperature dependence of V_{OC} becomes smaller for both systems, indicating the transition to the degenerate

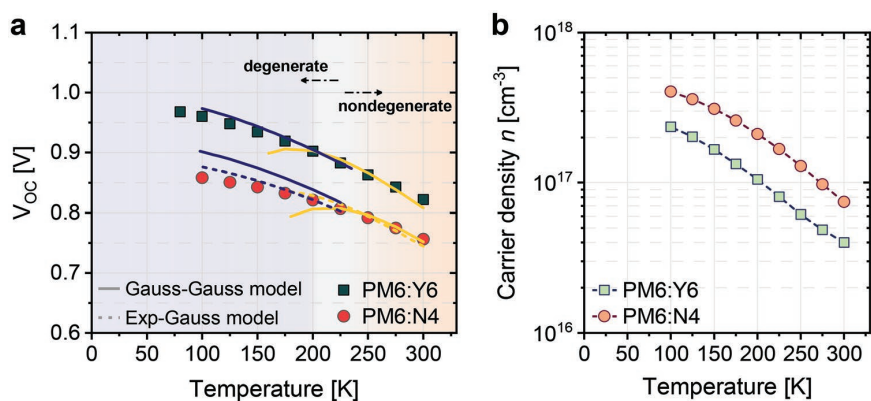


Figure 5. a) Open-circuit voltage V_{OC} as a function of temperature for PM6:Y6 and PM6:N4 devices (full symbols). The experimental data were fitted according to the Gaussian-Gaussian model (full lines) or the Gaussian-exponential model (dashed lines) using the expressions in the non-degenerate and degenerate regions, with the transition marked between 200 and 250 K depending on the blend and charge carrier density. The fitting parameters can be found in Table S3 (Supporting Information). b) Temperature dependence of the charge carrier density n for the blends PM6:Y6 and PM6:N4 devices (symbols), obtained via PIA. Dashed lines are a guide to the eye.

regime. The analytical description of the experimental $V_{OC}(T)$ data requires knowledge of the temperature-dependent carrier density. Determination of n at low temperatures with BACE is problematic as this method relies on the extraction of charges. We have therefore applied PIA spectroscopy, which is an extraction-less technique, with the results shown in Figure 5b for 1 sun illumination conditions. First, we observe that the carrier density n is consistently higher in PM6:N4, in agreement with the smaller k_2 reported above. More importantly, for both blends there is an increase of n over the entire temperature range, being stronger at first from 300 to 200 K.

With $n(T)$ at hand, we are now in a position to analytically describe the progression of the V_{OC} with temperature (Figure 5a). For PM6:Y6 with two Gaussian distributions, $V_{OC}(T)$ was fitted with a combination of Equation (3a); and Equation S3e (Supporting Information); see Note S4 (Supporting Information for the discussion of the applicability of the equations). The fitting parameters are collected in Table S3 (Supporting Information). N_0 was set to the number density of Y6/N4 molecules in the blend ($N_{Y6/N4} = 2.4 \times 10^{20} \text{ cm}^{-3}$)^[55] and the values of $\sigma_{L,A}$ and $\sigma_{H,D}$ were fixed as obtained from SCLC, leaving the HOMO–LUMO gap as the only free parameter. As shown by the solid lines in Figure 5a, this approach explains well the temperature dependence of V_{OC} , yielding a reasonable value for the bandgap, $E_g = 1.42 \pm 0.15 \text{ eV}$. Notably, when the system has fully entered the degenerate regime, the temperature does not appear as an independent variable anymore but influences V_{OC} only through the temperature dependence of the carrier density. Therefore, without knowledge of $n(T)$, the analysis of $V_{OC}(T)$ will likely lead to wrong conclusions. We note a small discontinuity of the predicted $V_{OC}(T)$ from Equation (3a); and Equation S3e (Supporting Information) at the transition from the non-degenerate to the degenerate regions at around 200 K. The reason is that Equation (3a) becomes inaccurate at this transition, but unfortunately, there is no analytical approximation to provide a description of the entire transition region. For the same reason, the bandgap from the fit is slightly different for the high and low temperature regimes.

The fit to the PM6:N4 device with the Gaussian–Gaussian model and the disorder values deduced from SCLC works well in the non-degenerate regime, but the model fails to explain the data in the low temperature region, where it predicts a stronger temperature dependence (Figure 5a). In contrast, the Gaussian-exponential model (Equation (3b); and Equation (S3f), Supporting Information), marked in the plot with dashed lines, reproduces the V_{OC} over the entire temperature range. As detailed above, the lack of a temperature dependence of the (quasi-)Fermi level causes a smaller dependence of the V_{OC} on temperature, exactly as we observe in the PM6:N4 experimental data. The data could be well fitted using $T_0 = 435 \text{ K}$, the value predicted from the $m(T)$ and $n_{id}(T)$ data (Figure 4a). We notice that the V_{OC} does not increase as much as the models would predict toward lower temperatures, in neither PM6:Y6 and PM6:N4 devices. To ensure that the reduction of the V_{OC} is not a consequence of high leakage current,^[75] we compared the light and dark J – V s in Figure S15 (Supporting Information). The dark current decreases with temperature, and it is much lower than the photocurrent at low temperatures. For both systems, at 100 K, subtracting the leakage current from the photo-

current increases the V_{OC} by less than 5 mV, thus we conclude that the leakage effect is negligible. Another potential source of V_{OC} saturation is a low built-in voltage, e.g., due to a too small difference between the electrodes or an injection barrier.^[20,76,77] We, therefore, measured $V_{OC}(T)$ for different illumination intensities (Figure S16, Supporting Information). Instead of converging towards a fixed V_{OC} , changing the intensity leads to a horizontal shift of the $V_{OC}(T)$, with little distortion of the shape. In fact, we could reproduce the entire data set with the parameters determined from the fit to the 1 sun $V_{OC}(T)$ data and assuming that recombination is bimolecular for all temperatures (the carrier density depends strictly on the square root of the intensity). We, therefore, believe that the slight deviation of the measured and predicted V_{OC} at low temperatures has other reasons. We, finally, point out that all published $V_{OC}(T)$ data for the PM6:Y6 blend exhibit very similar behavior, implying that the underlying phenomena are intrinsic to the blend.

3. Discussion

Our data show that energetic disorder has a pronounced effect on the absolute value of the V_{OC} but also on the steepness of its temperature dependence, already at room temperature. Consequently, disorder affects the interpretation of the linear extrapolation of the $V_{OC}(T)$ to $T = 0$, which is typically assigned to the energy of the recombining state; the charge transfer (CT) state (in organic solar cells). For PM6:Y6, the extrapolation gives $qV_{OC}(T = 0 \text{ K}) \cong 1.1 \text{ eV}$. Because of the strong contribution of the NFA singlet excitons to the absorption and emission of this blend, there is yet no accurate value of the CT energy of PM6:Y6. Moreover, because of the energetic disorder, the mean energy of the populated CT state manifold is itself a function of temperature and referring to one CT state energy is meaningless.^[78,79] The situation is similar for PM6:N4, where $qV_{OC}(T = 0 \text{ K}) \cong 1.0 \text{ eV}$ is an unreasonably low value. Therefore, the extrapolation of qV_{OC} will not provide a reasonable estimate of the mean energy of the CT state manifold in these blends.

For PM6:Y6, the temperature-dependent charge transport can be consistently described by a Gaussian-type donor HOMO and acceptor LUMO, with a width of 74 and 60 meV, respectively. This picture is confirmed by the recombination analysis, which yielded n_{id} and m independent of temperature and close to one. Importantly, the very same disorder parameters deduced from transport measurements explain the course of the temperature-dependent V_{OC} . It has been proposed that OSCs are non-equilibrium hot carrier devices, where photogenerated carriers leave the device before they equilibrate in the DOS.^[31,32] While there is consistent proof that hot carriers assist charge extraction for highly disordered blends,^[80] there is a current debate whether the same mechanism is functional at open-circuit conditions.^[28] Very recently, kinetic Monte Carlo (kMC) simulations on a PM6:Y6 blend suggested a 130 meV increase in V_{OC} compared to the case of fully equilibrated charges.^[81] It was also suggested that photogenerated charge carriers exit the device via one of the contacts, followed by reinjection and recombination of equilibrated charge. While we cannot fully rule out that nonequilibrium carriers affect the measured V_{OC} in our devices, we argue that experiments on PM6:Y6 blends without and with electrodes

gave the same recombination rate.^[53] Also, our steady-state approach reproduces the $V_{OC}(T)$ on the basis of the measured carrier densities and disorders, for different illumination intensities, with the HOMO–LUMO splitting as the only unknown parameter. We see this as a strong proof that the QFLS and with that the V_{OC} is mostly determined by equilibrated carriers.

For the PM6:N4 blend, the combination of two Gaussians yields a good prediction for $V_{OC}(T)$ at higher temperatures but does not provide a good fit of the low temperature regime. Here, the combination of a Gaussian-shaped N4 LUMO with a broader PM6 HOMO that has an exponential tail gives a much better description. Again, we find a very similar dependence of the carrier density on fluence for the neat PM6:N4 film and device (Figure S5, Supporting Information), meaning that the recombination properties are not affected by the presence of the electrodes. It is, however, unlikely that the replacement of Y6 by N4 transforms the entire PM6 HOMO into an exponential DOS. Rather than that, we presume that the larger distortion of the PM6 phase in the PM6:N4 blend but also the mixing of N4 molecules into the polymer phase broadens the tail of the DOS. As N4 and Y6 have the same conjugated core, we expect the same electric dipole and quadrupole moment for both molecules. It has been shown that a small concentration of randomly oriented electric dipoles creates a Lorentzian DOS.^[58] Similarly, a random distribution of point charges creates exponential band tails.^[59] Such tail broadening has been experimentally observed in doped organic molecules and polymers.^[62] Further experiments and simulations are needed to reveal the true origin and shape of the PM6 HOMO, which is however beyond the scope of this paper. As a side note, such nonuniform DOS explains why T_0 from the analysis of the SCLC transport is different from the value extracted from the recombination studies. The reason is that the SCLC current is proportional to the density of free charges while, in our model, the recombination concerns mainly charges in the tail of the distribution.

The lower V_{OC} of the PM6:N4 blend is consistent with a picture of equilibrated charges in a broader density of states distribution. This raises the questions whether a similar broadening concerns the CT state manifold. Because of additional disorder of the electrostatic interaction, it is predicted that the distribution of the CT energies is wider than that of the charge-separated states.^[83] Also, the larger morphological disorder at the donor–acceptor interface would potentially broaden the CT DOS.^[29] Unfortunately, the presence of a strong absorption and emission from Y6 excitons prevents the determination of the spectral position and width of the CT emission in PM6:Y6.^[55] In EL measurements, this is observed by injected free charges that are reformed into singlet excitons. Figure S17 (Supporting Information) shows the EL spectra of a PM6:N4 device as a function of temperature. At 300 K, the peak at 1.32 eV corresponds to the N4 singlet but we observe that, as the sample is cooled down, a low energy contribution becomes discernible. The peak is at 1.10 eV at 300 K and it overcomes the singlet below 240 K. This is different in PM6:Y6, where the low energy peak is at ≈ 1.15 eV at 300 K, but the singlet emission dominates at all temperatures.^[55] For both cases, the intensity of the low energy emission is independent of temperature for a given injection current, implying that it originates from the radiative recombination of the main recombining state—the CT state. These results point to

a lower energy of the populated CT manifold in PM6:N4, e.g., due to an overall lower CT energy or by more pronounced state broadening. Energetic disorder is indicated by the redshift of the low energy emission peak in Figure S17 (Supporting Information) with decreasing temperature. With respect to this, recent kMC simulations suggested that free charge encounter forms an athermal CT population, whose mean energy is not simply determined by the CT state properties but in addition by the energy of the encountering charges, which itself is a function of temperature.^[84] Irrespective of the exact mechanism, the data show that for PM6:N4, the offset between the populated CT and singlet state is larger, which explains the lower contribution by singlet emission and why the ELQY is more than one order of magnitude lower in PM6:N4 compared to PM6:Y6 (Figure S3, Supporting Information). This, in turn, explains the nonradiative voltage losses in PM6:N4.

Finally, we find that the free carrier density increases with decreasing temperature in both blends. At V_{OC} , CT states and free carriers (in the charge-separated, CS, state) are in dynamic equilibrium.^[85] Our data suggest that the CT–CS balance shifts toward free charges for a lower T . In other words, the reformation of CT states by free charge encounter is more affected by the lowering of the temperature than the redissociation of these states into free charges. Recent transient absorption and time-resolved photoluminescence experiments suggested that charges in PM6:Y6 have to overcome a substantial Coulomb-barrier to form free carriers, which would favor CT reformation at lower temperatures.^[86] On the other hand, recent simulations showed that this barrier due to mutual Coulomb attraction can be fully compensated by strong band bending across the D:A heterojunction.^[87] Energetic disorder will add complexity to these models as it provides additional low-lying states to host free charges.^[88,89] From the parameters deduced above, we conclude that the mean energy of the populated CS states is never larger than 1.1 eV in PM6:Y6 (see the Note S4 and Figure S14, Supporting Information). This is significantly smaller than the Y6 singlet energy and, according to the EL spectra, lower than the populated CT energy. As such, energetic disorder is likely to contribute to free charge formation in such high-performance NFA-based blends.

4. Conclusion

In summary, by comparing the temperature-dependent charge transport and recombination properties of PM6 blended with two Y-series NFAs, Y6, and N4, we show that energetic disorder plays an important role even in high-efficiency organic solar cells. Studies of the blend morphology reveal a different packing and larger structural disorder in the PM6:N4 blend, which translates into a larger energetic disorder but also different shape of the density of states distributions. This is confirmed by temperature-dependent BACE and JV measurements, which reveal that the blends exhibit different nongeminate recombination mechanism: in PM6:Y6, recombination occurs between carriers in two rather narrow Gaussian state distributions, while in PM6:N4, recombination is predominantly between carriers in a Gaussian-shaped LUMO DOS with carriers in the tail of a broader HOMO DOS with a more exponential character. This information combined with the carrier densities from photoinduced

absorption allows us to analytically describe the V_{OC} as a function of temperature and illumination intensity. Hereby, we find that the free carrier density increases with decreasing temperatures in both PM6:Y6 and PM6:N4, indicative of a down-hill driving force for free charge formation assisted by energetic disorder. Regarding the CT properties, electroluminescence measurements reveal a red-shifted CT emission in PM6:N4 compared to PM6:Y6, which becomes predominant over the singlet at low temperatures. This points to a lower energy of the populated CT state manifold, possibly due to a wider distribution of the CT energies in this more disordered blend, which goes along with a larger nonradiative voltage loss in PM6:N4. We conclude that energetic disorder has to be taken into account when considering the absolute value of the V_{OC} but also the steepness of its temperature dependence, and that the treatment of recombination and related properties with single CT and charge transporting levels is inappropriate. In this regard, PM6:Y6 benefits substantially from a narrower Gaussian-type density of state distribution, giving promise for the development of NFA-based solar cells with even smaller V_{OC} losses once the origin of energetic disorder is properly understood.

Supporting Information

Supporting Information is available from the Wiley Online Library or from the author.

Acknowledgements

This work has been funded by the Alexander von Humboldt Foundation (Sofja Kovalevskaja-Award) and from the Deutsche Forschungsgemeinschaft, DFG, German Research Foundation through the project Fabulous (project number 450968074) and HIOS (project number 182087777 – SFB 951), as well as project number 3923306670. E.M.H. and F.E. acknowledge funding from SolarEraNet (No. NFA4R2ROPV). F.E. thanks the Elite Study Program Macromolecular Science within the Elite Network of Bavaria (ENB) for support. This research used the Soft Matter Interfaces Beamline (SMI, Beamline 12-ID) of the National Synchrotron Light Source II, a U.S. Department of Energy (DOE) Office of Science User Facility operated for the DOE Office of Science by Brookhaven National Laboratory under Contract No. DE-SC0012704. This publication is based upon work supported by the King Abdullah University of Science and Technology (KAUST) Office of Sponsored Research (OSR) under Award No: OSR-CARF/CCF-3079. Q.W. and Y.Z. acknowledge National Natural Science Foundation of China (No. 52125306). A.A. acknowledges support from the Welsh Government's Sêr Cymru II Rising Star and Capacity Builder Accelerator Programs through the European Regional Development Fund, Welsh European Funding Office, and Swansea University Strategic Initiative in Sustainable Advanced Materials.

Open access funding enabled and organized by Projekt DEAL.

Conflict of Interest

The authors declare no conflict of interest.

Data Availability Statement

The data that support the findings of this study are available from the corresponding author upon reasonable request.

Keywords

energetic disorder, non-fullerene acceptors, open-circuit voltage, organic solar cells

Received: November 2, 2021

Revised: December 11, 2021

Published online: February 3, 2022

- [1] A. Armin, W. Li, O. J. Sandberg, Z. Xiao, L. Ding, J. Nelson, D. Neher, K. Vandewal, S. Shoaee, T. Wang, H. Ade, T. Heumüller, C. Brabec, P. Meredith, *Adv. Energy Mater.* **2021**, *11*, 2003570.
- [2] Q. Liu, Y. Jiang, K. Jin, J. Qin, J. Xu, W. Li, J. Xiong, J. Liu, Z. Xiao, K. Sun, S. Yang, X. Zhang, L. Ding, *Sci. Bull.* **2020**, *65*, 272.
- [3] Y. Cui, H. Yao, J. Zhang, K. Xian, T. Zhang, L. Hong, Y. Wang, Y. Xu, K. Ma, C. An, C. He, Z. Wei, F. Gao, J. Hou, *Adv. Mater.* **2020**, *32*, 1908205.
- [4] Y. Lin, Y. Firdaus, F. H. Isikgor, M. I. Nugraha, E. Yengel, G. T. Harrison, R. Hallani, A. El-Labban, H. Faber, C. Ma, X. Zheng, A. Subbiah, C. T. Howells, O. M. Bakr, I. McCulloch, S. De Wolf, L. Tsetseris, T. D. Anthopoulos, *ACS Energy Lett.* **2020**, *5*, 2935.
- [5] T. Zhang, C. An, P. Bi, Q. Lv, J. Qin, L. Hong, Y. Cui, S. Zhang, J. Hou, *Adv. Energy Mater.* **2021**, *11*, 2101705.
- [6] F. Liu, L. Zhou, W. Liu, Z. Zhou, Q. Yue, W. Zheng, R. Sun, W. Liu, S. Xu, H. Fan, L. Feng, Y. Yi, W. Zhang, X. Zhu, *Adv. Mater.* **2021**, *33*, 2100830.
- [7] J. Yuan, Y. Zhang, L. Zhou, G. Zhang, H.-L. Yip, T.-K. Lau, X. Lu, C. Zhu, H. Peng, P. A. Johnson, M. Leclerc, Y. Cao, J. Ulanski, Y. Li, Y. Zou, *Joule* **2019**, *3*, 1140.
- [8] L. Perdigón-Toro, H. Zhang, A. Markina, J. Yuan, S. M. Hosseini, C. M. Wolff, G. Zuo, M. Stolterfoht, Y. Zou, F. Gao, D. Andrienko, S. Shoaee, D. Neher, *Adv. Mater.* **2020**, *32*, 1906763.
- [9] G. Zhang, X. K. Chen, J. Xiao, P. C. Y. Chow, M. Ren, G. Kuppang, X. Jiao, C. C. S. Chan, X. Du, R. Xia, Z. Chen, J. Yuan, Y. Zhang, S. Zhang, Y. Liu, Y. Zou, H. Yan, K. S. Wong, V. Coropceanu, N. Li, C. J. Brabec, J. L. Bredas, H. L. Yip, Y. Cao, *Nat. Commun.* **2020**, *11*, 3943.
- [10] L. Zhu, M. Zhang, G. Zhou, T. Hao, J. Xu, J. Wang, C. Qiu, N. Prine, J. Ali, W. Feng, X. Gu, Z. Ma, Z. Tang, H. Zhu, L. Ying, Y. Zhang, F. Liu, *Adv. Energy Mater.* **2020**, *10*, 1904234.
- [11] Z. Bi, K. Chen, L. Gou, Y. Guo, X. Zhou, H. B. Naveed, J. Wang, Q. Zhu, J. Yuan, C. Zhao, K. Zhou, S. Chandrabose, Z. Tang, Y. Yi, J. M. Hodgkiss, L. Zhang, W. Ma, *J. Mater. Chem. A* **2021**, *9*, 16733.
- [12] G. Kuppang, X. K. Chen, J. L. Bredas, *Mater. Today Adv.* **2021**, *11*, 100154.
- [13] N. Tokmoldin, J. Vollbrecht, S. M. Hosseini, B. Sun, L. Perdigón-Toro, H. Y. Woo, Y. Zou, D. Neher, S. Shoaee, *Adv. Energy Mater.* **2021**, *11*, 2100804.
- [14] J. Wu, J. Lee, Y. C. Chin, H. Yao, H. Cha, J. Luke, J. Hou, J. S. Kim, J. R. Durrant, *Energy Environ. Sci.* **2020**, *13*, 2422.
- [15] S. M. Hosseini, N. Tokmoldin, Y. W. Lee, Y. Zou, H. Y. Woo, D. Neher, S. Shoaee, *Sol. RRL* **2020**, *4*, 2000498.
- [16] H. Bässler, *Phys. Status Solidi* **1993**, *175*, 15.
- [17] S. D. Baranovskii, *Phys. Status Solidi* **2014**, *251*, 487.
- [18] A. Hofacker, J. O. Oelerich, A. V. Nenashev, F. Gebhard, S. D. Baranovskii, *J. Appl. Phys.* **2014**, *115*, 223713.
- [19] V. Coropceanu, J. L. Bredas, S. Mehraeen, *J. Phys. Chem. C* **2017**, *121*, 24954.
- [20] J. C. Blakesley, D. Neher, *Phys. Rev. B* **2011**, *84*, 075210.
- [21] D. Credgington, J. R. Durrant, *J. Phys. Chem. Lett.* **2012**, *3*, 1465.
- [22] S. D. Collins, C. M. Proctor, N. A. Ran, T.-Q. Nguyen, *Adv. Energy Mater.* **2016**, *6*, 1501721.
- [23] A. Foertig, A. Baumann, D. Rauh, V. Dyakonov, C. Deibel, *Appl. Phys. Lett.* **2009**, *95*, 052104.

- [24] G. Garcia-Belmonte, J. Bisquert, *Appl. Phys. Lett.* **2010**, *96*, 113301.
- [25] T. Kirchartz, B. E. Pieters, J. Kirkpatrick, U. Rau, J. Nelson, *Phys. Rev. B* **2011**, *83*, 115209.
- [26] F. Etzold, I. A. Howard, R. Mauer, M. Meister, T. D. Kim, K. S. Lee, N. S. Baek, F. Laquai, *J. Am. Chem. Soc.* **2011**, *133*, 9469.
- [27] T. Kirchartz, J. Nelson, *Phys. Rev. B* **2012**, *86*, 165201.
- [28] S. Roland, J. Kniepert, J. A. Love, V. Negi, F. Liu, P. Bobbert, A. Melianas, M. Kemerink, A. Hofacker, D. Neher, *J. Phys. Chem. Lett.* **2019**, *10*, 1374.
- [29] W. Kaiser, A. Gagliardi, *J. Phys. Chem. Lett.* **2019**, *10*, 6097.
- [30] A. Melianas, V. Pranculis, A. Devižis, V. Gulbinas, O. Inganäs, M. Kemerink, *Adv. Funct. Mater.* **2014**, *24*, 4507.
- [31] A. Melianas, F. Etzold, T. J. Savenije, F. Laquai, O. Inganäs, M. Kemerink, *Nat. Commun.* **2015**, *6*, 8778.
- [32] A. Melianas, V. Pranculis, Y. Xia, N. Felekidis, O. Inganäs, V. Gulbinas, M. Kemerink, *Adv. Energy Mater.* **2017**, *7*, 1602143.
- [33] T. Upreti, Y. Wang, H. Zhang, D. Scheunemann, F. Gao, M. Kemerink, *Phys. Rev. Appl.* **2019**, *12*, 064039.
- [34] J. Kurpiers, T. Ferron, S. Roland, M. Jakoby, T. Thiede, F. Jaiser, S. Albrecht, S. Janietz, B. A. Collins, I. A. Howard, D. Neher, *Nat. Commun.* **2018**, *9*, 2038.
- [35] N. R. Tummala, S. Mehraeen, Y. T. Fu, C. Risko, J. L. Brédas, *Adv. Funct. Mater.* **2013**, *23*, 5800.
- [36] N. R. Tummala, Z. Zheng, S. G. Aziz, V. Coropceanu, J. L. Brédas, *J. Phys. Chem. Lett.* **2015**, *6*, 3657.
- [37] H. Cha, Y. Zheng, Y. Dong, H. H. Lee, J. Wu, H. Bristow, J. Zhang, H. K. H. Lee, W. C. Tsoi, A. A. Bakulin, I. McCulloch, J. R. Durrant, *Adv. Energy Mater.* **2020**, *10*, 2001149.
- [38] S. Liu, J. Yuan, W. Deng, M. Luo, Y. Xie, Q. Liang, Y. Zou, Z. He, H. Wu, Y. Cao, *Nat. Photonics* **2020**, *14*, 300.
- [39] J. Yuan, C. Zhang, H. Chen, C. Zhu, S. H. Cheung, B. Qiu, F. Cai, Q. Wei, W. Liu, H. Yin, R. Zhang, J. Zhang, Y. Liu, H. Zhang, W. Liu, H. Peng, J. Yang, L. Meng, F. Gao, S. So, Y. Li, Y. Zou, *Sci. China Chem.* **2020**, *63*, 1159.
- [40] A. Hofacker, D. Neher, *Phys. Rev. B* **2017**, *96*, 245204.
- [41] S. Xie, Y. Xia, Z. Zheng, X. Zhang, J. Yuan, H. Zhou, Y. Zhang, *Adv. Funct. Mater.* **2018**, *28*, 1705659.
- [42] V. V. Brus, N. Schopp, S. Ko, J. Vollbrecht, J. Lee, A. Karki, G. C. Bazan, T. Nguyen, *Adv. Energy Mater.* **2021**, *11*, 2003091.
- [43] C. He, Y. Li, Y. Liu, Y. Li, G. Zhou, S. Li, H. Zhu, X. Lu, F. Zhang, C. Z. Li, H. Chen, *J. Mater. Chem. A* **2020**, *8*, 18154.
- [44] C. Zhang, J. Yuan, K. L. Chiu, H. Yin, W. Liu, G. Zheng, J. K. W. Ho, S. Huang, G. Yu, F. Gao, Y. Zou, S. K. So, *J. Mater. Chem. A* **2020**, *8*, 8566.
- [45] C. Kaiser, O. J. Sandberg, N. Zarrabi, W. Li, P. Meredith, A. Armin, *Nat. Commun.* **2021**, *12*, 3988.
- [46] A. Karki, J. Vollbrecht, A. J. Gillett, S. S. Xiao, Y. Yang, Z. Peng, N. Schopp, A. L. Dixon, S. Yoon, M. Schrock, H. Ade, G. N. M. Reddy, R. H. Friend, T. Q. Nguyen, *Energy Environ. Sci.* **2020**, *13*, 3679.
- [47] P. Wan, X. Chen, Q. Liu, S. Mahadevan, M. Guo, J. Qiu, X. Sun, S.-W. Tsang, M. Zhang, Y. Li, S. Chen, *J. Phys. Chem. Lett.* **2021**, *12*, 10595.
- [48] K. Jiang, Q. Wei, J. Y. L. Lai, Z. Peng, H. K. Kim, J. Yuan, L. Ye, H. Ade, Y. Zou, H. Yan, *Joule* **2019**, *3*, 3020.
- [49] S. Li, C.-Z. Li, M. Shi, H. Chen, *ACS Energy Lett.* **2020**, *5*, 1554.
- [50] J. Kniepert, I. Lange, N. J. van der Kaap, L. J. A. Koster, D. Neher, *Adv. Energy Mater.* **2014**, *4*, 1301401.
- [51] S. M. Hosseini, S. Roland, J. Kurpiers, Z. Chen, K. Zhang, F. Huang, A. Armin, D. Neher, S. Shoaee, *J. Phys. Chem. C* **2019**, *123*, 6823.
- [52] L. Quang Phuong, S. Mehrdad Hosseini, C. Woo Koh, H. Young Woo, S. Shoaee, *J. Phys. Chem. C* **2019**, *123*, 27417.
- [53] L. Q. Phuong, S. M. Hosseini, O. J. Sandberg, Y. Zou, H. Y. Woo, D. Neher, S. Shoaee, *Sol. RRL* **2020**, *5*, 2000649.
- [54] J. Kniepert, A. Paulke, L. Perdigón-Toro, J. Kurpiers, H. Zhang, F. Gao, J. Yuan, Y. Zou, V. M. Le Corre, L. J. A. Koster, D. Neher, *J. Appl. Phys.* **2019**, *126*, 205501.
- [55] L. Perdigón-Toro, L. Quang Phuong, S. Zeiske, K. Vandewal, A. Armin, S. Shoaee, D. Neher, *ACS Energy Lett.* **2021**, *6*, 557.
- [56] S. Dong, T. Jia, K. Zhang, J. Jing, F. Huang, *Joule* **2020**, *4*, 2004.
- [57] L. Hong, H. Yao, Z. Wu, Y. Cui, T. Zhang, Y. Xu, R. Yu, Q. Liao, B. Gao, K. Xian, H. Y. Woo, Z. Ge, J. Hou, *Adv. Mater.* **2019**, *31*, 1903441.
- [58] A. Dieckmann, H. Bässler, P. M. Borsenberger, *J. Chem. Phys.* **1993**, *99*, 8136.
- [59] M. Silver, L. Pautmeier, H. Bässler, *Solid State Commun.* **1989**, *72*, 177.
- [60] K. Vandewal, J. Widmer, T. Heumueller, C. J. Brabec, M. D. McGehee, K. Leo, M. Riede, A. Salleo, *Adv. Mater.* **2014**, *26*, 3839.
- [61] A. Zusan, K. Vandewal, B. Allendorf, N. H. Hansen, J. Pflaum, A. Salleo, V. Dyakonov, C. Deibel, *Adv. Energy Mater.* **2014**, *4*, 1400922.
- [62] U. Rau, *Phys. Rev. B: Condens. Matter Mater. Phys.* **2007**, *76*, 085303.
- [63] N. I. Craciun, J. J. Brondijk, P. W. M. Blom, *Phys. Rev. B: Condens. Matter Mater. Phys.* **2008**, *77*, 035206.
- [64] N. Felekidis, A. Melianas, M. Kemerink, *Org. Electron.* **2018**, *61*, 318.
- [65] G. Zuo, Z. Li, O. Andersson, H. Abdalla, E. Wang, M. Kemerink, *J. Phys. Chem. C* **2017**, *121*, 7767.
- [66] G. Zuo, M. Linares, T. Upreti, M. Kemerink, *Nat. Mater.* **2019**, *18*, 588.
- [67] P. W. M. Blom, M. J. M. de Jong, J. J. M. Vleggaar, *Appl. Phys. Lett.* **1996**, *63*, 3308.
- [68] R. Steyrleuthner, S. Bange, D. Neher, *J. Appl. Phys.* **2009**, *105*, 064509.
- [69] G. A. H. Wetzelaer, M. Kuik, H. T. Nicolai, P. W. M. Blom, *Phys. Rev. B: Condens. Matter Mater. Phys.* **2011**, *83*, 165204.
- [70] D. Rauh, C. Deibel, V. Dyakonov, *Adv. Funct. Mater.* **2012**, *22*, 3371.
- [71] T. Ripolles-Sanchis, S. R. Raga, A. Guerrero, M. Welker, M. Turbiez, J. Bisquert, G. Garcia-Belmonte, *J. Phys. Chem. C* **2013**, *117*, 8719.
- [72] G. Paasch, S. Scheinert, *J. Appl. Phys.* **2010**, *107*, 104501.
- [73] N. Zarrabi, O. J. Sandberg, S. Zeiske, W. Li, D. B. Riley, P. Meredith, A. Armin, *Nat. Commun.* **2020**, *11*, 5567.
- [74] P. Mark, W. Helfrich, *J. Appl. Phys.* **1962**, *33*, 205.
- [75] Y. Tang, J. M. Bjuggren, Z. Fei, M. R. Andersson, M. Heeney, C. R. McNeill, *Sol. RRL* **2020**, *4*, 2000375.
- [76] F. Gao, W. Tress, J. Wang, O. Inganäs, *Phys. Rev. Lett.* **2015**, *114*, 128701.
- [77] A. Spiess, M. List, T. Sarkar, U. Würfel, *Adv. Energy Mater.* **2017**, *7*, 1601750.
- [78] T. M. Burke, S. Sweetnam, K. Vandewal, M. D. McGehee, *Adv. Energy Mater.* **2015**, *5*, 1500123.
- [79] J. Yan, E. Rezasoltani, M. Azzouzi, F. Eisner, J. Nelson, *Nat. Commun.* **2021**, *12*, 3642.
- [80] N. Gasparini, M. Salvador, T. Heumueller, M. Richter, A. Classen, S. Shrestha, G. J. Matt, S. Holliday, S. Strohm, H.-J. Egelhaaf, A. Wadsworth, D. Baran, I. McCulloch, C. J. Brabec, *Adv. Energy Mater.* **2017**, *7*, 1701561.
- [81] T. Upreti, S. Wilken, H. Zhang, M. Kemerink, *J. Phys. Chem. Lett.* **2021**, *12*, 9874.
- [82] P. Pingel, D. Neher, *Phys. Rev. B: Condens. Matter Mater. Phys.* **2013**, *87*, 115209.
- [83] Z. Zheng, N. R. Tummala, T. Wang, V. Coropceanu, J. Brédas, *Adv. Energy Mater.* **2019**, *9*, 1803926.
- [84] G. Zuo, S. Shoaee, M. Kemerink, D. Neher, *Phys. Rev. Appl.* **2021**, *16*, 034027.
- [85] O. J. Sandberg, A. Armin, *J. Phys. Chem. C* **2021**, *125*, 15590.

- [86] C. C. S. Chan, C. Ma, X. Zou, Z. Xing, G. Zhang, H. Yip, R. A. Taylor, Y. He, K. S. Wong, P. C. Y. Chow, *Adv. Funct. Mater.* **2021**, *31*, 2107157.
- [87] S. Karuthedath, J. Gorenflot, Y. Firdaus, N. Chaturvedi, C. S. P. De Castro, G. T. Harrison, J. I. Khan, A. Markina, A. H. Balawi, T. A. Dela Peña, W. Liu, R. Z. Liang, A. Sharma, S. H. K. Paleti, W. Zhang, Y. Lin, E. Alarousu, D. H. Anjum, P. M. Beaujuge, S. De Wolf, I. McCulloch, T. D. Anthopoulos, D. Baran, D. Andrienko, F. Laquai, *Nat. Mater.* **2020**, *20*, 378.
- [88] S. N. Hood, I. Kassal, *J. Phys. Chem. Lett.* **2016**, *7*, 4495.
- [89] S. Athanasopoulos, H. Bässler, A. Köhler, *J. Phys. Chem. Lett.* **2019**, *10*, 7107.

Supporting Information

for *Adv. Energy Mater.*, DOI: 10.1002/aenm.202103422

Understanding the Role of Order in Y-Series Non-Fullerene Solar Cells to Realize High Open-Circuit Voltages

*Lorena Perdigón-Toro, Le Quang Phuong, Fabian Eller, Guillaume Freychet, Elifnaz Saglamkaya, Jafar I. Khan, Qingya Wei, Stefan Zeiske, Daniel Kroh, Stefan Wedler, Anna Köhler, Ardalan Armin, Frédéric Laquai, Eva M. Herzig, Yingping Zou, Safa Shoaee, and Dieter Neher**

Supporting Information

The role of order in Y-series non-fullerene solar cells to realize high open-circuit voltages

Lorena Perdigón-Toro^{1,2}, Le Quang Phuong², Fabian Eller³, Guillaume Freychet⁴, Elifnaz Saglamkaya², Jafar I. Khan⁵, Qingya Wei⁶, Stefan Zeiske⁷, Daniel Kroh⁸, Stefan Wedler⁸, Anna Köhler⁸, Ardalan Armin⁷, Frédéric Laquai⁵, Eva M. Herzig³, Yingping Zou⁶, Safa Shoaee², Dieter Neher^{1}*

1. L. Perdigón-Toro, Prof. D. Neher.

Soft Matter Physics and Optoelectronics, Institute of Physics and Astronomy, University of Potsdam, Karl-Liebknecht-Str. 24-25, 14476 Potsdam-Golm, Germany
E-mail: neher@uni-potsdam.de

2. L. Perdigón-Toro, Dr. L. Q. Phuong, E. Saglamkaya, Prof. S. Shoaee.

Disordered Semiconductor Optoelectronics, Institute of Physics and Astronomy, University of Potsdam, Karl-Liebknecht-Str. 24-25, 14476 Potsdam-Golm, Germany

3. F. Eller, Prof. E.M. Herzig.

Physikalisches Institut, Dynamik und Strukturbildung – Herzig Group, Universität Bayreuth, Universitätsstr. 30, 95447 Bayreuth, Germany

4. Dr. G. Freychet.

NSLS-II, Brookhaven National Laboratory, Upton, New York 11973, USA

5. Dr. J.I. Khan, Prof. F. Laquai.

KAUST Solar Center (KSC), Physical Sciences and Engineering Division (PSE), King Abdullah University of Science and Technology (KAUST), Thuwal 23955-6900, Kingdom of Saudi Arabia

6. Q. Wei, Prof. Y. Zou.

College of Chemistry and Chemical Engineering, Central South University, Changsha, 410083, P.R. China

7. S. Zeiske, Dr. A. Armin.

Sustainable Advanced Materials (Sêr SAM), Department of Physics, Swansea University, Singleton Park, Swansea, SA2 8PP U.K

8. D. Kroh, Dr. S. Wedler, Prof. A. Köhler.

Soft Matter Optoelectronics, Bayreuth Institut of Macromolecular Research (BIMF), and Bavarian Polymer Institute (BPI), University of Bayreuth, Bayreuth 95440, Germany

Experimental section:

Device and sample preparation

The polymer PM6 and the small acceptor molecule Y6 were purchased from 1-Material Inc. The acceptor molecule N4 was synthesized as in Ref.^[1] The solvents chloroform (CHCl₃) and the additive chloronaphthalene (CN) were purchased from Carl Roth and Alfa Aesar, respectively. The devices with a regular configuration were fabricated with a structure ITO/PEDOT:PSS/active layer/PDINO/Ag. Patterned ITO (Lumtec) substrates were cleaned in an ultrasonic bath with acetone, Hellmanex, deionized water and isopropanol for 10 min, followed by microwave plasma treatment (4 min at 200 W). Subsequently, PEDOT:PSS (Clevios AI 4083) was filtered through a 0.2 μm PA filter and spin coated onto ITO at 5000 rpm under ambient conditions to obtain a ~30 nm layer. The PEDOT:PSS coated substrates were thermally annealed at 150°C for 10 min. PM6 and Y6 were dissolved in CHCl₃ to a total concentration of 16 mgmL⁻¹ with a 1 to 1.2 weight ratio, and 0.5% CN (v/v, CN/ CHCl₃) for the devices with additive. In case of PM6 and N4, the materials were dissolved in CHCl₃ to a total concentration of 16 mgmL⁻¹ with a 1 to 1.25 weight ratio and 0.5% CN (v/v, CN/ CHCl₃) as additive. The solutions were stirred for 3 hours inside the glovebox. Then, blends were spin coated (at 2500 rpm for PM6:Y6 and 2000 rpm for PM6:N4) onto the PEDOT:PSS layer to obtain a photoactive layer of thickness of ca. 110 nm, and annealed at 90°C for 5 min. To complete the devices, a very thin layer (~10 nm) of PDINO (1-Material Inc.) was spin coated onto the active layer, from a 1 mgmL⁻¹ solution in methanol (2000 rpm), and 100 nm of Ag as the top electrode were evaporated under a 10⁻⁶-10⁻⁷ mbar vacuum. For devices with semi-transparent cathode, only 45 nm of Ag were evaporated at this stage. The active area of the cells is A = 0.011 cm² for BACE measurement and A = 0.06 cm² for all other measurements.

For photoluminescence measurements of films, solutions of PS:NFA and PM6:NFA were spin coated on glass directly. PM6:NFA solutions were prepared as explained above. NFA and PS (Sigma Aldrich, 35 kDa) were dissolved on CF as well. The weight ratio 1 to 1.2 for the PS:Y6 blend and the ratio 1 to 1.25 for the PS:N4 were maintained.

Current density-voltage characteristics (J-V)

J-V curves were measured using a Keithley 2400 system in a 2-wire source configuration. Simulated AM1.5G irradiation at 100 mWcm⁻² was provided by a filtered Oriol Class AAA Xenon lamp and the intensity was monitored simultaneously with a Si photodiode. The sun simulator is calibrated with a KG5 filtered silicon solar cell (certified by Fraunhofer ISE).

For temperature-dependent measurements, the devices were loaded into a liquid nitrogen-cooled cryostat (Janis) and the temperature was adjusted in a range of 80 K to 300 K using a temperature controller (Lakeshore 335). J-V data were measured using a Keithley 2400 Source Meter in a two-wire configuration and illumination was done using a white LED. An automated filter wheel was used to measure different intensities.

Sensitive external quantum efficiency (s-EQE_{pv})

Sensitive external quantum efficiency (EQE) was measured with a home-built apparatus using a high-performance double grating monochromator (PerkinElmer, Lambda 950) as a light source providing excitation wavelengths from 175 nm up to 3300 nm. The probe light beam was physically chopped at 273 Hz by a multi-blade chopper wheel from Thorlabs (MC2000B). Long-pass filters (Edmunds Optics,

OD 4) were used to filter out remaining stray light, while the device photocurrent was passed through a low noise current-amplifier with variable gain (Femto, DLPCA-200) prior detecting the photocurrent signal with a lock-in amplifier (Stanford Research, SR860). Different electrical bandwidths between 1 Hz and 0.001 Hz were used to increase the dynamic range of the EQE measurement. A NIST-calibrated silicon (Newport, 818-UV) and germanium (Newport, 818-IR) photodiode sensor were used for the calibration process. A detailed description of the EQE apparatus is provided elsewhere.^[2]

Quasi-steady-state photoinduced absorption (PIA) and electromodulation injection absorption (EMIA)

In PIA measurements, the photoexcitation of a 405-nm continuous wave laser diode (Spectral Products) is modulated at a frequency of 570 Hz by an optical chopper (Thorlabs MC2000B). In EM measurements, a square voltage with a frequency fixed at 370 Hz and a tunable amplitude provided by a function generator (Keysight 33210A) is applied to the device. The white light emitted from a tungsten halogen lamp is optically directed into a monochromator (Spectral Products DK240), and the monochromatic light existing from the monochromator is used as the probe light, and focused on the studied device to overlap with the photoexcitation light. The change in the transmitted probe light ΔT induced by the photoexcitation in PIA and the dark injection in EMIA is recorded by a Si photodiode (Thorlabs) and a lock-in amplifier (SR830) and then corrected by a background subtraction. The transmitted probe light T through the unexcited sample is measured by using another optical chopper (Thorlabs MC2000B) to modulate the probe light, the same photodiodes and the lock-in amplifier. Our PIA system has a sensitivity on the order of 10^{-7} .

For temperature-dependent measurements, the devices were loaded into a liquid nitrogen-cooled cryostat (Janis) and the temperature was adjusted in a range of 80 K to 300 K using a temperature controller (Lakeshore 335). J-V data were measured using a Keithley 2400 Source Meter in a two-wire configuration.

Bias-assisted charge extraction (BACE)

In BACE, to establish steady-state conditions, we used a high power 1 W, 445 nm laser diode (insaneware) with a switch-off time of ~ 10 ns. The laser diode was operated at 500 Hz with a duty cycle of 50%, such that illumination lasted 1 ms and the diode was switched off for also 1 ms. During illumination, the device was held at the equivalent V_{OC} using an Agilent 81150A pulse generator. Right after switching-off the laser, a high reverse was applied to the sample by the same fast pulse generator (Agilent 81150A), allowing a fast extraction time of 10-20 ns. The current transients were measured via a 10Ω resistor in series with the sample and recorded with an oscilloscope (Agilent DSO9104H).

For temperature dependent measurements, the device was placed on the cooling finger of a closed cycle helium cryostat (ARS-CS202-X1.AL). The cryostat was heated and evacuated to $\sim 1 \times 10^{-4}$ mbar (Pfeiffer TCP121 Turbo pump and Edwards XDS-10 scroll pump). Electrical connection was done through a home-built amplifier which was directly attached as close as possible to the sample outside the cryostat.

Time-delayed collection field (TDCF)

In TDCF, the device was excited with a laser pulse from a diode pumped, Q-switched Nd:YAG laser (NT242, EKSPILA) with ~ 5 ns pulse duration at a typical repetition rate of 500 Hz. To compensate for

the internal latency of the pulse generator, the laser pulse was delayed and homogeneously scattered in an 85 m long silica fiber (LEONI). Then, charges were generated while the device was held at pre-bias V_{pre} . After a varying delay times, a high reverse bias, V_{coll} , was applied to extract all the charges in the device. V_{pre} and V_{coll} were set by an Agilent 81150A pulse generator through a home-built amplifier, which was triggered by a fast photodiode (EOT, ET-2030TTL). The current flowing through the device was measured via a 10 Ω resistor in series with the sample and recorded with an oscilloscope (Agilent DSO9104H). Great care was taken to avoid free carrier recombination prior to extraction. Therefore, a fast ramp-up (~ 2.5 ns) of the bias was applied.

Electroluminescence (EL) and ELQY

For EL measurements, the device is hold at a constant voltage, using a Keithley 2400, for 1 s. The emission spectra were recorded with an Andor Solis SR393i-B spectrograph with a silicon detector Indium Gallium Arsenide DU491A-1.7 detector. A calibrated Oriel 63355 lamp was used to correct the spectral response. EL spectra were recorded with different gratings with center wavelengths of 800, 1100, and 1400 nm, and merged afterwards.

For absolute EL measurements, a calibrated Si photodetector (Newport) connected to a Keithley 485 picoampere meter were used. The detector, with an active area of ~ 2 cm², was placed in front of the measured pixel with a distance < 0.5 cm, and the total photon flux was evaluated considering the emission spectrum of the device and the external quantum efficiency of the detector. The injected current was monitored with a Keithley 2400.

GIWAXS

The 2D GIWAXS measurements were performed in vacuum at the Soft Matter Interfaces beamline (12-ID) at the National Synchrotron Lightsource II (NSLS-II) at Brookhaven National Laboratory at an energy of 16.1 keV and an angle of incidence of 0.18° (clearly above the critical angle for all materials to probe the bulk). The FWHM of the beam profile was 25 μ m vertically and 250 μ m horizontally. A Pilatus300KW detector with a sample to detector distance of 275 mm was used at different rotational angles to cover a larger q-range. The single pictures were merged and converted into a linear q scale. The samples were prepared on PEDOT:PSS coated Si substrates. Neat films were spin-coated from CF and blends from CN/CF (0.5%v/v), to a thickness of ca. 100 nm. All measurements are averages over 6 positions on the sample each measured for 20 s to reduce effects due to inhomogeneities. Changes in intensity profiles with time were tested for all samples and no beam damage was determined for 20 s of exposure. The presented q-profiles in the vertical and horizontal direction are cake cuts covering a range of 20° being background corrected by the corresponding rescaled cuts of PEDOT:PSS on Si.

All performed fits are Pseudo-Voigt fits, described by the following expression for a single peak:

$$f(q) = A \cdot [\eta \cdot L(q) + (1 - \eta) \cdot G(q)] \text{ with } 0 < \eta < 1$$

$$G(q) = \exp\left[-\ln(2) \cdot \left(\frac{q-c}{b}\right)^2\right], \quad L(q) = \frac{1}{1 + \left(\frac{q-c}{b}\right)^2}$$

Where A is the peak amplitude, c is the peak position, $2b$ is the full width at half maximum of the Pseudo-Voigt peak and η the Pseudo-Voigt mixing parameter. When several peaks were overlapping

the sum of several Pseudo-Voigt peaks was fitted. Moreover, an additional constant background was fitted.

The Pseudo-Voigt mixing parameter η describes the contribution of cumulative disorder (described by a Lorentzian) while the other contribution is due to non-cumulative disorder (described by a Gaussian).^[3] When cumulative as well as non-cumulative contribute, the peak shape is described by a Voigt profile (convolution of Gaussian and Lorentzian), which can be approximated by a Pseudo-Voigt profile.^[3,4] For η close to 0, non-cumulative disorder is dominating and a coherence length can be calculated with the Scherrer equation:

$$L_c = \frac{2\pi \cdot K}{\Delta q} = \frac{2\pi \cdot K}{2b}$$

Where Δq is the full width at half maximum and $K = 0.94$ was chosen as shape factor. For higher η (especially the case for π - π peaks) the peak width is strongly influenced by cumulative disorder leading to significant deviation of the calculated coherence length.^[3,4]

In Figure S7 below, the peak areas of the π - π peak and the amorphous contribution are calculated by integrating the Pseudo-Voigt function obtained by fitting the contributions (fit curves also displayed in Figure S7). Then the ratios between the peak areas of the π - π peak and the amorphous contribution are calculated.

Time-resolved photoluminescence (TRPL)

TRPL measurements were performed using the output of a Chameleon (Coherent AG) fs laser operating at 80 MHz repetition rate. During measurements, thin films were kept in a small nitrogen-filled chamber, and the excitation laser fluence was kept around 500 nJ/cm² at 710 nm wavelength. The PL of the samples was collected by an optical telescope (consisting of two plano-convex lenses) and focused onto the slit of a grating spectrograph (PI Spectra Pro SP2300) and detected with a Streak Camera (Hamamatsu C10910) system with a temporal resolution of about 15 ps. The data was acquired in the photon counting mode using the Streak Camera software (HPDTA) and exported to Origin Pro 2020 for further analysis.

Space charge-limited currents (SCLC)

To prepare electron-only devices with the configuration ITO/ZnO/PM6:NFA/PDINO/Ag, ZnO nanoparticles (Avantama N-10) dissolved on isopropanol were filtered through a 0.45 μ m polytetrafluoroethylene filter and spin coated onto ITO at 5000 rpm for 30 s in air. The ZnO substrates were annealed at 120 °C for 30 min. The layers on top of ZnO are prepared as for solar cell devices. Hole-only devices with the configuration ITO/MoO₃/PM6:NFA/MoO₃/Ag were prepared by evaporating 8 nm of MoO₃ on top of ITO. Then, the active layer was prepared as for solar cell devices, followed by evaporation of 8 nm of MoO₃ under a 10⁻⁶-10⁻⁷ mbar vacuum.

For temperature-dependent measurements, the devices were loaded into a liquid nitrogen-cooled cryostat (Janis) and the temperature was adjusted in a range of 80 K to 300 K using a temperature controller (Lakeshore 335). J-V data were measured using a Keithley 2400 Source Meter in a two-wire configuration.

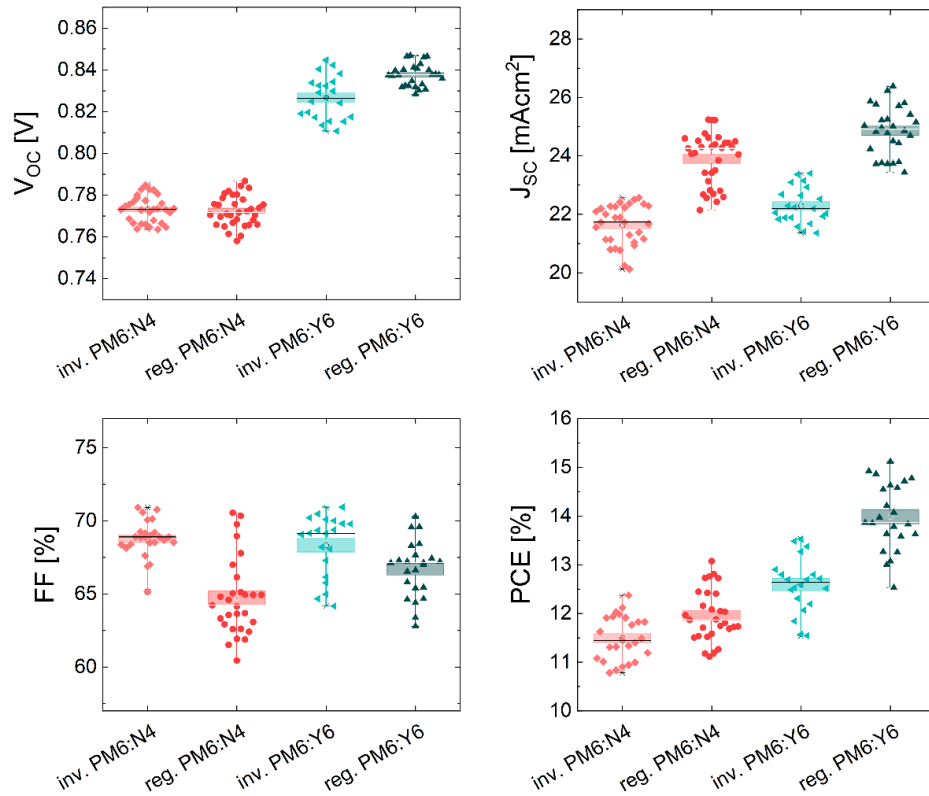


Figure S1: Photovoltaic performance parameters and cell statistics of PM6:Y6 and PM6:N4 in regular and inverted device architecture with fully reflecting electrode (100 nm Ag).

Table S1. Average photovoltaic parameters and standard deviations for PM6:Y6 (1:1.2 w/w CF, additive CN 0.5% v/v, 90°C for 5 min) and PM6:N4 (1:1.25 w/w CF, additive CN 0.5% v/v, 90°C for 5 min) devices with structure ITO/PEDOT:PSS/PM6:NFA/PDINO/Ag(fully reflecting 100nm). Active layer thickness is ca. 110 nm and A=6 mm².

Blend	V_{OC} [V]	J_{SC} [mAcm ⁻²]	FF [%]	PCE [%]
PM6:Y6	0.838 ±0.005	24.9 ±0.8	66.8 ±1.9	14.0 ±0.7
PM6:N4	0.773 ±0.007	23.9 ±0.9	64.7 ±2.6	12.0 ±0.5

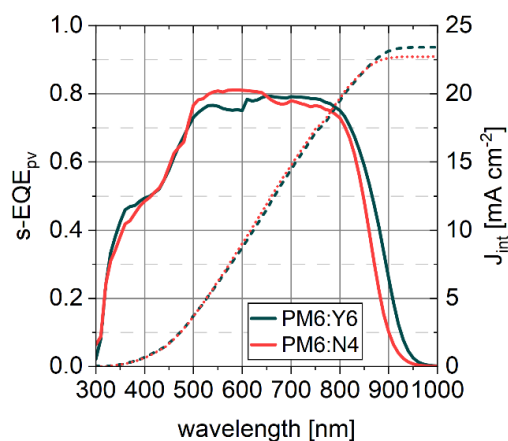


Figure S2: Linear photovoltaic external quantum efficiency (EQEpv), left axis, and the integrated J_{SC} , right axis. The J_{int} for PM6:Y6 is 23.4 mA cm^{-2} , and for PM6:N4 22.7 mA cm^{-2} . The lower integrated values in comparison to those in Table S1 might be due to slight degradation of the samples sent to for sensitive measurements to Swansea.

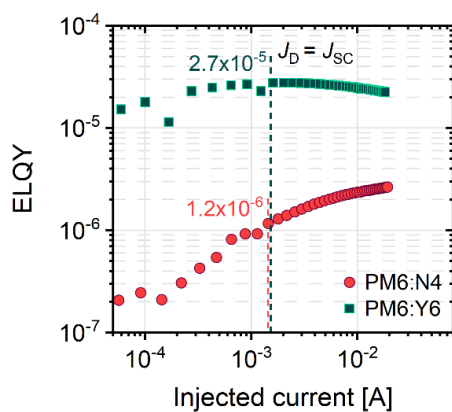


Figure S3: Electroluminescence quantum efficiency (ELQY) as a function of injected current for PM6:Y6 and PM6:N4 regular devices.

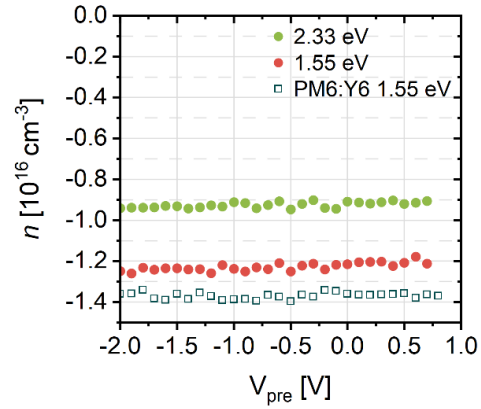


Figure S4: Bias-dependent free charge generation for PM6:N4 measured by TDCF for an excitation of 2.33 eV and 1.55 eV with a low fluence of $0.05 \mu\text{J cm}^{-2}$ and $V_{\text{coll}}=-2.5 \text{ V}$. For comparison, the equivalent measurement of PM6:Y6 at 1.55 eV is shown.

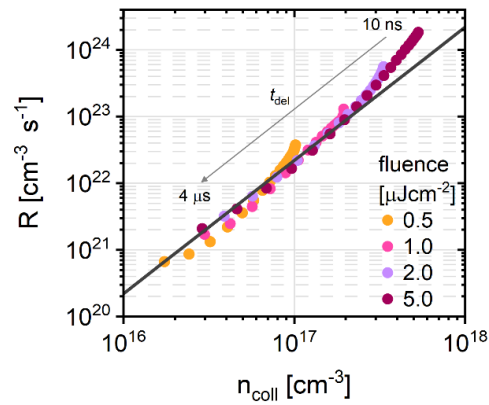


Figure S5: Recombination rate R as a function of the remaining charge in the device (n_{coll}) after a given certain delay time (t_{del}) for a PM6:N4 device by TDCF, for an excitation of 2.0 eV and $V_{\text{pre}}=0.6 \text{ V}$, $V_{\text{coll}}=-2.5 \text{ V}$. The dark line is a fit to $R = k_2 n^2$, with $k_2 = 2.2 \times 10^{-12} \text{ cm}^3 \text{ s}^{-1}$.

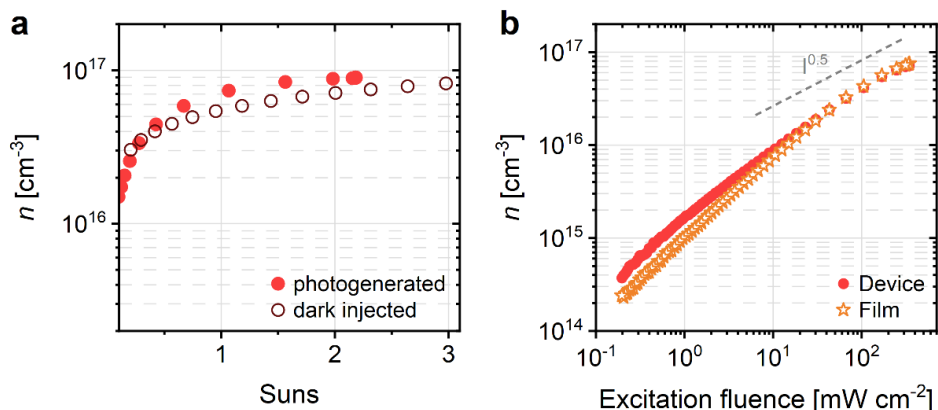


Figure S6: **a** Charge carrier density obtained from excitation-intensity-dependent photoinduced absorption (PIA) spectroscopy (photogenerated, full dots) and electromodulation injection absorption (EMIA) measurements (dark injected charges, open dots) measured for a PM6:N4 regular device with a semi-transparent cathode, both at a photon energy of 1.25 eV. The difference in the carrier concentration under photoexcitation and under dark injection is very little, causing only ~15 meV difference in QFLS at 1 sun. **b** Excitation-intensity-dependent photoinduced absorption (PIA) signals measured for a PM6:N4 regular device and on a PM6:N4 film on glass. The PIA data of the film is calibrated with a factor due to the back reflection from the Ag electrode. The calibration factor is evaluated by measuring the PIA signals with and without the Ag electrode. At 1 sun, we observe bimolecular recombination for both data sets and the agreement in carrier concentration points to small losses of carriers at the transport layer interfaces in the full device.

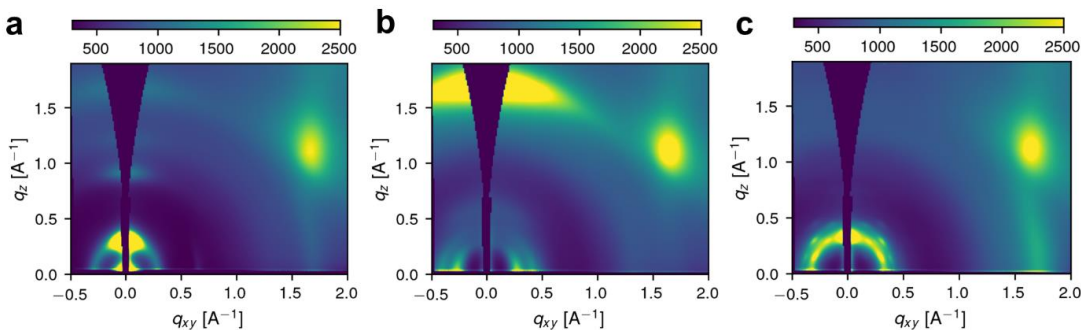


Figure S7: 2D-GIWAXS images of **a** neat PM6, **b** neat Y6 and **c** neat N4, measured on Si substrates (the strong diffraction signal at about $q_{xy}=1.7$ Å⁻¹, $q_z=1.2$ Å⁻¹ is due to substrate scattering).

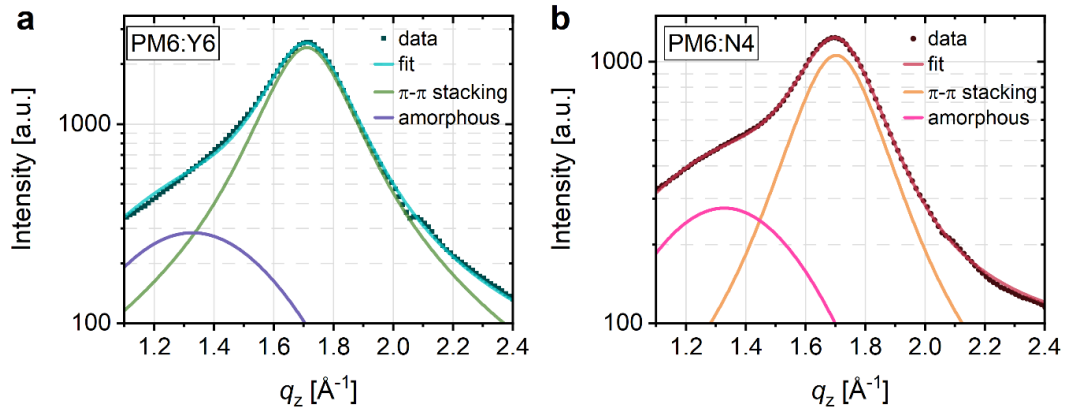


Figure S8: Pseudo-Voigt fits to the normalized vertical π - π stacking peak and the disordered contribution of **a** PM6:Y6 and **b** PM6:N4. The ratio in the vertical direction between the area of the π - π peak and the amorphous contribution is approximately 2.5 for PM6:N4 and 5.4 for PM6:Y6.

Supplementary Note 1. Fitting the TRPL kinetics

To calculate exciton quenching, PL lifetimes of the PM6:NFA blends are parametrized by fitting the experimental data with exponential decay curves. The TRPL of the two PS:NFA can be described by a monoexponential decay, representing the intrinsic lifetime of the exciton. In contrast, the blend TRPL consists of a fast decay, assigned to the quenching of the NFA exciton due to charge transfer at the D:A interface as well as a slow component. The latter may be due to the reformation of NFA excitons from the CT state but also due to the decay of excitons formed within large acceptors clusters which exhibit a longer lifetime. We have shown recently that the steady state PL of the PM6:Y6 blend is governed by such remaining non-dissociated excitons.^[5] To take this into account, the PL decay properties of the blends were described by a weighted-average lifetime^[6]:

$$t_{avg,wt} = \frac{A_1 t_1 + A_2 t_2}{A_1 + A_2}$$

where A is the signal amplitude and t is the decay. The PL quenching efficiency is then calculated by: $1 - (t_{avg,blend}/t_{1,neat})$.

Table S2. Parameters obtained by fitting the time-resolved PL data. A is the signal amplitude and t is the decay. The weighted-average lifetime $t_{avg,wt}$ is calculated as noted above.

Blend	A_1	A_2	t_1 [ps]	t_2 [ps]	$t_{avg,wt}$ [ps]
PS:Y6	0.98		723		723
PM6:Y6	0.78	0.15	47	304	88
PS:N4	0.98		800		800
PM6:N4	0.75	0.20	35	152	60

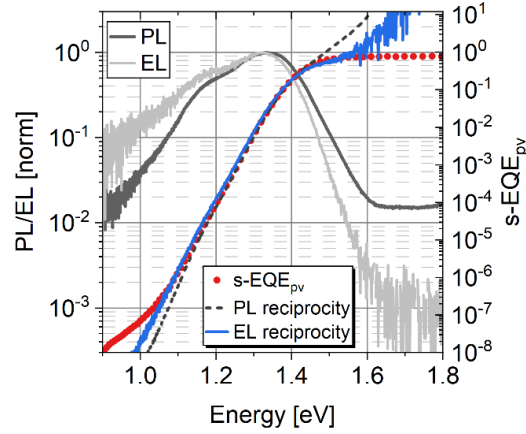


Figure S9: Normalized PL and EL spectra of a regular PM6:N4 device (gray lines, left axis), and sensitive photovoltaic external quantum efficiency (s-EQE_{pv}) of the same PM6:N4 device (dots, right axis). The absorption spectra calculated via the reciprocity relation from the depicted PL and EL are given in dotted black and full blue lines, respectively.

Supplementary Note 2. Space charge limited current (SCLC)

In the SCLC regime, the current density J depends quadratically on the voltage V , following the Mott-Gurney law

$$J = \frac{9}{8} \varepsilon_0 \varepsilon_r \mu \frac{V^2}{d^3} \quad (\text{S1a})$$

where μ is the charge carrier mobility and d is the film thickness. In most cases, the slope of the J - V curve on a double log-scale is larger than 2, due to disorder, traps or field-dependent mobilities.^[7-9] To account for the observed field enhancement, Murgatroyd and Gill (MG) extended Equation S1a, as^[10]

$$J = \frac{9}{8} \varepsilon_0 \varepsilon_r \mu_0 \frac{V^2}{d^3} \exp\left(0.891\gamma\sqrt{\frac{V}{d}}\right) \quad (\text{S1b})$$

with μ_0 being the zero-field mobility and γ , the field enhancement factor. Assuming a Gaussian DOS, the Gaussian disorder model (GDM) can be used to describe the zero-field mobility dependence on temperature T by^[7]

$$\mu_0(T) = \mu_\infty \exp\left[\left(\frac{2}{3} \frac{\sigma}{k_B T}\right)^2\right] \quad (\text{S1c})$$

where μ_∞ is the mobility at infinite temperature and σ is the static Gaussian disorder. k_B is the Boltzmann constant.

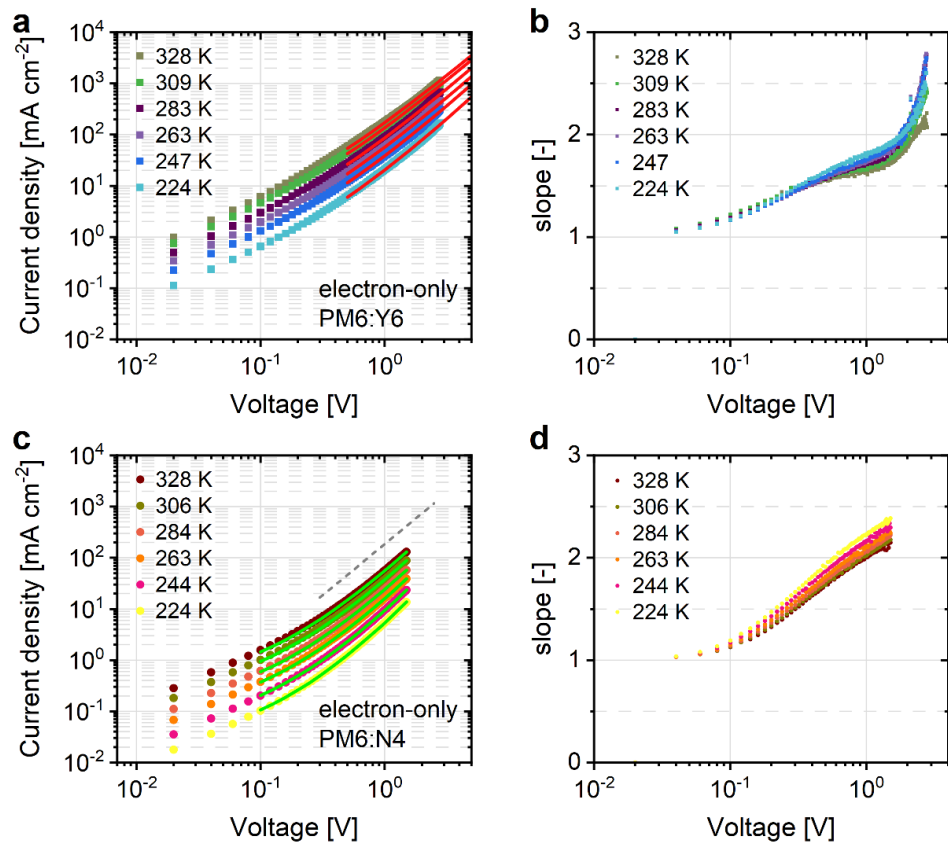


Figure S10: J - V characteristics of electron-only devices (ITO/ZnO/PM6:NFA/PDINO/Ag). **a** PM6:Y6, 150 nm layer (squares) and **c** PM6:N4, 150 nm layer (dots), and the corresponding slope= $d(\log J)/d(\log V)$ vs voltage of **b** PM6:Y6 and **d** PM6:N4. The solid lines in panels a and c are the SCLC fittings with the Murgatroyd and Gill equation.

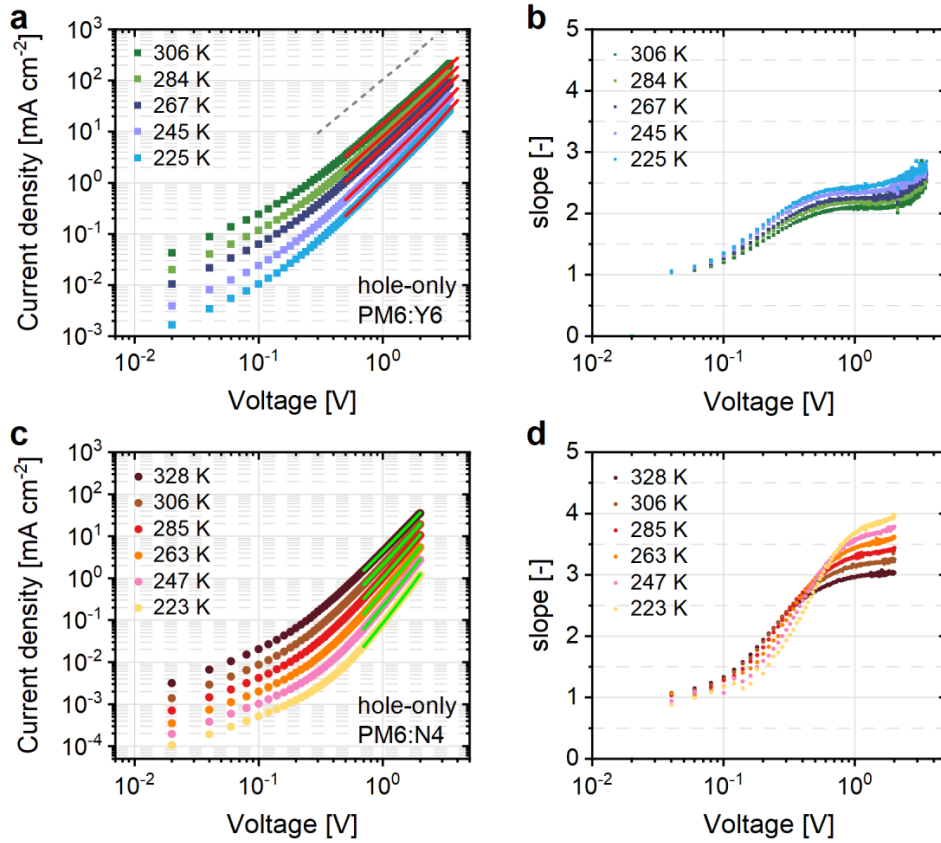


Figure S11: J - V characteristics of hole-only devices (ITO/MoO₃/PM6:NFA/ MoO₃/Ag). **a** PM6:Y6, 170 nm layer (squares) and **c** PM6:N4, 240 nm layer (dots), and the corresponding slope= $d(\log J)/d(\log V)$ vs voltage of **b** PM6:Y6 and **d** PM6:N4. The solid lines in panel **a** and **c** are the SCLC fittings with the Murgatroyd and Gill equation.

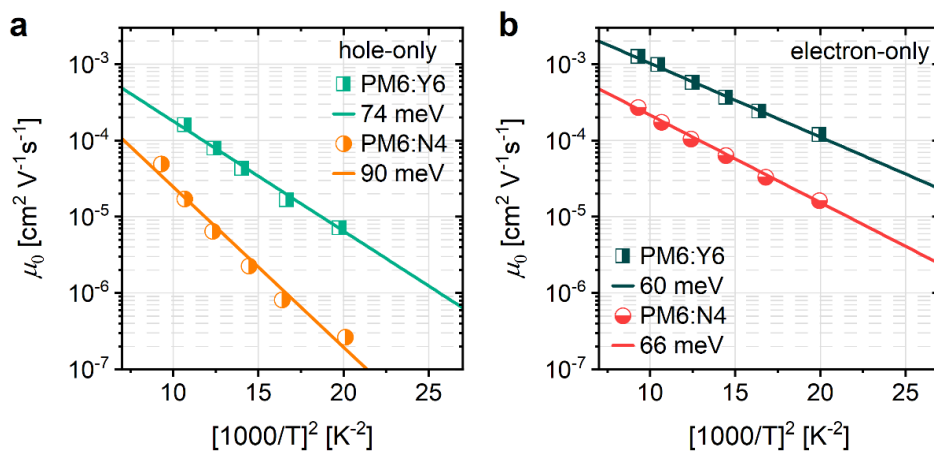


Figure S12: Zero-field charge carrier mobility μ_0 of **a** holes and **b** electrons in the blends PM6:Y6 and PM6:N4. The energetic disorder is calculated from the slope, following Equation S1c.

Supplementary Note 3. Fits to SCLC for an exponential trap distribution

Mark and Helfrich^[11] showed that under the assumption of an exponential trap distribution with a characteristic distribution temperature T_0 , the SCLC current density measured in only-devices follows the equation

$$J = qN_0\mu \left(\frac{l}{l+1} \frac{\epsilon_0\epsilon_r}{qN_t} \right)^l \left(\frac{2l+1}{l+1} \right)^{l+1} \frac{U^{l+1}}{D^{2l+1}} \quad (\text{S2a})$$

where q is the elementary charge, N_0 the effective density of states, N_t the total trap density and μ the trap-free charge mobility. Here, l is defined as $l = T_0/T$. N_t can be determined from the crossing point of all the J - V curves,^[12] which is denoted as V_c and calculated as follows

$$V_c = \frac{qN_t d^2}{2\epsilon_0\epsilon_r} \quad (\text{S2b})$$

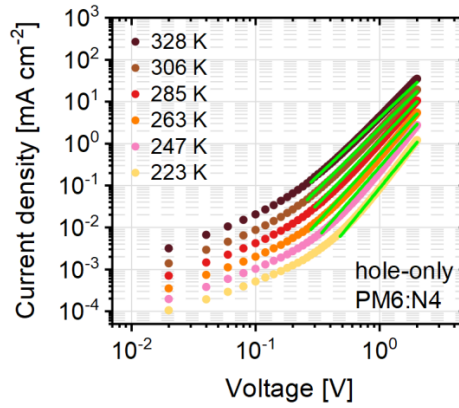


Figure S13: J - V characteristics of a PM6:N4 hole-only device (ITO/MoO₃/PM6:NFA/ MoO₃/Ag), same as in Figure S9c. The solid lines are fits using the Mark and Helfrich expression (see Supplementary Note 2). The fitting parameters are $N_0 = 2.4 \times 10^{20} \text{ cm}^{-3}$, $N_t = 5.5 \times 10^{17} \text{ cm}^{-3}$, $\mu = 1.7 \times 10^{-5} \text{ cm}^2 \text{ V}^{-1} \text{ s}^{-1}$ and $T_0 = 585 \text{ K}$.

Supplementary Note 4. V_{oc} for a Gaussian or exponential DOS

The relation between the (quasi-) Fermi level position and the density of equilibrated charges in a Gaussian DOS is generally described by the Gauss-Fermi integral for which an analytical solution is not available. However, analytical approximations exist for different regimes, as discussed in detail in the sentinel paper by G. Paasch and S. Scheinert.^[13] The case of high temperatures and low enough carrier densities can be described by the non-degenerate case. Here, carriers are situated at around the equilibrium energy, which is $\epsilon_{\infty,e} = E_{L,A} - \frac{\sigma_{L,A}^2}{k_B T}$ for electrons in the acceptor LUMO and

$\epsilon_{\infty,h} = E_{H,D} + \frac{\sigma_{H,D}^2}{k_B T}$ for holes in the donor HOMO, respectively. Also, the (quasi-) Fermi level for electrons (holes) is well below (above) the main carrier energy: $E_{F,e} < \epsilon_{\infty,e}$ and $E_{F,h} > \epsilon_{\infty,h}$. In this case, the Fermi-Dirac distribution can be approximated by the Boltzmann distribution and Eq. 3a in the main manuscript is valid for high enough temperatures. The transition to the degenerate case occurs when the (quasi-) Fermi levels cross the equilibrium energy. This is the case for low temperatures and/or high carrier densities. As a consequence, the mean carrier energy will be no more the equilibrium energy but it will be rather determined by the positions of the quasi-Fermi

levels. In the extreme case, $T = 0K$, the Fermi–Dirac distribution becomes a Heaviside step at the Fermi energy, which now must be situated deep in the DOS for a non-zero carrier density. Then, $E_{F,e} = E_{L,A} - \sqrt{2}\sigma_{L,A} \operatorname{erfc}^{-1}\left(2\frac{n}{N_0}\right)$ and $E_{F,h} = E_{H,D} + \sqrt{2}\sigma_{H,D} \operatorname{erfc}^{-1}\left(2\frac{p}{N_0}\right)$, with no dependence on temperature.

For $T > 0$. Paasch and Scheinert derived the following approximation for the degenerate regime:

$$E_{F,e} = E_{L,A} - \frac{\sqrt{2}\sigma_{L,A}}{H_{L,A}} \operatorname{erfc}^{-1}\left(2\frac{n}{N_0}\right) \quad (\text{S3a})$$

$$E_{F,h} = E_{H,D} + \frac{\sqrt{2}\sigma_{H,D}}{H_{H,D}} \operatorname{erfc}^{-1}\left(2\frac{p}{N_0}\right) \quad (\text{S3b})$$

The functions $H_{L,A}$ and $H_{H,D}$ for the acceptor and the donor are defined as

$$H_{L,A} = \frac{\sqrt{2}}{\sigma_{L,A}} k_B T \operatorname{erfc}^{-1}\left[\exp\left(-\frac{1}{2}\left(\frac{\sigma_{L,A}}{k_B T}\right)^2\right)\right] \quad (\text{S3c})$$

$$H_{H,D} = \frac{\sqrt{2}}{\sigma_{H,D}} k_B T \operatorname{erfc}^{-1}\left[\exp\left(-\frac{1}{2}\left(\frac{\sigma_{H,D}}{k_B T}\right)^2\right)\right] \quad (\text{S3d})$$

Then, under the assumption that the electron and hole densities are equal ($n = p$) under illumination at open-circuit conditions, the V_{OC} can be approximated analytically as

$$qV_{OC} = E_{F,e} - E_{F,h} = E_g - \frac{\sqrt{2}\sigma_{L,A}}{H_{L,A}} \operatorname{erfc}^{-1}\left(2\frac{n}{N_0}\right) - \frac{\sqrt{2}\sigma_{H,D}}{H_{H,D}} \operatorname{erfc}^{-1}\left(2\frac{n}{N_0}\right) \quad (\text{S3e})$$

As pointed out above, the transition between the high temperature non-degenerate case (Eq. 3a of the main manuscript) and low temperature approximation (Eq. S3e) occurs when the quasi-Fermi levels cross the equilibrium energy: $E_{F,e} = \epsilon_{\infty,e}$ and $E_{F,h} = \epsilon_{\infty,h}$. If $n = p$ and the acceptor LUMO has a similar width as the donor HOMO, this transition will occur at the same temperature and carrier density for both electrons and holes. Then, Eq. 3a will be valid for $qV_{OC} = E_{F,e} - E_{F,h} < \epsilon_{\infty,e} - \epsilon_{\infty,h}$ while Eq. S3e must be applied if $qV_{OC} = E_{F,e} - E_{F,h} > \epsilon_{\infty,e} - \epsilon_{\infty,h}$. In **Figure S14** below, we have plotted $\epsilon_{\infty,e} - \epsilon_{\infty,h}$ and qV_{OC} as function of temperature for the parameters derived for the PM6:Y6 blend and simulated for 1 sun conditions. Because of the term $-\frac{\sigma^2}{2k_B T}$, $\epsilon_{\infty,e} - \epsilon_{\infty,h}$ decreases strongly with decreasing temperature while $qV_{OC} = E_{F,e} - E_{F,h}$ increases, also because of the increasing carrier density. The crossing point is around 200 K, moving to higher temperatures for a higher carrier density or a broader DOS.^[13] Therefore, above 200 K, Eq.3a is suited to describe the temperature dependence of the V_{OC} but not below. We note here that Eq. 3a is no more a good approximation of $V_{OC}(T)$ very close to the transition point, where the Boltzmann-distribution is no more valid. In Ref.^[13], Paasch and Scheinert have provided an analytical approximation for the non-degenerate regime, which relates the carrier density to the position of the Fermi-level and temperature. Unfortunately, this relation cannot be inversed to provide the QFLS as a function of n and T .

As pointed out above, in the non-degenerate regime carriers are located at $\epsilon_{\infty,e}$ and $\epsilon_{\infty,h}$, meaning that $\epsilon_{\infty,e} - \epsilon_{\infty,h}$ is the energy of the equilibrated electron-hole pair i.e., the energy of the charge separate state, E_{CS} . To provide an upper limit for E_{CS} in the degenerate regime, we have taken the carrier density at a given temperature, and calculated the QFLS for the given density in the approximation of a step-wise state occupation ($T = 0K$), yielding $(E_{F,e} - E_{F,h})_n$. As expected, qV_{OC}

approximates $(E_{F,e} - E_{F,h})_n$ for low temperatures in **Figure S14**, while the increase of $(E_{F,e} - E_{F,h})_n$ with decreasing temperature mirrors the dependence of the carrier density on temperature.

In case of an exponential distribution, which has a shallower tail, the Fermi level will always dig into the DOS, the mean carrier energy is located close to the quasi-Fermi level and, for a given carrier density, is independent of temperature.^[11] Then, for the case that electrons in a Gaussian DOS recombine with holes in an exponential DOS, only $E_{F,e}(n)$ is explicitly temperature dependent, which for the transition region yields:

$$qV_{OC} = E_{F,e} - E_{F,h} = E_g - \frac{\sqrt{2}\sigma_A}{H_A} \operatorname{erfc}^{-1}\left(2\frac{n}{N_0}\right) + k_B T_0 \ln \frac{n}{N_0} \quad (\text{S3f})$$

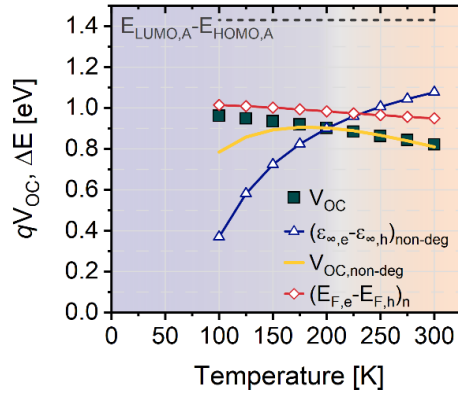


Figure S14: Temperature dependence of the relevant properties for the PM6:Y6 blend describing the transition between the non-degenerate and degenerate regime. $\epsilon_{\infty,e} - \epsilon_{\infty,h}$ is the energy difference between the equilibrium energy of the acceptor LUMO and donor HOMO, representing the energy of the charge-separated (CS) state. The transition to the degenerate regime occurs when this energy crosses the experimental qV_{OC} , representing the QFLS $E_{F,e} - E_{F,h}$. As expected, the non-degenerate model, Eq. 3a, fails to explain the experimental qV_{OC} below the transition temperature. Also shown is $(E_{F,e} - E_{F,h})_n$, which for the given temperature dependence of the carrier density is the Fermi level for a hypothetical step-wise distribution function and serves as an upper limit of the CS energy in the degenerate regime (see Supplementary Note 3).

Table S3: Measured and fitted parameters used to predict the open-circuit voltage as a function of temperature data shown in Figure 5a of the main text. G-G stand for Gauss-Gauss model and Exp-G for exponential-Gauss. For each model the parameters are divided into the non-degenerate (non-deg) and degenerate (deg) regimes. In all calculations, N_0 was set to the number density of Y6/N4 molecules in the blend ($N_{V6} = 2.4 \times 10^{20} \text{ cm}^{-3}$).

PM6:Y6				PM6:N4				
Model	E_g [eV] ^{a)}	σ_{EA} [meV] ^{b)}	σ_{IE} [meV] ^{b)}	Model	E_g [eV] ^{a)}	σ_{EA} [meV] ^{b)}	σ_{IE} [meV] ^{b)}	T_0 [K] ^{b)}
G-G non - deg	1.43	60	74	G-G non - deg	1.41	66	90	-
G-G deg	1.41	60	74	G-G deg	1.37	66	90	-
				Exp-G non - deg	1.34	66	-	435
				Exp-G	1.32	66	-	435

16

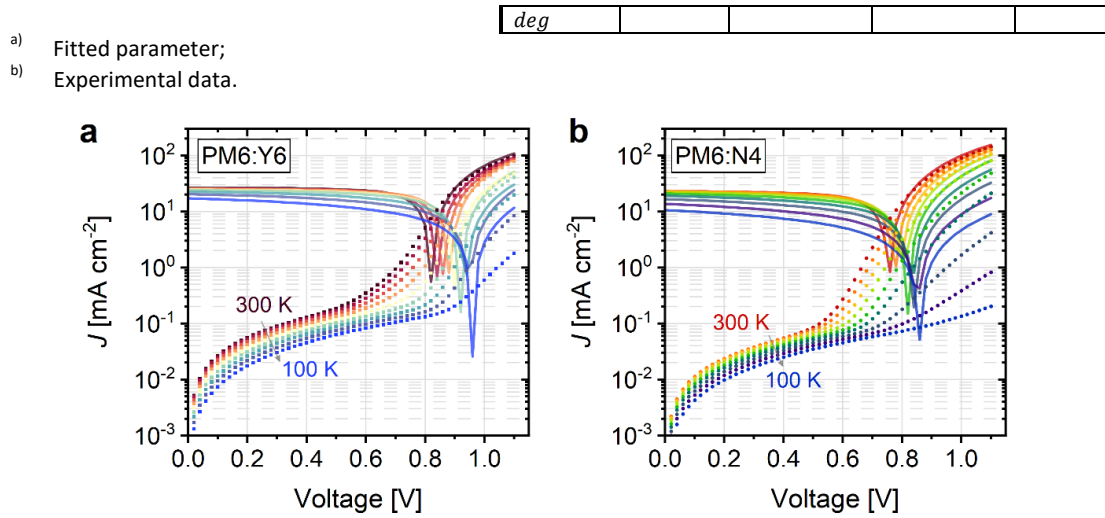


Figure S15: J - V characteristics measured at 1 sun equivalent (solid lines) with white light and in the dark (squares and dots) of **a** PM6:Y6 and **b** PM6:N4. The dark current decreases with temperature and is lower than the photocurrent at low temperatures, which shows that the V_{oc} is not limited by leakage current in this regime.

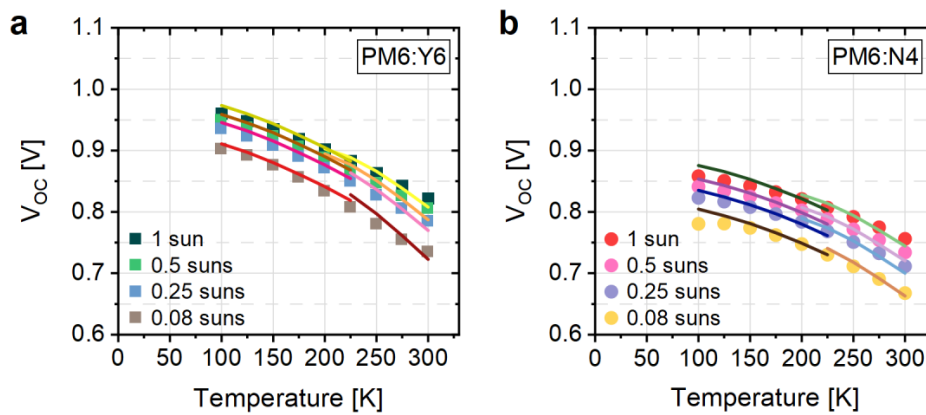


Figure S16: Open-circuit voltage V_{oc} as a function of illumination intensity and temperature for **a** PM6:Y6 and **b** PM6:N4 (full symbols). The experimental data were fitted at 1 sun according to the Gaussian-Gaussian model for PM6:Y6 and the exponential-Gaussian model for PM6:N4 using the expressions in the non-degenerate and degenerate regions, as shown in Figure 5 in the main text (see Supplementary Note 3). To fit the lower intensities, the carrier density at 1 sun was simply reduced by the factor $F = \sqrt{\frac{I_{low}}{I_{1sun}}}$, which assumes bimolecular recombination over all temperatures.

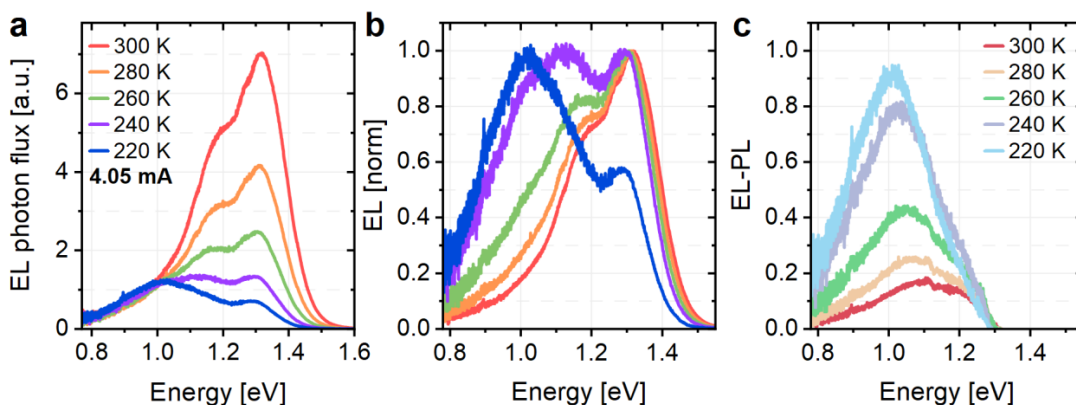
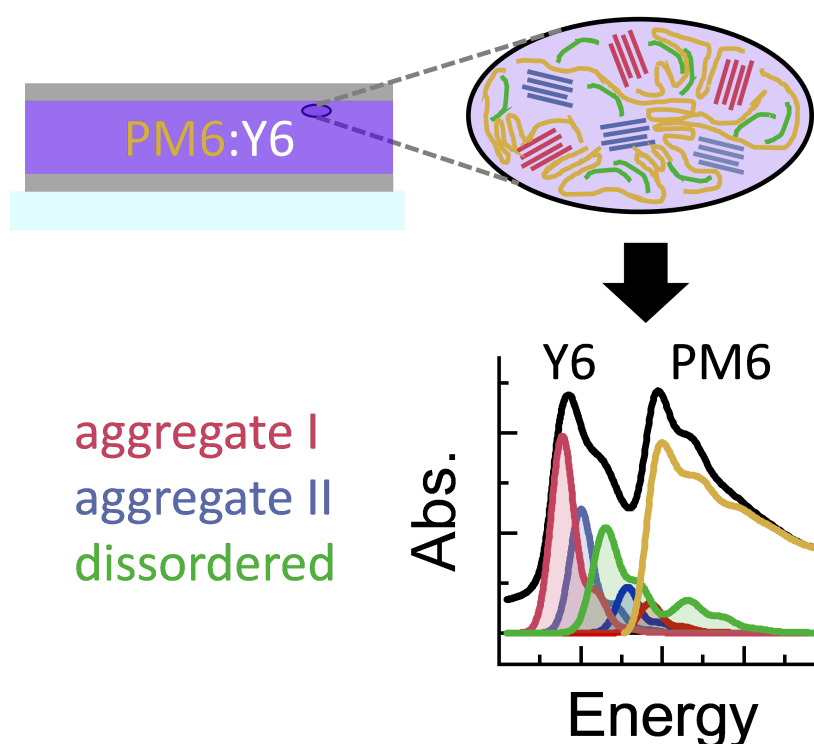


Figure S17: **a** Electroluminescence (EL) spectra as a function of temperature of a regular PM6:N4 device measured at a constant current of 4.05 mA. **b** Normalized EL spectra from panel a. **c** Resulting spectra after subtraction of the photoluminescence (PL) of the device from the normalized EL spectra in panel b. The subtraction reveals a broad emission with a maximum at 1.10 eV at 300 K.

References

- [1] K. Jiang, Q. Wei, J. Y. L. Lai, Z. Peng, H. K. Kim, J. Yuan, L. Ye, H. Ade, Y. Zou, H. Yan, *Joule* **2019**, 3, 3020.
- [2] S. Zeiske, C. Kaiser, P. Meredith, A. Armin, *ACS Photonics* **2020**, 7, 256.
- [3] J. Rivnay, R. Noriega, R. J. Kline, A. Salleo, M. F. Toney, *Phys. Rev. B - Condens. Matter Mater. Phys.* **2011**, 84, 045203.
- [4] T. J. Prosa, J. Moulton, A. J. Heeger, M. J. Winokur, *Macromolecules* **1999**, 32, 4000.
- [5] L. Perdigón-Toro, L. Quang Phuong, S. Zeiske, K. Vandewal, A. Armin, S. Shoaee, D. Neher, *ACS Energy Lett.* **2021**, 6, 557.
- [6] S. Karuthedath, J. Gorenflot, Y. Firdaus, N. Chaturvedi, C. S. P. De Castro, G. T. Harrison, J. I. Khan, A. Markina, A. H. Balawi, T. A. Dela Peña, W. Liu, R. Z. Liang, A. Sharma, S. H. K. Paleti, W. Zhang, Y. Lin, E. Alarousu, D. H. Anjum, P. M. Beaujuge, S. De Wolf, I. McCulloch, T. D. Anthopoulos, D. Baran, D. Andrienko, F. Laquai, *Nat. Mater.* **2020**, 1.
- [7] H. Bässler, *Phys. status solidi* **1993**, 175, 15.
- [8] N. Felekidis, A. Melianas, M. Kemerink, *Org. Electron.* **2018**, 61, 318.
- [9] G. Zuo, Z. Li, O. Andersson, H. Abdalla, E. Wang, M. Kemerink, *J. Phys. Chem. C* **2017**, 121, 7767.
- [10] P. N. Murgatroyd, *J. Phys. D. Appl. Phys.* **1970**, 3, 151.
- [11] P. Mark, W. Helfrich, *J. Appl. Phys.* **1962**, 33, 205.
- [12] R. Steyrlleuthner, S. Bange, D. Neher, *J. Appl. Phys.* **2009**, 105, 064509.
- [13] G. Paasch, S. Scheinert, *J. Appl. Phys.* **2010**, 107, 104501.

12 Identifying the Signatures of Intermolecular Interactions in Blends of PM6 with Y6 and N4 Using Absorption Spectroscopy



Daniel Kroh, **Fabian Eller**, Konstantin Schötz, Stefan Wedler, Lorena Perdigón-Toro, Guillaume Freychet, Qingya Wei, Maximilian Dörr, David Jones, Yingping Zou, Eva M. Herzig, Dieter Neher, and Anna Köhler

Published in
Advanced Functional Materials **2022**, 32, 2205711
(DOI: 10.1002/adfm.202205711)

Reprinted with permission according to the CC BY 4.0 license
Copyright 2022 The Authors. *Advanced Functional Materials* published by Wiley-VCH GmbH



Identifying the Signatures of Intermolecular Interactions in Blends of PM6 with Y6 and N4 Using Absorption Spectroscopy

Daniel Kroh, Fabian Eller, Konstantin Schötz, Stefan Wedler, Lorena Perdigón-Toro, Guillaume Freychet, Qingya Wei, Maximilian Dörr, David Jones, Yingping Zou, Eva M. Herzig, Dieter Neher, and Anna Köhler*

In organic solar cells, the resulting device efficiency depends strongly on the local morphology and intermolecular interactions of the blend film. Optical spectroscopy was used to identify the spectral signatures of interacting chromophores in blend films of the donor polymer PM6 with two state-of-the-art nonfullerene acceptors, Y6 and N4, which differ merely in the branching point of the side chain. From temperature-dependent absorption and luminescence spectroscopy in solution, it is inferred that both acceptor materials form two types of aggregates that differ in their interaction energy. Y6 forms an aggregate with a predominant J-type character in solution, while for N4 molecules the interaction is predominantly in a H-like manner in solution and freshly spin-cast film, yet the molecules reorient with respect to each other with time or thermal annealing to adopt a more J-type interaction. The different aggregation behavior of the acceptor materials is also reflected in the blend films and accounts for the different solar cell efficiencies reported with the two blends.

1. Introduction

The efficiency of organic solar cells (OSCs) has remarkably improved within the last years to power conversion efficiencies surpassing 19% for single layer bulk-heterojunctions,^[1-13] and beyond 20% for tandem cells.^[14] This mainly results from the recent developments of nonfullerene acceptors (NFAs).^[15] The NFAs adjustability in energy levels, electronic structure, and harvesting long-wavelength absorption allowed for significant advances of the solar cell efficiency over that obtained in fullerene-based acceptor devices.^[15-19] This approach proved particularly successful when the so-called Y series acceptors, based on a general A-DA'D-A structure (A = acceptor moiety, D = donor moiety) and absorbing from 1.4 eV onward,

D. Kroh, K. Schötz, S. Wedler, M. Dörr, A. Köhler
Soft Matter Optoelectronics
Experimentalphysik II
University of Bayreuth
95440 Bayreuth, Germany
E-mail: anna.koehler@uni-bayreuth.de

F. Eller, E. M. Herzig
Dynamik und Strukturbildung-Herzig Group
Physikalisches Institut
Universität Bayreuth
Universitätsstr. 30, 95447 Bayreuth, Germany

L. Perdigón-Toro, D. Neher
Soft Matter Physics and Optoelectronics
Institute of Physics and Astronomy
University of Potsdam
Karl-Liebknecht-Str. 24-25, 14476 Potsdam-Golm, Germany

G. Freychet
NLSL-II
Brookhaven National Laboratory
Upton, NY 11973, USA

Q. Wei, Y. Zou
College of Chemistry and Chemical Engineering
Central South University
Chansha 410083, P. R. China

D. Jones
School of Chemistry
Bio21 Institute
The University of Melbourne
30 Flemington Road, Parkville, VIC 3010, Australia

A. Köhler
Bayreuth Institute of Macromolecular Research (BIMF) and Bavarian
Polymer Institute (BPI)
University of Bayreuth
95447 Bayreuth, Germany

The ORCID identification number(s) for the author(s) of this article can be found under <https://doi.org/10.1002/adfm.202205711>.

© 2022 The Authors. Advanced Functional Materials published by Wiley-VCH GmbH. This is an open access article under the terms of the Creative Commons Attribution License, which permits use, distribution and reproduction in any medium, provided the original work is properly cited.

DOI: 10.1002/adfm.202205711

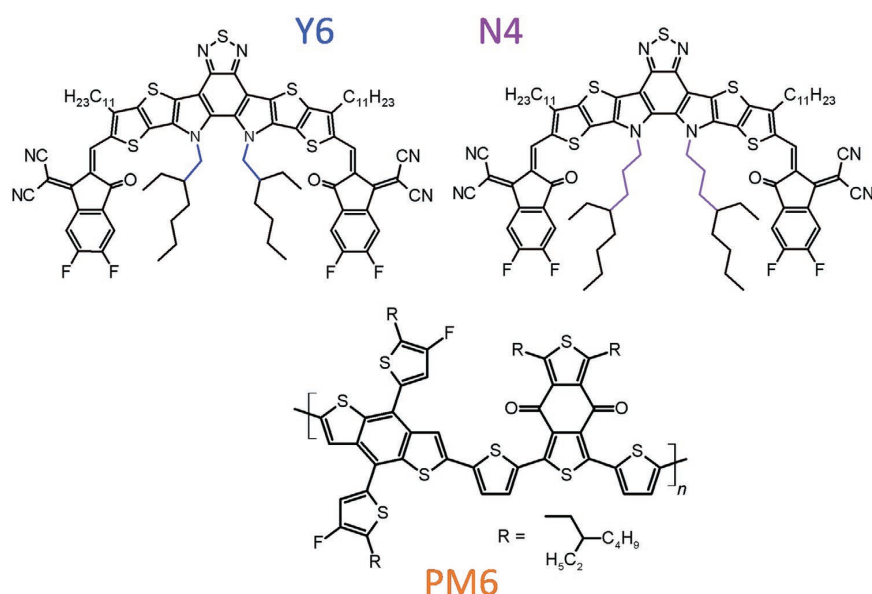


Figure 1. Chemical structures of Y6, N4, and PM6.

are combined with the polymer PM6 or related polymers (Figure 1).^[2–3,20–23] PM6 has a general D- π -A structure with an optical gap around 1.8 eV.

The outstanding performance of these Y-type acceptor materials especially blended with PM6 prompted many groups to dedicate significant effort to understanding the reason behind this. The observed dependence of the device performance on the processing conditions and blend composition suggested a strong role of the molecular arrangements and order in the blend film.^[24–27] This insight was further supported by the observation that side-chain modifications have a great impact on device performance. Side-chain modifications are well-known to alter the aggregation behavior and long-range order.^[23,25–26,28–40]

It is well-known that the performance of OSCs does not only depend on the material itself, but rather on the arrangement and orientation of individual molecules with respect to neighboring molecules. It is the local morphology and the resulting intermolecular interactions that control the energy levels as well as optical and electronic properties of the material, including the efficiency of exciton dissociation and charge extraction in a device.^[41–43] In consequence, the morphology of films with Y-type acceptors has been extensively studied by X-ray scattering. In single crystals, Y6 was found to form a “honeycomb” superstructure. Building blocks of this complex structure were identified in neat films of Y6 and in blend films made with Y6 and PM6. Molecular dynamics (MD) simulations and density functional theory (DFT) calculations allowed pinpointing dimer configurations that can make up these building blocks.^[7,44]

We complement these investigations on Y-type acceptors by identifying the associated intermolecular interactions using optical spectroscopy. This provides information about both, noninteracting and interacting chromophores not only in highly ordered but also in amorphous phases. Our aim is

to elucidate the presence and nature of such interactions in blend films of PM6 with two different Y-type acceptors. This requires first of all a clear identification of the optical signatures of intermolecular interactions in the neat materials. We therefore choose Y6 and N4 as electron acceptor materials (see Figure 1), which merely differ in the position of the branching point of the alkyl sidechains in the bay area of the molecule (2nd position branching of the alkyl side-chains for Y6, 4th position branching for N4).

It has been previously observed that both materials show differences in their long-range order, and thus, we expect concomitant differences in their aggregation behavior and intermolecular interactions that will help to understand the role of the backbone and sidechains.^[26,45] We are ultimately interested in blend films of PM6:Y6 and PM6:N4, which have previously been used by some of us to study the role of structural and energetic disorder on free charge recombination and open circuit voltage (V_{OC}).^[25] For this, we will first identify the signatures of intermolecular interactions that show in solutions upon cooling, which is a well-established approach.^[46–52] Cooling down the solution decreases the quality of the solvent. This induces interactions between the backbones of the sample molecules so that dimers or aggregates form. These interactions result in different absorption and photoluminescence spectra, which allows their identification and provides insight into the nature of the interactions.^[53–54] The spectral signatures of intermolecular interactions in solution will then be used to recognize interacting chromophores in the spectra of neat film of Y6, N4, and PM6, and subsequently in blend films of PM6:Y6 and PM6:N4, which are more complex as the spectra of the components superimpose.

For each of the acceptors, we assign the spectral signatures from two different types of interacting chromophores, one with a larger interaction energy and one with a smaller one, while

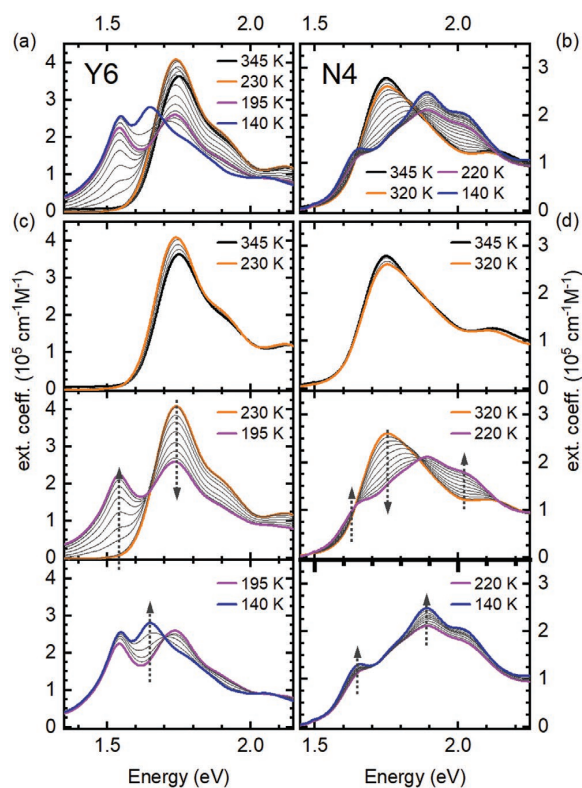


Figure 2. Absorption spectra of a) Y6 (left) and b) N4 (right) in MeTHF at a concentration of 0.15 mg mL^{-1} for different temperatures upon cooling from 345 to 140 K. Spectra taken at characteristic temperatures are drawn with colored solid lines and given in the legend. c,d) Spectra separated in three characteristic temperature ranges, respectively. Arrows indicate spectral changes in each temperature range.

there is only one type of interacting chromophores in the donor polymers PM6.

2. Results

2.1. Y6 and N4 in Solution

Figure 2 shows the absorption of Y6 and N4 in 2-Methyltetrahydrofuran (MeTHF) solution upon cooling from 345 to 140 K. A comparison of the full spectral evolution is shown in **Figure 2a,b**. Based on the spectral evolution of the absorption spectra upon cooling, we can group the spectra into three temperature ranges. These are displayed separately for clarity in **Figure 2c,d**. The corresponding emission spectra are shown in **Figures S1 and S2** (Supporting Information). For Y6, the first characteristic temperature range is between 345 and 230 K (**Figure 2b**). At 345 K, the absorption spectrum has a peak centered at 1.75 eV and a shoulder at 2.90 eV. The linewidth, corresponding to a Gaussian linewidth with $\sigma = 72 \text{ meV}$, is characteristic for noninteracting molecules with a distribution of conformations in solution. Upon cooling, the first absorption

band increases slightly in intensity and shifts to lower energies by 10 meV. This behavior is indicative of an increase in conjugation due to a more planarized molecular backbone.^[46–49,51–52] An additional analysis of the emission spectra and decay times (see **Figures S1–S3**, Supporting Information) confirms that the electronic interactions between the molecules do not change down to 230 K.

The second characteristic temperature range is between 230 and 195 K. In this range, a new spectral feature in absorption appears at 1.54 eV. Concomitantly, the absorption band at 1.75 eV decreases in intensity, resulting in an isosbestic point at 1.64 eV. The appearance of an additional absorption feature, accompanied by an isosbestic point, indicates the transformation of one phase into another. This can be considered as a disorder–order transition with an onset temperature of $T_{\text{onset}} = 230 \text{ K}$, which is the first temperature upon cooling where signatures of aggregates can be observed.^[47–48,51–52] Evidently, individual solvated Y6 molecules start to interact electronically, thus forming physical aggregates. We further observe a rise in the baseline, which is characteristic for light scattering from small particles.

The lowest investigated temperature range between 195 and 140 K is shown on the bottom panel of **Figure 2c**. Below 190 K, there is another phase transition as evidenced by the emergence of a new peak at 1.65 eV, accompanied by a new isosbestic point at 1.70 eV. The observation of a second isosbestic point with $T_{\text{onset}} = 195 \text{ K}$ hints to the formation of a second type of aggregate. This is unusual for organic semiconducting materials in solution and has only been reported in a few cases.^[49,55] This phenomenon will be discussed further after analyzing the spectra in more detail.

The temperature-dependent spectral changes of N4 upon cooling from 345 to 140 K, i.e., the derivative that differs from Y6 merely in the branching point of the side-chains, are displayed in **Figure 2b,d**. Despite this subtle change, a different evolution with temperature compared to Y6 is readily obvious when comparing **Figure 2a,b**. For N4, the first characteristic temperature range is from 345 to 320 K. At 345 K, N4 still shows a similar absorption spectrum to Y6 with a maximum in absorption at 1.75 eV and a shoulder at 1.90 eV. However, in contrast to Y6, the intensity of the absorption band at 1.75 eV does not increase upon cooling but rather decreases. Notably, in the second temperature range, from about 320 K downward, we observe the appearance of additional absorption features at 1.66, at 1.89, and at 2.02 eV, and with two isosbestic points at 1.64 and 1.87 eV. Evidently, there is a phase transition of N4 with an onset temperature at around $T_{\text{onset}} = 320 \text{ K}$. In contrast to Y6, the new phase in N4 is not characterized merely by an obvious new peak at lower energy (1.66 eV), but also by an intense band at higher energy (1.89, 2.02 eV), which is a more unusual observation. We again take these features as indication for the presence of electronically interacting chromophores, such as physical aggregates. In the lowest investigated temperature range, when cooling below 220 K the new absorption features increase in intensity and become more structured, while the intensity of the original contribution at 1.75 eV remains constant. This suggests that the number of aggregates formed remains constant below 220 K, yet the molecules in the aggregates further optimize their geometry, e.g., by planarization.^[47,49,56] In contrast to

Y6, we do not observe the separate appearance of a different type of aggregate below 220 K. Upon heating, the same spectral features are obtained than upon cooling, albeit with a small temperature hysteresis (Figure S4, Supporting Information). We also measured the spectra in chloroform solution for the temperature range from 330 K (close to the boiling point of CF) down to 215 K (close to the melting point of CF), and observe the same trends as detailed in Figure S5 (Supporting Information).

2.2. Spectral Analysis

The temperature-dependent absorption measurements suggest the formation of electronically interacting chromophores when the solubility of the molecule in solution is sufficiently poor. To identify the optical signatures of the interacting chromophores and to disentangle them from the spectra of the noninteracting chromophores, we use Kasha's dimer model as a simple yet sufficient approximation. This is illustrated for reference in Figure 3, though we note that the number of interacting chromophores may be larger than two.^[57] As widely known, in this framework interactions between adjacent molecules lead to an energetic splitting of the excited state, with one energy level above and one below the energy of the excited state of the monomer (see Figure 3). In the case that the dispersion shift is negligible compared to the splitting of the energy levels, the latter are located symmetrically around the energy level of the excited state of the monomer.^[57,58] Frequently, the molecules arrange so that all oscillator strength lies in the transitions to the lower or upper of the two levels, which is referred to as H- or J-type dimers (or aggregates, if more than two molecules are involved), and then consideration of only one level for the interacting chromophores is sufficient. The special curved geometry of the Y-type acceptor molecules however allows for various mutual interaction possibilities and arrangements.^[7] We therefore explicitly consider both energy levels to model the absorption from one type of interacting chromophores.

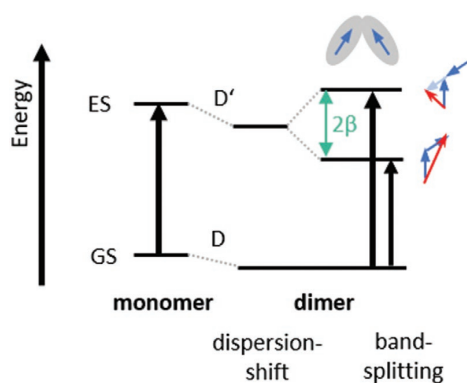


Figure 3. Oblique orientation of the dipoles of two molecules with the energy levels (GS: ground state, ES: excited state) for a monomer and the dimer, considering the dispersion shift $\Delta D = D - D'$ and the effect of the exchange energy β . The resulting transitions are displayed by the black arrows. The blue arrows indicate the transition dipoles of the corresponding molecules, the red arrows the total transition dipole moment.

Thus, to disentangle the different contributions to the absorption spectrum, we model the absorption spectra as a superposition of transitions, represented by Franck–Condon (FC) progressions. We first focus on the absorption spectra at a temperature just above the onset of the phase transition, where only noninteracting molecules prevail (i.e., at $T = 230$ K for Y6, at $T = 320$ K for N4). Based on Raman measurements of Y6,^[59] we use a single effective vibrational mode of $\hbar\omega = 162$ meV for both materials, Y6 and N4. This is justified since the two molecules only differ in the branching point of the alkyl side chains. We use one FC progression for the $S_0 \rightarrow S_1$ transition with a 0-0 energy of 1.74 eV and a second FC progression with the same Gaussian linewidth yet with a different Huang–Rhys parameter for the $S_0 \rightarrow S_2$ transition at about 2.15 eV. For both progressions, the Huang–Rhys parameter was optimized to best match the experimental spectra. The fit parameters are detailed in Table S1 and Figure S6 (Supporting Information).

We next considered the absorption spectra for Y6 at 230 and at 195 K, where we observed the additional absorption from interacting chromophores. To account for transitions to the two possible levels of one type of interacting chromophores, we add two further progressions, on redshifted and one blueshifted relative to the progression of the noninteracting molecules (marked by solid and dashed lines, respectively, in Figure 4). Even though we do not know whether the interacting chromophores are exactly two or maybe more molecules, we shall henceforth refer to them as aggregates in the implicit understanding that the limiting case of a dimer is included in this term. We constrain the two progressions pertaining to the lower and upper level of the aggregate to have the same dominant intramolecular effective vibrational mode of $\hbar\omega = 162$ meV as the noninteracting chromophores, yet since the aggregate may experience a narrower effective disorder, we allow the linewidth to differ from the noninteracting molecule. We further impose a symmetric splitting around the 0-0 energy of the noninteracting molecule, after accounting for a dispersion shift ΔD . It turns out that a satisfactory fit to the experimental data cannot be obtained by considering only one type of aggregate, as detailed further in c.f. Figure S7 (Supporting Information). Rather, a second type of aggregate needs to be included with low intensity. The same modeling approach was used for N4.

Figure 4 shows the spectral decomposition of the absorption spectra in solution of Y6 and N4 at two temperatures, respectively. Table 1 summarizes the Franck–Condon fit parameters for Y6 at 195 K and N4 at 220 K, i.e., 0-0 transition energy E_{00} , Gaussian linewidth parameter σ , Huang–Rhys parameter S_1 , vibrational energy $\hbar\omega$. Values for 140 K and for the S_2 transition of the noninteracting chromophores can be found in the Supporting Information. We name the aggregate with the larger energetic splitting *aggregate I* (colored in red in Figure 4) and the one with smaller splitting *aggregate II* (colored in blue). The indices LE and HE refer to the lower and higher energy level for each aggregate.

There are several noteworthy features. Table 1 allows us to derive the values for the dispersion shift ΔD and the interaction energy β simply by rewriting the 0-0 transition energies to the aggregate as $E_{00} = E_M + \Delta D \pm \beta$. The resulting values are summarized in Table 2, along with an indication of the intensity of the 0-0 transitions relative to that of the amorphous phase at

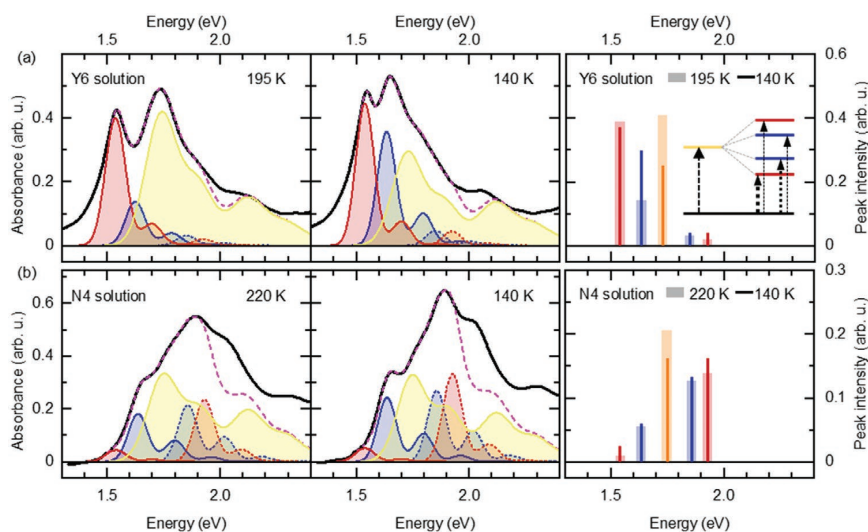


Figure 4. Spectral decomposition of the absorption spectra of a) Y6 and b) N4 in MeTHF solution at characteristic temperatures (195, 140 K for Y6 and 220, 140 K for N4) via a Franck–Condon Fit (detailed description in text). The disordered phase is colored in yellow, aggregate I in red and aggregate II in blue, each with their two progressions energetically below (solid line) and above (dashed line) the disordered phase. The global fit is displayed as pink dashed line. Additionally, we display the fractional intensity of each phase at 195/220 K as transparent bar and at 140 K as solid lines on the right side for both materials. A scheme of the underlying phenomenon of the energy level splitting is displayed in the top right graph.

195 K. The values for ΔD and β obtained for 140 K are almost identical except for the intensity of the transitions and can be found in the Supporting Information.

In summary, for Y6 we find that at 195 and at 140 K two different types of aggregates exist in the solution, in addition to the noninteracting chromophores. The absorption of aggregate I and aggregate II has some oscillator strength to both of the two split energy levels, yet the transition to the lower level dominates, akin to J-type aggregation. On the right side of Figure 4a, the associated intensities are displayed, normalized to sum up to one. The transparent bars show the intensities at 195 K, while the solid lines show the intensities at 140 K. At 195 K, the spectrum is dominated by comparable contributions from aggregate I and from noninteracting chromophores.

Upon cooling to 140 K, the contribution from noninteracting chromophores reduces further and concomitantly that from aggregate I increases, while the amount of aggregate II remains constant. Thus, below 195 K, a disorder–order transition takes place resulting almost without exception in the formation of aggregate II. Evidently, aggregate I has the stronger interaction energy and forms more readily even at a higher temperature, while aggregate II has a lower interaction energy and forms with less ease. As we performed the 140 K measurements on the same solution after the 195 K measurements, we cannot unambiguously distinguish whether aggregation II necessarily requires lower temperatures, i.e., a poorer solvent quality, or whether more time might already be sufficient for its formation.

Figure 4b shows the spectral decomposition of N4 in solution at 220 and 140 K with the corresponding intensities of the different species shown on the right side. We identify transitions to aggregates at about the same energetic positions as

Table 1. The parameters for the FC-progressions used in Figure 4.

	Transition	E_{00} [eV]	σ [meV]	S_1	$\hbar\omega$ [meV]
Y6 in MeTHF 195 K	Noninteracting	1.74	69	0.43	162
	Agg. I, LE	1.54	44	0.15	162
	Agg. I, HE	1.92	44	0.15	162
	Agg. II, LE	1.62	44	0.26	162
	Agg. II, HE	1.85	44	0.26	162
N4 in MeTHF 220 K	Noninteracting	1.74	68	0.55	162
	Agg. I, LE	1.54	44	0.18	162
	Agg. I, HE	1.93	44	0.18	162
	Agg. II, LE	1.64	43	0.40	162
	Agg. II, HE	1.86	43	0.40	162

Table 2. Dispersion shift, interaction energy, and fractional intensity for the aggregates in Y6 and N4 in MeTHF. The fractional intensity is shown for the low energy phase (LE) and high energy phase (HE) of the aggregates, respectively.

	ΔD [meV]	β [meV]	Fractional intensity	
			LE	HE
Y6, Noninteracting 195 K	–	–	0.41	
Y6, Agg. I at 195 K	–15	195	0.39	0.02
Y6, Agg. II at 195 K	–10	110	0.14	0.03
N4, Noninteracting 220 K			0.34	
N4, Agg. I at 220 K	–15	195	0.04	0.23
N4, Agg. II at 220 K	0	110	0.18	0.21

for Y6, and with similar interaction strength, yet with a clearly different intensity distribution. In contrast to Y6, at 220 K, the absorption of *aggregate I* (red) in N4 takes place mainly to the higher energy level, akin to a H-type aggregate, and the absorption to *aggregate II* (blue) takes place with almost equal intensity to both split energy levels.

Upon cooling down to 140 K, the distribution of oscillator strength remains nearly unchanged, except that the intensity of absorption from noninteracting chromophores reduces slightly relative to that from the aggregate. This very different distribution of oscillator strength in N4 compared to Y6 suggests that N4 forms dimers with similar interaction energy as Y6, yet with different relative orientations of the molecules. In simplified terms, one could associate the two aggregates in Y6 with a J-type character, and those in N4 with a more H-type character or oblique orientation of dipole moments. This assignment is consistent with the observed PL intensities (see the Supporting Information).

It is remarkable that this change in orientation of the interacting chromophores as well as the higher onset temperature of N4 is brought about merely by the change in the branching point of the side chain. In N4, the branching point is further away from the backbone than in Y6, reducing steric constraints for the mutual orientation of chromophore backbones and exposing the π -system. We speculate that this, first, increases the likelihood of π - π -stacking allowing for aggregation already at higher temperatures, and second permits a staggered backbone arrangement with partial overlap between donor and acceptor sites in N4, that may be precluded in Y6. The group of Brédas identified several dimer configurations by molecular dynamics simulations, either with more J-like or H-like character, which may correspond to the aggregate configurations observed with our spectroscopic analysis.^[7,44] This will be further discussed below. The observation of several aggregate types is not surprising in Y6 since a complex honeycomb structure has been previously confirmed, which consists of different dimer configurations.^[6–7,60]

2.3. Neat Y6 and N4 Films

Having identified the prevailing aggregates and their spectral characteristics in solution, the next step toward understanding the blend film composition is a spectral analysis of neat films for the acceptor materials, Y6 and N4. **Figure 5a,b** shows the absorption of Y6 and N4 films, spun from a solution of chloroform with 0.5% chloronaphthalene (CN) as-cast (ac, dotted lines) and after thermal annealing for 5 min at 90 °C (TA, blue and purple solid lines, respectively). These preparation conditions are well-known to achieve the best performances in solar cells made with blend films. For reference, the absorption in solution at 140 K is indicated as gray dotted line (sol.).

The first transition band of the neat, as-cast Y6 film has a dominant absorption peak at 1.55 eV with shoulders at 1.68 and 1.91 eV. Centered at 2.5 eV, a weak and structureless second transition band is evident. Annealing the neat Y6 film results in only small changes, where the low energy peak position slightly shifts to lower energies. Comparing the film spectra with the absorption in MeTHF solution at 140 K, it is evident that the observed peak at 1.55 eV and the shoulder at 1.68 eV of the films coincide with the energetic position of the peaks

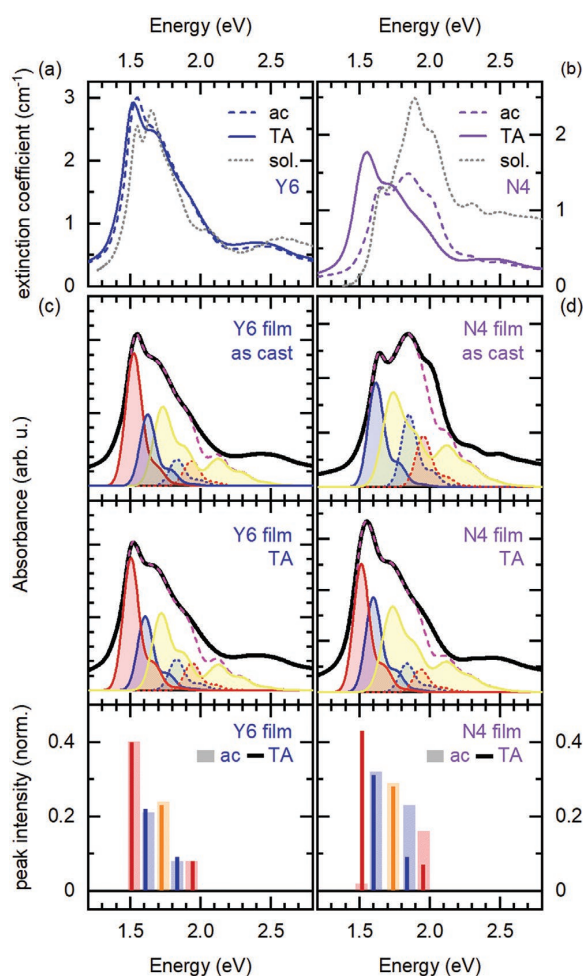


Figure 5. Absorption spectra of as-cast (dashed line) and thermally annealed (solid line) films of a) Y6 and b) N4. Additionally, the absorption in solution at 140 K is depicted (gray, dotted line), respectively. Spectral decomposition of the absorption spectra of the as-cast (top) and thermal annealed (middle) films of c) Y6 and d) N4 via a Franck–Condon Fit (detailed description in text). The disordered phase is colored in yellow, *aggregate I* in red and *aggregate II* in blue, each with their two progressions energetically below (solid line) and above (dashed line) the disordered phase. The global fit is displayed as pink dashed line. For a better comparison, we depict the peak intensity of each phase according to the spectral decomposition of the as-cast (transparent bar) and TA (solid line) film in one graph on the bottom.

of both aggregate types observed in solution, though the peak intensities differ slightly. For N4, the peak positions in the as-cast film also coincide with those in MeTHF at 140 K, yet the relative peak intensities differ strongly. Furthermore, and also in contrast to Y6, the absorption spectrum of the neat N4 film changes drastically in shape and position by thermal annealing, with a dominant lower energy peak emerging. As a result, the annealed N4 film appears similar to the spectrum of the Y6 film. Qualitatively the same spectral change is observed in N4 when, instead of annealing, the as-cast film is left to rest

Table 3. The parameters for the FC-progressions used in Figure 4.

	Phase ^{a)}	E_{00} [eV]	σ [meV]	S_1	$\hbar\omega$ [meV]
Y6 film as-cast	Noninteracting	1.73	64	0.42	162
	Agg. I, LE	1.52	57	0.13	162
	Agg. I, HE	1.93	57	0.13	162
	Agg. II, LE	1.62	55	0.20	162
	Agg. II, HE	1.83	55	0.20	162
N4 film as-cast	Noninteracting	1.73	70	0.48	162
	Agg. I, LE	1.51	55	0.18	162
	Agg. I, HE	1.95	55	0.18	162
	Agg. II, LE	1.61	55	0.20	162
	Agg. II, HE	1.85	55	0.20	162

^{a)}The FC-parameters for the TA films are very similar to the as-cast films for both, Y6 and N4, and can be found in the Supporting Information.

and measured again after 3 months (see Figure S8, Supporting Information). We point out that the extinction coefficient of the annealed Y6 film is almost twice the value of the annealed N4 film. Thus, the difference in the absorption of Y6 and N4 in the film is manifested in two features, that is an overall lower intensity of the N4 absorption, which is not present in solution, and a significant change in shape and position after annealing.

Figure 5c,d shows the spectral decompositions of the neat films, as-cast and thermal annealed, using the same approach as for the spectra in solution. For Y6, we find aggregates with similar energetic positions, Huang–Rhys parameters, coupling strength and even relative intensities in the as-cast or TA films as in solution, as detailed in Tables 3 and 4. Only the linewidth of the aggregates in the film is increased from roughly $\sigma = 44$ meV to $\sigma = 56$ meV when going from solution to film. This testifies that during film formation with the given preparation conditions, Y6 forms the same aggregates as in solution upon cooling. For N4, we also find two types of aggregates, at approximately the same energetic positions as in solution and as in Y6, and with similar Huang–Rhys factors. Even coupling strength and the change in linewidth from solution to film are similar to Y6. The feature that causes the strikingly different absorption in N4 is the different distribution of oscillator strength. Comparing the as-cast film to the MeTHF solution, we see a lesser contribution of the higher aggregate levels, a stronger contribution of the lower level of aggregate II, and, most prominently, a nearly complete absence of the lower level of aggregate I. Upon annealing, this level acquires significant oscillator strength, while that of the upper aggregate levels reduces, so that the distribution of oscillator strength is now closer to the case in Y6. Evidently, annealing N4 causes a significant reorientation of molecules with respect to each other toward a geometry that supports more J-type aggregation.

In summary, upon film formation we observe the formation of aggregates with similar energy levels as in solution. However, we find an overall lower absorption strength in the N4 film compared to the Y6 film, and we observe the signature of a significant change in geometric orientation between individual molecules after annealing. After annealing, the very similar

Table 4. Dispersion shift and interaction energy for the aggregates in Y6 and N4 in film.

		ΔD [meV]	β [meV]	Fractional intensity ^{a)}	
				LE	HE
Y6, as cast	Noninteracting	–	–	0.24	
	Agg. I	–5	205	0.40	0.08
	Agg. II	–5	105	0.21	0.08
Y6, TA	Noninteracting	–	–	0.23	
	Agg. I	+5	220	0.40	0.08
	Agg. II	+10	115	0.22	0.09
N4, as-cast	Noninteracting	–	–	0.29	
	Agg. I	–	215	0.0	0.16
	Agg. II	–5	120	0.32	0.23
N4, TA	Noninteracting	–	–	0.28	
	Agg. I	–5	215	0.43	0.07
	Agg. II	–15	120	0.31	0.09

^{a)}Intensities normalized so that intensities of all phases add up to 1 in the respective as-cast film.

spectra of Y6 and N4 suggest a similar orientation between molecules.

These findings can be compared against results obtained from grazing-incidence wide-angle X-ray scattering (GIWAXS) measurements. Figure 6a shows the 2D maps of the scattering patterns of N4 and Y6 films on silicon, as-cast and after thermal annealing, respectively. Reference measurements on glass, confirming the analogous behavior of the examined materials on both substrate types, can be found in the Supporting Information. Both N4 films, as-cast and thermally annealed, show intensity at around 1.8 \AA^{-1} predominantly in horizontal (q_{xy}) direction. This is indicative for π – π stacking with an edge-on orientation to the substrate. In contrast, the Y6 film shows intensity at around 1.8 \AA^{-1} in vertical (q_z) direction, indicating a π – π stacking in face-on orientation consistent with previous publications.^[2,6,25,61] This difference in backbone orientation between N4 and Y6 accounts for the higher absorption intensity of Y6. Since the transition dipole moment is in the plane of the molecules, more intense absorption is possible for the predominant face-on orientation of Y6 compared to the edge on orientation of N4. The scattering images show no changes in the fundamental orientation upon thermal annealing.

The nature of nanostructure of the aggregates, as obtained from the low q -values, also differs between Y6 and N4 films. The horizontal and vertical cuts at low q -values are shown in Figure 6b. For the Y6 as-cast film we observe multiple clearly defined peaks at 0.22, 0.34, and 0.44 \AA^{-1} in horizontal direction and at 0.52 and 0.62 \AA^{-1} in vertical direction. This suggests a sample containing a complex structure. Upon annealing, only the peak intensities slightly change, which can also arise from small differences of the film thickness. The as-cast N4 film, in contrast, shows only one peak in this q range at 0.32 \AA^{-1}

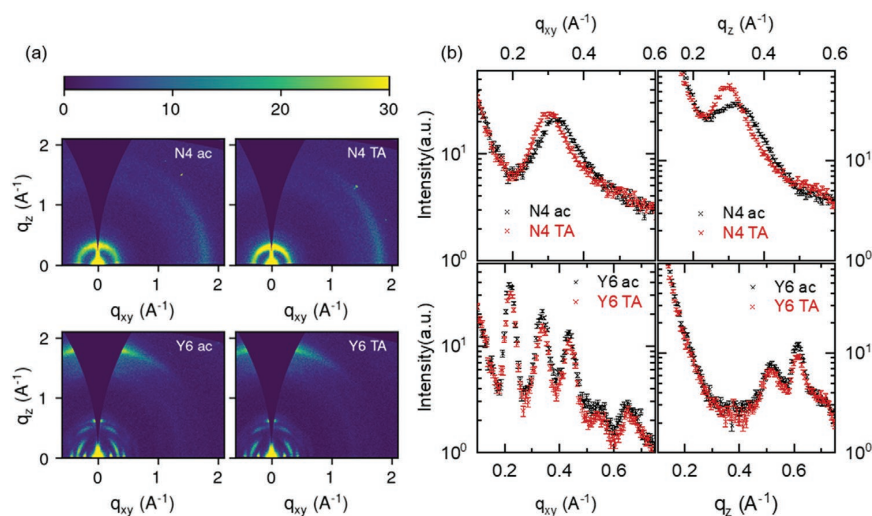


Figure 6. a) 2D-GIWAXS images of N4 (top) and Y6 (bottom) films, as-cast (left) and after thermal annealing (right) measured on Si substrates. b) Horizontal (left) and vertical (right) line cuts of the as-cast and thermal annealed films of N4 (top) and Y6 (bottom).

in horizontal and vertical direction. Hence, there is less pronounced order in as-cast films of N4 compared to Y6 which shows a clear superstructure beyond single molecules. Upon thermal annealing, we observe a significant change in the scattering pattern of N4. The main peak shifts to smaller q -values with a peak at 0.30 \AA^{-1} in both directions. This shift is accompanied by an intensity gain in vertical direction, indicating an increase in the preferred orientation. The change in peak position and intensity suggests a significant adjustment of the nanostructure including an increase of the lattice parameter.

Evidently, the shift to smaller q_z values upon annealing N4 correlates with the redistribution of oscillator strength to the lower aggregate levels, and thus a reorientation of the transition dipole moments. However, as displayed in Figure 5, after annealing, the films of N4 and Y6 are characterized by very similar intermolecular electronic interaction, that is two kinds of predominantly J-like aggregates, in addition to a disordered phase, while they still differ significantly in their nanostructure, as demonstrated by the strikingly different GIWAXS data (Figure 6b). The difference in the formed nanostructures in N4 is even more striking when considering that N4 has aggregates in solution already at room temperature at the start of film formation, so that extended structures could potentially form during the entire drying process. But even in the dried film the structural order is not as well defined for N4 as for Y6 as observed by scattering. This method includes the investigation of structural order beyond individual molecules in contrast to spectroscopy. The Y6 nanostructure shows smaller peak width in the scattering data due to larger coherence lengths which can be translated to a molecular ordering with a range of almost 20 nm, while it is only about 7 nm for N4. This well-defined honeycomb nanostructure occurs during film formation, although Y6 at room temperature does not yet show signatures of aggregation in solution. We speculate that on the one hand, the longer side chains of N4 allow for an easier aggregation of

individual molecules, however, on the other hand these longer side chains also induce steric hindrance such that larger complex nanostructures cannot be formed.

2.4. Aggregation of PM6 in Solution and Film

Having considered the optical and GIWAXS signatures of the acceptor materials, we now investigate the aggregation behavior of the electron donor material PM6. Figure 7 shows the temperature-dependent evolution of the PL and absorption spectra of PM6 in oDCB at a concentration of 0.25 mg mL^{-1} upon cooling from 450 to 270 K. Here, PM6 follows the typical behavior of a conjugated polymer that aggregates upon cooling in solution. It displays an initial redshift upon cooling, followed by the appearance of a lower energy absorption, and a final sharpening of the vibrational structure at lower temperature, here 270 K. The PL intensity reduces as the aggregate absorption grows, which points toward a more H-like character.^[47–48,50–51] Thus, PM6 undergoes a disorder–order transition with an onset temperature at $T_{\text{onset}} = 420 \text{ K}$, i.e., well above room temperature. Above 420 K PM6 has only noninteracting chains. The PL spectrum is broad, which is typical for donor–acceptor polymers.^[62–63] The spectral shape of the PL spectrum from the interacting chains corresponds to the spectra obtained at 270 K. For the absorption spectrum of the interacting chains, the contribution from the noninteracting chains needs to be subtracted (see the Supporting Information).^[49,64] This implies that PM6 is one of the frequently used donor polymers that already contain aggregates in room temperature solution, a feature that has an impact on the resulting morphology in the thin film.^[50–51] For applications such as solar cells, the amount of PM6 aggregates in room temperature solution can be modified through the usual parameters such as choice of solvent, temperature, molecular weight, polydispersity, and other approaches.^[48,65–74]

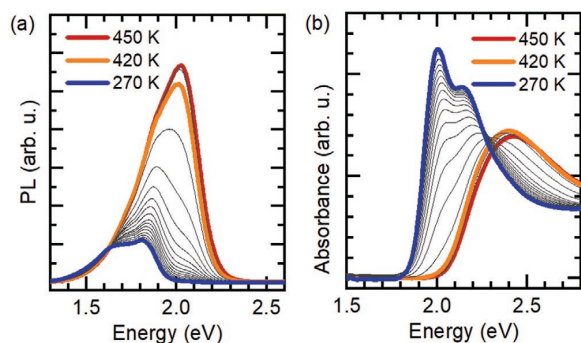


Figure 7. PL a) and absorption b) spectra of PM6 in oDCB at a concentration of 0.25 mg mL^{-1} upon cooling from 450 to 270 K in 10 K-steps. Spectra taken at characteristic temperatures are drawn with colored solid lines and given in the legend.

2.5. Blend Films

With the knowledge of the optical signatures of aggregates in Y6, N4, and PM6, we can now attempt to identify which species exist in blends of PM6:Y6 and PM6:N4. Solar cells made with such blends have previously been compared by Perdigón-Toro et al. They find a higher solar cell efficiency in the PM6:Y6 film, which is mainly a result of a higher open-circuit voltage V_{OC} . Perdigón-Toro et al. attributed this to a lower energetic disorder and higher phase purity in PM6:Y6. Temperature-dependent recombination studies revealed that free charge recombination is merely between a Gaussian-shaped highest occupied molecular orbital (HOMO) of the donor and a Gaussian-type lowest unoccupied molecular orbital (LUMO) density of states (DOS) of the acceptor in PM6:Y6, whereas recombination in PM6:N4 involves a wider Gaussian width of the acceptor LUMO and, in

addition, an exponential tail in the HOMO DOS, causing a significant decrease of the resulting V_{OC} .^[25]

In our work, we use blend films, prepared under the same conditions as Perdigón-Toro et al. and focus on the question how these blends differ regarding their content and nature of aggregated species. We use thermally annealed blend films with a material ratio of 1:1.2 for PM6:Y6 and 1:1.25 for PM6:N4 spun from chloroform with 0.5%/V CN as solvent additive. The absorption of the blend films is shown in **Figure 8a**. For both blend films, we observe two distinct absorption bands around 1.5 eV and around 2.0 eV, respectively, which are due to the absorption of the electron acceptor and the PM6, respectively. The absorption of N4 in the blend appears shifted to slightly higher energies compared to Y6. This suggests differences of the aggregation behavior between the acceptor compounds. The absorption of PM6 looks similar for both films, except for a slight difference in intensity, which may result from the slightly different material mixing ratios.

We can perform a spectral decomposition of the blend absorption by employing the parameters obtained from the Franck-Condon analysis of the neat films. It turns out that all values for the FC progression in Y6 and N4 are nearly identical in the blend and in the thermally annealed neat films (see the Supporting Information). For Y6, this is consistent with the results of molecular dynamics (MD) simulations, which show that the molecular packing of pristine Y6 is largely maintained in the blends.^[7] Differences occur only in the oscillator strength of the aggregates' components and their contribution relative to the noninteracting chains. The fractional intensities of the different aggregate levels are shown in **Figure 8b**.

The most obvious difference in the PM6:Y6 film is a higher contribution of the J-like aggregates relative to the noninteracting chains, and a particularly strong contribution of *aggregate I* (red). This feature has much less intensity in the PM6:N4 film, which accounts for the apparent blueshift of the spectrum.

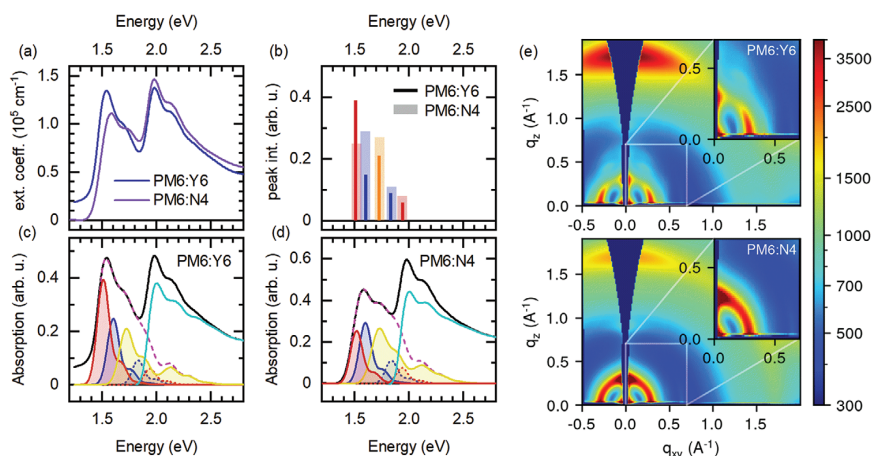


Figure 8. Absorption of TA blend films of a) PM6:Y6 (1:1.2) and PM6:N4 (1:1.25). b) Fractional intensities of the several phases of the acceptor compound in PM6:Y6 (solid line) and PM6:N4 (transparent bars) as obtained from the c,d) spectral decomposition of the absorption spectra of the blend films into a disordered phase of the acceptor compounds Y6 and N4 (dark yellow). The two acceptor aggregated phases (red, blue) with their low energy (solid line) and high energy (dotted line) progressions are shown respectively for N4 and Y6. The absorption contributed to PM6 is drawn with a turquoise line. e) 2D-GIWAXS images of PM6:Y6 (top) and PM6:N4 (bottom) measured on Si substrates. The inset shows a magnification of the low q -range (marked by the white square).

The higher degree of aggregation of Y6 in the blend film and the higher amount of *aggregate I* correlates to the better overall performance of the PM6:Y6 organic solar cell device than PM6:N4, which will be discussed below. The higher contribution of aggregates in the PM6:Y6 film is further consistent with GIWAXS measurements in the PM6:Y6 blend which show signatures of nanostructures arising from Y6 molecules, in contrast to the PM6:N4 film,^[25] as illustrated by the GIWAXS data shown in Figure 8e. Several connected Y6 molecules are required to form such superstructures.

3. Discussion

In recent years, many studies focused on unveiling the structural and morphological properties of Y-type NFA materials and their impact on the photophysical properties when blended with electron donors, such as PM6. For example, X-ray scattering revealed that Y6 and some of its derivatives form a complex “honeycomb” structure in single crystals.^[6–8,60,75] Molecular dynamics simulations show that pristine films of Y6 contain building blocks of this honeycomb structure, which are largely maintained when blended with PM6.^[7,44] Extracted from these simulations, four dimer configurations have been identified with different orientations of the molecular core (C) and terminal (T), as illustrated in Figure 9.

We put our results in context with the structures reported by Kupgan et al.^[44] For all samples in our study, we observe two aggregates, which differ in the interaction energy β and the distribution of the oscillator strength into the two levels. It is tempting to associate the dimers with the larger molecular overlap, i.e., CT–CT and CC–TT with the aggregates I that have a β just above 200 meV (c.f. Table 4), and the dimers with the smaller molecular overlap, such as TT and CT with aggregates II where β takes about half that value. The extent of the molecular overlap in the CC–TT arrangement appears to be similar

to the one in the CT–CT configuration. By visual inspection, it is reasonable to expect the transition dipole moments for CC–TT to align in a parallel fashion thus yielding a predominant H-type character, whereas the more sequential alignment in CT–CT will result in a J-type nature. In this framework, the observed reorientation and change from H-like to J-like character of aggregate I during the thermal annealing of the N4 neat film would correspond to a reorientation from the CC–TT to the CT–CT configuration. In Y6, the formation of a CC–TT orientation seems to be inhibited by the closer position of the side-chain branching to the backbone and its associated steric demand, while it is enabled by the more remote branching point in N4. This conclusion also fits to the observed scattering pattern. Previous spectroscopic and molecular dynamics studies on other D–A-type molecules revealed that for banana shaped molecules, like the shape of the Y-family, there are different pathways for dimer formation that lead to structures with CT–CT or CC–TT character. Which pathway is accessible depends on the steric demand of the sidechains.^[46,76]

The different branching point of the sidechain in N4 compared to Y6 can also account for the higher onset temperature of aggregate formation in MeTHF solution. Less steric hindrance of the sidechains enables electronic interaction of the backbones already at higher temperatures for N4, so that aggregation can occur. This is consistent with the observations by Lei et al. that moving the branching point away from a backbone results in stronger π -stacking interactions.^[77] We consider that this higher onset temperature for aggregation is also the cause for the different orientation of the aggregates toward the substrate that we observe by GIWAXS measurements. We found an edge-on orientation for N4 and face-on for Y6, in accordance with earlier reports.^[26] The higher onset temperature for aggregation, above room temperature, leads to the presence of aggregates already in solution prior to the film formation. Thereby, the π - π interactions are already saturated to a certain degree, and the ability of the π -system to interact with the

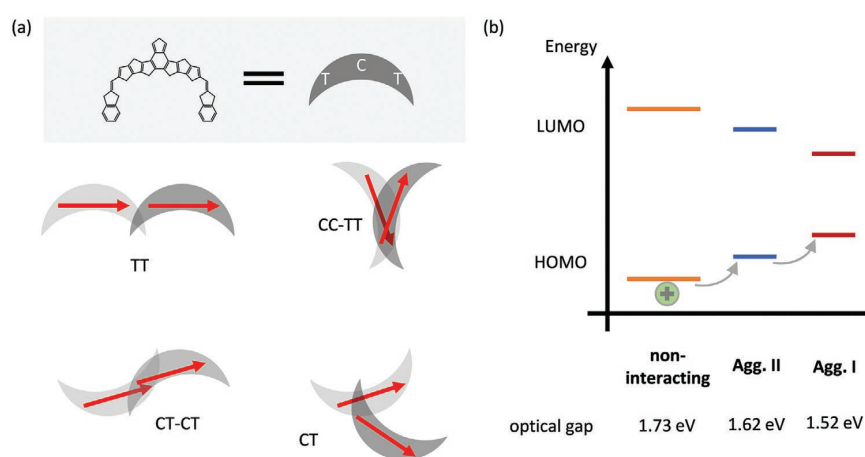


Figure 9. a) Schematic dimer configurations with interactions between the molecular core (C) and terminal (T) in different orientations as suggested by Kupgan et al. on the basis of MD simulations, along with our expected orientation of the transition dipole moments (red arrows). After.^[44] b) Schematic illustrating possible positions of HOMO/LUMO levels of aggregate I and II in a qualitative manner.

substrate is reduced. Consequently, preferably the side chains interact with the substrate, leading to a predominant edge-on orientation. In contrast, Y6 with a clearly lower onset temperature ($T_{\text{onset}} = 230$ K) is well dissolved until shortly prior to the complete evaporation of the solvent. Thereby, the π -system of the molecules can interact with the substrate unimpeded, resulting in a face-on orientation.

By influencing the short-range order in neat films, we also expect the sidechains to have an influence on the solar cell performance of blends with PM6. Both PM6 blend films with Y6 and N4 are reported to show excellent power conversion efficiencies. However, the Y6 based devices exceed the performance of devices with N4.^[25] Perdigón-Toro et al. attributed this to the unfavorable molecular edge-on orientation in the PM6:N4 blend, causing a reduced mobility. More importantly, the PM6:N4 blend was shown to exhibit a larger energetic disorder, in part with an exponential tail of trap states, which was shown to be the main reason for the smaller V_{OC} in PM6:N4 devices compared with PM6:Y6.^[25–26]

We find that the absorption spectra of PM6:Y6 contain a higher fraction of interacting chromophores than PM6:N4, and among them a particularly dominant proportion of aggregate I. While we do not know the HOMO and LUMO levels for Aggregate I and Aggregate II relative to those of the non-interacting molecules, their lower optical gap suggests a concomitant HOMO destabilization and LUMO stabilization. Consequently, charges will predominantly relax toward interacting chromophores of Aggregate I. (c.f. Figure 9) From the results of Perdigón-Toro we conclude that the number and distribution of Aggregate I-type chromophores in PM6:Y6 is sufficient to support a good percolation path for the charge carriers. In contrast, either the fraction or the distribution (or both) of Aggregate I-type chromophores in the PM6:N4 blend is such that transport is disrupted, with Aggregate I-type chromophores providing trap states for electrons. We consider that the long-range Coulomb potential fluctuations due to the presence of trapped negative charges lead to a nearly exponential tail in the HOMO DOS.^[54,78–79] We therefore conclude that the distribution of Aggregate I-type chromophores is responsible for the differences in the density of states (DOS) suggested by Perdigón-Toro et al., and the concomitant differences in solar cell performance.

We finally consider the effect of the different molecular packing in the two blends on the V_{OC} , which is found to be systematically lower in the PM6:N4 system.^[25–26] It was shown that free charge recombination in PM6:Y6 proceeds almost entirely through the CT state^[80] and we expect the same situation for the PM6:N4 blend. Then, the V_{OC} is determined by the energy, energetic disorder, and decay rate of the CT state.^[81] Unfortunately, the CT state absorption and emission is nearly hidden under the strong NFA exciton in both systems;^[25,80] therefore these properties are not attainable from optical spectroscopy. It has, however, been shown that the CT properties are largely linked to the energy, aggregation, and orientation of the molecules forming the CT states.^[82] As we point out earlier, the most obvious difference in the optical spectra is a higher contribution of the J-like aggregates in the PM6:Y6 film compared to the noninteracting chains but also the PM6:N4 blend. In addition, the GIWAXS measurements in the PM6:Y6 blend show

signatures of nanostructures arising from Y6 molecules, which require aggregates of several Y6 molecules to be present. Our GIWAXS results further reveal a more isotropic molecular orientation of the constituents in the PM6:N4 blend. In combination of these effects, we expect a larger energetic disorder of the CT state in the PM6:N4 blend, which will translate into a faster nonradiative decay and a smaller V_{OC} .^[83]

4. Conclusion

In this study, we identify and analyze the intermolecular interactions in Y series NFAs, and the role of the side chain branching point in the formation of aggregates, in highly efficient blend systems by optical spectroscopy in combination with a Franck–Condon analysis. For this, we used the well-established Y-type acceptors Y6, with 2nd position branching of the alkyl side-chains, and N4 (4th position branching), and combine these with the donor polymer PM6. PM6 shows a distinct aggregate formation in films as well as in solution with an aggregate onset temperature well above the room temperature. The two acceptor molecules are found to form two aggregate types, though with clearly different nature. Y6 forms two J-like aggregates with different interaction energies, which can also be observed in blend films with PM6. In contrast, N4 forms aggregates with more H-like character as the further branching point of the side chains enables a more parallel stacking due to less steric hinderance. Upon thermal annealing or for longer storage time, this H-character converts into a J-like character, which can be traced back to a molecular reorientation, in accordance with GIWAXS measurements. In the thermally annealed blend films with PM6, the aggregates of both acceptor materials show similar character, though the proportions of the aggregates differ. The PM6:Y6 blend contains a significant higher amount of the acceptor aggregate with higher interaction energy. This dominant absorption of acceptor aggregate correlates with good transport properties and low energetic disorder in the corresponding solar cells.^[25] This is not the case for the N4 phase in the PM6:N4 blend. There, an even distribution of the two types of aggregates and an overall lower contribution correlates with the appearance of an exponential tail in the DOS of the PM6 HOMO, consistent with the classical picture of DOS broadening by counter-charges on trapped isolated lower energy sites. In this way, the modification of the aggregation behavior through the slight extension of the side chain in the acceptor N4 causes a substantial change in the electronic structure of the donor PM6, with strong impact on the solar cell performance.

5. Experimental Section

The electron acceptor Y6 and the donor polymer PM6 were purchased by “1-material.” N4 was synthesized as described.^[26] For temperature-dependent solution measurements, N4 and Y6 at 0.15 mg mL⁻¹ in MeTHF were dissolved. This corresponds to a molar concentration of about 1×10^{-4} mol L⁻¹ for both materials. PM6 was dissolved in ortho-dichlorobenzene (ODB) at a concentration of 0.25 mg mL⁻¹. The solutions were stirred for at least 1 h at 50 °C to ensure complete dissolution of the materials. Temperature-dependent absorption and

emission measurements were carried out using a home-built setup. The solutions were filled in a 1 mm fused silica cuvette and placed in a temperature controlled continuous flow helium cryostat by Oxford Instruments. After reaching each temperature step of the measurement, waited for 15 min to ensure a fully equilibrated system before taking the measurement. The lowest accessible temperature was determined by the glass transition temperature of MeTHF, i.e., 137 K. A tungsten lamp is used as light source for absorption measurements. For emission measurements, a 405 nm continuous wave diode laser from Coherent was used to excite the PM6 samples and a 659 nm continuous wave diode laser for the Y6 and N4 samples. A spectrograph Andor Shamrock SR303i coupled to a CCD camera (Andor iDus 420) functions as detection system.

For neat film samples, solutions of neat Y6 and of neat N4 in chloroform at 12 mg mL⁻¹, and of neat PM6 in chlorobenzene at 8 mg mL⁻¹ were prepared. Solutions of blends with PM6:Y6 in weight ratios of 1:1.2, and of PM6:N4 (weight ratio 1:1.25) were prepared in chloroform at a total concentration of 16 mg mL⁻¹. All solutions were mixed with 0.5% chloronaphthalene (CN) and then stirred for at least 2 h at 50 °C. All films were prepared by spin-casting the solution in a glovebox with nitrogen atmosphere at room temperature with 1000 rpm. Thermal annealing (TA) was conducted at 90 °C for 5 min. UV–vis absorption spectra of films at room temperature were captured with a Cary 5000 UV–vis spectrometer.

GIWAXS on neat films coated on silicon substrates was performed in vacuum at RT on a laboratory system at the University of Bayreuth (Xeuss 3.0, Xenocs SAS, Grenoble, France) with a Cu K α source ($\lambda = 1.54 \text{ \AA}$), a Dectris EIGER 2R 1 m detector, and a sample-to-detector distance of 52.5 mm. Scattering experiments were carried out on silicon substrates due to decreased scattering background compared to glass. Figure S9 (Supporting Information) shows the GIWAXS data on glass for comparison. The presented q -profiles are cake cuts covering an azimuthal angle of 70°–110° for the cuts in the vertical direction and 0°–20° as well as 160°–180° for the cuts in the horizontal direction. The 2D GIWAXS measurements on blend films were performed on PEDOT:PSS (poly(3,4-ethylenedioxythiophene) polystyrene sulfonate) coated silicon substrates in vacuum at RT at the Soft Matter Interfaces beamline (12-ID) at the National Synchrotron Lightsource II (NSLS-II) at Brookhaven National Laboratory ($\lambda = 0.77 \text{ \AA}$), with a Dectris Pilatus200KW detector with a sample-to-detector distance of 275 mm at different rotational angles. These measurements are averages over 6 positions on the sample each measured for 20 s to reduce effects due to inhomogeneities. Changes in intensity profiles with time were tested and no beam damage was determined for 20 s of exposure.

Supporting Information

Supporting Information is available from the Wiley Online Library or from the author.

Acknowledgements

E.M.H. and F.E. acknowledge funding from SolarEraNet (No. NFA4R2ROPV) and the DFG (INST 91/443-1). F.E. thanks the Elite Study Program Macromolecular Science within the Elite Network of Bavaria (ENB) for support. This research used the Soft Matter Interfaces Beamline (SMI, Beamline 12-ID) of the National Synchrotron Light Source II, a US Department of Energy (DOE) Office of Science User Facility operated for the DOE Office of Science by Brookhaven National Laboratory under Contract No. DE-SC0012704. L.P.T. and D.N. acknowledge financial support by the DFG HIOS (Project No. 182087777 – SFB 951). A.K. and D.K. thank the Bayerisches Staatsministerium für Wissenschaft und Kunst for funding in the framework of the “SolTechGoHybrid” initiative.

Open access funding enabled and organized by Projekt DEAL.

Conflict of Interest

The authors declare no conflict of interest.

Data Availability Statement

The data that support the findings of this study are available from the corresponding author upon reasonable request.

Keywords

charge-transfer states, Frank–Condon analysis, morphology, organic solar cells

Received: May 19, 2022

Revised: July 1, 2022

Published online: August 23, 2022

- [1] L. Liu, S. Chen, Y. Qu, X. Gao, L. Han, Z. Lin, L. Yang, W. Wang, N. Zheng, Y. Liang, Y. Tan, H. Xia, F. He, *Adv. Mater.* **2021**, *33*, 2101279.
- [2] J. Yuan, Y. Zhang, L. Zhou, G. Zhang, H.-L. Yip, T.-K. Lau, X. Lu, C. Zhu, H. Peng, P. A. Johnson, M. Leclerc, Y. Cao, J. Ulanski, Y. F. Li, Y. Zou, *Joule* **2019**, *3*, 1140.
- [3] F. Liu, L. Zhou, W. Liu, Z. Zhou, Q. Yue, W. Zheng, R. Sun, W. Liu, S. Xu, H. Fan, L. Feng, Y. Yi, W. Zhang, X. Zhu, *Adv. Mater.* **2021**, *33*, 2100830.
- [4] L. Zhan, S. Li, T.-K. Lau, Y. Cui, X. Lu, M. Shi, C.-Z. Li, H. Li, J. Hou, H. Chen, *Energy Environ. Sci.* **2020**, *13*, 635.
- [5] J. Yuan, H. Zhang, R. Zhang, Y. Wang, J. Hou, M. Leclerc, X. Zhan, F. Huang, F. Gao, Y. Zou, Y. Li, *Chem* **2020**, *6*, 2147.
- [6] L. Zhu, M. Zhang, G. Q. Zhou, T. Y. Hao, J. Q. Xu, J. Wang, C. Q. Qiu, N. Prine, J. Ali, W. Feng, X. D. Gu, Z. F. Ma, Z. Tang, H. M. Zhu, L. Ying, Y. M. Zhang, F. Liu, *Adv. Energy Mater.* **2020**, *10*, 1904234.
- [7] G. C. Zhang, X. K. Chen, J. Y. Xiao, P. C. Y. Chow, M. R. Ren, G. Kugan, X. C. Jiao, C. C. S. Chan, X. Y. Du, R. X. Xia, Z. M. Chen, J. Yuan, Y. Q. Zhang, S. F. Zhang, Y. D. Liu, Y. P. Zou, H. Yan, K. S. Wong, V. Coropceanu, N. Li, C. J. Brabec, J. L. Bredas, H. L. Yip, Y. Cao, *Nat. Commun.* **2020**, *11*, 3943.
- [8] W. G. Zhu, A. P. Spencer, S. Mukherjee, J. M. Alzola, V. K. Sangwan, S. H. Amsterdam, S. M. Swick, L. O. Jones, M. C. Heiber, A. A. Herzog, G. P. Li, C. L. Stern, D. M. DeLongchamp, K. L. Kohlstedt, M. C. Hersam, G. C. Schatz, M. R. Wasielewski, L. X. Chen, A. Facchetti, T. J. Marks, *J. Am. Chem. Soc.* **2020**, *142*, 14532.
- [9] R. J. Ma, Y. Tao, Y. Z. Chen, T. Liu, Z. H. Luo, Y. Guo, Y. Q. Xiao, J. Fang, G. Y. Zhang, X. J. Li, X. Guo, Y. P. Yi, M. J. Zhang, X. H. Lu, Y. F. Li, H. Yan, *Sci. China: Chem.* **2021**, *64*, 581.
- [10] S. Bao, H. Yang, H. Fan, J. Zhang, Z. Wei, C. Cui, Y. Li, *Adv. Mater.* **2021**, *33*, 2105301.
- [11] J. Gao, X. Ma, C. Xu, X. Wang, J. H. Son, S. Y. Jeong, Y. Zhang, C. Zhang, K. Wang, L. Niu, J. Zhang, H. Y. Woo, J. Zhang, F. Zhang, *Chem. Eng. J.* **2022**, *428*, 129276.
- [12] Y. Cui, Y. Xu, H. Yao, P. Bi, L. Hong, J. Zhang, Y. Zu, T. Zhang, J. Qin, J. Ren, *Adv. Mater.* **2021**, *33*, 2102420.
- [13] K. Chong, X. Xu, H. Meng, J. Xue, L. Yu, W. Ma, Q. Peng, *Adv. Mater.* **2022**, *34*, 2109516.
- [14] Z. Zheng, J. Wang, P. Bi, J. Ren, Y. Wang, Y. Yang, X. Liu, S. Zhang, J. Hou, *Joule* **2021**, *6*, 171.

- [15] A. Armin, W. Li, O. J. Sandberg, Z. Xiao, L. M. Ding, J. Nelson, D. Neher, K. Vandewal, S. Shoaee, T. Wang, H. Ade, T. Heumüller, C. Brabec, P. Meredith, *Adv. Energy Mater.* **2021**, *11*, 2003570.
- [16] C. Yan, S. Barlow, Z. Wang, H. Yan, A. K.-Y. Jen, S. R. Marder, X. Zhan, *Nat. Rev. Mater.* **2018**, *3*, 18003.
- [17] J. Zhang, H. S. Tan, X. Guo, A. Facchetti, H. Yan, *Nat. Energy* **2018**, *3*, 720.
- [18] Q. Yue, W. Liu, X. Zhu, *J. Am. Chem. Soc.* **2020**, *142*, 11613.
- [19] W. Liu, X. Xu, J. Yuan, M. Leclerc, Y. Zou, Y. Li, *ACS Energy Lett.* **2021**, *6*, 598.
- [20] T. Zhang, C. An, P. Bi, Q. Lv, J. Qin, L. Hong, Y. Cui, S. Zhang, J. Hou, *Adv. Energy Mater.* **2021**, *11*, 2101705.
- [21] R. J. Ma, T. Liu, Z. H. Luo, K. Gao, K. Chen, G. Y. Zhang, W. Gao, Y. Q. Xiao, T. K. Lau, Q. P. Fan, Y. Z. Chen, L. K. Ma, H. L. Sun, G. L. Cai, T. Yang, X. H. Lu, E. G. Wang, C. L. Yang, A. K. Y. Jen, H. Yan, *ACS Energy Lett.* **2020**, *5*, 2711.
- [22] Z. H. Luo, R. J. Ma, T. Liu, J. W. Yu, Y. Q. Xiao, R. Sun, G. S. Xie, J. Yuan, Y. Z. Chen, K. Chen, G. D. Chai, H. L. Sun, J. Min, J. Zhang, Y. P. Zou, C. L. Yang, X. H. Lu, F. Gao, H. Yan, *Joule* **2020**, *4*, 1236.
- [23] G. D. Chai, Y. Chang, J. Q. Zhang, X. P. Xu, L. Y. Yu, X. H. Zou, X. J. Li, Y. Z. Chen, S. W. Luo, B. B. Liu, F. J. Bai, Z. H. Luo, H. Yu, J. E. Liang, T. Liu, K. S. Wong, H. Zhou, Q. Peng, H. Yan, *Energy Environ. Sci.* **2021**, *14*, 3469.
- [24] L. Zhu, M. Zhang, J. Xu, C. Li, J. Yan, G. Zhou, W. Zhong, T. Hao, J. Song, X. Xue, Z. Zhou, R. Zeng, H. Zhu, C.-C. Chen, R. C. I. MacKenzie, Y. Zou, J. Nelson, Y. Zhang, Y. Sun, F. Liu, *Nat. Mater.* **2022**, *21*, 656.
- [25] L. Perdigón-Toro, L. Q. Phuong, F. Eller, G. Freychet, E. Saglamkaya, J. I. Khan, Q. Wei, S. Zeiske, D. Kroh, S. Wedler, A. Köhler, A. Armin, F. Laquai, E. M. Herzig, Y. Zou, S. Shoaee, D. Neher, *Adv. Energy Mater.* **2022**, *12*, 2103422.
- [26] K. Jiang, Q. Wei, J. Y. L. Lai, Z. Peng, H. K. Kim, J. Yuan, L. Ye, H. Ade, Y. Zou, H. Yan, *Joule* **2019**, *3*, 3020.
- [27] G. Yao, Y. Ge, X. Xiao, L. Zhang, N. Yi, H. Luo, S. Yuan, W. Zhou, *ACS Appl. Energy Mater.* **2022**, *5*, 1193.
- [28] S. Li, C.-Z. Li, M. Shi, H. Chen, *ACS Energy Lett.* **2020**, *5*, 1554.
- [29] S. Dong, T. Jia, K. Zhang, J. Jing, F. Huang, *Joule* **2020**, *4*, 2004.
- [30] Y. Qin, Y. Xu, Z. Peng, J. Hou, H. Ade, *Adv. Funct. Mater.* **2020**, *30*, 2005011.
- [31] X. J. Li, H. Huang, I. Angunawela, J. D. Zhou, J. Q. Du, A. Liebman-Pelaez, C. H. Zhu, Z. J. Zhang, L. Meng, Z. Q. Xie, H. Ade, Y. F. Li, *Adv. Funct. Mater.* **2020**, *30*, 1906855.
- [32] J. Q. Zhang, F. J. Bai, I. Angunawela, X. Y. Xu, S. W. Luo, C. Li, G. D. Chai, H. Yu, Y. Z. Chen, H. W. Hu, Z. F. Ma, H. Ade, H. Yan, *Adv. Energy Mater.* **2021**, *11*, 2102596.
- [33] Z. H. Luo, R. J. Ma, Z. X. Chen, Y. Q. Xiao, G. Y. Zhang, T. Liu, R. Sun, Q. Zhan, Y. Zou, C. Zhong, Y. Z. Chen, H. L. Sun, G. D. Chai, K. Chen, X. G. Guo, J. Min, X. H. Lu, C. L. Yang, H. Yan, *Adv. Energy Mater.* **2020**, *10*, 2002649.
- [34] Z. Luo, R. Sun, C. Zhong, T. Liu, G. Zhang, Y. Zou, X. Jiao, J. Min, C. Yang, *Sci. China: Chem.* **2020**, *63*, 361.
- [35] Z.-F. Yao, J.-Y. Wang, J. Pei, *Cryst. Growth Des.* **2018**, *18*, 7.
- [36] L. Hong, H. F. Yao, Z. Wu, Y. Cui, T. Zhang, Y. Xu, R. N. Yu, Q. Liao, B. W. Gao, K. H. Xian, H. Y. Woo, Z. Y. Ge, J. H. Hou, *Adv. Mater.* **2019**, *31*, 1903441.
- [37] D. Mo, H. Chen, Y. Zhu, H.-H. Huang, P. Chao, F. He, *ACS Appl. Mater. Interfaces* **2020**, *12*, 28329.
- [38] Y. Guo, G. Han, Y. Yi, *J. Energy Chem.* **2019**, *35*, 138.
- [39] T. Yasuda, K. Sakamoto, *Org. Electron.* **2018**, *62*, 429.
- [40] C. Yan, Y. Wu, J. Wang, R. Li, P. Cheng, H. Bai, Z. Zhan, W. Ma, X. Zhan, *Dyes Pigm.* **2017**, *139*, 627.
- [41] S. Athanasopoulos, H. Bässler, A. Köhler, *J. Phys. Chem. Lett.* **2019**, *10*, 7107.
- [42] S. N. Hood, I. Kassal, *J. Phys. Chem. Lett.* **2016**, *7*, 4495.
- [43] M. Schubert, D. Dolfen, J. Frisch, S. Roland, R. Steyrleuthner, B. Stiller, Z. Chen, U. Scherf, N. Koch, A. Facchetti, D. Neher, *Adv. Energy Mater.* **2012**, *2*, 369.
- [44] G. Kupgan, X.-K. Chen, J.-L. Brédas, *Mater. Today Adv.* **2021**, *11*, 100154.
- [45] Y. Liu, J. Zhao, Z. Li, C. Mu, W. Ma, H. Hu, K. Jiang, H. Lin, H. Ade, H. Yan, *Nat. Commun.* **2014**, *5*, 5293.
- [46] S. Wedler, A. Bourdick, S. Athanasopoulos, S. Gekle, F. Panzer, C. McDowell, T.-Q. Nguyen, G. C. Bazan, A. Köhler, *J. Mater. Chem. C* **2020**, *8*, 4944.
- [47] F. Panzer, H. Bässler, A. Köhler, *J. Phys. Chem. Lett.* **2017**, *8*, 114.
- [48] F. Panzer, H. Bässler, R. Lohwasser, M. Thelakkat, A. Köhler, *J. Phys. Chem. Lett.* **2014**, *5*, 2742.
- [49] F. Panzer, M. Sommer, H. Bässler, M. Thelakkat, A. Köhler, *Macromolecules* **2015**, *48*, 1543.
- [50] M. Reichenberger, D. Kroh, G. M. Matrone, K. Schötz, S. Pröller, O. Filonik, M. E. Thordardottir, E. M. Herzig, H. Bässler, N. Stingelin, A. Köhler, *J. Polym. Sci. B: Polym. Phys.* **2018**, *56*, 532.
- [51] C. Scharsich, F. S. Fischer, K. Wilma, R. Hildner, S. Ludwigs, A. Köhler, *J. Polym. Sci. B: Polym. Phys.* **2015**, *53*, 1416.
- [52] A. Köhler, S. T. Hoffmann, H. Bässler, *J. Am. Chem. Soc.* **2012**, *134*, 11594.
- [53] F. C. Spano, *Acc. Chem. Res.* **2010**, *43*, 429.
- [54] A. Köhler, H. Bässler, *Electronic Processes in Organic Semiconductors: An Introduction*, John Wiley & Sons, New York **2015**.
- [55] K. Cai, J. Xie, D. Zhang, W. Shi, Q. Yan, D. Zhao, *J. Am. Chem. Soc.* **2018**, *140*, 5764.
- [56] M. Reichenberger, D. Kroh, G. M. Matrone, K. Schötz, S. Pröller, O. Filonik, M. E. Thordardottir, E. M. Herzig, H. Bässler, N. Stingelin, *J. Polym. Sci. B: Polym. Phys.* **2018**, *56*, 532.
- [57] M. Kasha, *Radiat. Res.* **1963**, *20*, 55.
- [58] M. Kasha, H. R. Rawls, M. A. El-Bayoumi, *Pure Appl. Chem.* **1965**, *11*, 371.
- [59] J. Gao, J. Wang, Q. An, X. Ma, Z. Hu, C. Xu, X. Zhang, F. Zhang, *Sci. China Chem.* **2020**, *63*, 83.
- [60] F. Lin, K. Jiang, W. Kaminsky, Z. Zhu, A. K.-Y. Jen, *J. Am. Chem. Soc.* **2020**, *142*, 15246.
- [61] Z. Bi, K. Chen, L. Gou, Y. Guo, X. Zhou, H. B. Naveed, J. Wang, Q. Zhu, J. Yuan, C. Zhao, K. Zhou, S. Chandrabose, Z. Tang, Y. Yi, J. M. Hodgkiss, L. Zhang, W. Ma, *J. Mater. Chem. A* **2021**, *9*, 16733.
- [62] L. Lin, Y. Morisaki, Y. Chujo, *Int. J. Polym. Sci.* **2010**, *2010*.
- [63] F. B. Dias, S. Pollock, G. Hedley, L.-O. Pålsson, A. Monkman, I. I. Perepichka, I. F. Perepichka, M. Tavasli, M. R. Bryce, *J. Phys. Chem. B* **2006**, *110*, 19329.
- [64] M. Reichenberger, S. Baderschneider, D. Kroh, S. Grauf, J. r. Köhler, R. Hildner, A. Köhler, *Macromolecules* **2016**, *49*, 6420.
- [65] Q. Liu, J. Fang, J. Wu, L. Zhu, X. Guo, F. Liu, M. Zhang, *Chin. J. Chem.* **2021**, *39*, 1941.
- [66] C. H. Guo, D. H. Li, L. Wang, B. C. Du, Z. X. Liu, Z. Q. Shen, P. Wang, X. Zhang, J. L. Cai, S. L. Cheng, C. Yu, H. Wang, D. Liu, C. Z. Li, T. Wang, *Adv. Energy Mater.* **2021**, *11*, 2102000.
- [67] D. Li, X. Chen, J. Cai, W. Li, M. Chen, Y. Mao, B. Du, J. A. Smith, R. C. Kilbride, M. E. O'Kane, X. Zhang, Y. Zhuang, P. Wang, H. Wang, D. Liu, R. A. L. Jones, D. G. Lidzey, T. Wang, *Sci. China Chem.* **2020**, *63*, 1461.
- [68] B. Du, R. Geng, W. Tan, Y. Mao, D. Li, X. Zhang, D. Liu, W. Tang, W. Huang, T. Wang, *J. Energy Chem.* **2021**, *54*, 131.
- [69] L. Zhan, S. Li, X. Xia, Y. Li, X. Lu, L. Zuo, M. Shi, H. Chen, *Adv. Mater.* **2021**, *33*, 2007231.
- [70] Y. P. Xie, Y. H. Cai, L. Zhu, R. X. Xia, L. L. Ye, X. Feng, H. L. Yip, F. Liu, G. H. Lu, S. T. Tan, Y. M. Sun, *Adv. Funct. Mater.* **2020**, *30*, 2002181.
- [71] T. Shan, Y. Zhang, Y. Wang, Z. Xie, Q. Wei, J. Xu, M. Zhang, C. Wang, Q. Bao, X. Wang, C. Chen, J. Huang, Q. Chen, F. Liu, L. Chen, H. Zhong, *Nat. Commun.* **2020**, *11*, 5585.

- [72] H. Fu, W. Gao, Y. Li, F. Lin, X. Wu, J. H. Son, J. Luo, H. Y. Woo, Z. Zhu, A. K. Y. Jen, *Small Methods* **2020**, *4*, 2000687.
- [73] Y. Wei, J. Yu, L. Qin, H. Chen, X. Wu, Z. Wei, X. Zhang, Z. Xiao, L. Ding, F. Gao, H. Huang, *Energy Environ. Sci.* **2021**, *14*, 2314.
- [74] L. Arunagiri, G. Zhang, H. Hu, H. Yao, K. Zhang, Y. Li, P. C. Chow, H. Ade, H. Yan, *Adv. Funct. Mater.* **2019**, *29*, 1902478.
- [75] C. Xiao, C. Li, F. Liu, L. Zhang, W. Li, *J. Mater. Chem. C* **2020**, *8*, 5370.
- [76] A. Bourdick, M. Reichenberger, A. Stradomska, G. C. Bazan, T.-Q. Nguyen, A. Köhler, S. Gekle, *J. Phys. Chem. B* **2018**, *122*, 9191.
- [77] T. Lei, J. H. Dou, J. Pei, *Adv. Mater.* **2012**, *24*, 6457.
- [78] V. Arkhipov, P. Heremans, E. Emelianova, H. Baessler, *Phys. Rev. B* **2005**, *71*, 045214.
- [79] I. Hulea, H. Brom, A. Houtepen, D. Vanmaekelbergh, J. Kelly, E. Meulenkamp, *Phys. Rev. Lett.* **2004**, *93*, 166601.
- [80] L. Perdigon-Toro, L. Q. Phuong, S. Zeiske, K. Vandewal, A. Armin, S. Shoaee, D. Neher, *ACS Energy Lett.* **2021**, *6*, 557.
- [81] T. M. Burke, S. Sweetnam, K. Vandewal, M. D. McGehee, *Adv. Energy Mater.* **2015**, *5*, 1500123.
- [82] X. K. Chen, M. K. Ravva, H. Li, S. M. Ryno, J. L. Brédas, *Adv. Energy Mater.* **2016**, *6*, 1601325.
- [83] Z. Zheng, N. R. Tummala, T. Wang, V. Coropceanu, J. L. Brédas, *Adv. Energy Mater.* **2019**, *9*, 1803926.



Supporting Information

for *Adv. Funct. Mater.*, DOI: 10.1002/adfm.202205711

Identifying the Signatures of Intermolecular Interactions
in Blends of PM6 with Y6 and N4 Using Absorption
Spectroscopy

*Daniel Kroh, Fabian Eller, Konstantin Schötz, Stefan
Wedler, Lorena Perdigón-Toro, Guillaume Freychet,
Qingya Wei, Maximilian Dörr, David Jones, Yingping
Zou, Eva M. Herzig, Dieter Neher, and Anna Köhler**

Supporting Information

Identifying the signatures of intermolecular interactions in blends of PM6 with Y6 and N4 using absorption spectroscopy

Daniel Kroh¹, Fabian Eller², Konstantin Schötz¹, Stefan Wedler¹, Lorena Perdigón-Toro³, Guillaume Freychet⁴, Maximilian Dörr¹, David Jones⁵, Eva M. Herzig², Dieter Neher³, Anna Köhler^{1,6*}

¹ Soft Matter Optoelectronics, Experimentalphysik II, University of Bayreuth, Bayreuth 95440, Germany

² Dynamik und Strukturbildung -Herzig Group, Physikalisches Institut, Universität Bayreuth, Universitätsstr. 30, 95447 Bayreuth, Germany

³ Soft Matter Physics and Optoelectronics, Institute of Physics and Astronomy, University of Potsdam, Karl-Liebknecht-Str. 24-25, 14476 Potsdam-Golm, Germany

⁴ NSLS-II, Brookhaven National Laboratory, Upton, NY 11973, USA

⁵ School of Chemistry, Bio21 Institute, The University of Melbourne, 30 Flemington Road, Parkville, Victoria 3010, Australia

⁶ Bayreuth Institute of Macromolecular Research (BIMF) and Bavarian Polymer Institute (BPI), University of Bayreuth, 95447 Bayreuth, Germany.

*e-mail: Anna.Koehler@uni-bayreuth.de

Keywords: Organic solar cells, Charge-transfer states, Frank-Condon Analysis, Morphology

Y6 in mTHF – emission and TCSPC

Figure S1 shows the corresponding emission spectra of Y6 in mTHF solution (left), displayed in the same temperature ranges as the absorption (right).

In the high temperature range, the shape of the emission spectra resembles a mirror image of the absorption spectra. However, while the absorption increases only moderately, the emission rises strongly, reaching its maximum at 250 K (solid black line) and then decreasing slightly to 230 K. This is accompanied by a slight bathochromic shift.

The increase in emission intensity far exceeds the increase in absorption. Evidently, there is a mechanism that increases the photoluminescence quantum yield, $\Phi = k_r/(k_r + k_{nr})$ with the radiative transition rate k_r and non-radiative transition rate k_{nr} . To establish whether k_r increases, or whether k_{nr} decreases, we measured the photoluminescence transients at 345 K, 295 K and 250 K, which gave mono-exponential decays with lifetimes of 386 ps, 1.0 ns, and 1.4 ns, respectively (see Figure S2). Evaluating the relative changes in Φ and τ lifetime shows that k_r remains unchanged implying that k_{nr} reduces upon decreasing the temperature, most likely by freezing out thermal deactivation through rotations between the Y6-core and the acceptor arms. The constant value of k_r implies that electronic interactions between the molecules in solution do not change down to 230 K. Consequently, Y6 remains completely in the disordered phase down to 230 K

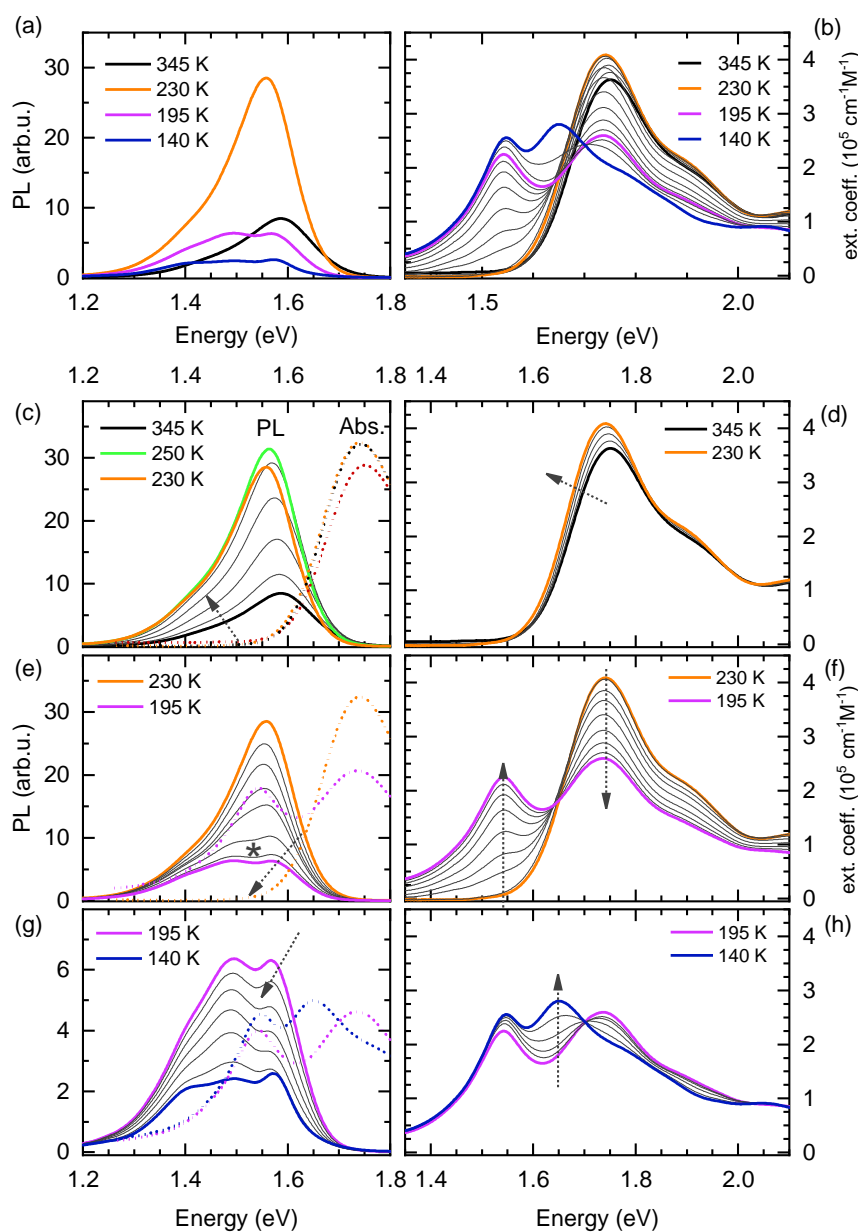


Figure S1: PL (a,c,e,g) and absorption (b,d,f,h) spectra of Y6 in mTHF at a concentration of 0.15 mg/ml for different temperatures upon cooling from (a,b) 345 K to 140 K. Spectra taken at characteristic temperatures are drawn with colored solid lines and given in the legend. Spectra are shown (c,d) between 345 K and 230 K in steps of 20K, (e,f) between 230 K and 195 K in steps of 5 K, and (g,h) between 195 K and 140 K in steps of 10 K. In the absorption spectra at characteristic temperatures outside the ranges are shown with dashed lines. In the PL spectra the absorption spectra at specific temperatures are additionally drawn in dotted lines.

N4 in mTHF – emission

Figure S2 shows the corresponding emission spectra of N4 in mTHF solution (left), displayed in the same temperature ranges as the absorption (right). The absorption spectra are described and discussed in the manuscript.

At 345 K, the PL spectrum is broad and a mirror image of the absorption spectrum with a peak at 1.58 eV. In the high temperature range, the PL slightly increases and the peak shifts to lower energies, implying an increase in oscillator strength by planarization of the molecules. Upon cooling below 320 K, the overall intensity strongly decreases at 1.58 eV, resulting in a spectrum with a peak at 1.40 eV at 220 K, while the absorption reveals that aggregate formation takes place in this temperature range. Further cooling to 140 K slightly increases the PL intensity and the spectrum shifts to lower energies, while the intensity at 1.58 eV goes down to zero. This is consistent with the observation, that in this temperature range the aggregates phase planarizes, which enhances the PLQY and enhances the energy transfer from the disordered phase to the aggregated phase. Thus, at 140 K, we only observe emission from the aggregated phase.

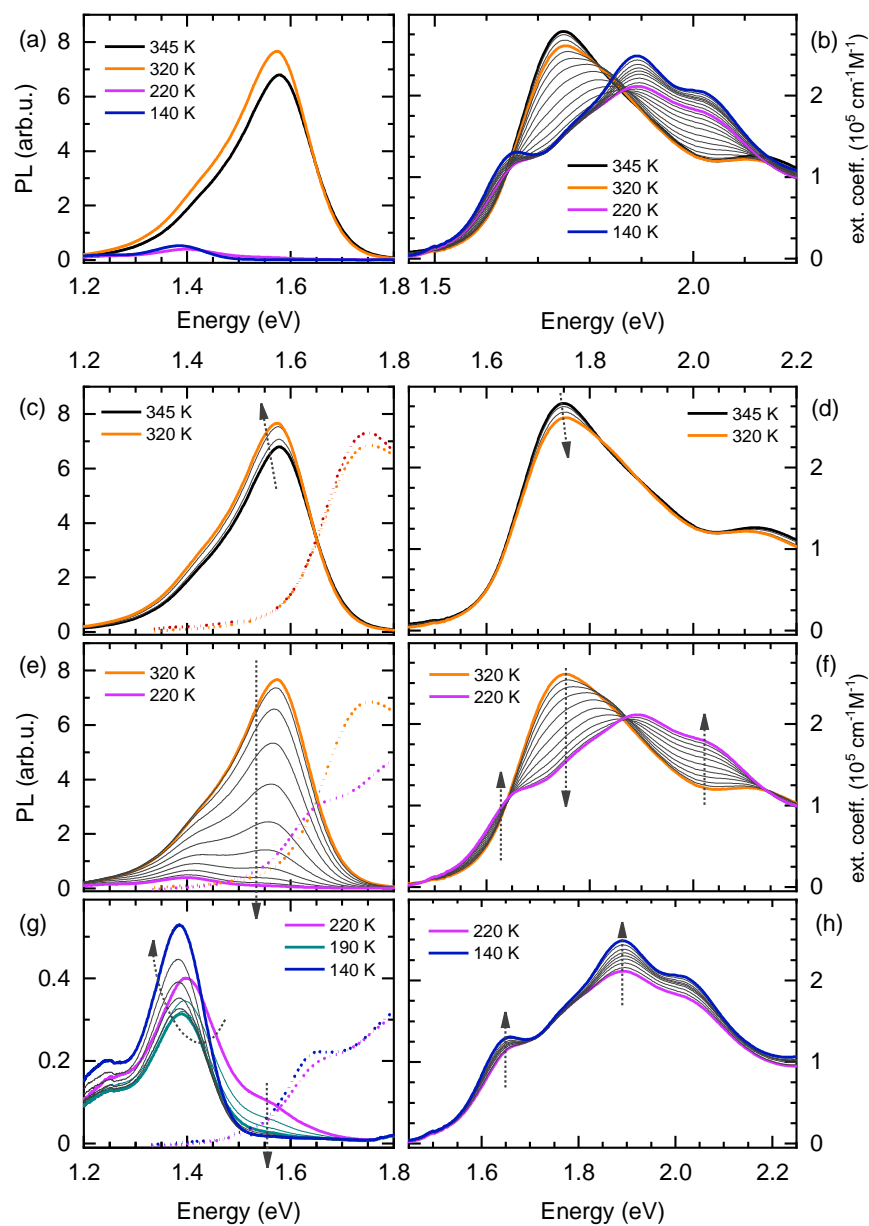


Figure S2: PL (a,c,e,g) and absorption (b,d,f,h) spectra of N4 in mTHF for different temperatures upon cooling from (a,b) 345 K to 140 K at a concentration of 0.15 mg/ml. Spectra taken at characteristic temperatures are drawn with colored solid lines and given in the legend. Spectra are shown (c,d) between 345 K and 320 K, (e,f) between 320 K and 220 K, and (g,h) between 220 K and 140 K in steps of 10 K. In the absorption spectra at characteristic temperatures outside the ranges are shown with dashed lines. In the PL spectra the absorption spectra at specific temperatures are additionally drawn in dashed lines.

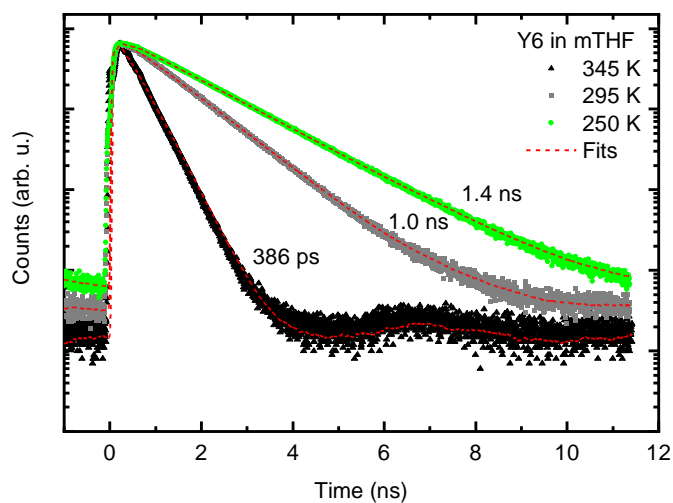


Figure S3: TCSPC measurements of Y6 in mTHF solution at 345 K, 295 K and 250 K with monoexponential decays with lifetimes of 386 ps, 1.0 ns, and 1.4 ns, respectively.

PLQY calculation:

$$\Phi = k_r * \tau$$

$$\frac{\Phi_{345K}}{\Phi_{250K}} = \frac{8.6}{31.4} = 0.27 \text{ (PL Peak intensity)}$$

$$\frac{\tau_{345K}}{\tau_{250K}} = \frac{386}{1434} = 0.27 \text{ (PL life - times)}$$

$$\Phi_{345K} = 0.27 \Phi_{250K}$$

$$k_r^{345K} * \tau^{345K} = 0.27 k_r^{250K} * \tau^{250K} \text{ with life - times}$$

$$k_r^{345K} = k_r^{250K}$$

Heating process of Y6 and N4 in mTHF solution

Figure S4 shows the absorption spectra during the heating process of Y6 and N4 in mTHF solution. Compared to the cooling process, the absorption spectra show a slight hysteresis. From 140 K to 170 K, we identify an isosbestic point at 1.73 eV accompanied by a decrease of the peak intensity at 1.65 eV and increase at 1.75 eV, indicating a dissolution of *aggregate II*. Between 170 K and 220 K we have a transition range, where the intensity below 1.73 eV decreases, which indicates a dissolution of both aggregated phases. Above 220 K we identify another isosbestic point at 1.65 eV accompanied by a decrease of the peak intensity at 1.53 eV and a strong increase of the intensity at 1.75 eV, which indicates a re-formation of *aggregate I* to non-interacting, disordered molecules. Thus, the heating process shows a slight hysteresis, which in a temperature-delayed manner.

In contrast, the absorption spectra of the heating process of N4 in mTHF shows almost no hysteresis compared to the cooling process.

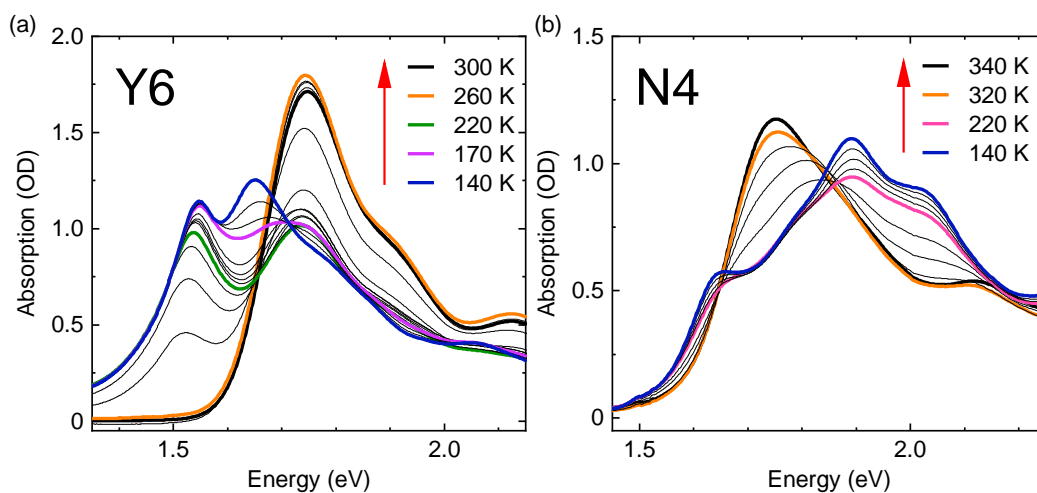


Figure S4: Absorption spectra of (a) Y6 in mTHF solution at a concentration of 0.2 mg/ml upon heating from 140 K (blue) to 300 K (black) in 10 K steps and (b) N4 in mTHF solution at a concentration of 0.2 mg/mL upon heating from 140 K (blue) to 340 K (black) in 20 K steps.

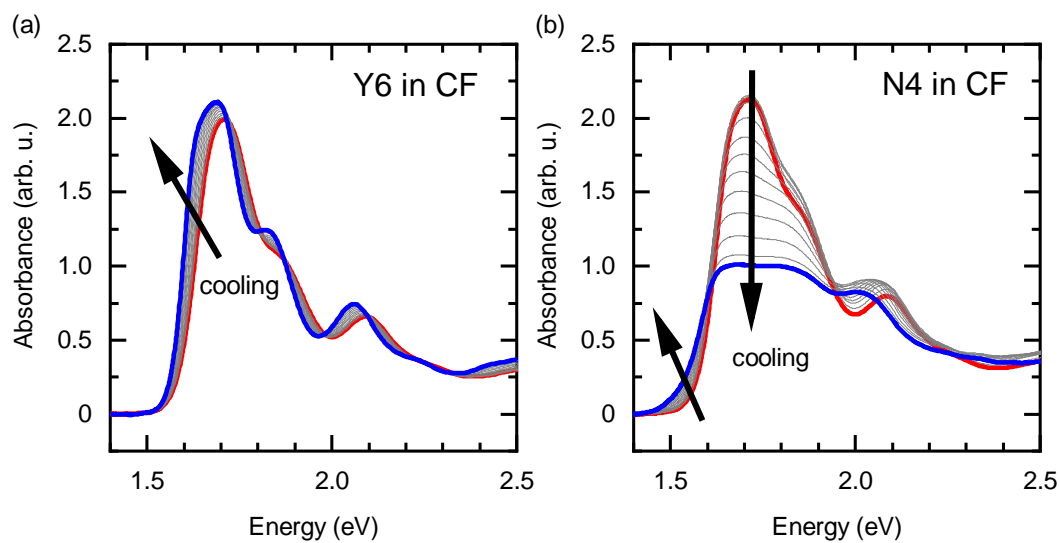


Figure S5: Absorption spectra of (a) Y6 and (b) N4 in CF solution at a concentration of 0.2 mg/ml upon cooling from 330 K (red) to 215 K (blue) in 10 K steps from 330 K to 220 K and the lowest measured temperature 215 K. Arrows indicate spectral changes upon cooling.

Franck-Condon analysis

Figure S6 shows the Franck-Condon fit for the absorption of Y6 in mTHF at 230 K, which we assign to the spectrum of the non-interacting conformation. Therefore, we used an effective mode of 162 eV to fit the $S_0 \rightarrow S_1$ transition with an E_{00} at 1.73 eV. We assign the peak at 2.13 eV to the $S_0 \rightarrow S_2$ transition and thus fitted it with a new progression with the same effective mode, but adjusted Huang-Rhys parameter. The values for the fits to the $S_0 \rightarrow S_2$ transition of the non-interacting conformations are shown in Table S1. For all other FC fits, the values of the $S_0 \rightarrow S_2$ transition are kept constant as well as the intensity ratio of $S_0 \rightarrow S_1$ to $S_0 \rightarrow S_2$.

Table S1: The parameters for the FC-progressions used for the non-interacting conformation of Y6 at 230 K

	<i>transition</i>	E_{00} (eV)	σ (meV)	S_1	$\hbar\omega$ (meV)
Y6 in mTHF 230 K	non-interacting, $S_0 \rightarrow S_1$	1.73	69	0.43	162
	non-interacting, $S_0 \rightarrow S_1$	2.13	72	0.50	162

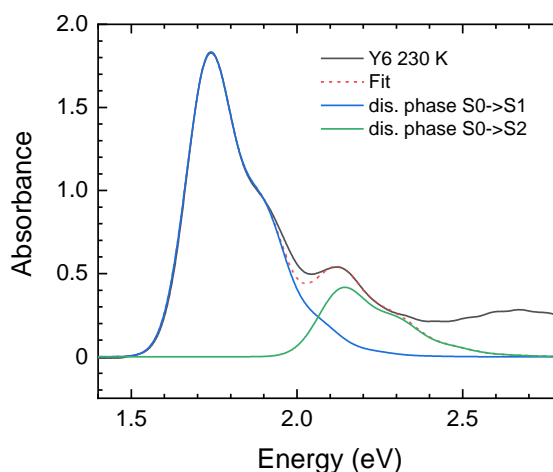


Figure S6: Absorption spectrum of Y6 in mTHF at 230 K with Franck-Condon fit with a progression at 1.73 eV fit with an effective mode at 162 meV to fit the $S_0 \rightarrow S_1$ transition and a second progression at 2.13 eV with an effective mode of 162 meV to fit the $S_0 \rightarrow S_2$ transition. The spectrum has been used as “monomer-phase” to decompose absorption spectra at lower temperatures, where spectral signatures of aggregate absorption appears.

Franck-Condon Fit: Y6 at 195 K in mTHF solution

Figure S7 shows a Franck-Condon Fit of the absorption spectrum of Y6 in mTHF solution at 195 K using a monomer/disordered phase and only one aggregate species. The peak at about 1.54 eV limits the linewidth of the aggregated phase (red) leading to a deviation of the global fit (red, dashed line) and the absorption spectrum at around 1.62 eV. Thus, we used a second aggregated phase to fit the absorption as described in the manuscript.

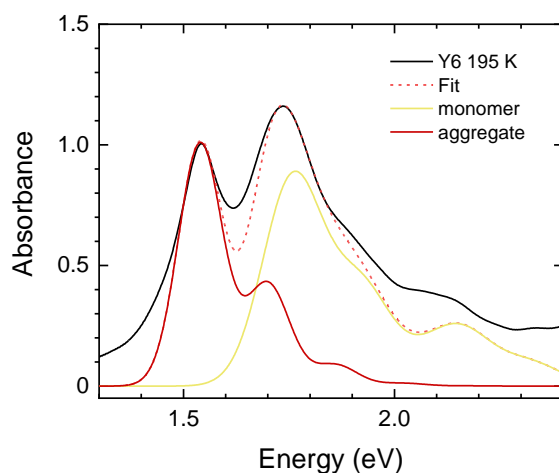


Figure S7: Absorption spectrum of Y6 in mTHF at 195 K with a Franck-Condon global fit (red dashed line) with a monomer phase (yellow) and only one aggregated phase (red).

N4 film after 3 months

Figure S8 shows the absorption spectra of the same N4 films, as-cast and thermally annealed, after 3 months. The spectrum of the thermally annealed film does not undergo spectral changes and only decreases a slightly in intensity. The spectrum of the as-cast N4 film has changed over time and almost resembles the spectrum of the thermal annealed film. Thus, giving the system of the as-cast film time results in a change of the morphology to the thermodynamic more stable morphology present in the TA films.

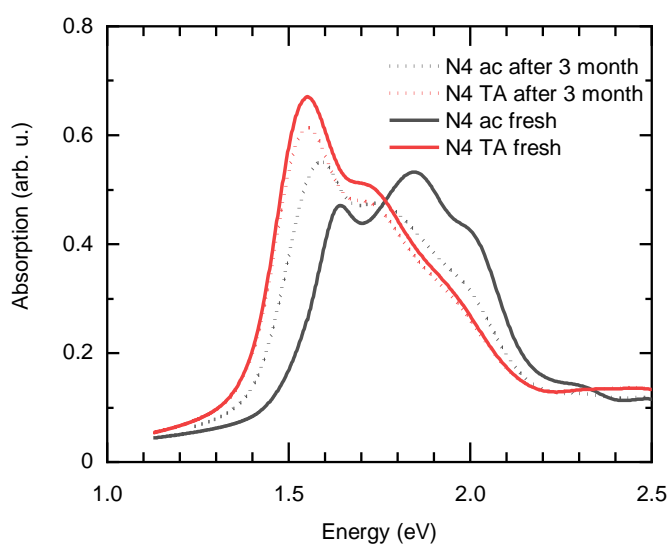


Figure S8: Absorption spectra of neat N4 films as-cast (black lines) and after thermal annealing (red lines), fresh after processing (solid lines) and 3 month later (dotted lines)

GIWAXS data of N4 films on glass

Figure S9 shows the comparison between GIWAXS measurements of N4 films, as-cast and after thermal annealing, on glass and silicon (Si) substrates. The 2D-maps are shown in Figure S9a,b and the corresponding horizontal and vertical cuts in Figure S8c,d, respectively. Comparing the 2D maps, the data on glass show a strongly increased intensity at q -values around 1.75 \AA^{-1} , which originates from the scattering background of the glass substrate. The scattering pattern of the lamellar stacking at lower q -values is almost identical, which can also be seen in the horizontal and vertical cuts. Additionally, the data on glass substrates show the same trend upon thermal annealing as on silicon. The scattering pattern shifts to lower q -values indicating a significant reorientation. Consequently, we observe the same scattering behaviour of N4 on glass and Si substrates. Thus, we assume, that a comparison of the GIWAXS data on Si (due to its decreased scattering background) with the absorption data on glass substrates is meaningful.

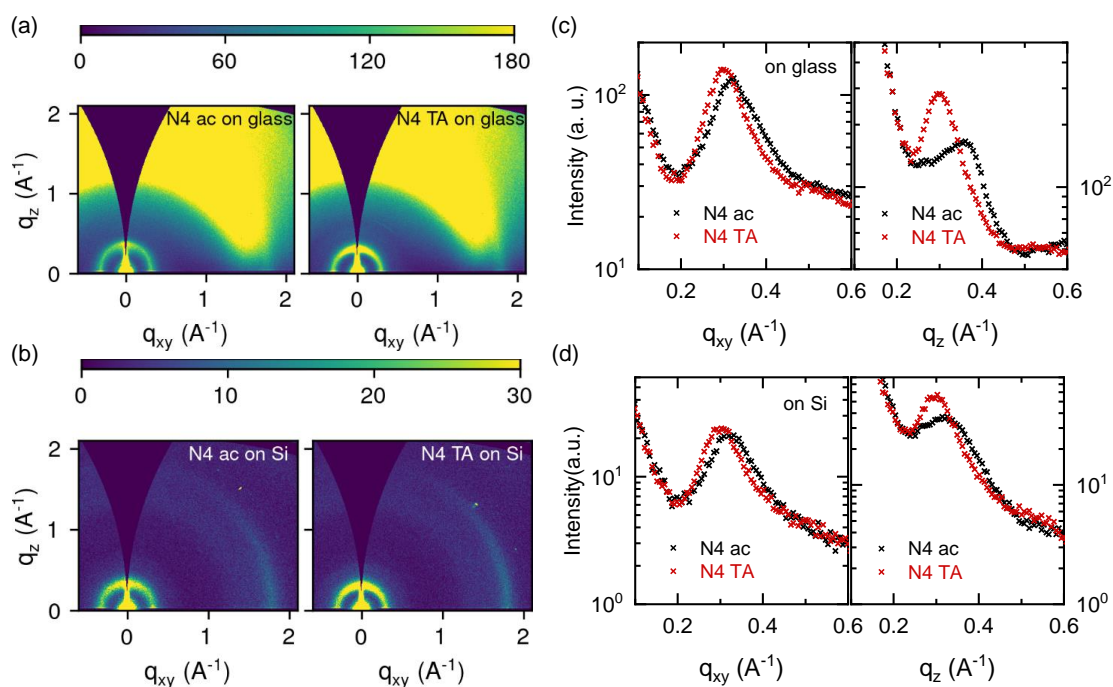


Figure S9: 2D-GIWAXS images of N4 films measured (a) on glass substrates and (b) on silicon substrates (Si), as-cast (ac) and after thermal annealing (TA). (c,d) Horizontal (left) and vertical (right) line cuts of the as-cast and thermally annealed films of N4 on (c) glass substrates and on (d) Si substrates, respectively.

Spectral decomposition of PM6 in solution and film

Fig. S10a,b show the temperature dependent PL and absorption spectra of PM6 in oDCB in a temperature range from 450 K to 270 K in 10 K steps. The spectral evolution is discussed in the manuscript. Additionally, a spectral decomposition into an aggregated and disordered phase of the absorption spectra of PM6 in solution at 270 K is shown in Fig. S10c and of a neat film in Fig. S10d. For the spectral decomposition we took the absorption spectrum at 420 K, which is right above the critical temperature and thus the absorption spectrum of the pure disordered phase, and scaled it to the absorption spectra at 270 K in solution and the neat film, respectively. Then we subtract the spectrum of the disordered phase resulting in the aggregate absorption (dashed lines). We scaled the spectrum of the disordered phase (orange) a bit below the absorption spectra, as in reality the absorption of the aggregate will not go down to zero at about 2.4 eV. This is a good approach to estimate the absorption spectra of the aggregated phase in solution and film. (REF, REICHI) For both, solution at 270 K and film, we find a similar pronounced aggregate absorption with a 0-0-peak at 2.00 eV and a shoulder at 2.13 eV.

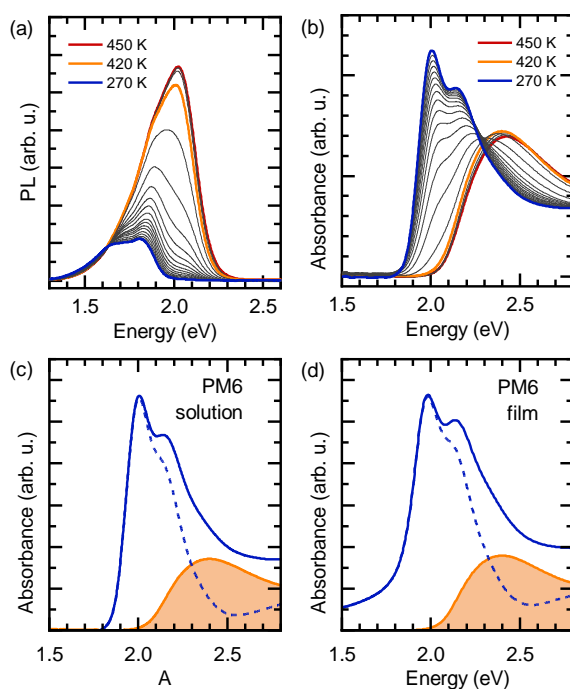


Figure S10: PL (a) and absorption (b) spectra of PM6 in oDCB at a concentration of 0.25 mg/ml. Spectra taken at characteristic temperatures are drawn with colored solid lines and given in the legend. Decomposition of absorption spectra into aggregated (dashed blue line) and disordered (orange area) phase (c) in solution at 270 K and (d) in a neat PM6 film.

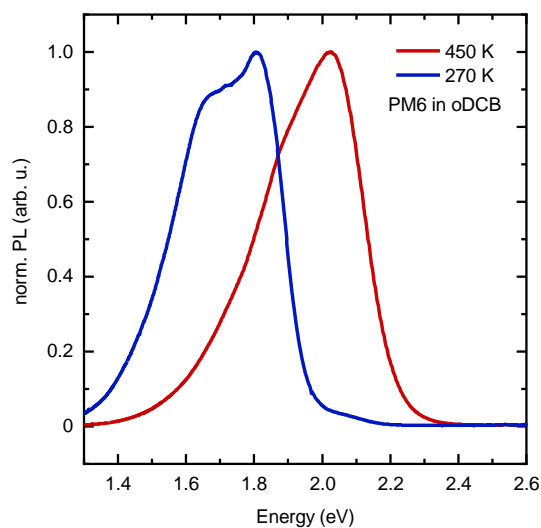


Figure S11: PL spectra of PM6 in oDCB at a concentration of 0.25 mg/ml at 450 K and 270 K normalized to their maxima.

Assuming, that the PM6 chains are fully solvated at 450 K, we assign the PL spectrum at 450 K with a maximum at 2.02 eV to the disordered phase. Upon cooling, the intensity at 2.02 eV decreases, while starting from 420 K spectral signatures of aggregation appear in absorption. The red-shifted PL at 270 K shows almost no intensity at 2.02 eV and we thus assign this PL spectrum to the aggregated phase of PM6 (see Figure S11).

Franck-Condon analysis parameters:

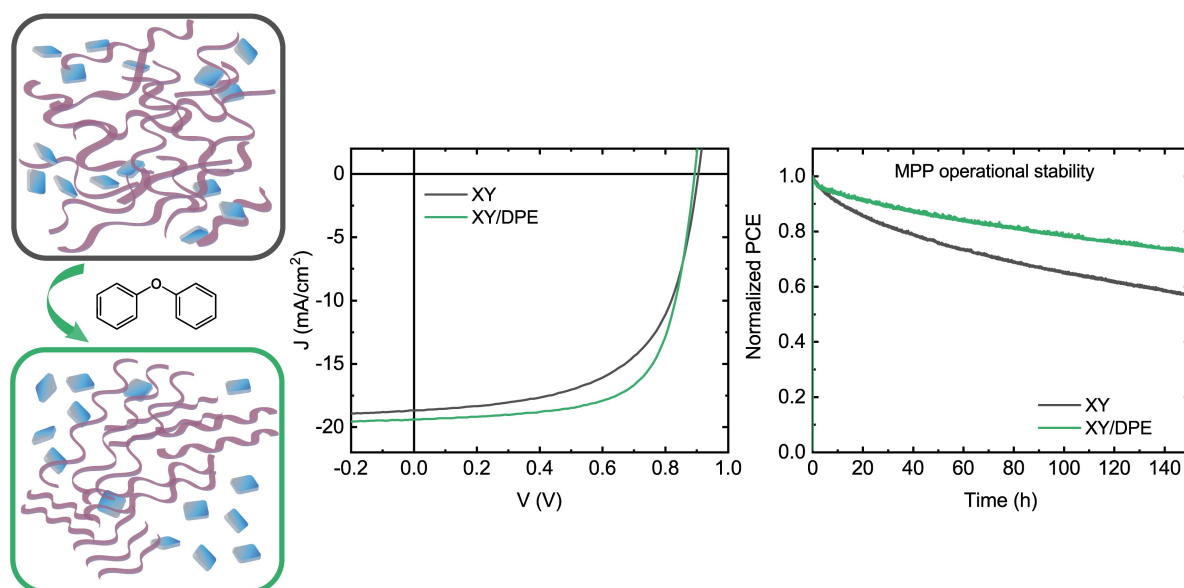
Table S2 shows the Franck-Condon fit parameters of the spectral decomposition of the electron acceptor materials Y6 and N4 in solution, neat films and blend films with PM6 according to Figure 3, Figure 4 and Figure 7.

Table S2: Fitting parameters of the Franck-Condon analysis for the decomposition of the absorption spectra of the electron acceptors Y6 and N4 in mTHF solution, in as-cast and TA films and in blend films with PM6; with the energetic position of the 0-0 transition E_{00} , the linewidth σ , the Huang-Rhys parameter S_1 and the effective vibrational mode $\hbar\omega$.

Y6 in mTHF	transition	E_{00} (eV)	σ (meV)	S_1	$\hbar\omega$ (meV)	
195 K	non-interacting	1.74	68.6	0.43	162	
	Agg. I, LE	1.54	44.4	0.15	162	
	Agg. I, HE	1.92	44.4	0.15	162	
	Agg. II, LE	1.62	43.5	0.26	162	
	Agg. II, HE	1.85	43.5	0.26	162	
140 K	non-interacting	1.74	66.8	0.43	162	
	Agg. I, LE	1.54	40.6	0.15	162	
	Agg. I, HE	1.92	40.6	0.15	162	
	Agg. II, LE	1.63	41.3	0.26	162	
	Agg. II, HE	1.85	41.3	0.26	162	
N4 in mTHF	transition	E_{00} (eV)	σ (meV)	S_1	$\hbar\omega$ (meV)	
	220 K	non-interacting	1.74	67.9	0.55	162
		Agg. I, LE	1.54	44.2	0.18	162
		Agg. I, HE	1.93	44.2	0.18	162
		Agg. II, LE	1.64	43.0	0.40	162
Agg. II, HE		1.86	43.0	0.40	162	
140 K	non-interacting	1.74	64.1	0.55	162	
	Agg. I, LE	1.54	42.6	0.18	162	
	Agg. I, HE	1.93	42.6	0.18	162	
	Agg. II, LE	1.64	40.5	0.40	162	
	Agg. II, HE	1.86	40.5	0.40	162	

Y6 film	<i>transition</i>	E_{00} (eV)	σ (meV)	S_1	$\hbar\omega$ (meV)
as-cast	non-interacting	1.73	64.1	0.42	162
	Agg. I, LE	1.52	57.2	0.13	162
	Agg. I, HE	1.93	57.2	0.13	162
	Agg. II, LE	1.62	54.7	0.20	162
	Agg. II, HE	1.83	54.7	0.20	162
TA	non-interacting.	1.72	62.1	0.42	162
	Agg. I, LE	1.50	55.1	0.18	162
	Agg. I, HE	1.94	55.1	0.18	162
	Agg. II, LE	1.60	54.0	0.20	162
	Agg. II, HE	1.83	54.0	0.20	162
N4 film	<i>transition</i>	E_{00} (eV)	σ (meV)	S_1	$\hbar\omega$ (meV)
as-cast	non-interacting	1.73	70.2	0.48	162
	Agg. I, LE	1.51	55.1	0.18	162
	Agg. I, HE	1.95	55.1	0.18	162
	Agg. II, LE	1.61	55.3	0.20	162
	Agg. II, HE	1.85	55.3	0.20	162
TA	non-interacting	1.73	69.7	0.48	162
	Agg. I, LE	1.51	55.1	0.18	162
	Agg. I, HE	1.93	55.1	0.18	162
	Agg. II, LE	1.60	55.3	0.20	162
	Agg. II, HE	1.84	55.3	0.20	162
Blend films	<i>transition</i>	E_{00} (eV)	σ (meV)	S_1	$\hbar\omega$ (meV)
PM6:Y6	non-interacting	1.72	62.1	0.42	162
	Agg. I, LE	1.51	55.0	0.19	162
	Agg. I, HE	1.94	55.0	0.19	162
	Agg. II, LE	1.60	54.0	0.20	162
	Agg. II, HE	1.83	54.0	0.20	162
PM6:N4	non-interacting	1.72	69.7	0.48	162
	Agg. I, LE	1.52	55.1	0.18	162
	Agg. I, HE	1.93	55.1	0.18	162
	Agg. II, LE	1.60	55.3	0.20	162
	Agg. II, HE	1.84	55.3	0.20	162

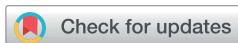
13 Effects of the diphenyl ether additive in halogen-free processed non-fullerene acceptor organic solar cells



Lorenzo Di Mario, David Garcia Romero, Meike J. Pieters, **Fabian Eller**, Chenhui Zhu, Giovanni Bongiovanni, Eva M. Herzig, Andrea Mura and Maria A. Loi

Published in
Journal of Materials Chemistry A **2023**, 11 (5), 2419-2430
(DOI: 10.1039/D2TA08603D)

Reprinted with permission from the Royal Society of Chemistry
Copyright 2022 The Royal Society of Chemistry

Cite this: *J. Mater. Chem. A*, 2023, **11**, 2419

Effects of the diphenyl ether additive in halogen-free processed non-fullerene acceptor organic solar cells†

 Lorenzo Di Mario,^a David Garcia Romero,^a Meike J. Pieters,^a Fabian Eller,^b Chenhui Zhu,^c Giovanni Bongiovanni,^d Eva M. Herzig,^b Andrea Mura^d and Maria A. Loi^{*a}

The development of an environmentally friendly fabrication process for non-fullerene acceptor organic solar cells is an essential condition for their commercialization. However, devices fabricated by processing the active layer with green solvents still struggle to reach, in terms of efficiency, the same performance as those fabricated with halogenated solvents. The reason behind this is the non-optimal nanostructure of the active layer obtained with green solvents. Additives in solution have been used to fine-tune the nanostructure and improve the performance of organic solar cells. Therefore, the identification of non-halogenated additives and the study of their effects on the device performance and stability are of primary importance. In this work, we propose the use of diphenyl ether (DPE) as additive, in combination with the non-halogenated solvent *o*-xylene, to fabricate organic solar cells with a completely halogen-free process. Thanks to the addition of DPE, a best efficiency of 11.7% have been obtained for the system TPD-3F:IT-4F, an increase over 15% with respect to the efficiency of devices fabricated without additive. Remarkably, the stability under illumination of the solar cells is also improved when DPE is used. The addition of DPE has effects on the molecular organization in the active layer, with an enhancement in the donor polymer ordering, showing a higher domain purity. The resulting structure improves the charge carrier collection, leading to a superior short-circuit current and fill factor. Furthermore, a reduction of the non-radiative recombination losses and an improved exciton diffusion, are the results of the superior molecular ordering. With a comprehensive insight of the effects of DPE when used in combination with a non-halogenated solvent, our study provides an approach to make the fabrication of organic solar cell environmentally friendlier and more suitable for large scale production.

Received 3rd November 2022
Accepted 15th January 2023

DOI: 10.1039/d2ta08603d

rsc.li/materials-a

Introduction

Organic solar cells (OSCs), based on the combination of polymer donors with small molecule acceptors, have seen in the last few years a surge in power conversion efficiency (PCE), driven by the development of novel non-fullerene acceptors (NFA), which, compared to fullerene derivatives, offer complementary light absorption and well-matched energy levels with the polymer donors.^{1,2} Efficiency values have already surpassed what is considered as the threshold for commercialization, with record

PCE above 19%.^{3–6} Therefore, the new challenge for the scientific community is the improvement of the stability and of the fabrication process, in order to allow large scale production of these devices.⁷

In solution-processed OSCs, the active layer deposition relies on the preparation of a solution containing both the donor and acceptor materials, in order to obtain the formation of a bulk heterojunction (BHJ) layer upon casting. The solvent employed to prepare the solution regulates the purity and crystallinity of donor- and acceptor-rich domains^{8,9} which can dramatically affect the nanostructure of the BHJ, and thus the performance of the final devices. This sets strict requirements for the selection of the solvent, which can be challenging to meet. Currently, the OSCs with the best performance are all obtained using halogenated solvents (*e.g.* chloroform, chlorobenzene, dichlorobenzene).^{4–6} Despite their proven effectiveness for the processing of the active layer in OSCs, halogenated solvents are toxic and harmful for the environment and therefore they are not suitable for industrial application. Finding green solvents able to guarantee device performance comparable to those

^aZernike Institute for Advanced Materials, University of Groningen, Nijenborgh 4, Groningen 9747 AG, The Netherlands. E-mail: m.a.loi@rug.nl

^bDynamics and Structure Formation – Herzig Group, Institute of Physics, University of Bayreuth, Universitätsstraße 30, Bayreuth 95447, Germany

^cLawrence Berkeley National Laboratory, Advanced Light Source, Berkeley, CA, 94720, USA

^dDipartimento di Fisica, Università degli Studi di Cagliari, Monserrato I-09042, Italy

† Electronic supplementary information (ESI) available. See DOI: <https://doi.org/10.1039/d2ta08603d>



obtained with halogenated solvents is crucial for the commercialization of OSCs.^{10,11} In the last few years, several halogen-free solvents (*e.g.* *o*-xylene, tetrahydrofuran, anisole, carbon disulfide, limonene) have been reported to successfully work for the fabrication of OSCs, although device performance is still lagging behind in comparison with the one obtained with the halogenated counterpart.^{12–15} While many donor and acceptor materials show a good solubility in non-halogenated solvents, the optimal nanostructure of the BHJ is hardly achieved when they are employed.

A simple and effective method to control the aggregation of donor and acceptor materials, in order to promote an optimal structure of the BHJ, consists in the use of solvent additives. Since their first successful use, strong efforts have been devoted to define the criteria for the selection of proper additives and to identify the most promising ones for the processing of OSCs of various composition.^{16,17} As happened for the solvents, the first effective additives that have been identified were halogenated additives. 1,8-Diiodooctane (DIO) and 1-chloronaphthalene (CN) are the most widely used solvent additives and their effects on BHJ nanostructure, device efficiency and stability have been thoroughly studied.^{18–20} While those additives are often reported to improve the device performance also when OSCs are fabricated using green solvents,^{13,14} their employment can hinder the compatibility with large scale production. Therefore, finding non-halogenated additives for OSCs, and investigating their effects, represents a further step toward OSCs commercialization.²¹

The use of diphenyl ether (DPE) as non-halogenated additive has been reported in the fabrication of diverse OSCs, showing his effectiveness in devices using fullerenes as acceptors, where improvements have been correlated with an effect of DPE on the polymer donor crystallization.^{22–25} More recently, DPE has also been used in the fabrication of OSCs with NFAs, both in bulk- as well as planar-heterojunction active layer.^{26–29} Despite those promising results, a fundamental understanding of the complex interaction between DPE, solvents, polymer donors and non-fullerene acceptors is still missing and most of the knowledge related to the effects of DPE as additive still relies on what was observed in systems using fullerene derivatives as acceptors. Additionally, DPE has been mostly used in combination with halogenated solvents and its use with green solvent is scarcely reported.^{26,27,30} Finally, the effects of DPE on the stability of OSCs has not yet been investigated, although it is widely reported that other additives remain in the active layer, with detrimental effects for the device stability.^{31–33}

In this work, we demonstrate that the use of the non-halogenated DPE as additive, in combination with a non-halogenated solvent, improves simultaneously the performance and the stability of NFA-OSCs. The OSCs were fabricated blending together the polymer poly[2,2'-(4,8-bis[4-fluoro-5-(2-hexyldecyl)-2-thienyl]benzo[1,2-*b*:4,5-*b'*]dithiophene-2,6-diyl)-2,5-thiophenediyl(5,6-dihydro-5-octyl-4,6-dioxo-4*H*-thieno[3,4-*c*]pyrrole-1,3-diyl)-2,5-thiophenediyl] (TPD-3F) and the small molecule 3,9-bis(2-methylene-((3-(1,1-dicyanomethylene)-6,7-difluoro)-indanone))-5,5,11,11-tetrakis(4-hexylphenyl)-dithieno[2,3-*d*:2',3'-*d'*]-*s*-indaceno[1,2-*b*:5,6-*b'*]dithiophene (IT-4F). We

used *o*-xylene as solvent and we investigated the effects of DPE as additive, depositing the active layer by both spin coating and blade coating.

Solar cells fabricated with the addition of DPE achieved a maximum PCE of 11.7%, with an improvement of over 15% compared with devices without additive. The operational stability of the solar cells is also improved when DPE is used, with devices able to preserve 73% of their initial efficiency after 150 h under constant illumination, where only 57% of the efficiency is maintained in devices fabricated without additive. In the DPE treated devices, the increase in J_{sc} and in FF, is the result of an improved charge carrier collection, especially when photons are absorbed by the donor. The consequence of the interaction of DPE with the donor molecules were investigated by Grazing-Incidence Wide-Angle X-ray Scattering (GIWAXS) measurements, which revealed how the additive leads to a higher ordering of the polymer molecules, inducing edge-on orientation in comparison to the dominantly face-on presented in the blend without additive. Photoluminescence and fast transient absorption measurements further support the correlation between the structural changes and device performance, showing a reduction of non-radiative recombination losses, together with an improved exciton diffusion. In particular, the increased exciton diffusion points towards a reduced energetic disorder, as result of the superior molecular ordering of the donor when DPE is used as an additive. The reduced energetic disorder not only promotes better device performance but is also the reason for the improved device stability.

Results and discussion

We fabricated OSCs using TPD-3F and IT-4F as donor and acceptor, respectively. Fig. 1a shows the chemical structures of the two molecules, together with the device structure used (Fig. 1b). The organic blend of donor and acceptor was spin coated starting from a solution in *o*-xylene with diphenyl ether (DPE) as additive. A solution without the additive was used to fabricate reference devices, with the same structure and employing the same processing parameters. Furthermore, for comparison, devices were fabricated with the commonly-used halogenated additive 1,8-diiodooctane (DIO). Device performance and characterizations of films made using DIO are reported in the ESI.†

Normalized UV-Vis absorption spectra of blend films spin coated from solution with and without the use of DPE (Fig. 1c) show the characteristic absorption features of TPD-3F with peaks around 560 and 610 nm, and IT-4F with a peak at 720 nm.^{34,35} The most noteworthy change in the absorption spectrum, due to the use of DPE, is an increased absorption in the spectral range of the donor material with respect to the peak of the acceptor, which suggests an effect of the additive in the formation of the donor-rich domains. A closer look at the absorption peak of the acceptor, as reported in the inset of Fig. 1c, reveals a small redshift of the absorption onset when DPE is used. Such effect is often observed when additives are used for non-fullerene acceptor OSCs and is associated with a higher ordering of the acceptor-rich domains.^{36,37} Overall, the



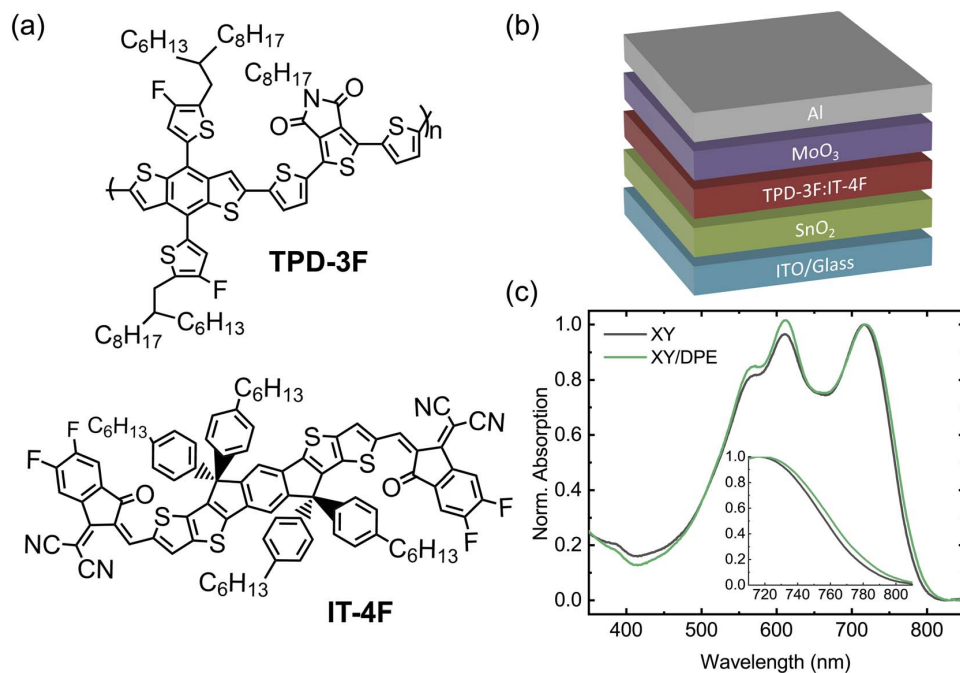


Fig. 1 (a) Chemical structures of the polymer donor TPD-3F and the non-fullerene acceptor IT-4F. (b) Schematic of the device structure used in this work. (c) Absorption spectra of TPD-3F:IT-4F blend films cast from *o*-xylene without additive and with 3 wt% of DPE. The inset shows a zoom-in of the absorption onset.

analysis of the absorption spectra suggests changes in the BHJ layer following the use of DPE, which are compatible with an improved molecular ordering in both donor-rich and acceptor-rich domains. This is consistent with an increased phase purity in the BHJ layer, since donor-acceptor intermixing generally hinders a proper ordering.

In Fig. 2 the performance of solar cells fabricated by spin coating the blend film with and without the addition of DPE is compared. J - V characteristics under illumination of the two best devices are reported in Fig. 2a, while Table 1 and Fig. S1† report a summary of the photovoltaic parameters obtained over multiple batches of devices. Devices fabricated with the use of DPE show superior photovoltaic performance, with a maximum efficiency of 11.7%, which represents an improvement of more than 15% over the best values obtained without additive. The improvement is the result of an increased J_{sc} and FF, both parameters that are strongly affected by the molecular ordering and phase purity in the BHJ. A reduction of the V_{oc} is observed for devices fabricated adding DPE. This result correlates well with the redshift of the absorption spectrum and is ascribed to a narrowing of the acceptor energy gap due to an increased crystallinity.³⁷

OSCs have also been fabricated casting the active layer by blade coating and their performance is shown in Fig. S2.† Despite the different deposition method, the addition of DPE leads to similar changes in J_{sc} , FF and V_{oc} as those observed when spin coating is employed. Remarkably, when blade coating is used, the

performance of devices without additive are poorer while devices with DPE are able to achieve performance comparable with spin coated devices.

Comparing the performance of devices fabricated with DPE with those of devices fabricated with DIO, as shown in Fig. S1,† both additives induce similar effects on the photovoltaic parameters. However, while DIO improves the performance of the devices with respect to those fabricated without additive, the overall effect on the efficiency is below 5% and for all photovoltaic parameters the improvement is less significant than with DPE.

To better understand the origin of the increased J_{sc} in devices fabricated using DPE, we measured the external quantum efficiency (EQE) (Fig. 2b). The value of the J_{sc} calculated from the EQE spectra is consistent with that extracted from the J - V curves. Devices with and without the additive exhibit similar EQE spectral shape with differences in the absolute values. While for devices fabricated with DPE a maximum EQE of 82% is measured, without the additive only 75% is reached. To better point out the differences of samples fabricated with and without additive, the difference between the two EQE spectra is displayed in Fig. S3.† The most significant changes are observed in the spectral range of absorption of the TPD-3F, which is in agreement with what has been discussed for the absorption spectra (Fig. 1c).

Fig. 2c shows the J - V characteristics of the solar cells measured in dark conditions. Devices fabricated using DPE are characterized by lower shunt current and diminished series resistance, which is consistent with the higher FF measured



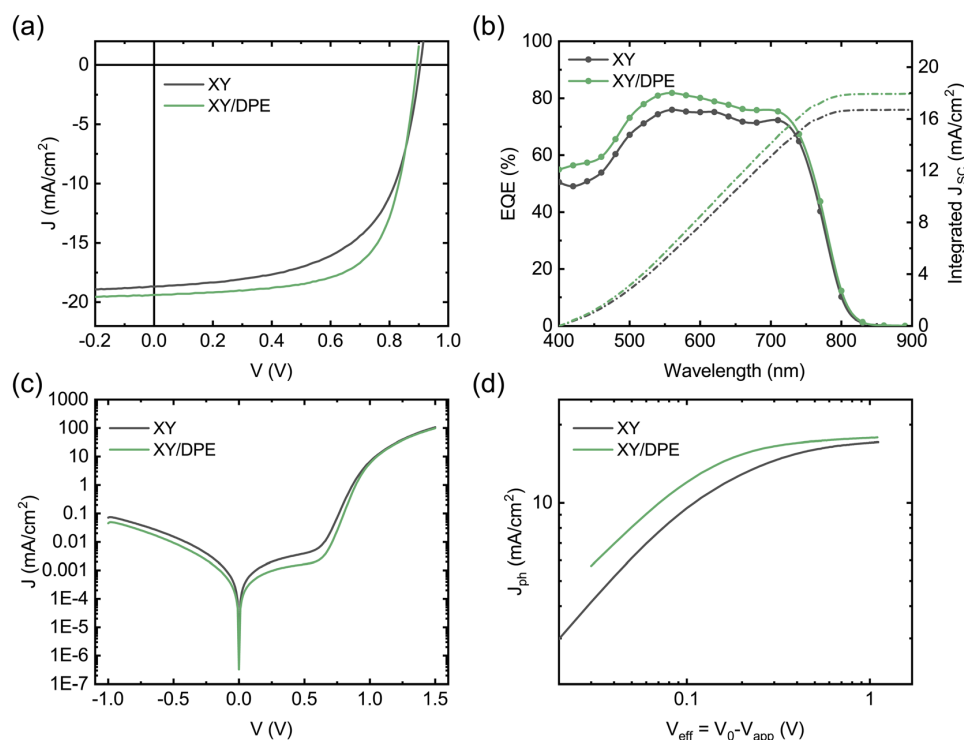


Fig. 2 Electrical characteristics of optimized solar cells, fabricated by spin coating from a *o*-xylene solution without additive and with 3 wt% of DPE: (a) J - V curves under illumination (AM 1.5, 100 mW cm^{-2}); (b) EQE spectra and integrated J_{sc} ; (c) J - V curves in dark condition; (d) J_{ph} as a function of V_{eff} .

under illumination. The reduced leakage current can be explained by a slower drying of the organic film after spin coating, due to the high boiling point of the additive, which leads to a more compact film. However, the lower series resistance hints at an improved BHJ nanostructure and, thus, at an increased charge carrier collection. This is confirmed by the study of the photocurrent J_{ph} as function of the effective voltage V_{eff} (Fig. 2d). J_{ph} is defined as the difference between light and dark current densities, while V_{eff} is the difference between the voltage V_0 at which dark and light current densities compensate and the applied voltage V_{app} . For large values of V_{eff} , the photon harvesting is maximized and J_{ph} reaches a saturation value. Devices fabricated adding DPE reach a saturation current of 17.88 mA cm^{-2} , which is higher than the 17.15 mA cm^{-2} of

devices fabricated without additive. This indicates an increased photon harvesting, which is in agreement with absorption and EQE spectra and points towards an improved nanostructure of the BHJ as result of the use of DPE. From the ratio between J_{ph} and the saturation current density at maximum power point conditions, it is possible to estimate the charge carrier collection probability P_{coll} .³⁸ A remarkable difference is observed on the collection probability with and without the additive, with an increase from 77.6% to 83.8% when DPE is used, which hint at a more favorable interpenetrating network of donor and acceptor and a better charge transport.

Charge carrier transport and collection were also investigated by impedance spectroscopy and the results are displayed in the Nyquist plot in Fig. 3, together with the best fits of the

Table 1 Photovoltaic parameters of champion solar cells, fabricated by spin coating a solution of TPD-3F:IT-4F with and without DPE. Average values obtained from 15 devices fabricated in different batches are reported in parenthesis

Solution	V_{oc} (V)	J_{sc} (mA cm^{-2})	FF (%)	PCE (%)
XY ^a	0.936 (0.935 ± 0.006)	16.49 (16.52 ± 0.35)	62.66 (60.21 ± 2.66)	9.67 (9.30 ± 0.29)
XY + 3% DPE ^a	0.922 (0.921 ± 0.004)	17.75 (17.35 ± 0.32)	66.05 (63.93 ± 1.58)	10.81 (10.20 ± 0.41)
XY ^b	0.905 (0.905 ± 0.002)	18.70 (18.59 ± 0.11)	59.77 (59.50 ± 0.58)	10.11 (9.98 ± 0.12)
XY + 3% DPE ^b	0.893 (0.892 ± 0.004)	19.39 (19.29 ± 0.20)	67.49 (66.75 ± 0.50)	11.68 (11.50 ± 0.18)

^a Devices with active area of 10 mm^2 . ^b Devices with active area of 4 mm^2 .



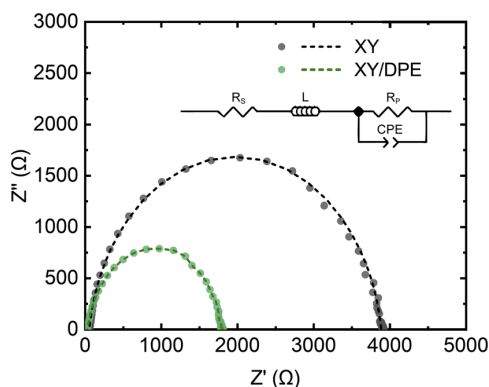


Fig. 3 Nyquist plot of solar cells fabricated with and without DPE. Experimental data (dots) and best fits (dash lines). Inset: equivalent circuit used to fit the experimental data.

experimental data. Devices fabricated either with or without the use of DPE, show a single semicircle in the Nyquist plot and, thus, their behavior can be fitted assuming a single RC component. The equivalent circuit used for the fitting is shown in Fig. 3 as inset and the values obtained for the different components can be found in Table S1.† As expected from the results previously discussed, the component R_p , which mainly represents the resistance of the organic layer, is reduced by the use of DPE, as further indication of the improvement in charge transport. The constant phase element (CPE) is a non-ideal capacitor, which considers dispersive processes, caused for instance by inhomogeneities in the BHJ. The dispersion parameter CPE-P (ideally equal to 1), is similar for devices fabricated with and without the use of DPE, suggesting no effects of the additive on the homogeneity of the film, which is an important aspect for the scaling up of the fabrication process. Furthermore, the higher RC time constant for devices fabricated using DPE with respect to the one of those without additive is an indication of longer charge carrier lifetimes.³⁹ Finally, the series resistance R_s , which takes into account the

resistance of contacts, interlayers and interfaces, is also remarkably reduced in the presence of DPE. Considering that there are no differences in the device structure, the observed change in R_s indicates the effect of the additive on the active layer and therefore also on the resistance at the interfaces. As reported in the case of DIO,^{18,20} the use of an additive for the active layer can affect the distribution of donor and acceptor in the direction perpendicular to the substrate, with the result of a higher concentration of one of the two components at the interface with the transport layer. While such a gradient of concentration of donor and acceptor along the film thickness is challenging to prove,⁴⁰ it could explain the significant difference in R_s observed.

To conclude the analysis of the effect of DPE on device performance, the stability of solar cells was tested, and the results are displayed in Fig. 4. Fig. 4a shows the operational stability of solar cells under illumination at the maximum power point. Solar cells fabricated adding DPE are characterized by an improved stability, preserving the 73% of their initial efficiency after 150 hours, while devices without additive maintain only the 57% of their efficiency. Looking at the decay dynamics, both solar cells have an initial rapid loss of performance, called burn-in, followed by a more gradual and significantly slower loss. The main difference in the stability of devices fabricated with and without the use of DPE is in the burn-in phase. For devices fabricated using DPE the burn-in lasts few hours and accounts for a loss in performance of around 5%. On the other hand, devices fabricated without additive have a burn-in phase of more than 20 hours, in which the efficiency drops below 80% of the initial value. While the origin of the burn-in in NFA-OSCs is still debated, morphological instabilities and disorder-induced losses have been identified as two of the main factors determining this phenomenon.⁴¹ Morphological instabilities arise when the BHJ nanostructure that is achieved after casting and post-processing is not the most thermodynamically stable. In this condition, the exposure to light provides enough energy to drive an evolution toward a more stable nanostructure. This often implies a de-mixing of the two blend components, which leads to performance reduction in the devices.

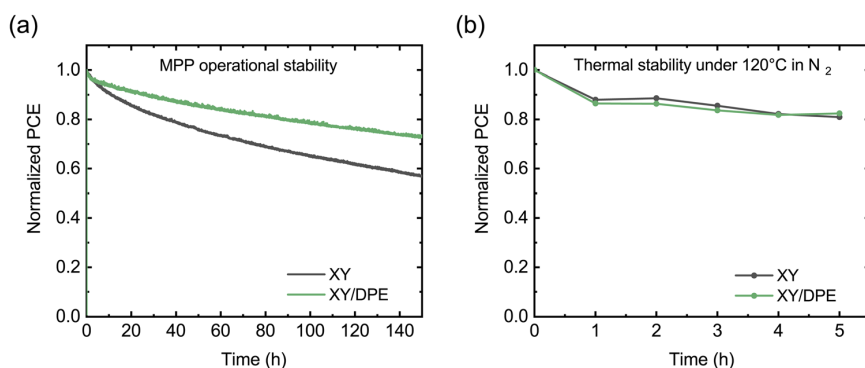


Fig. 4 Stability of solar cells fabricated casting the blend film from a solution without additive and with DPE: (a) stability in operation measured at maximum power point (MPP) under continuous illumination (AM 1.5, 100 mW cm⁻²); (b) thermal stability measured after annealing the solar cells at 120 °C in N₂ atmosphere.



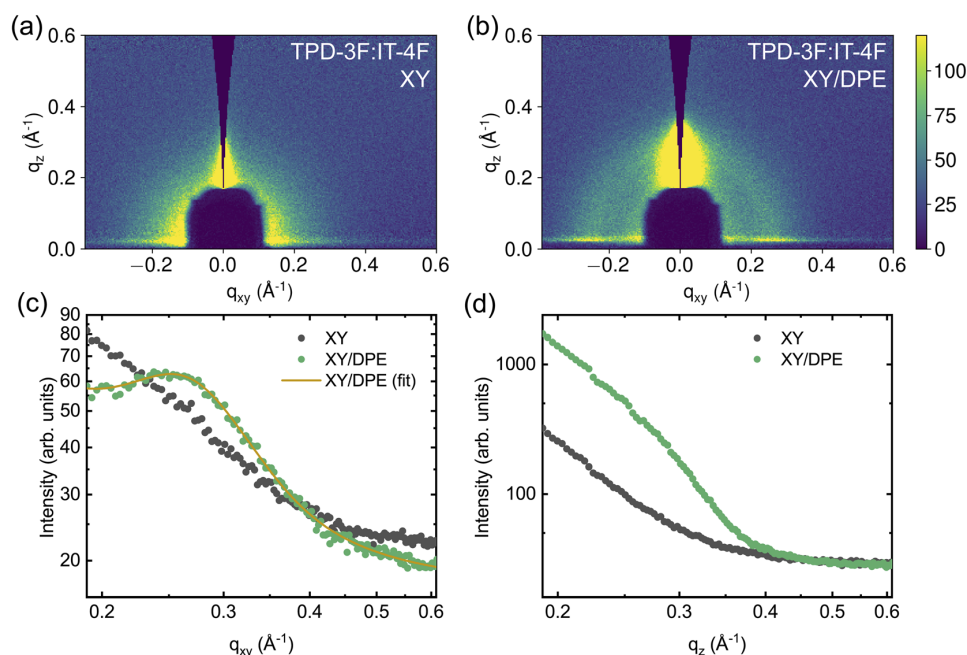


Fig. 5 2D GIWAXS data and cuts of measurements on TPD-3F:IT-4F blend films cast with and without the addition of DPE: 2D false-color maps for a blend film without additive (a) and with additive (b); corresponding in-plane (c) and out-of-plane (d) line cuts.

Since morphological instabilities are thermodynamically driven, heating the devices has a similar effect as light exposure. Thus, operational stability and thermal stability measurements are expected to return similar results. In Fig. 4b the thermal stability at 120 °C is reported for the two types of devices. Differently from the results with light exposure, under thermal stress solar cells with and without additive show comparable behaviors. This suggests that, despite the presence of thermodynamic instability, the difference in operational stability between device with and without DPE could arise from a different impact of disorder-induced losses. An increase in energetic disorder and, thus, in disorder-induced losses is generated in OSCs by the light exposure due to photochemical reactions in the BHJ.^{42,43} A higher molecular ordering of donor and acceptor is reported to reduce the sensitivity to the increased energetic disorder.^{44–46} Therefore, the improved stability when DPE is used could find an explanation in an increased molecular ordering in the BHJ with respect to when the additive is not used.

The stability of solar cells fabricated using DIO has also been tested and is displayed in the ESI (Fig. S4†). The operational stability in Fig. S4a† shows the same behavior as for devices without additive, proving that the improvement observed with DPE, strongly correlates with the characteristics of this specific additive. However, the often reported detrimental effects of DIO in solar cell stability due to photoinduced ionization^{33,47,48} is not present in our measurements, as an UV filter was used. On the other hand, as can be seen in Fig. S4b,† devices fabricated using DIO show worse stability under thermal stress than devices with DPE and without additive. While an in-depth study of the

mechanism that affect the stability of OSCs in the presence of different additives is out of the scope of this work, the comparison between DIO and DPE points to the superior stability of the devices fabricated with DPE, which is a crucial aspect for applications.

Due to the addition of DPE, both efficiency and stability of the solar cells show improvements, which derive from changes in BHJ nanostructure and in the molecular ordering of donor and acceptor molecules. To further investigate the variation induced by DPE in the nanostructure, Grazing Incidence Wide-Angle X-ray Scattering (GIWAXS) measurements have been performed on the active layers deposited on the glass/ITO/SnO₂ stack used for devices. Fig. 5 shows the measurements performed on the two active layers, while Fig. S5 and S6 in ESI† show the results of experiments on neat TPD-3F and IT-4F films, respectively. Only intermolecular separations bigger than the π - π stacking are here discussed, since a strong scattering from the layer stack under the active layer at q values similar to the π - π stacking makes impossible to isolate the peak. The measurements on neat donor (Fig. S5†), with and without additive, show a peak in the direction parallel to the substrate at around $q_{xy} = 0.247 \text{ \AA}^{-1}$ ($d = 25.4 \text{ \AA}$), which points to a preferential face-on orientation of the polymer with respect to the substrate. Differences in peak shape with and without the use of DPE are negligible. On the other hand, the use of DPE as additive results in an increase of the peak amplitude and peak area of around 37%, in comparison with the film prepared without additive. In addition, a weaker but similar TPD-3F lamellar peak seems to be induced by the DPE in the direction



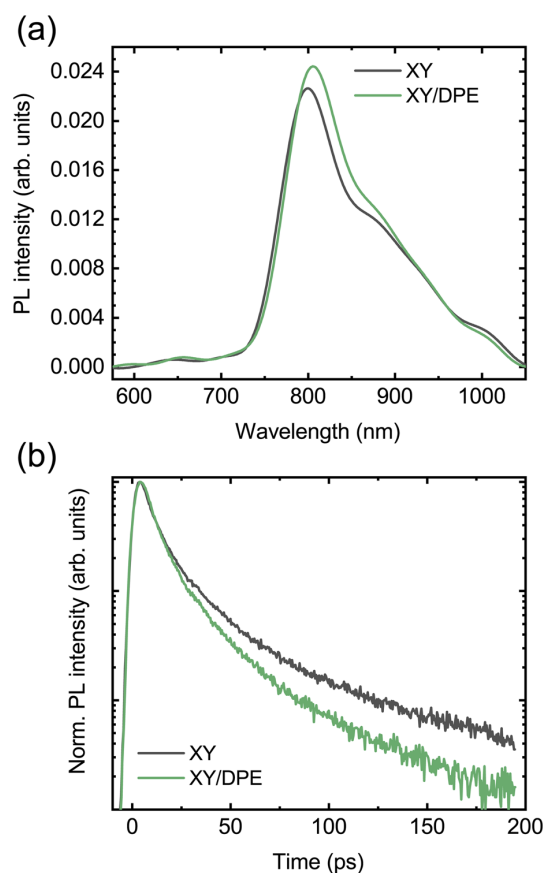


Fig. 6 Photoluminescence measurements on TPD-3F:IT-4F blend films cast with and without the use of DPE: (a) steady-state photoluminescence; (b) decay of the PL signal at 800 nm.

perpendicular to the substrate, as shown in Fig. S5d† by the increased scattering intensity for q_z values between 0.2 and 0.3 \AA^{-1} . Overall, the type of ordering in neat TPD-3F films, with and without DPE, appears to be the same. Nonetheless, with the addition of DPE, more TPD-3F molecules are in an ordered phase and, additionally to the dominant face-on orientation, a fraction of edge-on orientation occurs.

In the IT-4F films (Fig. S6†), no signs of well-defined nanostructure are observed when the film is spin coated from a solution without additive. However, when DPE is used, a clear peak appears in the direction perpendicular to the substrate, at about $q_z = 0.414 \text{\AA}^{-1}$. In the films of neat donor and acceptor the addition of DPE increases the amount of material possessing nanostructure. Since not only existing nanostructures are strengthened or reoriented, but new order appears with the addition of DPE, the effect of the additive is not limited to an increased drying time, but most likely also to an altered solubility.

The effects of the addition of DPE becomes even more important for the blend films, as can be seen in Fig. 5. Even though the neat TPD-3F film cast from a solution without

additive exhibits a clear nanostructure, the TPD-3F:IT-4F blend film does not show any signs of nanostructure of the donor without the use of the additive. This suggests a strong interaction between donor and acceptor molecules, which leads to highly mixed domains and, thus, hinders the nanostructure formation of TPD-3F. The addition of DPE enables nanostructure formation, with the appearance of a TPD-3F peak in the direction parallel to the substrate (Fig. 5c). Compared to the peak shown by the film of neat donor, an increase of about 90% of the peak width points towards a higher disorder in the blend. At the same time the peak position shifts to $q_{xy} = 0.258 \text{\AA}^{-1}$ ($d = 24.3 \text{\AA}$), which corresponds to a reduction of the spacing of about 4.3% in the blend with respect to the neat donor film. The addition of DPE also affects the ordering in the perpendicular direction, where a significant enhancement in scattering is observed in the film with the additive, compared to the one without (Fig. 5d). Similarly to the case of the neat donor films, such increased scattering can be correlated with an ordering of the TPD-3F in the perpendicular direction, with structure size analogous and larger with respect to that observed in the parallel direction. Therefore, with the addition of DPE, the nanostructure is not only strongly enhanced, but also reoriented with a significant fraction of the TPD-3F with an edge-on orientation, additionally to the dominant face-on orientation.

The effects of DPE on the blend nanostructure are also compared to those of DIO and the results are reported in the ESI (Fig. S7†). The addition of DIO also enables the nanostructure formation of TPD-3F in the blend. Peak position and line shape in the direction parallel to the substrate are comparable to those obtained with the use of DPE, suggesting a similar quality of ordering. Comparing the blend peak amplitudes, the amplitude is higher by about 69% when DIO is used instead of DPE, indicating that the occurrence of face-on orientation is higher with the halogenated additive. On the other hand, no clear sign of edge-on orientation for the TPD-3F is observed using DIO, in contrast to DPE.

To conclude, the analysis of GIWAXS measurements indicates that both DPE and DIO lead to a stronger aggregation of the TPD-3F molecules, which we attribute to a more pronounced phase separation. The lower order of the TPD-3F nanostructure in the blend films compared to the films of neat donor points out that IT-4F is present in the donor-rich domains. This induces a loss of order at shorter distances, but also increases the packing density of the TPD-3F. The effect of DPE and DIO on the phase separation appears to be similar. Nonetheless, the addition of DIO favors only a face-on orientation of the TPD-3F while DPE also promotes edge-on orientation, on both blend and neat donor films. Similar effects on the blend nanostructure when DPE is used as additive have been previously reported for other polymers.^{23,24,29} In general, DPE is considered a theta solvent for polymers such as the ones used as donors in OSCs.²⁴ This means that the polymer coils act as ideal chains in DPE, since the interaction between solvent and polymer is balanced at the theta point. The result, when DPE is used as additive, is an improved blend film nanostructure with a continuous and properly distributed polymer network, in both the directions parallel and perpendicular to



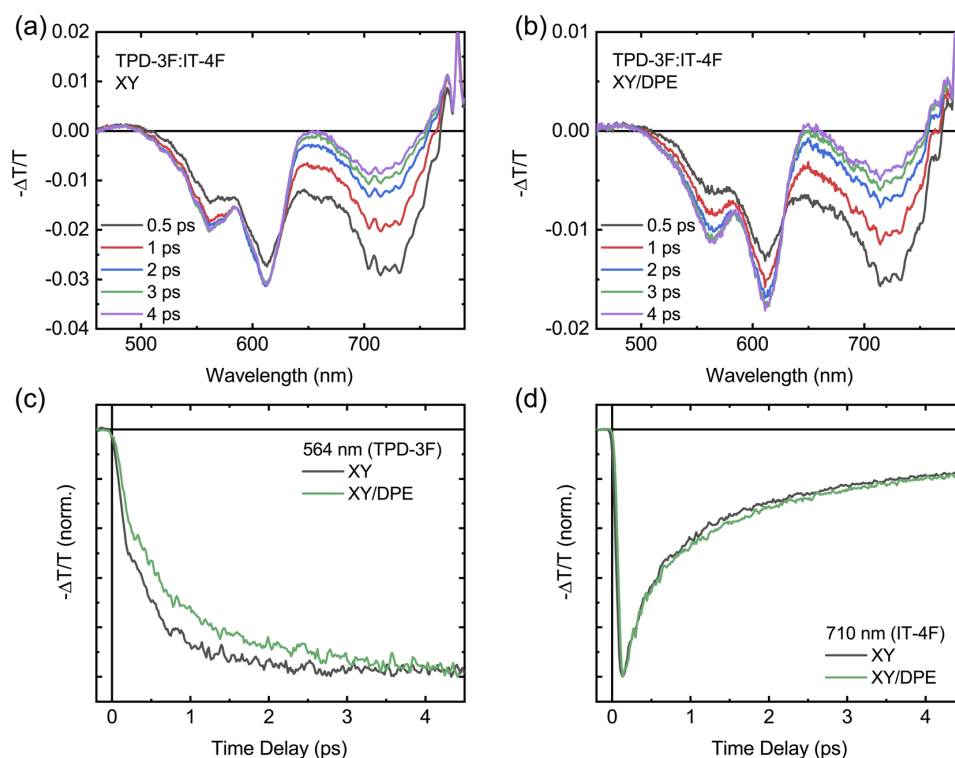


Fig. 7 Fast transient transmission spectroscopy measurements with an excitation wavelength of 700 nm on TPD-3F:IT-4F blend films cast with and without the use of DPE in solution: transient transmission spectra acquired at different time delays for the blend film cast without additive (a) and with additive (b); kinetics of the donor (c) and acceptor (d) signals for the two blend films.

the substrate, a condition that is expected to enhance charge transport and suppress non-radiative losses.^{23,24} As already reported in other works in literature, the use of DPE as additive can lead to a remarkable improvement of both charge carrier mobilities, a result that is consistent with the changes in nanostructure here pointed out.^{23,26,27}

To further understand how the change in nanostructure induced by the DPE affects the charge carrier dynamics in the blend and to reveal the correlation with the device performance improvement, photoluminescence (PL) and fast transient transmission spectroscopy (FTTS) have been employed. The steady state PL spectra of blend films deposited by spin coating from a solution with and without DPE are compared in Fig. 6a. Both spectra display the typical acceptor emission, while the emission from the donor is totally quenched.^{34,35} Comparing the two spectra, the addition of DPE leads to slightly increased PL intensity, together with a redshift of the peak, which is consistent with that observed for the absorption spectra.

Moving to the time-resolved PL measurements (Fig. 6b), a faster decay of the PL intensity measured at the peak (800 nm) and, thus, a faster exciton quenching is observed in blend films processed with DPE with respect to films without additive. The time-resolved PL decays are fitted with multiexponential curves and the extracted parameters are reported in Table S2,[†] together

with the calculated average PL lifetimes. A significantly shorter average PL lifetime is obtained when DPE is used, despite comparable time-constants in both the picoseconds and tens of picoseconds regimes. The shorter PL lifetime can be associated with an increased chance for the excitons of reaching the donor-acceptor interface to be dissociated. This can be the result of both a reduction in domain size or an increased exciton diffusion length. A reduction in domain size is unlikely considering the results of the GIWAXS characterization, which point out a higher phase purity likely associated with an increased phase separation. An increase of the exciton diffusion length can be explained by a reduced energetic disorder, which is a direct consequence of the improved ordering of the donor molecules induced by the DPE.⁴⁹⁻⁵¹ The correlation between improved exciton dissociation and ordering of the polymer in the blend film is also consistent with the increase of the EQE in the range of absorption of the donor.

FTTS can be used to further investigate the exciton diffusion and dissociation at the sub-picosecond time scale (Fig. 7). Upon excitation with pump pulses at 700 nm, the transient spectra of films with and without DPE show similar features, as displayed in Fig. 7a and b. For both films the transient spectra are characterized by a broad band centered around 720 nm and two peaks at around 600 nm. All signals are negative in sign and are



ascribed to the ground state bleaching of acceptor and donor, for the signals at 720 nm and 600 nm, respectively. Fig. S8† shows the transient spectra obtained by exciting the neat donor and acceptor films with pump pulses at 360 nm. Similar transient spectra have been reported for analogous donor:acceptor blend systems.^{34,36} Despite the fact that the 700 nm wavelength used to excite the blend is above the edge of absorption of the donor, located around 650 nm,^{34,35} a photobleaching of its ground state is observed in both blend films, confirming a fast hole transfer following the exciton generation in the acceptor. The comparison of the transient spectra at different times after excitation reveals a difference in the evolution of the donor signal and, thus, in the charge carrier dynamics, when DPE is used. In the film processed without the additive, the donor signal reaches the maximum intensity much faster in comparison with the film processed with DPE. The difference in the rise time of the bleaching of the donor signal is even more evident in Fig. 7c, where the kinetics of the signal at 564 nm are displayed for both films. This wavelength has been selected to avoid any overlap between the donor and acceptor signals (see Fig. S8†). For comparison the acceptor bleaching kinetics at 710 nm are displayed in Fig. 7d. Fitting the kinetics of the donor signal, a rise time of around 500 fs is obtained for the film without additive and of about 700 fs for the film with DPE. A slower hole transfer when comparing two different donor:acceptor systems can be associated with a slower exciton dissociation, which can lead to worse device performance. In this case, being the composition of the blend exactly the same with and without the additive, the difference in rise time should not be correlated with the energetic landscape, but most likely with the change in nanostructure induced by the DPE.⁵² Therefore, in agreement with the results of the GIWAXS measurements, the longer rise time hints to an increased phase separation, with bigger and more pure domains. The slight difference in hole transfer is not enough to negatively impact the overall exciton dissociation process, which is still more efficient in the blend film made with DPE, thanks to the longer exciton diffusion length.

In summary, the results of the optical spectroscopies further confirm how the blend nanostructure induced by the DPE leads to improved device performance, with an optimized balance between exciton dissociation and charge carrier transport, which is the result of the favorable domain size and purity.⁵³ At the same time, the improved molecular ordering when DPE is used, promotes the exciton diffusion at the donor-acceptor interface and reduce the non-radiative recombination losses. All this contributes to increase the charge carrier collection and, thus, to reduce the non-radiative recombination losses.⁵⁴

Conclusions

In conclusion, this work demonstrates the fabrication of NFA-OSCs by spin coating as well as blade coating with a fully halogen-free process, using *o*-xylene as solvent and DPE as additive. The addition of DPE determines an improvement above 15% of the efficiency of the solar cells, in comparison with devices fabricated without additive. A best PCE of 11.7% is obtained with DPE, as result of increases in short-circuit current

and fill factor. Device performance improvements are correlated with an optimized nanostructure of the active layer induced by the additive, which increases the phase purity and promotes the ordering of the donor molecules. In particular, the improved molecular ordering in the presence of DPE, and the resulting decreased energetic disorder, is revealed to reduce non-radiative energy losses and to enhance exciton diffusion, for a more efficient charge carrier collection in the solar cells. Additionally, the reduced energetic disorder is also found to improve the operational stability of the OSCs. All these results prove the potential of DPE as additive in combination with non-halogenated solvents for the fabrication of efficient and stable NFA-OSCs on large scale.

Experimental

Materials

Organic donor (TPD-3F) and acceptor (IT-4F) materials were purchased from Raynergy Tek. *o*-Xylene (99%) was purchased from Acros Organics. Diphenyl ether (>98%) and 1,8-diiodooctane (98%) were purchased from Sigma Aldrich. Tin oxide nanoparticles dispersion in H₂O (15 wt%) was purchased from Alfa Aesar. All chemicals were used as received, without any further purification.

Solar cells fabrication

Solar cells with inverted structure ITO/SnO₂/TPD-3F:IT-4F/MoO₃/Al were fabricated on pre-patterned glass/ITO substrates. A 5 wt% solution of tin oxide nanoparticles was prepared diluting a SnO₂ dispersion with ultrapure water. The solution was kept stirring for at least 4 h and it was filtered before use. The organic blend solutions were prepared dissolving TPD-3F and IT-4F, with a concentration of 9 mg ml⁻¹ (1 : 1), in *o*-xylene with and without the addition of an additive. DIO was added in a concentration of 0.5 wt%, while DPE in a concentration of 3 wt%. The concentration of DPE in solution was adjusted following a systematic study on solar cells, in order to maximize their performance (see Table S3†). The blend solutions were stirred for 12 h at 120 °C and filtered before use. The pre-patterned substrates were cleaned with soapy water, deionized water, acetone and isopropyl alcohol, then dried and treated with UV/ozone for 20 min. The SnO₂ solution was spin-coated at 3000 rpm for 40 s and annealed at 150 °C for 30 min in air, to obtain films of about 40 nm. The samples were then treated with UV/ozone for 20 min, before transferring them into a glove box. The blend solutions were spin-coated at 1500 rpm for 60 s, to obtain a BHJ layer of about 120 nm. After annealing at 120 °C for 10 min, the samples were transferred in an evaporator, where 10 nm of MoO₃ and 100 nm of Al were sequentially evaporated at a base pressure of 10⁻⁶ mbar.

Device measurements

The *J*-*V* characteristics were measured in nitrogen atmosphere and at a controlled temperature of 295 K, using a Keithley 2400 source meter and under a simulated AM 1.5 G spectrum from a Steuernagel solar constant 1200 metal halide lamp. The light



intensity was calibrated using a monocrystalline silicon solar cell (WRVS reference cell, Fraunhofer ISE). The measured current density J was corrected for the spectral mismatch. Operational stability measurements were performed keeping the solar cells under illumination and tracking their maximum power point. Thermal stability was tested annealing the solar cells at 120 °C on a hotplate for a total of 5 h and measuring their J - V characteristics every hour. All measurements were performed in a glove box, on non-encapsulated samples.

The external quantum efficiency (EQE) of the solar cells was measured using a xenon lamp and a set of three filter wheels to illuminate the samples, scanning a spectral range of 400–1400 nm, at intervals of 20 nm below 680 nm and 30 nm above. After passing the filter wheels, the light was directed through a chopper and then focused on the solar cells. A lock-in amplifier (Stanford Research Systems SR830 DSP) was used to measure the photocurrent. The photon flux was calibrated before the measurements, using two Newport optical power detectors (Newport 818-SL and 818-IR). The solar cells were kept in nitrogen atmosphere during the measurements.

Impedance spectroscopy measurements

For impedance spectroscopy measurements a Solartron 1260 impedance gain-phase analyzer was used. The DC voltage was set to open circuit conditions and the AC voltage was set to 20 mV. The samples were measured fresh and the thickness of the active layers was the same for all the sample measured. The solar cells were kept in nitrogen atmosphere and in dark conditions during the measurements.

GIWAXS measurements

GIWAXS measurements were performed on samples with structure ITO/SnO₂/organic film, on glass substrate. Substrate cleaning and SnO₂ deposition were the same as for solar cells. Blend films were spin coated and annealed as for the solar cells, starting from the same solutions. Films of neat donor and acceptor were spin coated and annealed using the same parameter as for the other samples, starting from solutions in *o*-xylene, with and without DPE.

GIWAXS experiments were conducted at the beamline 7.3.3 at the Advanced Light Source at Lawrence Berkeley National Lab (Berkeley, USA).⁵⁵ The samples were illuminated with 10 keV radiation ($\lambda = 1.24 \text{ \AA}$) at an incident angle (α_i) of 0.1° at room temperature. The beam size was 300 μm (height) \times 700 μm (width). The scattering signal was captured on a Pilatus 2M (172 μm pixel size, file format EDF, 1475 \times 1679 pixels) located 274 mm from the sample.

The 2D maps are corrected by rescaled background scattering of ITO/SnO₂ on glass. Using these background corrected cake cuts covering an azimuthal angle of 70–110° for the cuts in the vertical direction and 0–20° as well as 160–180° for the cuts in the horizontal direction were used to obtain the presented cuts.

The data analysis is based on fitting the lamellar peak in the horizontal cuts. The fits are Pseudo-Voigt fits, described by the following expression:

$$f(q) = A \cdot [\eta \cdot L(q) + (1 - \eta) \cdot G(q)] \text{ with } 0 < \eta < 1$$

$$G(q) = \exp \left[-\ln(2) \cdot \left(\frac{q-c}{b} \right)^2 \right], L(q) = \frac{1}{1 + \left(\frac{q-c}{b} \right)^2}$$

where A is the peak amplitude, c is the peak position, $2b$ is the full width at half maximum of the Pseudo-Voigt peak and η the Pseudo-Voigt mixing parameter. An additional background covering small angle scattering and a constant accounting for the scattering of the substrate were included in the fitting procedure.

Photoluminescence measurements

Steady state and time-resolved photoluminescence were measured exciting the samples with the second harmonic (400 nm) of a mode-locked Ti:Sapphire laser (Coherent Mira 900), emitting at a repetition rate of 76 MHz. The laser beam was adjusted in size through an iris and then focused on the sample with a lens of 150 mm focal length. For all the measurements a laser power of 40 μW was used, which corresponds to a fluence of about 46 nJ cm^{-2} per pulse. The spectra were taken in reflection geometry. The PL emission from the sample was collected with an achromatic doublet to a monochromator with a 50 lines mm^{-1} grating. Steady-state PL spectra were acquired with a Hamamatsu C9100-13 spectral-calibrated EM-CCD camera. Time-resolved PL traces were recorded with a Hamamatsu C5680-24 picosecond streak camera, in synchroscan mode. A time resolution of 2 ps was evaluated from the scattering of the laser beam. Blend films were prepared the same way as those used for GIWAXS measurements and kept in nitrogen atmosphere during the measurements.

Transient transmission spectroscopy measurements

Fast transient transmission spectroscopy was performed using as pump the output of an optical parametric amplifier (Light Conversion Topas 800), seeded by a regenerative amplifier (794 nm, 4 mJ, 1 kHz) with an integrated Ti:Sapphire oscillator (Coherent Libra). Pump pulses of 100 fs, at wavelengths of 360 nm and 700 nm have been used to excite the samples. A white light supercontinuum (450–850 nm), generated inside a transient absorption spectrometer (Ultrafast Systems Helios), was used as probe. The spot size of the focused pump on the sample was around 150 μm and the pulse energy was adjusted to be 60 nJ per pulse and 10 nJ per pulse, for the 700 nm and 360 nm wavelength, respectively. The time delay (up to 8 ns) between pump and probe have been controlled modifying the optical path of the probe through a delay line with sub micrometer spatial resolution. The organic films were spin coated on pre-cleaned quartz substrates, following the same procedure used for devices, and encapsulated with a quartz lid and epoxy glue, in order to be measured without air exposure.

Conflicts of interest

The authors declare no conflict of interest.



Acknowledgements

L. D. M., F. E., E. M. H. and M. A. L. acknowledge funding from SolarEraNet (No. NFA4R2ROPV). D. G. R. acknowledges the financial support from NWO organization. F. E. and E. M. H. acknowledge funding from the DFG (INST 91/443-1). F. E. thanks the Elite Study Program Macromolecular Science within the Elite Network of Bavaria (ENB) for support. Portions of this research were carried out at beamline 7.3.3 of the Advanced Light Source, which is supported by the Director of the Office of Science, Office of Basic Energy Sciences, of the U.S. Department of Energy under Contract No. DE-AC02-05CH11231. A. M. acknowledge access to research infrastructure in CeSAR—Centro Servizi di Ateneo per la Ricerca – at Università degli Studi di Cagliari and thank Dr M. Marceddu for technical assistance. L. D. M., D. G. R. and M. A. L. thank A. F. Kamp and T. Zaharia for their technical support.

References

- J. Hou, O. Inganäs, R. H. Friend and F. Gao, *Nat. Mater.*, 2018, **17**, 119–128.
- A. Karki, A. J. Gillett, R. H. Friend and T. Q. Nguyen, *Adv. Energy Mater.*, 2021, **11**, 1–30.
- Y. Cui, Y. Xu, H. Yao, P. Bi, L. Hong, J. Zhang, Y. Zu, T. Zhang, J. Qin, J. Ren, Z. Chen, C. He, X. Hao, Z. Wei and J. Hou, *Adv. Mater.*, 2021, **33**, 2102420.
- K. Chong, X. Xu, H. Meng, J. Xue, L. Yu, W. Ma and Q. Peng, *Adv. Mater.*, 2022, **34**, 2109516.
- L. Zhu, M. Zhang, J. Xu, C. Li, J. Yan, G. Zhou, W. Zhong, T. Hao, J. Song, X. Xue, Z. Zhou, R. Zeng, H. Zhu, C. C. Chen, R. C. I. MacKenzie, Y. Zou, J. Nelson, Y. Zhang, Y. Sun and F. Liu, *Nat. Mater.*, 2022, **21**, 656–663.
- Y. Wei, Z. Chen, G. Lu, N. Yu, C. Li, J. Gao, X. Gu, X. Hao, G. Lu, Z. Tang, J. Zhang, Z. Wei, X. Zhang and H. Huang, *Adv. Mater.*, 2022, 2204718.
- R. Xue, J. Zhang, Y. Li and Y. Li, *Small*, 2018, **14**, 1–24.
- S. Guo, E. M. Herzog, A. Naumann, G. Tainter, J. Perlich and P. Müller-Buschbaum, *J. Phys. Chem. B*, 2014, **118**, 344–350.
- Z. Du, M. Mainville, J. Vollbrecht, A. L. Dixon, N. Schopp, M. Schrock, Z. Peng, J. Huang, S. Chae, H. Ade, M. Leclerc, G. N. M. Reddy and T.-Q. Nguyen, *Sol. RRL*, 2021, **5**, 2100213.
- S. Zhang, L. Ye, H. Zhang and J. Hou, *Mater. Today*, 2016, **19**, 533–543.
- C. McDowell and G. C. Bazan, *Curr. Opin. Green Sustainable Chem.*, 2017, **5**, 49–54.
- L. Ye, Y. Xiong, Z. Chen, Q. Zhang, Z. Fei, R. Henry, M. Heeney, B. T. O'Connor, W. You and H. Ade, *Adv. Mater.*, 2019, **31**, 1808153.
- H. Chen, H. Lai, Z. Chen, Y. Zhu, H. Wang, L. Han, Y. Zhang and F. He, *Angew. Chem., Int. Ed.*, 2021, **60**, 3238–3246.
- H. Chen, R. Zhang, X. Chen, G. Zeng, L. Kobera, S. Abbrent, B. Zhang, W. Chen, G. Xu, J. Oh, S.-H. Kang, S. Chen, C. Yang, J. Brus, J. Hou, F. Gao, Y. Li and Y. Li, *Nat. Energy*, 2021, **6**, 1045–1053.
- X. Song, P. Sun, D. Sun, Y. Xu, Y. Liu and W. Zhu, *Nano Energy*, 2022, **91**, 106678.
- K. L. Jae, L. M. Wan, C. J. Brabec, J. Yuen, S. M. Ji, Y. K. Jin, K. Lee, G. C. Bazan and A. J. Heeger, *J. Am. Chem. Soc.*, 2008, **130**, 3619–3623.
- K. R. Graham, P. M. Wieruszewski, R. Stalder, M. J. Hartel, J. Mei, F. So and J. R. Reynolds, *Adv. Funct. Mater.*, 2012, **22**, 4801–4813.
- L. Zhao, S. Zhao, Z. Xu, B. Qiao, D. Huang and X. Xu, *Org. Electron.*, 2016, **34**, 188–192.
- C. McDowell, M. Abdelsamie, M. F. Toney and G. C. Bazan, *Adv. Mater.*, 2018, **30**, 1707114.
- L. Zhao, H. Ji, S. Li, Q. Shi, C. Zhu, W. Wang and D. Huang, *Appl. Surf. Sci.*, 2021, **569**, 151120.
- L. Ye, Y. Xiong, M. Zhang, X. Guo, H. Guan, Y. Zou and H. Ade, *Nano Energy*, 2020, **77**, 105310.
- T. L. Nguyen, H. Choi, S. J. Ko, M. A. Uddin, B. Walker, S. Yum, J. E. Jeong, M. H. Yun, T. J. Shin, S. Hwang, J. Y. Kim and H. Y. Woo, *Energy Environ. Sci.*, 2014, **7**, 3040–3051.
- H. Choi, S.-J. Ko, T. Kim, P.-O. Morin, B. Walker, B. H. Lee, M. Leclerc, J. Y. Kim and A. J. Heeger, *Adv. Mater.*, 2015, **27**, 3318–3324.
- T. H. Lee, S. Y. Park, B. Walker, S. J. Ko, J. Heo, H. Y. Woo, H. Choi and J. Y. Kim, *RSC Adv.*, 2017, **7**, 7476–7482.
- S. Rasool, D. Van Vu, C. E. Song, H. K. Lee, S. K. Lee, J. Lee, S. Moon and W. S. Shin, *Adv. Energy Mater.*, 2019, **9**, 1900168.
- W. Zhao, L. Ye, S. Li, X. Liu, S. Zhang, Y. Zhang, M. Ghasemi, C. He, H. Ade and J. Hou, *Sci. China Mater.*, 2017, **60**, 697–706.
- J. E. Yu, S. J. Jeon, J. Y. Choi, Y. W. Han, E. J. Ko and D. K. Moon, *Small*, 2019, **15**, 1–10.
- Z. Zheng, E. He, J. Wang, Z. Qin, T. Niu, F. Guo, S. Gao, Z. Ma, L. Zhao, X. Lu, Q. Xue, Y. Cao, G. T. Mola and Y. Zhang, *J. Mater. Chem. A*, 2021, **9**, 26105–26112.
- X. Ma, Q. Jiang, W. Xu, C. Xu, S. Young Jeong, H. Young Woo, Q. Wu, X. Zhang, G. Yuan and F. Zhang, *Chem. Eng. J.*, 2022, **442**, 136368.
- L. Ye, Y. Xiong, S. Li, M. Ghasemi, N. Balar, J. Turner, A. Gadisa, J. Hou, B. T. O'Connor and H. Ade, *Adv. Funct. Mater.*, 2017, **27**, 1702016.
- A. Tournebise, A. Rivaton, H. Peisert and T. Chassé, *J. Phys. Chem. C*, 2015, **119**, 9142–9148.
- W. Kim, J. K. Kim, E. Kim, T. K. Ahn, D. H. Wang and J. H. Park, *J. Phys. Chem. C*, 2015, **119**, 5954–5961.
- B. J. Tremolet De Villers, K. A. O'Hara, D. P. Ostrowski, P. H. Biddle, S. E. Shaheen, M. L. Chabinyc, D. C. Olson and N. Kopidakis, *Chem. Mater.*, 2016, **28**, 876–884.
- C. Y. Liao, Y. Chen, C. C. Lee, G. Wang, N. W. Teng, C. H. Lee, W. L. Li, Y. K. Chen, C. H. Li, H. L. Ho, P. H. S. Tan, B. Wang, Y. C. Huang, R. M. Young, M. R. Wasielewski, T. J. Marks, Y. M. Chang and A. Facchetti, *Joule*, 2020, **4**, 189–206.
- D. Garcia Romero, L. Di Mario, G. Portale and M. A. Loi, *J. Mater. Chem. A*, 2021, **9**, 23783–23792.
- Q. Yang, X. Li, H. Tang, Y. Li, Y. Fu, Z. Li and Z. Xie, *J. Mater. Chem. C*, 2020, **8**, 6724–6733.
- Q. He, W. Sheng, M. Zhang, G. Xu, P. Zhu, H. Zhang, Z. Yao, F. Gao, F. Liu, X. Liao and Y. Chen, *Adv. Energy Mater.*, 2021, **11**, 1–11.



- 38 J. Gao, R. Ming, Q. An, X. Ma, M. Zhang, J. Miao, J. Wang, C. Yang and F. Zhang, *Nano Energy*, 2019, **63**, 103888.
- 39 G. Garcia-Belmonte, A. Munar, E. M. Barea, J. Bisquert, I. Ugarte and R. Pacios, *Org. Electron.*, 2008, **9**, 847–851.
- 40 M. P. Felicissimo, D. Jarzab, M. Gorgoi, M. Forster, U. Scherf, M. C. Scharber, S. Svensson, P. Rudolf and M. A. Loi, *J. Mater. Chem.*, 2009, **19**, 4899–4901.
- 41 E. M. Speller, A. J. Clarke, J. Luke, H. K. H. Lee, J. R. Durrant, N. Li, T. Wang, H. C. Wong, J. S. Kim, W. C. Tsoi and Z. Li, *J. Mater. Chem. A*, 2019, **7**, 23361–23377.
- 42 A. Tournebise, P.-O. Bussière, P. Wong-Wah-Chung, S. Thérias, A. Rivaton, J.-L. Gardette, S. Beaupré and M. Leclerc, *Adv. Energy Mater.*, 2013, **3**, 478–487.
- 43 R. A. Street and D. M. Davies, *Appl. Phys. Lett.*, 2013, **102**, 1–4.
- 44 T. Heumueller, W. R. Mateker, I. T. Sachs-Quintana, K. Vandewal, J. A. Bartelt, T. M. Burke, T. Ameri, C. J. Brabec and M. D. McGehee, *Energy Environ. Sci.*, 2014, **7**, 2974–2980.
- 45 T. Heumueller, T. M. Burke, W. R. Mateker, I. T. Sachs-Quintana, K. Vandewal, C. J. Brabec and M. D. McGehee, *Adv. Energy Mater.*, 2015, **5**, 1500111.
- 46 M. B. Upama, M. Wright, M. A. Mahmud, N. K. Elumalai, A. Mahboubi Soufiani, D. Wang, C. Xu and A. Uddin, *Nanoscale*, 2017, **9**, 18788–18797.
- 47 A. J. Pearson, P. E. Hopkinson, E. Couderc, K. Domanski, M. Abdi-Jalebi and N. C. Greenham, *Org. Electron.*, 2016, **30**, 225–236.
- 48 N. Y. Doumon, G. Wang, X. Qiu, A. J. Minnaard, R. C. Chiechi and L. J. A. Koster, *Sci. Rep.*, 2019, **9**, 1–14.
- 49 T. A. Papadopoulos, L. Muccioli, S. Athanasopoulos, A. B. Walker, C. Zannoni and D. Beljonne, *Chem. Sci.*, 2011, **2**, 1025–1032.
- 50 J. D. A. Lin, O. V. Mikhnenko, J. Chen, Z. Masri, A. Ruseckas, A. Mikhailovsky, R. P. Raab, J. Liu, P. W. M. Blom, M. A. Loi, C. J. Garcia-Cervera, I. D. W. Samuel and T. Q. Nguyen, *Mater. Horiz.*, 2014, **1**, 280–285.
- 51 I. Rörich, O. V. Mikhnenko, D. Gehrig, P. W. M. Blom and N. I. Crăciun, *J. Phys. Chem. B*, 2017, **121**, 1405–1412.
- 52 N. D. Eastham, J. L. Logsdon, E. F. Manley, T. J. Aldrich, M. J. Leonardi, G. Wang, N. E. Powers-Riggs, R. M. Young, L. X. Chen, M. R. Wasielewski, F. S. Melkonyan, R. P. H. Chang and T. J. Marks, *Adv. Mater.*, 2018, **30**, 1–8.
- 53 Z. Chen, X. Chen, B. Qiu, G. Zhou, Z. Jia, W. Tao, Y. Li, Y. M. Yang and H. Zhu, *J. Phys. Chem. Lett.*, 2020, **11**, 3226–3233.
- 54 D. He, F. Zhao, C. Wang and Y. Lin, *Adv. Funct. Mater.*, 2022, **32**, 2111855.
- 55 A. Hexemer, W. Bras, J. Glossinger, E. Schaible, E. Gann, R. Kirian, A. MacDowell, M. Church, B. Rude and H. Padmore, *J. Phys.: Conf. Ser.*, 2010, **247**, 012007.



Effects of the diphenyl ether additive in halogen-free processed non-fullerene acceptor organic solar cell

Supplementary Information

Lorenzo Di Mario¹, David Garcia Romero¹, Meike J. Pieters¹, Fabian Eller², Eva M. Herzig²,
Chenhui Zhu³, Giovanni Bongiovanni⁴, Andrea Mura⁴, Maria A. Loi^{1*}

Affiliations

1) Zernike Institute for Advanced Materials, University of Groningen, Nijenborgh 4,
Groningen 9747 AG, The Netherlands

2) Dynamics and structure formation – Herzig Group, Institute of Physics, University of
Bayreuth, Universitätsstraße 30, Bayreuth 95447, Germany

3) Lawrence Berkeley National Laboratory, Advanced Light Source, Berkeley, CA, 94720 USA

4) Dipartimento di Fisica, Università degli studi di Cagliari, Monserrato I-09042, Italy

* Corresponding author email: m.a.loi@rug.nl

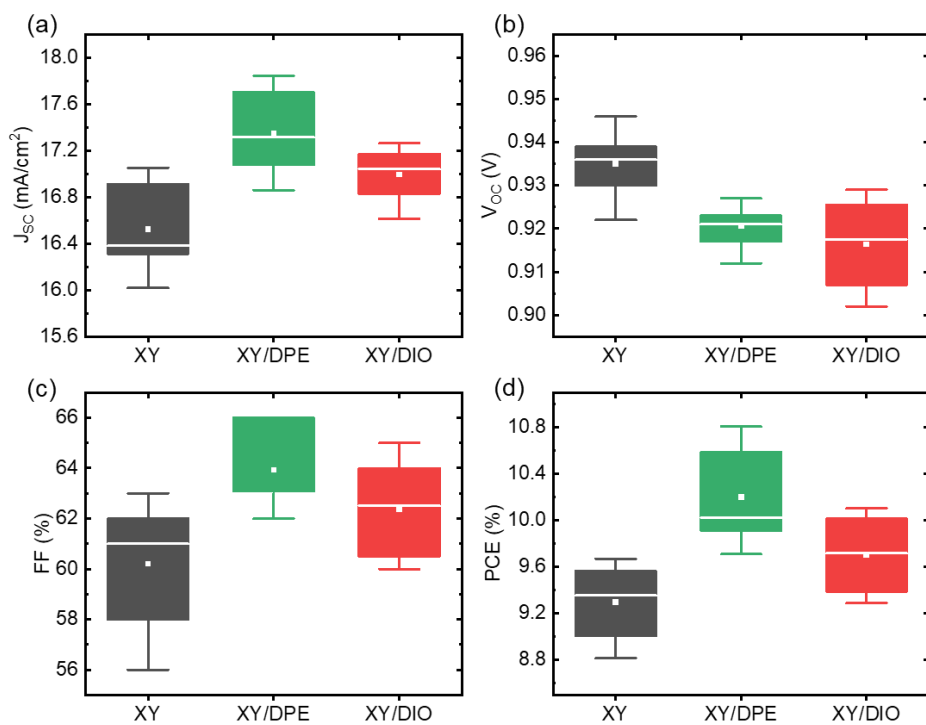


Figure S1 Box charts of the photovoltaic parameter distributions for devices fabricated spin coating the blend solution without additive, with DPE and with DIO. Values from 15 devices for each condition. The active area of the devices is 10 mm².

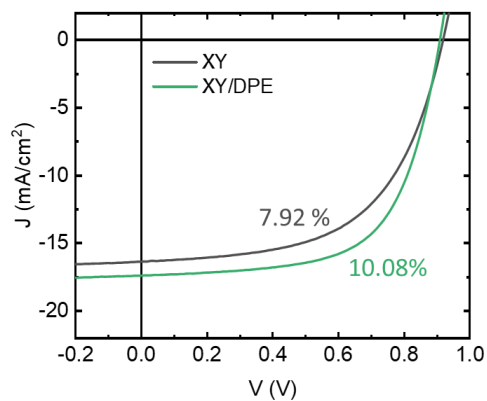


Figure S2 J-V curves under illumination (AM 1.5, 100 mW cm⁻²) of TPD-3F:IT-4F devices fabricated depositing the active layer by blade coating, from a solution without additive and with 3 wt% of DPE. Numbers indicate the PCE obtained for each device.

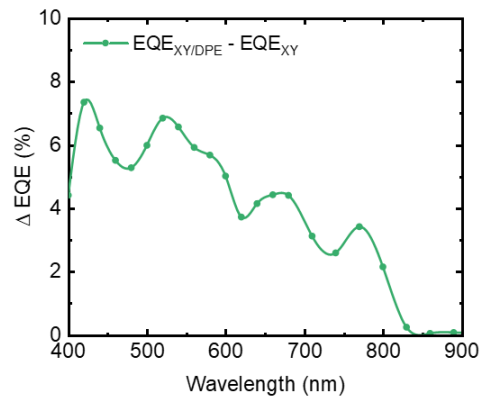


Figure S3 Difference of external quantum efficiency (ΔEQE) between TPD-3F:IT-4F devices fabricated with DPE and devices fabricated without additive.

Table S1 Components of the equivalent circuit as extracted by fitting the Nyquist plot data for TPD-3F:IT-4F devices fabricated with and without the use of DPE.

Solution	R_s (ohm)	L (μH)	R_p (kohm)	CPE (nF)	CPE-P	τ (μs)
XY	54.02	2.493	3.831	12.66	0.918	48.50
XY/DPE	22.20	2.524	1.786	29.49	0.887	52.67

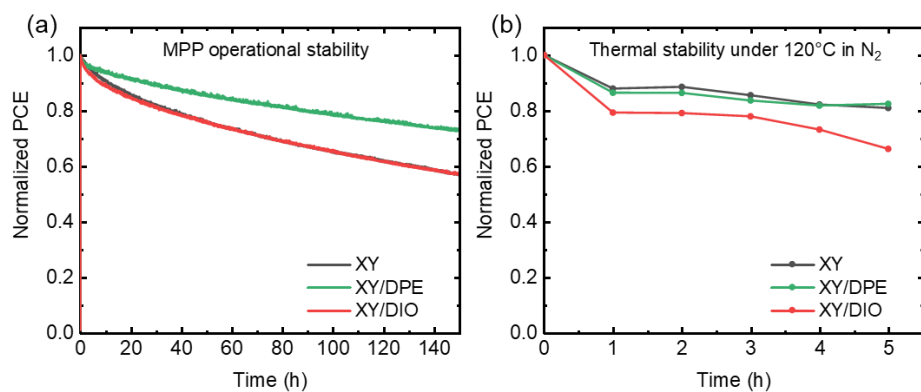


Figure S4 Stability of TPD-3F:IT-4F solar cells fabricated casting the blend film from a solution without additive, with DPE and with DIO: (a) stability in operation at maximum power point (MPP), under continuous illumination (AM 1.5, 100 mW cm⁻²); (b) thermal stability, annealing solar cells at 120 °C in N₂ atmosphere.

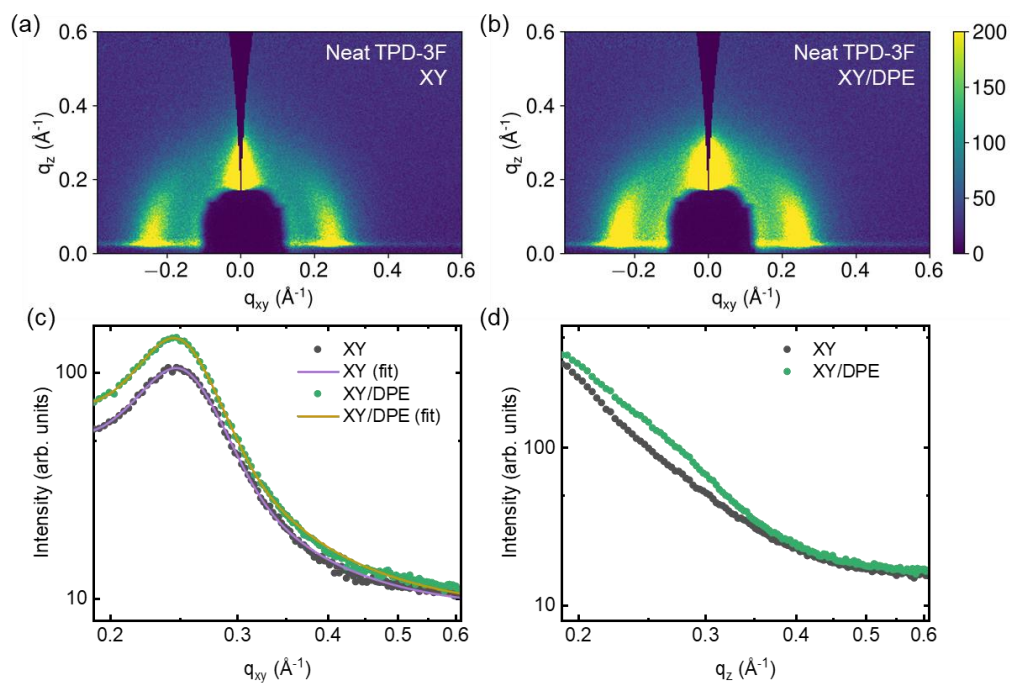


Figure S5 2D GIWAXS data and cuts of measurements on films of pure TPD-3F donor cast with and without the use of DPE in solution: 2D false-color maps for a film without additive (a) and with additive (b); corresponding in-plane (c) and out-of-plane (d) line cuts.

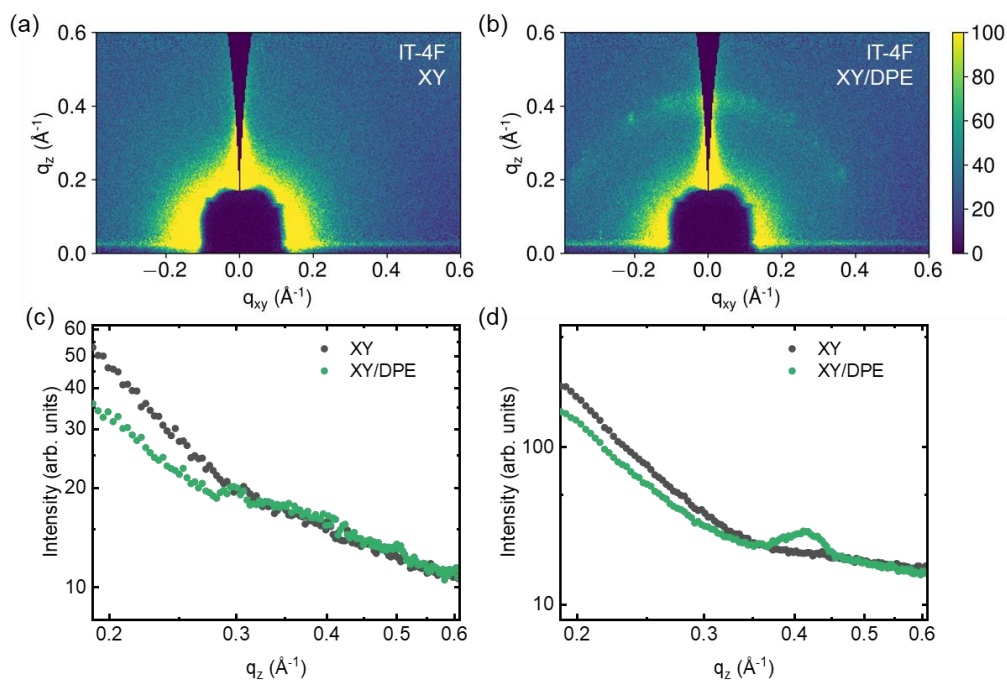


Figure S6 2D GIWAXS data and cuts of measurements on films of neat IT-4F acceptor cast with and without the use of DPE in solution: 2D false-color maps for a film without additive (a) and with additive (b); corresponding in-plane (c) and out-of-plane (d) line cuts.

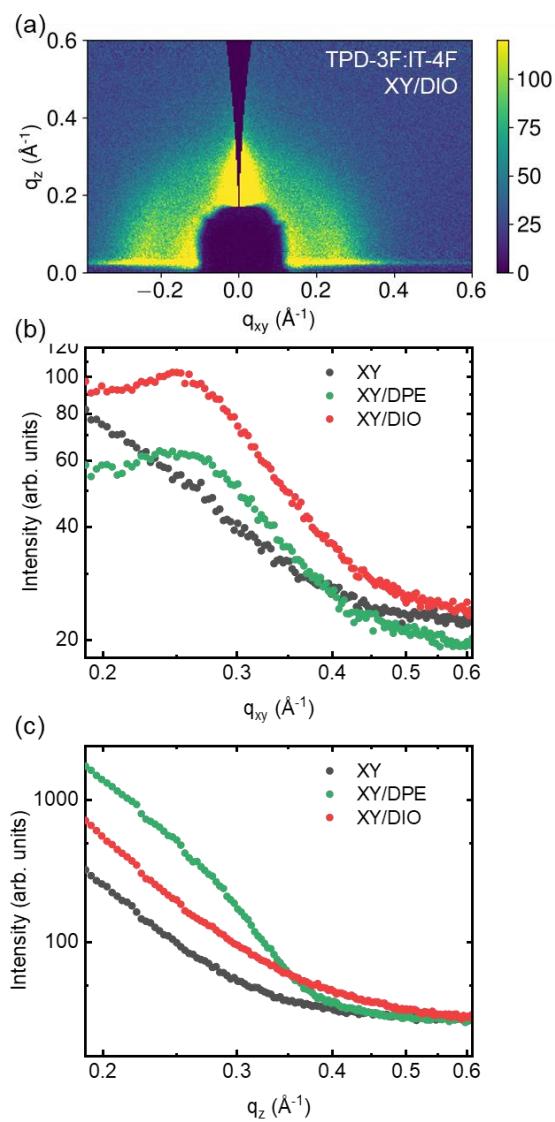


Figure S7 2D GIWAXS data and cuts of measurements on TPD-3F:IT-4F blend films cast with the use of DIO in solution: 2D false-color maps (a) and corresponding in-plane (b) and out-of-plane (c) line cuts.

Table S2 Fitting parameters for the time-resolved PL decays and calculated average lifetimes.

Solution	A₁	τ_1 (ps)	A₂	τ_2 (ps)	A₃	τ_3 (ps)	τ_{avg} (ps)
XY	0.59	4.5	0.25	15.5	0.03	68.3	24.6
XY/DPE	0.71	5.2	0.20	16.7	0.01	64.2	16.4

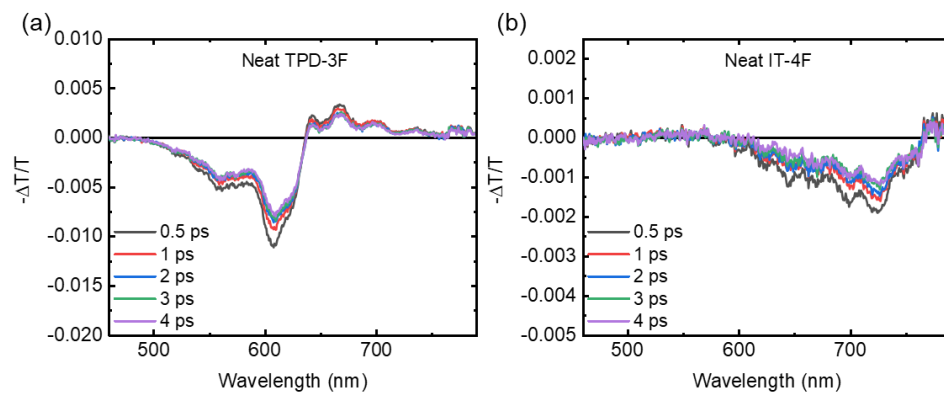


Figure S8 Transient transmission spectra acquired at different time delays for the films of pure TPD-3F donor (a) and of pure IT-4F acceptor. Excitation wavelength 360 nm. Films cast without using any additive.

Table S3 Photovoltaic parameters of solar cells fabricated casting the blend film from a solution without additive and with DPE in different concentrations.

Solution	V_{oc} (V)	J_{sc} (mA cm⁻²)	FF (%)	PCE (%)
XY	0.921	16.49	51.59	7.83
XY/1% DPE	0.931	15.19	60.10	8.50
XY/3% DPE	0.915	16.88	62.27	9.62
XY/5% DPE	0.911	17.14	60.23	9.41

From the results of the characterizations reported in the manuscript for the concentration of 3% in comparison with the sample without additive, it is reasonable to expect differences in the nanostructure with a different concentration of DPE. This indeed, it is expected to affect the solar cell performance. The concentration of 1% is not enough to achieve a sufficient phase separation of the two blend components, with the result of a not optimal charge carrier collection (as supported by the low short circuit current of the solar cells). On the other hand, a concentration of 5% leads to an excessive segregation of the two components, with big domain size and, thus, with increased non-radiative recombination (as supported by the low open circuit voltage and fill factor of the solar cells).

14 Microstructural and Thermal Transport Properties of Regioregular Poly(3-hexylthiophene-2,5-diyl) Thin Films

Kai Herrmann, Simon Freund, **Fabian Eller**, Tamino Rößler, Georg Papastavrou, Eva
M. Herzig and Markus Retsch

Published in
Materials **2022**, 15 (21), 7700
(DOI: 10.3390/ma15217700)

Reprinted with permission according to the CC BY 4.0 license
Copyright 2022 by the authors

Article

Microstructural and Thermal Transport Properties of Regioregular Poly(3-hexylthiophene-2,5-diyl) Thin Films

Kai Herrmann ¹, Simon Freund ¹ , Fabian Eller ² , Tamino Rößler ³, Georg Papastavrou ^{3,4}, Eva M. Herzig ²  and Markus Retsch ^{1,4,*} 

¹ Department of Chemistry, Physical Chemistry 1, University of Bayreuth, Universitätsstraße 30, 95447 Bayreuth, Germany

² Dynamics and Structure Formation—Herzig Group, Department of Physics, University of Bayreuth, Universitätsstraße 30, 95447 Bayreuth, Germany

³ Physical Chemistry 2, University of Bayreuth, Universitätsstr 30, 95447 Bayreuth, Germany

⁴ Bavarian Polymer Institute, Bayreuth Center for Colloids and Interfaces and Bavarian Center for Battery Technology (BayBatt), University of Bayreuth, Universitätsstraße 30, 95447 Bayreuth, Germany

* Correspondence: retsch@uni-bayreuth.de

Abstract: Polymeric thin films offer a wide range of exciting properties and applications, with several advantages compared to inorganic counterparts. The thermal conductivity of such thin films ranges typically between $0.1\text{--}1\text{ W m}^{-1}\text{ K}^{-1}$. This low thermal conductivity can cause problems with heat dissipation in various applications. Detailed knowledge about thermal transport in polymeric thin films is desired to overcome these shortcomings, especially in light of the multitude of possible microstructures for semi-crystalline thin films. Therefore, poly(3-hexylthiophene-2,5-diyl) (P3HT) is chosen as a model system to analyze the microstructure and optoelectronic properties using X-ray scattering and absorption spectra along with the thermal transport properties using the photoacoustic technique. This combination of analysis methods allows for determining the optoelectronic and thermal transport properties on the same specimen, supplemented by structural information. The effect of different molecular weights and solvents during film preparation is systematically examined. A variation of the optoelectronic properties, mainly regarding molecular weight, is apparent, while no direct influence of the solvent during preparation is discernible. In contrast, the thermal conductivities of all films examined fall within a similar range. Therefore, the microstructural properties in the ordered regions do not significantly affect the resulting thermal properties in the sample space investigated in this work. We conclude that it is mainly the amorphous regions that determine the thermal transport properties, as these represent a bottleneck for thermal transport.

Keywords: polymeric thin film; microstructure; morphology; thermal conductivity; poly(3-hexylthiophene-2,5-diyl)



Citation: Herrmann, K.; Freund, S.; Eller, F.; Rößler, T.; Papastavrou, G.; Herzig, E.M.; Retsch, M.

Microstructural and Thermal Transport Properties of Regioregular Poly(3-hexylthiophene-2,5-diyl) Thin Films. *Materials* **2022**, *15*, 7700. <https://doi.org/10.3390/ma15217700>

Academic Editor: Nelson Wilbur Pech-May

Received: 2 October 2022

Accepted: 28 October 2022

Published: 2 November 2022

Publisher's Note: MDPI stays neutral with regard to jurisdictional claims in published maps and institutional affiliations.



Copyright: © 2022 by the authors. Licensee MDPI, Basel, Switzerland.

This article is an open access article distributed under the terms and conditions of the Creative Commons Attribution (CC BY) license (<https://creativecommons.org/licenses/by/4.0/>).

1. Introduction

Polymeric thin films have become increasingly important in recent decades and are now used in various applications. Their usage includes separation membranes for fuel cells, electrodes in batteries, or active layers in organic photovoltaics [1–3]. Low cost, mechanical flexibility, solvent processability, and tailor-made functionalities make polymeric thin films attractive alternatives compared to their inorganic counterparts. Conjugated polymers are particularly interesting as they exhibit a backbone chain of alternating single- and double bonds, leading to the formation of a delocalized π -electron system when adequately doped [4,5]. Delocalized π -electron systems often result in interesting optical and electronic properties [6]. A well-established class of conjugated polymers are polythiophenes. In polythiophenes, charge conduction occurs via intrachain and interchain charge transport in the crystalline regions, while the amorphous part conducts via hopping or tunneling [7–9]. Within the material class of polythiophenes, the most studied system is poly(3-hexylthiophene-2,5-diyl) (P3HT) due to its electrical and optical properties [7,10,11].

To extract information about the aggregation behavior of P3HT in thin films through a relatively simple measurement, Spano developed a model to describe the absorption from H-aggregates comprising parallelly aligned, cofacially packed conjugated chains in the case of weak excitonic coupling [12,13]. Using this model, the UV-vis absorption A as a function of the photon energy E results via [14]:

$$A(E) \propto \sum_{m=0} \left(\frac{S^m}{m!} \right) \left(1 - \frac{W e^{-S}}{2E_p} \sum_{n \neq m} \frac{S^n}{n!n-m} \right)^2 \exp \left(-\frac{(E - E_{0-0} - mE_p - 0.5WS^m e^{-S})^2}{2\sigma^2} \right) \quad (1)$$

through transitions between the vibrational levels m and n . Herein, S is the Huang–Rhys factor, E_p —the intermolecular vibrational energy, E_{0-0} —the 0–0 transition energy, W —the exciton bandwidth, and σ —the Gaussian linewidth [15].

A characteristic feature of both bulk polymers and polymeric thin films is their low thermal conductivity, mainly in the order of 0.1–1 W m^{−1} K^{−1} [16]. Depending on the application, this low thermal conductivity can be disadvantageous if generated heat is not supposed to accumulate. It can also be advantageous if heat losses need to be prevented or a thermal gradient should be maintained. For P3HT, several investigations have examined the influence of film thickness, blending, or preparation parameters on their thermal transport properties [17–20]. As pointed out by many studies, a holistic understanding of thermal transport in polymer thin films is still missing. Up to now, most investigations have focused on the influence of structural properties such as the degree of crystallinity or the thin film thickness. Particularly in the case of semiconducting polymers, the interplay between the optoelectronic and thermal transport properties has not been investigated. Nevertheless, it is difficult to establish a consistent understanding since many parameters simultaneously influence the thermal properties of polymeric thin films. Our approach, consequently, is to relate the thermal properties to the structural properties.

This work, therefore, explores possible structure–property relationships between the thermal conductivity and nanostructure as well as morphology-related properties of P3HT thin films. We systematically investigate the optoelectronic and structural properties of three regioregular P3HT polymers with distinct molecular weights and solvent-processing conditions. After providing details on the employed materials and methods, the extracted morphologic information based on the absorption spectra and scattering analysis are presented. The set of samples analyzed using UV-vis absorption spectra is subsequently thermally analyzed using the photoacoustic technique, resulting in the direct determination of the thin film cross-plane thermal conductivity without requiring further measurements. We finally correlate our structural analysis to the thermal transport properties. Potential correlations are discussed, focusing on the fraction of aggregates and the exciton binding energy.

2. Materials and Methods

Regioregular P3HT with different molecular weights was purchased from Sigma-Aldrich (average M_w 20–45 kg mol^{−1}, 50–75 kg mol^{−1}, and 85–100 kg mol^{−1} with regioregularity $\geq 90\%$) and used as received. Chlorobenzene, CB (anhydrous $\geq 99.8\%$), 1,2-dichlorobenzene, 1,2-DCB (anhydrous 99%) and 1,2,4-trichlorobenzene, 1,2,4-TCB (anhydrous $\geq 99\%$) were also purchased from Sigma-Aldrich and used as received.

Thin films were prepared by dissolving the respective polymer in the respective solvent at 100 °C for 20 min and spin-coating the solutions on Quartz substrates (Präzisions Glas und Optik GmbH). The spin-coating parameters are presented in Table 1. The films were annealed for about 16 h at 40 °C in a vacuum oven.

Table 1. Utilized spin-coating parameters (concentration c and rotation speed ω) for all combinations of molecular weights and solvents.

Solvent	$\overline{M}_w = 32.5 \text{ kg mol}^{-1}$	$\overline{M}_w = 62.5 \text{ kg mol}^{-1}$	$\overline{M}_w = 92.5 \text{ kg mol}^{-1}$
Chlorobenzene	$c = 50 \text{ mg mL}^{-1}$, $\omega = 750 \text{ rpm}$	$c = 50 \text{ mg mL}^{-1}$, $\omega = 750 \text{ rpm}$	$c = 30 \text{ mg mL}^{-1}$, $\omega = 500 \text{ rpm}$
1,2-Dichlorobenzene	$c = 55 \text{ mg mL}^{-1}$, $\omega = 500 \text{ rpm}$	$c = 55 \text{ mg mL}^{-1}$, $\omega = 500 \text{ rpm}$	$c = 55 \text{ mg mL}^{-1}$, $\omega = 1000 \text{ rpm}$
1,2,4-Trichlorobenzene	$c = 70 \text{ mg mL}^{-1}$, $\omega = 500 \text{ rpm}$	$c = 70 \text{ mg mL}^{-1}$, $\omega = 500 \text{ rpm}$	$c = 70 \text{ mg mL}^{-1}$, $\omega = 1000 \text{ rpm}$

UV–vis absorption was measured with a UV–vis spectrometer (Cary 5000, Agilent Technologies) between 350 nm and 750 nm, corresponding to 1.65 eV to 3.54 eV, with an integration time of 0.1 ms in transmission geometry. To ensure a good resolution also at high absorption for thicker samples ($A_{\max} \geq 3$), the reference beam was attenuated using an attenuation grid and the integration time increased to 0.5 ms.

The data analysis on the absorption spectra was performed according to Ref. [14]. For the fit to Equation (1), a lower boundary of 1.95 eV and an upper boundary of 2.35 eV were applied using the Matlab function *nlinfit* employing the Levenberg–Marquardt algorithm [15]. The 95% confidence intervals were calculated using the Matlab function *nlparci* based on the residuals for the fitted model and the estimated variance-covariance matrix for the fitted coefficients.

Grazing incidence wide-angle X-ray scattering (GIWAXS) was performed on a laboratory system at the University of Bayreuth (Xeuss 3.0, Xenocs SAS, Grenoble, France) with a Cu $K\alpha$ source ($\lambda = 1.54 \text{ \AA}$), a Dectris EIGER 2R 1M detector, and a sample-to-detector distance of 72 mm. Scattering experiments were carried out at room temperature under vacuum on samples on Quartz substrates with a length of 4 mm. The incident angle was set to 0.20° well above the critical angle of 0.16° , which probes the full depth of the films. The presented q -profiles are cake cuts covering an azimuthal angle of $70\text{--}110^\circ$ for the cuts in the vertical direction and $0\text{--}20^\circ$ as well as $160\text{--}180^\circ$ for the cuts in the horizontal direction.

The data analysis is based on fitting the horizontal and vertical cuts. All performed fits are Pseudo-Voigt fits, described by the following expression for a single peak:

$$f(q) = A \cdot [\eta \cdot L(q) + (1 - \eta) \cdot G(q)], \quad \text{with } 0 < \eta < 1 \quad (2)$$

$$G(q) = \exp \left[-\ln(2) \cdot \left(\frac{q-c}{b} \right)^2 \right], \quad L(q) = \frac{1}{1 + \left(\frac{q-c}{b} \right)^2} \quad (3)$$

where A is the peak amplitude, c is the peak position, $2b$ is the full width at half maximum of the Pseudo-Voigt peak, and η the Pseudo-Voigt mixing parameter. To fit the superposition of various peaks, we fitted the sum of five Pseudo-Voigt peaks for both directions. Moreover, background scattering was fitted with the functional form of $d_h \cdot q^{-4} + e_h$ in the horizontal and of $d_v \cdot q^{-5} + f \cdot q^{-2} + e_v$ in the vertical direction, where d_h , e_h , d_v , e_v , and f are constants. For the fitting, we used *lmfit* in Python. Normalization of the peak amplitude is based on the absorption spectra of the respective samples. The areas of the aggregate and amorphous fit are added, while the aggregate area is divided by 1.39 due to its higher molar extinction coefficient [21].

The samples for thermal transport characterization and a thermally thick reference material (quartz) were coated with a 100 nm gold layer by thermal evaporation to ensure high and near-surface absorption for the photoacoustic characterization. The layer thickness was monitored using a quartz crystal microbalance. Photoacoustic measurements were performed with a continuous wave Coherent Genesis MX488-1000, Utrecht, The Netherlands laser. The laser was modulated with a ConOptics 350-160 electro-optic modulator, operated by a sinusoidal signal of a Zurich Instruments lock-in amplifier HF2LI, Zurich,

Switzerland. The acoustic signal was measured using a Bruel & Kjaer 4398-A-011, Bremen, Germany microphone, which is subsequently demodulated in the lock-in amplifier.

The pressure in the photoacoustic cell was set to 1.379 bar of helium, corresponding to 20 psi. A comprehensive explanation of the experimental setup is given in Ref. [22] for more practical information.

The data analysis on the photoacoustic measurements is performed according to Ref. [22]. To determine the sample's thermal properties using the multilayer model from Hu et al., the thermal properties of the substrate (quartz) and transducer (gold) are required [23]. Therefore, the thermal effusivity and diffusivity of gold are taken as $\varepsilon_{Au} = 22,271 \text{ W s}^{1/2} \text{ m}^{-2} \text{ K}^{-1}$ and $D_{Au} = 8.06 \times 10^{-5} \text{ m}^2 \text{ s}^{-1}$ [24]. The thermal effusivity and diffusivity of quartz are taken as $\varepsilon_{Quartz} = 1499.8 \text{ W s}^{1/2} \text{ m}^{-2} \text{ K}^{-1}$ and $D_{Quartz} = 8.47 \times 10^{-7} \text{ m}^2 \text{ s}^{-1}$ [24]. Again, the least-squares fitting function *nlinfit* is used to determine the sample's thermal effusivity and diffusivity. The thermal conductivity is subsequently calculated from these parameters. The approach for error estimation is described in Ref. [22]. In doing so, two independent measurements are analyzed using a Monte Carlo approach for the controlled parameters sample and transducer thickness. Therefore, 1000 iterations with randomly selected controlled parameters on two data sets, measured on the same sample but at different positions, were performed. Simultaneously, the uncertainty of every fit procedure is taken into account by the respective residuals and the estimated variance–covariance matrix.

The thicknesses of the polymeric films were determined using an Olympus OLS5000, Hamburg, Germany laser confocal microscope and a 50× microscope objective. The error is calculated by measuring five areas of $260 \mu\text{m} \times 260 \mu\text{m}$ at the top, left, center, right, and bottom of the circular area with a radius of 2 mm probed by the photoacoustic measurement and assuming a Gaussian distribution.

3. Results

To enable both the optical and the photoacoustic characterization, specific requirements for the sample thickness have to be met. For optical characterization, the samples should not be excessively thick to ensure a detectable transmission. In contrast, due to the limited frequency regime of the photoacoustic technique, the samples should have a certain thickness to allow the significant determination of the thermal conductivity [22]. Therefore, the film thickness should be about 500 nm to allow quantitative measurements of both optoelectronic and thermal properties. This is also an adequate thickness for GIWAXS characterization [25,26]. Quartz substrates are well suited for all these measurements because they exhibit high optical transparency in the wavelength regime of interest and thermal effusivity in a similar order of magnitude as polymers.

First, the parameters displayed in Table 1 were determined to produce films in the desired thickness range from the different solvents chlorobenzene, 1,2-dichlorobenzene, and 1,2,4-trichlorobenzene to achieve a variation in the microstructure [21,27]. An exemplary resulting film for the molecular weight of 32.5 kg mol^{-1} spin-coated from chlorobenzene is shown in Figure 1a. The polymeric films are partially removed from the substrate by scraping off with a glass pipette to produce a sharp edge. The color code here contains information about the z-axis, where the height of the substrate is normalized to zero. Based on this, the film thickness can be determined as shown with a cumulative frequency distribution in Figure 1b. In addition to the average film thickness, the surface roughness can also be determined from the respective measurements as a further quality characteristic. For this, we use the root mean square roughness S_q as one of the most widely used ones as defined by

$$S_q = \sqrt{\frac{1}{A} \iint_A Z^2(x, y) \partial x \partial y}, \quad (4)$$

where A represents the evaluated area and Z the respective height [28]. The parameter S_q , therefore, corresponds to the standard deviation of the height distribution. For all samples

examined, S_q is in the range of 10 nm to 40 nm, allowing a proper data analysis. This surface roughness is corroborated by atomic force microscopy measurements on P3HT samples spin cast from chlorobenzene solutions. The height images reveal a granular surface topology with undulations of a few 10 nm (Figure S1). Neither in the height, nor in the phase image were we able to resolve microcrystalline regions regardless of the molecular weight.

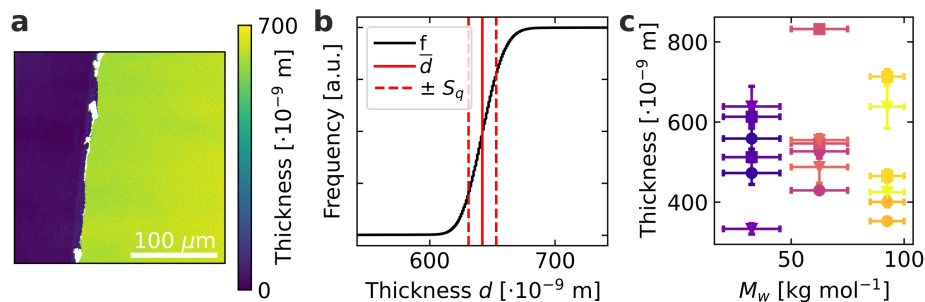


Figure 1. (a) Exemplary confocal microscopy image of $\bar{M}_w = 32.5 \text{ kg mol}^{-1}$ spin-coated from chlorobenzene. The height is color-coded, visualizing the quartz substrate as blue and the thin film as green. (b) Exemplary cumulative frequency distribution f as a function of thickness, as well as the average thickness \bar{d} and the surface roughness S_q calculated from subfigure (a). (c) Resulting film thicknesses, errors are derived from the inhomogeneities at different measurement points. Circular symbols represent films spin-coated from chlorobenzene, squares films from 1,2-dichlorobenzene, and triangles films from 1,2,4-trichlorobenzene.

For the cross-plane thermal conductivity determination, however, not only the local surface roughness is of interest, but especially inhomogeneities and fluctuations of the film thickness in the investigated measuring area, which corresponds to approximately 12.6 mm^2 [22]. To represent these inhomogeneities realistically, the film thickness was determined at five locations in the area of the thermal measurement, and the mean value and standard deviation were determined under the assumption of a Gaussian distribution. The film thickness results obtained from this procedure are shown in Figure 1c. To map a sample to sample variation, two separate films were examined for every combination of molecular weight and solvent. All produced films are in the required range between 330 nm to 830 nm, ensuring a significant analysis of optoelectronic and thermal properties.

Having verified the fundamental requirements for the thin films, we can now turn to optoelectronic characterization. The acquired absorption spectra are evaluated according to Equation (1), which is demonstrated for the example of a molecular weight of 32.5 kg mol^{-1} spin-coated from chlorobenzene in Figure 2a. For the data analysis, W , E_{0-0} , σ , and a global proportionality factor were varied as free parameters, while S was taken as 1.0 and E_p was taken as 0.179 eV, as reported in the literature [21,29,30]. Certain deviations between the model and measured values can be seen, but they are taken into account by the uncertainty estimation discussed in Section 2. The most common deviations are based on the model's assumptions, simplifying the actual situation. It, therefore, would be expected that the amorphous residual is unstructured. However, it can be seen that the amorphous contribution resulting from the analysis exhibits structuring [15]. This structuring above approximately 2.5 eV is most likely an artifact due to electronic transitions at higher energies [12,14,15]. Furthermore, slightly structured residuals in the energy range below 2.5 eV are recognizable, suggesting that the Gaussian disorder is too simple to describe the thin films' absorption spectrum fully [14,15]. Despite these deviations, the model used is nevertheless a practical possibility to estimate certain microstructural properties of the thin films.

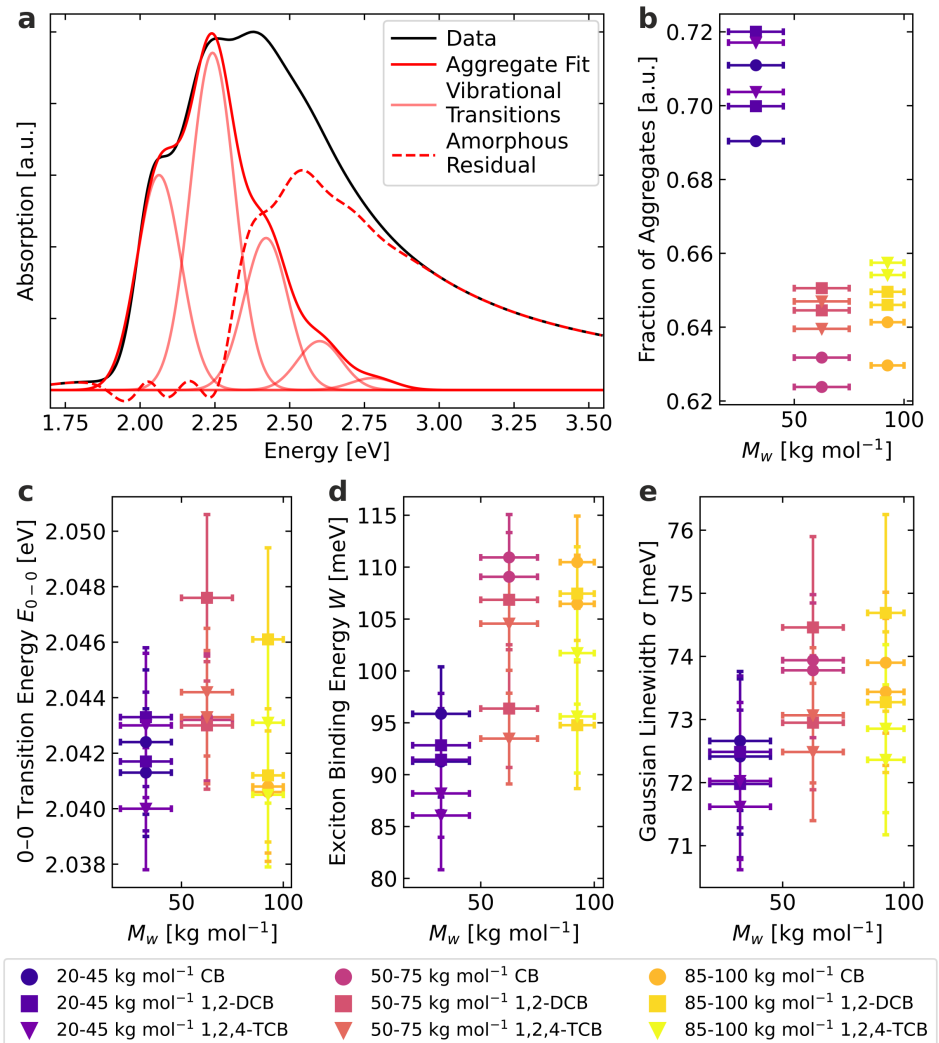


Figure 2. Performed UV-vis absorption spectra data analysis: (a) Exemplary fit on the absorption spectrum of $\bar{M}_w = 32.5$ kg mol⁻¹ spin-coated from chlorobenzene. The individual vibrational transitions sum up to the aggregate fit. (b–e) Extracted fraction of aggregates, 0–0 transition energy, exciton binding energy and Gaussian linewidth.

The fraction of aggregates extracted from the absorption spectra is displayed in Figure 2b and calculated from the numerically integrated absorptions of the aggregate fit and the amorphous residual. Normalizing the aggregate integral with the factor of 1.39 is based on the different extinction coefficients of aggregated and non-aggregated P3HT [31,32]. The low molecular weight ($\bar{M}_w = 32.5$ kg mol⁻¹) exhibits the highest fraction of aggregates, with the two higher molecular weights ($\bar{M}_w = 62.5$ kg mol⁻¹ and $\bar{M}_w = 92.5$ kg mol⁻¹) being at a lower and similar level. Furthermore, it can be seen that the different films of the same molecular weight polymer display slightly different microstructures. However, we could not establish a direct and unambiguous correlation between the solvent used for spin-coating and the fraction of aggregates.

There is an inverted dependency for the extracted fit parameters in Figure 2c–e. Generally, the low molecular weight exhibits the lowest 0–0 transition energy, exciton binding energy, and Gaussian linewidth, while the two higher molecular weights are at a higher and similar level. Again, no direct influence of the solvent is discernible. The 0–0 transition energy is related to the peak position of the first vibrational transition in

Figure 2a. The similar transition energies for the two higher molecular weights suggest that the local electronic properties of the chains in the ordered domains are only weakly affected by the molecular weight in this range [14]. The lower 0–0 transition energy is possibly due to fewer local torsions of the conjugated backbones within the aggregates for the low molecular weight [14]. Still, the relative differences appear to be minor. The exciton binding energy is related to the relative intensities of the vibrational transitions. It can be interpreted as a measure of the average conjugation length of planarized chain segments in the ordered domains [33]. A lower exciton binding energy is related to a higher conjugation length above a certain minimum length, which is the case for all films examined here [33]. Therefore, the fraction of aggregates is higher for the low molecular weight, and the conjugation length inside the aggregate domains is increased. The Gaussian linewidth is a measure of the energetic disorder inside the ordered domains and is related to the width of the vibrational transitions in Figure 2a. Again, the energetic disorder is the lowest for the lower molecular weight, while for the two higher molecular weights, it is higher and on a similar level.

In summary, the lower molecular weight exhibits the highest fraction of aggregates, the highest average conjugation length, and the lowest energetic disorder. The two higher molecular weights are more disordered in all respects, with both being at a similar level. The apparent cause is probably the increased entanglements in the forming film and the number of refolded or bridging polymer chains between the aggregates [14,34,35]. In any case, the used spin-coating solvent plays a minor role in influencing the optoelectronic properties compared to the molecular weight for our preparation parameters.

While the UV-vis absorption measurements examine the electronic interaction of neighboring polymer chains, we can characterize the stacking of polymer chains using x-ray diffraction. To examine the influence of molecular weight and processing solvent on the nanostructure beyond individual chains, we perform GIWAXS measurements.

In Figure 3a, example 2D GIWAXS data are displayed. P3HT is known to stack in two directions within a single crystallite, i.e., along the side chains (lamellar stacking) and by stacking the backbones via π - π stacking. As the short intermolecular distance of the π - π stacking enables electronic coupling, it more strongly regulates the optoelectronic and thermal properties than the lamellar stacking with its larger intermolecular distance across the non-conductive hexyl sidechains. Therefore, the lamellar stacking serves as an indicator for the aggregate quantity and quality, but the π - π stacking is expected to relate to transport properties.

We examine both stacking directions using GIWAXS. The spin-coating procedure yielded P3HT films with a variation in layer thicknesses, as outlined in Figure 1c. Therefore, we used the weighted combination of amorphous (weight = 1.39) and aggregated (weight = 1.0) material obtained from the individual absorption spectra of each film as a measure for the amount of scattering polymer in the X-ray beam to normalize the peak amplitudes. We are then able to use the normalized peak amplitudes for a quantitative comparison of stacking features between different molecular weight samples. For all samples, in the vertical direction at about $q = 0.39 \text{ \AA}^{-1}$ ((100) peak, $d = 16 \text{ \AA}$), 0.78 \AA^{-1} ((200) peak), and 1.16 \AA^{-1} ((300) peak), the first three orders of the lamellar stacking scattering are clearly visible. In the horizontal direction, only the (100) lamellar peak stands out significantly from the background. Moreover, at about $q = 1.66 \text{ \AA}^{-1}$ ($d = 3.79 \text{ \AA}$) in the horizontal direction, the well-defined π - π peak can be observed. This is a typical signature of edge-oriented P3HT. Between about 1.2 \AA^{-1} and 1.7 \AA^{-1} , scattering of disordered P3HT can be seen, but also scattering of the Quartz substrate (reference measurement, see Figure S4) is contributing to the same q -range, especially in the vertical direction. To extract information on the lamellar and π - π stacking, we include the broad peaks of the disordered P3HT and Quartz underneath the π - π stacking peak into our fitting routine. The fit of the horizontal cut of the example data from Figure 3a in the horizontal direction is displayed in Figure 3b.

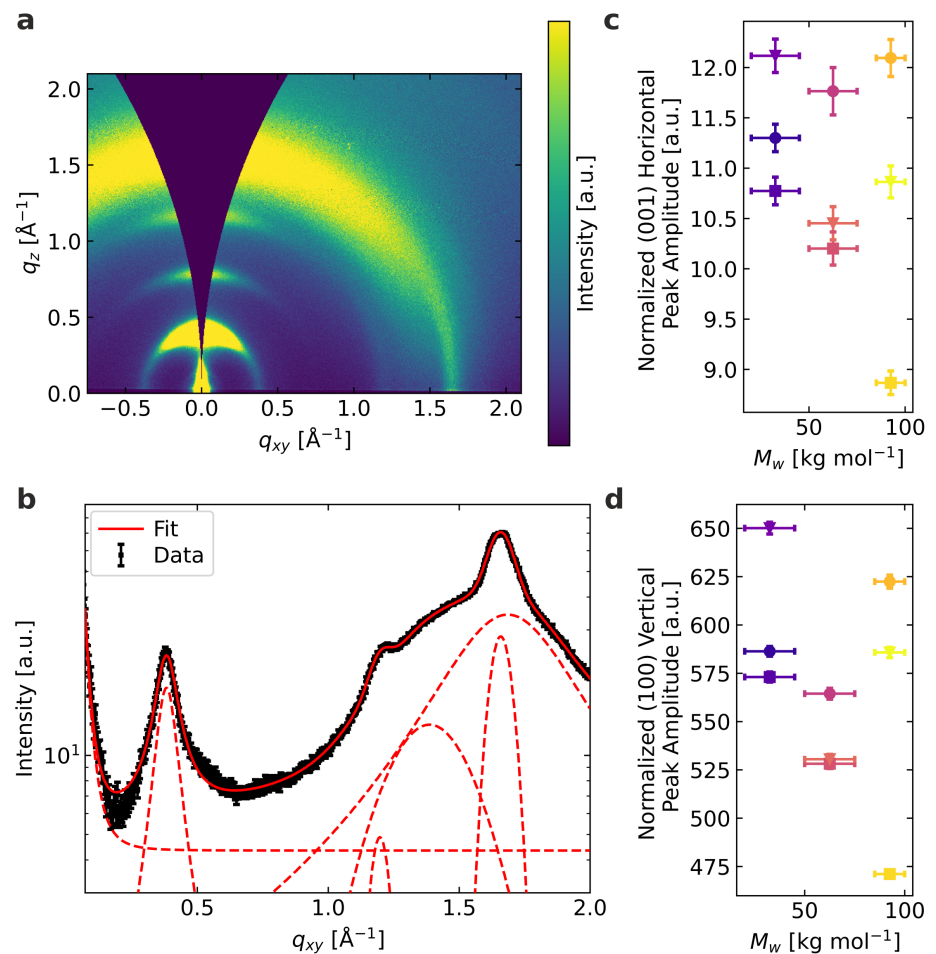


Figure 3. Performed GIWAXS analysis: (a) 2D GIWAXS data of $\overline{M}_w = 92.5 \text{ kg mol}^{-1}$ spin-coated from 1,2,4-trichlorobenzene. (b) Horizontal cut of the 2D data showing the individual fitting contributions. (c) Normalized peak amplitude of the horizontal π - π stacking signal (001). (d) Normalized peak amplitude of the vertical lamellar stacking signal (100). The shown data sets are carried out on samples with a comparable thickness. The obtained peak amplitudes are normalized with the amount of examined material from individual absorption measurements.

In Figure 3c,d, the normalized peak amplitudes of the (001) peak in the horizontal direction (π - π stacking) and the (100) peak in the vertical direction (dominant lamellar peak) are shown. The normalized peak amplitudes resemble the amount of material involved in π - π stacking and lamellar stacking, respectively. In all samples, we observed material containing polymer π - π stacking and lamellar stacking. However, we could not determine a systematic trend concerning the relative amounts among the different samples. Neither the different molecular weights, nor the various spin-coating solvents resulted in a systematic trend favoring one or the other stacking type quantitatively. The variability of the normalized peak amplitudes is highest for samples with the highest molecular weight, indicating that this polymer seems the most challenging to reproduce the nanostructures in a controllable way.

In contrast to the optical analysis presented in Figure 2, the GIWAXS data do not confirm a higher degree of order, in particular, in the case of the low molecular weight species. This does not contradict the optoelectronic properties, but is based on the differences in length scales probed. In Figures S5a and S4b, the peak widths of the same

peaks are displayed. For the π - π stacking as well as the lamellar stacking, the differences between the values for the various solvents and molecular weights are rather small, and no systematic behavior is observable. The peak width is a measure for the range of ordering, where a smaller peak width signals a longer-range order. Neither for the lamellar, nor the π - π stacking does the peak width indicate the highest order for the low molecular weight as observed in the optoelectronic characterization, where shorter length scales are probed. Therefore, we conclude that despite systematic differences in the backbone ordering and energetic disorder, this does not translate to a systematic impact on the longer-range π - π and lamellar stacking, as measured by GIWAXS.

Having discussed the microstructural properties, we now turn to the thermal properties. An exemplary measurement of the photoacoustic phase shift $\Delta\phi$ as a function of frequency, and the performed multilayer fit, are shown for the molecular weight of 32.5 kg mol^{-1} spin-coated from chlorobenzene in Figure 4a. The frequency position in combination with the sample thickness determines mainly the thermal diffusivity, while the phase shift values determine mainly the thermal effusivity in the one-dimensional limit of the thermal diffusion equation, which can be applied here [22,36]. The combination of both parameters then provides the thermal conductivity. The thermal conductivity for all samples investigated in this work is reported in Figure 4b.

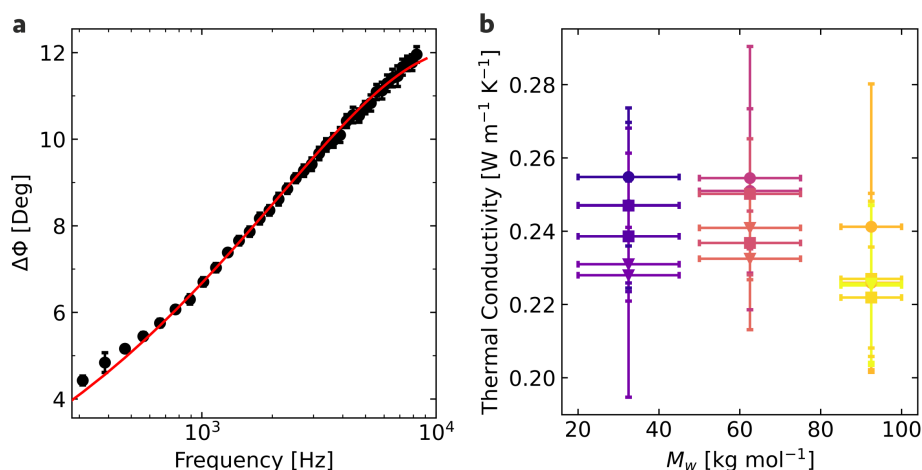


Figure 4. Performed photoacoustic data analysis: (a) Exemplary fit on the measured phase shift of $\bar{M}_w = 32.5 \text{ kg mol}^{-1}$ spin-coated from chlorobenzene. (b) Extracted thermal conductivities for the different molecular weights and solvents. Circular symbols represent films spin-coated from chlorobenzene, squares films from 1,2-dichlorobenzene, and triangles films from 1,2,4-trichlorobenzene.

The primary sources of errors are the inhomogeneities and fluctuations in the film thickness. Since layer thickness is one of the most critical parameters of the multilayer model, these uncertainties directly affect the resulting thermal conductivity. The thermal conductivity for all samples is between $0.22 \text{ W m}^{-1} \text{K}^{-1}$ and $0.26 \text{ W m}^{-1} \text{K}^{-1}$, which are generally in line with or slightly above literature values [18,20]. Furthermore, no thickness dependence effects are apparent for the investigated thickness regime, as shown in the Supporting Information (Figure S2). No direct influence of the solvent on the resulting properties is discernible for the thermal properties, similar to the microstructural properties. However, the impact of the molecular weight seems to be different here. The two lower molecular weights appear to be on a similar level at approximately $0.24 \text{ W m}^{-1} \text{K}^{-1}$ on average, while the high molecular weight exhibits an average thermal conductivity of roughly $0.23 \text{ W m}^{-1} \text{K}^{-1}$. This molecular weight dependency contrasts with the microstructure parameters, where the two higher molecular weights are at a similar level, while the lowest molecular weight deviates from them. Nevertheless, the relative deviations in thermal conductivity between the different molecular weights are comparatively small.

Since all structural, optoelectronic, and thermal transport properties have been determined on the same specimen, we can now correlate these properties to identify possible relationships.

4. Discussion

Correlations between the microstructural properties, determined by absorption spectra analysis, and thermal properties determined on the same samples are investigated below. The microstructural properties are plotted against the thermal conductivity to identify possible correlations or independencies. Figure 5 shows this for the fraction of aggregates and the exciton binding energy.

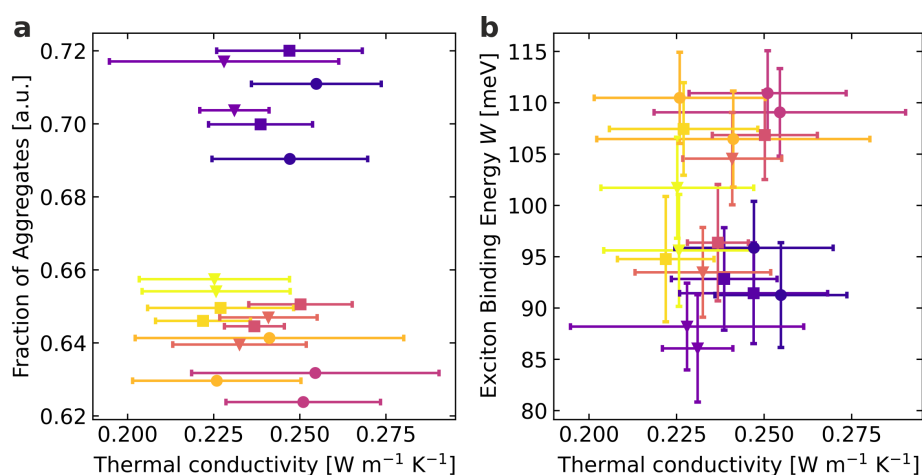


Figure 5. Correlations between extracted microstructural properties and thermal conductivity: (a) Relation between the fraction of aggregates and the thermal conductivity. (b) Relation between the exciton binding energy and the thermal conductivity. Color code: violet: low \bar{M}_w samples, red: medium \bar{M}_w samples, yellow: high \bar{M}_w samples. Circular symbols represent films spin-coated from chlorobenzene, squares films from 1,2-dichlorobenzene, and triangles films from 1,2,4-trichlorobenzene.

Within the accuracy of the measurement, we do not find a correlation between the fraction of aggregates and the thermal conductivity in the investigated range of molecular weights and generated microstructures. Although a significant variation in the fraction of aggregates can be seen depending on the molecular weight, it does not affect the thermal conductivity. The thermal conductivity proves robust concerning the present fraction of aggregates and is, therefore, not affected in the evaluated domain. This is supported by the structural investigations on the longer length scales obtained from the GIWAXS measurements. While the fraction of aggregates obtained from spectroscopy correlates with the trend of peak amplitudes with molecular weight and solvent, the peak widths of the scattering data, which correlate with the length scale of ordered domains, do not show any systematic changes. For the exciton binding energy, a more complex situation emerges. For the high molecular weight, a similar situation as for the fraction of aggregates is present, where similar thermal conductivities for different exciton binding energies can be identified. In contrast, for the low and especially medium molecular weight, one could infer a connection between the exciton binding energy and the thermal conductivity. Slightly higher thermal conductivities accompany higher exciton binding energies. Considering the scatter and accuracy of our data, such a potential trend needs to be interpreted cautiously. Taking into account the 0–0 transition energy and the Gaussian linewidth, this trend is not confirmed (Supporting Information, Figure S3). Overall, we have to conclude that a correlation between the structure, the optoelectronic properties, and the thermal conductivity cannot be resolved in the P3HT thin films investigated here.

We interpret the main obstruction to a consistent identification of correlations between the microstructural properties and the thermal conductivity by the lack of sufficiently high

difference in the thermal conductivity of the crystalline and amorphous regions, respectively. The fundamental factor underlying these results is the semi-crystalline structure of the investigated thin films. The amorphous regions mainly affect macroscopic thermal transport in semi-crystalline polymeric thin films with molecular weights above the critical entanglement molecular weight [37–39]. The critical entanglement molecular weight for P3HT is assumed to be approximately 35 kg mol^{-1} [37,40,41]. Especially for the high concentrations used in this work during spin-coating to enable a sufficient film thickness for the thermal characterization, chain entanglements are likely to have a very significant influence. The molecular weights used in this work are either on the order or above the critical entanglement molecular weight, which presumably leads to the amorphous domains forming the bottleneck for macroscopic thermal transport. Even though preferential chain orientation can significantly enhance the thermal conductivity of the amorphous phase, mostly through increased short-range ordering while long-range order remains absent, this is only achieved with special preparation procedures [42]. The amorphous phase for the relatively high film thickness and preparation by spin-coating examined in this work is, therefore, not considered to be oriented.

In contrast, the extracted microstructural properties are assigned to the ordered regions, as only these are included in the optoelectronic model and detectable in X-ray diffraction [12]. This reinforces our findings that a change in the microstructural properties in the ordered regions does not affect the resulting macroscopic thermal transport properties in the examined range of molecular weights. The bottleneck for macroscopic thermal transport remains the amorphous regions, which separate the ordered parts.

5. Conclusions

This work investigated possible relationships between nanostructure, optoelectronic, and thermal transport properties for regioregular P3HT thin films. Three different molecular weights ($\bar{M}_w = 32.5 \text{ kg mol}^{-1}$, 62.5 kg mol^{-1} , and 92.5 kg mol^{-1}) and three different solvents (chlorobenzene, 1,2-dichlorobenzene, and 1,2,4-trichlorobenzene) were chosen for this purpose. Absorption spectra were analyzed using the model from Spano, which showed that the two higher molecular weights exhibit similar optoelectronic properties [12]. In contrast, the lower molecular weight shows slight differences with a higher fraction of aggregates and a lower 0–0 transition energy, a lower exciton binding energy, and a lower Gaussian linewidth, corresponding to the highest degree of order in the crystalline domains. The spin-coating solvent used played a minor role in influencing the optoelectronic properties compared to the molecular weight of the P3HT. GIWAXS measurements also support this behavior. The spatial extension of the ordered domains shows no systematic changes with molecular weight or processing solvent. The thermal conductivity was determined on the same set of samples, revealing very similar values in the range of $0.22\text{--}0.26 \text{ W m}^{-1} \text{ K}^{-1}$. The fraction of aggregates proved to be unrelated to the thermal conductivity in the investigated sample space. In general, we find the microstructural properties not to be related to the thermal conductivity. This can be explained by the fact that non-oriented amorphous regions separate the ordered regions. These apparently dictate the macroscopic heat transport. The optoelectronic properties, however, are mainly governed by the ordered parts. Consequently, we cannot resolve an unambiguous relation between the optoelectronic and the thermal transport properties. Therefore, we would like to further encourage the field to explore possible relationships between microstructure and thermal properties, at best with a stronger focus on the amorphous region. This will be of immediate relevance for a range of polymer-based materials, where the thermal performance strongly depends on the structural arrangement across several length scales. Important related materials are polymer-based photovoltaics, organic light-emitting diodes, hybrid thermoelectric systems, or thermal interface materials. Similar to the structure of P3HT investigated in this study, these materials comprise ordered and disordered regions with significant contributions of the involved interfaces. Efficient heat transfer between the various compartments of these materials will only be possible with stringent control of the polymer morphology in each

of these nanostructured spaces and requires a better fundamental understanding of this intricate interplay.

Supplementary Materials: The following are available online at <https://www.mdpi.com/article/10.3390/ma15217700/s1>, Figure S1: Height and phase AFM images of P3HT films, Figure S2: Thickness Dependency of Thermal Conductivity, Figure S3: Additional Correlations of Microstructure and Thermal Conductivity. Figure S4: GIWAXS of Quartz Reference. Figure S5: Additional Extracted GIWAXS Parameters.

Author Contributions: Conceptualization, K.H.; methodology, K.H.; data analysis and validation, K.H., S.F.; investigation, K.H., S.F.; GIWAXS measurements, F.E.; data analysis GIWAXS, F.E.; AFM measurement, T.R.; writing—original draft preparation, K.H.; writing—original draft preparation scattering, F.E.; writing—review and editing, E.M.H., G.P. and M.R.; visualization, K.H.; supervision, M.R., E.M.H., G.P.; project administration, K.H.; funding acquisition, E.M.H., G.P. and M.R. All authors have read and agreed to the published version of the manuscript.

Funding: This work was funded by the German Research Foundation (DFG, SFB 840, project B7).

Institutional Review Board Statement: Not applicable.

Informed Consent Statement: Not applicable.

Data Availability Statement: The datasets generated and analyzed during the current study are available from the corresponding author on reasonable request.

Acknowledgments: The authors thank Tobias Lauster for assistance and advice on the UV–vis measurements. F.E. and E.M.H. thank for funding from SolarEraNet (No. NFA4R2ROPV) and the DFG (INST 91/443-1). F.E. thanks the Elite Study Program Macromolecular Science within the Elite Network of Bavaria (ENB) for support.

Conflicts of Interest: The authors declare no conflict of interest.

References

1. Zhang, H.; Shen, P.K. Recent Development of Polymer Electrolyte Membranes for Fuel Cells. *Chem. Rev.* **2012**, *112*, 2780–2832. [[CrossRef](#)] [[PubMed](#)]
2. Du, W.; Du, X.; Ma, M.; Huang, S.; Sun, X.; Xiong, L. Polymer Electrode Materials for Lithium-Ion Batteries. *Adv. Funct. Mater.* **2022**, *1*, 2110871. [[CrossRef](#)]
3. Li, G.; Zhu, R.; Yang, Y. Polymer solar cells. *Nat. Photonics* **2012**, *6*, 153–161. [[CrossRef](#)]
4. Stott, T.L.; Wolf, M.O. Electronic interactions in metallated polythiophenes: What can be learned from model complexes. *Coord. Chem. Rev.* **2003**, *246*, 89–101. [[CrossRef](#)]
5. Derewjanko, D.; Scheunemann, D.; Järsvall, E.; Hofmann, A.I.; Müller, C.; Kemerink, M. Delocalization Enhances Conductivity at High Doping Concentrations. *Adv. Funct. Mater.* **2022**, *32*, 2112262. [[CrossRef](#)]
6. Guo, X.; Cui, C.; Zhang, M.; Huo, L.; Huang, Y.; Hou, J.; Li, Y. High efficiency polymer solar cells based on poly(3-hexylthiophene)/indene-C70 bisadduct with solvent additive. *Energy Environ. Sci.* **2012**, *5*, 7943. [[CrossRef](#)]
7. Agbolaghi, S.; Zenoozi, S. A comprehensive review on poly(3-alkylthiophene)-based crystalline structures, protocols and electronic applications. *Org. Electron.* **2017**, *51*, 362–403. [[CrossRef](#)]
8. Brinkmann, M. Structure and morphology control in thin films of regioregular poly(3-hexylthiophene). *J. Polym. Sci. Part B Polym. Phys.* **2011**, *49*, 1218–1233. [[CrossRef](#)]
9. Salleo, A. Charge transport in polymeric transistors. *Mater. Today* **2007**, *10*, 38–45. [[CrossRef](#)]
10. Joshi, S.; Grigorian, S.; Pietsch, U.; Pingel, P.; Zen, A.; Neher, D.; Scherf, U. Thickness Dependence of the Crystalline Structure and Hole Mobility in Thin Films of Low Molecular Weight Poly(3-hexylthiophene). *Macromolecules* **2008**, *41*, 6800–6808. [[CrossRef](#)]
11. Wu, Z.; Petzold, A.; Henze, T.; Thurn-Albrecht, T.; Lohwasser, R.H.; Sommer, M.; Thelakkat, M. Temperature and Molecular Weight Dependent Hierarchical Equilibrium Structures in Semiconducting Poly(3-hexylthiophene). *Macromolecules* **2010**, *43*, 4646–4653. [[CrossRef](#)]
12. Spano, F.C. Modeling disorder in polymer aggregates: The optical spectroscopy of regioregular poly(3-hexylthiophene) thin films. *J. Chem. Phys.* **2005**, *122*, 234701. [[CrossRef](#)] [[PubMed](#)]
13. Spano, F.C. Absorption in regio-regular poly(3-hexyl)thiophene thin films: Fermi resonances, interband coupling and disorder. *Chem. Phys.* **2006**, *325*, 22–35. [[CrossRef](#)]
14. Pingel, P.; Zen, A.; Abellón, R.D.; Grozema, F.C.; Siebbeles, L.D.; Neher, D. Temperature-Resolved Local and Macroscopic Charge Carrier Transport in Thin P3HT Layers. *Adv. Funct. Mater.* **2010**, *20*, 2286–2295. [[CrossRef](#)]
15. Turner, S.T.; Pingel, P.; Steyrlleuthner, R.; Crossland, E.J.W.; Ludwigs, S.; Neher, D. Quantitative Analysis of Bulk Heterojunction Films Using Linear Absorption Spectroscopy and Solar Cell Performance. *Adv. Funct. Mater.* **2011**, *21*, 4640–4652. [[CrossRef](#)]

16. Henry, A. Thermal Transport in Polymers. *Annu. Rev. Heat Transf.* **2014**, *17*, 485–520. [[CrossRef](#)]
17. Rausch, S.; Rauh, D.; Deibel, C.; Vidi, S.; Ebert, H.P. Thin-Film Thermal-Conductivity Measurement on Semi-Conducting Polymer Material Using the 3ω Technique. *Int. J. Thermophys.* **2012**, *34*, 820–830. [[CrossRef](#)]
18. Duda, J.C.; Hopkins, P.E.; Shen, Y.; Gupta, M.C. Thermal transport in organic semiconducting polymers. *Appl. Phys. Lett.* **2013**, *102*, 251912. [[CrossRef](#)]
19. Smith, M.K.; Singh, V.; Kalaitzidou, K.; Cola, B.A. Poly(3-hexylthiophene) Nanotube Array Surfaces with Tunable Wetting and Contact Thermal Energy Transport. *ACS Nano* **2015**, *9*, 1080–1088. [[CrossRef](#)]
20. Xu, Y.; Wang, X.; Zhou, J.; Song, B.; Jiang, Z.; Lee, E.M.Y.; Huberman, S.; Gleason, K.K.; Chen, G. Molecular engineered conjugated polymer with high thermal conductivity. *Sci. Adv.* **2018**, *4*, eaar3031. [[CrossRef](#)]
21. Clark, J.; Chang, J.F.; Spano, F.C.; Friend, R.H.; Silva, C. Determining exciton bandwidth and film microstructure in polythiophene films using linear absorption spectroscopy. *Appl. Phys. Lett.* **2009**, *94*, 163306. [[CrossRef](#)]
22. Herrmann, K.; Pech-May, N.; Retsch, M. Photoacoustic thermal characterization of low thermal diffusivity thin films. *Photoacoustics* **2021**, *22*, 100246. [[CrossRef](#)] [[PubMed](#)]
23. Hu, H.; Wang, X.; Xu, X. Generalized theory of the photoacoustic effect in a multilayer material. *J. Appl. Phys.* **1999**, *86*, 3953–3958. [[CrossRef](#)]
24. Yang, J.; Ziade, E.; Schmidt, A.J. Uncertainty analysis of thermorefectance measurements. *Rev. Sci. Instrum.* **2016**, *87*, 014901. [[CrossRef](#)] [[PubMed](#)]
25. Zhong, Y.; Seeberger, D.; Herzig, E.M.; Köhler, A.; Panzer, F.; Li, C.; Huettner, S. The impact of solvent vapor on the film morphology and crystallization kinetics of lead Halide perovskites during annealing. *ACS Appl. Mater. Interfaces* **2021**, *13*, 45365–45374. [[CrossRef](#)]
26. Yamamoto, K. Grazing-Incidence Small Angle X-Ray Scattering in Polymer Thin Films Utilizing Low-Energy X-Rays. In *X-ray Scattering*; InTech: Houston, TX, USA, 2017. [[CrossRef](#)]
27. Niefind, F.; Karande, S.; Frost, F.; Abel, B.; Kahnt, A. Solvent influence on the surface morphology of P3HT thin films revealed by photoemission electron microscopy. *Nanoscale Adv.* **2019**, *1*, 3883–3886. [[CrossRef](#)]
28. DeGarmo, E. *Materials and Processes in Manufacturing*; John Wiley & Sons: Hoboken, NJ, USA, 2003.
29. Chang, J.F.; Clark, J.; Zhao, N.; Siringhaus, H.; Breiby, D.W.; Andreasen, J.W.; Nielsen, M.M.; Giles, M.; Heeney, M.; McCulloch, I. Molecular-weight dependence of interchain polaron delocalization and exciton bandwidth in high-mobility conjugated polymers. *Phys. Rev. B* **2006**, *74*, 115318. [[CrossRef](#)]
30. Clark, J.; Silva, C.; Friend, R.H.; Spano, F.C. Role of Intermolecular Coupling in the Photophysics of Disordered Organic Semiconductors: Aggregate Emission in Regioregular Polythiophene. *Phys. Rev. Lett.* **2007**, *98*, 206406. [[CrossRef](#)]
31. Scharsich, C.; Lohwasser, R.H.; Sommer, M.; Asawapirom, U.; Scherf, U.; Thelakkat, M.; Neher, D.; Köhler, A. Control of aggregate formation in poly(3-hexylthiophene) by solvent, molecular weight, and synthetic method. *J. Polym. Sci. Part B Polym. Phys.* **2011**, *50*, 442–453. [[CrossRef](#)]
32. Kajiya, D.; Ozawa, S.; Koganezawa, T.; Saitow, K.I. Enhancement of Out-of-plane Mobility in P3HT Film by Rubbing: Aggregation and Planarity Enhanced with Low Regioregularity. *J. Phys. Chem. C* **2015**, *119*, 7987–7995. [[CrossRef](#)]
33. Gierschner, J.; Huang, Y.S.; Averbeke, B.V.; Cornil, J.; Friend, R.H.; Beljonne, D. Excitonic versus electronic couplings in molecular assemblies: The importance of non-nearest neighbor interactions. *J. Chem. Phys.* **2009**, *130*, 044105. [[CrossRef](#)]
34. Zen, A.; Saphiannikova, M.; Neher, D.; Grenzer, J.; Grigorian, S.; Pietsch, U.; Asawapirom, U.; Janietz, S.; Scherf, U.; Lieberwirth, I.; et al. Effect of Molecular Weight on the Structure and Crystallinity of Poly(3-hexylthiophene). *Macromolecules* **2006**, *39*, 2162–2171. [[CrossRef](#)]
35. Brinkmann, M.; Rannou, P. Molecular Weight Dependence of Chain Packing and Semicrystalline Structure in Oriented Films of Regioregular Poly(3-hexylthiophene) Revealed by High-Resolution Transmission Electron Microscopy. *Macromolecules* **2009**, *42*, 1125–1130. [[CrossRef](#)]
36. Du, H.; Hu, H. Comparison of three-dimensional photoacoustic effect with different Gaussian radii. *IOP Conf. Ser. Earth Environ. Sci.* **2017**, *69*, 012176. [[CrossRef](#)]
37. Koch, F.P.V.; Rivnay, J.; Foster, S.; Müller, C.; Downing, J.M.; Buchaca-Domingo, E.; Westacott, P.; Yu, L.; Yuan, M.; Baklar, M.; et al. The impact of molecular weight on microstructure and charge transport in semicrystalline polymer semiconductors—poly(3-hexylthiophene), a model study. *Prog. Polym. Sci.* **2013**, *38*, 1978–1989. [[CrossRef](#)]
38. Lu, T.; Kim, K.; Li, X.; Zhou, J.; Chen, G.; Liu, J. Thermal transport in semicrystalline polyethylene by molecular dynamics simulation. *J. Appl. Phys.* **2018**, *123*, 015107. [[CrossRef](#)]
39. Selezneva, E.; Pietro, R.D.; Jiao, X.; McNeill, C.R.; Siringhaus, H. Investigation of the effect of microstructural changes on thermal transport in semicrystalline polymer semiconductors. *APL Mater.* **2019**, *7*, 081118. [[CrossRef](#)]
40. Hu, H.; Zhao, K.; Fernandes, N.; Boufflet, P.; Bannock, J.H.; Yu, L.; de Mello, J.C.; Stingelin, N.; Heeney, M.; Giannelis, E.P.; et al. Entanglements in marginal solutions: A means of tuning pre-aggregation of conjugated polymers with positive implications for charge transport. *J. Mater. Chem. C* **2015**, *3*, 7394–7404. [[CrossRef](#)]
41. Tummala, N.R.; Risko, C.; Bruner, C.; Dauskardt, R.H.; Brédas, J.L. Entanglements in P3HT and their influence on thin-film mechanical properties: Insights from molecular dynamics simulations. *J. Polym. Sci. Part B Polym. Phys.* **2015**, *53*, 934–942. [[CrossRef](#)]
42. Singh, V.; Bougher, T.L.; Weathers, A.; Cai, Y.; Bi, K.; Pettes, M.T.; McMennamin, S.A.; Lv, W.; Resler, D.P.; Gattuso, T.R.; et al. High thermal conductivity of chain-oriented amorphous polythiophene. *Nat. Nanotechnol.* **2014**, *9*, 384–390. [[CrossRef](#)]

Supplementary Materials: Microstructural and Thermal Transport Properties of Regioregular Poly(3-hexylthiophene-2,5-diyl) Thin Films

Kai Herrmann ¹, Simon Freund ¹, Fabian Eller ², Tamino Rößler ³, Georg Papastavrou ^{3,4}, Eva M. Herzig ² and Markus Retsch ^{1,4,*}

S1. Height and phase atomic force microscopy images

Height and phase images of spin cast P3HT films from chlorobenzene are shown in Figure S1. The granular surface exhibits height undulations of a few 10 nm. P3HT lamellar stacks could not be resolved.

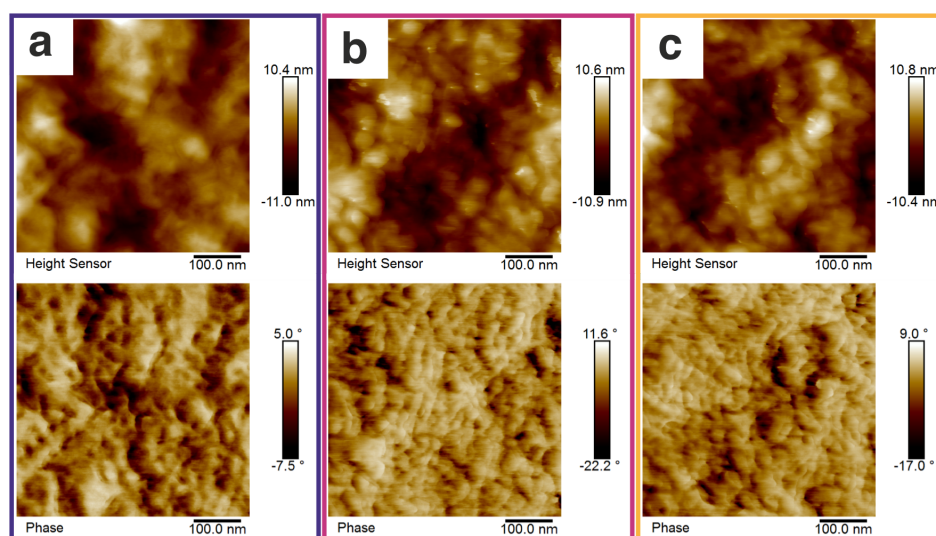


Figure S1. AFM measurement of the surface topography of spin cast films. a) $\bar{M}_w=32.5 \text{ kg mol}^{-1}$, b) $\bar{M}_w=62.5 \text{ kg mol}^{-1}$, c) $\bar{M}_w=92.5 \text{ kg mol}^{-1}$. All AFM images were acquired at a Bruker Dimension Icon equipped with a Nanoscope V Controller. Tapping mode was applied under ambient conditions ($f_{nom} = 300 \text{ kHz}$, $k_{nom} = 26 \text{ N m}^{-1}$). Topography and phase data is depicted.

S2. Thickness Dependency of Thermal Conductivity

The thickness dependency of the thermal conductivity for all samples examined in this work is shown in Figure S2. No influence of the film thickness can be seen here, which verifies that the thermal conductivity in the investigated thickness range is independent of the film thickness. Typically, the influence of the film thickness on the thermal conductivity of polymers is only present below 100 nm.

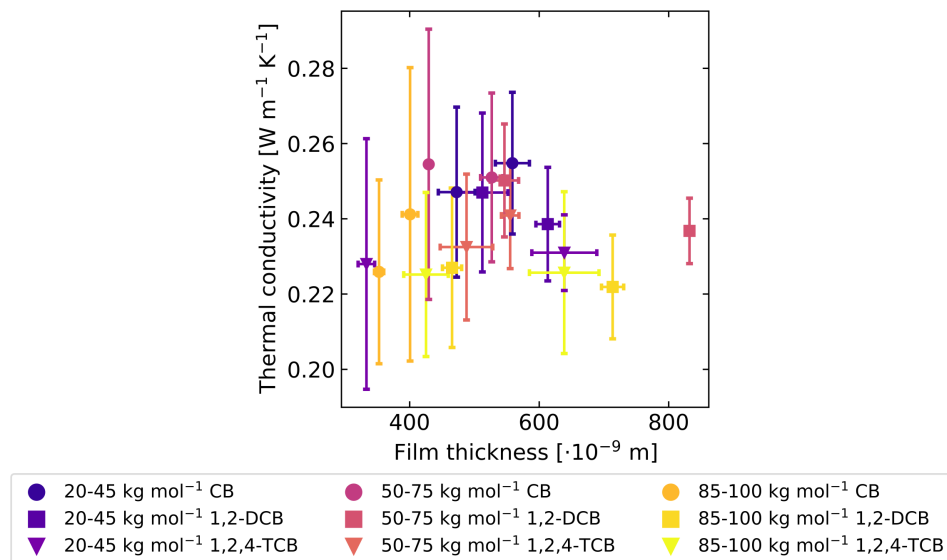


Figure S2. Thermal conductivity as a function of film thickness.

S3. Additional Correlations of Microstructure and Thermal Conductivity

Further correlations between microstructure parameters and thermal conductivity not shown in the main manuscript are shown in Figure S3. In this respect, there do not appear to be any direct correlations between the 0-0 transition energy or the Gaussian linewidth and the thermal conductivity in the range of measurement inaccuracies.

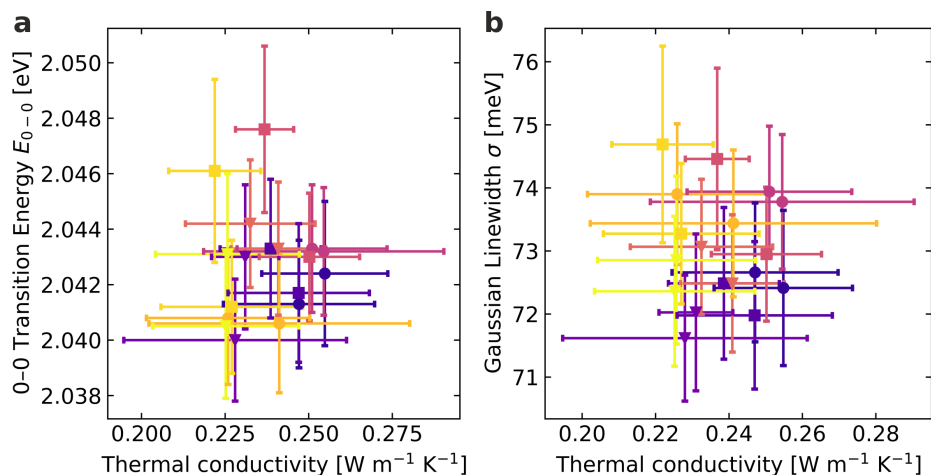


Figure S3. Correlations between extracted microstructural properties and thermal conductivity: **a** Relation between the 0-0 transition energy and the thermal conductivity. **b** Relation between the Gaussian linewidth and the thermal conductivity.

S4. GIWAXS of Quartz Reference

The background scattering of the GIWAXS measurements originating from substrate scattering is a broad feature as shown in the GIWAXS measurement of a Quartz substrate in Figure S4. This feature is found underneath the π - π stacking signal.

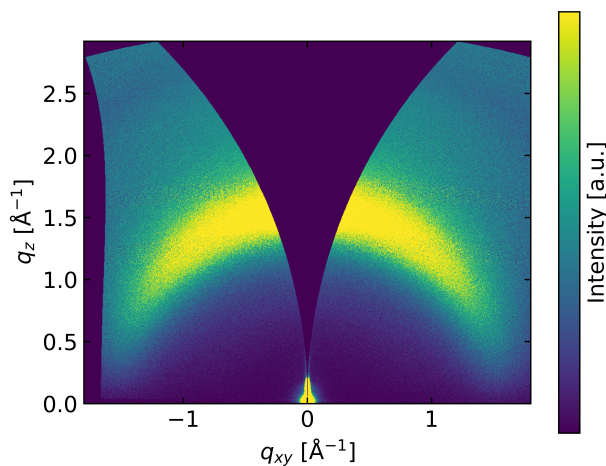


Figure S4. 2D GIWAXS data of the Quartz substrate.

S5. Additional Extracted GIWAXS Parameters

Figure S5 shows the peak widths of the π - π and the dominant lamellar peak from the GIWAXS measurements, two further fit parameters of the data presented in the main manuscript. The color code is analogous to that of the main manuscript.

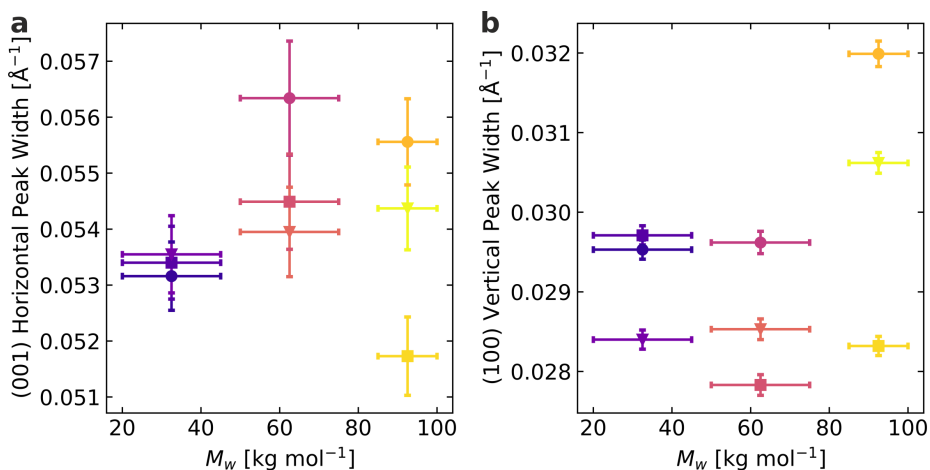
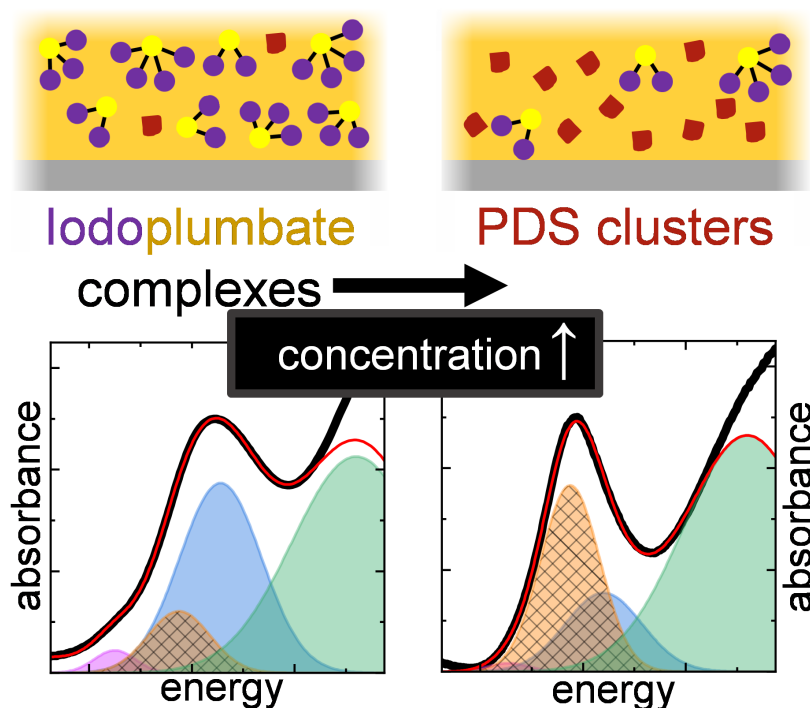


Figure S5. Fit parameters from GIWAXS data: **a** Peak width of the horizontal π - π stacking signal (001). **b** Peak width of the vertical lamellar stacking signal (100).

15 Solvated PbI_2 Clusters preceding the Crystallization of Lead Halide Perovskites – a UV/VIS In-Situ Study



Maximilian Spies, Simon Biberger, **Fabian Eller**, Eva M. Herzig, Anna Köhler

Submitted in
Advanced Electronic Materials

Solvated PbI₂ Clusters preceding the Crystallization of Lead Halide Perovskites – a UV/VIS In-Situ Study

Maximilian Spies¹, Simon Biberger¹, Fabian Eller², Eva M. Herzig², Anna Köhler^{1*}

¹Soft Matter Optoelectronics (EP II) and Bayreuth Institute of Macromolecular
Research (BIMF), University of Bayreuth, Bayreuth 95440, Germany

²Dynamics and Structure Formation - Herzig Group, University of Bayreuth, Bayreuth
95440, Germany

Corresponding Author:

*E-Mail: <mailto:anna.koehler@uni-bayreuth.de>

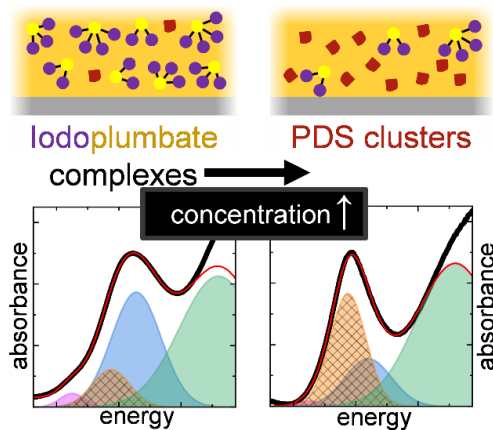
Keywords: optical in-situ spectroscopy, methylammonium lead iodide, iodoplumbate complexes, sol-
gel, precursor chemistry

1
2
3
4
5
6
7
8
9
10
11
12
13
14
15
16
17
18
19
20
21
22
23
24
25
26
27
28
29
30
31
32
33
34
35
36
37
38
39
40
41
42
43
44
45
46
47
48
49
50
51
52
53
54
55
56
57
58
59
60
61
62
63
64
65

Abstract

The solution-based fabrication of reproducible, high-quality lead iodide perovskite films demands a detailed understanding of the crystallization dynamics, which is mainly determined by the perovskite precursor solution and its processing conditions. We conducted a systematic *in-situ* study during the critical phase before the nucleation in solution to elucidate the formation dynamics of lead iodide perovskite films. Using UV absorption spectroscopy during spin coating allows us to track the evolution of iodoplumbate complexes present in the precursor solution. We find that prior to film formation, a novel absorption signature at 3.15 eV arises. We attribute this to the emergence of a PbI_2 -DMF solvated (PDS) phase. The amount of PDS phase is closely connected to the concentration of the solution layer during spin coating. We also propose that PDS clusters are a predecessor of crystalline perovskite phases and act as nucleation seeds in the precursor solution. In this way, our work provides insights into the early stages of perovskite crystallization.

TOC Figure



Introduction

1 The use of hybrid metal halide perovskites in solar cells has led to remarkable
2 photovoltaic performances in the recent years. Devices with a single active perovskite layer
3 (26.1 % power conversion efficiency), as well as tandem devices with silicon and perovskite
4 working in conjunction (33.9 %) have demonstrated the potential for photovoltaic applications.¹
5 In addition, in a solution-based approach, low-cost processing techniques make perovskite film
6 fabrication very affordable. For this, the perovskite precursors are often dissolved in a polar
7 aprotic solvent. However, further processing such as spin coating or blade coating of the
8 solution poses challenges in obtaining a suitable layer of polycrystalline perovskite on the
9 substrate.^{2,3} The resulting film should be fully covering, pin-hole free and consist of large crystal
10 grains with only few defects.² Therefore, understanding the mechanisms during processing
11 that dictate the crystallization in the precursor solution is important for the reproducible
12 fabrication of neat perovskite films.

13 The properties of perovskite precursor solutions have already been extensively
14 investigated. For instance, the optical properties of the precursor solution of methylammonium
15 lead iodide (MAPbI₃), i.e. a solution made with the educts methylammonium iodide (MAI) and
16 lead iodide (PbI₂), are known to result from iodoplumbate complexes.^{4,5} In fact, iodide as well
17 as solvent molecules are able to coordinate to the lead atom and the metal-to-halide charge
18 transfer determines the absorption properties of these complexes.⁵ Therefore, an absorption
19 peak can be assigned to each lead complex with a specific iodine coordination (i.e. PbI⁺, PbI₂,
20 PbI₃⁻, PbI₄²⁻, ...).^{5,6} The energetic positions of these highly absorbing species are located in the
21 UV region and are not affected by the solvent.⁵⁻⁷ However, solvent molecules compete with
22 iodine for coordination sites to the lead.⁷ Consequently, solvents with greater coordinating
23 abilities result in an iodoplumbate complex distribution favoring complexes with lower iodine
24 coordination.⁷ Another property of the lead iodide perovskite precursor solution is its colloidal
25 nature with size distributions in the range of 100 – 1000 nm, measured using dynamic light
26 scattering, as well as in the range of 1 – 10 nm obtained from small angle neutron scattering
27 and cryo-electron microscopy.⁸⁻¹¹ The nanometer sized colloids outweigh the larger colloids
28 substantially.¹⁰ Despite these extensive investigations, the process of precursor formation and
29 subsequent perovskite crystallization is still not fully understood.

30 In this work, we optically investigate the precursor solution of lead iodide perovskites
31 with dimethylformamide (DMF) and dimethyl sulfoxide (DMSO) as solvents. The two solvents
32 differ in their ability to coordinate with the iodoplumbate complexes, with DMSO being the more
33 strongly coordinating solvent. We focus on the dynamic process of film formation. For both,
34 *as-prepared* solutions and during spin coating (*in-situ*), we obtain UV absorption data at
35 concentrations suitable for thin film fabrication (0.2 – 0.9 mol/L). For all investigated solutions,

1
2
3
4
5
6
7
8
9
10
11
12
13
14
15
16
17
18
19
20
21
22
23
24
25
26
27
28
29
30
31
32
33
34
35
36
37
38
39
40
41
42
43
44
45
46
47
48
49
50
51
52
53
54
55
56
57
58
59
60
61
62
63
64
65

we observe the emergence of a novel optical signature during spin coating. We ascribe this signature to a PbI_2 -DMF solvated (PDS) phase. We propose that PDS clusters form in the precursor solution and act as nucleation seeds for the crystallization of subsequent perovskite phases. By modeling the solution layer thickness during spin coating, we estimate the precursor concentration in solution and find that the *in-situ* observed optical evolution of the perovskite precursor solution is mainly concentration driven.

Experimental Section

Preparation of solutions

All materials were used as received. Lead(II) iodide (PbI₂, 98%), methylammonium iodide (MAI, 99%) and formamidinium iodide (FAI, 99%) were purchased from TCI. The solvents dimethylformamide (DMF) and dimethyl sulfoxide (DMSO) were purchased from Acros. For MAPbI₃ (/FAPbI₃) solutions, PbI₂ and MAI (/FAI) were weighed in a stoichiometry of 1:1 and dissolved in DMF or in a solvent mixture DMF:DMSO = 12:1 at various concentrations (0.2 – 0.9 mol/L). For PbI₂ solutions, PbI₂ was dissolved in DMF at a concentration of 0.3 mol/L, making it comparable with the 0.6 mol/L MAPbI₃ (/FAPbI₃) precursor solutions.

As-prepared measurements

The *as-prepared* measurements were conducted with the Thinning Fluid Film Spectroscopy (TFFS) method recently introduced by Eller et al.¹² In this method, quartz tubes, partially filled with solution and sealed in inert N₂ atmosphere, are rapidly shaken with a home-built robotic setup. Transmission is measured through the thin fluid film on the walls of the tubes. This solution layer is thinning with time as it is flowing down the walls. Below a certain thickness, the absorption of the liquid layer is within the detection limits of the setup and can hence be measured. This procedure yields the spectral shape of the absorption, albeit the extinction cannot be determined quantitatively as the thickness of the solution layer on the wall of the tube is not known. The light source was a deuterium lamp from Ocean Optics and the spectrometer an AvaSpec-HSC1024x58 TEC-EVO from Avantes.

In-situ measurements

All optical *in-situ* data were recorded with a home-built setup. A detailed description of this setup is provided by Buchhorn et al.¹³ In brief, solutions were spin coated on a quartz glass substrate at 2000 RPM for 60 s and a ramp-up time of 1 s and the transmitted light was recorded at a frame rate of 7 Hz. A halogen lamp in combination with a deuterium lamp was used as light source. To ensure reproducibility, we recorded at least two coatings for each sample, which turned out to be quasi-identical.

Results

Unraveling spectral signatures in concentrated precursor solution

We first focus on identifying the various spectral signatures in concentrated precursor solutions. Absorption spectra of a perovskite precursor solution at concentrations suitable for film fabrication (~1 mol/L) are generally difficult to obtain due to the strongly absorbing properties of the iodoplumbate complexes. In previous studies, absorption spectra were obtained only by diluting the precursor solution to the mmol/L range.^{5,6,14} However, since the colloidal nature of the precursor solution is strongly concentration dependent, the properties of dilute solutions may not necessarily be identical to solutions with higher concentrations.⁸ It is therefore essential to investigate the precursor solution at concentrations that are relevant for the fabrication of perovskite-based optoelectronic devices.

We measured the absorption of precursor solutions up to a concentration of 0.9 mol/L, using the Thinning Fluid Film Spectroscopy (TFFS) method described above.¹² We employed a sealed quartz glass tube containing solution and nitrogen gas to avoid solvent evaporation and exposure to oxygen or water. In contrast to the *in-situ* method described later in this work, we refer to measurements of the perovskite precursor solution in the TFFS setup as *as-prepared*. Fig. 1 shows the spectra obtained by absorption measurements of stoichiometric MAPbI₃ *as-prepared* precursor solutions made with pure dimethylformamide (DMF) in Fig. 1a. The absorption spectra of precursor solutions made with DMF and dimethyl sulfoxide (DMSO) (DMF:DMSO = 12:1) as solvents are displayed in Fig. 1b. The spectra are normalized to the area under the curve from 2.7 eV to 3.7 eV. (At energies above 3.7 eV there is an increased risk of artefacts from scattering, *vide infra*).

For the 0.2 mol/L DMF solution (Fig. 1a), we observe three peaks at 2.90 eV, 3.36 eV and 3.86 eV superimposed on a general increase of the absorption towards even higher energies. Other groups that investigated solutions in the mmol/L range observed the same features and attributed them to absorption from PbI₄²⁻, PbI₃⁻, and PbI₂ complexes, respectively.^{5,6,14} Upon increasing the concentration up to 0.9 mol/L we find the peaks associated with PbI₂ and PbI₄²⁻ to reduce in intensity relative to the feature attributed to PbI₃⁻. Moreover, an isosbestic point is clearly visible at 3.32 eV.

In solutions containing a mixture of DMF and DMSO (Fig. 1b), we observe a similar evolution, with an isosbestic point at 3.37 eV. Furthermore, we find a more pronounced PbI₂ signature compared to PbI₃⁻ and PbI₄²⁻, especially at the lower concentration of 0.2 mol/L. We attribute this to the higher Gutmann Donor Number of DMSO ($D_N = 29.8$) compared to DMF ($D_N = 26.6$).⁷ The Gutmann Donor Number is a measure for the coordination ability of a solvent. Since the iodide competes with the solvent for coordination sites to the lead, a more strongly coordinating solvent shifts the distribution of iodoplumbate complexes towards those with

1
2
3
4
5
6
7
8
9
10
11
12
13
14
15
16
17
18
19
20
21
22
23
24
25
26
27
28
29
30
31
32
33
34
35
36
37
38
39
40
41
42
43
44
45
46
47
48
49
50
51
52
53
54
55
56
57
58
59
60
61
62
63
64
65

fewer iodide atoms. This effect is more pronounced in solutions with lower concentrations as they contain a higher ratio of solvent to iodide.

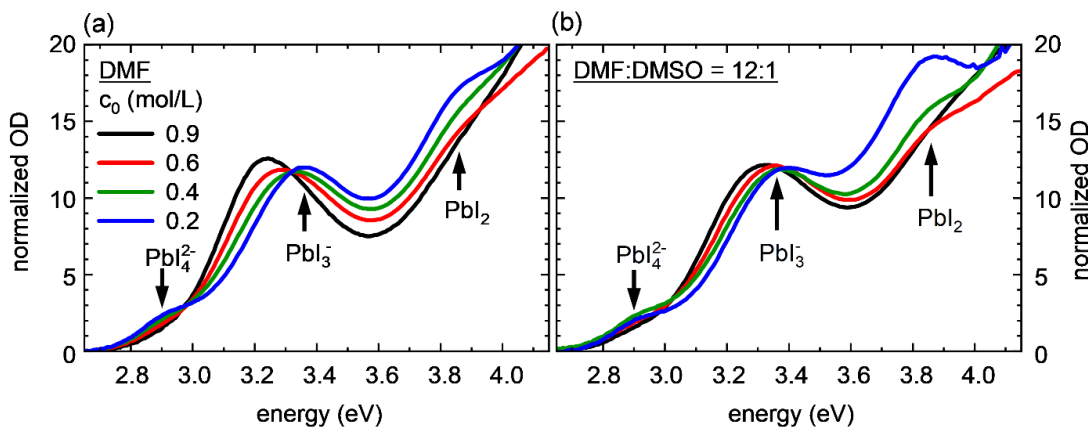


Fig. 1: Absorption measurements of the *as-prepared* precursor solution of MAPbI₃ at various concentrations c_0 , normalized by area up to 3.7 eV. In (a) the solvent in use is pure DMF, in (b) a small amount (1:12 by volume) of DMSO is added to DMF. Arrows indicate literature values for energies of the complexes PbI_2 , PbI_3^- and PbI_4^{2-} .

The concentration range in Fig. 1 allows for a first tentative assignment of the spectral features. However, when preparing a perovskite film by spin-coating a precursor solution, the precursor concentration increases even further during processing and the film eventually crystallizes. The changes in absorption during one-step spin coating (*in-situ*) of MAPbI₃ precursor solutions are captured in Fig. 2.

Fig. 2a depicts an *in-situ* measurement during spin coating of stoichiometric MAPbI₃ precursor in DMF at a concentration of 0.6 mol/L (see Fig. S1 for 0.4 mol/L and 0.2 mol/L). We observe an evolution of the absorption at energies usually associated with the PbI_3^- peak, i.e. in the spectral range of 3.0 – 3.5 eV. “Spinning time = 0 s” marks the beginning of spin coating. In the first few seconds, the spectra cannot be fully resolved as the absorption of the solution layer is still too high. After about 2 s, the optical density (OD) decreases due to material throw-off, so that absorption spectra suitable for analysis can be recorded. At this point, the spectra obtained in general, and in particular the PbI_3^- peak positions, are in good agreement with the peak positions of the *as-prepared* solution measurements. Up to 5 s the OD decreases whereas, from 6 s onwards, the OD maximum increases until it saturates the detector after 14 s. We ascribe the broad increase of the OD after 14 s to the formation of the highly scattering and absorbing intermediate phase $(\text{MA})_2\text{Pb}_3\text{I}_8(\text{DMF})_2$.^{15,16}

1
2
3
4
5
6
7
8
9
10
11
12
13
14
15
16
17
18
19
20
21
22
23
24
25
26
27
28
29
30
31
32
33
34
35
36
37
38
39
40
41
42
43
44
45
46
47
48
49
50
51
52
53
54
55
56
57
58
59
60
61
62
63
64
65

Within the time between 2 – 14 s, we observe a narrowing of the band initially between 3.0 – 3.5 eV and a continuous shift of the band maximum (at 3.27 eV at 2 s) to the red (to 3.15 eV) until spectra can no longer be recorded. Additionally, we note an isosbestic point at 3.32 eV between 7 – 12 s, displayed in the bottom panel of Fig. 2a as zoom-in. This isosbestic point occurs in the film formation at a stage where material throw-off no longer contributes to spectral changes. Hence, it suggests that the observed optical signatures do not originate from a single PbI_3^- peak but rather from two peaks with different widths and energetic positions and with varying intensity. Therefore, we conjecture that the spectral band in the range from 3.0 eV to 3.6 eV in the beginning (2 – 5 s) contains a significant contribution from the well-known PbI_3^- peak, whereas in the end (6 – 13 s) the emergence of a novel optical signature with its maximum at 3.15 eV modifies the absorption spectra.

To explain the spectral evolution over the range of 2.6 to 4.0 eV, we explore whether the spectra can be reproduced by assuming a superposition of absorption from the iodoplumbate complexes PbI_4^{2-} , PbI_3^- , and PbI_2 . Therefore, we employed a model of three gaussian line shapes with fixed widths and at fixed positions, chosen at the literature energies of PbI_4^{2-} , PbI_3^- , and PbI_2 , in agreement with the peaks in the low-concentrated *as-prepared* measurements.^{5,6,14} Fitting the spectrum of the *as-prepared* precursor solution results in a discernible residual, which is depicted by the orange hatched area in Fig. 2c. The residual consists of a nearly Gaussian peak centered at 3.18 – 3.15 eV and a general increase above 3.6 eV. We attribute the residual to an absorption band of a novel species.

We next studied the spectral composition of precursor solution during spin coating. To avoid artifacts from interferences below 2.8 eV and from scattering above 3.7 eV, we chose to keep the relative heights (and hence the areas) of the Gaussians associated with the iodoplumbate complexes fixed to the values obtained in the *as-prepared* solution. We find that the novel optical signature increases with spinning time relative to the iodoplumbate contributions (see Fig. 2b). Additionally, the energetic position of the near Gaussian part slightly shifts from 3.18 eV to 3.15 eV with time. When we allow the heights of all Gaussians to vary, we still obtain essentially the same result, i.e. the new optical signature increases and red-shifts with spinning time, and the heights of the Gaussian peaks associated with the iodoplumbate complexes increase from PbI_4^{2-} to PbI_2 . (see Fig. S2). To keep the number of fitting parameters low, we hence kept the relative heights of the iodoplumbate Gaussians fixed for all further analysis. Fits to spectra at other initial concentrations (0.2 – 0.9 mol/L) show qualitatively similar evolutions, albeit the magnitude of the novel optical signature increases with initial concentration (Fig. 2c). The fits to *in-situ* measurements with different initial concentrations are displayed in Fig. S3 and the supporting video files.

1 Hence, the data so far support the notion of a novel species forming in proportion to
2 the precursor concentration, be it the initial concentration or the increase in concentration
3 during spin coating. The evolution of the spectra with increasing concentration, notably the
4 shift of the band centered around 3.2 eV, its narrowing and the emergence of an isosbestic
5 point are difficult to account for without postulating an additional species. We can rule out a
6 sole solvatochromic effect as explanation for the observed shift, since this cannot account for
7 the isosbestic point and would affect all iodoplumbate signatures, yet the energetic positions
8 of PbI_4^{2-} and PbI_2 are noticeably unaffected by concentration. Fig. S4 shows that fits with a
9 shifting Gaussian near 3.2 eV give poor agreement with the measurements.
10
11
12
13
14
15
16
17
18
19
20
21
22
23
24
25
26
27
28
29
30
31
32
33
34
35
36
37
38
39
40
41
42
43
44
45
46
47
48
49
50
51
52
53
54
55
56
57
58
59
60
61
62
63
64
65

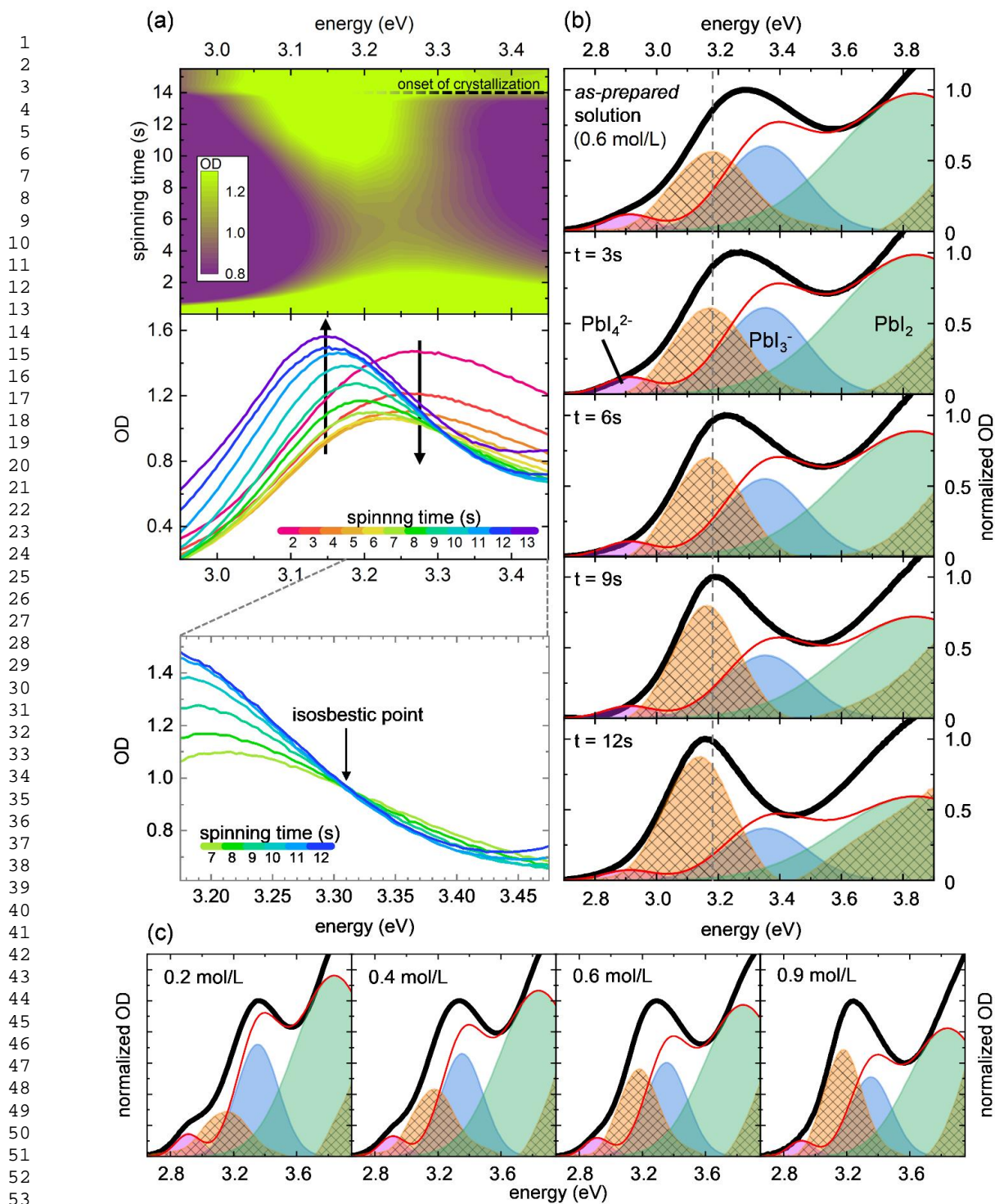


Fig. 2: (a) & (b): *In-situ* absorption measurements of the MAPbI₃ precursor solution in DMF at 0.6 mol/L during spin coating, highlighting the evolution of the central peak around 3.2 eV. (a): 2D map of the OD with respect to energy and spinning time (top), temporal cuts through the OD map (middle) and zoom to an isosbestic point after 6 s

1
2
3
4
5
6
7
8
9
10
11
12
13
14
15
16
17
18
19
20
21
22
23
24
25
26
27
28
29
30
31
32
33
34
35
36
37
38
39
40
41
42
43
44
45
46
47
48
49
50
51
52
53
54
55
56
57
58
59
60
61
62
63
64
65

(bottom). (b): Fits (red) to absorption spectra (black) at different spinning times and for *as-prepared* solution (i.e. $t = 0$). A novel optical signature (hatched orange) emerges from the residual of a fit consisting of the known complexes PbI_2 , PbI_3^- and PbI_4^{2-} . Spectra are normalized to the central peak maximum near 3.2 eV. (c): Fitting *as-prepared* absorption data reveals an increase of the novel signature with precursor concentration.

Origin of the novel optical signature

1
2 A possible origin for the novel optical signature could be the formation of polynuclear
3 iodoplumbate complexes (i.e. complexes with more than one Pb atom). The delocalization of
4 the electronic system upon forming dimers and trimers leads to an energetic shift of the PbI_3^-
5 signature.^{14,17} However, the energies attributed to these polynuclear complexes are not
6 consistent with the observed evolution in the band centered around 3.2 eV.¹⁴
7
8
9

10
11 We therefore explored whether the novel optical signature, indicated by the hatched
12 orange peak in Fig. 2, might result from the formation of a crystalline PbI_2 -DMF solvated (PDS)
13 phase. Such a crystalline solvated phase has previously been observed when spin coating a
14 PbI_2 -DMF solution.^{18–20} This highly crystalline PDS phase exhibits x-ray diffraction (XRD)
15 peaks at lower angles compared to PbI_2 , indicating a larger lattice spacing due to the
16 incorporation of DMF.^{19,20} A formation of such a PDS phase has, however, not yet been
17 associated with processes in a precursor solution, nor has its optical signature been identified.
18
19
20
21
22

23
24 To probe this, we conducted two experiments. First, we investigated the effect of the
25 organic cation by spin coating a formamidinium lead iodide (FAPbI_3) precursor dissolved in
26 DMF and analyzing the spectra analogous to the MAPbI_3 precursor solution in Fig. 2b. From
27 the right panel in Fig. 3 we see that there are no significant differences between the
28 compositions of the MAPbI_3 and FAPbI_3 spectra, implying a negligible influence of the organic
29 cation on the formation of the novel optical signature (see Fig. S5c). Second, we spin coat a
30 solution of PbI_2 in DMF and analyze the resulting spectra as before (Fig. 3, center panel).
31 Remarkably, omitting the organic cation entirely has only a minor effect on the spectral
32 evolution. The spectral shape still results from a superposition of the absorption features
33 attributed to iodoplumbate complexes and the novel optical signature, with the latter increasing
34 in the course of spin coating as the solution concentration increases. Moreover, the spectral
35 evolution happens on approximately the same time scale as in the MAPbI_3 and FAPbI_3
36 precursor solutions (see Fig. S5a). The differences between the spectra obtained without and
37 with organic cation are mainly a lower fraction of PbI_4^{2-} and PbI_3^- , straightforwardly accounted
38 for by the lower iodide concentration, and a lower final energetic position of the novel feature's
39 peak at 3.0 eV.
40
41
42
43
44
45
46
47
48
49
50

51 The formation of a crystalline PbI_2 -DMF solvated (PDS) phase upon spin coating PbI_2
52 in DMF has been identified previously by XRD and GIWAXS.^{18–20} We therefore associate the
53 residue in the fits the data for the PbI_2 solution in Fig. 3 (center panel), i.e. the hatched orange
54 area obtained when subtracting the signatures of iodoplumbate complexes from the overall
55 absorption, with the PDS phase. For clarification, here with PDS we exclusively refer to the
56 sole PbI_2 -DMF solvated phase, since sometimes PDS is also used for intermediate perovskite
57 phases such as $(\text{MA})_2\text{Pb}_3\text{I}_8(\text{DMF})_2$.¹⁶
58
59
60
61
62
63
64
65

1
2
3
4
5
6
7
8
9
10
11
12
13
14
15
16
17
18
19
20
21
22
23
24
25
26
27
28
29
30
31
32
33
34
35
36
37
38
39
40
41
42
43
44
45
46
47
48
49
50
51
52
53
54
55
56
57
58
59
60
61
62
63
64
65

When we thermally anneal the film obtained from spin coating the PbI₂ solution at 100 °C for 10 minutes, we observe the formation of an absorption edge at approximately 2.4 eV, indicating the formation of crystalline PbI₂ (see Fig. S6).²¹ This is consistent with the transformation of a PbI₂-DMF solvated phase into crystalline PbI₂ upon annealing observed by XRD measurements and further supports our assignment.¹⁹ In passing, we note that we observed the absorption edge at 2.4 eV to also appear without annealing when just allowing the film to dry over time.

From the similar evolution in the optical signatures during spin coating of MAPbI₃ or FAPbI₃ precursors it is straightforward to identify the hatched orange peak around 3.2 eV in the analysis of the respective precursor solution spectra with absorption from the same PDS phase. We speculate that the rising feature above 3.7 eV might also be associated with the PDS phase, either as absorption, or perhaps as light scattering from the PDS phase.

Since perovskites are frequently prepared not from a DMF solution but from a DMF:DMSO mixture, we investigated if the signature of the PDS phase also forms in a MAPbI₃-DMF:DMSO precursor solution (Fig. 3). Fitting the spectra with the same restrictions as before, we find the spectra for the initial solution as well as “just before crystallization” to be very similar to the spectra without DMSO. The time scale of the evolution is, however, decelerated roughly by a factor of 2 compared to pure DMF as solvent (see Fig. S5b).

We finally comment on the energetic shifts in the optical signature of this PDS-related peak. In the perovskite precursor data just before perovskite formation, this peak occurs at 3.15 eV, in contrast to the value of 3.0 eV in the PbI₂-DMF solution. We suggest this indicates a quantum confinement effect in the PDS structure in precursor solutions, with 3.0 eV being the energy of the absorption in the bulk PDS phase. In fact, during spin coating of PbI₂ in DMF (see Fig. S5a) this peak red shifts after 7 s, indicating the growth of PDS structures when no organic cation is present. Analogously, during spin coating of the precursor solution, we observe a small red shift in the PDS signal of about 0.03 eV, which we similarly attribute to a growth of the PDS phase in the course of spin coating.

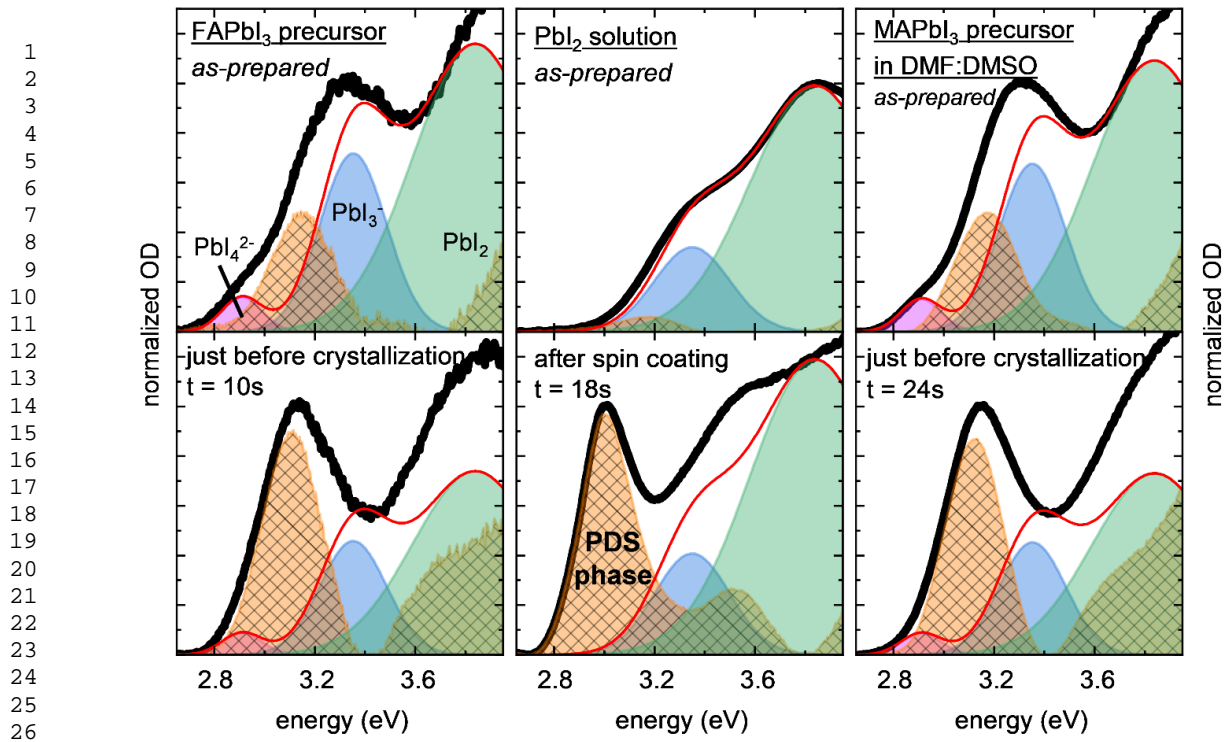


Fig. 3: Fits (red) to the absorption spectra (black) of FAPbI₃ precursor (0.6 mol/L) in DMF, and PbI₂ (0.3 mol/L) in DMF and MAPbI₃ precursor (0.6 mol/L) in a solvent mixture DMF:DMSO (12:1). Top row: spectra of *as-prepared* solutions. Bottom row: spectra of the solution films obtained by *in-situ* measurements just before crystallization occurs or after spin coating. The optical signature of the PDS phase (PbI₂ solution, bottom) resembles the novel signatures in the perovskite precursor solutions. Spectra are normalized to the central peak maximum.

The kinetics of PDS phase formation

So far, we have assigned the novel optical feature to the formation of a PDS phase, and we could observe that its intensity seems to increase with the concentration of the solution. To address this aspect in a more quantitative way, we analyzed the *in-situ* absorption data. From a sinusoidal pattern due to thin film white light interference in the absorption at 1.6 – 2.3 eV, we can extract the thickness of the perovskite solution layer during spin coating (see Fig. S7). A comprehensive description of this method is provided by Biberger et al.²² Fig. 4a shows the evolution of the solution layer's thickness during spin coating of precursor solutions for different initial concentrations (c_0). The interference pattern allows to determine the thickness of the solution layer until rapid crystallization occurs after about 10 – 15 s of spinning time, depending on c_0 . The time of crystallization is determined by the broad overall increase of the OD (see Fig. 2a), and hence the plots in Fig. 4 end when the film crystallizes.

We observe several features. Generally, the higher the initial concentration of the precursor solution, the longer it takes for crystallization to occur, as evidenced by the later termination of the curves in Fig. 4 (see Fig. S8). All measurements show a fast reduction in thickness at the beginning and a slower reduction at later times. Furthermore, the general trend is that the higher the initial concentration, the thicker the solution layer at all times.

In order to gain a deeper insight into the kinetics that govern the solution layer thinning during spin coating, we model the process as hydrodynamic-evaporative thinning. This assumes that there are two effects that determine the film thickness evolution: hydrodynamic thinning (h_{hydro}) and evaporative thinning (h_{evap}).^{23,24} The hydrodynamic thinning is due to the spinning of the substrate and therefore material being thrown off. It can be described by the following equation:²⁵

$$h_{\text{hydro}}(t) = h_0 \left(1 + \frac{4\omega^2 h_0^2 (t-t')}{3 \nu_{\text{kin}}} \right)^{-1/2} \quad \text{eq. 2}$$

h_0 is the solution layer thickness before spin coating, ω is the rotational velocity of the spin coater, ν_{kin} is the kinematic viscosity of the solution and t is the time after starting the spin coater with an instant ramp-up in velocity. To account for the finite ramp-up time of our spin coater, we shift the model by $t' = 0.5$ s compared to the time $t = 0.0$ s where the spin coater starts accelerating. To describe the evaporative thinning, we consider that the evaporation of solvent is mainly determined by the surface area of the liquid. This holds for solutions with a negligible amount of dissolved material compared to solvent molecules, which is the case in our experiments until shortly before crystallization. Due to the large substrate area (4 cm²), this

surface stays approximately constant during the solution layer thinning. Therefore, we can assume a constant rate of evaporation E :^{23,24}

$$h_{\text{evap}}(t) = -Et \quad \text{eq. 3}$$

Combining eq. 2 and eq. 3 yields the solution layer height model:

$$h_{\text{model}}(t) = h_{\text{hydro}}(t) + h_{\text{evap}}(t) \quad \text{eq. 4}$$

The initial thickness h_0 has only a minor influence on the evolution of the solvent layer thickness. We approximate h_0 as 1 mm as an estimate for the height of the droplet on the substrate before spin coating. The rotational velocity ω is 2000 RPM, whereas the parameters ν_{kin} and E remain as fitting parameters. The yellow dotted lines in Fig. 4a illustrate the best fit of eq. 4 to the data. The fit agrees with the data very well and only deviates slightly 1 – 2 s before crystallization occurs. As detailed below, the evaporation rate can reduce with increasing concentration. We therefore consider that 1 – 2 s before crystallization, the concentration has increased to a level where eq. 3 no longer applies.

The obtained fitting parameters are depicted in the inset in Fig. 4a. With increasing c_0 , we find an increase in kinematic viscosity and a decrease of the evaporation rate. The increase in viscosity with increasing concentration is intuitive due to an increased amount of dissolved material. Furthermore, the fitted viscosity values seem plausible when comparing them to the kinematic viscosity of DMF ($0.85 \text{ mm}^2/\text{s}$)²⁶ since we expect a higher viscosity when DMF contains dissolved material. We stress that the viscosity values obtained are only valid in the hydrodynamic regime when the concentration has not changed substantially from its initial value c_0 (see S9). The fitting parameters also show a decrease in evaporation rate with increasing concentration. We explain this by the high coordinating ability of the lead complexes: solvent molecules tend to adhere to the lead, rather than to evaporate from the solution layer. This effect is greater in more concentrated solutions. The limitations of the model and the extent of the two regimes (hydrodynamic and evaporative) are further discussed in S9.

By separating the solution layer thickness evolution into a hydrodynamic and an evaporative part in our model (transition at approx. $1.3 \text{ }\mu\text{m}$ film thickness, see S9), we are not only able to obtain viscosities and evaporation rates. We can also estimate the evolution of the concentration during spin coating. Throw-off of material (i.e. h_{hydro}) affects the solvent as well as the solvated material in the same way. Therefore, the amount of solvated material $M(t)$ is proportional to h_{hydro} . On the other hand, the volume of solution $V(t)$ is proportional to the solution layer thickness (i.e. h_{model}). Thus, the concentration of the solution during spin coating $c(t)$ can be expressed in the following way (see S10 for details):

$$c(t) = \frac{M(t)}{V(t)} = \frac{c_0}{1 + \frac{h_{\text{evap}}(t)}{h_{\text{hydro}}(t)}} \quad \text{eq. 5}$$

Fig. 4b shows the evolution of the concentration according to eq. 5, based on the fit to Fig. 4a. The concentration $c(t)$ for each sample starts from its respective c_0 . The subsequent dynamics differ for each sample: the lower the initial concentration, the faster the increase in concentration. This can be easily understood. A lower concentration implies firstly a higher solvent evaporation rate, and secondly a larger material throw-off due to the lower viscosity (inset of Fig. 4a). The combined effect results in a thinner film and hence a larger surface to volume ratio, thus promoting a stronger concentration increase upon evaporation from the surface. Eventually, the samples with lower c_0 exceed the concentration of the samples with initially higher c_0 .

To determine the concentration dependent rates of the iodoplumbates and PDS phase formation, we analyzed the *in-situ* absorption data of MAPbI₃ precursors in DMF as follows. For every time frame, we fitted the absorption spectra with the model described above (see supporting video files). Fig. 4c shows the evolution of the absorption intensity of the PbI₃⁻ peak, normalized to the initial concentration c_0 . Since the ratio between the different iodoplumbates is kept constant during the fit, the PbI₃⁻ peak height is proportional to the overall iodoplumbate absorption. We find that the PbI₃⁻ peak height decreases in the beginning of spin coating and plateaus after a certain time for each c_0 . The slight increase a few seconds before crystallization can most likely be explained by a minor increase in scattering (see supporting video files) and may mask a potential actual decrease of the signal. The observed decrease in the first few seconds due to material throw-off and the transition into the plateau region roughly coincide with the transition from the hydrodynamic into the evaporative regime (see S9).

The evolution of the PDS peak height, normalized to initial concentration, (Fig. 4d) exhibits a more intricate dynamic. At first, the PDS phase decreases, similar to the PbI₃⁻ complexes. However, after about 6 s, the PDS phase increases at different rates depending on the initial concentration of the precursor solution. The lower the initial concentration c_0 , the faster the increase after about 6 s. Furthermore, the increase of PDS phase slows down shortly before crystallization occurs. When comparing the evolution of the concentration (Fig. 4b) with the evolution of the PDS phase (Fig. 4d), similarities in the dynamic become apparent. Especially after 6 s, we note that the evolution of the PDS peak height qualitatively matches the concentration evolution. In particular, in both data sets we observe that the curves for different concentrations all seem to cross near 9.5 s. In Fig. 4b, the crossing point implies that there is one time when all samples have identical concentrations. This matches with an identical PDS peak height in all samples at the same time in Fig. 4c. The similar time evolution of both data sets suggests that the evolution of the PDS phase is mainly concentration driven.

17

1
2
3
4
5
6
7
8
9
10
11
12
13
14
15
16
17
18
19
20
21
22
23
24
25
26
27
28
29
30
31
32
33
34
35
36
37
38
39
40
41
42
43
44
45
46
47
48
49
50
51
52
53
54
55
56
57
58
59
60
61
62
63
64
65

However, there is one difference between the time evolution of the calculated concentration and the PDS phase. After the crossing point near 9.5 s, the evolution of the PDS peak changes slope and curvature. In fact, the crossing point is the point of inflection for all curves. This is not observed in the calculated concentrations in Fig. 4b, which are derived from fits to the solution layer thickness, assuming a constant rate of evaporation (eq. 3). The time when a noticeable deviation occurs between the two data sets (Fig. 4b and 4d) matches roughly with the time when the modelled solution layer thickness (yellow dotted lines in Fig. 4a) deviates from the measured thickness. The observed slower reduction in solution layer thickness in Fig. 4a than predicted by the hydrodynamic-evaporative thinning model (eq. 4) implies an actually slower increase in concentration than extrapolated with the dots in Fig. 4b. An actual evolution of the concentration $c(t)$ analogous to the evolution observed for the PDS peak height in Fig. 4d is hence conceivable.

The plots of the solution layer thickness in Fig. 4a end when the absorption increased strongly over the entire spectral range and saturated the detector. We took this to indicate the formation of a strongly absorbing or scattering crystalline species, i.e. either the final perovskite MAPbI_3 or an intermediate perovskite phase $(\text{MA})_2\text{Pb}_3\text{I}_8(\text{DMF})_2$. It is intriguing that the time at which this crystallization step occurs increases with initial concentration. This can be rationalized from our insights into the evolution of the solution concentration. In the classical thermodynamic view, crystallization occurs in a supersaturated solution, i.e. when the concentration of the solution exceeds its equilibrium solubility. Since we observe that the precursor solution with a lower initial concentration crystallizes earlier (see end of plots in Fig. 4 or Fig. S8), supersaturation therefore also occurs earlier for initially lower concentrated solutions. This may appear counterintuitive because one could argue that lower concentrated solutions need to evaporate more solvent before reaching supersaturation. However, Fig. 4b shows, that mainly the late increase in concentration after 6 s determines which solution reaches supersaturation first. In fact, lower concentrated solutions reach supersaturation earlier due to the concentration dependent evaporation and viscosity, and thereby affecting the spin coating hydrodynamics.

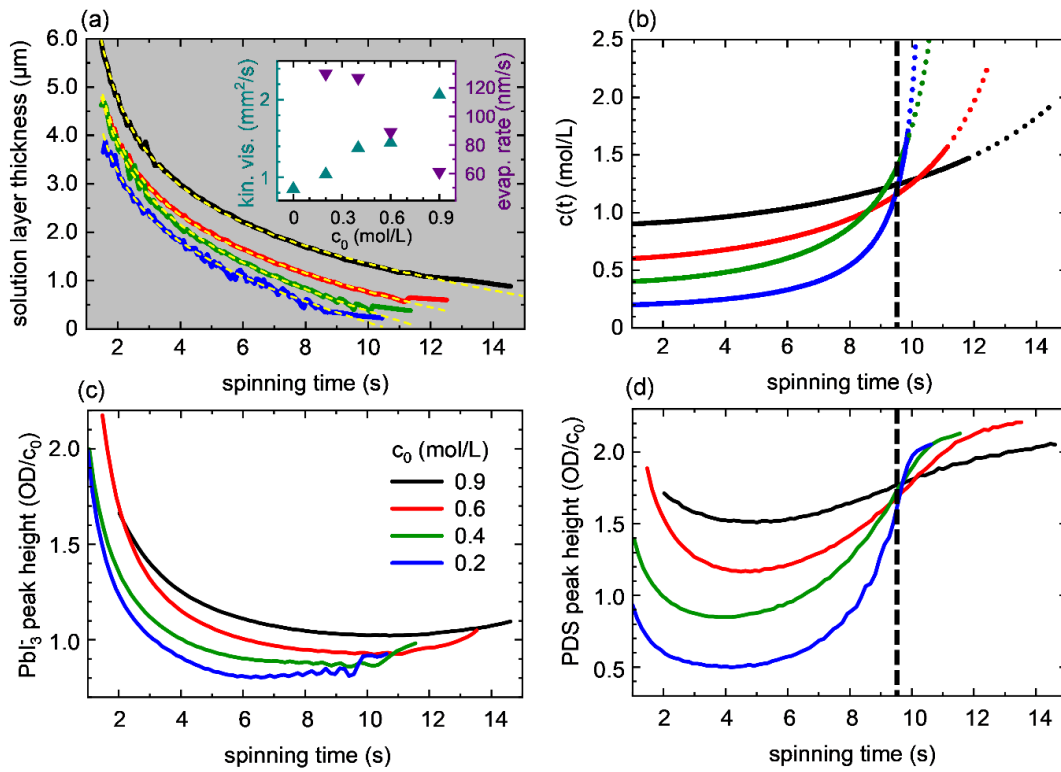


Fig. 4: Analysis of *in-situ* measurements of MAPbI_3 precursor in DMF. (a): Thickness of the perovskite solution layer during spin coating. The kinematic viscosity (cyan) and evaporation rate (purple) are obtained from a fit (yellow) to the solution layer thickness (exception: literature value for $c_0 = 0$).²⁶ (b): Estimated concentration evolution $c(t)$ of the perovskite precursor solution during spin coating, according to eq. 5. (c) and (d): Height evolutions of the spectral signatures of PbI_3^- and the PDS phase, obtained from fits to *in-situ* measurements depicted in Fig. 2. These evolutions resemble vaguely the film thickness and the concentration evolution. c_0 denotes the perovskite precursor concentration in the beginning of spin coating. The plots end when the film crystallizes. Dashed vertical lines in (b) and (d) highlight the time of intersection at 9.5 s.

1
2
3
4
5
6
7
8
9
10
11
12
13
14
15
16
17
18
19
20
21
22
23
24
25
26
27
28
29
30
31
32
33
34
35
36
37
38
39
40
41
42
43
44
45
46
47
48
49
50
51
52
53
54
55
56
57
58
59
60
61
62
63
64
65

Discussion

Our UV absorption measurements, both *as-prepared* and *in-situ*, give new insights into the lead iodide perovskite precursor solutions at concentrations suitable for film fabrication. Notably, fits to the absorption data reveal the emergence of a PbI_2 -DMF-solvated (PDS) phase, independently of the organic cation (MA^+ or FA^+) (Fig. 2 and 3). We observe that this PDS phase forms in the precursor solution with increasing concentration until the perovskite formation sets in. Hence, the PDS phase seems to be a predecessor of crystalline perovskite phases. The earlier precipitation of MA^+ -free PbI_2 -like phases is also consistent with the lower solubility of PbI_2 , compared to MA^+ . In fact, Yan et al. describe a soft coordination framework consisting of iodine and lead that appears in solution before the formation of a perovskite phase.⁸ In-situ grazing incidence wide-angle x-ray scattering (GIWAXS) measurements show no high-order structures prior to the formation of the perovskite phases but rather signatures of a sol-gel phase.^{15,20,27,28} Such a broad sol-gel-like signal in GIWAXS measurements would be consistent with the presence of individual, small structures in a suspension. In particular, they need to be small enough that no significant long-range order can be detected. Hence, we propose that the PDS phase in the perovskite precursor solution appears only as very small structures. This limitation on the structure size is further supported by observed peak shifts (during formation as well as when comparing PbI_2 -solution with precursor signal), which we attributed to quantum confinement effects (Fig. 3). It is also supported by the observations of Hu et al.²⁹ They observe PbI_6^{4-} octahedral cage nanoparticles in precursor solutions. Molecular dynamics simulations show that these octahedral complexes form PbI_2 -like amorphous clusters by sharing edges with neighboring octahedra.^{30,31} Further research needs to clarify whether the PDS phase observed here is identical to the crystalline, nanometer-scale colloids that have been observed in DMF-based MAPbI_3 precursor solution.^{8,10,11} Importantly, our analysis enabled us to identify the optical signatures of the PDS phase.

Having identified the formation of a PDS phase and its optical signature, we were able to compare the growth of the PDS fraction in the solution layer to the evolution to the solutions' concentration as determined by eq. 4. The strong temporal correlation suggested that the formation of PDS phase is concentration driven. We found that as concentration increases during spin-coating, PDS formation is replaced by the formation of crystalline perovskite or intermediate perovskite. This step occurs later for higher initial concentrations. This time difference has previously been attributed to the formation of large colloids (0.1 – 1 μm) in the precursor solution.³² We have instead interpreted the data in the framework of classical nucleation theory and attributed the earlier perovskite crystallization to the faster increase in concentration in the initially less concentrated solution.

The bend in the curves of Fig. 4d after about 10 s also tells us that growth of the PDS fraction reduces strongly and approaches saturation as the perovskite-based crystallites begin to form. Classical nucleation theory alone cannot account for this. One possible mechanism is the transformation of PDS into a perovskite-based phase. Cao et al. show that PDS, i.e. the PbI_2 -DMF solvated phase, can transform into crystalline MAPbI_3 through a molecular exchange of the DMF in the PDS phase with MA^+ and I^- ions.¹⁹ During spin coating, however, solvated intermediate perovskite phases typically form prior to unsolvated MAPbI_3 .^{33,34} Therefore, we tentatively suggest that PDS clusters primarily convert into $(\text{MA})_2\text{Pb}_3\text{I}_8(\text{DMF})_2$ via interdiffusion of MAI, before finally changing over to MAPbI_3 , consistent with simulations from Ahlawat et al..³¹

Based on the results presented in this work, in combination with those of other research groups,^{7,8,15,19,28,34,35} we propose a mechanism (Fig. 5) for the evolution of the precursor chemistry and the resulting film formation in the one-step spin coating process that includes the appearance of a temporary PDS phase. At first, iodoplumbate complexes as well as few small PDS clusters are present in the *as-prepared* lead iodide perovskite precursor solution (see Fig. 2).^{6,8} During spin coating and with increasing concentration, the number of PDS clusters increases. This process is mainly concentration driven. Eventually, at larger concentrations (roughly in the range exceeding 1.7 mol/l, see Fig. 4b), the organic cation begins to diffuse into the PDS clusters. This prevents further PDS formation and instead enables the formation of primarily intermediate perovskite. In this way, the original PDS clusters become nucleation seeds for the further growth of the intermediate perovskites, which occurs in an anisotropic way to result in a needle-like structure.³⁶ Finally, the complete solvent removal (typically accelerated via heat treatment) results in the solvent-free perovskite phase. The final needle-like structure illustrated in Fig. 5 is predetermined by the structure of the intermediate phase.³⁶

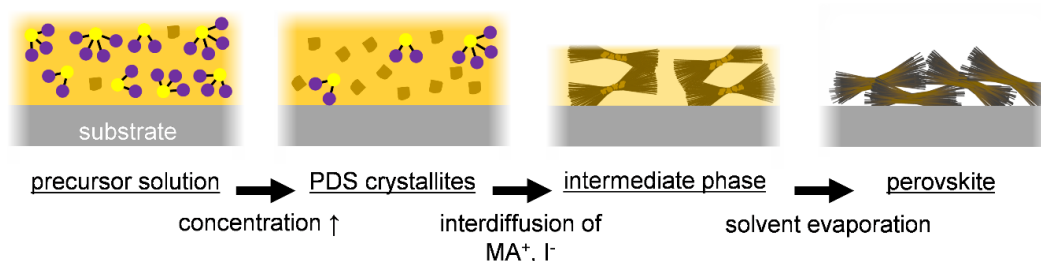


Fig. 5: Mechanistic picture of the one-step spin coating process of MAPbI_3 precursor in DMF. We propose that PbI_2 -DMF solvated (PDS) clusters in the precursor solution act

as nucleation seeds for subsequent perovskite phases. In the end, the needle like perovskite morphology is predetermined by the solvated intermediate phase.

1
2
3
4
5
6
7
8
9
10
11
12
13
14
15
16
17
18
19
20
21
22
23
24
25
26
27
28
29
30
31
32
33
34
35
36
37
38
39
40
41
42
43
44
45
46
47
48
49
50
51
52
53
54
55
56
57
58
59
60
61
62
63
64
65

Conclusion

1
2 In summary, we investigated the precursor chemistry and its evolution in different
3 concentrated solutions both before (*as-prepared*) and during spin coating (*in-situ*). We identify
4 absorption features from iodoplumbate complexes as well as from PbI₂-DMF solvated (PDS)
5 clusters. Quantum confinement effects suggest that this PDS phase appears only as small
6 structures during processing of lead iodide perovskites, rather than as bulk crystalline
7 structures with long-range order. Based on our analysis of the solutions' concentration and the
8 observed absorption features, we infer that the PDS phase evolves into intermediate
9 perovskite and hence plays a central role in the perovskite crystallization process.
10
11

12
13
14
15
16 Therefore, PDS phase engineering presents itself as a promising way to refine
17 perovskite crystallization and optimize film morphology without additional post treatments. In
18 particular, we anticipate that PDS crystallites are not only involved in the one-step spin coating
19 process but also in other coating processes and fabrication procedures. Hence, two-step
20 procedures, gas quenching or antisolvent methods should consider the PDS phase in their
21 protocol for film fabrication. For instance, the amount of PDS clusters in the solution may also
22 be useful for determining when antisolvent should be added in an automated way (*“reactive
23 concept”*).²² Additive engineering of the precursor solution would be a further promising
24 approach to modify the PDS phase.
25
26
27
28
29
30

31
32 Our study elucidates the critical role of PDS clusters in the formation of lead iodide
33 perovskites, offering a better understanding of the precursor chemistry and crystallization
34 dynamics. An optical signature reveals the amount of this PDS phase (even during fabrication)
35 and can be used to optimize the film formation, for instance by controlling the amount of
36 nucleation sites during perovskite crystallization. Future research should further explore film
37 fabrication methods and their impact on the PDS phase, subsequent perovskite phases and
38 film morphology. The integration of these insights into existing fabrication techniques holds
39 promise for innovative approaches in perovskite solar cell production.
40
41
42
43
44
45
46
47
48
49
50
51
52
53
54
55
56
57
58
59
60
61
62
63
64
65

Acknowledgements

1
2 We thank Fabian Panzer and Konstantin Schötz for initiating this work. FE and EMH thank the
3
4 Deutsche Forschungsgemeinschaft (DFG Research Unit FOR 5387 POPULAR, Project No.
5 461909888) for their support. EMH and AK acknowledge DFG PA 3373/7-1 for funding.
6
7

Author Contributions

8
9
10 MS and SB planned the experiments. MS modified the in-situ setup and conducted all in-situ
11
12 measurements and their analysis. FE under the supervision of EMH conducted the *as-*
13
14 *prepared* UV-VIS absorption spectroscopy measurements with the thinning fluid film
15
16 spectroscopy (TFFS) method. MS developed the precursor states fitting, the model for the film
17
18 thickness and concentration evolution and modelled all absorption spectra. MS, SB and AK
19
20 discussed the results and outlined the manuscript. MS with help from SB wrote the first version
21
22 of the manuscript. AK edited the manuscript. All authors critically read the manuscript and
23
24 commented on the manuscript. AK supervised the project.
25
26
27
28
29
30
31
32
33
34
35
36
37
38
39
40
41
42
43
44
45
46
47
48
49
50
51
52
53
54
55
56
57
58
59
60
61
62
63
64
65

References

- 1 Best Research-Cell Efficiency Chart, <https://www.nrel.gov/pv/cell-efficiency.html>,
(accessed May 28, 2024).
- 2 W. Nie, H. Tsai, R. Asadpour, J.-C. Blancon, A. J. Neukirch, G. Gupta, J. J. Crochet, M.
Chhowalla, S. Tretiak, M. A. Alam, H.-L. Wang and A. D. Mohite, *Science*, 2015, **347**,
522–525.
- 3 M. Saliba, J.-P. Correa-Baena, C. M. Wolff, M. Stollerfoht, N. Phung, S. Albrecht, D.
Neher and A. Abate, *Chem. Mater.*, 2018, **30**, 4193–4201.
- 4 O. Horváth and I. Mikó, *J. Photochem. Photobiol. Chem.*, 1998, **114**, 95–101.
- 5 K. G. Stamplecoskie, J. S. Manser and P. V. Kamat, *Energy Environ. Sci.*, 2015, **8**, 208–
215.
- 6 E. Radicchi, E. Mosconi, F. Elisei, F. Nunzi and F. De Angelis, *ACS Appl. Energy Mater.*,
2019, **2**, 3400–3409.
- 7 J. C. Jr. Hamill, J. Schwartz and Y.-L. Loo, *ACS Energy Lett.*, 2018, **3**, 92–97.
- 8 K. Yan, M. Long, T. Zhang, Z. Wei, H. Chen, S. Yang and J. Xu, *J. Am. Chem. Soc.*, 2015,
137, 4460–4468.
- 9 J. Kim, B. Park, J. Baek, J. S. Yun, H.-W. Kwon, J. Seidel, H. Min, S. Coelho, S. Lim, S.
Huang, K. Gaus, M. A. Green, T. J. Shin, A. W. Y. Ho-baillie, M. G. Kim and S. I. Seok, *J.*
Am. Chem. Soc., 2020, **142**, 6251–6260.
- 10 M. E. O’Kane, J. A. Smith, R. C. Kilbride, E. L. K. Spooner, C. P. Duif, T. E. Catley, A. L.
Washington, S. M. King, S. R. Parnell and A. J. Parnell, *Chem. Mater.*, 2022, **34**, 7232–
7241.
- 11 N. S. Dutta, N. K. Noel and C. B. Arnold, *J. Phys. Chem. Lett.*, 2020, **11**, 5980–5986.
- 12 F. Eller and E. M. Herzig, *J. Phys. Chem. A*, 2024, **128**, 9682–9687.
- 13 M. Buchhorn, S. Wedler and F. Panzer, *J. Phys. Chem. A*, 2018, **122**, 9115–9122.
- 14 A. M. Valencia, O. Shargaieva, R. Schier, E. Unger and C. Cocchi, *J. Phys. Chem. Lett.*,
2021, **12**, 2299–2305.

- 1
2
3
4
5
6
7
8
9
10
11
12
13
14
15
16
17
18
19
20
21
22
23
24
25
26
27
28
29
30
31
32
33
34
35
36
37
38
39
40
41
42
43
44
45
46
47
48
49
50
51
52
53
54
55
56
57
58
59
60
61
62
63
64
65
- 15R. Munir, A. D. Sheikh, M. Abdelsamie, H. Hu, L. Yu, K. Zhao, T. Kim, O. E. Tall, R. Li, D.-M. Smilgies and A. Amassian, *Adv. Mater.*, 2017, **29**, 1604113.
- 16L. Ke, S. Luo, X. Ren and Y. Yuan, *J. Phys. Appl. Phys.*, 2021, **54**, 163001.
- 17J. Jiang, J. M. Vicent-Luna and S. Tao, *J. Energy Chem.*, 2022, **68**, 393–400.
- 18H. Zheng, W. Wang, S. Yang, Y. Liu and J. Sun, *RSC Adv.*, 2016, **6**, 1611–1617.
- 19X. B. Cao, Y. H. Li, F. Fang, X. Cui, Y. W. Yao and J. Q. Wei, *RSC Adv.*, 2016, **6**, 70925–70931.
- 20D. Barrit, P. Cheng, M.-C. Tang, K. Wang, H. Dang, D.-M. Smilgies, S. (Frank) Liu, T. D. Anthopoulos, K. Zhao and A. Amassian, *Adv. Funct. Mater.*, 2019, **29**, 1807544.
- 21D.-Y. Lin, B.-C. Guo, Z.-Y. Dai, C.-F. Lin and H.-P. Hsu, *Crystals*, 2019, **9**, 589.
- 22S. Biberger, M. Spies, K. Schötz, F.-J. Kahle, N. Leupold, R. Moos, H. Grüninger, A. Köhler and F. Panzer, *J. Mater. Chem. C*, DOI:10.1039/D3TC04361D.
- 23J. Danglad-Flores, S. Eickelmann and H. Riegler, *Eng. Rep.*, 2021, **3**, e12390.
- 24S. Karpitschka, C. M. Weber and H. Riegler, *Chem. Eng. Sci.*, 2015, **129**, 243–248.
- 25N. Sahu, B. Parija and S. Panigrahi, *Indian J. Phys.*, 2009, **83**, 493–502.
- 26P. S. Nikam and S. J. Kharat, *J. Chem. Eng. Data*, 2005, **50**, 455–459.
- 27Y. Zhong, R. Munir, J. Li, M.-C. Tang, M. R. Niazi, D.-M. Smilgies, K. Zhao and A. Amassian, *ACS Energy Lett.*, 2018, **3**, 1078–1085.
- 28J. Li, R. Munir, Y. Fan, T. Niu, Y. Liu, Y. Zhong, Z. Yang, Y. Tian, B. Liu, J. Sun, D.-M. Smilgies, S. Thoroddsen, A. Amassian, K. Zhao and S. (Frank) Liu, *Joule*, 2018, **2**, 1313–1330.
- 29Q. Hu, L. Zhao, J. Wu, K. Gao, D. Luo, Y. Jiang, Z. Zhang, C. Zhu, E. Schaible, A. Hexemer, C. Wang, Y. Liu, W. Zhang, M. Grätzel, F. Liu, T. P. Russell, R. Zhu and Q. Gong, *Nat. Commun.*, 2017, **8**, 15688.
- 30B. Li, Q. Dai, S. Yun and J. Tian, *J. Mater. Chem. A*, 2021, **9**, 6732–6748.
- 31P. Ahlawat, A. Hinderhofer, E. A. Alharbi, H. Lu, A. Ummadisingu, H. Niu, M. Invernizzi, S. M. Zakeeruddin, M. I. Dar, F. Schreiber, A. Hagfeldt, M. Grätzel, U. Rothlisberger and M. Parrinello, *Sci. Adv.*, 2021, **7**, eabe3326.

- 1
2
3
4
5
6
7
8
9
10
11
12
13
14
15
16
17
18
19
20
21
22
23
24
25
26
27
28
29
30
31
32
33
34
35
36
37
38
39
40
41
42
43
44
45
46
47
48
49
50
51
52
53
54
55
56
57
58
59
60
61
62
63
64
65
- 32C. Rehermann, V. Schröder, M. Flatken, F. Ünlü, O. Shargaieva, A. Hoell, A. Merdasa, F. Mathies, S. Mathur and E. L. Unger, *RSC Adv.*, 2022, **12**, 32765–32774.
- 33W. Xiang, J. Zhang, S. (Frank) Liu, S. Albrecht, A. Hagfeldt and Z. Wang, *Joule*, 2022, **6**, 315–339.
- 34K. Schötz, C. Greve, A. Langen, H. Gorter, I. Dogan, Y. Galagan, A. J. J. M. van Breemen, G. H. Gelinck, E. M. Herzig and F. Panzer, *Adv. Opt. Mater.*, 2021, **9**, 2101161.
- 35M. A. Reus, L. K. Reb, A. F. Weinzierl, C. L. Weindl, R. Guo, T. Xiao, M. Schwartzkopf, A. Chumakov, S. V. Roth and P. Müller-Buschbaum, *Adv. Opt. Mater.*, 2022, **10**, 2102722.
- 36A. A. Petrov, I. P. Sokolova, N. A. Belich, G. S. Peters, P. V. Dorovatovskii, Y. V. Zubavichus, V. N. Khrustalev, A. V. Petrov, M. Grätzel, E. A. Goodilin and A. B. Tarasov, *J. Phys. Chem. C*, 2017, **121**, 20739–20743.

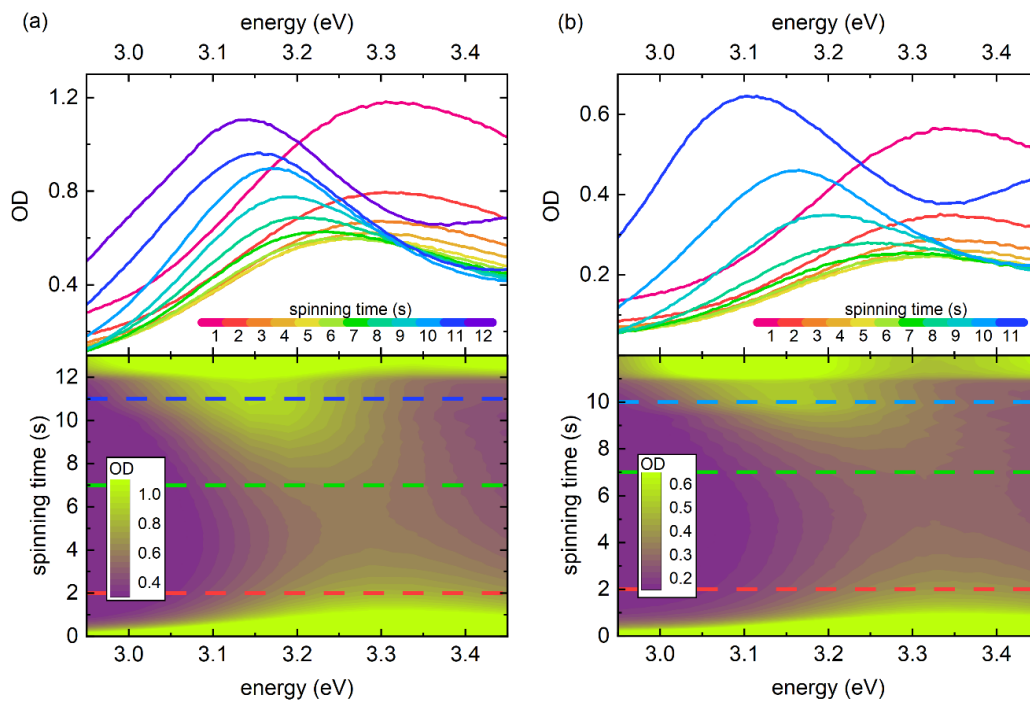


Fig. S1: *In-situ* absorption measurements of the precursor solution in DMF at (a) 0.4 mol/L and (b) 0.2 mol/L during spin coating, highlighting the PbI_3^- evolution. Bottom: 2D map of the OD with respect to energy and spinning time. Top: Temporal cuts through the OD map with three cuts also depicted as dashed lines with their respective colour in the OD map below.

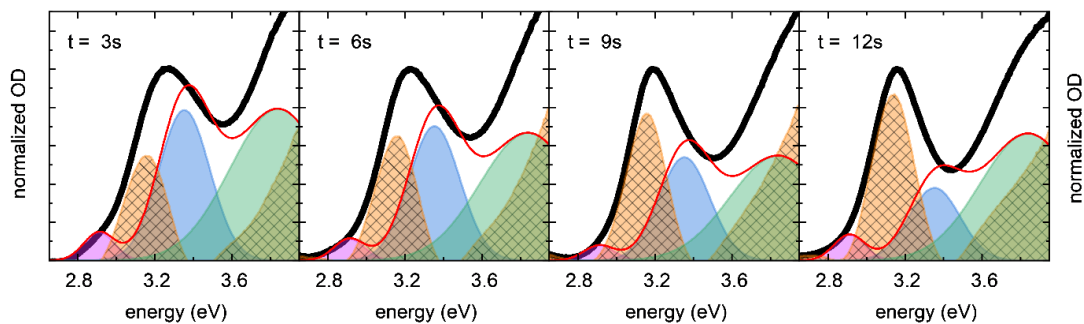


Fig. S2: Fits to *in-situ* absorption measurements of 0.6 mol/L MAPbI_3 precursor similar to Fig. 2b but without a fixed iodoplumbate peak ratio. Peak heights are allowed to vary independently from each other, resulting in an increased number of fitting parameters. The results are essentially the same as with the fitting method used throughout the main text.

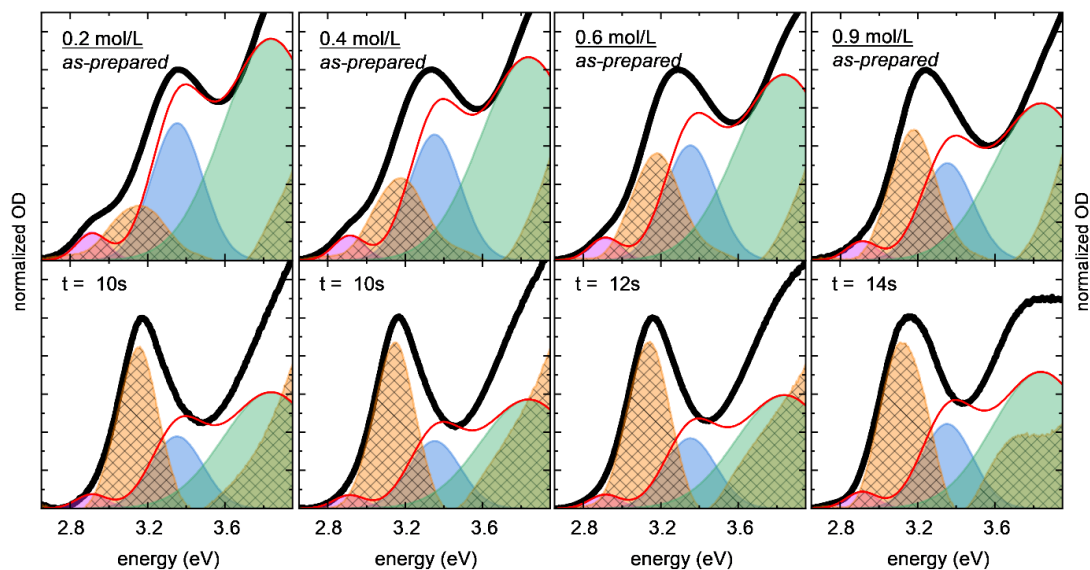


Fig. S3: Fits (red) to the absorption spectra (black) of MAPbI₃ precursor in DMF at different initial concentrations c_0 . Upper row: spectra of *as-prepared* precursor solutions. Lower row: spectra of precursor solutions obtained by *in-situ* measurements just before crystallization occurs. Spectra are normalized to the central peak maximum. The fit is composed of a sum of gaussians, indicated by the shaded areas. The novel optical signature at 3.15 eV emerges as the residual of the fit. See video files for times in between *as-prepared* and *just before crystallization*.

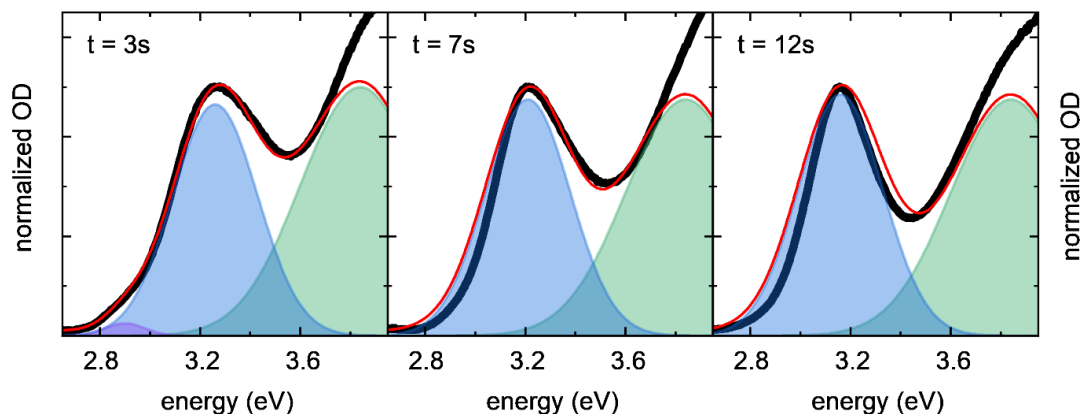


Fig. S4: Fits (red) to the absorption spectra (black) of MAPbI_3 precursor in DMF at 0.6 mol/L obtained from *in-situ* measurements during spin coating. The fits consist of three gaussian line shapes, fixed in width and variable in height. Additionally, the blue gaussian is not fixed to a reported iodoplumbate energy, but is able to shift. While the fit deviates only slightly for $t = 3$ s, for later times, the discrepancies of this model become obvious, especially when considering the width of the Gaussian line shape of PbI_3^- . Therefore, a model without an additional signature at 3.15 eV (PDS phase signature) is insufficient to reproduce the data.

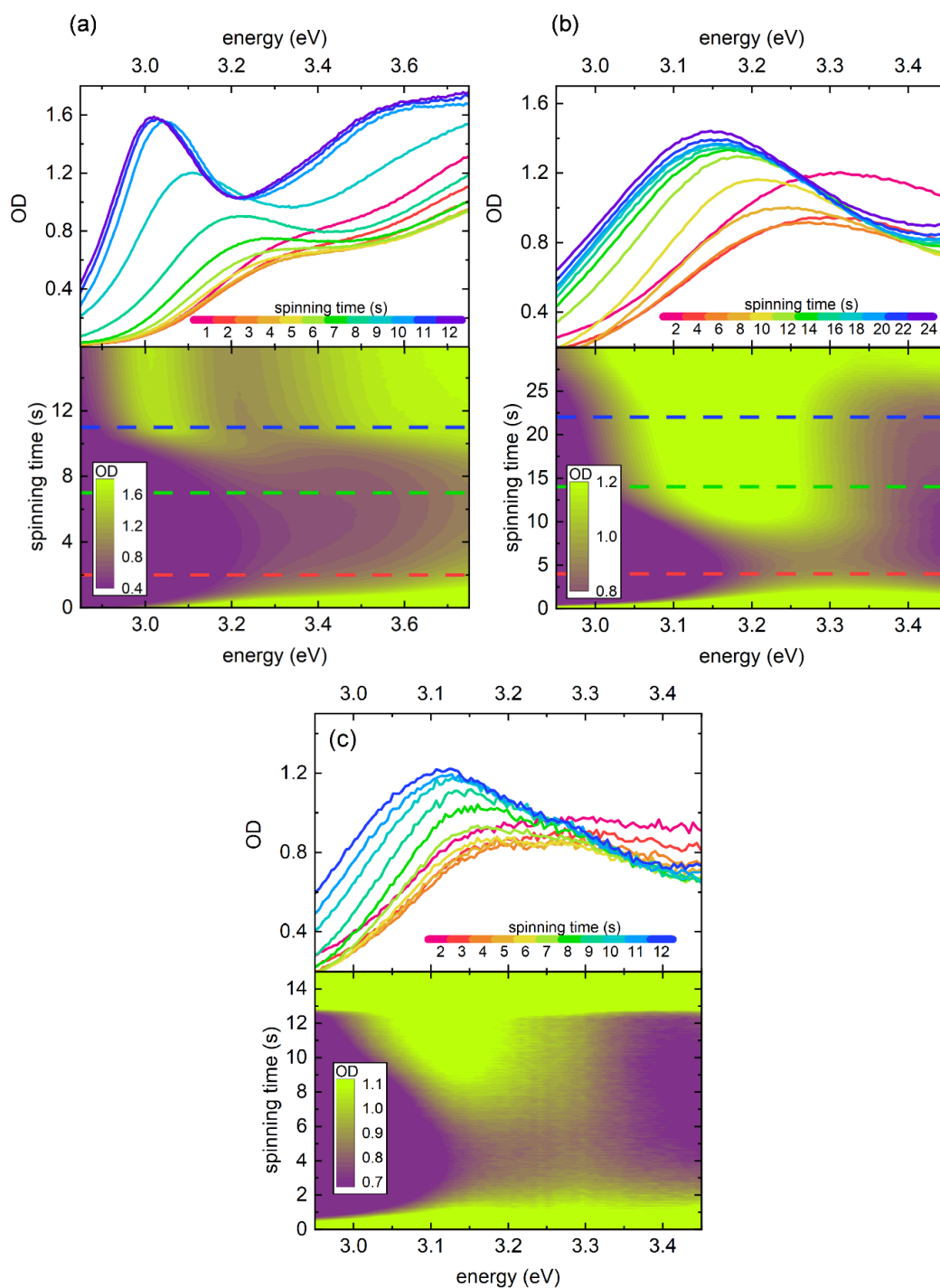


Fig. S5: *In-situ* absorption measurements of PbI_2 in DMF at 0.3 mol/L (a) and MAPbI_3 in DMF:DMSO = 12:1 (b) and FAPbI_3 in DMF at 0.6 mol/L (c). Bottom panels: 2D map of the OD with respect to energy and spinning time. Top panels: Temporal cuts through the OD map with three cuts also depicted as dashed lines with their respective colour in the OD map below. A concentration of 0.3 mol/L PbI_2 in DMF corresponds to the same amount as in the MAPbI_3 precursors at 0.6 mol/L. In (a), from 7 – 11 s the novel optical signature red shifts, indicating crystallite growth. In (b), the dynamic is decelerated by a factor of 2 compared to the samples with pure DMF as solvent.

5

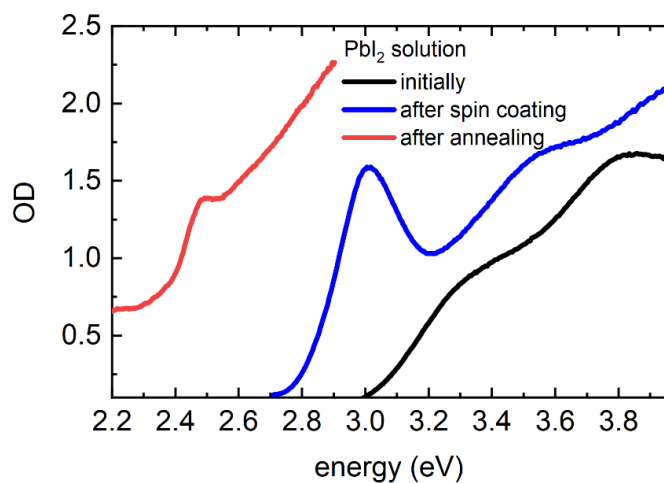


Fig. S6: Absorption measurements of PbI_2 solution (in DMF, 0.3 mol/L) during spin coating (black), of the spin coated film (i.e. PbI_2 -DMF solvated phase, blue) and of the annealed film (i.e. crystalline PbI_2 , red).

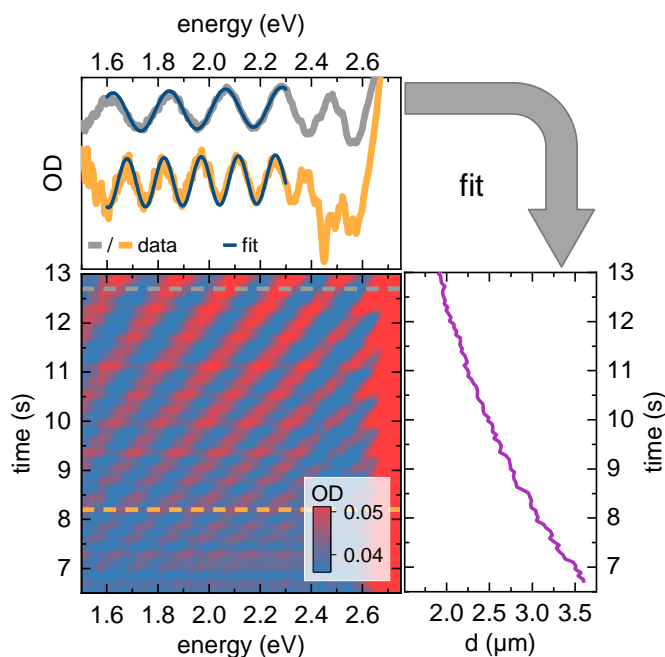


Fig. S7: Illustration of the extraction of solvent layer thickness using in-situ absorption spectroscopy (lower left panel).¹ For every time frame (e.g., at the grey/orange dashed lines) a sine-like function is fitted to the absorption data (upper panel) to calculate the solvent layer thickness d from the frequency ω of the sine wave using [eq. S2](#).

The pattern in the heat map in fig. S9 is caused by a white-light thin film interference effect. This pattern can be used to extract the solvent layer thickness d using the equation

$$d = \frac{\lambda_1 \lambda_2}{2(\lambda_1 n_2 - \lambda_2 n_1)} \quad \text{eq. S1}$$

where λ_1 and λ_2 are the wavelengths of two consecutive extrema in the OD. n_1 and n_2 are the refractive indices of the sample at the respective wavelengths. We can assume n to be constant in the spectral range and given by the refractive index of the solvent DMF ($n_{DMF} = 1.43$). Therefore, the equation for d can be expressed in terms of the frequency of the observed sine wave (ω) since the extrema are uniformly spaced in units of energy:

$$d = \frac{h c \omega}{4 \pi n_{DMF}} \quad \text{eq. S2}$$

where h is the Planck constant and c is the speed of light in vacuum.

¹ S. Biberger, M. Spies, K. Schötz, F.-J. Kahle, N. Leupold, R. Moos, H. Grüninger, A. Köhler and F. Panzer, *J. Mater. Chem. C*, DOI:10.1039/D3TC04361D.

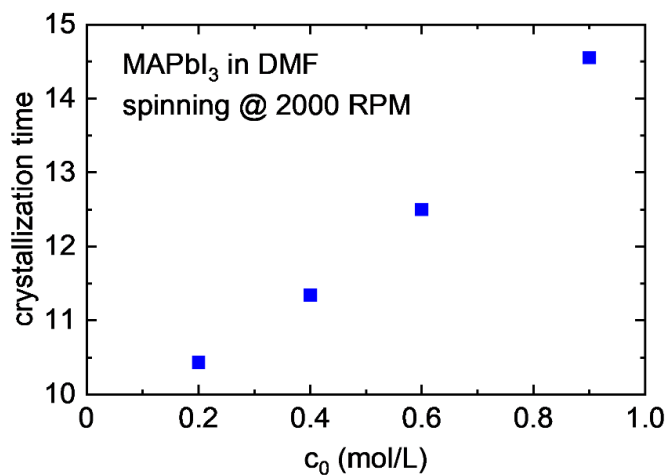


Fig. S8: Timings of crystallization of MAPbI_3 precursor, dissolved in DMF at different initial concentrations c_0 , when spin coating at 2000 RPM.

S9: Critical discussion of the film thickness model

When reflecting film thickness model critically, the question might arise if it is justified to assume the kinematic viscosity to be constant during spin coating. After all, during spin coating one would expect an increase in concentration due to evaporation of the solvent. In fact, the inset in Fig. 4a suggests that the viscosity is concentration dependent. However, the model still holds for a qualitative analysis since the parameters ν_{kin} and E affect the solution layer thickness evolution in different regimes. Danglad-Flores et al.² show that during spin coating the solution dynamic transitions from the hydrodynamic into the evaporative regime. Within the first few seconds of spin coating, when the solution layer is still fairly thick, the hydrodynamic thinning dominates the thinning process. Here, only the viscosity of the solution affects the thickness evolution, while the effect of solvent evaporation is negligible within this time range. Consequently, the viscosity values obtained from fitting should be only assigned to the concentration in the hydrodynamic regime, i.e. c_0 . On the other hand, only in the evaporative regime at later times, the evaporation of the solvent dictates the concentration evolution. Thus, changes in viscosity during hydrodynamic thinning (due to an increase in concentration) are negligible and do not significantly affect the thickness evolution. Since the fitting parameters suggest a concentration dependent evaporation rate (see inset in Fig. 4a), the parameter E should be considered as an average evaporation rate.

Karpitschka et al.³ show that the regimes transitions from the hydrodynamic to the evaporative regime at the transition film thickness h_{tr} :

$$h_{tr} = \left(\frac{3 E \nu_{kin}}{2 \omega^2} \right)^{1/3}$$

eq. S3

E is the rate of evaporation, ν_{kin} is the kinematic viscosity and ω is the rotational speed of the spin coater. For all investigated samples, the transition height is similar, ranging from 1.29 – 1.44 μm . Likewise, a transition time can be obtained by determining the time when the film thickness reaches the transition height:

initial concentration c_0 in mol/L	transition height h_{tr} in μm	transition time in s
0.2	1.33	5.0
0.4	1.44	5.8
0.6	1.30	7.2
0.9	1.29	10.2

² J. Danglad-Flores, S. Eickelmann and H. Riegler, *Eng. Rep.*, 2021, **3**, e12390.

³ S. Karpitschka, C. M. Weber and H. Riegler, *Chem. Eng. Sci.*, 2015, **129**, 243–248.

S10: Derivation of eq. 5

The concentration $c(t)$ of the solution is given by the ratio of solvated material $M(t)$ and the volume of the solution $V(t)$.

$$c(t) = \frac{M(t)}{V(t)} = c(0) \frac{\frac{M(t)}{M(0)}}{\frac{V(t)}{V(0)}} \quad \text{eq. S4}$$

Since h_{hydro} affects the solvent as well as the solvated material, the amount of solvated material is directly proportional to h_{hydro} . The volume of the solution is proportional to the film thickness h . (These assumptions only hold if the area of the film does not change during spin coating.)

$$c(t) = \frac{M(t)}{V(t)} = c(0) \frac{\frac{M(t)}{M(0)}}{\frac{V(t)}{V(0)}} = c(0) \frac{\frac{h_{hydro}(t)}{h_{hydro}(0)}}{\frac{h(t)}{h(0)}} \quad \text{eq. S5}$$

$h(t)$ is composed of $h_{hydro}(t)$ and $h_{evap}(t)$. Since $h_{evap}(0) = 0$ the following holds:

$$h(0) = h_{hydro}(0) \quad \text{eq. S6}$$

Therefore, the concentration can be written as

$$c(t) = c(0) \frac{h_{hydro}(t)}{h(t)} \quad \text{eq. S7}$$

Expanding $h(t)$ yields:

$$c(t) = c(0) \frac{h_{hydro}(t)}{h_{hydro}(t) + h_{evap}(t)} = \frac{c(0)}{1 + \frac{h_{evap}(t)}{h_{hydro}(t)}} \quad \text{eq. S8}$$

A. List of Abbreviations

AgBeh	Silver Behenate
AI	Artificial Intelligence
BACE	Bias Assisted Charge Extraction
CCD	Charge-Coupled Device
CID	Current-Induced Doping
CMOS	Complementary Metal–Oxide–Semiconductor
CN	1-Chloronaphthalene
Cu	Copper
DFT	Density Functional Theory
DFTB3	An Extension of the Self-Consistent-Charge Density-Functional Tight-Binding Method
DIO	1,8-Diiodooctane
DOS	Density Of States
DPE	Diphenyl ether
DSC	Differential Scanning Calorimetry
EQE	External Quantum Efficiency
FWHM	Full Width at Half Maximum
GISAXS	Grazing Incidence Small-Angle X-ray Scattering
GIWAXS	Grazing Incidence Wide-Angle X-ray Scattering
MeTHF	2-Methyltetrahydrofuran
NFA	Non-Fullerene Acceptor
OD	Optical Density
OEET	Organic Electrochemical Transistor
OFET	Organic Field-Effect Transistor
OLED	Organic Light-Emitting Diode
OPV	Organic Photovoltaics
PbI ₂	Lead(II) iodide
PCE	Power Conversion Efficiency
PIA	Photo-Induced Absorption Spectroscopy
ROI	Region Of Interest

RSoXS	Resonant Soft X-ray Scattering
SCLC	Space Charge Limited Current
SCM	Spectral Change Metric
SDD	Sample-to-Detector Distance
SNR	Signal-to-Noise Ratio
SVA	Solvent Vapor Annealing
TDCF	Time-Delayed Collection Field
TFFS	Thinning Fluid Film Spectroscopy
TMB	3, 3', 5, 5'-Tetramethylbenzidine
TRPL	Time Resolved Photoluminescence Spectroscopy
UV	Ultraviolet
UV-Vis	Ultraviolet-Visible
V_{OC}	Open-Circuit Voltage
WA	Warren-Averbach

The trivial names of organic semiconductor molecules are not defined in the list of abbreviations, as the full IUPAC names are hardly used. In contrast, almost exclusively trivial names are used in literature and do not require a definition. However, sometimes, several trivial names are used for the same molecule. Hence, the following list summarizes some commonly used synonyms for trivial names utilized in this thesis:

DTY6	BTP-4F-24, Y6-DT
IT-4F (IT4F)	ITIC-4F, ITIC-2F
N2200	P(NDI2OD-T2), PNDI-2T, Polynaphthalene-bithiophene
PM6	PBDB-T-2F, PBDB-T-F, PBDB-TF
Y6	BTP-4F
Y7	BTP-4Cl
Y12	BTP-4F-12, Y6-BO, BO-4F

B. Danksagung

Am Ende möchte ich mich noch herzlich bei allen bedanken, die mich bei der Entstehung dieser Arbeit unterstützt haben und ohne die diese Arbeit nie möglich gewesen wäre. Zuerst möchte ich Prof. Eva M. Herzig danken, die mir die Promotion in ihrer Arbeitsgruppe ermöglicht hat und mich all die Jahre von meiner Bachelor-Arbeit, über die Master-Arbeit bis hin zur Promotion betreut hat. Du hast mir immer dein volles Vertrauen geschenkt und mich stets dabei unterstützt, meine vielen Ideen umzusetzen. Ich habe mir nicht den einfachsten Weg herausgesucht als ich eine unerwartet explodierende Lösung genauer untersuchen wollte. Du warst davon und von diversen kreativen Automatisierungsideen aber stets begeistert, hast mich motiviert und mir jegliches benötigte Material unverzüglich bereitgestellt. Nur durch den Glauben an diese außergewöhnlichen Konzepte konnten wir die ausgesprochen starke Nanostrukturkontrolle und die viele Automatisierung in dieser Doktorarbeit erreichen und haben auch noch einiges mehr in der Pipeline. Vielen Dank auch dafür, dass du mir die Teilnahme an verschiedensten Konferenzen, Workshops, Auslandsaufenthalten und sogar einem eingeladenen Vortrag ermöglicht hast, wodurch ich über die ganze Welt unterwegs sein konnte – von China bis nach Hawaii und bald auch Australien.

Ein besonderer Dank geht auch an Irene Bauer, Christina Gräbner und Frank Schirmer. Ihr habt mich stets bei diversen (teils auch abenteuerlichen) Fragen, Problemen und Anliegen im Labor und technischer Natur unterstützt und den ganzen Laborbetrieb im Hintergrund am Laufen gehalten. Christina, ich weiß gar nicht, wie viele Substrate du für mich geschnitten und gereinigt hast und wie unglaublich viel Arbeit du mir dadurch in stressigen Zeiten abgenommen hast.

Vielen Dank auch an unsere Sekretärinnen Michaela Fischer, Laura Schwarze, Diana Margerie und Andrea Ludwig. Wie viel Papierkram und organisatorische Arbeit ihr uns immer abnehmt hat man gemerkt und dadurch erst so richtig schätzen gelernt als das Sekretariat zwischenzeitlich nicht besetzt war.

Nicht genug danken kann ich auch Thomas Dabisch. Du hast in deiner Werkstatt mit großem Einsatz spontan jeden Aufbau möglich gemacht, dein Netzgerät wurde schon so ein bisschen zur Dauerleihgabe in meinem Versuchsaufbau und deine ansteckende Fröhlichkeit und Hilfsbereitschaft sind unübertroffen.

Ich möchte mich auch ganz herzlich bei allen Kollaborationspartnern für die vielen spannenden Kollaborationen bedanken. Die Vielzahl verschiedener Methoden und Konzepte und der wertvolle Austausch haben meinen Horizont stets erweitert. Nicht zu vergessen sind auch die vielen lieben persönlichen Kontakte. Es war mir hierbei auch eine große Ehre, Teil vom SOLAR-ERA.NET Projekt NFA4R2ROPV zu sein und nach wie vor von der DFG Forschergruppe POPULAR.

Ein besonderer Dank geht auch an Prof. Remco Havenith und seine ganze Arbeitsgruppe, die mich so herzlich für einen Auslandsaufenthalt in Groningen aufgenommen haben und mich so stark im für mich neuen Feld von quantenchemischen Simulationen

und High-Performance-Computing unterstützt haben.

Ganz besonders bedanken möchte ich mich auch bei all meinen ehemaligen und aktuellen Kollegen aus der Herzig- und auch Köhler-Gruppe. Es ist mehr als nur der viele wertvolle wissenschaftliche Austausch und die gute Zusammenarbeit und ihr seid mehr als nur Kollegen. Vor allem die unübertroffene Gemeinschaft und Arbeitsatmosphäre hat dafür gesorgt, dass man jeden Tag gerne in die Uni geht und wenn auch mal alles schief gegangen ist, man von Leidensgenossen wieder aufgebaut wird. Besonderer Dank geht hier an Christopher Greve und Meike Kuhn. Ihr seid schon die ganze Zeit treue Begleiter auf demselben Weg, mit denen man über alles reden kann und die jegliche auftretenden Probleme nur zu gut kennen und verstehen.

Manuel Lippert und Paul Schwanitz, ihr seid zwar noch recht neu dabei, aber habt unser Büro im Sturm erobert. Mit euch im Büro ist stets ein riesiger Spaß garantiert und ihr seid auch genauso begeistert von jeglicher Automatisierungs- und 3D-Druck-Eskalation. Ich bin so froh, dass ich euch im Praktikum für meine Automatisierungspläne gewinnen konnte und euch jetzt auch in kürzester Zeit von einer Promotion bei uns überzeugen konnte.

Zu guter Letzt gilt mein größter Dank meiner wundervollen Frau Elena. Du hast mich immer bedingungslos unterstützt und hattest stets Verständnis, wenn Experimente mal wieder länger gedauert haben als gedacht, etwas unbedingt noch fertig werden musste, internationale Meetings zu seltsamen Zeiten stattfinden, ich noch ganz akut ein Visum gebraucht habe oder was sonst auch immer angefallen ist. Es ist auch stets sehr motivierend, abends und am Wochenende nicht alleine am Schreibtisch zu sitzen, sondern dich neben mir sitzen zu haben, wie du auch produktiv arbeitest. Vielen Dank auch für die viele schöne Zeit, in der du es mir ermöglichst, entspannt abzuschalten und an etwas anderes als nur Experimente und Daten zu denken. Ich freu mich schon so auf die nächsten Jahrzehnte mit dir!

C. Eidesstattliche Versicherung

Hiermit versichere ich an Eides statt, dass ich die vorliegende Arbeit selbstständig verfasst und keine anderen als die von mir angegebenen Quellen und Hilfsmittel verwendet habe.

Weiterhin erkläre ich, dass ich die Hilfe von gewerblichen Promotionsberatern bzw. –vermittlern oder ähnlichen Dienstleistern weder bisher in Anspruch genommen habe, noch künftig in Anspruch nehmen werde.

Zusätzlich erkläre ich hiermit, dass ich keinerlei frühere Promotionsversuche unternommen habe.

Bayreuth, den

Fabian Eller